First-principles investigation of magnetic and electronic transport properties of transition metal alloys

Dissertation

zur Erlangung des Grades
Doktor der Naturwissenschaften

genehmigt von der Fakultät für Physik
der Universität Duisburg-Essen

vorgelegt von
Denis Comtesse

Erstgutachter: Prof. Dr. P. Entel
Zweitgutachter: Prof. Dr. P. H. Dederichs

Tag der mündlichen Prüfung:
04. September 2014

meinen lieben Eltern

Ingrid und Klaus Comtesse

Abstract

In this work the electronic structure as well as magnetic and thermoelectric properties of alloy systems containing the $3d$-transition metals manganese, iron and cobalt have been investigated by means of first-principles methods and Monte Carlo simulations. In addition, a new analysis of magnetic exchange interaction in nickel-manganese based alloys is carried out by decomposing the magnetic coupling constants into contributions associated with orbital symmetries.

The survey starts with the investigation of the binary alloys $Fe_{1-x}Mn_x$, $Fe_{1-x}Co_x$ and $Co_{1-x}Mn_x$. Interesting new insight into ground state properties and finite temperature magnetism of $Fe_{1-x}Mn_x$ is obtained from the combination of *ab initio* methods and Monte Carlo simulations. The evaluated Curie temperatures are in good agreement with experiment and predicted ground state configurations of magnetic moments match the state-of-the-art theory of these alloys. Results of the investigation of $Fe_{1-x}Co_x$ allow an excellent mapping onto the experimental phase diagram and contribute to the current discussion on the occurrence of superstructures in these systems. As there is only few theoretical work concerning $Co_{1-x}Mn_x$ up to now, the investigation of these alloys delivers valuable new information. The first modeling of the complex magnetic properties of $Co_{1-x}Mn_x$ on a first-principles basis has been carried out and additionally, the occurrence of an unexpected structural phase is predicted.

In the second step, a series of Heusler alloys based on the three transition metals Mn, Fe, Co and the main group elements Al and Si is carried out. In this part, the focus is on half-metallic ferromagnetism of such systems. Almost all combinations of these elements turn out to be half-metallic and certain compositions are half-metallic antiferromagnets. The influence of disorder on the specific electronic structure and the magnetic properties is analyzed and it turns out that disorder does not necessarily destroy half-metallicity if it is restricted to certain sublattices. On the other hand, magnetism and Curie temperature can be strongly affected. Comparing the results to the investigation of corresponding binary alloys reveals a clear relation but also the outstanding position of Heusler alloys.

During the investigation of magnetic exchange interactions in nickel-manganese based Heusler alloys the decomposition of the interaction into contributions associated with electron states of certain symmetry allows to understand how the strength of the interaction arises from particular contributions. In addition the contribution of magnetism to the driving force of the martensitic transition of such systems is qualitatively understood because the analysis reveals a certain type of magneto-structural instability. This opens an entirely new view on martensitic transitions in magnetic alloys.

The last part of this work concerns the thermoelectric properties of half-metallic Heusler layers in contact with platinum leads. Here, focus is on the spin dependence of the Seebeck coefficient. It turns out that the half-metallic property of the Heusler systems significantly affects the contributions arising from the two spin channels. The results show the possibility to design thermally driven spin generators and contribute to the modern field of spincaloritronics.

Zusammenfassung

In dieser Arbeit werden die elektronische Struktur sowie die magnetischen und thermoelektrischen Eigenschaften von Systemen welche die Übergangsmetalle Mangan, Eisen und Cobalt enthalten mit einer Kombination aus *ab initio* Methoden und Monte Carlo Simulationen untersucht. Darüber hinaus ist ein weiterer Abschnitt der Untersuchung der magnetischen Austauschwechselwirkung in Nickel-Mangan basierten Systemen gewidmet, in dem eine neue Strategie für die Zerlegung dieser Wechselwirkung in Beiträge bestimmter Symmetrie verwendet wird.

Die Studie beginnt mit der Untersuchung der binären Legierungen $Fe_{1-x}Mn_x$, $Fe_{1-x}Co_x$ und $Co_{1-x}Mn_x$. Interessante neue Einsichten in die Grundzustandseigenschaften und den Magnetismus bei endlichen Temperaturen von $Fe_{1-x}Mn_x$ werden durch das Kombinieren von *ab initio* Rechnungen und Monte Carlo Simulationen gewonnen. Die Bestimmung der Curie Temperatur der System ist in guter Übereinstimmung mit dem Experiment und die vorhergesagten Grundzustandskonfigurationen der magnetischen Momente passen zu der modernen Theorie dieser Legierungen. Die Resultate für $Fe_{1-x}Co_x$ könne sehr gut auf das experimentelle Phasendiagramm abgebildet werden und tragen insbesondere zur aktuellen Diskussion über das Auftreten von Superstrukturen in diesen Systemen bei. Da bisher nur wenige theoretische Arbeiten über $Co_{1-x}Mn_x$ existieren ergibt die Analyse dieser Legierungen wertvolle neue Informationen. Diese Arbeit bietet die erste Modellierung der komplexen magnetischen Eigenschaften auf reiner *ab initio* Basis. Darüber hinaus wird das Auftreten einer unerwarteten strukturellen Phase vorhergesagt.

In einem zweiten Schritt wird eine Serie von Heusler Legierungen untersucht die auf Mn, Fe, Co und den Hauptgruppen Elementen Al und Si basieren. Hier liegt besonderes Augenmerk auf dem halb-metallischen Ferromagnetismus dieser Systeme. Fast alle Kombinationen genannten Elements ergeben halb-metallische Legierungen wobei manche halb-metallische Antiferromagneten sind. Es wird untersucht wie Unordnung die speziellen elektronischen und magnetischen Eigenschaften beeinflusst. Dabei stellt sich heraus das Unordnung die Halb-Metallizität nicht zwingen zerstört wenn sie sich auf bestimmte Untergitter beschränkt. Andererseits kann jede Form von Unordnung starken Einfluss auf die magnetischen Eigenschaften und besonders die Curie Temperatur haben.

Bei der Analyse der magnetischen Austauschwechselwirkung in Nickel-Mangan basierten Heusler Legierungen erlaubt die Zerlegung in Beiträge von Elektronenzuständen bestimmter Symmetrie, die Stärke der Wechselwirkungen auf bestimmte Anteile zurückzuführen. Im weiteren stellt sich heraus, dass durch diese Zerlegung der Beitrag des Magnetismus zu der den Martensit Übergang, der in diesen Legierungen auftritt, erzeugenden Kraft qualitativ verstanden werden da die Analyse eine Art magneto-strukturelle Instabilität aufzeigt.

Der letzte Teil dieser Arbeit beschäftigt sich mit den thermoelektrischen Eigenschaften von Heusler Legierungen die mit Platin Elektroden kontaktiert sind. Dabei liegt der Focus auf der Spin-Abhängigkeit des Seebeck Effektes. Es zeigt sich das es möglich ist mit diesen Systemen einen thermisch getriebenen Spin-Generator zu designen und damit zum modernen Feld der Spincaloritronic bezutragen.

Contents

1 Introduction

The objective of this work is threefold. On one hand, groups of materials based on manganese, iron and cobalt are investigated by means of density functional theory methods in combination with Monte Carlo simulations. The focus of this survey is on magnetic properties at absolute zero and finite temperature. Binary alloys such as $Fe_{1-x}Mn_x$, $Fe_{1-x}Co_x$ and $Co_{1-x}Mn_x$ are considered first, followed by an analysis of the Heusler alloys X_2YZ (X,Y = Mn, Fe and Co). Besides the transition metal components, Heusler alloys contain an additional main group element Z. Throughout this first investigation, the main group elements taken into account are Al and Si. Properties of the Heusler and the corresponding binary alloy are compared in order to gain insight into the dependence of electronic and magnetic properties on the composition of the 3*d*-metals and the particular role of the main group element. This improves the understanding of mechanisms which are responsible for the multifunctionallity of Heusler alloys and in particular for the occurrence of half-metallicity.

On the other hand, an additional chapter is devoted to the detailed investigation of magnetic exchange parameters of nickel-manganese based Heusler alloys which can undergo a martensitic phase transition. In particular, a decomposition of the exchange interactions into contributions of different symmetry is presented. It turns out that this decomposition allows valuable insight into the magnetic contribution to the driving force of the martensitic transition which is a topic of great importance and of current interest. In addition, the understanding of the magnetocaloric effect which is also observed in some Ni-Mn based Heusler systems, can be improved. From a more general point of view, this decomposition is interesting because it shows that the long and short range contributions to the total magnetic exchange interaction arise from electron states with different symmetry.

Finally, thermoelectric properties of layered structures containing two platinum leads and a thin film of half-metallic Heusler alloy in between are studied. The focus is on the spin dependence of the thermoelectric properties and possible spin caloritronic applications. As half-metallic alloys are promising candidates in this field but since the generation of highly spin-polarized currents is often hindered by the influence of interfaces, platinum leads are investigated because platinum can be accurately grown onto Heusler alloys including only a small lattice mismatch that introduces almost no relaxations. On the other hand, spin currents can be directly measured in platinum by using the inverse spin Hall effect. In order, to account for the spin-orbit coupling of Pt, the calculations are carried out in the fully relativistic framework and to distinguish between the two spin channels in relativistic theory, a particular projection scheme is employed. The results show that the Pt-Heusler-Pt systems can be used to drive currents with high polarization and are therefore promising for a practical use in spin caloritronic devices.

In the following a more detailed motivation for the investigations carried out in the present treatise is given. Afterwards, theoretical concepts used in this work are outlined, followed by a list of computational details. This guides the way to the central part of this work.

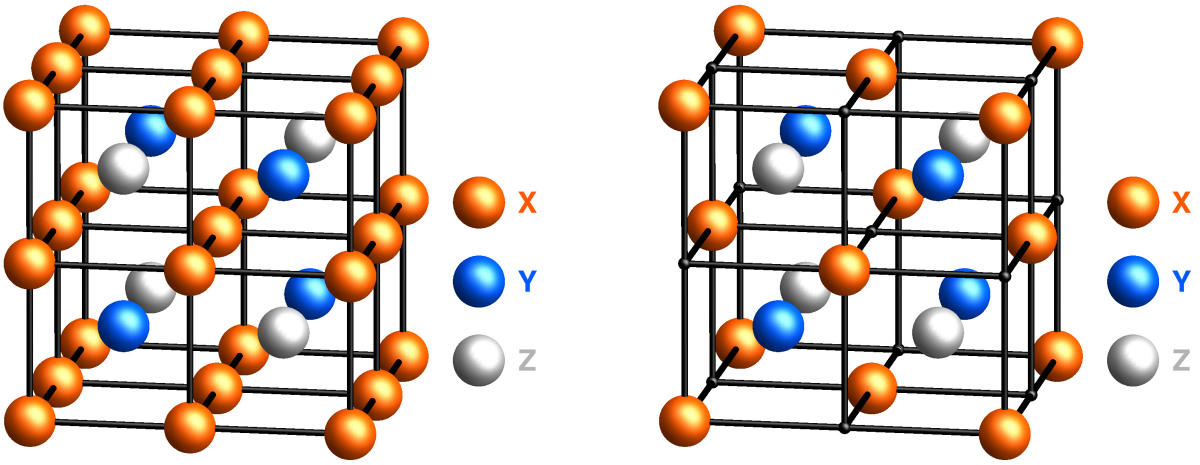

(a) (b)

Figure 1.1: (a) Lattice structure of $L2_1$ ordered full-Heusler alloys. It consists of four interpenetrating fcc lattices where two are occupied by the X species and the other two by Y and Z. (b) Lattice structure of the corresponding $C1_b$ ordered half-Heusler. Here, one of the four fcc lattices is left unoccupied.

1.1 Motivation

The microscopic understanding of basic properties of transition metal alloys which contain Mn, Fe and Co is a matter of ongoing debate as well as of particular interest because these elements are constituents of materials that are present in the every days live and also in modern high-tech compounds. A very popular class of materials in which these three elements play a role, are the so called Heusler alloys. A Heusler alloy contains three types of elements X, Y, Z with composition X_2YZ. Usually, X and Y are transition metals and Z is a main group element. The atoms are arranged in the $L2_1$ structure, which is shown in Fig. 1.1(a). This structure consists of four merged fcc sublattices arranged on the cubic diagonal and shifted by 1/4 and is often called full-Heusler.

Heusler alloys are named after the German mining engineer and chemist Friederich Heusler (1866 - 1947). He synthesized and studied the compound Cu_2MnAl [1]. This first Heusler alloy immediately became famous since it showed extraordinary properties. Although, non of the constituents is ferromagnetic, the Heusler compound Cu_2MnAl is. Especially, the variation of the magnetization with heat treatment and composition caught lots of attention. Careful heat treatment increases the magnetization because it improves the structural order and changes in composition can lead to linear changes of the magnetization which is connected to the concentration of valence electrons.

Nowadays, Heusler alloys are of great interest in many fields of materials physics because of their manifold properties. One of the most interesting properties is the magnetic shape-memory effect. This effect is closely related to the phenomenon of the martensitic phase transition.

The martensitic phase transformation is a diffusionless structural phase transition between a cubic and a tetragonal distorted structure. In other cases martensitic transformations occur between cubic structures and hexagonal closed packed structures. The low temperature phase

which is of lower symmetry is called the martensitic phase and the high temperature phase is the parent austenitic phase. This short description suffices here, but the interested reader finds a detailed introduction of martensitic transformations in the book of Nishiyama [2].

Alloys which exhibit martensitic phase transitions can additionally show the shape-memory effect. This effects describes the following phenomenon: A sample of particular shape is mechanically deformed at low temperatures in its martensitic phase and when it is heated up above the transition temperature to the austenitic phase, it recovers the original shape. This definition is taken from the book of Otsuka and Wayman [3], which contains a comprehensive discussion of the shape-memory effect.

The shape-memory effect can be qualitatively understood in the following sense: During the martensitic transformation the macroscopic shape of the workpiece does not change. Although, the change of the microstructure could have affected the macroscopic shape, it is conserved due to the introduction of complicated multiply twinned microstructures. Otherwise, the involved strain energies would be too high to be overcome by the driving forces of the transition. The high mobility of the twin boundaries in the martensitic phase is responsible for the macroscopically possible shape changes that can be achieved by active deformation. During a subsequent phase transformation back to the austenitic phase the twin boundary motions are reversed and the workpiece recovers its original shape. This implies that the shape-memory is obtained from some sort of twin boundary motion memory. The details of the microscopic mechanisms are mater of ongoing debate.

The magnetic shape-memory effect can occur in materials where the martensitic phase transition temperature is below the Curie temperature. One idea is to manipulate the shape of the magnetic alloy by a field driven structural transformation instead of a temperature driven transformation. The other idea is to move the twin boundaries in the martensitic phase by applying an external field. This field is the magnetic field. It couples to the magnetic moments, which are coupled to the lattice and therefore to the structure of the alloy. The most prominent Heusler compound which shows the magnetic shape-memory effect is Ni_2MnGa. For a more detailed discussion the reader is referred to Ref. [4] and references therein.

The investigation of the magnetic exchange interactions of Ni based Heusler alloys carried out in the present work (see Section 7.10) opens an interesting new perspective concerning the connection between magnetism and structure responsible for the shape-memory effect and related mechanisms.

A different but also very prominent property that occurs in some Heusler alloys is half-metallic ferromagnetism. In a half-metallic ferromagnet the electronic density of states (DOS) of one spin channel shows a gap at the Fermi energy whereas the density of states of the other channel is that of a metal. In other words, one spin channel is metallic and the other is insulating or semi-conducting. This implies that two distinct electronic properties are found within one and the same material.

Half-metallicity was first predicted by de Groot et. al. [6] in 1983. The authors proposed that this property occurs in some half-Heusler alloys because unusual magneto-optical properties of these alloys motivated the theoretical study of their electronic structure (see references in Ref. [6]). The quantitative composition of half-Heusler alloys is given by XYZ. This means that, compared to the full-Heusler, one of the X sublattices is unoccupied. The lattice structure is called $C1_b$ and is shown in Fig. 1.1(b).

As half-metallicity implies a 100% spin polarization of the DOS at the Fermi level, half-metallic compounds are of great interest in the field of spintronics because it should in principle be possible to extract highly spin-polarized currents from such materials. Within

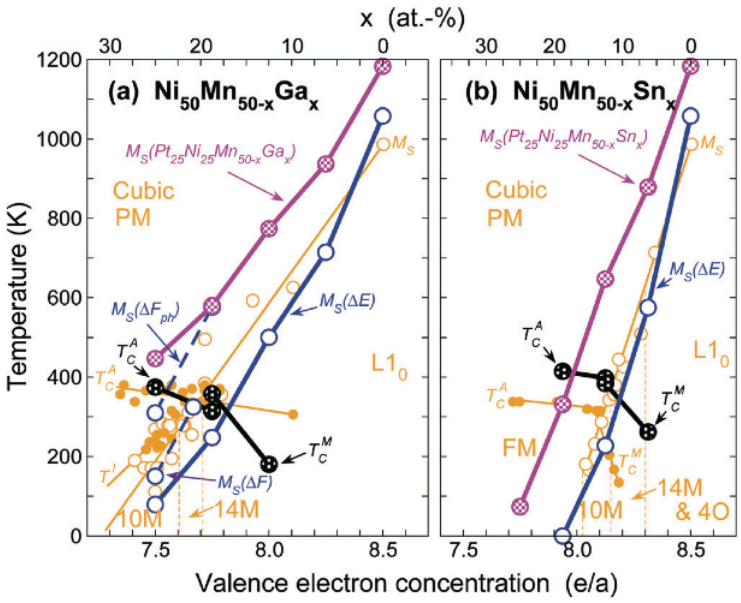

Figure 1.2: Phase diagrams of two Heusler alloys which are promising candidates for magnetic shape-memory applications. Experimental data is shown in orange (Picture is taken from Ref. [5]).

the different classes of materials which show half-metallic ferromagnetism, the Heusler alloys attracted much interest and therefore half- and full-Heuslers have been extensively studied experimentally and theoretically [7].

The investigations are motivated by the fact that many properties of Heusler alloys can be tuned by adjusting the composition. This is easily done because many intermetallic compounds can nucleate in the Heusler structure providing a variety of possibilities to combine elements. This allows in particular a good control of the valence electron concentration and many properties of Heusler alloys often show a linear dependence on the valence electron concentration. An example of this linear dependence is shown in Fig. 1.2 where experimental and theoretical data for the dependence of the transition temperatures of magnetic and martensitic phase transformations on the electron concentration is shown for two nickel-manganese based Heusler alloys.

Theoretical investigations of promising candidates for half-metallic ferromagnetism are of special interest because there is no unique feature that can be measured in experiments which explicitly determines a half-metallic ferromagnet [8]. This is associated with the problem of measuring the spin polarization of the DOS exactly. Therefore, theoretical results are essential for the interpretation of experimental results that give indirect evidence of half-metallicity.

A different but very recent topic is initiated by the discovery that some Heusler system show a spin-glass type of behavior [9]. Although, spin-glasses are not of obvious practical use for applications, their non-ergodic magnetic behavior is of great interest for general theoretical considerations and a matter of ongoing discussion (for a comprehensive introduction see Ref. [10]). As some Fe, Mn and Co based binary and Heuslers alloys exhibit long-range as well as competing ferro- and antiferromagnetic interactions and chemical disorder as well as dilution by main group elements can be introduced, the necessary ingredients for the

occurrence of spin-glasses are present in such systems.

The main aim of this work is to gain understanding of magnetism of binary alloys of Mn, Fe and Co as well as the corresponding ternary full-Heusler alloys at absolute zero and finite temperature. In addition, it is discussed in how far Heusler alloys might be interesting for spintronic and thermoelectric applications. It is discussed how properties of binary alloys change when a third element is added. The focus is on Mn, Fe and Co based alloys because the Co based Heuslers are already known to exhibit half-metallic behavior (see e.g. Ref [11]).

The binary alloys $Fe_{1-x}Mn_x$, $Fe_{1-x}Co_x$ and $Co_{1-x}Mn_x$ are of particular interest because they exhibit various properties that are often strongly connected to magnetism in these materials and in many cases subject of ongoing discussion. Iron and manganese are fundamental constituents of many modern steels for example the TRIP (Transformation Induced Plasticity) and TWIP (Twinning Induced Plasticity) steels (see Ref. [12] and references therein). Therefore, the connection between mechanical and magnetic properties of these alloys is of technological interest. Iron-cobalt alloys show very high saturation magnetizations combined with very high Curie temperatures and are known to show Invar as well as anti-Invar behavior (see e.g. Ref. [13] and [14]). The Invar and anti-Invar behavior is also found in cobalt-manganese alloys which are additionally interesting because of their complex magnetic properties like super-paramagnetic and spin-glass behavior (see Ref. [15] and references therein).

Almost all Heusler alloys based on the three elements Mn, Fe and Co together with the main group element, e.g Al, Si, Ga, Ge, exhibit trends of half-metallic behavior. Those based on Co can be ferromagnetic half-metals and some based on Fe or Mn are considered to show a different type of half-metallic magnetism namely the half-metallic antiferromagnetism. This type of material was also first proposed by de Groot in 1995 [16].

The remainder of this work is organized as follows: First, the general theoretical background of density functional theory is outlined. Afterwards, the two schemes which are used to carry out practical calculations are described. The first is based on an expansion of the many-body wave function in terms of plane waves and the second is an application of multiple scattering theory (MST) which is called Korringa-Kohn-Rostocker (KKR) formalism. In addition, the methods to derive magnetic exchange parameters and transport properties from the calculated electronic structure are presented. The following part addresses binary alloys. At first $Fe_{1-x}Mn_x$ systems are considered. As they are interesting for steel applications, the influence of carbon, which is also an important constituent of steel, on the magnetic properties is investigated in detail. Subsequently, $Fe_{1-x}Co_x$ alloys are discussed. Here, the focus is on their Invar properties. Afterwards, $Co_{1-x}Mn_x$ is taken into account. Only very few work exists which is addressed to $Co_{1-x}Mn_x$ and therefore interesting new results are presented. Afterwards, an extensive discussion of Mn, Fe and Co based Heusler alloys is presented. Special attention is paid to the possible occurrence of half-metallicity. This discussion is followed by the presentation of results obtained from the decomposition of magnetic exchange interactions into symmetry associated contributions. Here, the focus is on Ni-Mn based alloys because this analysis allows specific insight into the martensitic driving force and other related properties of such alloys. Finally, a discussion of thermoelectric properties of Heusler films between platinum leads is given to investigate the spin-dependence of thermoelectric effects in such systems.

2 Theoretical Background

2.1 Density functional theory

The investigations presented in this work rely on theoretical calculations of electronic properties of solid state systems. They are carried out within the framework of quantum mechanics. The fundamental equation of this theory is the well known Schödinger equation. In cases where relativistic effects are not negligible, the basis of the calculations can be founded on relativistic quantum mechanics and the fundamental Dirac equation.

The many-body problem that arises from the non-relativistic or relativistic quantum mechanical description of a solid state systems is not exactly solvable in an analytical or numerical way. An appropriate procedure to find an adequate approximate solution is therefore desirable and can be found within density functional theory. This formalism provides the possibility to describe atomic systems quantum mechanically with high accuracy and in good agreement with experiment. Therefore, it serves as the major theoretical background of this work.

In the following the basic concepts of quantum mechanics of systems consisting of many atoms are outlined. At first, this introduction is restricted to the non-relativistic formalism for matters of transparency. In Section 2.1.3, some aspects of the more complicated nature of quantum mechanical many-body theory in the relativistic framework are described. Subsequently, density functional theory is introduced for the non-relativistic case and aspects of its relativistic generalization are presented. During this introduction the complicated character of the relativistic formalism becomes evident in a natural way.

2.1.1 Preliminaries

This section is devoted to a very short summary of the basic language of quantum mechanics before the introduction of many-body theory is started in the next section.

In quantum theory observables are mathematically represented by operators. The eigenvalue problem associated with these operators, in general

$$\hat{O}\psi_n = o_n\psi_n \ , \tag{2.1}$$

yields eigenvalues o_n which are often measurable values of the observable. The corresponding eigenfunctions ψ_n are interpreted in a probabilistic way. The eigenfunction depends on one or a set of dynamic variables of the system and the square of the eigenfunction $|\psi_n|^2$ is interpreted as the probability density to find the system in a state defined by specific values of the dynamical variables. If the variable is spatial, e.g. $\psi_n(\boldsymbol{r})$, one obtains the probability density to find a particle at a particular position $\boldsymbol{r}$ in space.

As the operators in quantum mechanics are linear, the space of functions to which the eigenfunctions belong is also linear and, in general, form a Hilbert space. Therefore, all eigenfunctions can be represented by a linear combination of a basis of functions which is, in general, infinitely large and can be represented by a vector, denoted by $|\Psi\rangle$. The basis

functions or vectors $|\psi_n\rangle$ have the usual properties of a basis of a linear space and are therefore normalized and orthogonal.

A detailed introduction into basic quantum mechanics can be found in e.g. Ref. [17] or Ref. [18].

2.1.2 Basic concepts

In this section non-relativistic quantum mechanics of systems consisting of many atoms is introduced. The corresponding Hamiltonian is discussed together with some necessary simplifications, and a scheme to find an approximate solution of this many-body problem is presented.

If the atomic nuclei are assumed to be point charges, the stationary wave function of an atomic system with N electrons and K nuclei is determined by the time independent Schrödinger equation

$$\hat{H}\Psi\left(\boldsymbol{r}_1, \boldsymbol{r}_2, ..., \boldsymbol{r}_N; \boldsymbol{R}_1, \boldsymbol{R}_2, ..., \boldsymbol{R}_K\right) = E\Psi\left(\boldsymbol{r}_1, \boldsymbol{r}_2, ..., \boldsymbol{r}_N; \boldsymbol{R}_1, \boldsymbol{R}_2, ..., \boldsymbol{R}_K\right) \tag{2.2}$$

where the $\{\boldsymbol{r}_i\}$ are the spatial variables of the electrons and $\{\boldsymbol{R}_i\}$ those of the nuclei. The spin degree of freedom is omitted here for simplicity but is introduced later.

In the absence of external fields, the non-relativistic Hamiltonian $\hat{H}$ consists of five contributions:

$$\hat{H} = \hat{T}_{\mathrm{el}} + \hat{T}_{\mathrm{nuc}} + \hat{V}_{\mathrm{el\,el}} + \hat{V}_{\mathrm{el\,nuc}} + \hat{V}_{\mathrm{nuc\,nuc}} \ . \tag{2.3}$$

The first two contributions correspond to the kinetic energy of the electrons and the nuclei. In position-space representation they are given by

$$\hat{T} = \hat{T}_{\mathrm{el}} + \hat{T}_{\mathrm{nuc}} = -\sum_{i=1}^{N} \frac{\hbar^2}{2m_{\mathrm{e}}} \nabla_i^2 - \sum_{\kappa=1}^{K} \frac{\hbar^2}{2M_\kappa} \nabla_\kappa^2 \ , \tag{2.4}$$

where $\hbar = h/2\pi$ is the Planck constant, m_e is the mass of the electron and the $\{M_\kappa\}$ are the masses of the nuclei which can in general be different for every nucleus. The remaining three contributions in Eq. (2.3) account for the interaction between the electrons, the nuclei and the interaction between electrons and nuclei. They are written as

$$\begin{aligned} \hat{V} &= \hat{V}_{\mathrm{el\,el}} + \hat{V}_{\mathrm{el\,nuc}} + \hat{V}_{\mathrm{nuc\,nuc}} \\ &= \sum_{i=1}^{N-1} \sum_{j=i+1}^{N} \frac{e^2}{|\boldsymbol{r}_i - \boldsymbol{r}_j|} - \sum_{\kappa=1}^{K} \sum_{i=1}^{N} \frac{Z_\kappa e^2}{|\boldsymbol{R}_\kappa - \boldsymbol{r}_i|} + \sum_{\kappa=1}^{K-1} \sum_{\lambda=\kappa+1}^{K} \frac{Z_\kappa Z_\lambda e^2}{|\boldsymbol{R}_\kappa - \boldsymbol{R}_\lambda|} \end{aligned} \tag{2.5}$$

where Z_κ denotes the proton number of nucleus κ and e the elementary electric charge. This Hamiltonian is the general mathematical foundation for the description of an arbitrary system of atoms.

As the mass of the electron is three orders of magnitude smaller than the mass of the proton, the corresponding timescale of motion of the electrons compared to that of the nuclei (at the same energy) is more than two orders of magnitude smaller. This implies that on timescales of the electrons the nuclei are almost at rest. In other words, the electrons follow the motion of the nuclei almost instantly. This fact leads directly to the so called adiabatic or Born-Oppenheimer approximations [19] where the coordinates of the nuclei serve only as parameters instead of dynamical variables. This separates the system of electrons from

the nuclei in a way that the influence of the nuclei is that of an external time independent potential

$$V_{\text{ext}}(\boldsymbol{r}_i) = -\sum_{\kappa=1}^{K} \frac{Z_\kappa e^2}{|\boldsymbol{R}_\kappa - \boldsymbol{r}_i|} \ . \tag{2.6}$$

Adopting the Born-Oppenheimer approximation, it is justified to restrict the discussion to the electronic system. Therefore, the associated Hamiltonian is of the form

$$\hat{H}_{\text{el}} = -\sum_{i=1}^{N} \frac{\hbar^2}{2m_{\text{e}}} \nabla_i^2 + \sum_{i=1}^{N-1} \sum_{j=i+1}^{N} \frac{e^2}{|\boldsymbol{r}_i - \boldsymbol{r}_j|} - \sum_{i=1}^{N} V_{\text{ext}}(\boldsymbol{r}_i) \ , \tag{2.7}$$

which is much simpler compared to Eq. (2.3) because it depends only on the dynamical variables $\boldsymbol{r}_i$ of the electrons.

So far, spin degrees of freedom are neglected. As the Hamiltonian (2.7) is used to describe only one type of particles, namely the electrons, spin can be introduced in a straightforward way. In non-relativistic quantum mechanics the spin operator of the electron, which is known to be a fermionic particle with spin 1/2, is introduced in an *a priori* way [18]. It is given by

$$\hat{\boldsymbol{s}} = \frac{\hbar}{2} \hat{\boldsymbol{\sigma}} \tag{2.8}$$

where $\hat{\boldsymbol{\sigma}}$ is the vector of the Pauli matrices [17]

$$\hat{\sigma}_x = \begin{pmatrix} 0 & 1 \\ 1 & 0 \end{pmatrix}, \qquad \hat{\sigma}_y = \begin{pmatrix} 0 & -i \\ i & 0 \end{pmatrix}, \qquad \hat{\sigma}_z = \begin{pmatrix} 1 & 0 \\ 0 & -1 \end{pmatrix} \ . \tag{2.9}$$

Within this representation the z-component is preferred because $\hat{s}_z$ is diagonal. Therefore, the spin quantization refers to the z-axis of the coordinate system. The eigenfunctions of $\hat{\sigma}_z$ are

$$\chi_{1/2} = \begin{pmatrix} 1 \\ 0 \end{pmatrix}, \qquad \chi_{-1/2} = \begin{pmatrix} 0 \\ 1 \end{pmatrix} \tag{2.10}$$

where the subscript corresponds to the two associated eigenvalues of $\hat{\sigma}_z$, which are $1/2$ and $-1/2$.

In quantum theory, the angular momentum state is specified by the eigenvalues of the square and one particular component of the associated angular momentum operator. As the eigenvalue of the square of the spin operator $\hat{\boldsymbol{s}}$ is always $3/4$, the spin state is already uniquely defined by the eigenvalue of the z-component.

In non-relativistic theory, spin has to be introduced as an additional property in this *a priori* way. In relativistic quantum theory the spin degree of freedom arises in a natural way as will be discussed in Section 2.1.3.

Due to the introduction of the spin degree of freedom the wave function of a system of electrons depends now on the coordinate and spin variable of every electron. To keep the notation compact the wave function is written as $\Psi(\boldsymbol{x}_1, ..., \boldsymbol{x}_N)$, where $\boldsymbol{x}_i = (\boldsymbol{r}_i, \sigma_i)$ is a composite index containing the coordinate dependence $\boldsymbol{r}_i$ and the spin variable $\sigma_i = 1/2, -1/2$. This wave function is determined by the time independent Schrödinger equation of the electronic system

$$\hat{H}_{\text{el}} \Psi(\boldsymbol{x}_1, ..., \boldsymbol{x}_N) = E \Psi(\boldsymbol{x}_1, ..., \boldsymbol{x}_N) \ . \tag{2.11}$$

Two additional requirements of the wave function Ψ need to be introduced. As the square of Ψ gives the probability to find all N electron in the system, the normalization condition

$$\int \Psi\left(\boldsymbol{x}_1, ..., \boldsymbol{x}_N\right) \mathrm{d}\boldsymbol{r}_1 ... \mathrm{d}\boldsymbol{r}_N = N \tag{2.12}$$

has to be fulfilled. And as a spin 1/2 identifies the electron as a fermion, the wave function has to be antisymmetric with respect to the exchange of two particles [18] which implies that

$$\Psi\left(..., \boldsymbol{x}_i, ..., \boldsymbol{x}_j, ...\right) = -\Psi\left(..., \boldsymbol{x}_j, ..., \boldsymbol{x}_i, ...\right) \ . \tag{2.13}$$

This restricts the set of possible wave functions to the Hilbert space of antisymmetric and normalized functions of N variables which is usually denoted by $\mathcal{H}^N$. In relativistic theory there is no need to establish this symmetry property as an additional requirement because it is directly connected to the natural occurrence of the spin [20].

In the following, the wave function Ψ_0, which corresponds to the smallest eigenvalue E_0 and is called the ground state of the system, is of particular interest because from this ground state many important physical properties can be derived. The variational principle states that the ground state energy E_0 serves as the lower bound for the expectation value of the Hamilton operator $\hat{H}_{el}$ (see Eq. 2.7) with respect to all functions of the corresponding Hilbert space $\mathcal{H}^N$ [21]. This statement may be written in the form

$$E_0 = \min_{\Psi \in \mathcal{H}^N} \langle \Psi | \hat{H}_{\mathrm{el}} | \Psi \rangle \, . \tag{2.14}$$

As it is additionally required that the wave function is normalized and antisymmetric, an appropriate basis set of $\mathcal{H}^N$ is needed in order to perform such variations. A possible orthonormal basis of antisymmetric functions is provided by the set of all Slater determinants given by

$$\Phi_n\left(\boldsymbol{x}_1, ..., \boldsymbol{x}_N\right) = \frac{1}{\sqrt{N}} \begin{vmatrix} \varphi_i\left(\boldsymbol{x}_1\right) & \cdots & \varphi_j\left(\boldsymbol{x}_N\right) \\ \vdots & \ddots & \vdots \\ \varphi_k\left(\boldsymbol{x}_1\right) & \cdots & \varphi_l\left(\boldsymbol{x}_N\right) \end{vmatrix} . \tag{2.15}$$

This Slater determinants are constructed from a complete orthonormal set $\{\varphi_i\left(\boldsymbol{x}\right)\}$ of spin-dependent single particle eigenfunctions. The φ_i can be single particle solution of of the underlying system which is a common choice. In this case a zeroth order approximation to a ground state is given by the Slater determinant which is constructed from the first N states that correspond to the first N eigenvalues. In the case of an atomic or molecular system the φ_i are called orbitals.

In principle, it is possible to expand the ground state wave function by using the set of Slater determinants

$$\Psi\left(\boldsymbol{x}_1, ..., \boldsymbol{x}_N\right) = \sum_n a_n \Phi_n\left(\boldsymbol{x}_1, ..., \boldsymbol{x}_N\right) \tag{2.16}$$

and to obtain the ground state energy by minimizing the expectation value of the total energy $\langle \Phi | \hat{H}_{\mathrm{el}} | \Phi \rangle$ with respect to the coefficients a_n. As this task is not feasible in practice, because of the high computational demand, it is useful to restrict to certain sub-spaces of $\mathcal{H}^N$. A strong simplification is obtained if only one term of the expansion is taken into account. In this case the single particle wave functions $\{\varphi_i\left(x\right)\}$ are varied in order to find a single Slater determinant which minimizes the total energy. This approach is known as the Hartree-Fock method [22, 23, 24] and is sketched in the following.

As spin and motion of the electron are independent in non-relativistic theory, the single electron wave function is a product of the function of the position and the function of the spin variable $\varphi(\boldsymbol{x}) = \psi^{\sigma}(\boldsymbol{r})\,\xi(\sigma)$. Writing the expectation value of the total energy of the electron system in terms of a single Slater determinant and adopting that the single particle wave functions are orthogonal and normalized, the expression

$$\begin{aligned} E_{\mathrm{HF}} = \langle\Phi|\hat{H}_{\mathrm{el}}|\Phi\rangle &= \sum_{i,\sigma}\int \mathrm{d}\boldsymbol{r}\psi_i^{\sigma *}(\boldsymbol{r})\left[-\frac{1}{2}\nabla^2 + V_{\mathrm{ext}}(\boldsymbol{r})\right]\psi_i^{\sigma}(\boldsymbol{r}) \\ &+ \frac{1}{2}\sum_{i,j,\sigma_i,\sigma_j}\int \mathrm{d}\boldsymbol{r}\mathrm{d}\boldsymbol{r}'\psi_i^{\sigma_i *}(\boldsymbol{r})\,\psi_j^{\sigma_j *}(\boldsymbol{r}')\,\frac{1}{|\boldsymbol{r}-\boldsymbol{r}'|}\psi_i^{\sigma_i}(\boldsymbol{r})\,\psi_j^{\sigma_j}(\boldsymbol{r}') \\ &- \frac{1}{2}\sum_{i,j,\sigma}\int \mathrm{d}\boldsymbol{r}\mathrm{d}\boldsymbol{r}'\psi_i^{\sigma *}(\boldsymbol{r})\,\psi_j^{\sigma *}(\boldsymbol{r}')\,\frac{1}{|\boldsymbol{r}-\boldsymbol{r}'|}\psi_j^{\sigma}(\boldsymbol{r})\,\psi_i^{\sigma}(\boldsymbol{r}') \\ &= \sum_i h_i + \sum_{i,j}(U_{ij} - J_{ij}) \end{aligned} \tag{2.17}$$

is obtained [25], because the Hamiltonian (2.7) is independent of spin and therefore diagonal in the basis of the spin functions. To keep the notation more transparent, atomic units are introduced here. Therefore, space is now measured in units of the Bohr radius $a_{\mathrm{B}} = \hbar/(2m_{\mathrm{e}}e^2)$ and energy in units of the Hartree energy $E_{\mathrm{H}} = m_{\mathrm{e}}e^4\hbar^2$.

Expression (2.17) consists of three contributions. The first one is the sum of the single particle contributions h_i arising from the kinetic energy of the electron and its interaction with the nuclei. The second term U_{ij} includes the Coulomb interactions between the electrons. In this conventional form it includes the self interaction of the electron with its own charge distribution. This spurious contribution is canceled by the last term J_{ij}, which is the exchange interaction and reflects the antisymmetric character of the many-body wave function. It vanishes for electrons with different spin since the spin part of the wave functions is orthogonal for opposite spins.

If the variational principle is applied to this energy functional, a set of single particle equations called Hartree-Fock equations [25]

$$\begin{aligned} &\left[-\frac{1}{2}\nabla^2 + \sum_{j,\sigma_j}\int \mathrm{d}\boldsymbol{r}'\psi_j^{\sigma_j *}(\boldsymbol{r}')\,\frac{1}{|\boldsymbol{r}-\boldsymbol{r}'|}\psi_j^{\sigma_j}(\boldsymbol{r}') + V_{\mathrm{ext}}\right]\psi_i^{\sigma}(\boldsymbol{r}) \\ &- \sum_j\int \mathrm{d}\boldsymbol{r}'\psi_j^{\sigma *}(\boldsymbol{r}')\,\frac{1}{|\boldsymbol{r}-\boldsymbol{r}'|}\psi_i^{\sigma}(\boldsymbol{r}')\,\psi_j^{\sigma}(\boldsymbol{r}) = \varepsilon_i^{\sigma}\psi_i^{\sigma}(\boldsymbol{r}) \end{aligned} \tag{2.18}$$

is found. These equations have to be solve self-consistently to find the set of single particle wave functions that builds up a Slater determinant which minimizes the energy E_{HF}. In order to carry out calculations within the Hartree-Fock formalism in an efficient way, the single particle wave functions are expanded with respect to a set of basis functions

$$\psi_i^{\sigma}(\boldsymbol{r}) = \sum_{\alpha} c_{\alpha,i}\chi_{\alpha} \tag{2.19}$$

and the coefficients $c_{\alpha,i}$ are determined in order to minimize the energy [26, 27, 28].

The ε_i^{σ} in Eq. (2.18) serve as Lagrange parameters of the variation [29] which ensure the normalization. The last parameter with the highest value can be interpreted due to Koopmans

theorem [30], which states that it is the first ionization energy. But this is only approximately true because the theorem assumes that although one electron is removed from the system the other states remain self-consistent.

All other ε_i^σ may also be interpreted as the eigenvalues of different energy levels of the system which are occupied by lower energy electrons. This assumes the one particle picture which neglects the many-body nature of the quantum mechanical system. Therefore, the interpretation of the ε_i^σ includes assumptions that cannot be neglected.

The previous discussion leads to the main drawback of the entire method: In Hartree-Fock approximation the many-body problem is reduced to an effective single particle problem. Every particle moves in a potential, which by construction reflects the average charge density of all other particles. This implies that the correlations, which couple the motions of the electrons is disregarded, except for the fact that particles with the same spin cannot be found in the same volume element due to the exchange interaction. This can be a serious problem because in certain systems the electrons are strongly correlated and therefore their description within the Hartree-Fock formalism fails completely.

Many methods exist which intend to cure the lack of missing correlation effects. One of these methods is the *Configuration Interaction* (CI) method [31], where a systematic improvement is achieved by enlarging the space of trial functions. Single particle states, which are exited with respect to the reference Hartree-Fock ground state are included in this method. Therefore, more single particle wave functions M as there are particles N in the considered system have to be determined within the usual Hartree-Fock calculation. This means that occupied and unoccupied states are calculated together. Afterwards, the Slater determinant of the Hartree-Fock ground state is constructed by choosing the N functions which are of lowest energies. Replacing occupied states by unoccupied states in the construction of the Slater determinants and building up linear combinations

$$\Psi = a_0 \Phi_{\mathrm{HF}} + \sum_i a_i \Phi_i \,, \tag{2.20}$$

an additional variation with respect to the coefficients a_i of the Slater determinants can be performed. More sophisticated formulations of this idea are given in Ref. [25]. The drawback of the CI method is that the computational demand scales with the fifth or higher power of the system size.

The computational demand is considerably lowered in density functional theory which is introduced in Section 2.1.4. In this method the high dimensional problem of searching the ground state wave function, depending on N positional variables is replaced by the determination of the ground state electron density, which is only a function of the three spatial coordinates. Before this theory is explained in more detail the relativistic theory of the is electron introduced.

2.1.3 Relativistic formalism

In this section, basic facts about relativistic quantum mechanics are presented. The origin of the Dirac equation, which is the fundamental equation of motion in relativistic theory, is discussed together with its solution for the case of a free particle. During the discussion of this simple problem many characteristic aspects of the relativistic theory emerge. It becomes apparent how the formulation of a relativistic many-body theory leads to problems that need to be solved within a more developed formalism, namely the relativistic quantum field theory.

These facts are important because a relativistic formulation of density functional theory is used in later chapters. Special issues of this formulation partially arise from the problems discussed in this subsection.

It should be noted that the Dirac equation cannot be derived from non-relativistic theory because this equation is more general. On the opposite, it is required that the non-relativistic theory is recovered as a limiting case of slow velocities. Therefore, the description of the origin has to follow heuristic arguments. For reasons of compactness these arguments are not discussed extensively but details can be found in textbooks [20, 32, 33].

First, two fundamental requirements have to be fulfilled [32]: The relativistic equation of motion has to be linear in order to ensure the principle of superposition. Furthermore, the derivatives of time and space have to be of the same order to ensure invariance under Lorentz transformations [1].

A starting point of the formulation of the relativistic equation is found in the relation which determines the energy W of a free particle in classical relativity [32]

$$W^2 = p^2c^2 + m^2c^4 \,. \tag{2.21}$$

Following the correspondence principle [17], energy and momentum can be replaced by the associated operators. If this replacement is carried out in Eq. (2.21), a relativistic equation of motion called the Klein-Gordon equation is obtained. Although this equation fulfills the necessary requirements, it turns out that it is not the suitable equation for the description of electrons. The Klein-Gordon equation is suitable for bosons with zero spin but what is needed here is an equation for fermions with spin 1/2 [32]. Therefore, a different strategy has to be found. At this point Dirac proposed to start from the ansatz

$$W = \boldsymbol{\alpha} \cdot \boldsymbol{p}\, c + \beta mc^2 = \hat{\mathcal{H}}_{\mathrm{D}} \,. \tag{2.22}$$

In order to give this ansatz a physical justification, the square of Eq. (2.22) should recover (2.21). This implies that the coefficients α_i and β have to fulfill the conditions

$$\begin{aligned}
\alpha_x^2 = \alpha_y^2 = \alpha_z^2 = \beta^2 = I \,, \\
\{\boldsymbol{\alpha}, \beta\} = \boldsymbol{\alpha}\beta + \beta\boldsymbol{\alpha} = 0 \,, \\
\{\alpha_x, \alpha_y\} = \alpha_x\alpha_y + \alpha_y\alpha_x = 0 \,, \\
\{\alpha_y, \alpha_z\} = \alpha_y\alpha_z + \alpha_z\alpha_y = 0 \,, \\
\{\alpha_x, \alpha_z\} = \alpha_x\alpha_z + \alpha_z\alpha_x = 0
\end{aligned} \tag{2.23}$$

where I is the identity and the curly brackets denote anti-commutators [17]. It is obvious, that these conditions cannot be fulfilled by real numbers or in general by elements of a field. But it is possible to fulfill them with appropriate matrices. There is some freedom in defining such matrices [32] but here only the most widely used representation, the famous Dirac matrices, is introduced. This representation is four dimensional, its identity is given by

$$I_4 = \begin{pmatrix} 1 & 0 & 0 & 0 \\ 0 & 1 & 0 & 0 \\ 0 & 0 & 1 & 0 \\ 0 & 0 & 0 & 1 \end{pmatrix} = \begin{pmatrix} I_2 & 0 \\ 0 & I_2 \end{pmatrix} \tag{2.24}$$

[1] This is not fulfilled by the Schrödinger equation where the time derivative is of first and the space derivative is of second order.

and β and the α_i are defined by [2]

$$\beta = \begin{pmatrix} 1 & 0 & 0 & 0 \\ 0 & 1 & 0 & 0 \\ 0 & 0 & -1 & 0 \\ 0 & 0 & 0 & -1 \end{pmatrix} = \begin{pmatrix} I_2 & 0 \\ 0 & -I_2 \end{pmatrix}, \quad \alpha_x = \begin{pmatrix} 0 & 0 & 0 & 1 \\ 0 & 0 & 1 & 0 \\ 0 & 1 & 0 & 0 \\ 1 & 0 & 0 & 0 \end{pmatrix} = \begin{pmatrix} 0 & \sigma_x \\ \sigma_x & 0 \end{pmatrix} \tag{2.25}$$

$$\alpha_y = \begin{pmatrix} 0 & 0 & 0 & -i \\ 0 & 0 & i & 0 \\ 0 & -i & 0 & 0 \\ i & 0 & 0 & 0 \end{pmatrix} = \begin{pmatrix} 0 & \sigma_y \\ \sigma_y & 0 \end{pmatrix}, \quad \alpha_z = \begin{pmatrix} 0 & 0 & 1 & 0 \\ 0 & 0 & 0 & -1 \\ 1 & 0 & 0 & 0 \\ 0 & -1 & 0 & 0 \end{pmatrix} = \begin{pmatrix} 0 & \sigma_z \\ \sigma_z & 0 \end{pmatrix} \tag{2.26}$$

where the σ_i are the Pauli matrices which have already been introduced in Section 2.1.2. The matrices need to have at least four dimensions because in lower dimensions it is not possible to find four distinct matrices fulfilling the required anti-commutation rules.

Putting all the definitions and requirements together, the time-dependent Dirac equation is written as

$$i\hbar\frac{\partial}{\partial t}\boldsymbol{\psi}(\boldsymbol{r},t) = \left(-i\hbar c\,\boldsymbol{\alpha}\cdot\nabla + \beta mc^2\right)\boldsymbol{\psi}(\boldsymbol{r},t) \tag{2.27}$$

where the wave function $\boldsymbol{\psi}(\boldsymbol{r},t)$ is now a four dimensional vector and is called spinor. Spinors are elements of a complex vector space and the special name stems from the particular transformation behavior (see Ref. [35] for details).

As the statistical interpretation of the wave function remains the same as in non-relativistic quantum mechanics, the square of a spinor

$$|\boldsymbol{\psi}(\boldsymbol{r},t)|^2 = \sum_{i=1}^{4} |\psi_i(\boldsymbol{r},t)|^2 \tag{2.28}$$

gives a probability density to find a particle in an infinitesimal volume element around $\boldsymbol{r}$.

In summary: A wave equation is derived which fulfills the requirement of linearity and Lorentz invariance. As result of the required Lorentz invariance the equation is now four dimensional. The probabilistic interpretation of the wave function is kept by using equation (2.28). In the following, solutions of this equation for a single free particle are determined.

As in the non-relativistic case the time dependence may be separated from the spatial dependence by assuming a wave function of the form

$$\boldsymbol{\psi}(\boldsymbol{r},t) = \boldsymbol{\psi}(\boldsymbol{r})\,e^{-iWt/\hbar} = \begin{pmatrix} \psi_1(\boldsymbol{r}) \\ \psi_2(\boldsymbol{r}) \\ \psi_3(\boldsymbol{r}) \\ \psi_4(\boldsymbol{r}) \end{pmatrix} e^{-iWt/\hbar}\,. \tag{2.29}$$

Substitution into the Dirac equation (2.27) leads to the time independent analogue of the time independent Schrödinger equation,

$$\left(-i\hbar c\,\boldsymbol{\alpha}\cdot\nabla + \beta mc^2\right)\boldsymbol{\psi}(\boldsymbol{r}) = W\boldsymbol{\psi}(\boldsymbol{r}) \tag{2.30}$$

[2] The matrices α_i and β build up a so called Clifford algebra [34].

where the eigenvalue W is the relativistic energy. In order to solve this equation an ansatz for plane wave functions with four components is employed

$$\boldsymbol{\psi}(\boldsymbol{r}) = \begin{pmatrix} U_1 \\ U_2 \\ U_3 \\ U_4 \end{pmatrix} e^{-i\boldsymbol{p}\cdot\boldsymbol{r}/\hbar}\,, \tag{2.31}$$

where the U_i are amplitudes. In order to simplify the following mathematical effort considerably, the particle is assumed to move in the xy-plane. Substitution of (2.31) into Eq. (2.30) leads to four equations that determine the amplitudes U_i

$$\begin{aligned} \left(mc^2 - W\right) U_1 + c\left(p_x - ip_y\right) U_4 &= 0 \\ c\left(p_x + ip_y\right) U_1 - \left(mc^2 + W\right) U_4 &= 0 \\ \left(mc^2 - W\right) U_2 + c\left(p_x + ip_y\right) U_3 &= 0 \\ c\left(p_x - ip_y\right) U_2 - \left(mc^2 + W\right) U_3 &= 0\,, \end{aligned} \tag{2.32}$$

where p_x and p_y are the x and y components of the momentum [3]. This homogeneous system of equations decouples into two independent homogeneous systems for the pairs U_1, U_4 and U_2, U_3. It is known from basic linear algebra that homogenous systems always have a trivial solution and under certain circumstances, which are determined by the coefficients, an additional general non-trivial solution, which depends on free parameters. This is the case if the determinant of the coefficient matrix is zero. The determinant of the coefficient matrix of both pairs of equations is equal and gives

$$\begin{vmatrix} \left(mc^2 - W\right) & c\left(p_x - ip_y\right) \\ c\left(p_x + ip_y\right) & \left(mc^2 + W\right) \end{vmatrix} = W - c^2\boldsymbol{p}^2 - m^2c^4\,. \tag{2.33}$$

Requiring the determinants to be zero the relativistic energy relation (2.21) is recovered. This means that there are only non-trivial solutions if the energy W and the momentum $\boldsymbol{p}$ fulfill this relations which is of course a natural requirement that has to be valid for every physical solution.

From the two pairs of equations two relations are obtained which determine the relative values of the U_i

$$\frac{U_1}{U_4} = \frac{c\left(p_x - ip_y\right)}{W - mc^2} = \frac{W + mc^2}{c\left(p_x + ip_y\right)} \tag{2.34}$$

$$\frac{U_2}{U_3} = \frac{c\left(p_x + ip_y\right)}{W - mc^2} = \frac{W + mc^2}{c\left(p_x - ip_y\right)}\,. \tag{2.35}$$

From the middle and the right hand site of both Eq. (2.21) is obtained again which indicates that one can identify the U_i with the nominators or denominators of the last two equations.

In other words, each system of two corresponding equations of Eq. (2.32) has three solutions. One is the trivial solution and the other two physically relevant solutions are directly obtained from the relative values of the U_i. These solutions are

$$\begin{aligned} U_1 = W + mc^2 \quad &\vee \quad U_1 = c\left(p_x - ip_y\right) \\ U_2 = W + mc^2 \quad &\vee \quad U_2 = c\left(p_x + ip_y\right) \\ U_3 = c\left(p_x - ip_y\right) \quad &\vee \quad U_3 = W - mc^2 \\ U_4 = c\left(p_x + ip_y\right) \quad &\vee \quad U_4 = W - mc^2\,. \end{aligned} \tag{2.36}$$

[3] Without the restriction that the particle moves only in the xy-plane all four equations are coupled [32].

Insertion of these solutions in Eq. (2.32) gives again the energy relation Eq. (2.21) and therefore a valid expression. An alternative way of evaluating the U_i is shown in Appendix A.1.

All in all, four linear independent solutions of the free particle problem can be identified from the previous considerations. The first two arise from the non-trivial solutions of one pair of equations (2.32) when the solution of the other pair is chosen to be the trivial one and vice versa. Neglecting the normalization, the free particle wave functions are given by

$$\psi_p^{\uparrow} \propto \begin{pmatrix} W+mc^2 \\ 0 \\ 0 \\ c\,(p_x+ip_y) \end{pmatrix} e^{-i\boldsymbol{p}\cdot\boldsymbol{r}/\hbar} \quad , \quad \psi_p^{\downarrow} \propto \begin{pmatrix} 0 \\ W+mc^2 \\ c\,(p_x-ip_y) \\ 0 \end{pmatrix} e^{-i\boldsymbol{p}\cdot\boldsymbol{r}/\hbar}$$
$$\psi_n^{\uparrow} \propto \begin{pmatrix} c\,(p_x-ip_y) \\ 0 \\ 0 \\ W-mc^2 \end{pmatrix} e^{-i\boldsymbol{p}\cdot\boldsymbol{r}/\hbar} \quad , \quad \psi_n^{\downarrow} \propto \begin{pmatrix} 0 \\ c\,(p_x+ip_y) \\ W-mc^2 \\ 0 \end{pmatrix} e^{-i\boldsymbol{p}\cdot\boldsymbol{r}/\hbar} \,. \tag{2.37}$$

Now, the implications following from the four solutions need to be discussed. If the four solutions are inserted in Eq. (2.30) it becomes apparent that the eigenvalue W on the right hand side is W for the first two solutions but needs to be $-W$ for the second pair of solutions. This means that solutions for particles with positive as well as negative energies are obtained. Noting that Eq. (2.21) has the two solutions

$$W = \pm\sqrt{c^2\boldsymbol{p}^2 + m^2c^4} \tag{2.38}$$

where one gives a positive and the other a negative energy, it becomes apparent that negative energies occur naturally in relativistic theory.

It needs to be understood how two solutions for positive as well as for negative energies have to be interpreted. To simplify this discussion, a transformation into the rest frame of the particle where p_x and p_y are zero is helpful. Due to the vanishing momentum $\boldsymbol{p} = 0$ the energy is $W = \pm mc^2$ according to Eq. (2.38). If $W = +mc^2$ is set for the first two solutions they become

$$\psi_p^{\uparrow} \propto \begin{pmatrix} 2mc^2 \\ 0 \\ 0 \\ 0 \end{pmatrix} \quad , \quad \psi_p^{\downarrow} \propto \begin{pmatrix} 0 \\ 2mc^2 \\ 0 \\ 0 \end{pmatrix} \,. \tag{2.39}$$

It is argued in Ref. [33] that there must be an operator, which commutes with the momentum operator and distinguishes between the two energetically degenerated solutions. This operator gives both solutions an independent physical meaning. It can be shown that the operator of the spin orientation in z-direction fulfills these requirements. In contrast to the non-relativistic theory the spin operator is written in a form that accounts for the four components of the wave function [32]

$$\hat{S}_z = \frac{\hbar}{2}\tilde{\sigma}_z = \frac{\hbar}{2}\begin{pmatrix} 1 & 0 & 0 & 0 \\ 0 & -1 & 0 & 0 \\ 0 & 0 & 1 & 0 \\ 0 & 0 & 0 & -1 \end{pmatrix} . \tag{2.40}$$

By applying this operator to the wave functions $\psi_p^{\uparrow}$ and $\psi_p^{\downarrow}$ one obtains

$$\hat{S}_z\psi_p^{\uparrow} = \frac{\hbar}{2}\tilde{\sigma}_z \begin{pmatrix} 2mc^2 \\ 0 \\ 0 \\ 0 \end{pmatrix} = \frac{\hbar}{2}\psi_p^{\uparrow}\,, \qquad \hat{S}_z\psi_p^{\downarrow} = \frac{\hbar}{2}\tilde{\sigma}_z \begin{pmatrix} 0 \\ 2mc^2 \\ 0 \\ 0 \end{pmatrix} = -\frac{\hbar}{2}\psi_p^{\downarrow}\,. \tag{2.41}$$

This shows that the solutions $\psi_p^{\uparrow}$ and $\psi_p^{\downarrow}$ are eigenfunctions of the spin operator of the z-direction. It is easily proven that they are not eigenfunctions the four dimensional x- and y-component of the total spin operator. Therefore, $\psi_p^{\uparrow}$ is interpreted as a wave function of a spin-up particle and $\psi_p^{\downarrow}$ as a wave function of a spin-down particle.

It is important to note that $\psi_p^{\uparrow}$ and $\psi_p^{\downarrow}$ are only eigenfunctions of the z-component of the spin if the particle is studied in its rest frame. In any other frame of reference where the particle has a finite momentum, this is no longer true. This implies that momentum and spin of a particle have a fundamental relation in relativistic quantum theory. A well known effect connected to this property is the spin-orbit coupling. To describe the influence of such effects on properties of solids a relativistic description of the electronic structure is needed.

In a next step the first two functions of Eq. (2.37) have to be written in an appropriate normalized form for all frames of reference. As they are not yet normalized they can be multiplied with an arbitrary factor without changing their meaning. Here, they are multiplied with $(W + mc^2)^{-1}$ which leads to

$$\begin{aligned} \psi_p^{\uparrow} &\propto \begin{pmatrix} 1 \\ 0 \\ 0 \\ \frac{c(p_x+ip_y)}{W+mc^2} \end{pmatrix} e^{-i\boldsymbol{p}\cdot\boldsymbol{r}/\hbar} = \begin{pmatrix} \chi_{1/2} \\ \frac{c\hat{\boldsymbol{\sigma}}\boldsymbol{p}}{W+mc^2}\chi_{1/2} \end{pmatrix} e^{-i\boldsymbol{p}\cdot\boldsymbol{r}/\hbar} \\ \psi_p^{\downarrow} &\propto \begin{pmatrix} 0 \\ 1 \\ \frac{c(p_x-ip_y)}{W+mc^2} \\ 0 \end{pmatrix} e^{-i\boldsymbol{p}\cdot\boldsymbol{r}/\hbar} = \begin{pmatrix} \chi_{-1/2} \\ \frac{c\hat{\boldsymbol{\sigma}}\boldsymbol{p}}{W+mc^2}\chi_{-1/2} \end{pmatrix} e^{-i\boldsymbol{p}\cdot\boldsymbol{r}/\hbar} \end{aligned} \tag{2.42}$$

where the $\chi^{\pm 1/2}$ are the two component basis spinors introduced in Eq. (2.10). In addition the compact notation

$$c\hat{\boldsymbol{\sigma}}\boldsymbol{p} = \begin{pmatrix} 0 & c\,(p_x - ip_y) \\ c\,(p_x + ip_y) & 0 \end{pmatrix} \tag{2.43}$$

is used. Now, the normalization can be carried out in a straightforward way. As in the non-relativistic case, the exponential part is normalized with respect to the volume of the system. Due to the requirement that $U^{\uparrow(\downarrow)}U^{\uparrow(\downarrow)} = 1$, the second part of the normalization constant is found (see Appendix A.2 for details). Therefore, the normalized wave functions are

$$\begin{aligned} \psi_p^{\uparrow} &= \frac{1}{\sqrt{V}}\left(\frac{W+mc^2}{2W}\right)^{\frac{1}{2}} \begin{pmatrix} \chi_{1/2} \\ \frac{c\hat{\boldsymbol{\sigma}}\boldsymbol{p}}{W+mc^2}\chi_{1/2} \end{pmatrix} e^{-i\boldsymbol{p}\cdot\boldsymbol{r}/\hbar} \\ \psi_p^{\downarrow} &= \frac{1}{\sqrt{V}}\left(\frac{W+mc^2}{2W}\right)^{\frac{1}{2}} \begin{pmatrix} \chi_{-1/2} \\ \frac{c\hat{\boldsymbol{\sigma}}\boldsymbol{p}}{W+mc^2}\chi_{-1/2} \end{pmatrix} e^{-i\boldsymbol{p}\cdot\boldsymbol{r}/\hbar} \end{aligned} \tag{2.44}$$

which are the physical eigenfunctions of a spin-up and a spin-down particle with positive energy.

Now, the third and fourth function of Eq. (2.37) are examined in more detail. Again, the functions are investigated in the rest frame of the particle, where the momentum is zero. To get the non-trivial solutions, $W = -mc^2$ has to be chosen which leads to

$$\psi_n^{\uparrow} \propto \begin{pmatrix} 0 \\ 0 \\ 0 \\ -2mc^2 \end{pmatrix} \quad , \quad \psi_n^{\downarrow} \propto \begin{pmatrix} 0 \\ 0 \\ -2mc^2 \\ 0 \end{pmatrix} . \tag{2.45}$$

These negative energy solutions are also eigenfunctions of $\hat{S}_z$ in the rest frame of the particle. Therefore, they also describe particles with spin-up $\psi_n^{\uparrow}$ and spin-down $\psi_n^{\downarrow}$. In a general frame of reference the normalized functions are

$$\begin{aligned} \psi_n^{\uparrow} &= \frac{1}{\sqrt{V}} \left(\frac{W - mc^2}{2W} \right)^{\frac{1}{2}} \begin{pmatrix} -\frac{c\hat{\boldsymbol{\sigma}}\boldsymbol{p}}{W+mc^2} \chi_{1/2} \\ \chi_{1/2} \end{pmatrix} e^{-i\boldsymbol{p}\cdot\boldsymbol{r}/\hbar} \\ \psi_n^{\downarrow} &= \frac{1}{\sqrt{V}} \left(\frac{W - mc^2}{2W} \right)^{\frac{1}{2}} \begin{pmatrix} -\frac{c\hat{\boldsymbol{\sigma}}\boldsymbol{p}}{W+mc^2} \chi_{-1/2} \\ \chi_{-1/2} \end{pmatrix} e^{-i\boldsymbol{p}\cdot\boldsymbol{r}/\hbar} \end{aligned} \tag{2.46}$$

where the normalization constant is slightly different to that of the positive energy wave functions. It contains $W - mc^2$ instead of $W + mc^2$ (see again Appendix A.2 for details).

It should be noted that the first component of the solutions $\psi_p^{\uparrow}$ and $\psi_p^{\downarrow}$ (see Eq. (2.44)) is large and the second is small for velocities far below c. This is the other way around for the negative energy solutions $\psi_n^{\uparrow}$ and $\psi_n^{\uparrow}$. This can be immediately understood by examining the prefactor $c\hat{\boldsymbol{\sigma}}\boldsymbol{p}/W + mc^2$ in front of the spinors $\chi^{\sigma}(\sigma = 1/2, -1/2)$. The nominator of this factor is of order c and the denominator of order c^2. Both become of the same order when the moment $\boldsymbol{p}$ becomes large and therefore the velocity of the particle approaches c.

The occurrence of states with negative energies requires an adequate interpretation. These solutions cannot be ignored and skipped just because they appear to have no physical meaning. The mathematical argument is that solutions with negative energy belong to the set of basis functions, which would become incomplete if the negative energy solutions are ignored. A physical argument is that finite transition probabilities to negative states are obtained from perturbation theory [33]. In other words, although states with negative energy might be neglected at the start they can appear again during a calculation.

Unfortunately, a naive interpretation of this solutions immediately leads to a problem. If it is accepted that there are empty states with negative energy then particles with positive energy would decay down into these states due to finite transition probabilities. As the energy spectrum is not bound this decay would go on forever. As the particles would emit photons during this decay to release the excess energy, and as these photons are not observed, this interpretation is inconsistent compared to reality. In other words, it is not reasonable to assume that the whole universe is on its way to infinitely large negative energy.

Dirac proposed a solution to this problem by assuming that all negative energy states are filled with electrons [36]. This infinite amount of electrons occupying negative energy states and interspersing the whole universe is usually known as the Dirac sea. An electron which is excited from one of these states leaves a hole, that can be interpreted as a particle with positive charge. From this interpretation the existence of the positron, which in this sense

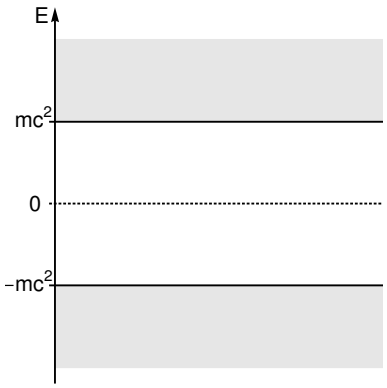

Figure 2.1: Energy spectrum of the free Dirac equation. There is a continuous spectrum of positive energy states and a continuous one of the negative energy states. Both are separated by a gap of two times the rest energy.

is the remaining hole in the Dirac sea, is predicted. In addition, the pairwise creation of electrons and positrons is understood in this way. The positive and negative energy states are separated by $2mc^2$ because the total energy cannot be smaller then the rest energy mc^2 (see Fig. 2.1). Therefore, the energy needed to create an electron-positron pair is two times the rest energy of the electron.

But unfortunately, the concept of the Dirac sea still leaves open questions: At first, the Dirac sea has, in principle, an infinitely large charge as well as mass. Therefore, the vacuum state suffers from serious divergences that have to be treated somehow. Another problem is the antisymmetry between particles and antiparticles in nature when every particle leaves its corresponding hole in the Dirac sea. This implies an equal amount of matter and antimatter in the universe which is also not observed. Further problems arise, as negative energy electrons of the Dirac sea should interact with the usual positive energy electrons and also with external electric fields. Therefore, the field of an electron interacts with the Dirac sea and the sea acts back onto the electron leading to a self-interaction that needs to be treated within a many-body theory approach and is not directly included in the simple Dirac theory. Moreover, though a symmetric and homogeneous distribution of the negative energy electrons does not lead to a finite polarization of a vacuum, the application of an external electric field and the resulting shift of the distribution leads to an infinite polarization of the vacuum.

In summary: The Dirac theory leads to serious drawbacks in a single particle picture and instead needs to be a many-body theory. This many-body theory leads to the occurrence of diverging quantities.

A consistent solution of these problems was given by the invention of a relativistic many-body theory, namely the theory of quantum electrodynamics [37, 38, 33]. An introduction of this theory exceeds the scope of this work.

The circumstances are simpler in applications of the relativistic theory together with density functional methods for the description of the electronic structure of solids. The usual total energy of the electron is well below twice its rest energy, which separates the positive and negative energy states. In this case the particles can be separated from antiparticles in a mathematically rigor way by using the Fouldy-Wouthuysen transformation [32].

But in order to formulate a consistent relativistic density functional one still needs to start from quantum electrodynamics. How this is done will be discussed in Section 2.1.5. One

reason for starting from quantum electrodynamic is that this theory already includes the retardation of the electromagnetic interaction, which has not been discussed yet. It needs to be included because otherwise the relativistic description would be incomplete. Effects of retardation can be included within the Dirac theory by adding the so called Breit interaction [32] by hand, but starting from QED is of course more convenient. Therefore, a many electron Dirac-Hamiltonian and its possible treatment within the Hartree-Fock picture is not discussed here but can be found in Ref. [32].

2.1.4 Foundations of density functional theory

In this section, the non-relativistic formulation of density functional theory (DFT) is outlined. At first the basic ideas are discussed followed by a presentation of the fundamental theorems on which the entire theory relies together with their proofs. In the end the generalization to spin-dependent DFT is carried out. A discussion of how this theory can be extended to include relativity is outlined in Section 2.1.5.

The basic idea of density functional theory is to use the particle density as the central quantity instead of the wave function because the density depends only upon one spatial variable. This choice is reasonable because it turns out that the density contains all necessary information just like the wave function itself. For a normalized wave function of N particles, e.g. electrons, it is defined by the expectation value

$$n(\boldsymbol{r}) = \langle \Psi | \hat{n}\,(\boldsymbol{r}) | \Psi \rangle = N \int \mathrm{d}^3 r_2 ... \mathrm{d}^3 r_N \, |\Psi(\boldsymbol{r}, \boldsymbol{r}_2, ..., \boldsymbol{r}_N)|^2 \;, \tag{2.47}$$

where the electron density operator is given by

$$\hat{n}(\boldsymbol{r}) = \sum_{i=1}^{N} \delta(\boldsymbol{r} - \boldsymbol{r}_i) \;. \tag{2.48}$$

Originally, DFT is founded on the work of Thomas [39] and Fermi [40]. They introduced the first energy functional based on the electron density. An approximate form of the kinetic energy, that assumes the electrons to be non-interacting and homogeneously distributed, is employed and all effects of exchange and correlation are neglected. Later, Dirac proposed a local approximation for the exchange [41], which is still of great importance today (see Appendix A.3). In the total functional

$$\begin{aligned} E_{\mathrm{TF}}\,[n] = \frac{3}{10}\left(3\pi^2\right)^{2/3} \int \mathrm{d}^3 r \, n^{5/3}(\boldsymbol{r}) + \int \mathrm{d}\boldsymbol{r} \, V_{\mathrm{ext}}(\boldsymbol{r})\, n(\boldsymbol{r}) \\ + \frac{1}{2} \int \mathrm{d}^3 r \int \mathrm{d}^3 r' \, \frac{n(\boldsymbol{r})\, n(\boldsymbol{r}')}{|\boldsymbol{r} - \boldsymbol{r}'|} - \frac{3}{4}\left(\frac{3}{\pi}\right)^{1/3} \int \mathrm{d}^3 r \, n^{4/3}(\boldsymbol{r}) \;, \end{aligned} \tag{2.49}$$

the first part represents the kinetic energy, the second and third are the Coulomb interaction of the electron density with an external potential, e.g. the potential of the atomic cores in a solid, and the electrostatic repulsion between the electrons. The last one is the local approximation of the exchange energy. A variation of this density functional with respect to stationarity of the energy gives the ground state electron density. The resulting equations are more easy to solve compared to a many-body Schrödinger equation but the involved approximations are to crude to capture the essential physics.

The modern and general as well as rigorous formulation of DFT is based on the fundamental work of Hohenberg and Kohn [42]. Their work provides the central theorems and their proofs, which serve as the first exact foundation of DFT. The two central theorems can be stated as follows [31]:

Theorem I: For any system of interacting particles in an external potential $V_{\text{ext}}(\boldsymbol{r})$, the potential $V_{\text{ext}}(\boldsymbol{r})$ is determined uniquely, except for a constant, by the ground state particle density $n_0(\boldsymbol{r})$. Since the Hamiltonian is thus fully determined, except for a constant shift of energy, the many-body wave functions of all states (ground and excited) are determined. Therefore all properties of the system are completely determined by the ground state density $n_0(\boldsymbol{r})$.

Theorem II: A universal functional for the energy $F_{\text{HK}}[n]$ in terms of the density $n(\boldsymbol{r})$ can be defined, which is valid for any external potential $V_{\text{ext}}(\boldsymbol{r})$. For any particular $V_{\text{ext}}(\boldsymbol{r})$, the exact ground state energy of the system is the global minimum of the functional

$$E_{V_{\text{ext}}}[n] = F_{\text{HK}}[n] + \int \mathrm{d}^3 r \, V_{\text{ext}}(\boldsymbol{r}) \, n(\boldsymbol{r}) \,, \tag{2.50}$$

and the density $n(\boldsymbol{r})$ that minimizes the functional is the exact ground state density $n_0(\boldsymbol{r})$.

To proof the theorems a set of local one-particle potentials $\mathcal{V}$ is defined, for which each eigenvalue problem [4]

$$\hat{H}|\phi\rangle = (\hat{T} + \hat{V}_{\text{int}} + \hat{V}_{\text{ext}})|\phi\rangle = E|\phi\rangle, \quad \hat{V}_{\text{ext}} \in \mathcal{V} \tag{2.51}$$

gives a non-degenerated ground state for a system of N fermions. Here, $\hat{V}_{\text{int}}$ represents the inter-particle interactions. The ground state corresponding to $\hat{V}_{\text{ext}} \in \mathcal{V}$ is denoted by $|\psi_0\rangle$ and the associated eigenvalue of the ground state by E_{GS}. Therefore, one may write

$$\hat{H}|\psi_0\rangle = E_{\text{GS}}|\psi_0\rangle \,. \tag{2.52}$$

This implies that a set of ground states $\boldsymbol{\Psi}$ can be defined and the Schrödinger equation serves as a map

$$C : \mathcal{V} \to \boldsymbol{\Psi} \tag{2.53}$$

which is surjective by definition. For all ground states $\psi_0 \in \boldsymbol{\Psi}$ the prescription in Eq. (2.47) defines a second map

$$D : \boldsymbol{\Psi} \to \mathcal{N} \tag{2.54}$$

onto the set of ground state densities $\mathcal{N}$, which is again trivially surjective. The essential statement of the Hohenberg-Kohn theorems is that both maps are injective, therefore bijective and thus invertible. To fulfill this requirement it has to be shown that for two different potentials $\hat{V}_{\text{ext}}, \hat{V}'_{\text{ext}} \in \mathcal{V}$ which differ by more than a constant ($\hat{V}_{\text{ext}} \neq \hat{V}'_{\text{ext}} + \text{const}$), the map C gives two different ground states $|\psi_0\rangle, |\psi'_0\rangle \in \boldsymbol{\Psi}$. Starting from the Schrödinger equations

$$(\hat{T} + \hat{V}_{\text{int}} + \hat{V}_{\text{ext}})|\psi_0\rangle = E_{\text{GS}}|\psi_0\rangle \tag{2.55}$$

$$(\hat{T} + \hat{V}_{\text{int}} + \hat{V}'_{\text{ext}})|\psi'_0\rangle = E'_{\text{GS}}|\psi'_0\rangle \tag{2.56}$$

[4] The proofs of the Hohenberg-Kohn theorems as presented here follow the considerations given in Ref. [43].

and assuming that $|\psi_0\rangle = |\psi_0'\rangle$ the subtraction of both equations leads to $\hat{V}_{\text{ext}} - \hat{V}'_{\text{ext}} = E_{\text{GS}} - E'_{\text{GS}}$, because $\hat{V}_{\text{ext}}$ and $\hat{V}'_{\text{ext}}$ are multiplicative operators. This is an obvious contradiction because it implies that the potentials differ only by a constant shift. Therefore, the invertibility of the map C is proven and its inverse is denoted by

$$C^{-1} : \mathbf{\Psi} \to \mathcal{V} \,. \tag{2.57}$$

To proof the bijectivity of the map D, it has to be shown that if $|\psi_0\rangle \neq |\psi_0'\rangle$ then $n \neq n'$. The variation principle states that

$$E_{\text{GS}} = \langle\psi_0|\hat{H}|\psi_0\rangle < \langle\psi_0'|\hat{H}|\psi_0'\rangle = \langle\psi_0'|\hat{H}' + \hat{V}_{\text{ext}} - \hat{V}'_{\text{ext}}|\psi_0'\rangle = E'_{\text{GS}} + \int \mathrm{d}^3r\, n'(\boldsymbol{r})\Big[\hat{V}_{\text{ext}}(\boldsymbol{r}) - \hat{V}'_{\text{ext}}(\boldsymbol{r})\Big] \tag{2.58}$$

and with the corresponding argument based on E'_{GS} gives

$$E'_{\text{GS}} < E_{\text{GS}} + \int \mathrm{d}^3r\, n(\boldsymbol{r})\Big[\hat{V}'_{\text{ext}}(\boldsymbol{r}) - \hat{V}_{\text{ext}}(\boldsymbol{r})\Big] \,. \tag{2.59}$$

From the addition of both inequalities and the assumption that $n = n'$, the contradiction $E_{\text{GS}} + E'_{\text{GS}} < E'_{\text{GS}} + E_{\text{GS}}$ is obtained. This proofs the existence of the inverse map

$$D^{-1} : \mathcal{N} \to \mathbf{\Psi} \tag{2.60}$$

and therefore the existence of the full inverse map

$$(CD)^{-1} : \mathcal{N} \to \mathcal{V} \,. \tag{2.61}$$

Thereby, the first Hohenberg-Kohn theorem is rigorously proven.

□

In the second theorem a functional for the determination of the energy is established. For a specific system with external potential $\hat{V}_{\text{ext}}$ and ground state density n_0, this functional is defined by

$$E_{V_{\text{ext}}}[n_0] = \langle\psi_0[n_0]|\hat{T} + \hat{V}_{\text{int}} + \hat{V}_{\text{ext}}|\psi_0[n_0]\rangle \,. \tag{2.62}$$

As the states $|\psi_0\rangle$ are obtained from D^{-1} from the elements of $\mathcal{N}$, the property

$$E_0 < E_{V_{\text{ext}}}[n] \quad \text{for} \quad n \neq n_0 \quad \text{and} \quad E_0 = E_{V_{\text{ext}}}[n_0] \,, \tag{2.63}$$

where E_0 is the ground state energy, follows from the variation principle. The proof of the existence of D^{-1} does not assume a specific form of the potential. Therefore, this map is independent of the potential. The energy functional, which has to be minimized to find the ground state density is thus defined by

$$E_{\text{V}_{\text{ext}}}[n] = \langle\psi_0[n]|\hat{T} + \hat{V}_{\text{int}}|\psi_0[n]\rangle + \langle\psi_0[n]|\hat{V}_{\text{ext}}|\psi_0[n]\rangle \tag{2.64}$$

$$= F_{\text{HK}}[n] + \int \mathrm{d}^3r\, V_{\text{ext}}(\boldsymbol{r})\, n(\boldsymbol{r}) \,. \tag{2.65}$$

Here, the Hohenberg-Kohn functional $F_{\text{HK}}[n]$ is a universal functional which does not depend on the potential of the system because the kinetic energy and the Coulomb interaction between electrons can always be treated on the same footing. Only the interaction with the external potential, e.g. the nuclei, which is included in the second term varies for different systems. This immediately proofs the universality stated by the second theorem.

□

The Hohenberg-Kohn functional $F_{\mathrm{HK}}[n]$ can be split into two parts

$$F_{\mathrm{HK}}[n] = G[n] + \frac{1}{2}\int \mathrm{d}^3r \int \mathrm{d}^3r' \, \frac{n(\boldsymbol{r})\, n(\boldsymbol{r}')}{|\boldsymbol{r}-\boldsymbol{r}'|} \, , \tag{2.66}$$

where the second part is the naturally present classical Coulomb term describing the electrostatic interaction between electrons. For later purposes it is useful to note already here that the universal functional $G[n]$ can be decomposed into a kinetic energy term of a non-interacting system and an unknown part, which contains all effects of exchange and correlation [44]

$$G[n] = T_0[n] + E_{\mathrm{xc}}[n] \ . \tag{2.67}$$

Here, the fundamental drawback of DFT shows up because the missing piece in the expression for the energy functional is the exchange-correlation part, for which no analytical representation is known. In Appendix A.3 successful approximations of this functional, frequently used in practical calculations, are discussed.

There is another missing piece in the consideration above and this is the exact prescription for mapping the ground state density onto its corresponding ground state wave function. To gain the understanding of this problem some more details of the Hohenberg-Kohn theorems and their proofs have to be discussed.

The proofs of the Hohenberg-Kohn theorems as presented above suffer from two certain restrictions. The first is the assumption of a non-degenerated ground state. This lack can be easily cured by an extension of the proofs to degenerated ground states (see Ref. [43]). The second is associated with the assumption that a functional $\psi_0[n]$ is known which relates the ground state density with a ground state wave function. This implies that the functional $F_{\mathrm{HK}}[n]$ is only well defined for densities that belong to ground states of Hamiltonians with a particular external potential. Densities of this kind are called V-representable densities [45, 43]. All other densities, e.g. densities that belong to excited states, are excluded.

Problems arise from the restriction to V-representable densities. A practical implementation of the variation principle in the space of V-representable densities is not possible, because it turns out that not every reasonable well behaved and non-negative function is V-representable [43]. Therefore, a variation could only be carried out by employing additional constraints which are not well defined.

A more sufficient basis of DFT was given by Levy and Lieb [46, 47, 48]. They established a new definition of the functional associated with the kinetic and the internal energy contributions. This Levy-Lieb functional is of the form

$$F_{\mathrm{LL}}[n] = \min_{\psi \to n} \langle \psi | \hat{T} + \hat{V}_{\mathrm{int}} | \psi \rangle \tag{2.68}$$

where the notation $\psi \to n$ indicates that the search for the minimum is performed over all normalized N-particle wave functions, which are connected to one particular density n. In other words: Given a particular density $n(\boldsymbol{r})$, the wave function $|\psi\rangle$ that reproduces this density by $n(\boldsymbol{r}) = \langle \psi | \hat{n}(\boldsymbol{r}) | \psi \rangle$ and reveals the minimum of $\langle \psi | \hat{T} + \hat{V}_{\mathrm{int}} | \psi \rangle$ is the wave function associated with the density $n(\boldsymbol{r})$ in terms of the map D^{-1} (see Eq. 2.60). This implies that

$$F_{\mathrm{LL}}[n_0] = F_{\mathrm{HK}}[n_0] \tag{2.69}$$

for every V-representable density. Therefore, the Levy-Lieb functional is an extension of the Hohenberg-Kohn functional. In order to check if this extension is reasonable, it has to be proven that the total energy functional

$$E_{v_{\text{ext}}}[n] = F_{\text{LL}}[n] + \int \mathrm{d}^3 r \, V_{\text{ext}}(\boldsymbol{r}) \, n(\boldsymbol{r}) \tag{2.70}$$

exhibits a minimum at the correct ground state density n_0. This is immediately seen by employing the variational principle in the sense that

$$E_0 = \min_{\psi \to n} \langle \psi | \hat{T} + \hat{V}_{\text{int}} + \hat{V}_{\text{ext}} | \psi \rangle \; . \tag{2.71}$$

Therein, the search for the minimum over all N-particle wave functions can be split into two consecutive minima. Thus, one may write

$$\begin{aligned} E_0 =& \min_n \left[\min_{\psi \to n} \langle \psi | \hat{T} + \hat{V}_{\text{int}} + \hat{V}_{\text{ext}} | \psi \rangle \right] && (2.72) \\ =& \min_n \left[\min_{\psi \to n} \langle \psi | \hat{T} + \hat{V}_{\text{int}} | \psi \rangle + \int \mathrm{d}^3 r \, V_{\text{ext}}(\boldsymbol{r}) \, n(\boldsymbol{r}) \right] && (2.73) \\ =& \min_n \left[F_{\text{LL}}[n] + \int \mathrm{d}^3 r \, V_{\text{ext}}(\boldsymbol{r}) \, n(\boldsymbol{r}) \right] \; . && (2.74) \end{aligned}$$

This shows that the Levy-Lieb functional also leads to the correct ground state density.

The improvement of this formulation is that the new functional is defined over the space of all densities associated with an antisymmetric N-particle wave function which must not necessarily be the ground state wave function of a certain Hamiltonian. Such densities are called N-representable if the additional conditions

$$n(\boldsymbol{r}) \geq 0, \qquad \int \mathrm{d}^3 r \, n(\boldsymbol{r}) = N, \qquad \int \mathrm{d}^3 r \, |\nabla n(\boldsymbol{r})| < \infty \tag{2.75}$$

are fulfilled. These conditions are met by every reasonable function. An important fact about N-representable densities concerning a practicable application of DFT is pointed out by Gilbert [49], who showed that any N-representable density can be represented in terms of N orthonormal orbitals. Therefore, the formulation of Levy and Lieb points towards a practical application of DFT.

The basic idea of Levy and Lieb can be understood by considering the space of all N-particle wave functions to be partitioned into subspaces of wave functions, which are connected to a particular density. The first minimization is carried out in the subspaces and gives the $F_{\text{LL}}[n]$. The second minimization is carried out over all densities associated with the partitions of the wave function space and leads to the ground state density of the system under consideration. Therefore, it is in principle possible to carry out a variation by starting with an arbitrary, although somewhat reasonable, trial function. But as the definition of the Levy-Lieb functional still has only a theoretical meaning, a practical procedure is needed to carry out the variational search for the ground state density. How this can be achieved is shown in Section 2.1.6.

In order to apply DFT to magnetic systems, the spin degree of freedom needs to be taken into account. This is of great importance since all materials investigated in this work are

magnetic and therefore reveal a spin polarized ground state. The representation of the spin-dependent wave function as a bispinor is used (this is introduced in Section 2.1.2) and the corresponding operators acting on this bispinors are 2×2 matrices of the form

$$\hat{T}_{\alpha\beta} = -\delta_{\alpha\beta} \sum_{i=1}^{N} \nabla_i^2 \tag{2.76}$$

$$\hat{V}_{\alpha\beta}^{\mathrm{int}} = \sum_{i=1}^{N-1} \sum_{j=i+1}^{N} \frac{\delta_{\alpha\beta}}{|\boldsymbol{r}_i - \boldsymbol{r}_j|} \tag{2.77}$$

$$\hat{V}_{\alpha\beta}^{\mathrm{ext}} = \sum_{i=1}^{N} v_{\alpha\beta}\left(\boldsymbol{r}_i\right) \tag{2.78}$$

where the α and β are spin indices and atomic units are used ($e = m = \hbar = 1$). The density is now given by the matrix

$$n_{\alpha\beta}(\boldsymbol{r}) = N \sum_{\sigma_2,\ldots,\sigma_N} \int \mathrm{d}^3 r_2 \ldots \mathrm{d}^3 r_N \, \Psi(\boldsymbol{r}, \alpha; \boldsymbol{r}_2, \sigma_2; \ldots; \boldsymbol{r}_N, \sigma_N) \, \Psi(\boldsymbol{r}, \beta; \boldsymbol{r}_2, \sigma_2; \ldots; \boldsymbol{r}_N, \sigma_N) \ . \tag{2.79}$$

Starting from here, a similar procedure as for the spin independent case can be carried out. A calculation as in Eq. (2.58) leads to an inequality of the form

$$E'_{\mathrm{GS}} < E_{\mathrm{GS}} + \int \mathrm{d}^3 r \, n(\boldsymbol{r}) \left[v'_{\alpha\beta}(\boldsymbol{r}) - v_{\alpha\beta}(\boldsymbol{r}) \right] \tag{2.80}$$

and the corresponding inequality which gives a contradiction. With this, it is shown that the first Hohenberg-Kohn theorem is also valid for the spin-dependent case. The second theorem follows immediately from the original considerations with the additional condition that the number of electrons is conserved and given by

$$N = \sum_{\alpha,\beta} \int \mathrm{d}\boldsymbol{r} \, n_{\alpha\beta}\left(\boldsymbol{r}\right) \ . \tag{2.81}$$

Details of the considerations described above can be found in Ref. [50] as well as in Ref. [51] or in the book of Kübler [52].

Therewith, the foundations of non-relativistic DFT are introduced and a subsequent discussion of its relativistic generalization can be carried out in the next subsection.

2.1.5 Relativistic density functional theory

In this subsection, some basic facts and corresponding references of the formulation of relativistic density functional theory are given. As discussed in Section 2.1.3, the Dirac theory exhibits an intrinsic many-body character which leads to serious problems. These problems can be solved in the more developed relativistic quantum field theory which is known as the theory of quantum electrodynamics (a standard and often cited introduction to this topic can be found in Ref. [53]).

The first relativistic generalization of the Hohenberg-Kohn theory was reported by Rajagopal and Callaway (see Ref. [54]). But in this work the focus is on the formulation of a

spin-dependent theory rather than on relativistic effects. Later publications of Rajagopal (see Ref. [55]), Mac Donald and Vosko (see Ref. [56]) aimed on formulating an explicitly relativistic theory. All derivations are based on quantum electrodynamics (QED) which guarantees that the relativistic formulation of DFT relies on a solid basis because QED is the theory of choice for the relativistic description of interacting electrons. It includes e.g. the retardation of the interaction between the electrons by describing it as being mediated by photons moving with the velocity of light. But the quantization of the electric field that leads to the concept of photons is neglected in relativistic DFT because this simplifies the involved derivations considerably and is not necessary for the description of the electronic structure of condensed mater. In addition, the interaction with the nucleus is still treated as an interaction with an instantaneous external potential. This remains reasonable in terms of the Born-Oppenheimer approximation.

The fundamental difference of relativistic DFT compared to non-relativistic DFT is that it naturally becomes a current density functional theory (CDFT) in terms of the relativistic four-current that includes the particle density and the three components of the current density [57]. As one is interested in stationary problems the current is assumed to be independent of time.

Following the assumption of stationarity, the proof procedure of Hohenberg and Kohn can be applied onto the four-current density in exactly the same manner [54, 55]. This procedure is now sketched in the form proposed in Ref. [43]. Two maps connecting the external potential with the wave function and the wave function with the density as in Section 2.1.4 have to be introduced. These maps are proven to be surjective and therefore invertible. The first map is now the one that maps a given external four potential A^{μ}_{ext} onto the ground state of an N-electron system $|\Psi_{\text{g}}\rangle$ denoted by

$$C : \{A^{\mu}_{\text{ext}}\} \rightarrow \{|\Psi_{\text{g}}\rangle\} \tag{2.82}$$

where the curly brackets indicate that this is a map between the two spaces of external potentials and the corresponding ground states (compare to $\mathbf{\Psi}$, $\mathcal{V}$ in Section 2.1.4). The map C is given by the stationary eigenvalue problem

$$\hat{H}_{\text{QED}}(A)\,|\Psi_{\text{g}}\rangle = E_g(A)\,|\Psi_{\text{g}}\rangle \tag{2.83}$$

which is no longer valid in a Hilbert space but in a Fock space [18] because in QED particles can be created and annihilated. As the quantization of the electromagnetic field is neglected here, the implications of the QED can be fully absorbed in a Hamiltonian acting on wave functions in Fock space (for details see Ref. [43] and the references therein).

The second map is the one that maps the ground state onto the corresponding four-current density $J^{A}_{\mu}(\boldsymbol{r})$

$$D : \{|\Psi_{\text{g}}\rangle\} \rightarrow \{J^{A}_{\mu}\,(\boldsymbol{r})\} \tag{2.84}$$

which is given by the expectation value

$$J^{A}_{\mu}(\boldsymbol{r}) = \langle\Psi_{\text{g}}|\hat{j}_{\mu}(\boldsymbol{r})|\Psi_{\text{g}}\rangle\,. \tag{2.85}$$

Here, $\hat{j}_{\mu}$ are the components of the four-current operator

$$\hat{j} = \begin{pmatrix} c\hat{\rho} \\ \hat{j}_x \\ \hat{j}_y \\ \hat{j}_z \end{pmatrix}\,, \tag{2.86}$$

where the electron density operator is denoted by $\hat{\rho}$ and the $\hat{j}_i$ are the cartesian components of the current operator. A simple repetition of the Hohenberg-Kohn procedure proofs the invertibility of these maps as well as the existence of an energy functional which is given by

$$\langle \Psi_\mathrm{g} | \hat{H}_\mathrm{QED}\,(A) | \Psi_\mathrm{g} \rangle = E_A\left[J^A\right] = F\left[J^A\right] + \int \mathrm{d}^3 r\, J^A_\mu(\boldsymbol{r})\, A^\mu_\mathrm{ext}(\boldsymbol{r})\ . \tag{2.87}$$

This proofs the existence of a relativistic generalization of the Hohenberg-Kohn theory. It is discussed in Section 2.1.7 how a couple of additional considerations lead to a relativistic density functional theory (RDFT) which is analogue to the standard DFT and no longer a current density theory.

2.1.6 Non-relativistic Kohn-Sham theory

In order to use density functional theory in practical calcualtions, a scheme is needed that allows the direct calculation of the ground state density. Such a scheme was proposed by Kohn and Sham [44]. The idea of their approach is to define a system of non-interacting particles exposed to a local single particle potential such that the ground state density of this auxiliary system equals the ground state density of the interacting system under consideration. The auxiliary system is given in terms of the Hamiltonian

$$\hat{H}_a = \hat{T}_a + \hat{V}_a\,, \tag{2.88}$$

which is assumed to have a non-degenerated ground state (for simplicity the spin degree of freedom is again omitted here). According to Hohenberg and Kohn, the existence of a unique energy functional

$$E_a\,[n] = T_a\,[n] + \int \mathrm{d}^3 r\, V_a(\boldsymbol{r})\, n(\boldsymbol{r}) \tag{2.89}$$

is guaranteed and a variation of this functional leads to the ground state density $n_a(\boldsymbol{r})$ of the auxiliary system.

The central statement of Kohn and Sham is that a potential $V_a(\boldsymbol{r})$ exists, such that the density $n_a(\boldsymbol{r})$ of this specific auxiliary system equals the density of the interacting system, $n(\boldsymbol{r}) = n_a(\boldsymbol{r})$. The case that the ground state density of an interacting system is equal to that of a non-interacting system is called non-interacting-V-representability [43]. Therefore, Kohn-Sham theory assumes the density of the system under consideration to be non-interacting-V-representable. Unfortunately, this assumption has not been rigorously proven in general, but the success of the Kohn-Sham theory has led to a wide acceptance.

As the particles of the auxiliary system are non-interacting, its density and therefore the density of the interacting system can be expressed by

$$n(\boldsymbol{r}) = n_a(\boldsymbol{r}) = \sum_{i=1}^{N} \left|\phi_i(\boldsymbol{r})\right|^2\ , \tag{2.90}$$

where the $\phi_i(\boldsymbol{r})$ are the lowest N single particle states, obtained from the Schrödinger equation

$$\left(-\frac{\hbar^2}{2m}\nabla^2 + V_a(\boldsymbol{r})\right)\phi_i(\boldsymbol{r}) = \epsilon_i \phi_i(\boldsymbol{r}) \qquad , \qquad \epsilon_1 \leq \epsilon_2 \leq \ldots\,, \tag{2.91}$$

which is usually called Kohn-Sham equation. The fermionic property of the particles is considered within the potential $V_a(\boldsymbol{r})$ by assuming that the N particles occupy the N lowest eigenstates of the Schrödinger equation without occupying an eigenstate twice or more. Therefore, the eigenstates determine the density directly as shown in Eq. (2.90). There is no need to construct an antisymmetric many-body wave function from which the density is obtained because the exchange is included in the potential $V_a(\boldsymbol{r})$ and therefore the eigenfunctions of Eq. (2.91) contain all information needed to obtain the correct fermionic density by summing up the squares of their absolute values.

As the potential $V_a(\boldsymbol{r})$ generates the density $n(\boldsymbol{r})$, the uniqueness of $V_a(\boldsymbol{r})$ follows from the Hohenberg-Kohn theorems. This includes that the single particle eigenstates of Eq. (2.91) are functionals of the density $n(\boldsymbol{r})$ and one may write

$$\phi_i(\boldsymbol{r}) = \phi_i([n], \boldsymbol{r})\,. \tag{2.92}$$

Therefore, it follows that the non-interacting kinetic energy

$$T_a\,[n] = \sum_{i=1}^{N} \int \mathrm{d}^3 r\, \phi_i^*(\boldsymbol{r}) \left(-\frac{\hbar^2}{2m}\nabla^2\right) \phi_i(\boldsymbol{r}) \tag{2.93}$$

is also a unique functional of the density $n\,(\boldsymbol{r})$. Thus, it is possible to calculate the ground state density of the interacting system by determining the eigenfunctions of a Schödinger equation of a non-interacting system with a particular external potential $V_a(\boldsymbol{r})$. The remaining question is how this particular potential can obtained.

The decomposition of the general energy functional, introduced in Section 2.1.4 is given by

$$E_{\mathrm{V_{ext}}}\,[n] = G\,[n] + \frac{1}{2}\int \mathrm{d}^3 r \int \mathrm{d}^3 r'\, \frac{n(\boldsymbol{r})n(\boldsymbol{r}')}{|\boldsymbol{r}-\boldsymbol{r}'|} + \int \mathrm{d}^3 r\, V_{\mathrm{ext}}(\boldsymbol{r})n(\boldsymbol{r}) \tag{2.94}$$

where the functional $G\,[n] = T_0\,[n] + E_{\mathrm{xc}}\,[n]$ contains the kinetic energy of non-interacting electrons and a correction due to many-body effects, which is called the exchange-correlation energy. A variation of this functional with respect to the density requires that

$$\frac{\delta E_{\mathrm{V_{ext}}}\,[n]}{\delta n(\boldsymbol{r})} = \frac{\delta T_0\,[n]}{\delta n(\boldsymbol{r})} + \frac{\delta E_{\mathrm{xc}}\,[n]}{\delta n(\boldsymbol{r})} + \int \mathrm{d}^3 r'\, \frac{n(\boldsymbol{r}')}{|\boldsymbol{r}-\boldsymbol{r}'|} + V_{\mathrm{ext}}(\boldsymbol{r}) = 0\,. \tag{2.95}$$

On the other hand, a variation of the energy functional of the auxiliary system (see Eq. (2.89)) requires

$$\frac{\delta E_{\mathrm{V_{ext}}}\,[n]}{\delta n(\boldsymbol{r})} = \frac{\delta T_a\,[n]}{\delta n(\boldsymbol{r})} + V_{\mathrm{a}}(\boldsymbol{r}) = 0\,. \tag{2.96}$$

As $T_a\,[n] = T_0\,[n]$, the potential of the auxiliary system is given by

$$V_{\mathrm{a}}(\boldsymbol{r}) = \int \mathrm{d}^3 r'\, \frac{n(\boldsymbol{r}')}{|\boldsymbol{r}-\boldsymbol{r}'|} + V_{\mathrm{ext}}(\boldsymbol{r}) + \frac{\delta E_{\mathrm{xc}}\,[n]}{\delta n(\boldsymbol{r})}\,. \tag{2.97}$$

Equation (2.97) together with (2.91) and (2.90) provide a self-consistent set of equations for the determination of the ground state density of the interacting system of interest. An initial guess for the density gives the potential and by solving the associated Kohn-Sham equation a new density can be calculated and a new cycle can be started. Such a self-consistent calculation would, in principle, be exact if the exchange-correlation contribution

were known. As already mentioned in Section 2.1.4, no exact exchange-correlation functional exists and only approximations are used in practical calculations.

In addition, as the self-consistent calculations have to be carried out numerically, efficient algorithms are needed to achieve reasonable convergence. Two such methods are discussed in Section 2.2 and Appendix A.5. But first the relativistic formulation of the Kohn-Sham theory is discussed.

2.1.7 Relativistic Kohn-Sham theory

In the last section the non-relativistic version of the Kohn-Sham theory is discussed. This theory gives the possibility to use DFT in practical calculations of the electronic structure of real materials. In Section 2.1.5 the existence and uniqueness of a relativistic Hohenberg-Kohn functional based on the theory of quantum electrodynamics is proven. Now, the development of the relativistic Kohn-Sham theory is outlined. The derivations are much more involved and therefore can only be sketched (details can be found in Ref. [58] and references therein).

The considerations in Section 2.1.5 lead to a current density functional theory. Therefore, the relativistic four-current density is the central quantity in this theory. It can be shown that the considerations of Kohn and Sham can be adopted in this case leading to the following equation [57]

$$\left[c\boldsymbol{\alpha}\cdot\left(\frac{\hbar}{i}\nabla+\frac{e}{c}\boldsymbol{A}_{\mathrm{eff}}(\boldsymbol{r})\right)+\beta mc^2+V_{\mathrm{eff}}(\boldsymbol{r})\right]\Psi_i(\boldsymbol{r})=\epsilon_i\Psi_i(\boldsymbol{r}) \tag{2.98}$$

which is the Dirac equation of a non-interacting particle in a general external effective vector and scalar potential defined by

$$V_{\mathrm{eff}}(\boldsymbol{r})=-e\left[V^0_{\mathrm{ext}}(\boldsymbol{r})+\frac{1}{c}\int \mathrm{d}^3r'\,\frac{J^0(\boldsymbol{r}')}{|\boldsymbol{r}-\boldsymbol{r}'|}+c\frac{\partial E_{\mathrm{xc}}[J^\mu]}{\partial J^0(\boldsymbol{r})}\right], \tag{2.99}$$

$$\boldsymbol{A}_{\mathrm{eff}}(\boldsymbol{r})=-e\left[\boldsymbol{A}_{\mathrm{ext}}(\boldsymbol{r})+\frac{1}{c}\int \mathrm{d}^3r'\,\frac{\boldsymbol{J}(\boldsymbol{r}')}{|\boldsymbol{r}-\boldsymbol{r}'|}+c\frac{\partial E_{\mathrm{xc}}[J^\mu]}{\partial \boldsymbol{J}(\boldsymbol{r})}\right]. \tag{2.100}$$

The electronic four-current density $J^\mu=(J^0,J^k)$ is defined by summing over the four-component spinors

$$\begin{aligned}J^0(\boldsymbol{r})&=-ec\sum_i\Psi_i^\dagger(\boldsymbol{r})\Psi_i(\boldsymbol{r}),\\ J^k(\boldsymbol{r})&=-ec\sum_i\Psi_i^\dagger(\boldsymbol{r})\beta\alpha^k\Psi_i(\boldsymbol{r}).\end{aligned} \tag{2.101}$$

This simple summation is justified because the spinors $\Psi_i(\boldsymbol{r})$ are the solutions for the non-interacting auxiliary system (see Section 2.1.6 for comparison). The component J^0/c includes the electronic charge density and the other three are the spatial components of the electronic current density. Equation (2.98) together with (2.99) and (2.100) form a self-consistent set which is a relativistic analogue of the Kohn-Sham equations. Unfortunately, this general scheme leads to problems that prevent a practical implementation [58]. Therefore, approximative versions of a relativistic spin density functional theory have been derived by various authors. In the following the main features of how this is achieved are outlined.

Rajagopal and Callaway [54] applied the so called Gordon decomposition [32] to separate the orbital and spin part of the current density. As the spin part can be properly separated

from the orbital part and as the contribution of the latter to magnetic properties is small, it is neglected. By introducing the magnetization density

$$\boldsymbol{m} = -\mu_{\mathrm{B}} \sum_i \Psi_i^\dagger(\boldsymbol{r}) \beta \boldsymbol{\sigma} \Psi_i(\boldsymbol{r}) \,, \tag{2.102}$$

where $\boldsymbol{\sigma}$ is the vector of Pauli matrices, the coupling of the spin part of the current density to the effective potential is expressed by $-\boldsymbol{m} \cdot \boldsymbol{B}_{\mathrm{eff}}$. Here, an effective magnetic field $\boldsymbol{B}_{\mathrm{eff}}$ corresponding to the vector potential $\boldsymbol{A}_{\mathrm{eff}}$ is introduced. This yields the Kohn-Sham-Dirac equation

$$\left[\frac{c\hbar}{i} \boldsymbol{\alpha} \cdot \nabla + \beta m c^2 + V_{\mathrm{eff}}(\boldsymbol{r}) + \beta \boldsymbol{\sigma} \cdot \boldsymbol{B}_{\mathrm{eff}}(\boldsymbol{r}) \right] \Psi_i(\boldsymbol{r}) = \epsilon_i \Psi_i(\boldsymbol{r}) \,, \tag{2.103}$$

which is analogous to the non-relativistic theory. The effective magnetic field is given by

$$\boldsymbol{B}_{\mathrm{eff}}(\boldsymbol{r}) = \boldsymbol{B}_{\mathrm{ext}}(\boldsymbol{r}) + \frac{\partial E_{\mathrm{xc}}\left[n, \boldsymbol{m}\right]}{\partial \boldsymbol{m}(\boldsymbol{r})} \tag{2.104}$$

and the effective scalar potential is the same as in Eq. (2.99). This set of equations depends only on the charge and magnetization density and no longer on the current density.

Now, all tools to perform self-consistent relativistic DFT calculations are developed. Relativistic approximations of the exchange-correlation functional are outlined in Appendix A.4.

2.1.8 Practical solution of the Kohn-Sham equations

In the previous subsections the foundation of DFT is introduced. In this subsection a method to carry out practical calculations is presented. Therefore, schemes to solve the Kohn-Sham equation numerically have to be developed. The basic idea of such numerical schemes is to expand the wave function in a certain basis set and to determine the coefficients of this expansion by carrying out a matrix diagonalization. As the basis set has to be finite in practice, it has to be chosen in an appropriate way, e.g., localized functions are usually used for electronic structure calculations of molecules. Here, the focus is on methods that are suitable for the calculation of the electronic structure of solids. The periodicity of solids allows to expand the wave function in a plane wave basis set. For a discussion of the various implications of periodicity the reader is referred to Ref. [31] where the following derivation is adopted from.

The first step to start the DFT calculation is to guess an initial potential V_{eff}. In the case of a solid the periodicity (in general the symmetry) of the system under consideration should be incorporated. Afterwards, the Kohn-Sham equations

$$\hat{H}_{\mathrm{eff}}(\boldsymbol{r}) \psi_i(\boldsymbol{r}) = \left[-\frac{\hbar^2}{2m} \nabla^2 + V_{\mathrm{eff}}(\boldsymbol{r}) \right] \psi_i(\boldsymbol{r}) = \epsilon_i \psi_i(\boldsymbol{r}) \,. \tag{2.105}$$

introduced in Section 2.1.6 have to be solved. Due to the periodicity the wave function $\psi_i(\boldsymbol{r})$ is now expanded in a Fourier series

$$\psi_i(\boldsymbol{r}) = \frac{1}{\sqrt{\Omega}} \sum_{\boldsymbol{q}} c_{i,\boldsymbol{q}} \exp\left(i \boldsymbol{q} \cdot \boldsymbol{r}\right) = \frac{1}{\sqrt{\Omega}} \sum_{\boldsymbol{q}} c_{i,\boldsymbol{q}} |\boldsymbol{q}\rangle \tag{2.106}$$

where Ω is a large but finite volume. This basis set of plane wave functions is orthonormal and discrete. Inserting this expansion into Eq. (2.105) and multiplying from the left by $\langle \boldsymbol{q}'|$ one obtains

$$\sum_{\boldsymbol{q}} \langle \boldsymbol{q}'|\hat{H}_{\text{eff}}|\boldsymbol{q}\rangle c_{i,\boldsymbol{q}} = \epsilon_i \sum_{\boldsymbol{q}} \langle \boldsymbol{q}'|\boldsymbol{q}\rangle c_{i,\boldsymbol{q}} = \epsilon_i c_{i,\boldsymbol{q}'} \,. \tag{2.107}$$

The matrix elements of the kinetic energy part of $\hat{H}_{\text{eff}}$ can be evaluated immediately:

$$\langle \boldsymbol{q}'| - \frac{\hbar^2}{2m}\nabla^2|\boldsymbol{q}\rangle = \frac{\hbar^2}{2m}|q^2|\delta_{\boldsymbol{q},\boldsymbol{q}'} \,. \tag{2.108}$$

In order to calculate the potential part, one utilizes that the effective potential naturally exhibits the lattice periodicity. Therefore, it can also be expressed as a sum of Fourier components

$$V_{\text{eff}}(\boldsymbol{r}) = \sum_m \tilde{V}_{\text{eff}}(\boldsymbol{G}_m) \exp(i\boldsymbol{G}_m \cdot \boldsymbol{r}) \tag{2.109}$$

where the $\boldsymbol{G}_m$ are reciprocal lattice vectors. The coefficients $\tilde{V}_{\text{eff}}$ are given by

$$\tilde{V}_{\text{eff}}(\boldsymbol{G}) = \frac{1}{\Omega_{\text{cell}}} \int_{\Omega_{\text{cell}}} \mathrm{d}^3 r V_{\text{eff}}(\boldsymbol{r}) \exp(-i\boldsymbol{G} \cdot \boldsymbol{r}) \,, \tag{2.110}$$

and Ω_{cell} is the volume of the primitive unit cell. Hence, the matrix elements of the potential are given by

$$\langle \boldsymbol{q}'|V_{\text{eff}}|\boldsymbol{q}\rangle = \sum_m \tilde{V}_{\text{eff}}(\boldsymbol{G}_m)\delta_{\boldsymbol{q}'-\boldsymbol{q},\boldsymbol{G}_m} \,. \tag{2.111}$$

It is noted that these matrix elements are only finite if $\boldsymbol{q}$ and $\boldsymbol{q}'$ differ by a reciprocal lattice vector and are zero otherwise.

By defining $\boldsymbol{q} = \boldsymbol{k} + \boldsymbol{G}_m$ and $\boldsymbol{q}' = \boldsymbol{k} + \boldsymbol{G}_{m'}$ which differ by the reciprocal lattice vector $\boldsymbol{G}_{m''} = \boldsymbol{G}_m - \boldsymbol{G}_{m'}$, the above Kohn-Sham equation (2.105) can be rewritten as a matrix equation

$$\sum_{m'} H_{m,m'}(\boldsymbol{k}) c_{i,m'}(\boldsymbol{k}) = \epsilon_i(\boldsymbol{k}) c_{i,m}(\boldsymbol{k}) \tag{2.112}$$

where the matrix elements $H_{m,m'}$ are defined by

$$H_{m,m'}(\boldsymbol{k}) = \langle \boldsymbol{k} + \boldsymbol{G}_m|\hat{H}_{\text{eff}}|\boldsymbol{k} + \boldsymbol{G}_{m'}\rangle = \frac{\hbar^2}{2m}|\boldsymbol{k} + \boldsymbol{G}_m|^2\delta_{m,m'} + \tilde{V}_{\text{eff}}(\boldsymbol{G}_m - \boldsymbol{G}_{m'}) \,. \tag{2.113}$$

This equation determines a discrete set of of eigenvectors labeled by $i = 1, 2, ...$ for every k-point in the Brillouin zone. As the components of the eigenvectors are the expansion coefficients, the wave function is fully determined. In other words, the whole band structure $E_i(\boldsymbol{k})$ of a solid can be calculated by solving the eigenvalue problem (2.112) for each k-point. In practice, only a special set or mesh of k-point is chosen to reduce the numerical effort to a manageable amount (see Ref. [31]). The wave functions determine the density which allows to calculate the effective potential of the next self-consistent step.

The derivation above outlines the basic idea of how the numerical solution of the Kohn-Sham equations is turned into a solution of a matrix equation. Such matrix equations can be solved numerically with efficient algorithms. In practice some modifications of the basis set are made to make the calculations of the electronic structure of solids more efficient and accurate. For details about the different methods the reader is referred to the book of Martin

[31] and Kübler [52]. In Appendix A.5 one of those schemes is outlined which is the so called projector augmented plane wave method because this method is implemented in the Vienna *ab initio* simulation Package (VASP) [59, 60], commonly used to obtain results presented in this treatise.

2.2 Multiple scattering theory

In this section the multiple scattering theory (MST) is introduced because it is the basis of many of the calculations performed to obtain the results of this thesis. It provides an alternative approach for electronic structure calculations based on density functional theory. The approaches discussed in the last section are based on the solution of the Kohn-Sahm equation where wave functions are the central objects. In MST the Green's function $G(\boldsymbol{r}, \boldsymbol{r}')$ of the system is the central object. Vividly speaking, $G(\boldsymbol{r}, \boldsymbol{r}')$ describes how an electron propagates from point $\boldsymbol{r}$ to $\boldsymbol{r}'$ in the system under consideration. Therefore, it is closely related to the scattering properties of the system. In addition, the particle density can be directly evaluated from the Green's function. This establishes the possibility to employ $G(\boldsymbol{r}, \boldsymbol{r}')$ in DFT calculations.

The MST calculation consists of three basic parts: In the first part the single-site scattering problem of electrons scattered at a certain potential located in free space is solved. The second part is the evaluation of the so called structure constants which contain the information about how the scattering potentials are arranged in space. In other words: the solution of the scattering problem of a single potential and the evaluation of how the scatterers are distributed in space is treated independently. In a third step both informations are combined to calculate the so called scattering path operator. This operator contains all information of the electronic system and is closely related to the Green's function and therefore to the electron density. DFT links the calculated density to the potential including Coulomb and exchange-correlation contributions.

From these steps a self-consistent cycle can be constructed which is employed for electronic structure calculations and is called Korringa-Kohn-Rostoker (KKR) method [61, 62]. This method is of particular interest because it allows to derive properties from the Green's function which are not easily accessible in wave function based methods.

But the great advantage arising from the distinct treatment of single-site scattering and structure evaluation is that the KKR method can be applied to various geometries. Although the first realizations were designed to handle the problem of translational invariant systems the method can be applied to systems with lower or even no translational symmetry like surfaces or nanoparticles.

In addition, the KKR method allows to treat structural as well as magnetic disorder on a mean field basis. This is a striking advantage, because the computational demand for the description of disorder within a wave function based approach is much higher.

In the following subsections the foundations of MST are introduced. The description of the theory follows the book of Zabloudil *et al.* [63] but other descriptions can be found in Ref. [64] and [65].

2.2.1 Resolvents and Green's functions

Before the basics of MST can be discussed, the concept of resolvents and Green's functions has to be introduced. Therefore, the definitions and the most important properties of these

objects are presented in this section.

For a linear hermitian and time-independent operator, e.g., the Hamiltonian $\hat{H}$ of the system under consideration, with the corresponding eigenvalue equation

$$\hat{H}|\psi_i\rangle = \epsilon_i|\psi_i\rangle\,, \tag{2.114}$$

the associated resolvent is defined by

$$\hat{G}(z) = (z - \hat{H})^{-1} \tag{2.115}$$

where $z = \epsilon - i\delta$ is a complex number. As linear operators can be written in terms of their eigenfunctions and eigenvalues the Hamiltonian can be expressed by

$$\hat{H} = \sum_i \epsilon_i|\psi_i\rangle\langle\psi_i| \tag{2.116}$$

which means that the operator is represented by all projections onto the complete system of eigenfunctions weighted by the corresponding eigenvalues. A similar representation can be derived for the resolvent. As the resolvent is a function of the Hamiltonian they share the same system of eigenvectors, because as the Hamiltonian fulfills Eq. (2.114), any well behaved function F fulfills $F(\hat{H})|\psi_i\rangle = F(\epsilon_i)\,|\psi_i\rangle$ (a short justification of this statement is given in Appendix A.7). Therefore, the resolvent satisfies

$$\hat{G}(z)|\psi_i\rangle = (z - \hat{H})^{-1}|\psi_i\rangle = (z - \epsilon_i)^{-1}|\psi_i\rangle \tag{2.117}$$

which leads to the following representation

$$\hat{G}(z)|\Psi\rangle = \frac{1}{z - \hat{H}}|\Psi\rangle = \sum_i \frac{|\psi_i\rangle\langle\psi_i|}{z - \epsilon_i}|\Psi\rangle\ . \tag{2.118}$$

This representation can be directly applied to derive the Green's function $G(z, \boldsymbol{r}, \boldsymbol{r}')$ which is the configuration space representation of the resolvent and is given by

$$G(z, \boldsymbol{r}, \boldsymbol{r}') = \langle\boldsymbol{r}|\hat{G}(z)|\boldsymbol{r}'\rangle = \sum_i \frac{\langle\boldsymbol{r}|\psi_i\rangle\langle\psi_i|\boldsymbol{r}'\rangle}{z - \epsilon_i} = \sum_i \frac{\psi_i(\boldsymbol{r})\psi_i^*(\boldsymbol{r}')}{z - \epsilon_i}\ . \tag{2.119}$$

Here, the common notation $\langle\boldsymbol{r}|\psi_i\rangle = \psi_i(\boldsymbol{r})$ and $\langle\psi_i|\boldsymbol{r}'\rangle = \psi_i^*(\boldsymbol{r}')$ is employed. Therewith, the Green's function can be evaluated from the eigenvectors and eigenvalues of the underlying Hamiltonian.

In other contexts, it is also usual to define the configuration space Green's function directly from the following equation

$$(z - \hat{H})G(z, \boldsymbol{r}, \boldsymbol{r}') = \delta(\boldsymbol{r} - \boldsymbol{r}') \tag{2.120}$$

which is derived from the completeness relation $\sum_i \psi_i(\boldsymbol{r})\psi_i^*(\boldsymbol{r}') = \delta(\boldsymbol{r} - \boldsymbol{r}')$ by expanding the left hand side with $z - \epsilon_i$.

To finish the discussion, some commonly used properties of the resolvent and its Green's function are summarized. The first important property concerns the complex conjugation of the argument which leads to

$$\hat{G}(z^*) = \hat{G}^\dagger(z)\,, \tag{2.121}$$

where $\hat{G}^\dagger$ denotes the hermitian conjugate of the resolvent. The side-limits of the resolvent are defined by

$$\lim_{|\delta|\to 0} \hat{G}(z) = \begin{cases} \hat{G}^+(\epsilon); \delta > 0 \\ \hat{G}^-(\epsilon); \delta < 0 \end{cases} \tag{2.122}$$

and are connected by the property

$$\hat{G}^+(\epsilon) = \hat{G}^{-\,\dagger}(\epsilon) \; . \tag{2.123}$$

The Green's functions of the two side-limits $G^+(\epsilon, \boldsymbol{r}, \boldsymbol{r}')$ and $G^-(\epsilon, \boldsymbol{r}, \boldsymbol{r}')$ are called the advanced and retarded Green's function. The most important property concerning the KKR formalism is that the Green's function is connected to the particle density by

$$n(\boldsymbol{r}) = -\frac{1}{\pi} \mathrm{Im} \int \mathrm{d}\epsilon \, G^+(\epsilon, \boldsymbol{r}, \boldsymbol{r}) \; . \tag{2.124}$$

Therewith, the basic facts about resolvents and Green's functions are present. In the next subsection two very essential equations of common use in scattering and perturbation theory are introduced.

2.2.2 The Dyson and the Lippmann-Schwinger equation

In this subsection the Dyson and the Lippmann-Schwinger equation are introduced. The first is a central equation of many-body theory and the latter the central equation of scattering theory. They are both related because they connect the solution of systems without interaction to associated systems with interaction. This relies on perturbation theory where the solution of an interacting system can be formulated as a sum of the solution of the non-interacting system and subsequent terms that treat the interaction analogous to a series expansion. In terms of scattering theory it means that in a stationary scattering situation the full wave function is a sum of the incident and scattered wave. The following is adopted from Ref. [63] and [64] where a more detailed overview and additional references are given.

If the Hamiltonian $\hat{H}$ of a system is given in terms of an unperturbed Hamiltonian $\hat{H}_0$, which is usually called the free system, and a perturbation part $\hat{V}$

$$\hat{H} = \hat{H}_0 + \hat{V} \, , \tag{2.125}$$

the associated resolvents

$$\hat{G}(z) = (z - \hat{H}) \;\; , \;\; \hat{G}_0(z) = (z - \hat{H}_0) \tag{2.126}$$

are coupled by the self-consistent Dyson equation ,

$$\hat{G}(z) = \hat{G}_0(z) + \hat{G}(z)\hat{V}\hat{G}_0(z) \; . \tag{2.127}$$

The derivation of this equation can be reproduced in a few steps. Starting from $\hat{G}(z)$ an expansion by $z - \hat{H}_0$ gives

$$\begin{aligned} \hat{G}(z) =& \frac{1}{z - \hat{H}_0 - \hat{V}} = \frac{z - \hat{H}_0}{z - \hat{H}_0} \left(\frac{1}{z - \hat{H}_0 - \hat{V}} \right) \\ =& \frac{1}{z - \hat{H}_0} \left(\frac{z - \hat{H}_0 - \hat{V} + \hat{V}}{z - \hat{H}_0 - \hat{V}} \right) = \hat{G}_0(z) \left(1 + \frac{\hat{V}}{z - \hat{H}_0 - \hat{V}} \right) \\ =& \hat{G}_0(z)(1 + \hat{V}\hat{G}(z)) \; . \end{aligned} \tag{2.128}$$

The Dyson equation can be iteratively solved by subsequent insertion of the right hand side into $\hat{G}$ on the same side. This results in the expansion

$$\hat{G}(z) = \hat{G}_0(z) + \hat{G}_0(z)\hat{V}\hat{G}_0(z) + \hat{G}_0(z)\hat{V}\hat{G}_0(z)\hat{V}\hat{G}_0(z) + ... \ . \tag{2.129}$$

Rearranging the free resolvents

$$\hat{G}(z) = \hat{G}_0(z) + \hat{G}_0(z)(\hat{V} + \hat{V}\hat{G}_0(z)\hat{V} + ...)\hat{G}_0(z) \tag{2.130}$$

together with the definition of the T-operator

$$\hat{T}(z) = \hat{V} + \hat{V}\hat{G}_0(z)\hat{V} + \hat{V}\hat{G}_0(z)\hat{V}\hat{G}_0(z)\hat{V} + ... \tag{2.131}$$

leads to a reformulation of the Dyson equation in the following form

$$\hat{G}(z) = \hat{G}_0(z) + \hat{G}_0(z)\hat{T}(z)\hat{G}_0(z) \ . \tag{2.132}$$

An analogous procedure leads to a self-consistent equation of the T-operator given by

$$\hat{T}(z) = \hat{V} + \hat{V}\hat{G}_0(z)\hat{T}(z) \ . \tag{2.133}$$

As it is reasonable to assume the perturbation operator $\hat{V}$ to be hermitian, the T-operator has similar properties as the resolvent concerning the conjugation of the argument z and the side limits (see Eq. (2.121) and (2.123)). The T-operator also contains all physical information about the system under consideration. It should be noted that the equations above hold for any representation (Green's function) of the resolvent and therefore lead to a corresponding T-function.

A physical interpretation of the resolvent and the corresponding Green's function should be given here in order to gain a more intuitive understanding of multiple scattering theory. The Green's function $G(\epsilon, \boldsymbol{r}, \boldsymbol{r}')$ which is often called propagator contains information about the combined probability that a particle in a stationary state at energy ϵ is sometimes located at $\boldsymbol{r}$ and sometimes at $\boldsymbol{r}'$. It is more intuitive to describe the same for a time-dependent Green's function $G(\epsilon, \boldsymbol{r}, \boldsymbol{r}, t - t')$, which gives information about the probability that a particle located at $\boldsymbol{r}$ at time t can be found at $\boldsymbol{r}'$ at time t'. The essential statement is that the Green's function contains information about the motion of a particle in a quantum mechanical sense. In this sense the expansion of the Dyson equation Eq. (2.129) states that the propagation of a particle can be calculated as a sum of a free propagation and a propagation followed by various scattering events followed by another free propagation. The set of all these scattering processes and subsequent propagations can be represented by the T-operator (see Eq. (2.133)). More detailed information about the Green's function and its interpretation can be found in Ref. [65].

Now, the Lippmann-Schwinger equation is introduced. In contrast to the Dyson equation which connects the free Green's function to the Green's function of the interacting system, it connects the wave function of the free system to the wave function of the interacting system. If $|\varphi\rangle$ and $|\psi\rangle$ are eigenfunctions of $\hat{H}_0$ and $\hat{H} = \hat{H}_0 + \hat{V}$, the corresponding eigenvalue equations can be written in the following form

$$\begin{aligned} (z - \hat{H}_0)|\varphi(z)\rangle &= 0 \\ (z - \hat{H}_0)|\psi(z)\rangle &= \hat{V}|\psi(z)\rangle \end{aligned} \tag{2.134}$$

where all objects are defined on the continuous and complex energy plane. By employing the ansatz

$$|\psi(z)\rangle = |\varphi(z)\rangle + |\delta\psi(z)\rangle \tag{2.135}$$

where the full wave function is written as a sum of the unperturbed and a perturbative part, one can write

$$(z - \hat{H}_0)(|\varphi(z)\rangle + |\delta\psi(z)\rangle) = (z - \hat{H}_0)|\delta\psi(z)\rangle = \hat{V}|\varphi(z)\rangle + \hat{V}|\delta\psi(z)\rangle \tag{2.136}$$

by using Eq. (2.134). This yields

$$(z - \hat{H})|\delta\psi(z)\rangle = \hat{V}|\varphi(z)\rangle\,. \tag{2.137}$$

which connects the free solution $|\varphi\rangle$ and the perturbation part $|\delta\psi\rangle$. An inversion provides an alternative formulation of $|\delta\psi\,(z)\rangle$ in terms of the resolvent. Carrying out the side limits, the full wave function is given by

$$|\psi^{\pm}(\epsilon)\rangle = |\varphi(\epsilon)\rangle + \hat{G}^{\pm}\hat{V}|\varphi(\epsilon)\rangle \tag{2.138}$$

where ϵ is now a real number. This equation is the Lippmann-Schwinger equation. Reformulations using the T-operator as in the case of the Dyson equation are also possible. From the definition of the full Green's function and the T-operator in Eq. (2.129) and (2.130) the identity $\hat{T}(z)\hat{G}_0(z) = \hat{V}\hat{G}(z)$ follows. Therefore Eq.(2.138) can be written as

$$|\psi^{\pm}(\epsilon)\rangle = |\varphi(\epsilon)\rangle + \hat{G}_0^{\pm}(\epsilon)\hat{T}^{\pm}(\epsilon)|\varphi(\epsilon)\rangle\,. \tag{2.139}$$

A multiplication with $\hat{V}$ on both sides leads to

$$\hat{V}|\psi^{\pm}(\epsilon)\rangle = (\hat{V} + \hat{V}\hat{G}_0^{\pm}(\epsilon)\hat{T}^{\pm}(\epsilon))|\varphi(\epsilon)\rangle = \hat{T}^{\pm}(\epsilon)|\varphi(\epsilon)\rangle \tag{2.140}$$

where Eq. (2.130) is used again. This leads to a different form of the Lippmann-Schwinger equation given by

$$|\psi^{\pm}(\epsilon)\rangle = |\varphi(\epsilon)\rangle + \hat{G}_0^{\pm}(\epsilon)\hat{V}|\psi^{\pm}(\epsilon)\rangle\,. \tag{2.141}$$

This equation connects the free resolvent, the potential and the wave functions. The $|\psi^{+}(\epsilon)\rangle$ are called incoming and the $|\psi^{-}(\epsilon)\rangle$ outgoing waves. The incoming wave describes how a free wave is altered when undergoing the scattering event. The outgoing wave describes how the wave must have looked like if it is scattered in a specific way.

Hence, all necessary tools and important relations are introduced to present the general formalism of MST.

2.2.3 Multiple scattering expansion

In this section the scattering of electrons (or in general waves) propagating through an area of scattering centers is described in terms of a specific expansion. Another important operator called the scattering path operator is introduced which includes all multiple scattering information. But at first, a restriction of the underlying potential is introduced. In the following, the complex energy argument z is neglected to keep the notation more transparent.

The potential of the considered system is assumed to be a sum of N individual potentials at positions $\boldsymbol{R}_i$,

$$V(\boldsymbol{r}) = \sum_{i=1}^{N} V_i(\boldsymbol{r}_i) \quad , \quad \boldsymbol{r}_i = \boldsymbol{r} - \boldsymbol{R}_i \tag{2.142}$$

where the domains D_{V_i} of the potentials V_i are disjoint such that

$$D_{V_i} \cap D_{V_j} = \delta D_{V_i} \, . \tag{2.143}$$

The potential in the region between the scattering centers is assumed to be constant. Due to this assumptions, two simplifications are introduced. If the scattering centers are considered to be the regions around the nuclei of a solid, the space between those centers is of course much flatter than close to the nuclei but it is not constant. The other simplification is that the potential of the scattering center is assumed to be spherical which is of course a good assumption for regions close to nuclei but also not exactly valid, but simplifies the calculation because the angular momentum is conserved. Experience shows that despite these assumptions real systems are still well described. The approximation introduced in Eq. (2.142) and (2.143) is called muffin tin approximation. Formally speaking, it is a good approximation if the potential of the scattering centers decays with r^{-n}, $n \geq 2$ because for such potentials the assumption that the incident and scattered wave are only affected in a spatially bound region, is reasonable.

In the following the T-operator associated with a single potential V_i called single-site T-operator and the T-operator of N scatterers have to be distinguished. Equation (2.133) shows that the T-operator of a single potential is given by

$$\hat{t}_n = \hat{V}_n + \hat{V}_n \hat{G}_0 \hat{t}_n \, . \tag{2.144}$$

On the basis of the interpretation of the free Green's function given in Section 2.2.2 it is possible to understand how the T-operator of N scatterers can be constructed in terms of an infinite series: A particle might be scattered at only one center but might also travel to the next and so on. This is represented by

$$\hat{T} = \sum_n \hat{V}_n + \sum_{n,m} \hat{V}_n \hat{G}_0 \hat{V}_m + \sum_{n,m,k} \hat{V}_n \hat{G}_0 \hat{V}_m \hat{G}_0 \hat{V}_k + ... \quad , \quad n, m, k, ... \leq N \tag{2.145}$$

which contains information of all possible single-site scattering events as well as information about all possible multiple-scattering processes. A rigorous derivation of this equation is found in Ref. [63] and [64]. Equation (2.145) can be reformulated by employing the single-site scattering operator defined in Eq. (2.144) in combination with an iterative replacement of V_n which gives

$$\hat{T} = \sum_n \hat{t}_n + \sum_{n,m} \hat{t}_n \hat{G}_0 \left(1 - \delta_{nm}\right) \hat{t}_m + \sum_{n,m,k} \hat{t}_n \hat{G}_0 \left(1 - \delta_{nm}\right) \hat{t}_m \hat{G}_0 \left(1 - \delta_{mk}\right) \hat{t}_k + ... \, , \tag{2.146}$$

where the δ-terms prevent that a particle is subsequently scattered two times at the same center. Such terms are neglected because they are non-physical.

In order to obtain the scattering path operator (SPO), the summations over n and m of the last equation have to be factorized which leads to

$$\hat{T} = \sum_{n,m} \hat{\tau}_{nm} \, , \tag{2.147}$$

where the SPO $\hat{\tau}_{nm}$ is defined by

$$\hat{\tau}_{nm} = \hat{t}_n \delta_{nm} + \hat{t}_n \hat{G}_0 \left(1 - \delta_{nm}\right) \hat{t}_m + \sum_k \hat{t}_n \hat{G}_0 \left(1 - \delta_{nk}\right) \hat{t}_k \hat{G}_0 \left(1 - \delta_{km}\right) \hat{t}_m + ... \, . \tag{2.148}$$

This equation can be written in the compact form

$$\hat{\tau}_{nm} = \hat{t}_n \delta_{nm} + t_n \hat{\mathcal{G}}_{nm} \hat{t}_m \tag{2.149}$$

where $\mathcal{G}_{nm}$ is the important (full) structural resolvent

$$\hat{\mathcal{G}}_{nm} = \hat{G}_0 \left(1 - \delta_{nm}\right) + \sum_{k,j} \hat{G}_0 \left(1 - \delta_{nk}\right) \hat{\tau}_{kj} \hat{G}_0 \left(1 - \delta_{jm}\right) . \tag{2.150}$$

Now, the resolvent can be reformulated in terms of the SPO

$$\hat{G} = \hat{G}_0 + \sum_{n,m} \hat{G}_0 \hat{\tau}_{nm} \hat{G}_0 . \tag{2.151}$$

The introduction of the full structural resolvent is important because its free counterpart plays an important role in MST. This free structural resolvent is introduced in Section 2.2.4 as part of a particular expansion of the free Green's function. This expansion employes spherical functions which are directly connected to the single-site scattering problem and are discussed Appendix A.6.

2.2.4 The free Green's function expressed in terms of scattering solutions

The basics of MST are introduced in previous subsections. In this subsection, two types of expansions of the Green's function in terms of spherical functions are introduced (details about spherical functions can be found Appendix A.6). The second expansion named the two-center expansion is rudimentary for MST because it leads to a representation of the important free structure constants which depend only on distances between scattering centers. The derivations and in particular the notation is adopted from Ref. [63].

In oder to keep the notation more transparent, a composite index for angular momentum quantum numbers is introduced by $L = l(l+1) + m + 1$. In addition the notation

$$\begin{aligned} j_L\left(\epsilon; \boldsymbol{r}\right) &= j_l\left(pr\right) Y_L\left(\hat{\boldsymbol{r}}\right) \\ n_L\left(\epsilon; \boldsymbol{r}\right) &= n_l\left(pr\right) Y_L\left(\hat{\boldsymbol{r}}\right) \\ h_L^{\pm}\left(\epsilon; \boldsymbol{r}\right) &= h_l^{\pm}\left(pr\right) Y_L\left(\hat{\boldsymbol{r}}\right) \end{aligned} \tag{2.152}$$

is introduced where $p = \sqrt{\epsilon}$ together with a particular type of conjugation given by

$$f_L\left(\epsilon; \boldsymbol{r}\right)^{\times} = f_l\left(pr\right) Y_L\left(\hat{\boldsymbol{r}}\right)^* , \quad f_L = j_L,\, n_L,\, h_L . \tag{2.153}$$

An orthornormal set of basis functions given by

$$\phi_L\left(\epsilon; \boldsymbol{r}\right) = \frac{\epsilon^{1/4}}{\pi^{1/2}} j_L\left(\epsilon; \boldsymbol{r}\right) . \tag{2.154}$$

can be constructed from the j_L and a spectral representation of the free Green's function in terms of these functions can be defined by

$$G_0\left(z; \boldsymbol{r}, \boldsymbol{r}'\right) = \int_0^{\infty} \mathrm{d}\epsilon \sum_L \frac{\sqrt{\epsilon}}{\pi} \frac{j_L\left(\epsilon; \boldsymbol{r}\right) j_L^*\left(\epsilon; \boldsymbol{r}'\right)}{z - \epsilon} \tag{2.155}$$

where the energy integral can be evaluated by employing a similar procedure that leads to Eq. (A.82) in the Appendix. Therefore, the representation of G_0 in Eq. (2.155) can be transformed to

$$G_0\left(z;\boldsymbol{r},\boldsymbol{r}'\right) = ip\sum_L j_L\left(z,\boldsymbol{r}_<\right) h_L^+\left(z,\boldsymbol{r}_>\right)^\times = -ip\sum_L h_L^+\left(z,\boldsymbol{r}_>\right) j_L\left(z,\boldsymbol{r}_<\right)^\times \tag{2.156}$$

where $r_< = \min(r,r')$ and $r_> = \max(r,r')$ (see Ref. [63]). The energy argument of j_L and h_L^+ is now complex because it is associated with the complex energy argument z of G_0 on the left hand side and the energy variable ϵ is integrated out. It should be noted that Eq. (2.156) and (A.82) represent the same functions.

From the properties of the Green's function concerning the complex conjugation the relation

$$G_0\left(z^*;\boldsymbol{r},\boldsymbol{r}'\right) = G_0\left(z;\boldsymbol{r}',\boldsymbol{r}\right)^*, \qquad \epsilon > 0 \tag{2.157}$$

follows. This relation implies an expression of the side limits given by

$$\begin{aligned} G_0^\pm(\epsilon;\boldsymbol{r},\boldsymbol{r}') &= \mp ip\sum_L j_l(p\boldsymbol{r}_<)h_l^\pm(p\boldsymbol{r}_>)Y_L(\hat{\boldsymbol{r}})Y_L(\hat{\boldsymbol{r}}')^*, \quad \epsilon > 0, \quad p = \sqrt{\epsilon} \\ G_0^\pm(\epsilon;\boldsymbol{r},\boldsymbol{r}') &= p\sum_L j_l(p\boldsymbol{r}_<)h_l^+(ip\boldsymbol{r}_>)Y_L(\hat{\boldsymbol{r}})Y_L(\hat{\boldsymbol{r}}')^*, \quad \epsilon < 0, \quad p = \sqrt{-\epsilon}\,. \end{aligned} \tag{2.158}$$

It can be shown that it is sufficient to consider only G_0^+ because G_0^- is recovered by a simple transformation of p into $-p^*$. Therefore, the superscripts $+$ and $-$ are dropped and the identification $G_0(\epsilon;\boldsymbol{r},\boldsymbol{r}') = G_0^+(\epsilon;\boldsymbol{r},\boldsymbol{r}')$ is used.

In order to get a more compact notation, the vectors

$$\mathbf{f}\left(\epsilon;\boldsymbol{r}\right) = \left[f_1\left(\epsilon;\boldsymbol{r}\right), f_2\left(\epsilon;\boldsymbol{r}\right), f_3\left(\epsilon;\boldsymbol{r}\right), \dots\right] \tag{2.159}$$

$$\mathbf{f}\left(\epsilon;\boldsymbol{r}\right)^\times = \begin{bmatrix} f_1\left(\epsilon;\boldsymbol{r}\right) \\ f_2\left(\epsilon;\boldsymbol{r}\right) \\ f_3\left(\epsilon;\boldsymbol{r}\right) \\ \vdots \end{bmatrix} \tag{2.160}$$

are introduced where the f_i are defined according to Eq. (2.153). Hence, G_0 can be written as

$$G_0\left(\epsilon;\boldsymbol{r},\boldsymbol{r}'\right) = -ip\mathbf{j}\left(\epsilon,\boldsymbol{r}_<\right)\mathbf{h}^+\left(\epsilon,\boldsymbol{r}_>\right)^\times = -ip\mathbf{h}^+\left(\epsilon,\boldsymbol{r}_>\right)\mathbf{j}\left(\epsilon,\boldsymbol{r}_<\right)^\times\,. \tag{2.161}$$

and rewritten in a close form by using the Heavyside step-function

$$G_0\left(\epsilon;\boldsymbol{r},\boldsymbol{r}'\right) = -ip\left[\mathbf{j}\left(\epsilon,\boldsymbol{r}\right)\mathbf{h}^+\left(\epsilon,\boldsymbol{r}'\right)^\times\Theta(r'-r) + \mathbf{h}^+\left(\epsilon,\boldsymbol{r}\right)\mathbf{j}\left(\epsilon,\boldsymbol{r}'\right)^\times\Theta(r-r')\right]\,. \tag{2.162}$$

This is a spectral representation of the free Green's function in terms of spherical functions obtained from the radial Schrödinger equation and spherical harmonics.

Now, the two-center expansion of the Green's function is discussed. This provides important insight into the principles of the actual multiple scattering formalism, because a specific representation of the free structure constants is found during the derivation. The two-center

expansion assumes that the two arguments of G_0 refer to different origins. This is achieved by using the following definitions

$$\boldsymbol{r} = \boldsymbol{r}_n + \boldsymbol{R}_n \quad , \quad \boldsymbol{r}' = \boldsymbol{r}_m + \boldsymbol{R}_m \tag{2.163}$$

$$n \neq m \quad , \quad |\boldsymbol{r}_n - \boldsymbol{r}_m| < |\boldsymbol{R}_{nm}| \quad , \quad \boldsymbol{R}_{nm} = \boldsymbol{R}_m - \boldsymbol{R}_n \tag{2.164}$$

which additionally reflect the muffin tin geometry conditions. Relying on this assumption, the following expansion of the Green's function is proposed

$$G_0\left(\epsilon; \boldsymbol{r}_n + \boldsymbol{R}_n, \boldsymbol{r}_m + \boldsymbol{R}_m\right) = \sum_{LL'} j_L\left(\epsilon, \boldsymbol{r}_n\right) \mathcal{G}^{nm}_{0,LL'} j_L\left(\epsilon, \boldsymbol{r}_m\right) = \mathbf{j}\left(\epsilon, \boldsymbol{r}_n\right) \boldsymbol{\mathcal{G}}^{nm}_0 \mathbf{j}\left(\epsilon, \boldsymbol{r}_n\right)^{\times} . \tag{2.165}$$

where the expansion coefficients $\boldsymbol{\mathcal{G}}^{nm}_0 = \{\mathcal{G}^{nm}_{0,LL'}\}$ are called real-space free structure constants. As is known from the last section that the free particle Green's function depends only on the difference $\boldsymbol{r} - \boldsymbol{r}'$, one can write

$$G_0\left(\epsilon; \boldsymbol{r}_n + \boldsymbol{R}_n, \boldsymbol{r}_m + \boldsymbol{R}_m\right) = G_0\left(\epsilon; \boldsymbol{r}_n - \boldsymbol{r}_m, \boldsymbol{R}_{nm}\right) \tag{2.166}$$

because $\boldsymbol{r}_n - \boldsymbol{r}_m - \boldsymbol{R}_{nm} = \boldsymbol{r}_n + \boldsymbol{R}_n - (\boldsymbol{r}_m + \boldsymbol{R}_m)$. As by definition $|\boldsymbol{r}_n - \boldsymbol{r}_m| < |\boldsymbol{R}_{nm}|$, the one-center expansion

$$G_0\left(\epsilon; \boldsymbol{r}_n + \boldsymbol{R}_n, \boldsymbol{r}_m + \boldsymbol{R}_m\right) = -ip \sum_{L} h^+_L\left(\epsilon, \boldsymbol{R}_{nm}\right) j_L\left(\epsilon, \boldsymbol{r}_n - \boldsymbol{r}_m\right)^{\times} . \tag{2.167}$$

applies which is adopted from Eq. (2.162). The spherical Bessel functions are now replaced by (see Appendix A.8)

$$\begin{aligned} j_L\left(\epsilon, \boldsymbol{r}_n - \boldsymbol{r}_m\right)^{\times} &= \frac{i^{-l}}{4\pi} \int \mathrm{d}\hat{\boldsymbol{k}} \mathrm{e}^{i\boldsymbol{k}\left(\boldsymbol{r}_n - \boldsymbol{r}_m\right)} Y_L(\hat{\boldsymbol{k}})^* \\ &= 4\pi \sum_{L'L''} i^{l'-l''-l} j_{L'}\left(\epsilon, \boldsymbol{r}_n\right) j_{L''}\left(\epsilon, \boldsymbol{r}_m\right)^{\times} C^{L''}_{LL'} , \end{aligned} \tag{2.168}$$

where the $C^{L''}_{LL'}$ are the Gaunt coefficients

$$C^{L''}_{LL'} = \int \mathrm{d}\hat{\boldsymbol{k}}\, Y_L(\hat{\boldsymbol{k}})^* Y_{L'}(\hat{\boldsymbol{k}})^* Y_{L''}(\hat{\boldsymbol{k}}) = \int \mathrm{d}\hat{\boldsymbol{k}}\, Y_L(\hat{\boldsymbol{k}}) Y_{L'}(\hat{\boldsymbol{k}}) Y_{L''}(\hat{\boldsymbol{k}})^* . \tag{2.169}$$

This allows to write Eq. (2.167) in the following form

$$G_0\left(\epsilon; \boldsymbol{r}_n + \boldsymbol{R}_n, \boldsymbol{r}_m + \boldsymbol{R}_m\right) = -4\pi pi \sum_{L'L''L'''} h^+_L\left(\epsilon, \boldsymbol{R}_{nm}\right) i^{l'-l''-l} j_{L'}\left(\epsilon, \boldsymbol{r}_n\right) j_{L''}\left(\epsilon, \boldsymbol{r}_m\right)^{\times} C^{L''}_{LL'} . \tag{2.170}$$

By introducing the index change $(LL'L'') \rightarrow (L''L'L')$ one can specify the real-space structure constants by writing

$$\mathcal{G}^{nm}_{0,LL'}\left(\epsilon\right) = -4\pi pi \sum_{L''} i^{l-l'-l''} h^+_L\left(\epsilon, \boldsymbol{R}_{nm}\right) C^{L''}_{LL'} . \tag{2.171}$$

In summary the free-particle Green's function can be written as

$$\begin{aligned} G_0\left(\epsilon; \boldsymbol{r}_n + \boldsymbol{R}_n, \boldsymbol{r}_m + \boldsymbol{R}_m\right) = &\left(1 - \delta_{nm}\right) \mathbf{j}\left(\epsilon, \boldsymbol{r}_n\right) \boldsymbol{\mathcal{G}}^{nm}_0 \mathbf{j}\left(\epsilon, \boldsymbol{r}_m\right)^{\times} \\ &- ip\delta_{nm} \left\{ \mathbf{j}\left(\epsilon, \boldsymbol{r}_n\right) \mathbf{h}^+\left(\epsilon, \boldsymbol{r}_m\right)^{\times} \Theta\left(r_m - r_n\right) \right. \\ &\left. + \mathbf{h}^+\left(\epsilon, \boldsymbol{r}_n\right) \mathbf{j}\left(\epsilon, \boldsymbol{r}_m\right)^{\times} \Theta\left(r_n - r_m\right) \right\} . \end{aligned} \tag{2.172}$$

This is the important two-center expansion of the free Green's function in terms of spherical functions and structure constants. It shows that the structure constants are fully determined by the distance vectors $\boldsymbol{R}_{nm}$ which are given by the spatial arrangement of the scattering centers in the actual system under consideration.

2.2.5 Scattering solutions and T-matrix

In this subsection a special form of the Lippmann-Schwinger equation is presented which automatically leads to a matrix representation of the single-site T-operator $\hat{t}^n$. The derivation starts from Eq. (2.139) which is for simplicity written in the form

$$|\psi\rangle = |\varphi\rangle + \hat{G}_0 \hat{t}^n |\varphi\rangle \;, \tag{2.173}$$

where $\hat{T} = \hat{t}^n$ in the single-site case. All superscripts and arguments are omitted for reasons of transparency and the insertion of the completeness relation $\int \mathrm{d}\boldsymbol{r}\, |\boldsymbol{r}\rangle\langle\boldsymbol{r}|$ together with a multiplication by $\langle\boldsymbol{r}|$ leads to

$$\langle\boldsymbol{r}|\psi\rangle = \langle\boldsymbol{r}|\varphi\rangle + \langle\boldsymbol{r}|\hat{G}_0|\boldsymbol{r}'\rangle\langle\boldsymbol{r}'|\hat{t}^n|\boldsymbol{r}''\rangle\langle\boldsymbol{r}''|\varphi\rangle \,. \tag{2.174}$$

The matrix $\langle\boldsymbol{r}|\hat{t}^n|\boldsymbol{r}'\rangle = t^n(\boldsymbol{r},\boldsymbol{r}')$ defines a configuration space representation of the single-site scattering operator.

As spherical Bessel functions are eigenfunctions of the free Hamiltonian $\hat{H}_0$, the Lippmann-Schwinger equation

$$R_L^n(\epsilon;\boldsymbol{r}_n) = j_L(\epsilon;\boldsymbol{r}_n) + \int\int\limits_{\{\boldsymbol{x}_n,\boldsymbol{y}_n\in D_{V_n}\}} \mathrm{d}\boldsymbol{x}_n \mathrm{d}\boldsymbol{y}_n G_0(\epsilon;\boldsymbol{r}_n,\boldsymbol{x}_n)\, t^n(\epsilon;\boldsymbol{x}_n,\boldsymbol{y}_n)\, j_L(\epsilon;\boldsymbol{y}_n) \tag{2.175}$$

is obtained for $\boldsymbol{r}_n \in D_{V_n}$, where R_L^n is the full wave function (here the energy argument ϵ is again added in the notation). For $\boldsymbol{r}_n \notin D_{V_n}$ the one center expansion given in Eq. (2.161) can be used and as $\boldsymbol{r}_n$ lies outside the region D_{V_n} it is definitively larger than $\boldsymbol{R}_n$. This leads to

$$R_L^n(\epsilon;\boldsymbol{r}_n) = j_L(\epsilon;\boldsymbol{r}_n) - ip\sum_{L'} h_{L'}^+(\epsilon;\boldsymbol{r}_n)\, t_{L'L}^n(\epsilon) \;, \tag{2.176}$$

where the matrix elements $t_{L'L}^n$ are the partial wave representations of the single-site T-operator defined by

$$t_{L'L}^n(\epsilon) = \int\int\limits_{\{\boldsymbol{x}_n,\boldsymbol{y}_n\in D_{V_n}\}} \mathrm{d}\boldsymbol{x}_n \mathrm{d}\boldsymbol{y}_n\, j_{L'}(\epsilon;\boldsymbol{x}_n)^{\times}\, t^n(\epsilon;\boldsymbol{x}_n,\boldsymbol{y}_n)\, j_L(\epsilon;\boldsymbol{y}_n) \;. \tag{2.177}$$

In order to keep the formulas more transparent the shorthand notation

$$\boldsymbol{t}^n(\epsilon) = \{t_{L'L}^n\} \tag{2.178}$$

is introduced and therefore Eq. (2.177) becomes

$$\boldsymbol{t}^n(\epsilon) = \int\int\limits_{\{\boldsymbol{x}_n,\boldsymbol{y}_n\in D_{V_n}\}} \mathrm{d}\boldsymbol{x}_n \mathrm{d}\boldsymbol{y}_n\, \mathbf{j}(\epsilon;\boldsymbol{x}_n)^{\times}\, t^n(\epsilon;\boldsymbol{x}_n,\boldsymbol{y}_n)\, \mathbf{j}(\epsilon;\boldsymbol{y}_n) \;. \tag{2.179}$$

In addition, the expression of the scattering function outside the muffin tin sphere which explicitly depends on the single-site scattering matrix, is now given by

$$\mathbf{R}^n(\epsilon;\boldsymbol{r}_n) = \mathbf{j}(\epsilon;\boldsymbol{x}_n) - ip\mathbf{h}^+(\epsilon;\boldsymbol{x}_n)\,\boldsymbol{t}^n(\epsilon) \quad , \quad \boldsymbol{r}_n \notin D_{V_n}\,. \tag{2.180}$$

Here, only the regular solutions are used but it should be kept in mind that also irregular scattering solutions can be defined (see Appendix A.6 for details). Since irregular solutions are usually not needed and occur only in special purpose calculations, a discussion of such functions is omitted here.

2.2.6 The fundamental equation of multiple scattering theory

In this section the focus is on the full and free structural Green's function because it turns out that a matrix representation of the latter, together with the matrix of the single-site operator obtained in the last section, form the fundamental MST equation.

At first a partial wave representation of the full structural Green's function, which is the configuration representation of the full structural resolvent, in term of a two-center expansion is needed. From the definition of the structural Green's function in Section 2.2.3 given by

$$\hat{\mathcal{G}}_{nm} = \hat{G}_0\,(1-\delta_{nm}) + \sum_{k\neq n}\sum_{j\neq m}\hat{G}_0\hat{\tau}_{kj}\hat{G}_0\,. \tag{2.181}$$

the insertion of the completeness relation as in Eq. (2.174) leads to

$$\langle\boldsymbol{r}|\hat{\mathcal{G}}_{nm}|\boldsymbol{r}'\rangle = \langle\boldsymbol{r}|\hat{G}_0|\boldsymbol{r}'\rangle\,(1-\delta_{nm}) + \sum_{k\neq n}\sum_{j\neq m}\int \mathrm{d}\boldsymbol{r}''\int \mathrm{d}\boldsymbol{r}'''\langle\boldsymbol{r}|\hat{G}_0|\boldsymbol{r}''\rangle\langle\boldsymbol{r}''|\hat{\tau}_{kj}|\boldsymbol{r}'''\rangle\langle\boldsymbol{r}'''|\hat{G}_0|\boldsymbol{r}'\rangle \tag{2.182}$$

where all matrices are the configuration space representations. The representation of the full structural resolvent is assumed to have the two center expansion

$$\mathcal{G}^{nm}(\epsilon;\boldsymbol{r}_n+\boldsymbol{R}_n,\boldsymbol{r}_m+\boldsymbol{R}_m) = \mathbf{j}(\epsilon;\boldsymbol{r}_n)\,\boldsymbol{\mathcal{G}}^{nm}(\epsilon)\,\mathbf{j}(\epsilon;\boldsymbol{r}_m)^{\times} \tag{2.183}$$

where $\boldsymbol{\mathcal{G}}^{nm}$ is called structural Green's function matrix which is evaluated by inserting the two center expansion of the free Green's function given by Eq. (2.165). This leads to

$$\boldsymbol{\mathcal{G}}^{nm}(\epsilon) = \boldsymbol{\mathcal{G}}_0^{nm}(\epsilon)\,(1-\delta_{nm}) + \sum_{k(\neq n)}\sum_{j(\neq m)}\boldsymbol{\mathcal{G}}_0^{nk}(\epsilon)\,\boldsymbol{\tau}^{kj}(\epsilon)\,\boldsymbol{\mathcal{G}}_0^{jm}(\epsilon)\,. \tag{2.184}$$

Since

$$\hat{\tau}^{kj}(\epsilon;\boldsymbol{x}_k+\boldsymbol{R}_k,\boldsymbol{y}_j+\boldsymbol{R}_j) = 0 \quad , \quad \boldsymbol{x}_k \notin D_{V_k} \vee \boldsymbol{y}_j \notin D_{V_j} \tag{2.185}$$

the matrix of the scattering path operator is given by

$$\boldsymbol{\tau}^{kj}(\epsilon) = \int\limits_{\{\boldsymbol{x}_k\in D_{V_k}\}}\mathrm{d}\boldsymbol{x}_k\int\limits_{\{\boldsymbol{y}_j\in D_{V_j}\}}\mathrm{d}\boldsymbol{y}_j\,\mathbf{j}(\epsilon;\boldsymbol{x}_k)^{\times}\,\hat{\tau}^{kj}(\epsilon;\boldsymbol{x}_k,\boldsymbol{y}_j)\,\mathbf{j}(\epsilon;\boldsymbol{y}_j)\,, \tag{2.186}$$

and is connected to the single-site scattering matrix and the structural Green's function matrix by

$$\boldsymbol{\tau}^{nm}(\epsilon) = \delta_{nm}\boldsymbol{t}^n(\epsilon) + \boldsymbol{t}^n(\epsilon)\,\boldsymbol{\mathcal{G}}^{nm}(\epsilon)\,\boldsymbol{t}^m(\epsilon) \tag{2.187}$$

or to the free structure constants by

$$\boldsymbol{\tau}^{nm}(\epsilon) = \delta_{nm}\boldsymbol{t}^{n}(\epsilon) + \sum_{k} \boldsymbol{t}^{n}(\epsilon)\,\boldsymbol{\mathcal{G}}_{0}^{km}(\epsilon)\,\boldsymbol{\tau}^{km}(\epsilon)\ . \tag{2.188}$$

Now, an overall shorthand notation is introduced that unifies the angular momentum and site indices. Therefore, the important quantities are given by

$$\begin{aligned} \underline{\boldsymbol{\mathcal{G}}}(\epsilon) &= \{\boldsymbol{\mathcal{G}}^{nm}(\epsilon)\} \quad , \quad \underline{\boldsymbol{t}}(\epsilon) = \{\boldsymbol{t}^{n}(\epsilon)\,\delta_{nm}\} \\ \underline{\boldsymbol{\mathcal{G}}}_{0}(\epsilon) &= \{\boldsymbol{\mathcal{G}}_{0}^{nm}(\epsilon)\,(1-\delta_{nm})\} \quad , \quad \underline{\boldsymbol{\tau}}(\epsilon) = \{\boldsymbol{\tau}^{nm}(\epsilon)\}\ . \end{aligned} \tag{2.189}$$

Using this notation in Eq. (2.188) one obtains

$$\underline{\boldsymbol{\tau}}(\epsilon) = \underline{\boldsymbol{t}}(\epsilon) + \underline{\boldsymbol{t}}(\epsilon)\underline{\boldsymbol{\mathcal{G}}}_{0}(\epsilon)\underline{\boldsymbol{\tau}}(\epsilon)\,. \tag{2.190}$$

which is solved by the fundamental equation of MST given by

$$\underline{\boldsymbol{\tau}}(\epsilon) = \left[\underline{\boldsymbol{t}}^{-1}(\epsilon) - \underline{\boldsymbol{\mathcal{G}}}_{0}(\epsilon)\right]^{-1}\ . \tag{2.191}$$

This equation brings the single-site scattering part together with the information of the underlying structure of the system. If Eq. (2.187) is inserted in Eq. (2.191) a simple rearrangement proofs that Eq. (2.191) is the correct expression of the SPO.

Throughout the last subsections the principles of the determination of the single-site scattering operator $\hat{t}^{n}$ and the evaluation of the free structure constants in real space $\mathcal{G}_{0,LL'}^{nm}$ are presented. The result of both procedures can be condensed in super matrices as they are shown in Eq. (2.189). What is left to be done is an inversion of the matrix in Eq. (2.191) to evaluate the scattering path operator. How the full Green's function is calculated from this operator is shown in the next section.

2.2.7 Representation of the full Green's function in terms of scattering solutions

A frequently used form of scattering solutions is defined by

$$\mathbf{Z}^{n}(\epsilon;\boldsymbol{r}_{n}) = \mathbf{R}^{n}(\epsilon;\boldsymbol{r}_{n})\,\boldsymbol{t}^{n}(\epsilon)^{-1} \quad , \quad \boldsymbol{r}_{n} \in D_{V_{n}} \tag{2.192}$$

$$\mathbf{Z}^{n}(\epsilon;\boldsymbol{r}_{n}) = \mathbf{j}(\epsilon;\boldsymbol{r}_{n})\,\boldsymbol{t}^{n}(\epsilon)^{-1} - ip\mathbf{h}^{+}(\epsilon;\boldsymbol{r}_{n}) \quad , \quad \boldsymbol{r}_{n} \notin D_{V_{n}}\ . \tag{2.193}$$

The full Green's function represented in terms of this functions is given by

$$\begin{aligned} G(\epsilon;\boldsymbol{r}_{n}+\boldsymbol{R}_{n},\boldsymbol{r}_{m}+\boldsymbol{R}_{m}) = {} & \mathsf{Z}^{n}(\epsilon;\boldsymbol{r}_{n})\,\underline{\tau}^{nm}(\epsilon)\,Z^{m}(\epsilon;\boldsymbol{r}_{m}) \\ & - \delta_{nm}\{\mathsf{Z}^{n}(\epsilon;\boldsymbol{r}_{n})\,\mathsf{J}^{m}(\epsilon;\boldsymbol{r}_{m})\,\Theta(r_{m}-r_{n}) \\ & \mathsf{J}^{n}(\epsilon;\boldsymbol{r}_{n})\,\mathsf{Z}^{m}(\epsilon;\boldsymbol{r}_{m})\,\Theta(r_{n}-r_{m})\} \end{aligned} \tag{2.194}$$

where $\mathsf{J}^{n}(\epsilon;\boldsymbol{r}_{n}) = \mathsf{j}(\epsilon;\boldsymbol{r}_{n})$. One can summarize that the full Green's function of the system under consideration is given by the scattering solutions that are determined from the Lippmann-Schwinger equation which basically include detailed information about the scattering at a single center and the scattering path operator which includes all multiple scattering information. Details of how this representation is derived from the considerations of the last sections can be found in Ref. [63].

The determination of the Green's function, which is the main task of MST has been derived now. As mentioned in the introduction of MST, the density of the system can be calculated

from this function and by calculating the new effective potential from the density a new MST calculation can be started to perform the second step of the self-consistent calculation. This means that all ingredients necessary to perform KKR calculations are discussed. But it should be mentioned that there are practical aspects actual KKR calculations that are not entirely described here for reasons of compactness. In particular the numerical treatment of the single-site scattering problem and the specific evaluation of the structure constant are beyond the scope of this introduction. All practical issues can be found in Ref. [63].

2.2.8 Spin-dependent multiple scattering theory

Since throughout the discussion of MST the spin degree of freedom is omitted a short comment to how a spin including extension of this theory is constructed should be given. Therefore, the spin-dependent Kohn-Sham Hamiltonian

$$\mathcal{H}(\boldsymbol{r}) = (-\nabla + V^{\text{eff}}(\boldsymbol{r}))\mathsf{I}_2 + \sigma_z \cdot \boldsymbol{B}^{\text{eff}}(\boldsymbol{r}) \tag{2.195}$$

given in Rydberg unit needs to be considered. Here, the effective potential and the effective magnetic field are muffin tin like and therefore

$$V^{\text{eff}}(\boldsymbol{r}) = \begin{cases} V^{\text{eff}}(\boldsymbol{r}) \\ 0 \end{cases}, \begin{array}{l} r \in D_V \\ r \notin D_V \end{array} \quad \text{and} \quad \boldsymbol{B}^{\text{eff}}(\boldsymbol{r}) = \begin{cases} \boldsymbol{B}^{\text{eff}}(\boldsymbol{r}) \\ 0 \end{cases}, \begin{array}{l} r \in D_V \\ r \notin D_V \end{array} . \tag{2.196}$$

The effective potential V^{eff} and the effective magnetic field $\boldsymbol{B}^{\text{eff}}$ are functionals of the particle and magnetization density and therefore given by

$$V^{\text{eff}}\left[n, \boldsymbol{m}\right] = V^{\text{ext}} + V^{\text{Hartree}} + \frac{\delta E_{\text{ex}}\left[n, \boldsymbol{m}\right]}{\delta n} \tag{2.197}$$

$$\boldsymbol{B}^{\text{eff}}\left[n, \boldsymbol{m}\right] = \boldsymbol{B}^{\text{ext}} + \frac{\delta E_{\text{ex}}\left[n, \boldsymbol{m}\right]}{\delta \boldsymbol{m}} . \tag{2.198}$$

As the Hamiltonian in Eq. (2.195) is diagonal in spin space, it can be rewritten in terms of two separate equations

$$\mathcal{H}(\boldsymbol{r}) = -\nabla + V^{\text{eff}}(\boldsymbol{r}) + sB_z^{\text{eff}}(\boldsymbol{r}), \quad s = \pm 1 . \tag{2.199}$$

This implies that the Green's function of the system is a 2×2 matrix which is diagonal and can be written as

$$G(z, \boldsymbol{r}, \boldsymbol{r}') = \begin{pmatrix} G_\uparrow(z, \boldsymbol{r}, \boldsymbol{r}') & 0 \\ 0 & G_\downarrow(z, \boldsymbol{r}, \boldsymbol{r}') \end{pmatrix} . \tag{2.200}$$

As both spin channels do not mix in non-relativistic theory, the MST problem can be independently solved for both channels. The interaction between the spin channels enters the calculation due to the $\boldsymbol{m}$-dependence of the effective potential and field.

The intrinsic two dimensional structure of the spin-dependent problem becomes four dimensional in the relativistic case which is considered in the following.

2.3 Relativistic MST

Since non-relativistic formulation of MST is introduced in the last section, this section is devoted to the relativistic theory. This formalism is basically similar to the non-relativistic

case but as the derivations are much longer, it is only outlined here. Facts and notations introduced during this outline are essential for the derivations carried out in Section 2.7.1 which concerns the formalism used in the study of spin-dependent transport within the relativistic framework as reported in Chapter 8. Details of the relativistic MST can again be found in Ref. [63].

2.3.1 The Dirac equation revisited

At first the relativistic Kohn-Sham-Dirac Hamiltonian is presented and a different index representation for the angular momentum quantum numbers which allows a more systematic treatment, is introduced. The Kohn-Sham-Dirac Hamiltonian is given by

$$\mathcal{H}(\boldsymbol{r}) = c\,\boldsymbol{\alpha}\cdot\boldsymbol{p} + \beta mc^2 + U(\boldsymbol{r}) \tag{2.201}$$

where the potential U is defined by

$$U(\boldsymbol{r}) = V^{\text{eff}}(\boldsymbol{r})\,\mathsf{I}_4 + \beta\Sigma\cdot\boldsymbol{B}^{\text{eff}}(\boldsymbol{r}) \tag{2.202}$$

and the effective potential and field are of the same form as introduced in Section 2.2.8. The eigenfuctions can be assumed to be linear combinations of bi-spinors

$$\Psi(\epsilon,\boldsymbol{r}) = \sum_{\kappa\mu}\begin{pmatrix} g_{\kappa\mu}(\epsilon,\boldsymbol{r})\,\chi_{\kappa\mu}(\hat{\boldsymbol{r}}) \\ if_{\kappa\mu}(\epsilon,\boldsymbol{r})\,\chi_{-\kappa\mu}(\hat{\boldsymbol{r}}) \end{pmatrix}, \tag{2.203}$$

where in contrast to Section 2.1.3 a notation that already adopts the spherical symmetry of the muffin tin approximation is used. This is a traditional notation of relativistic MST. The $g_{\kappa\mu}$ and $f_{\kappa\mu}$ are energy depended radial parts, called the large and small component and the $\chi_{\kappa\mu}$ are the angular parts, called spin spherical harmonics.

To distinguish the contributions arising from different angular momentum channels, the so called $\kappa\mu$-representation is used. These indices are connected to the usual angular momentum quantum number l and the total angular momentum number $j = l + s$ in the following way

$$\kappa = \begin{cases} l & , \quad j = l - 1/2 \\ -l-1 & , \quad j = l + 1/2 \end{cases} \quad ; \quad j = l \pm \frac{1}{2} \tag{2.204}$$

$$\mu \in \{-j, -j+1, \ldots, j-1, j\}\,. \tag{2.205}$$

In addition, it is convenient to introduce

$$\bar{l} = l - S_\kappa \quad , \quad S_\kappa = \kappa/|\kappa|\,, \tag{2.206}$$

and the composite index $(\kappa\mu)$ which is often abbreviated by Λ. The spin spherical harmonics are given by

$$\chi_{\kappa\mu}(\hat{\boldsymbol{r}}) = \sum_{s=\pm 1/2} C(l,\kappa,1/2|\mu-s,s)\,Y_{l,\mu-s}(\hat{\boldsymbol{r}})\,\Phi_s \tag{2.207}$$

where the $C(l,\kappa,1/2|\mu-s,s)$ are the Clebsch-Gordan coefficients and the Φ_s are the two dimensional unit spinors [5].

[5] In contrast to the preceding sections where the two dimensional spinor is denoted by χ_s it is now denoted by Φ_s in order to avoid confusion with the notation of spin spherical harmonics.

Using spherical coordinates and inserting the definitions above into the Kohn-Sham-Dirac equation, a separation of the radial from the angular part can be performed and the former is given by

$$\sum_{\Lambda} \begin{bmatrix} W - mc^2 - u^{+}_{\Lambda\Lambda'}(r) & -i\hbar c\left(\frac{\mathrm{d}}{\mathrm{d}r} + \frac{1}{r} - \frac{\kappa}{r}\right) \\ -i\hbar c\left(\frac{\mathrm{d}}{\mathrm{d}r} + \frac{1}{r} + \frac{\kappa}{r}\right) & W + mc^2 - u^{-}_{\Lambda\Lambda'}(r) \end{bmatrix} \begin{bmatrix} g_{\Lambda'}(\epsilon, \boldsymbol{r}) \\ i f_{\Lambda'}(\epsilon, \boldsymbol{r}) \end{bmatrix} = 0 \tag{2.208}$$

where

$$u^{\pm}_{\Lambda\Lambda'}(r) = \langle \pm\Lambda | V^{\mathrm{eff}}(\boldsymbol{r}) \pm \boldsymbol{\sigma} \cdot \boldsymbol{B}^{\mathrm{eff}}(\boldsymbol{r}) | \pm\Lambda' \rangle \quad , \quad |\pm\Lambda'\rangle = \begin{pmatrix} g_{\kappa\mu}(\epsilon, \boldsymbol{r})\, \chi_{\kappa\mu}(\hat{\boldsymbol{r}}) \\ i f_{\kappa\mu}(\epsilon, \boldsymbol{r})\, \chi_{-\kappa\mu}(\hat{\boldsymbol{r}}) \end{pmatrix} . \tag{2.209}$$

This is the relativistic equation for the determination of the stationary scattering solutions. It is a coupled set of differential equations which in general can only be solved numerically.

The Dirac equation for the free particle can be written as

$$\begin{bmatrix} (W - mc^2)\,\mathsf{I}_2 & -c\boldsymbol{\sigma} \cdot \hat{\boldsymbol{p}} \\ -c\boldsymbol{\sigma} \cdot \hat{\boldsymbol{p}} & (W + mc^2)\,\mathsf{I}_2 \end{bmatrix} \begin{bmatrix} \psi_b(\epsilon, \boldsymbol{r}) \\ \psi_s(\epsilon, \boldsymbol{r}) \end{bmatrix} = 0 \tag{2.210}$$

where the bispinors ψ_l is the large and ψ_s the small component. If spherical coordinates are introduced the corresponding solutions are

$$\Psi_{\kappa\mu}(\epsilon, \boldsymbol{r}) = \begin{bmatrix} f_l\left(\frac{pr}{\hbar}\right) \chi_{\kappa\mu}(\hat{\boldsymbol{r}}) \\ \frac{iS_\kappa pc}{W + mc^2} f_l\left(\frac{pr}{\hbar}\right) \chi_{-\kappa\mu}(\hat{\boldsymbol{r}}) \end{bmatrix} \tag{2.211}$$

where $f_l = j_l, n_l, h_l^{\pm}$ are spherical Bessel, Neumann or Hankel functions and $p = \sqrt{W^2 - m^2c^4}$. The conjugate of Eq. (2.211) is given by

$$\Psi_{\kappa\mu}(\epsilon, \boldsymbol{r})^{\times} = \left[f_l\left(\frac{pr}{\hbar}\right) \chi_{\kappa\mu}(\hat{\boldsymbol{r}})^{+} , \frac{-iS_\kappa pc}{W + mc^2} f_{\bar{l}}\left(\frac{pr}{\hbar}\right) \chi_{-\kappa\mu}(\hat{\boldsymbol{r}})^{+} \right] . \tag{2.212}$$

This shows that the free Dirac equation written in spherical coordinates can also be solved in terms of spherical functions. Hereby, the basic objects of relativistic scattering theory and the associated and commonly used notations are introduced.

2.3.2 The relativistic Green's function and its representations

In this section the relativistic Green's function and its relation to the non-relativistic Green's function is introduced. In addition, the single as well as two center expansion of the relativistic Green's function is presented. In order to avoid confusion, the relativistic quantities are labelled by the subscript D (Dirac) and the non-relativistic by S (Schrödinger).

In analogy to the non-relativistic case the relativistic resolvent is defined by

$$(W\mathsf{I}_4 - \hat{H}_0^{\mathrm{D}})\hat{G}_0^{\mathrm{D}}(\epsilon) = \mathsf{I}_4 \tag{2.213}$$

and is connected to its non-relativistic counterpart by

$$\hat{G}_0^{\mathrm{D}}(\epsilon) = \frac{1}{2mc^2}(W\mathsf{I}_4 - \hat{H}_0^{\mathrm{D}})\hat{G}_0^{\mathrm{S}}(p^2/2m)\mathsf{I}_4 . \tag{2.214}$$

The single center expansion of the non-relativistic Green's function introduced in Eq. 2.156 can be transformed to the $\kappa\mu$-representation. This leads to the following form

$$G_0^{\mathrm{S}}(\epsilon, \boldsymbol{r}, \boldsymbol{r}')\mathsf{I}_2 = -ip \sum_{\Lambda} j_l(pr_<) h_l^+(pr_>) \chi_\Lambda(\hat{\boldsymbol{r}}) \chi_\Lambda(\hat{\boldsymbol{r}})^+ \tag{2.215}$$

$$= -ip \sum_{\Lambda} j_{\bar{l}}(pr_<) h_{\bar{l}}^+(pr_>) \chi_{\bar{\Lambda}}(\hat{\boldsymbol{r}}) \chi_{\bar{\Lambda}}(\hat{\boldsymbol{r}})^+ \tag{2.216}$$

where $\chi_\Lambda(\hat{\boldsymbol{r}})^+$ denotes the conjugated $\chi_\Lambda(\hat{\boldsymbol{r}})$ and the last equation is obtained by changing κ to $-\kappa$. Thus, the relativistic Green's function can be written in term of the matrix

$$G_0^{\mathrm{D}}(\epsilon, \boldsymbol{r}, \boldsymbol{r}') = \begin{bmatrix} G_{0,11}^{\mathrm{D}}(\epsilon, \boldsymbol{r}, \boldsymbol{r}') & G_{0,12}^{\mathrm{D}}(\epsilon, \boldsymbol{r}, \boldsymbol{r}') \\ G_{0,21}^{\mathrm{D}}(\epsilon, \boldsymbol{r}, \boldsymbol{r}') & G_{0,22}^{\mathrm{D}}(\epsilon, \boldsymbol{r}, \boldsymbol{r}') \end{bmatrix} \tag{2.217}$$

where the different components can be evaluated from Eq. (2.214) and (2.216). Using the definitions in Eq. (2.211) and (2.212) and following similar steps as in the non-relativistic theory presented in Section 2.2.4, the compact form

$$G_0^{\mathrm{D}}(\epsilon, \boldsymbol{r}, \boldsymbol{r}')\mathsf{I}_2 = -ip \frac{W + mc^2}{2mc^2} \sum_{\Lambda} \left(h_\Lambda^+(\epsilon, \boldsymbol{r}) j_\Lambda(\epsilon, \boldsymbol{r}')^\times \Theta(r - r') + j_\Lambda(\epsilon, \boldsymbol{r}) h_\Lambda^+(\epsilon, \boldsymbol{r}')^\times \Theta(r' - r) \right) \tag{2.218}$$

of the single center expansion of the relativistic Green's function is obtained. It becomes apparent that using the notations introduced in Section 2.3.1, the relativistic objects can be written in analogy to the non-relativistic case. Therefore, the derivation of a two center expansion of the relativistic Green's function and the relativistic solution of the scattering path operator are given in a similar way as in the non-relativistic case (details can be found in Ref [63]).

A frequently used approximation of the full relativistic form of MST and DFT in general, is the so called scalar relativistic approximation. This approximation is also used in the present work and therefore outlined in Appendix A.10.

2.4 Screened KKR

In this section, a particular formulation of the KKR method, namely the screened KKR (SKKR) formalism [66, 67, 68] is outlined. A great advantage of this formalism is that the electronic structure of systems which exhibit only a two dimensional translational invariance can be calculated. This is important for transport calculations of realistic systems, which usually consist of two leads and the investigated structure in between. But it should be mentioned that variations of this method are also used for other geometries such as clusters.

The basic idea is that by applying a certain transformation the structure constants turn out to be of short range. This transformation is a scaling transformations of the Hamilton operator. Taking into account a so called scaling potential $\hat{W}$, the Hamilton operator can be rewritten as

$$\hat{H} = \hat{H}_0 + \hat{V} = \hat{H}_0 + \hat{V} + \hat{W} - \hat{W} = \hat{H}_0' + \hat{V}' \tag{2.219}$$

where

$$\hat{H}_0' = \hat{H}_0 + \hat{W}\,, \quad \hat{V}' = \hat{V} + \hat{W}\,. \tag{2.220}$$

A corresponding resolvent $\hat{\mathcal{G}}_0'$ can be defined for $\hat{H}_0'$ which is connected to the unscaled free resolvent $\hat{\mathcal{G}}_0$ by

$$\hat{\mathcal{G}}_0'(z) = \hat{\mathcal{G}}_0(z)[1 - \hat{W}\hat{\mathcal{G}}_0'(z)] \; . \tag{2.221}$$

Therefore, the Dyson equation determining the full resolvent can be written as

$$\hat{\mathcal{G}}(z) = \hat{\mathcal{G}}_0(z)[1 - \hat{V}\hat{\mathcal{G}}(z)] = \hat{\mathcal{G}}_0'(z)[1 - \hat{V}'\hat{\mathcal{G}}(z)] \; . \tag{2.222}$$

Now, the scaling potential is assumed to have the following muffin tin properties:

$$W(\boldsymbol{r}) = \sum_i W_i(\boldsymbol{r}_i) \tag{2.223}$$

$$W_i(\boldsymbol{r}_i) = \begin{cases} W_\mathrm{r} & |\boldsymbol{r}_i| \leq b \\ 0 & \text{otherwise} \end{cases} \; . \tag{2.224}$$

Here, W_r is an appropriate constant and b corresponds to the muffin tin radius. From now on the index r denotes the reference system defined by $W(\boldsymbol{r})$. The full Green's function of this reference system, written in terms of the supermatrix notation defined in Section 2.2.6, is given by

$$\underline{\boldsymbol{G}}^\mathrm{r}(\epsilon) = \underline{\boldsymbol{G}}^0(\epsilon)[1 - \underline{\boldsymbol{t}}^\mathrm{r}(\epsilon)\underline{\boldsymbol{G}}^0(\epsilon)]^{-1} \; . \tag{2.225}$$

Using the single-site scattering matrix of the system under investigation together with the single-site scattering matrix of the reference system, the difference

$$\underline{\boldsymbol{t}}_\Delta(\epsilon) = \underline{\boldsymbol{t}}(\epsilon) - \underline{\boldsymbol{t}}^\mathrm{r}(\epsilon) \; . \tag{2.226}$$

can be defined. Hereby, the full Green's function can be represented in terms of the full Green's function of the reference system and the difference between the single-site scattering matrices of the reference and the investigated system

$$\underline{\boldsymbol{G}}(\epsilon) = \underline{\boldsymbol{G}}^\mathrm{r}(\epsilon)[1 - \underline{\boldsymbol{t}}_\Delta(\epsilon)\underline{\boldsymbol{G}}^\mathrm{r}(\epsilon)]^{-1} \; . \tag{2.227}$$

As the structure constants of the investigated system and the reference system are assumed to be the same, a difference scattering path operator can be defined by

$$\underline{\boldsymbol{\tau}}_\Delta(\epsilon) = \left[\underline{\boldsymbol{t}}_\Delta^{-1}(\epsilon) - \underline{\boldsymbol{\mathcal{G}}}_0(\epsilon)\right]^{-1} \; . \tag{2.228}$$

Therefore, the full Green's function $\underline{\boldsymbol{G}}$ can be expressed by

$$\underline{\boldsymbol{G}}(\epsilon) = \underline{\boldsymbol{G}}^\mathrm{r}(\epsilon) + \underline{\boldsymbol{G}}^\mathrm{r}(\epsilon)\underline{\boldsymbol{\tau}}_\Delta(\epsilon)\underline{\boldsymbol{G}}^\mathrm{r}(\epsilon) \tag{2.229}$$

and the scattering path operator $\underline{\boldsymbol{\tau}}$ by

$$\underline{\boldsymbol{\tau}}(\epsilon) = \underline{\boldsymbol{t}}(\epsilon)[\underline{\boldsymbol{t}}_\Delta^{-1}(\epsilon)\underline{\boldsymbol{\tau}}_\Delta(\epsilon)\underline{\boldsymbol{t}}_\Delta^{-1}(\epsilon) + (\underline{\boldsymbol{t}}^{-1}(\epsilon) - \underline{\boldsymbol{t}}_\Delta^{-1}(\epsilon))]\underline{\boldsymbol{t}}(\epsilon) \; . \tag{2.230}$$

This means that once the difference scattering path operator $\underline{\boldsymbol{\tau}}_\Delta$ is determined all MST objects of the system under investigation can be determined.

The great advantage of this reformulation of MST is that by choosing an appropriate W_r, Eq. (2.225) can be solved such that

$$\underline{G}^{\mathrm{r},ij}(\epsilon) \sim \underline{0} \quad \forall \quad |\boldsymbol{R}_i - \boldsymbol{R}_j| \geq d \; . \tag{2.231}$$

The distance d is small and includes only the first and second nearest neighbors. The $\underline{G}^{\mathrm{r},ij}$ are usually called screened structure constants.

Now, the potential of the Hamiltonian $\hat{H} = \hat{H}_0 + \hat{V}$ is assumed to have only two dimensional translation symmetry and is still a superposition of non-overlapping functions

$$V(\boldsymbol{r}) = \sum_i V_i(\boldsymbol{r}_i + \boldsymbol{R}_{i,||} + R_{i,z}\hat{\boldsymbol{z}}) \tag{2.232}$$

such that the same two dimensional lattice $\mathcal{L}^{(2)}$ with $\boldsymbol{R}_{i,||} \in \mathcal{L}^{(2)}$ applies in all layers (a detailed treatment of two-dimensional translational invariance in terms of group theory is given in Ref. [69]). By introducing the notation

$$\boldsymbol{R}_{p,i} = \boldsymbol{C}_p + \boldsymbol{R}_{i,||} \quad ; \quad \boldsymbol{C}_p = R_{i,z}\hat{\boldsymbol{z}} \tag{2.233}$$

a lattice Fourier transformation of the screened structure constants

$$\underline{G}^{\mathrm{r},pq}(\boldsymbol{k}_{||}, \epsilon) = \sum_{\boldsymbol{R}_{||} \in \mathcal{L}^{(2)}} \exp(i\boldsymbol{k}_{||}\boldsymbol{R}_{||}) \underline{G}^{\mathrm{r}}(\boldsymbol{C}_p + \boldsymbol{R}_{||}, \epsilon) \tag{2.234}$$

is performed, where $\boldsymbol{k}_{||}$ is an element of the two dimensional Brillouin zone of $\mathcal{L}^{(2)}$. Now, the statement in Eq (2.231) can be rewritten in the form

$$\underline{G}^{\mathrm{r},pq}(\boldsymbol{k}_{||}, \epsilon) = \underline{0} \quad \text{if} \quad |p - q| < N \tag{2.235}$$

where N is suitably chosen and turns out to be the number of considered atomic layers within which the structure constants are completely screened. A block of N elements $\underline{G}^{\mathrm{r},pq}(\boldsymbol{k}_{||}, \epsilon) \neq \underline{0}$, $|p - q| \leq N$ can be understood as an element of a tridiagonal supermatrix labeled by P and Q

$$\underline{\boldsymbol{G}}^{\mathrm{r}}(\boldsymbol{k}_{||}, \epsilon) = \{\underline{G}^{\mathrm{r},pq}(\boldsymbol{k}_{||}, \epsilon)\} = \{\underline{\boldsymbol{G}}^{\mathrm{r},PQ}(\boldsymbol{k}_{||}, \epsilon)\} \; . \tag{2.236}$$

As all involved matrices are now tridiagonal the numerical treatment is far more efficient [70]. The $\boldsymbol{k}_{||}$-th projection of $\underline{\boldsymbol{G}}(\epsilon)$ is given by

$$\underline{\boldsymbol{G}}(\boldsymbol{k}_{||}, \epsilon) = \left[\underline{\boldsymbol{t}}_{\Delta}^{-1}(\epsilon) - \underline{\boldsymbol{G}}^{\mathrm{r}}(\boldsymbol{k}_{||}, \epsilon)\right]^{-1} \tag{2.237}$$

where

$$\underline{\boldsymbol{t}}_{\Delta}(\epsilon) = \left\{\underline{t}_{\Delta}^{P}(\epsilon)\delta_{PQ}\right\} \quad ; \quad \underline{t}_{\Delta}^{P}(\epsilon) = \{t_{\Delta}^{p}(\epsilon)\delta_{pq}\} \tag{2.238}$$

$$\underline{\boldsymbol{\tau}}_{\Delta}(\boldsymbol{k}_{||}, \epsilon) = \left\{\underline{\tau}_{\Delta}^{P}(\boldsymbol{k}_{||}, \epsilon)\right\} \quad ; \quad \underline{\tau}_{\Delta}^{P}(\boldsymbol{k}_{||}, \epsilon) = \left\{\tau_{\Delta}^{p}(\boldsymbol{k}_{||}, \epsilon)\right\} \; . \tag{2.239}$$

If the configuration space is now partitioned into a left, right and an intermediate region according to the following scheme

$$\begin{array}{lccc} \mathrm{L}: & -\infty & < P \leq & 0 \\ \mathrm{I}: & 1 & \leq P \leq & n \\ \mathrm{R}: & n+1 & \leq P \leq & \infty \end{array} \tag{2.240}$$

the inverse of the difference scattering path operator can be partitioned like

$$\left[\underline{\boldsymbol{\tau}}_{\Delta}(\boldsymbol{k}_{||}, \epsilon)\right]^{-1} = \begin{pmatrix} \left[\underline{\boldsymbol{\tau}}_{\Delta}(\boldsymbol{k}_{||}, \epsilon)\right]^{-1}_{\mathrm{L,L}} & \left[\underline{\boldsymbol{\tau}}_{\Delta}(\boldsymbol{k}_{||}, \epsilon)\right]^{-1}_{\mathrm{L,I}} & 0 \\ \left[\underline{\boldsymbol{\tau}}_{\Delta}(\boldsymbol{k}_{||}, \epsilon)\right]^{-1}_{\mathrm{I,L}} & \left[\underline{\boldsymbol{\tau}}_{\Delta}(\boldsymbol{k}_{||}, \epsilon)\right]^{-1}_{\mathrm{I,I}} & \left[\underline{\boldsymbol{\tau}}_{\Delta}(\boldsymbol{k}_{||}, \epsilon)\right]^{-1}_{\mathrm{I,R}} \\ 0 & \left[\underline{\boldsymbol{\tau}}_{\Delta}(\boldsymbol{k}_{||}, \epsilon)\right]^{-1}_{\mathrm{R,I}} & \left[\underline{\boldsymbol{\tau}}_{\Delta}(\boldsymbol{k}_{||}, \epsilon)\right]^{-1}_{\mathrm{R,R}} \end{pmatrix} \; . \tag{2.241}$$

In order to evaluate $\underline{\boldsymbol{\tau}}_{\Delta}(\boldsymbol{k}_{||},\epsilon)_{\mathrm{I,I}}$, the so called surface scattering path operators are used which are given by

$$\underline{\boldsymbol{\tau}}^{00}_{\Delta,\mathrm{L}}(\boldsymbol{k}_{||},\epsilon) = \left[\underline{t}^{\mathrm{L}}_{\Delta}(\epsilon)^{-1} - \underline{G}^{\mathrm{r},00}(\boldsymbol{k}_{||},\epsilon) - \underline{G}^{\mathrm{r},10}(\boldsymbol{k}_{||},\epsilon)\underline{\boldsymbol{\tau}}^{00}_{\Delta,\mathrm{L}}(\boldsymbol{k}_{||},\epsilon)\underline{G}^{\mathrm{r},01}(\boldsymbol{k}_{||},\epsilon)\right]^{-1} \tag{2.242}$$

$$\underline{\boldsymbol{\tau}}^{00}_{\Delta,\mathrm{R}}(\boldsymbol{k}_{||},\epsilon) = \left[\underline{t}^{\mathrm{R}}_{\Delta}(\epsilon)^{-1} - \underline{G}^{\mathrm{r},00}(\boldsymbol{k}_{||},\epsilon) - \underline{G}^{\mathrm{r},10}(\boldsymbol{k}_{||},\epsilon)\underline{\boldsymbol{\tau}}^{00}_{\Delta,\mathrm{R}}(\boldsymbol{k}_{||},\epsilon)\underline{G}^{\mathrm{r},01}(\boldsymbol{k}_{||},\epsilon)\right]^{-1} \tag{2.243}$$

and have to be evaluated recursively. In case that there are no lattice relaxations the difference scattering path operator is now given by

$$\begin{aligned}\left[\left[\underline{\boldsymbol{\tau}}_{\Delta}(\boldsymbol{k}_{||},\epsilon)\right]^{-1}_{\mathrm{I,I}}\right]^{PQ} &= \left(\underline{t}^{\mathrm{L}}_{\Delta}(\epsilon)^{-1} - \underline{G}^{\mathrm{r},00}(\boldsymbol{k}_{||},\epsilon)\right)\delta_{PQ} \\ &\quad - \underline{G}^{\mathrm{r},01}(\boldsymbol{k}_{||},\epsilon)\delta_{PQ-1} - \underline{G}^{\mathrm{r},10}(\boldsymbol{k}_{||},\epsilon)\delta_{PQ+1} \\ &\quad - \underline{G}^{\mathrm{r},10}(\boldsymbol{k}_{||},\epsilon)\underline{\boldsymbol{\tau}}^{00}_{\Delta,\mathrm{L}}(\boldsymbol{k}_{||},\epsilon)\underline{G}^{\mathrm{r},01}(\boldsymbol{k}_{||},\epsilon)\delta_{P1}\delta_{Q1} \\ &\quad - \underline{G}^{\mathrm{r},10}(\boldsymbol{k}_{||},\epsilon)\underline{\boldsymbol{\tau}}^{00}_{\Delta,\mathrm{R}}(\boldsymbol{k}_{||},\epsilon)\underline{G}^{\mathrm{r},01}(\boldsymbol{k}_{||},\epsilon)\delta_{Pn}\delta_{Qn}\,. \end{aligned} \tag{2.244}$$

The case of lattice relaxations is not discussed here. To get a site representation of the scattering path operator the two dimensional Brillouin integration ,

$$\underline{\boldsymbol{\tau}}^{nm}_{\Delta}(\epsilon) = \frac{1}{\Omega_{\mathrm{SBZ}}}\int \mathrm{d}\boldsymbol{k}_{||}\exp[-i\boldsymbol{k}_{||}(\boldsymbol{R}_{n,||} - \boldsymbol{R}_{m,||})]\underline{\boldsymbol{\tau}}^{pq}_{\Delta}(\boldsymbol{k}_{||},\epsilon)\,, \tag{2.245}$$

has to be performed, where Ω_{SBZ} is the area of the two dimensional Brillouin zone.

As already mentioned, the main advantage of the SKKR method is that the scattering path operator is tridiagonal. This implies the $O(N^3)$ problem is reduced to a $O(N^1)$. The screening in one direction that has been discussed here is sufficient to achieve this tridiagonal form. In addition, the partitioning of space allows to include the influence of the left and right semi-infinite part by the evaluation of the surface scattering path operator. Speaking in terms of transport this means that the perfect leads are separated from the interaction region in between but their influence in this region is taken into account by the surface scattering properties.

2.5 KKR in practice

As the last sections are devoted to a detailed description of MST, here, practical aspects and in particular the way to construct the KKR cycle is discussed.

The first step to start a KKR calculation is the solution of the single-site scattering problem. Therefore, a numerical determination of the scattering solution within the muffin tin radius is performed by solving the underlying equation of motion which can be the Schrödinger or Dirac equation for a given energy and a given effective potential. This solution is matched to the free solution outside the muffin tin radius which yields the full scattering solution, from which the the phase shift and therewith the matrix elements of the single-site scattering operator are obtained. In addition, the structure constants of the system are evaluated. This is done in k-space if a periodic solid is considered. The difference of the inverse matrix of the single-site scattering operator and the structure constant matrix have to be inverted to find the k-dependent scattering path operator. Afterwards, a Brillouin zone integration is performed to obtain the real space scattering path operator. From the real space scattering

path operator and the single-site scattering functions, the Green's function of the system is obtained for the given energy.

This procedure is repeated for different complex energies on a semi-circle contour. The contour is chosen to avoid the singularities of the Green's function on the real axis. An integration can be performed to obtain the charge density of the system given by

$$n(\boldsymbol{r}) = -\frac{2}{\pi} \int_{\curvearrowright} \mathrm{d}z \, G(z, \boldsymbol{r}, \boldsymbol{r}) \, . \tag{2.246}$$

From this charge density an external potential can be obtained via the Poisson equation. This external potential becomes the effective potential by adding Hartree and exchange-correlation contributions which are obtained from the exchange-correlation energy by

$$E_{\mathrm{xc}}\left[n\right] = \int \mathrm{d}\boldsymbol{r} \, n\left(\boldsymbol{r}\right) \epsilon_{\mathrm{xc}}\left(\left[n\right], \boldsymbol{r}\right) \, , \tag{2.247}$$

whereas, the Hartree part stems from the Coulomb energy,

$$U\left[n\right] = \int \mathrm{d}\boldsymbol{r} \int \mathrm{d}\boldsymbol{r}' \, \frac{n(\boldsymbol{r}) \, n(\boldsymbol{r})}{|\boldsymbol{r} - \boldsymbol{r}'|} \, . \tag{2.248}$$

The sum of all contributions, evaluated from the density, gives the total potential that serves as the potential for the subsequent self-consistent step. In the spin-dependent case, the magnetization density has to be additionally calculated for the construction of the exchange-correlation part.

2.6 Magnetic exchange parameters and the Lichtenstein Formula

In this section, Lichtensteins formula [71, 72] is introduced which allows to calculate magnetic exchange interactions between pairs of atoms from multiple scattering quantities. The exchange parameters calculated via this formula are associated with the Heisenberg Hamiltonian

$$\mathcal{H} = -\frac{1}{2} \sum_{i \neq j} J_{ij} \boldsymbol{S}_i \boldsymbol{S}_j \, . \tag{2.249}$$

However, this requires some inherent assumptions: Magnetism is assumed to arise from localized moments, which is not self-evident *a priori* for an itinerant electron system since valence electrons can be strongly delocalized (for details see Ref. [52]). On the other hand, it is assumed that the moments can only fluctuate in direction and not in length. This is also not always valid because the strength of a magnetic moment in a real material depends on the local and even global environment. But it turns out and is shown in this treatise that the exchange parameters calculated from Lichtensteins formula are sufficient for theoretical predictions of critical temperatures and also for general aspects of finite temperature magnetism. This is connected to the observation that even in itinerant magnets the moments arise from partially localized states.

The derivation of the Lichtenstein formula relies on the local force theorem [73] which states that, by assuming small perturbations, the variation of the total energy is expressed as the sum of energy changes of all occupied one-particle states given by

$$\delta E = \int_{-\infty}^{E_{\mathrm{f}}} \mathrm{d}E \, (E - E_{\mathrm{F}}) \delta N(E) \, , \tag{2.250}$$

where $\delta N(E)$ is the variation of the density of states. Here, small perturbation means small rotations of the magnetic moment at site i with angle θ and a corresponding rotation at site j with angle $-\theta$. To define changes of the single-site scattering in terms of an angle the following representation of $\hat{t}^i$ is used

$$\hat{t}^i = \frac{1}{2}(\hat{t}^i_\uparrow + \hat{t}^i_\downarrow) + \frac{1}{2}(\hat{t}^i_\uparrow + \hat{t}^i_\downarrow)\boldsymbol{\sigma} \cdot \boldsymbol{m}_i \tag{2.251}$$

where $\boldsymbol{m}_i = (\sin(\theta_i), 0, \cos(\theta_i))$. Therefore, changes in the single-site scattering $\delta\hat{t}^i$ can be expressed in terms of $\delta\boldsymbol{m}_i$. According to Lloyd's formula [74] and the possibility to express the variation $\delta N(E)$ in terms of the scattering path operator (see Ref. [75]), Eq. 2.250 can be rewritten as

$$\delta E = \frac{1}{\pi}\int_{-\infty}^{E_\mathrm{f}} \mathrm{d}E\, \mathrm{Im}\, \mathrm{Tr} \ln(1 - \delta\hat{t}^{-1}\hat{\tau})\,. \tag{2.252}$$

This leads to the actual form of Lichtenstein's formula [72],

$$J_{ij} = \frac{1}{4\pi}\mathrm{Im}\int_{-\infty}^{E_\mathrm{f}} \mathrm{d}E\, \mathrm{Tr}(t^{-1}_{i\uparrow} - t^{-1}_{i\downarrow})\tau_{ij\uparrow}(t^{-1}_{j\uparrow} - t^{-1}_{j\downarrow})\tau_{ji\downarrow}\,. \tag{2.253}$$

Hereby, the magnetic exchange parameters are fully determined by quantities evaluated within MST. As the energy integration has to be carried out in more detail compared to the evaluation of the potential in SCF calculations the integration is not performed on a semi-circle in the complex plane. Instead it is is carried out on a straight line parallel to the real axis with a small imaginary part (details are found in Ref. [63]). Therefore, the potential is calculated first and afterwards the J_{ij} of this potential are evaluated.

Strictly speaking the exchange interactions obtained from this formalism are only valid in the limit of small perturbations of the magnetic structure. No self-consistent relaxation of the electronic structure is taken into account. In particular, the angles of the rotations of the moments with respect to each other have to be small. Fortunately, it turns out that this formalism captures the most important features. If the exchange interactions are employed within Monte Carlo simulations, reasonable results even for high temperatures are obtained.

2.7 Linear response formalism for electronic transport

In this section an introduction to the linear response formalism is given which is used In this thesis to calculate electronic transport properties. Originally, the formalism stems from the pioneering work of Kubo [76] who derived a general formula which is not restricted to the description of electronic transport but provides a general linear response formalism.

Here, a derivation of the method which allows the calculation of the electronic conductance of a mesoscopic sample is described which follows Baranger and Stone [77]. Their formulation is general and is not restricted to a specific number of leads and also includes arbitrary magnetic fields. Therefore, it can also be employed for the calculation of transverse effects like, e.g., the Hall effect. In addition, Ref. [77] provides a proof of the equivalence of the Landauer-Büttiker approach [78] and the standard Kubo-Greenwood approach [79].

First, some basic facts about ballistic transport described by linear response theory need to be noted: Only elastic scattering of the conduction electrons is taken into account. This means that the considered sample is small enough and also temperature is low enough that no inelastic scattering events occur.

Now, a multiprobe structure is considered which consists of a finite region of arbitrary shape with certain geometric constraints which may lead to additional scattering of electrons. This region is connected to N perfectly ordered and straight semi-infinite leads. It is assumed that voltages are applied to these leads and the resulting current response is calculated. The electronic system is described by the Hamiltonian

$$\hat{H}_0 = \frac{1}{2m}\left(\boldsymbol{p} - \frac{e}{c}\boldsymbol{A}(\boldsymbol{x})\right) + U(\boldsymbol{x}) \tag{2.254}$$

where the spin degree of freedom is neglected for simplicity. This implies that the non-interacting electrons move in an external potential U and a magnetic field characterized by the vector potential $\boldsymbol{A}$. The Hamiltonian exhibits a continuous set of eigenfunctions with eigenvalues ϵ_α which exhibit the properties

$$\begin{aligned}\int \mathrm{d}\boldsymbol{r}\, \psi^*_\alpha(\boldsymbol{x})\psi_\beta(\boldsymbol{x}) &= \delta(\alpha-\beta)\\ \int \mathrm{d}\alpha\, \psi^*_\alpha(\boldsymbol{x})\psi_\alpha(\boldsymbol{x}') &= \delta(\boldsymbol{x}-\boldsymbol{x}')\end{aligned} \tag{2.255}$$

which assure orthogonality and completeness. The eigensystem is continuous because due to the semi-infinite leads the entire system in infinite.

A perturbing voltage $V(\boldsymbol{x}, t)$ applied to the system is introduced, which leads to the total Hamiltonian,

$$\hat{H} = \hat{H}_0 + \hat{H}_1 = \hat{H}_0 + eV(\boldsymbol{x}, t)\,. \tag{2.256}$$

The voltage is assumed to vary slow enough in time to keep the associated magnetic fields negligible. In addition, it is assumed that $V(\boldsymbol{x}, t)$ reaches a certain constant value in the leads which implies a vanishing electric field far enough from the sample. The spatial variation and time dependence of $V(\boldsymbol{x}, t)$ are given by

$$V(\boldsymbol{x}, t) = V(\boldsymbol{x})\cos(\Omega t)e^{-\delta|t|} \tag{2.257}$$

and therefore the time-dependent electric field yields [6]

$$\boldsymbol{E}(\boldsymbol{x}, t) = \boldsymbol{E}(\boldsymbol{x})\cos(\Omega t)e^{-\delta|t|}\,. \tag{2.258}$$

The purpose of the following considerations is to calculate the current density responding to the external electric field in the limit $\delta \to 0$ and $\Omega \to 0$ in exactly this order which is mathematically expressed by

$$\lim_{\Omega\to 0}\lim_{\delta\to 0} \boldsymbol{J}(\boldsymbol{x}, t, \Omega, \delta)\,. \tag{2.259}$$

The current density operator is given by

$$\hat{\boldsymbol{J}}(\boldsymbol{x}) = \frac{e}{2m}(n(\boldsymbol{x})(\hat{\boldsymbol{p}} - \frac{e}{c}\boldsymbol{A}(\boldsymbol{x})) + (\hat{\boldsymbol{p}} - \frac{e}{c}\boldsymbol{A}(\boldsymbol{x}))n(\boldsymbol{x})) \tag{2.260}$$

and in order to keep the notation more transparent the gauge invariant derivative

$$\boldsymbol{D} = \boldsymbol{\nabla} - \frac{ie}{\hbar c}\boldsymbol{A}(x) \tag{2.261}$$

[6] For the later purpose one should note that basic mathematics give $\lim_{\delta\to 0} e^{-\delta|t|} = 1$ and $\lim_{\Omega\to 0}\cos(\Omega t) = 1$

is defined together with the double-sided derivative

$$f(\boldsymbol{x})\overleftrightarrow{\boldsymbol{D}}g(\boldsymbol{x}) = f(\boldsymbol{x})\boldsymbol{D}g(\boldsymbol{x}) - g(\boldsymbol{x})\boldsymbol{D}f(\boldsymbol{x}) = -g(\boldsymbol{x})\overleftrightarrow{\boldsymbol{D}}^* f(\boldsymbol{x}) \tag{2.262}$$

where f and g are arbitrary functions. The calculation of the matrix elements of the current density operator yields

$$[\hat{\boldsymbol{J}}(\boldsymbol{x})]_{\beta\alpha} = -\frac{ie\hbar}{2m}\psi^*_\beta(\boldsymbol{x})\overleftrightarrow{\boldsymbol{D}}\psi_\alpha(\boldsymbol{x}) = -\frac{ie\hbar}{2m}\boldsymbol{W}_{\beta\alpha}(\boldsymbol{x})\,. \tag{2.263}$$

In order to introduce the basic linear response consideration the equilibrium density matrix of a non-interacting system represented by $\hat{H}_0$

$$\hat{\rho}_0 = \int \mathrm{d}\alpha\, f(\epsilon_\alpha)|\psi_\alpha\rangle\langle\psi_\alpha| \tag{2.264}$$

is reminded, where $f(\epsilon_\alpha)$ is the Fermi function. The time evolution of the full density matrix associated with $\hat{H}$

$$i\hbar\frac{\mathrm{d}\rho}{\mathrm{d}t} = [\hat{H}, \rho] \tag{2.265}$$

is in first order perturbation theory determined by

$$i\hbar\frac{\mathrm{d}\hat{\rho}_1}{\mathrm{d}t} = [\hat{H}_0, \hat{\rho}_1] + [\hat{H}_1, \hat{\rho}_0] \tag{2.266}$$

where $\hat{\rho}_1 = \hat{\rho} - \hat{\rho}_0$. This can be rewritten in matrix notation and leads to

$$i\hbar\frac{\mathrm{d}}{\mathrm{d}t}\rho_{1,\alpha\beta} = -\epsilon_{\beta\alpha}\rho_{1,\alpha\beta} + ef_{\beta\alpha}V_{\alpha\beta}\cos(\Omega t)e^{-\delta|t|}\,, \tag{2.267}$$

where $\epsilon_{\beta\alpha} = \epsilon_\beta - \epsilon_\alpha$, $f_{\beta\alpha} = f(\epsilon_\beta) - f(\epsilon_\alpha)$ and $\int \mathrm{d}\boldsymbol{r}\,\psi^*_\alpha(\boldsymbol{x})V(\boldsymbol{x})\psi_\beta(\boldsymbol{x}) = V_{\alpha\beta}$. In zeroth order, the time evolution of the current is given by

$$\boldsymbol{J}_0(\boldsymbol{x}) = \mathrm{Tr}(\rho_0\hat{\boldsymbol{J}}) = -\frac{ie\hbar}{2m}\int \mathrm{d}\alpha\, f(\epsilon_\alpha)\boldsymbol{W}_{\beta\alpha}(\boldsymbol{x})\,. \tag{2.268}$$

As it can be shown that $\nabla\boldsymbol{J}_0 = 0$ it does not contribute to net current and therefore drops out of the following considerations. Solving Eq. (2.267) by using an integrating factor, the first order response of the current is given by

$$\boldsymbol{J}_1(\boldsymbol{x}) = -\frac{ie^2\hbar}{4m}\int \mathrm{d}\alpha \int \mathrm{d}\beta\, f_{\beta\alpha}V_{\alpha\beta}\boldsymbol{W}_{\beta\alpha}(\boldsymbol{x})e^{\delta t}\left[\frac{e^{i\Omega t}}{\epsilon_{\beta\alpha} - \hbar\Omega + i\hbar\delta} + \frac{e^{-i\Omega t}}{\epsilon_{\beta\alpha} + \hbar\Omega + i\hbar\delta}\right]. \tag{2.269}$$

In this equation the limits $\delta \to 0$ and $\Omega \to 0$ have to be carried out. A discussion of all involved mathematical considerations that allow to carry out the limits is beyond the scope of this treatise. Here, only the result is presented (for details see the original work of Baranger and Stone [77]). The first order response of the current is

$$\boldsymbol{J}_1(\boldsymbol{x}) = -\frac{e^2\hbar^3\pi}{4m^2}\int \mathrm{d}\alpha \int \mathrm{d}\beta\, \left[f'(\epsilon_\alpha)\delta(\epsilon_{\beta\alpha}) + \frac{i}{\pi}\frac{f_{\beta\alpha}}{\epsilon_{\beta\alpha}}\mathrm{P}\left(\frac{1}{\epsilon_{\beta\alpha}}\right)\right]\boldsymbol{W}_{\beta\alpha}(\boldsymbol{x})\int_A \mathrm{d}^3x'\,\boldsymbol{W}_{\alpha\beta}(\boldsymbol{x}')\boldsymbol{E}(\boldsymbol{x}') \tag{2.270}$$

where A is the finite region of the sample which is limited by surfaces in the asymptotic region of the leads. Obviously, the first order current response is given by a sum of two terms. The first is the δ-function part denoted by $\delta(\epsilon_{\beta\alpha})$ and the second the principle value part denoted by $\mathrm{P}(1/\epsilon_{\beta\alpha})$. If the last result is expressed in terms of a non-local response function

$$\boldsymbol{J}_1(\boldsymbol{x}) = \int \mathrm{d}^3x' \underline{\sigma}(\boldsymbol{x}, \boldsymbol{x}')\boldsymbol{E}(\boldsymbol{x}')\,, \tag{2.271}$$

the conductivity tensor $\underline{\sigma}$ is given by

$$\underline{\sigma}(\boldsymbol{x}, \boldsymbol{x}') = -\frac{e^2\hbar^3\pi}{4m^2}\int \mathrm{d}\alpha \int \mathrm{d}\beta \left[f'(\epsilon_\alpha)\delta(\epsilon_{\beta\alpha}) + \frac{i}{\pi}\frac{f_{\beta\alpha}}{\epsilon_{\beta\alpha}}\mathrm{P}\left(\frac{1}{\epsilon_{\beta\alpha}}\right)\right]\boldsymbol{W}_{\beta\alpha}(\boldsymbol{x})\boldsymbol{W}_{\alpha\beta}(\boldsymbol{x}') \tag{2.272}$$

which is the first central result of this derivation. It should be noted that the principle value part is zero when no external magnetic field is applied. Therefore, this term is treated here for completeness but is neglected in later discussions because external magnetic field are not considered in this treatise.

The total current in lead m is related to the current density and the voltage by

$$I_m = \int_{C_m} \mathrm{d}y_m \boldsymbol{J}_1(\boldsymbol{x}_m)\hat{\boldsymbol{x}}_m = \sum_n g_{nm}V_n \tag{2.273}$$

where g_{nm} are the conductance coefficients. They can be identified with the conductance between two leads n and m. The C_m denotes a cross sectional area in the asymptotic region of the leads. In the case of two leads which is investigated later, g_{nm} gives the specific conductance of the system. Inserting Eq. (2.271) and using integration theorems, it can be shown that the conductance coefficient can be expressed as

$$g_{nm} = -\int_{C_m} \mathrm{d}y_m \int_{C_n} \mathrm{d}y_n' \hat{\boldsymbol{x}}_m \underline{\sigma}(\boldsymbol{x}, \boldsymbol{x}')\hat{\boldsymbol{x}}_n\,. \tag{2.274}$$

Therefore, Eq. (2.272) determines the conductivity tensor from which the total conductance between the leads (2.274) can be determined. In order to use the method derived so far within the KKR formalism the following representation in terms of the Green's function is employed,

$$\begin{aligned}\Delta G(\epsilon, \boldsymbol{x}, \boldsymbol{x}') &= G^+(\epsilon, \boldsymbol{x}, \boldsymbol{x}') - G^-(\epsilon, \boldsymbol{x}, \boldsymbol{x}') = -2\pi i \int \mathrm{d}\alpha \psi_\alpha(\boldsymbol{x})\psi_\alpha^*(\boldsymbol{x}')\delta(\epsilon - \epsilon_\alpha) \\ \Sigma G(\epsilon, \boldsymbol{x}, \boldsymbol{x}') &= G^+(\epsilon, \boldsymbol{x}, \boldsymbol{x}') + G^-(\epsilon, \boldsymbol{x}, \boldsymbol{x}') = 2\int \mathrm{d}\alpha \psi_\alpha(\boldsymbol{x})\psi_\alpha^*(\boldsymbol{x}')\mathrm{P}\left(\frac{1}{\epsilon - \epsilon_\alpha}\right)\,.\end{aligned} \tag{2.275}$$

With these identities Eq. (2.272) can be written as

$$\underline{\sigma}(\boldsymbol{x}, \boldsymbol{x}') = \frac{e^2\hbar^3}{16\pi m^2}\int_{-\infty}^{\infty} \mathrm{d}\epsilon\, f'(\epsilon_\alpha)\Delta G(\epsilon, \boldsymbol{x}, \boldsymbol{x}')\overleftrightarrow{\boldsymbol{D}}^*\overleftrightarrow{\boldsymbol{D}}'\Delta G(\epsilon, \boldsymbol{x}', \boldsymbol{x}) \tag{2.276}$$

where the principle value part is omitted assuming that no magnetic field is applied.

If additional considerations concerning the asymptotic behavior of wave functions in the leads are taken into account [77] one finally ends up with

$$g_{nm} = \frac{e^2\hbar^3}{8\pi m^2}\int \mathrm{d}\epsilon\, f'(\epsilon)\int_{C_m}\mathrm{d}y_m\int_{C_n}\mathrm{d}y_n'\Delta G^+(\epsilon, \boldsymbol{x}_m, \boldsymbol{x}_n')(\overleftrightarrow{\boldsymbol{D}}^* \cdot \hat{\boldsymbol{x}}_m)(\overleftrightarrow{\boldsymbol{D}}' \cdot \hat{\boldsymbol{x}}_n)\Delta G^+(\epsilon, \boldsymbol{x}_n', \boldsymbol{x}_m)\,. \tag{2.277}$$

The last equations can be written as a trace over operators by using the identity (see Ref. [77])

$$f(\boldsymbol{x},\boldsymbol{x}')\overleftrightarrow{\boldsymbol{D}}^{*}\overleftrightarrow{\boldsymbol{D}}' g(\boldsymbol{x}',\boldsymbol{x}) = -\left(\frac{2mi}{e\hbar}\right)^2 \mathrm{Tr}[\hat{J}(\boldsymbol{x})\hat{f}\hat{J}(\boldsymbol{x})\hat{g}]\,. \tag{2.278}$$

Therefore, the conductivity tensor is given by

$$\underline{\sigma} = \frac{\hbar}{4\pi}\mathrm{Tr}[\hat{J}(\boldsymbol{x})\Delta\hat{G}\hat{J}(\boldsymbol{x}')\Delta\hat{G}]\,. \tag{2.279}$$

This is the central result which is employed in the following subsection. It is independent of a certain representation and therefore it is used to derive the explicit expression for the conductivity in the relativistic KKR framework. For justification that this formula is valid in the relativistic framework the reader is referred to literature (see Ref. [58] and references therein).

2.7.1 Spin polarized current in the relativistic screened KKR framework

On the basis of Eq. 2.279 theoretical preparatory work for using linear response theory in the calculation of spin projected currents in the relativistic framework is presented.

The discussion is specified for the case of muffin tin potentials associated with a certain lattice. Therefore, the current density operator is replaced by the current operator and the connection to the density is given by a normalization to the volume per atom Ω and the number of atoms N_a.

As the imaginary part of the resolvent is given in terms of retarded and advanced Green's functions by $\mathrm{Im}\,G^{+} = \frac{1}{2i}\left(G^{+} - G^{-}\right)$, Eq. (2.279) can also be written as

$$\sigma_{\mu\nu} = \frac{\hbar}{\pi N_a \Omega}\mathrm{Tr}[\hat{J}_\mu \mathrm{Im}\hat{G}^{+}(z)\,\hat{J}_\nu \mathrm{Im}\hat{G}^{+}(z)] \tag{2.280}$$

which is the common form of the Kubo formula for the conductivity tensor. The $\hat{J}_\mu$ are the cartesian components of the current operator.

Now, the imaginary part of the Green's function is again written as a difference of advanced and retarded Green's functions and the notation

$$\sigma_{\mu\nu} = \frac{1}{4}\left[\tilde{\sigma}_{\mu\nu}(\hat{G}^{+},\hat{G}^{+}) + \tilde{\sigma}_{\mu\nu}(\hat{G}^{-},\hat{G}^{-}) - \tilde{\sigma}_{\mu\nu}(\hat{G}^{+},\hat{G}^{-}) - \tilde{\sigma}_{\mu\nu}(\hat{G}^{-},\hat{G}^{+})\right] \tag{2.281}$$

with

$$\tilde{\sigma}_{\mu\nu}(G^{\pm},G^{\pm}) = \tilde{\sigma}_{\mu\nu}(z_1,z_2) = -\frac{\hbar}{\pi N_a \Omega}\mathrm{Tr}[\hat{J}_\mu G(z_1)\,\hat{J}_\nu G(z_2)]\,. \tag{2.282}$$

is introduced. Carrying out the trace in the relativistic framework, this becomes

$$\begin{aligned}
\tilde{\sigma}_{\mu\nu}(z_1,z_2) &= -\frac{\hbar}{\pi N_a \Omega}\int \mathrm{d}\mathbf{r}\langle\mathbf{r}|\hat{J}_\mu G(z_1)\hat{J}_\nu G(z_2)|\mathbf{r}\rangle \\
&= -\frac{\hbar}{\pi N_a \Omega}\int \mathrm{d}\mathbf{r}\int \mathrm{d}\mathbf{r}'\langle\mathbf{r}|\hat{J}_\mu \sum_i \frac{|\psi_i\rangle\langle\psi_i|}{z_1-\epsilon_i}\hat{J}_\nu|\mathbf{r}'\rangle\langle\mathbf{r}'|\sum_j \frac{|\psi_j\rangle\langle\psi_j|}{z_2-\epsilon_j}|\mathbf{r}\rangle \\
&= -\frac{\hbar}{\pi N_a \Omega}\int \mathrm{d}\mathbf{r}\int \mathrm{d}\mathbf{r}'\int \mathrm{d}\mathbf{r}''\int \mathrm{d}\mathbf{r}'''\langle\mathbf{r}|\hat{J}_\mu|\mathbf{r}''\rangle G(\mathbf{r}'',\mathbf{r}''';z_2)\langle\mathbf{r}'''|\hat{J}_\nu|\mathbf{r}'\rangle G(\mathbf{r}',\mathbf{r};z_2) \\
&= -\frac{\hbar}{\pi N_a \Omega}\int \mathrm{d}\mathbf{r}\int \mathrm{d}\mathbf{r}'\int \mathrm{d}\mathbf{r}''\int \mathrm{d}\mathbf{r}'''(-ec\alpha_\mu)\delta(\mathbf{r}-\mathbf{r}'')G(\mathbf{r}'',\mathbf{r}''';z_2) \\
&\qquad\qquad \times(-ec\alpha_\nu)\delta(\mathbf{r}'''-\mathbf{r}')G(\mathbf{r}',\mathbf{r};z_2) \\
&= -\frac{\hbar}{\pi N_a \Omega}\int \mathrm{d}\mathbf{r}\int \mathrm{d}\mathbf{r}'(-ec\alpha_\mu)G(\mathbf{r},\mathbf{r}';z_2)(-ec\alpha_\nu)G(\mathbf{r}',\mathbf{r};z_2)
\end{aligned} \tag{2.283}$$

where the current operator is now given in terms of its relativistic configuration space representation

$$\hat{J}_\mu = -ec\alpha_\mu \tag{2.284}$$

which can be derived from the continuity equation in the same manner as in non-relativistic theory [32]. The relativistic Green's functions are written in multiple scattering form and muffin tin approximation,

$$\begin{aligned}
G(\mathbf{r}_n,\mathbf{r}'_m;z) &= \sum_{\Lambda,\Lambda'} Z^n_\Lambda(\mathbf{r}_n,z)\,\tau^{nm}_{\Lambda,\Lambda'} Z^{m\times}_{\Lambda'}(\mathbf{r}'_m,z) \\
&\quad -\sum_\Lambda \left[J^n_\Lambda(\mathbf{r}_n,z)\,Z^{n\times}_\Lambda(\mathbf{r}'_n,z)\,\Theta(r_n-r'_n)+Z^n_\Lambda(\mathbf{r}_n,z)\,J^{n\times}_\Lambda(\mathbf{r}'_n,z)\,\Theta(r'_n-r_n)\right]\delta_{nm}\,,
\end{aligned} \tag{2.285}$$

with a complex energy argument $z = E \pm i\delta$ and the composite index $\Lambda = (\kappa,\mu)$. The J^n_Λ denote the four-component free-particle solutions in terms of spherical Bessel functions j_l. The second term is hereafter neglected because it is purely real for real potentials and real energies do not contribute (see Ref. [80]). Inserting Eq. (2.285) into (2.283) yields

$$\begin{aligned}
\tilde{\sigma}_{\mu\nu}(z_1,z_2) &= -\frac{\hbar}{\pi N_a\Omega}\sum_{n,m}\int\limits_{\{\mathbf{r}\in\mathbf{D_{V_m}}\}}\mathrm{d}\mathbf{r}\int\limits_{\{\mathbf{r}'\in\mathbf{D_{V_m}}\}}\mathrm{d}\mathbf{r}'(-ec\alpha_\mu)\sum_{\Lambda,\Lambda'}Z^n_\Lambda(\mathbf{r}_n,z_1)\tau^{nm}_{\Lambda,\Lambda'}(z_1)Z^{m\times}_{\Lambda'}(\mathbf{r}_m,z_1) \\
&\qquad\qquad\times(-ec\alpha_\nu)\sum_{\Lambda'',\Lambda'''}Z^m_{\Lambda''}(\mathbf{r}_m,z_2)\tau^{mn}_{\Lambda'',\Lambda'''}(z_2)Z^{n\times}_{\Lambda'''}(\mathbf{r}_n,z_2) \\
&= -\frac{\hbar}{\pi N_a\Omega}\sum_{n,m}\int\limits_{\{\mathbf{r}\in\mathbf{D_{V_m}}\}}\mathrm{d}\mathbf{r}\int\limits_{\{\mathbf{r}'\in\mathbf{D_{V_m}}\}}\mathrm{d}\mathbf{r}'\sum_{\Lambda,\Lambda',\Lambda'',\Lambda'''}Z^{n\times}_{\Lambda'''}(\mathbf{r}_n,z_2)(-ec\alpha_\mu)Z^n_\Lambda(\mathbf{r}_n,z_1)\tau^{nm}_{\Lambda,\Lambda'}(z_1) \\
&\qquad\qquad\times Z^{m\times}_{\Lambda'}(\mathbf{r}_m,z_1)(-ec\alpha_\nu)Z^m_{\Lambda''}(\mathbf{r}_m,z_2)\tau^{mn}_{\Lambda'',\Lambda'''}(z_2) \\
&= -\frac{\hbar}{\pi N_a\Omega}\sum_{n,m}\sum_{\Lambda,\Lambda',\Lambda'',\Lambda'''}\underline{J}^{n\mu}(z_2,z_1)\,\underline{\tau}^{nm}(z_1)\,\underline{J}^{m\nu}(z_1,z_2)\,\underline{\tau}^{mn}(z_2)
\end{aligned} \tag{2.286}$$

The underline denotes a matrix in angular momentum representation indexed by Λ, Λ' with the elements

$$\begin{aligned} J^{n\mu}_{\Lambda,\Lambda'}(z_2, z_1) &= \int_{D_{\mathbf{R}_n}} \mathrm{d}\mathbf{r}\, Z^{n\times}_{\Lambda}(\mathbf{r}_n, z_2)\, \hat{J}_\mu Z^{n}_{\Lambda'}(\mathbf{r}_n, z_1) \\ J^{m\nu}_{\Lambda,\Lambda'}(z_1, z_2) &= \int_{D_{\mathbf{R}_m}} \mathrm{d}\mathbf{r}\, Z^{m\times}_{\Lambda}(\mathbf{r}_m, z_1)\, \hat{J}_\nu Z^{n}_{\Lambda'}(\mathbf{r}_m, z_2)\ . \end{aligned} \tag{2.287}$$

As these matrix elements are on-site quantities, the site indices will be neglected from now on. The Z_Λ are given by

$$\begin{aligned} Z_\Lambda(\mathbf{r}, z) &= \sum_{\Lambda'} \begin{pmatrix} g_{\Lambda'\Lambda}(r, z)\, \chi_{\Lambda'}(\hat{\mathbf{r}}) \\ i f_{\Lambda'\Lambda}(r, z)\, \chi_{\bar{\Lambda}'}(\hat{\mathbf{r}}) \end{pmatrix} \\ Z^{\times}_\Lambda(\mathbf{r}, z) &= \sum_{\Lambda'} \left(g_{\Lambda'\Lambda}(r, z)\, \chi^{\dagger}_{\Lambda'}(\hat{\mathbf{r}}), -i f_{\Lambda'\Lambda}(r, z)\, \chi^{\dagger}_{\bar{\Lambda}'}(\hat{\mathbf{r}}) \right) \end{aligned} \tag{2.288}$$

where g and f are components of the radial scattering solutions as introduced in Section 2.3.1.

In the following, the matrix elements of the spin projected current operator, which is defined by

$$\hat{\mathcal{J}}_{\mu l} = \hat{\mathcal{P}}_l \hat{J}_\mu \tag{2.289}$$

are evaluated where

$$\hat{\mathcal{P}}_l = \frac{1}{2}\left[1 \pm \left(\beta\Sigma_l - \frac{\gamma_5(\hat{p}_l + A_l)}{mc}\right)\right] \tag{2.290}$$

is the relativistic spin projection operator introduced in Ref. [81]. The elements are calculated by

$$\begin{aligned} \mathcal{J}^{il}_{\Lambda\Lambda'}(z_2, z_1) = -\frac{ec}{2}\int \mathrm{d}^3 r \sum_{\Lambda'',\Lambda'''} &\left(g_{\Lambda''\Lambda}(r, z_2)\, \chi^{\dagger}_{\Lambda''}(\hat{\mathbf{r}}), -i f_{\Lambda''\Lambda}(r, z_2)\, \chi^{\dagger}_{\bar{\Lambda}''}(\hat{\mathbf{r}}) \right) \\ \times \left[\alpha_i \pm \left(\beta\Sigma_l - \frac{\gamma_5\left(\hat{p}_l + \frac{e}{c}A_l\right)}{mc}\right)\alpha_i\right] &\begin{pmatrix} g_{\Lambda'''\Lambda'}(r, z_1)\, \chi_{\Lambda'''}(\hat{\mathbf{r}}) \\ i f_{\Lambda'''\Lambda'}(r, z_1)\, \chi_{\bar{\Lambda}'''}(\hat{\mathbf{r}}) \end{pmatrix}. \end{aligned} \tag{2.291}$$

Terms including the vector potential are neglected from now on because external magnetic fields are neglected. Separating the additive terms and using the Dirac notation, the matrix elements can be rewritten in the form

$$\begin{aligned} \mathcal{J}^{il}_{\Lambda\Lambda'}(z_2, z_1) = &-\frac{ec}{2}\left\langle Z_\Lambda(z_2)\left|\alpha_i\right| Z_{\Lambda'}(z_1)\right\rangle \mp \frac{ec}{2}\left\langle Z_\Lambda(z_2)\left|\beta\Sigma_l\alpha_i\right| Z_{\Lambda'}(z_1)\right\rangle \\ &\pm \frac{e}{2m}\left\langle Z_\Lambda(z_2)\left|\gamma_5\alpha_i\hat{p}_l\right| Z_{\Lambda'}(z_1)\right\rangle\ . \end{aligned} \tag{2.292}$$

Focussing on the first part on the right hand side one finds

$$\begin{aligned} -\frac{ec}{2}\left\langle Z_\Lambda\left|\alpha_i\right| Z_{\Lambda\prime}\right\rangle = -\frac{eci}{2}\sum_{\Lambda'',\Lambda'''} \Bigg[&\int r^2 \mathrm{d}r\, g_{\Lambda''\Lambda}(r, z_2)\, f_{\Lambda'''\Lambda\prime}(r, z_1)\left\langle \Lambda''\left|\sigma_i\right|\bar{\Lambda}'''\right\rangle \\ &- \int r^2 \mathrm{d}r\, f_{\Lambda''\Lambda}(r, z_2)\, g_{\Lambda'''\Lambda\prime}(r, z_1)\left\langle \bar{\Lambda}''\left|\sigma_i\right|\Lambda'''\right\rangle \Bigg] \end{aligned} \tag{2.293}$$

with

$$\langle \Lambda \left| \sigma_i \right| \Lambda' \rangle = \int \mathrm{d}\Omega \, \chi^{\dagger}_{\Lambda} \left(\hat{\mathbf{r}} \right) \sigma_i \chi_{\Lambda'} \left(\hat{\mathbf{r}} \right) \tag{2.294}$$

and

$$\chi_{\Lambda} \left(\hat{\mathbf{r}} \right) = \sum_{s=\pm 1/2} C \left(l \, j \, 1/2 | \mu - s, s \right) Y_{l,\mu-s} \phi_s \tag{2.295}$$

which is introduced in Section 2.3.1. Therefore, the angular part of the matrix element yields

$$\langle \Lambda \left| \sigma_i \right| \Lambda' \rangle = \sum_{s,s'} C \left(l \, j \, 1/2 | \mu - s, s \right) C \left(l \, j \, 1/2 | \mu' - s', s' \right) \langle \phi_s \left| \sigma_i \right| \phi_{s'} \rangle \, \delta_{l,l'} \delta_{\mu-s,\mu'-s'} \, . \tag{2.296}$$

Matrix elements of the different σ_i are immediately evaluated by

$$\begin{aligned} \langle \phi_s \left| \sigma_x \right| \phi_{s'} \rangle &= \delta_{s,1/2} \delta_{s',-1/2} + \delta_{s,-1/2} \delta_{s',1/2} \\ \langle \phi_s \left| \sigma_y \right| \phi_{s'} \rangle &= i \delta_{s,-1/2} \delta_{s',1/2} - i \delta_{s,1/2} \delta_{s',-1/2} \\ \langle \phi_s \left| \sigma_z \right| \phi_{s'} \rangle &= \delta_{s,1/2} \delta_{s',1/2} - \delta_{s,-1/2} \delta_{s',-1/2} \, . \end{aligned} \tag{2.297}$$

In order to keep the notation more transparent, the radial integration is denoted by the symbol

$$I \left(g_{\Lambda'' \Lambda}, f_{\Lambda''' \Lambda'} \right) = \int r^2 \mathrm{d}r \, g_{\Lambda'' \Lambda} \left(r, z_2 \right) f_{\Lambda''' \Lambda'} \left(r, z_1 \right) \, . \tag{2.298}$$

Hence, the first term in Eq. (2.292) can be expressed in compact form,

$$-\frac{ec}{2} \langle Z_{\Lambda} \left| \alpha_i \right| Z_{\Lambda \prime} \rangle = -\frac{eci}{2} \sum_{\Lambda'', \Lambda'''} \left[I \left(g_{\Lambda'' \Lambda}, f_{\Lambda''' \Lambda'} \right) \left\langle \Lambda'' \left| \sigma_i \right| \bar{\Lambda}''' \right\rangle - I \left(f_{\Lambda'' \Lambda}, g_{\Lambda''' \Lambda'} \right) \left\langle \bar{\Lambda}'' \left| \sigma_i \right| \Lambda''' \right\rangle \right] \, . \tag{2.299}$$

Now, the second part of the right hand side of Eq. (2.292) is analyzed. Here, it is convenient to rewrite the product of the matrix operators in order to obtain two additive contributions in the sense that

$$\begin{aligned} \beta \Sigma_l \alpha_i &= \begin{pmatrix} \mathbb{I}_2 & 0 \\ 0 & -\mathbb{I}_2 \end{pmatrix} \begin{pmatrix} \sigma_l & 0 \\ 0 & \sigma_l \end{pmatrix} \begin{pmatrix} 0 & \sigma_i \\ \sigma_i & 0 \end{pmatrix} = \begin{pmatrix} 0 & \sigma_l \sigma_i \\ -\sigma_l \sigma_i & 0 \end{pmatrix} \\ &= \delta_{il} \begin{pmatrix} 0 & \mathbb{I}_2 \\ -\mathbb{I}_2 & 0 \end{pmatrix} + i \epsilon_{lik} \begin{pmatrix} 0 & \sigma_k \\ -\sigma_k & 0 \end{pmatrix} \, . \end{aligned} \tag{2.300}$$

Therefore, the entire second part is given by

$$\begin{aligned} \mp \frac{ec}{2} \langle Z_{\Lambda} \left| \beta \Sigma_l \alpha_i \right| Z_{\Lambda'} \rangle = \mp \frac{ec}{2} \delta_{l,i} \sum_{\Lambda'', \Lambda'''} \int \mathrm{d}^3 r \, & \left(g_{\Lambda'' \Lambda} \left(r, z_2 \right) \chi^{\dagger}_{\Lambda''} \left(\hat{\mathbf{r}} \right), -i f_{\Lambda'' \Lambda} \left(r, z_2 \right) \chi^{\dagger}_{\bar{\Lambda}''} \left(\hat{\mathbf{r}} \right) \right) \\ & \times \begin{pmatrix} 0 & \mathbb{I}_2 \\ -\mathbb{I}_2 & 0 \end{pmatrix} \begin{pmatrix} g_{\Lambda''' \Lambda'} \left(r, z_1 \right) \chi_{\Lambda'''} \left(\hat{\mathbf{r}} \right) \\ i f_{\Lambda''' \Lambda'} \left(r, z_1 \right) \chi_{\bar{\Lambda}'''} \left(\hat{\mathbf{r}} \right) \end{pmatrix} \\ \mp \frac{eci}{2} \epsilon_{lik} \sum_{\Lambda'', \Lambda'''} \int \mathrm{d}^3 r \, & \left(g_{\Lambda'' \Lambda} \left(r, z \right) \chi^{\dagger}_{\Lambda''} \left(\hat{\mathbf{r}} \right), -i f_{\Lambda'' \Lambda} \left(r, z \right) \chi^{\dagger}_{\bar{\Lambda}''} \left(\hat{\mathbf{r}} \right) \right) \\ & \times \begin{pmatrix} 0 & \sigma_k \\ -\sigma_k & 0 \end{pmatrix} \begin{pmatrix} g_{\Lambda''' \Lambda'} \left(r, z \right) \chi_{\Lambda'''} \left(\hat{\mathbf{r}} \right) \\ i f_{\Lambda''' \Lambda'} \left(r, z \right) \chi_{\bar{\Lambda}'''} \left(\hat{\mathbf{r}} \right) \end{pmatrix} \, . \end{aligned} \tag{2.301}$$

The first term on the right hand side of Eq. (2.301) can be rewritten by using the notation introduced in Eq. (2.298) which yields

$$\mp\frac{eci}{2}\delta_{l,i}\sum_{\Lambda'',\Lambda'''}\left[I\left(g_{\Lambda''\Lambda},f_{\Lambda'''\Lambda'}\right)\,\delta_{\Lambda'',\bar{\Lambda}'''}+I\left(f_{\Lambda''\Lambda},g_{\Lambda'''\Lambda'}\right)\,\delta_{\bar{\Lambda}'',\Lambda'''}\right]\,, \tag{2.302}$$

where the Kronecker symbols follow from the orthonormality of the angular functions [7]. Turning to the second part of Eq. (2.301) one finds

$$\mp\frac{eci}{2}\epsilon_{lik}\sum_{\Lambda'',\Lambda'''}\left[I\left(g_{\Lambda''\Lambda},f_{\Lambda'''\Lambda'}\right)\,\left\langle\Lambda''\left|\sigma_k\right|\bar{\Lambda}'''\right\rangle+I\left(f_{\Lambda''\Lambda},g_{\Lambda'''\Lambda'}\right)\,\left\langle\bar{\Lambda}''\left|\sigma_k\right|\Lambda'''\right\rangle\right]\,, \tag{2.304}$$

where the matrix elements of the σ_k are already introduced in Eq. (2.297). Summarizing, the results of the second part gives

$$\begin{aligned}\mp\frac{ec}{2}\left\langle Z_\Lambda\left|\beta\Sigma_l\alpha_i\right|Z_{\Lambda'}\right\rangle=&\mp\frac{eci}{2}\delta_{l,i}\sum_{\Lambda'',\Lambda'''}\left[I\left(g_{\Lambda''\Lambda},f_{\Lambda'''\Lambda'}\right)\,\delta_{\Lambda'',\bar{\Lambda}'''}+I\left(f_{\Lambda''\Lambda},g_{\Lambda'''\Lambda'}\right)\,\delta_{\bar{\Lambda}'',\Lambda'''}\right]\\&\pm\frac{ec}{2}\epsilon_{lik}\sum_{\Lambda'',\Lambda'''}\left[I\left(g_{\Lambda''\Lambda},f_{\Lambda'''\Lambda'}\right)\,\left\langle\Lambda''\left|\sigma_k\right|\bar{\Lambda}'''\right\rangle+I\left(f_{\Lambda''\Lambda},g_{\Lambda'''\Lambda'}\right)\,\left\langle\bar{\Lambda}''\left|\sigma_k\right|\Lambda'''\right\rangle\right]\,.\end{aligned} \tag{2.305}$$

Now, the third part of Eq. (2.292) which is given by

$$\pm\frac{e}{2m}\left\langle Z_\Lambda\left|\gamma_5\alpha_i\hat{p}_l\right|Z_{\Lambda'}\right\rangle=\mp\frac{e}{2m}\left\langle Z_\Lambda\left|\Sigma_i\hat{p}_l\right|Z_{\Lambda'}\right\rangle \tag{2.306}$$

where

$$\gamma_5\alpha_i=\begin{pmatrix}0&-\mathbb{I}_2\\-\mathbb{I}_2&0\end{pmatrix}\begin{pmatrix}0&\sigma_i\\\sigma_i&0\end{pmatrix}=-\begin{pmatrix}\sigma_i&0\\0&\sigma_i\end{pmatrix}=-\Sigma_i \tag{2.307}$$

is used, needs to be evaluated. Writing

$$\begin{aligned}\mp\frac{e}{2m}\left\langle Z_\Lambda\left|\Sigma_i\hat{p}_l\right|Z_{\Lambda'}\right\rangle=\pm\frac{e}{2m}\sum_{\Lambda'',\Lambda'''}\Bigg[&\int\mathrm{d}^3r\,g_{\Lambda''\Lambda}\left(r,z_2\right)\chi^\dagger_{\Lambda''}\left(\hat{\mathbf{r}}\right)\,\sigma_i\hat{p}_l\,g_{\Lambda'''\Lambda'}\left(r,z_1\right)\chi_{\Lambda'''}\left(\hat{\mathbf{r}}\right)\\&+\int\mathrm{d}^3r\,f_{\Lambda''\Lambda}\left(r,z_2\right)\chi^\dagger_{\bar{\Lambda}''}\left(\hat{\mathbf{r}}\right)\,\sigma_i\hat{p}_l\,f_{\Lambda'''\Lambda'}\left(r,z_1\right)\chi_{\bar{\Lambda}'''}\left(\hat{\mathbf{r}}\right)\Bigg]\end{aligned} \tag{2.308}$$

[7]

$$\begin{aligned}\left\langle\Lambda\middle|\bar{\Lambda}'\right\rangle=\int\mathrm{d}\Omega\,\chi^\dagger_\Lambda\left(\hat{\mathbf{r}}\right)\chi_{\bar{\Lambda}'}\left(\hat{\mathbf{r}}\right)&=\sum_{s,s'}C\left(l\,j\,1/2|\mu-s,s\right)C\left(\bar{l}'\,j'\,1/2|\mu'-s',s'\right)\,\delta_{l,\bar{l}'}\,\delta_{\mu-s,\mu'-s'}\,\delta_{s,s'}\\&=\delta_{l,\bar{l}'}\,\delta_{\mu,\mu'}\underbrace{\sum_s C\left(l\,j\,1/2|\mu-s,s\right)C\left(l\,j'\,1/2|\mu-s,s\right)}_{\delta_{j,j'}}=\delta_{\Lambda,\bar{\Lambda}'}\end{aligned} \tag{2.303}$$

and using the definition of the χ_Λ and the momentum operator one finds

$$\begin{aligned}\mp\frac{e}{2m}\left\langle Z_\Lambda\left|\Sigma_i\hat{p}_l\right|Z_{\Lambda'}\right\rangle = \pm\frac{e}{2m}\sum_{\Lambda'',\Lambda'''}\Bigg[&\sum_{s'',s'''}C\left(l''\,j''\,1/2|\mu''-s'',s''\right)C\left(l'''\,j'''\,1/2|\mu'''-s''',s'''\right)\\&\times\int \mathrm{d}^3r\, g_{\Lambda''\Lambda}\left(r,z_2\right)Y^*_{l'',\mu''-s''}\left(\hat{\mathbf{r}}\right)\,\partial_l\left[g_{\Lambda'''\Lambda'}\left(r,z_1\right)Y_{l''',\mu'''-s'''}\left(\hat{\mathbf{r}}\right)\right]\left\langle\phi_{s''}\left|\sigma_i\right|\phi_{s'''}\right\rangle\\&+\sum_{s,s'}C\left(\bar{l}''\,j''\,1/2|\mu''-s'',s''\right)C\left(\bar{l}'''\,j'''\,1/2|\mu'''-s''',s'''\right)\\&\times\int \mathrm{d}^3r\, f_{\Lambda''\Lambda}\left(r,z_2\right)Y^*_{\bar{l}'',\mu''-s''}\left(\hat{\mathbf{r}}\right)\,\partial_l\left[f_{\Lambda'''\Lambda'}\left(r,z_1\right)Y_{l'',\mu'''-s'''}\left(\hat{\mathbf{r}}\right)\right]\left\langle\phi_{s''}\left|\sigma_i\right|\phi_{s'''}\right\rangle\Bigg]\,.\end{aligned} \tag{2.309}$$

In order to simplify the following the focus is on $l = z$ because with this assumption the remaining integrals can be written as follows

$$\begin{aligned}\frac{\partial}{\partial z}f\left(r\right)Y_{l,m}\left(\hat{\mathbf{r}}\right) = &\sqrt{\frac{(l+m)(l-m)}{(2l+1)(2l-1)}}\left[\frac{df\left(r\right)}{dr}+\frac{l+1}{r}f\left(r\right)\right]Y_{l-1,m}\left(\hat{\mathbf{r}}\right)\\&+\sqrt{\frac{(l+m+1)(l-m+1)}{(2l+1)(2l+3)}}\left[\frac{df\left(r\right)}{dr}-\frac{l}{r}f\left(r\right)\right]Y_{l+1,m}\left(\hat{\mathbf{r}}\right)\,.\end{aligned} \tag{2.310}$$

A proof of this formula is given in Appendix A.11. The proof also includes the formulas for $l = x, y$. But as the z-axis is usually the reference of the spin quantization and since in the application of the formulas derived here only out-of-plane magnetizations are considered, the focus on $l = z$ is sufficient. Applying the gradient formula to the first integral in Eq. (2.309) it becomes

$$\begin{aligned}&\int \mathrm{d}^3r\, g_{\Lambda''\Lambda}\left(r,z_2\right)Y^*_{l'',\mu''-s''}\left(\hat{\mathbf{r}}\right)\partial_z\left[g_{\Lambda'''\Lambda'}\left(r,z_1\right)Y_{l''',\mu'''-s'''}\left(\hat{\mathbf{r}}\right)\right]\\&=\delta_{\mu''-s'',\mu'''-s'''}\,\delta_{l'',l'''-1}\sqrt{\frac{(l'''+(\mu'''-s'''))(l'''-(\mu'''-s'''))}{(2l'''+1)(2l'''-1)}}\\&\times\int r^2\mathrm{d}r\, g_{\Lambda''\Lambda}\left(r,z_2\right)\left[\frac{dg_{\Lambda'''\Lambda'}\left(r,z_1\right)}{dr}+\frac{l'''+1}{r}g_{\Lambda'''\Lambda'}\left(r,z_1\right)\right]\\&+\delta_{\mu''-s'',\mu'''-s'''}\,\delta_{l'',l'''+1}\sqrt{\frac{(l'''+1+(\mu'''-s''')\,(l'''+1-(\mu'''-s''')))}{(2l'''+1)(2l'''+3)}}\\&\times\int r^2\mathrm{d}r\, g_{\Lambda''\Lambda}\left(r,z_2\right)\left[\frac{dg_{\Lambda'''\Lambda'}\left(r,z_1\right)}{dr}-\frac{l'''}{r}g_{\Lambda'''\Lambda'}\left(r,z_1\right)\right]\,.\end{aligned} \tag{2.311}$$

Again a shorthand notation can be introduced to keep the notation compact by using

$$\begin{aligned}K^+\left(g_{\Lambda''\Lambda},g_{\Lambda'''\Lambda'}\right) &= \int r^2\mathrm{d}r\, g_{\Lambda''\Lambda}\left(r,z_2\right)\left[\frac{dg_{\Lambda'''\Lambda'}\left(r,z_1\right)}{dr}+\frac{l'''+1}{r}g_{\Lambda'''\Lambda'}\left(r,z_1\right)\right]\\K^-\left(g_{\Lambda''\Lambda},g_{\Lambda'''\Lambda'}\right) &= \int r^2\mathrm{d}r\, g_{\Lambda''\Lambda}\left(r,z_2\right)\left[\frac{dg_{\Lambda'''\Lambda'}\left(r,z_1\right)}{dr}-\frac{l'''}{r}g_{\Lambda'''\Lambda'}\left(r,z_1\right)\right]\,,\end{aligned} \tag{2.312}$$

which leads to

$$\begin{aligned}
&\int \mathrm{d}^3 r\, g_{\Lambda'' \Lambda}\left(r, z_2\right) Y^*_{l'', \mu''-s''}\left(\hat{\mathbf{r}}\right) \partial_z \left[g_{\Lambda''' \Lambda'}\left(r, z_1\right) Y_{l''', \mu'''-s'''}\left(\hat{\mathbf{r}}\right)\right] \\
&= \delta_{\mu''-s'', \mu'''-s'''} \left[\delta_{l'', l'''-1} \sqrt{\frac{(l'''+(\mu'''-s'''))(l'''-(\mu'''-s'''))}{(2l'''+1)(2l'''-1)}} K^+\left(g_{\Lambda''\Lambda}, g_{\Lambda'''\Lambda'}\right)\right. \\
&\qquad \left. + \ \delta_{l'', l'''+1} \sqrt{\frac{(l'''+1+(\mu'''-s''')\,(l'''+1-(\mu'''-s''')))}{(2l'''+1)(2l'''+3)}} K^-\left(g_{\Lambda''\Lambda}, g_{\Lambda'''\Lambda'}\right)\right] .
\end{aligned} \tag{2.313}$$

Using the matrix elements of σ_i which can be written as $\sigma_i^{s,s'}$ one finds

$$\begin{aligned}
&\sum_{\Lambda'', \Lambda'''} \sum_{s'', s'''} \delta_{\mu''-s'', \mu'''-s'''}\, C\left(l''\, j''\, 1/2 | \mu''-s'', s''\right) C\left(l'''\, j'''\, 1/2 | \mu'''-s''', s'''\right)\, \sigma_i^{s'', s'''} \\
&\qquad \left[\delta_{l'', l'''-1} \sqrt{\frac{(l'''+(\mu'''-s'''))(l'''-(\mu'''-s'''))}{(2l'''+1)(2l'''-1)}} K^+\left(g_{\Lambda''\Lambda}, g_{\Lambda'''\Lambda'}\right)\right. \\
&\qquad \left. + \ \delta_{l'', l'''+1} \sqrt{\frac{(l'''+1+(\mu'''-s''')\,(l'''+1-(\mu'''-s''')))}{(2l'''+1)(2l'''+3)}} K^-\left(g_{\Lambda''\Lambda}, g_{\Lambda'''\Lambda'}\right)\right] .
\end{aligned} \tag{2.314}$$

Conveniently, the first contribution to $\mp \frac{e}{2m} \left\langle Z_\Lambda \left| \Sigma_i \hat{p}_l \right| Z_{\Lambda'} \right\rangle$ can be written as

$$\begin{aligned}
&\pm \frac{e}{2m} \sum_{\Lambda'', \Lambda'''} \sum_{\substack{m=\mu'''\pm\frac{1}{2} \\ m=\mu''\pm\frac{1}{2}}} C\left(l''\, j''\, 1/2 | m, \mu''-m\right) C\left(l'''\, j'''\, 1/2 | m, \mu'''-m\right)\, \sigma_i^{\mu''-m, \mu'''-m} \\
&\qquad \left[\delta_{l'', l'''-1} \sqrt{\frac{(l'''+m)(l'''-m)}{(2l'''+1)(2l'''-1)}} K^+\left(g_{\Lambda''\Lambda}, g_{\Lambda'''\Lambda'}\right)\right. \\
&\qquad \left. + \ \delta_{l'', l'''+1} \sqrt{\frac{(l'''+1+m)(l'''+1-m)}{(2l'''+1)(2l'''+3)}} K^-\left(g_{\Lambda''\Lambda}, g_{\Lambda'''\Lambda'}\right)\right]
\end{aligned} \tag{2.315}$$

and the second as

$$\begin{aligned}
&\pm \frac{e}{2m} \sum_{\Lambda'', \Lambda'''} \sum_{\substack{m=\mu'''\pm\frac{1}{2} \\ m=\mu''\pm\frac{1}{2}}} C\left(\bar{l}''\, j''\, 1/2 | m, \mu''-m\right) C\left(\bar{l}'''\, j'''\, 1/2 | m, \mu'''-m\right)\, \sigma_i^{\mu''-m, \mu'''-m} \\
&\qquad \left[\delta_{\bar{l}'', \bar{l}'''-1} \sqrt{\frac{(\bar{l}'''+m)(\bar{l}'''-m)}{(2\bar{l}'''+1)(2\bar{l}'''-1)}} K^+\left(f_{\Lambda''\Lambda}, f_{\Lambda'''\Lambda'}\right)\right. \\
&\qquad \left. + \ \delta_{\bar{l}'', \bar{l}'''+1} \sqrt{\frac{(\bar{l}'''+1+m)(\bar{l}'''+1-m)}{(2\bar{l}'''+1)(2\bar{l}'''+3)}} K^-\left(f_{\Lambda''\Lambda}, f_{\Lambda'''\Lambda'}\right)\right]
\end{aligned} \tag{2.316}$$

With this, the matrix elements of the spin-projected current operator are evaluated which allows to calculate spin-dependent contributions to the total current within linear response theory.

Details of how the conductance is evaluated in the case of the screened KKR formalism is discussed in Ref. [82].

Highlight

The derivation described in this subsection is necessary to obtain the formulas needed for the implementation of the relativistic spin-projection operator. This implementation and an additional extension of the transport Code to allow the treatment of complex structures were carried out by the author within the scope of this work.

2.7.2 Calculation of Seebeck coefficients from linear response theory

Before the evaluation of Seebeck coefficients is introduced a short discussion of the assumptions made in the calculation of thermoelectric properties discussed in the present work is given. The subsequent derivation of the necessary formulas is basically taken from Ref. [83].

It is important to note that the calculation of thermoelectric properties and their generalized spin dependence relies on the calculation of the conductance in the linear response regime, as referred in the chapter before. This implies that the conductance is calculated for cases where the ballistic transport is the only relevant mechanism. This is proven by the equivalence of the linear response theory of transport and the Landauer-Büttiker theory given in Ref. [77]. Therefore, no temperature dependent scattering mechanisms are considered. The assumption of ballistic transport can only be ensured within length scales below the characteristic diffusion scattering length scale of the system.

The thermoelectric properties are determined by the energy dependence of the ballistic conductance. Therefore, the bulk Seebeck coefficient results from the asymmetry of the energy dependence of the conductance around the Fermi energy in an interval determined by the temperature.

The formalism used to evaluate the Seebeck coefficient can be derived from the Landauer-Büttiker theory as shown in the work of Sivan and Imry [84]. They derived formulas for the calculation of thermoelectric properties from the so called multichannel Landauer formula. On the other hand, the Kubo formalism can be employed to relate the electric current j_c and the heat current density j_q to gradients of the electrochemical potential μ and the temperature [76, 85]. This result can be extended to include the spin current density [86] which leads to the following set of equations

$$\begin{aligned} j^c &= -L^{cc}\nabla\mu - L^{cq}\nabla T/T + \mathcal{L}^{cs}F_s \\ j^q &= -L^{qc}\nabla\mu - L^{qq}\nabla T/T + \mathcal{L}^{qs}F_s \\ J^s &= -\mathcal{L}^{sc}\nabla\mu - \mathcal{L}^{sq}\nabla T/T + \mathcal{L}^{ss}F_s\,, \end{aligned} \tag{2.317}$$

with $\nabla\mu = \nabla\mu_c + eE$, where μ_c is the chemical potential and F_s which is a fictitious spin accumulation driving force. The temperature dependent response tensors in Eq. (2.317) can be calculated from conductivities in the athermal limit (see Ref. [87] and [88]) and first and second response tensor in the first equation is given by

$$\begin{aligned} L^{qq}(T) &= -\int \mathrm{d}E\, g(E)\left[\frac{\partial}{\partial E}f(E,\mu,T)\right]\mathrm{d}E \\ L^{cq}(T) &= -\int \mathrm{d}E\, g(E)(E-\mu)\left[\frac{\partial}{\partial E}f(E,\mu,T)\right]\mathrm{d}E \end{aligned} \tag{2.318}$$

In cases where no external electric field is applied, the electronic current vanishes if open boundary conditions are considered. Therefore, the first part of Eq. 2.317 implies

$$E = -\frac{1}{eT}(L^{cc})^{-1}L^{cq}\nabla T = S\nabla T\,. \tag{2.319}$$

This means that the Seebeck coefficient is determined by the following ratio

$$S = -\frac{1}{eT}\frac{L^{cq}(\mu,T)}{L^{cc}(\mu,T)}\,, \tag{2.320}$$

and can be evaluated by calculating the conductivity in a certain energy interval that correspond to the width of the derivative of the Fermi-function at a given temperature and integrating this according to Eq. (2.318) and (2.320).

Using this approach two types of spin-dependent thermoelectric quantities can be defined by employing the formalism introduced in the last section. The first one is obtained by splitting the numerator of Eq. (2.320) into two additive contributions, which leads to the definition

$$\tilde{S}_\sigma = -\frac{1}{eT}\frac{L^{cq}_\sigma(\mu,T)}{L^{cc}(\mu,T)}, \quad \sigma = \uparrow,\downarrow\ . \tag{2.321}$$

where the quantities $\tilde{S}$ should not be confused with the Seebeck coefficient of a single spin channel. Results obtained from this definition give insight into how the two spin channels give additive contributions to the total Seebeck coefficient. It allows to determine which of the both channels is responsible for the major contribution.

As by definition, the difference between the two spin contribution to the total conductance evaluated in the last section can be interpreted as the spin current density (see Ref. [81]), the definition

$$S_{\text{spin}} = -\frac{1}{eT}\frac{L^{cq}_\uparrow(\mu,T) - L^{cq}_\downarrow(\mu,T)}{L^{cc}(\mu,T)} \tag{2.322}$$

is understood as a measure of how strong a spin accumulation is driven by the thermal gradient. A more detailed description of the evaluation of spin-dependent thermoelectric properties using the relativistic spin projection operator is given in Ref.[83].

3 Computational details

This chapter is devoted to the technical details of the numerical investigations reported within this treatise. In particular, detail of the combination of DFT calculations and MC simulations as well as transport calculations are described. At first, details of the DFT-MC combination are presented.

A standard computation procedure reported here, consists of the following three steps: First, the lattice parameters of the system under consideration is determined using the Vienna *ab initio* simulation package (VASP) [59]. Subsequently, the lattice parameters and magnetic structures are transferred to calculations of the magnetic exchange parameters, $J_{ij} = J(\boldsymbol{r}_{ij})$ ($\boldsymbol{r}_{ij}$ denotes the separation vector of the atoms), employing Lichtenstein's method [71, 72] which is implemented in the Spin-Polarized Relativistic-KKR (SPR-KKR) code [89]. In other words, the zero temperature magnetic configuration obtained from VASP is employed as the magnetic reference state for the calculation of exchange parameters. The lattice constant obtained with VASP is used instead of the experimental lattice constant within the SPR-KKR calculations to proceed in a pure theoretical way.

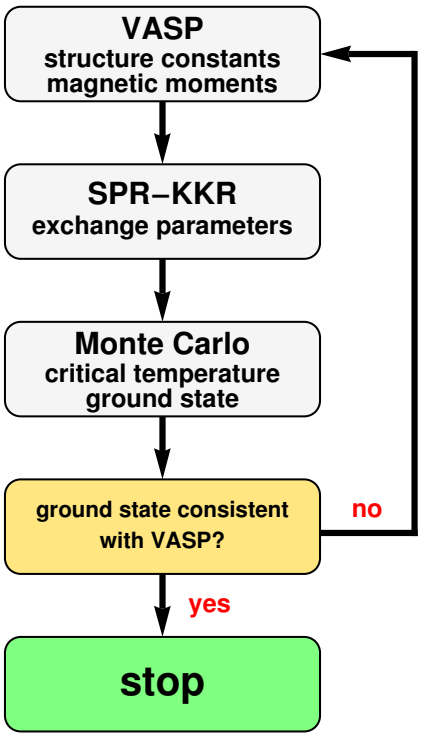

Figure 3.1: Computational flow-chart.

In the last step, Monte Carlo simulations of the classical Heisenberg model are carried out employing the calculated J_{ij}. Thereby, the investigation of the magnetic properties is extended to finite temperatures and the stability of the magnetic ground state configurations is analyzed.

The calculations of structural parameters like equilibrium volume and tetragonal distortion performed with VASP are based on the projector augmented wave (PAW) method [90] (see Appendix A.5). The GGA exchange correlation functional of Perdew, Burke and Ernzernhof [91] is used together with an energy cutoff of 390 eV and a k-point mesh of $15 \times 15 \times 15$ points in the irreducible wedge of the Brillouin zone.

Different possibilities of the collinear arrangement of the individual magnetic moments are considered. Usually the focus is on states with lowest total energy because such states can reasonably be considered as the ground state. Sometimes ,a particular magnetic configuration cannot be stabilized in the calculation and drops out of the consideration. As it is shown in detail for the case of FeMn (see Section 4.2.2), it is sometimes possible to start with an almost arbitrary magnetic configuration because the MC simulations guide the way to the most stable ones.

The SPR-KKR calculations are performed within the scalar relativistic framework (see Appendix A.10) using the the atomic sphere approximation (ASA) [92]. This means that the scattering matrices are evaluated at the boundary of overlapping and space filling spheres during the solution of the multiple scattering problem.

The calculation of charge densities and magnetic moments of the atoms also refers to those spheres.

In KKR calculations the local density approximation (LDA) in the formulation of Vosko, Wilk and Nusair (VWN) [93] is used. The use of GGA in the calculations with VASP guarantees good agreement of the predicted lattice constant in comparison with the experiment. In the KKR calculations the LDA is favored because no additional structural optimization is performed. Only the scattering matrices and the scattering path operator needed in the Lichtenstein formalism are calculated self-consistently. The use of LDA leads to good results for the magnetic properties such as magnetic moments and the exchange parameters J_{ij}. For a more detailed discussion of how the different types of LDA and GGA affect the calculated properties the reader is referred to Ref. [94] and references therein.

In the calculation of the J_{ij} the angular momentum expansion is cut off at $l = 3$. A mesh of 30^3 k-points and for the sampling of the complex contour up to the Fermi energy 30 points are used. The complex energy integration contour used in the self consistence run is a semicircle but in the calculation of the exchange parameters a straight line parallel to the real axis is used.

As mentioned above, additional MC simulations of the classical Heisenberg model are performed. This model is given by

$$\mathcal{H} = -\frac{1}{2}\sum_{i\neq j} J_{ij}\boldsymbol{S}_i\boldsymbol{S}_j \ , \tag{3.1}$$

where $\boldsymbol{S}_i = (S_i^x, S_i^y, S_i^z)$ are three dimensional unit vectors representing the magnetic moments and the J_{ij} are the exchange coupling parameters determined in the *ab initio* calculations. Although the classical Heisenberg model exhibits some disadvantageous properties for low temperatures such as a non-physical limit value of the entropy for zero temperature [95] it gives reasonable results for the critical temperature and the magnetic ground state.

The magnetization per unit cell of a particular sublattice a is defined by

$$\boldsymbol{m}_a = \frac{\mu_a}{N_{\mathrm{uc}}}\sum_{i=1}^{N_a}\boldsymbol{S}_{a,i} \tag{3.2}$$

where N_{uc} is the number of unit cells in the simulation box. The μ_a is the magnetic moment and N_a the number of atoms of the particular atomic species.

As the ensemble average of the magnetization $\langle\boldsymbol{m}_a\rangle$ of the Heisenberg model vanishes in finite systems because of rotational invariance of spin space, the norm of the magnetization $|\boldsymbol{m}_a|$ of the sublattices is measured and its ensemble average $m_a = \langle|\boldsymbol{m}_a|\rangle$ is calculated. In the case of collinear ground states, the atom species with the highest magnetic moment obtained from the *ab initio* calculations is used as a reference for the sign, which is assigned to the norm of the magnetization. This means that the atoms with the highest moments get a positive sign as well as all sublattices that are parallel aligned to this reference. All sublattices that are antiparallel aligned, get a negative sign. In the following $\|\boldsymbol{m}_a\|_s$ stands for this sign afflicted norm and $m_{s,a} = \langle\|\boldsymbol{m}_a\|_s\rangle$ for its ensemble average.

The MC simulation cells contain up to 10^3 elementary unit cells and periodic boundary conditions are employed. It turns out that for all investigated systems, the magnetic exchange parameters may be cut for distances larger than three lattice constants. For larger distances the exchange interactions have decayed to values below 0.1 meV and the effect on the resulting spin configuration can be safely neglected. Taking into account more of the longer range

behavior of the magnetic exchange mechanisms, affects the critical temperatures only weakly and the computational demand would be significantly increased. But as the critical temperature is even stronger affected by other approximations, such as the choice of the magnetic reference state and approximations during the determination of the electronic structure, a cut of the J_{ij} at three lattice constants turn out to be sufficient.

In some cases, the magnetic configuration obtained from MC simulations at low temperatures differs from the reference state obtained with VASP. This occurs because in the MC simulations the constraint of collinearity is released in contrast to the *ab initio* calculations. Therefore, a non-collinear magnetic structure can be obtained if the collinear configuration is frustrated. In addition, a specific collinear configuration can be obtained from the MC simulations when cooling from high temperatures, because the system gets trapped in a different local energy minimum provided by this configuration. In this case, the low temperature state obtained from the MC simulation is used as a new initial magnetic configuration in VASP and SPR-KKR calculations. The whole computational procedure can be iterated according to the scheme in Fig. 3.1. It turns out that this iterative procedure helps to find the magnetic ground state. This is of particular interest when the magnetic ground state is non-collinear because without the constraint of collinearity the number of possible ground state configurations rises significantly. This situation is discussed in detail below for the FeMn-system.

Please note that one may allow for non-collinear spin configurations in the DFT calculations right from the start. However, this is extremely time-consuming for larger cells, containing many atoms. The combination of DFT and MC methods as proposed here is speeding up the convergence towards the actual spin configuration of lowest energy considerably.

It should mention that the use of the classical Heisenberg model for the description of itinerant magnets is approximative because it assumes the moments to be localized. In addition, it is assumed that exchange parameters calculated at zero temperature can be used for MC simulations at elevated temperatures of more than 1000 K. This is again approximative because at high temperatures volume changes occur which can considerably change the exchange parameters. However, it is shown that the calculated critical temperatures and magnetic structures are in good agreement with previous theoretical and experimental work. In certain cases, the influence of the included approximations is discussed in detail.

It is only noted here that there is the possibility to use other approximations to model an itinerant magnet that are beyond bilinear models such as the Heisenberg model and which include more than only two body interactions (see, e.g., Ref. [96]) but this is beyond the scope of this treatise.

The computational details of the calculations presented in Section 7.10 and Chapter 8 are discussed in the introductions of these parts.

4 Iron Manganese

In this chapter binary iron-manganese alloys are investigated. Special attention is paid to complex magnetic structures which play an important role in this alloy system. Trends for non-collinear magnetism are found and investigated by means of first-principles calculations and Monte Carlo simulations. Additionally, the influence of carbon on the magnetic properties is investigated. Such investigations are of great technological interest because carbon is one of the most important constituents of steels.

4.1 Introduction

The magnetic properties of transition metals and their alloys are of particular theoretical interest since in these elements and alloys, structure as well as structural transitions are closely related to magnetism. The search for the magnetic ground state configurations, the role of magnetic excitations and the influence of temperature and substitutional disorder are subjects of ongoing discussions.[97, 98, 99, 100, 101]

Regarding the microscopic properties, iron-manganese systems are investigated intensively with focus on the magnetic structure [102, 103, 104, 105, 106] using different theoretical methods, such as the Korringa-Kohn-Rostocker (KKR), the Linear-Muffin-Tin-Orbital (LMTO) or the Exact-Muffin-Tin-Orbital (EMTO) Green's function method, often in combination with the coherent potential approximation (CPA) or a supercell approach in order to account for chemical disorder. A strong dependence of magnetism on composition and atomic order as well as tendencies for non-collinear magnetism are observed in the calculations. However, there is still no consensus on the exact nature of the magnetic ground state.

Most experimental work concentrates on the influence of lattice defects such as stacking faults, dislocations and twin boundaries because these types of defects are closely connected to the extraordinary mechanical properties of modern steels. The stability of the various phases is studied in combination with theoretical calculations using the CALPHAD (Computer Coupling of Phase Diagrams and Thermochemistry) package [107]. Such investigations have been very useful as they allowed to establish a phase diagram using the stacking fault energy (SFE) and composition as parameters [108, 109]. The influence of magnetism is retained only recently in the CALPHAD calculation by combining it with *ab initio* investigations [110].

Carbon, as an interstitial constituent, is known to increase the hardness of steels significantly within a certain concentration range. In addition, it leads to the formation of carbide phases like cementite in carbon rich environments [111]. Manganese acts as a carbide stabilizer and removes oxidic and sulfurous impurities that lead to technologically disadvantageous properties [112]. Both elements, Mn and C stabilize the austenitic high temperature fcc-phase in contrast to the low temperature martensitic bcc- or hcp-phase. This is of great interest because the austenitic phase is of particular technological importance.

Focussing on the magnetic phase transition in elemental bcc-iron the authors of Ref. [113] and [114] combined MC simulations with *ab initio* and CALPHAD calculations. Boukhvalov *et al.* [115] considered γ-iron with carbon at octahedral interstitial sites and investigated

structural relaxations as well as changes of magnetic exchange parameters in the neighborhood of the carbon impurities. Special attention is paid to the Fe_3C structure cementite and to cementite-type structures in which iron is partially substituted by manganese [116, 110, 117]. In the latter work, structural, elastic as well as thermodynamic properties are discussed. However, only few calculations have been performed up to now which would allow to discuss the impact of substitutional manganese and interstitial carbon simultaneously. One exception is the investigation of Medvedeva *et al.* [118] where the arrangement of the magnetic moments around a carbon impurity is investigated but relaxation effects were neglected (relaxation effects are deviations of the atomic positions from the perfect lattice structure). The influence of Al and Si on the lattice stability of Fe-Mn alloys has recently been investigated by Gebhardt *et al.* [103].

In this chapter, iron-manganese alloys of $Fe_{1-x}Mn_xC_y$ type with $x = 0.25$, 0.5, 0.75 and $y = 0$, 1 are considered in order to study the dependence on composition and addition of carbon simultaneously. Results of density functional theory (DFT) calculations and finite-temperature MC simulations of the classical Heisenberg model are presented. By combining DFT calculations using VASP [59, 119] and the SPR-KKR code [89, 120] with the Monte Carlo (MC) method, spin configurations over a temperature range up to 1200 K are taken into account. Similar investigations are carried out in Ref. [121] and [122] using mean field or random phase approximation (RPA) [123] to determine the critical temperature. But as these methods neglect important statistical fluctuations of the order parameter their description of finite temperature magnetism is incomplete and, e.g., leads to the overestimation of critical temperatures (see e.g. Ref. [95]).

Because of the competition of ferro- and antiferromagnetic interactions in Fe-Mn alloys, which is one of the key features of these systems, the magnetic ground state is difficult to find. Therefore, the main aspect of this chapter is to gain insight into the complex nature of possible magnetic ground states of Fe-Mn alloys and their variation with increasing temperature. It is shown that the Monte Carlo simulations in combination with *ab initio* calculations can be used to find the magnetic ground state in an efficient way even in case of non-collinear spin configurations. The flow-chart for this kind of calculations is shown in Fig. 3.1 and a description of the implementation of this procedure is given in Chapter 3 and Section 4.2.

4.2 Computational Results

4.2.1 Elemental bcc and fcc iron

In order to check the reliability of the theoretical investigations carried out throughout this treatise, in particular the accuracy of the prediction of critical temperatures T_C in comparison to experiments and other theoretical investigations, the first discussion concerns results for bcc and fcc iron. Figure 4.1(a) shows the ferromagnetic spin configuration of α-Fe. In (b) the magnetic exchange parameters and in (c) the magnetization curve obtained from the MC simulation together with the calculated critical temperature of $T_C = 955\,\mathrm{K}$ and the experimental value of 1043 K are shown. The deviation of the theoretical prediction from the experimental value is around 100 K. The lattice constant, $a_0 = 2.84\,\text{Å}$, and magnetic moment, $\mu = 2.24\,\mu_B$, evaluated with VASP, are close to the experimental values of $a_0^{exp} = 2.857\,\text{Å}$

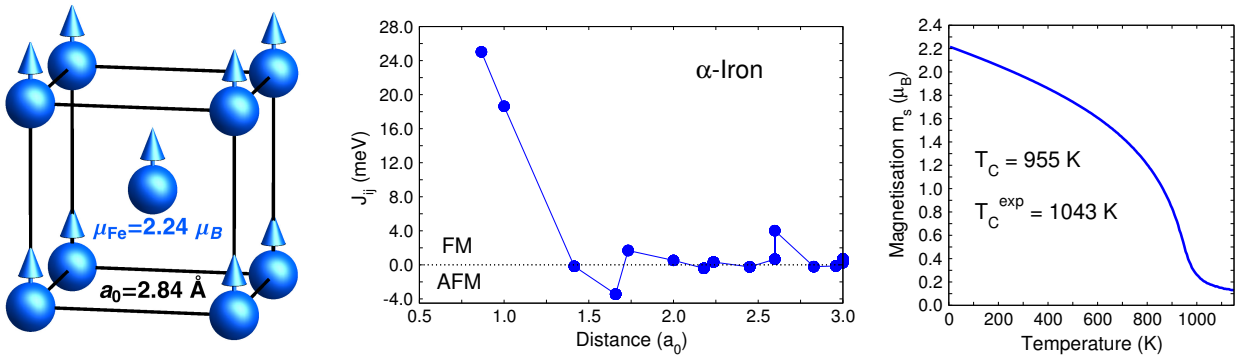

(a) (b) (c)

Figure 4.1: (a) Lattice constant and magnetic moment of α-Fe obtained from DFT calculations using VASP. (b) Magnetic exchange parameters as a function of the distance between the atoms in units of the lattice constant. The exchange parameters between nearest and next nearest neighbors show strong ferromagnetic interactions. The interactions for larger distances exhibit an oscillating RKKY [126, 127, 128] character. (c) Magnetization of α-iron as a function of temperature and the resulting critical temperature of 955 K obtained from the MC simulations.

and $\mu^{\text{exp}} = 2.24\,\mu_{\text{B}}$ [124] [1]. The magnetic exchange parameters shown in Fig. 4.1(b) reveal a strong ferromagnetic coupling of Fe moments of nearest and next nearest neighbors while the coupling is strongly reduced for larger distances where only weak oscillations of RKKY type remain [126, 127, 128].

It should be kept in mind that using the classical Heisenberg model for the description of itinerant magnets as well as using zero-temperature exchange parameters of the zero-temperature reference state leads to systematic errors. In addition, the cutoff of the exchange interactions for bcc Fe at $3\,a_0$ in the MC simulation may be too small in view of the long-range nature of the J_{ij} in this system. On the other hand, a deviation of the critical temperature of only 100 K from the experimental result shows that the essential physics is captured within the method used here. The systematic analysis of errors from the different sources is beyond the scope of this work but is in details discussed in Ref. [97] and the references therein.

Using the exchange parameters of α-Fe in a mean-field approximation, a critical temperature $T_{\text{C}}^{\text{MFT}} = 1313\,\text{K}$ is obtained, which is much larger than the experimental value. This shows that MC simulations based on zero-temperature *ab initio* exchange parameters yield more reliable results for the critical temperature compared to mean-field theory. This is assured by a comparison to other computational work listed in Ref. [129]. The MC simulations reported in Ref. [96] employed a generalized Stoner-Wolfarth model [130] instead of the Heisenberg model which explains the different T_{C} value of 1060 K. The generalized Stoner-Wolfarth model takes interactions of higher order between magnetic moments into account. This improves the description of itinerant magnets. Ležaić *et al.* [131] used a method similar to the procedure used here for the calculation of the critical temperature of α-Fe. They found $T_{\text{C}} = 900\,\text{K}$ which is close to the value obtained here. They used the experimental lattice constant $a_0^{\text{exp.}} = 2.857\,\text{Å}$, the full potential KKR method and the GGA correlation functional.

[1] It should be mentioned that the calculated magnetic moment does not account for spin-orbit coupling and orbital moment. The orbital moment gives a contribution of about 3% to the total moment measured in experiments but for details the reader is referred to Ref. [125].

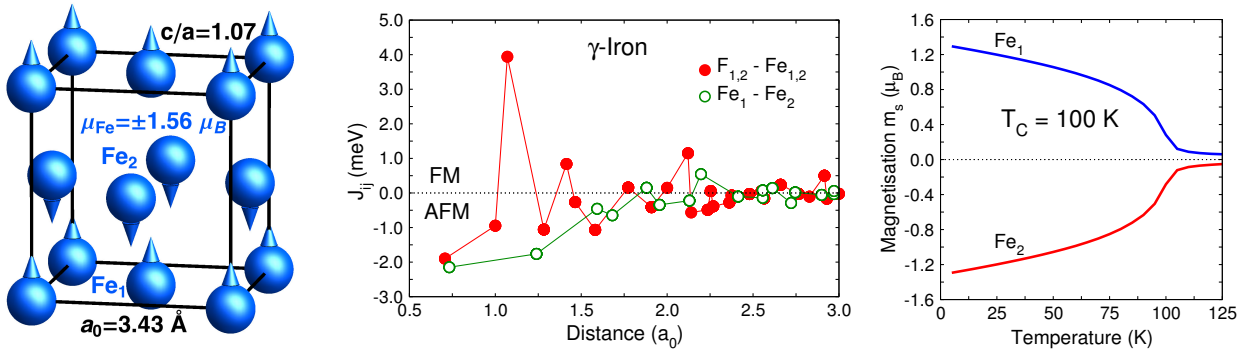

(a) (b) (c)

Figure 4.2: (a) Magnetic structure and lattice parameters of γ-Fe obtained from VASP calculations. The layerwise antiferromagnetic configuration is of lowest energy in a cell containing four atoms. The magnetic moments are strongly decreased compared to α-Fe. (b) Magnetic exchange parameters obtained from SPR-KKR calculations. As the magnetic moments, the exchange parameters are also strongly reduced compared to those of α-Fe and in particular the nearest neighbor interaction is now antiferromagnetic. There is still an oscillatory behavior for large distances but on a smaller scale. (c) Magnetization of the two sublattices of γ-Fe as a function of temperature in terms of the sign afflicted absolute value (see Chapter 3). The calculated critical temperature of 100 K is considerably lower compared to α-Fe. This is an obvious a consequence of smaller magnetic moments and exchange parameters and of the competing interactions.

Ruban *et al.* [99] investigated α-iron by using a longitudinal spin-fluctuation (LSF) model. They chose the disordered local moment (DLM) state as the reference state instead of the ferromagnetic state and reproduced the critical temperature of α-iron very accurately obtaining $T_C = 1065\,K$. In summary, it can be stated that the method of calculating the critical temperature used throughout this work gives reliable results. In particular, the results for the critical temperature shown here are of important significance because they are obtained from purely theoretical considerations and no experimentally determined parameters enter the calculation.

In the next step γ-Fe (fcc) is considered. Many investigations of γ-Fe have already been carried out [132, 133, 134, 135]. In most of them, almost degenerated spin spiral states are found to mark the magnetic ground state configuration. In addition, a strong dependence of the magnetic ground state configuration on the volume is observed. It appears that small volume changes (less than 0.1 Å difference in the lattice constant) can result in considerable changes of the magnetic configuration. A very accurate investigation is presented in Ref. [136] where in addition the main results of the aforementioned investigations are summarized.

In order to model complicated magnetic configurations like spin spirals, large unit cells have to be used to allow for complex arrangement of individual magnetic moments within periodic boundary conditions. In addition, volume changes have to be taken into account when finite temperatures are considered. Here, only a small cell is used in the DFT calculations and temperature associated volume changes are neglected in order to see if the combined approach gives still new insight. A cell containing four atoms is employed and the magnetic configuration is assumed to be layerwise antiferromagnetic, see Fig. 4.2(a).

In Fig. 4.2(a) and (b) structure, magnetic moments and exchange parameters of γ-Fe are

shown. As expected, γ-Fe exhibits considerably lower magnetic moments and smaller J_{ij} compared to α-Fe, *cf.* Fig. 4.2(a) and (b). It is particularly interesting that the exchange parameters between the nearest and next nearest neighbors are a factor of two and more smaller compared to the strongest interaction which is the one to the third nearest neighbor shell. This can be attributed to the different distances found in the fcc arrangement of atoms compared to the bcc case. Figure 4.2(c) shows the results of the MC simulation from which a critical temperature of 100 K is obtained. This is about 30 K higher compared with the experimental value of 67 K [137]. In Ref. [137] samples of γ-Fe encapsulated in a Cu matrix are analyzed and a helical spin structure is assumed to be the low temperature state. This spin configuration is not reproduced in the *ab initio* calculations since a small four atomic unit cell is used. The differences in structure and magnetism of our model compared to the experimental situation can explain the different result for the critical temperature.

It is obvious that the method applied here is less successful for γ-iron than for α-iron, because of the approximative nature of the Heisenberg model, the neglected temperature induced volume changes, and the small unit cell in which complex magnetic structures suggested by many authors cannot be realized. The magnetic configuration used here is only a rough estimate of the real magnetic state. However, the use of this small cell with a simple layerwise antiferromagnetic configuration is still reasonable because it is energetically very close to the double layered antiferromagnetic configuration which is found in larger unit cells [138, 139]. In addition, a deviation of around 30% compared to the experimental value of T_{C} is still good if the number of approximations is taken into account.

Therewith, it is shown that the method as it is used here gives reasonable results, extends understanding of magnetism from zero to finite temperatures and is therefore from now on used in the investigations of binary alloys and later on for Heusler systems.

4.2.2 γ-FeMn

In this subsection, it is discussed in how far Monte Carlo simulations of $L1_0$ structured γ-FeMn can be used to determine the non-collinear spin structure of the ground state. The magnetic order of this particular alloy is less well-known although an antiferromagnetic type of order has been reported in literature [124].

Starting point for the *ab initio* calculations is again a unit cell containing four atoms and a layerwise structural as well as antiferromagnetic configuration is adopted, i.e. the moments of Fe and Mn layers are antiparallel aligned to each other. The computational procedure follows the scheme shown in Fig. 3.1: First, the lattice constant is determined with VASP which is afterwards used in the SPR-KKR code for the calculation of magnetic exchange parameters followed by MC simulations. In contrast to the investigation of α- and γ-Fe, γ-FeMn is an example where an inconsistency between the low temperature spin configuration determined with the MC method in comparison to the one obtained from the *ab initio* calculation is encountered (compare Fig. 4.3(a) and 4.3(c)). All subsequent steps are also listed in Fig. 4.3.

The layerwise antiferromagnetic structure which is obtained after the initial VASP run is shown in Fig. 4.3(a). The middle column (Fig. 4.3(b)) shows the corresponding exchange parameters calculated with the SPR-KKR code by using the unit cell parameters obtained from the VASP calculations. Figure 4.3(c) shows the low temperature spin configuration which is obtained from the MC simulation with the structural parameters from VASP and the J_{ij} from SPR-KKR. The MC configuration is also of layerwise character but here the layers of Fe and Mn show each an antiferromagnetic type of order, see Fig. 4.3(c). This

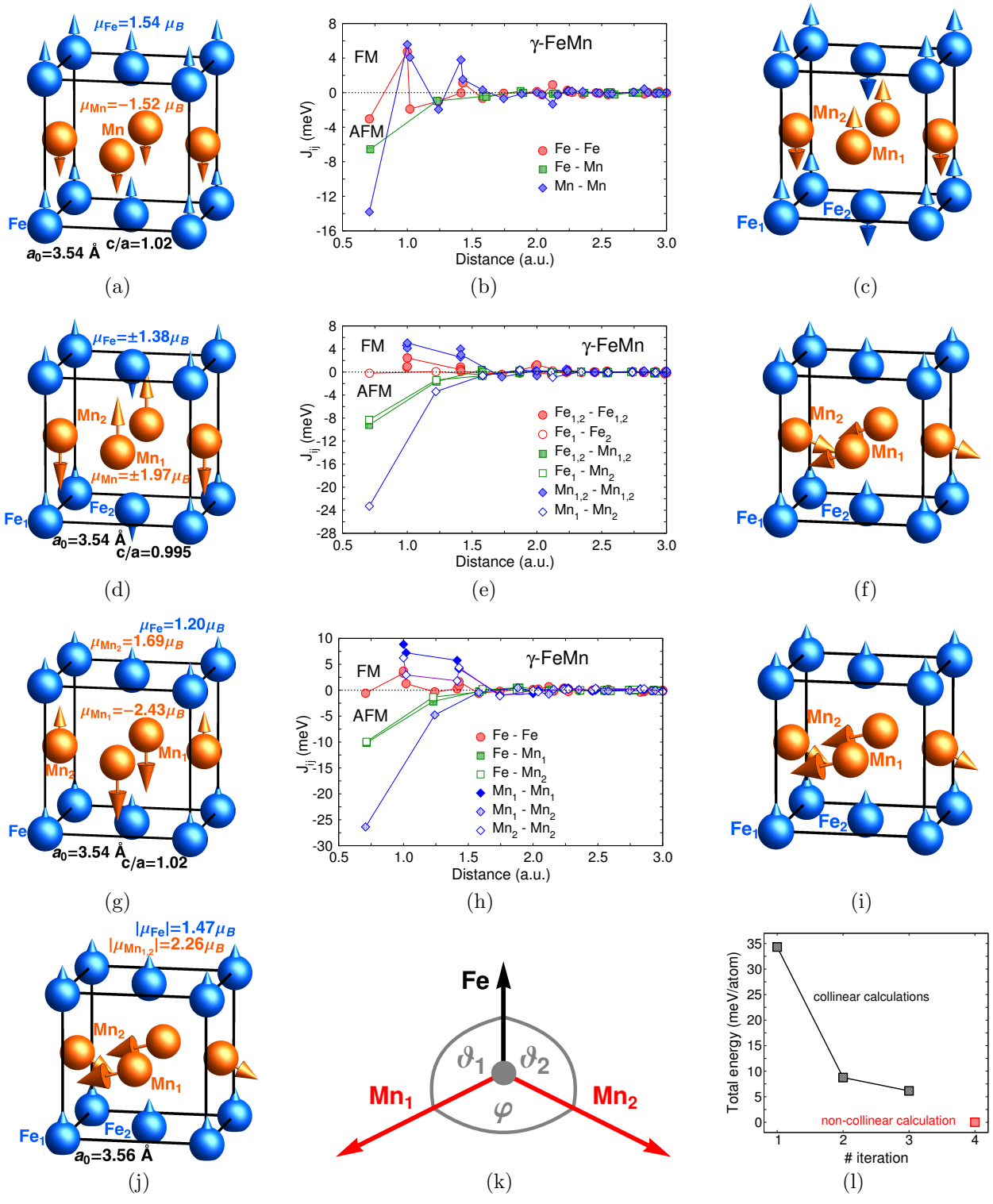

Figure 4.3: (a-i) show three iterative steps of the procedure introduced in Chapter 3 for γ-FeMn. The left column shows the lattice parameters and magnetic moments, the middle column the magnetic exchange parameters and the right column shows the low temperature magnetic configurations obtained from MC simulations. (j-l) show the result of a non-collinear VASP calculation, a schematic plot of the orientation of the magnetic moments and the total energy of the iteration steps presented in (a-i), respectively.

Atom	L_x	L_y	L_z
Fe_1	0.00	0.00	0.04
Fe_2	0.00	0.00	0.04
Mn_1	0.02	0.00	0.01
Mn_2	0.02	0.00	0.01

Table 4.1: Orbital moments of the different atoms in FeMn obtained from VASP calculations in units of μ_B.

structure can be explained by investigating the exchange parameters in more detail. All nearest neighbor interactions are antiferromagnetic and in the MC result eight of twelve nearest neighbors are antiparallel which reduces the frustration significantly and is therefore preferred. This means that the reference state of the J_{ij} calculation is intrinsically frustrated but marks a local energy minimum.

In the following step the low-temperature configuration of the MC simulation of Fig. 4.3(c) is used in a new VASP and SPR-KKR calculations of structural and magnetic parameters, i.e. the spin configuration found in the MC simulation is used to set the initial orientations of the magnetic moments for the next VASP calculation. The results of this subsequent VASP run are shown in Fig. 4.3(d). The new magnetic configuration leads to a lower total energy compared to the energy of the configuration shown Fig. 4.3(a). Subsequently, the J_{ij} of this configuration are calculated and a MC simulation is performed. The results are shown in Fig. 4.3(e) and 4.3(f). Figure 4.3(f) shows that the low temperature spin configuration obtained from the MC simulation bears now features of non-collinear magnetism. This configuration occurs because the iron moments interact ferromagnetically and antiferromagnetically with manganese. The manganese atoms of equal type are ferromagnetically coupled and those of different type antiferromagnetically. The non-collinear arrangement reduces the associated frustration. Therefore, the second reference state is still intrinsically frustrated.

In a final step the non-collinear state is modeled by a collinear one and another VASP calculation performed. To accomplish this modeling, the collinear spin configuration of the iron sublattices (MC) shown in Fig. 4.3(f) is used as a reference and all Fe atoms are initialized with spin-up. In order to take care of the antiferromagnetic tendencies of the moments in the Mn_1 and Mn_2 sublattices (see Fig. 4.3(e) and 4.3(f)), one sublattice, Mn_1, is chosen to be parallel to the iron sublattices and the other, Mn_2, to be antiparallel to the iron sublattices. The magnetic state which is obtained starting from these initial conditions is shown in Fig. 4.3(g). The total energy of the resulting configuration is again lower in energy compared to the one shown in Fig. 4.3(d).

In each cycle the total energy of the new collinear state obtained from VASP is lower (see Fig. 4.3(l)). This results from the successive reduction of frustration in the collinear reference states. Regarding the J_{ij}, each iteration leads to an increase of the nearest neighbor exchange interactions which are damped in more frustrated environments. The low temperature spin configuration of the final MC simulation shown in Fig. 4.3(i) is again a non-collinear configuration. The only difference to the configuration shown in Fig. 4.3(f) is that the magnetization direction of the Mn sublattices is slightly rotated. But as effects of magnetocrystalline anisotropy are neglected, both states are equal because without anisotropy the directions of

both Mn sub-lattlices can be rotated around the axes given by the magnetization of the Fe sublattice. However, they may not be rotated with respect to each other. This maintenance of the non-collinear state in the MC simulation shows that frustration cannot be completely avoided in a collinear arrangement of the individual magnetic moments.

The calculated J_{ij} in Fig. 4.3(h) show that the frustration occurs due the competing exchange interactions of the nearest neighbors. It is easy to see that if the constraint of collinearity is released as it is done in the MC simulation of a Heisenberg model, a non-collinear state is preferred. Although a collinear state which is lowest in energy for the four atom cell is found, the subsequent MC simulation still prefers a non-collinear configuration. Therefore, a final *ab initio* calculation is performed with VASP. Now, non-collinearity of the moments is allowed and an optimization of the total energy with respect to the orientation of the magnetic moments is performed. The MC result of Fig. 4.3(i) is used as the initial state. A comparable non-collinear configuration as shown in Fig. 4.3(i) is obtained. The lattice parameters and magnetic moments are given in Fig. 4.3(j). Figure 4.3(l) shows the variation of the total energy obtained from VASP calculations with the number of iterations of the DFT-MC cycle, including the non-collinear calculation. It shows that the total energy of the non-collinear state is lower compared to all collinear states.

A similar configuration like the one shown in Fig. 4.3(j) can be found in Fig. 2 of Ref. [106], where the authors performed non-collinear *ab initio* calculations using the LMTO approach [140]. The arrangement of the magnetic moments of the ground state found by these authors is sketched in Fig. 4.3(k). The arrows denote the directions of the magnetic moments of the iron and the two manganese sublattices which are all in the same plane. The angles ϑ_1, ϑ_2 and φ denote the plane angles between the orientations of the moments. A good agreement is found if the value of the angle $\varphi = 138.5°$ obtained from the non-collinear VASP calculation presented above, is compared to the result of Ref. [106] which is $\varphi = 128°$. The result of the MC simulations in Fig. 4.3(i) yields $\varphi = 138°$, which is almost the same value as the one obtained from non-collinear VASP calculations. This shows again the consistency of the combined *ab initio*-MC approach. The difference between the MC state (Fig. 4.3(i)) and the VASP result (Fig. 4.3(g)) is that the magnetizations of the two manganese sublattices differ because the collinear *ab initio* calculation results in different magnetic moments for the sublattices. In the non-collinear VASP calculation the magnetic moment of the two manganese sublattices is again the same.

The difference of the angle between the magnetizations of the manganese sublattices obtained by VASP in comparison to Ref. [106] may originate from the different approaches used in the calculation. However, it is remarkable that the angles obtained in VASP calculations and MC simulations are almost the same. This explicitly shows the powerful ability and consistency of the approach used here.

The total energy of the non-collinear state obtained from VASP is lower compared to the values of all collinear configurations. The energy difference between the non-collinear ground state and the lowest collinear state of Fig. 4.3(g) is $\Delta E = 3.41\,\mathrm{meV/atom}$. Furthermore, the lattice constant is slightly increased from 3.54 Å to 3.56 Å in the non-collinear case. It may be tentatively concluded that the magnetic state which minimizes the energy in the given four atom cell is found.

In addition, the possible influence of spin-orbit coupling on the relative orientations of the magnetic moments is checked. It turns out that the spin-orbit coupling is small and the same relative orientation of the magnetic moments as in the non-collinear case without spin-orbit coupling is found. The components of the orbital moments are summarized in Table 4.1.

Composition	Lattice	Magnetic order	a (Å)	c/a	$T_C(K)$
Fe	bcc	FM	2.84	1	955
Fe_3Mn	fcc	AF2	3.55	1	690
Fe_3MnC	fcc + i	AF2	3.77	1	420
FeMn	fcc	AF3	3.54	1.02	625*
$FeMn_3$	fcc	AF1	3.56	1	440*
$FeMn_3C$	fcc + i	AF4	3.8	0.98	780

Table 4.2: Lattice parameters and magnetic order obtained from VASP (GGA) calculations. The "i" indicates that the carbon atoms occupy interstitial sites in the fcc lattices. The column "Magnetic order" describes the magnetic order of the Fe and Mn atoms obtained in the collinear VASP calculations regardless of the orientation of the carbon atoms which are very small. The stars denote that non-collinear spin ordering is obtained from the MC simulation at low temperatures.

The remark in Ref. [106] that the magnetic exchange parameters between Fe and Mn fulfill the relation $J_{\mathrm{Fe-Mn}} \approx 0.5\, J_{\mathrm{Mn-Mn}}$ is of great interest because it is confirmed by the calculations presented here: $J_{\mathrm{Fe-Mn_1}}$ and $J_{\mathrm{Fe-Mn_2}}$ are by a factor of 2.6 smaller compared to the $J_{\mathrm{Mn_1-Mn_2}}$ couplings of the nearest neighbor shell shown in Fig. 4.3(h).

It should also be mentioned that the calculated lattice constant of $a_0 = 3.56\,\text{Å}$ of the non-collinear run is close to the experimental value of $a_0 = 3.60\,\text{Å}$ of disordered γ-FeMn [141]. The remaining difference between experimental and theoretical values may be due to disorder and approximations included in the theoretical calculations (e.g. the exchange-correlation functional).

Taking γ-FeMn as an example, it is demonstrated that the iterative computational procedure illustrated in Fig. 3.1 leads to the magnetic ground state of a particular cell. It is not claimed that the overall magnetic ground state of γ-FeMn is determined because for this one needs to include larger super cells with more atoms for the modeling of more complex magnetic configurations and of course compositional disorder. But as shown below, this iterative procedure works also for other systems, for example, Fe_3Mn and $FeMn_3$. Thus, it is concluded that it should in principle be possible to use the scheme to find magnetic ground states of other alloys as well.

Furthermore, the MC simulations give insight into the complex finite temperature magnetism that occurs in alloys with competing exchange interactions. It turns out, that the use of the magnetic low temperature reference state used in the calculations of the exchange parameters leads to interesting finite temperature behavior of the magnetically ordered phases below T_C although the use of the disordered local moment state (DLM) [142, 143] as a reference should in principle lead to better results for the critical temperature. This assumption is justified because the DLM state models the paramagnetic phase and therefore should reproduce effects of elevated temperatures. On the other hand, it is shown below that sometimes the DLM picture leads to strong quenching of individual moments of certain atoms and therefore fails to give a reasonable estimate of the critical temperature (see Chapter 5 and 6).

Figure 4.4 shows the variation of the norm of the magnetization of the sublattices of γ-

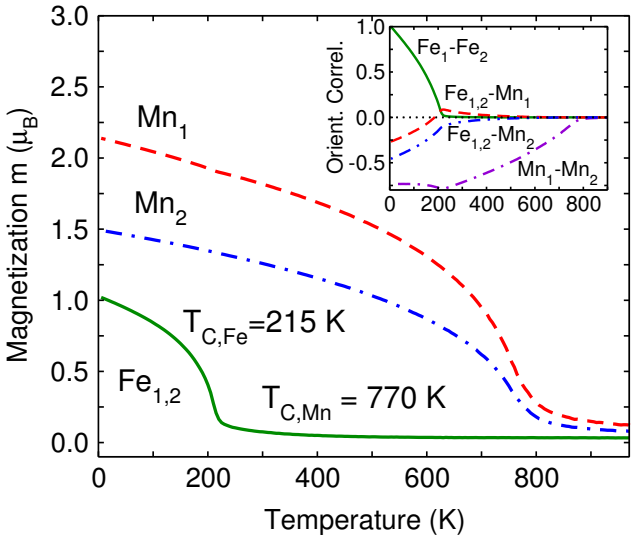

Figure 4.4: Variation of the magnetization as a function of temperature of the two different sublattices of γ-FeMn corresponding to Figures 4 (g-i). The magnetization is given by its absolute value instead of the sign afflicted absolute value. The inset shows the orientation correlation function.

FeMn with temperature. These magnetization curves show that the magnetic ordering of the manganese sublattices starts at almost a factor of four higher temperatures compared to the iron sublattices. The onset of magnetic ordering of the manganese sublattices starts at 770 K, whereas the iron sublattices order at 215 K. This can be explained by considering that the exchange interaction between the Mn atoms is much larger than the interactions between the Fe moments. The inset of Fig. 4.4 gives more detailed insight into this behavior. It shows the orientation correlation function of different pairs of sublattices which is defined by

$$G_{ab} = \frac{\langle \boldsymbol{m}_a \boldsymbol{m}_b \rangle}{\mu_a \mu_b} \tag{4.1}$$

with $G_{ab} = 1$ if the magnetization of the sublattices a and b are perfectly parallel, and -1 if they are antiparallel. The orientation correlation function reveals that the manganese sublattices start to align antiparallel at 770 K but as the iron sublattices start to order, they change their relative orientation and end up with the angle $\varphi = 138°$. The two iron sublattices start to align in a parallel manner at 215 K until they are perfectly aligned at $T = 0$ K. From the orientational correlation of the $Fe_{1,2}$-Mn_1 and $Fe_{1,2}$-Mn_2 sublattice pairs one recognizes that iron shows first a tendency to align parallel to the Mn_1 sublattice but then the behavior rapidly changes and finally an angle of $\vartheta_1 = 105.5°$ is found between Fe_1 and Mn_1. This shows that the magnetizations of the different sublattices undergo complex changes with decreasing temperature until they end up in the configuration sketched in Fig. 4.3(k) at $T = 0$ K.

Before the discussion of FeMn is finished some additional remarks concerning the use of the Heisenberg model are given: As it is found that the qualitative behavior of the exchange parameters does not change very much when the magnetic configurations of the reference state is changed (see Fig. 4.3) it can be concluded that the assumption of a Heisenberg like magnetism in FeMn is justified. In a completely Heisenberg like system the exchange parameters would not change with the reference state and the energy difference between

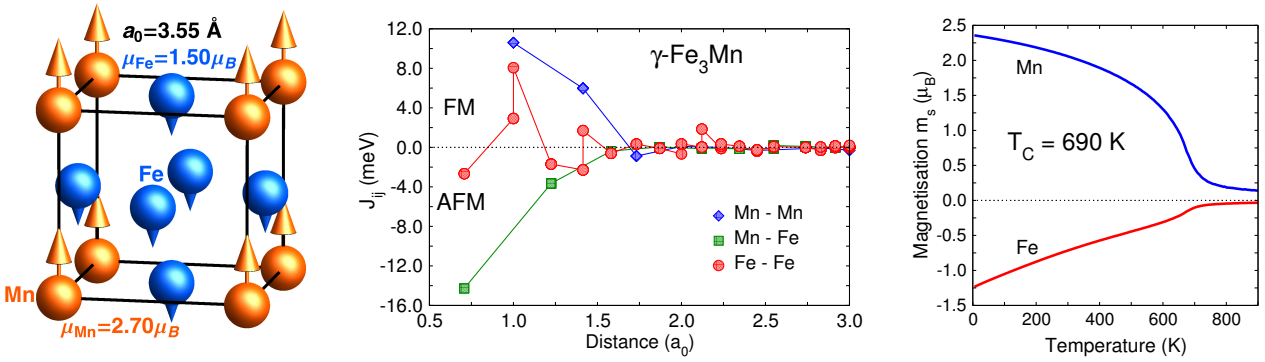

(a) (b) (c)

Figure 4.5: (a) Lattice constant and magnetic moments of Fe_3Mn obtained from VASP calculations. (b) Magnetic exchange parameters of Fe_3Mn. Manganese seems to prevent the long range oscillating behavior of the exchange parameters between iron pairs. Though there is only 25% manganese involved, all exchange parameters are close to zero beyond distances of three lattice constants. (c) Variation of the magnetization of γ-Fe_3Mn as a function of temperature. The magnetization of the iron sublattice shows an unusual behavior: With decreasing temperature it decreases linearly but shows a slightly stronger decrease at the critical point.

two magnetic configurations would be fully determined by the J_{ij}. Therefore, quantitative changes of the J_{ij} can be attributed to the non-Heisenberg tendencies of the system. These tendencies can occur due to, e.g., itinerant magnetism and many-body effects. But it can be concluded that if the reference state is reasonable enough, the MC simulation ends up in the correct ground state because the exchange parameters include the information about this ground state if the magnetism of the system is Heisenberg like.

In the following iron-manganese alloys containing 25 and 75% manganese are discussed. Regarding the influence of carbon on the magnetic properties of Fe-Mn alloys, carbon atoms are considered to occupy the energetically preferred octahedral coordinated interstitial sites.

The results concerning the lattice parameters, magnetic ordering, and critical temperatures of the systems studied here are summarized in Table 4.2. All structures and magnetic configurations in this table correspond to the lowest energy states of unit cells containing four atoms in the *ab initio* calculations. Obviously, the lattice constants are only little affected by the manganese content. This changes when carbon is added, which causes a significant increase of the cell volume. But this effect is again approximately independent of the manganese content. This can be understood by considering that iron and manganese atoms are almost of the same size and that the occupation of interstitial sites trivially increases the volume if the atoms occupying these sites are of considerable size.

The following discussion begins with γ-Fe_3Mn followed by Fe_3MnC. Further below, γ-$FeMn_3$ on the manganese rich side of the phase diagram is investigated in order to study the complex nature of the antiferromagnetic exchange interactions which are dominant in this system. Finally, $FeMn_3C$ is discussed and it turns out that the influence of carbon on the critical temperature on this side of the phase diagram is contrary to that on the iron rich side. Here, carbon increases the critical temperature compared to the system without carbon while in Fe_3MnC the critical temperature is decreased compared to Fe_3Mn.

Composition	$\mu_{\mathrm{Fe}}\,(\mu_{\mathrm{B}})$	$\mu_{\mathrm{Mn}}\,(\mu_{\mathrm{B}})$	$\mu_{\mathrm{C}}\,(\mu_{\mathrm{B}})$
Fe_3Mn	-1.57 (-1.25)	2.75 (2.36)	
Fe_3MnC	(1) -1.42 (-0.63) (2) -2.84 (-3.03)	1.95 (2.18)	-0.03 (-0.03)

Table 4.3: Comparison of the magnetic moments of Fe_3Mn and Fe_3MnC. The enumeration denotes the different types of iron atoms in Fe_3MnC. The values in brackets denote the magnetic moments obtained by using the SPR-KKR code. Results of the VASP calculations are shown without brackets. The difference between these values are due to the different methods and to the fact that GGA is used in VASP and LDA in SPR-KKR calculations.

4.2.3 γ-Fe_3Mn alloys

In this subsection, γ-Fe_3Mn in the $L1_2$ structure is investigate. Again, a unit cell consisting of four atoms is used. The magnetic structure which is lowest in energy, see Fig. 4.5(a), is antiferromagnetic and exhibits the same cubic symmetry as the chemical ordering (space group No. 221). However, the exchange interaction between next nearest neighbor iron atoms is split into two values. To understand this, it has to be noted that, e.g., the connecting lines between two next nearest neighbor iron atoms can be subjected to different environments. For example, the interaction between the iron atom at the bottom of the cell shown in Fig. 4.5(a) and the iron atom on its top is considered now: The connecting line between these atoms passes only iron atoms, whereas connecting line between the iron atom at the bottom and its periodic image at the right or left side as well to those in the front and back also passes manganese atoms. In both cases, the atoms are next nearest neighbors separated by one lattice constant. The stronger interaction is associated with the cases where the connection lines pass only iron atoms and the smaller one to those where the connection line also passes manganese atoms. The same occurs also for neighbors of higher order.

Figure 4.5(b) shows that all nearest neighbor iron atoms interact antiferromagnetically. But this coupling is rather weak compared to the stronger antiferromagnetic coupling between iron and manganese atoms and the ferromagnetic coupling to the next nearest neighbor iron atoms, at least to those which are connected within an iron environment as discussed above. The competing interactions strongly affect the temperature evolution of the magnetization obtained from the MC simulation. In Fig. 4.5(c) the magnetization of the iron and manganese sublattices is shown. The Fe sublattice shows clear indications of frustration effects because after a small bump in the vicinity of the critical temperature it increases almost linearly whereas the magnetization of the manganese sublattice develops in the usual manner. The behavior of the Fe sublattice originates from the competition of the antiferromagnetic interaction of nearest and the ferromagnetic of next nearest neighbors.

A critical temperature of $T_{\mathrm{C}} = 690\,\mathrm{K}$ is obtained from the MC simulation. A mean field analysis of the exchange parameters gives a critical temperature $T_{\mathrm{C}}^{\mathrm{MF}} = 863\,\mathrm{K}$.

Experimental phase diagrams (see for example Ref. [124]) show that the measured critical temperature of $Fe_{75}Mn_{25}$ is about 400 K. This is a significant deviation of the theoretical prediction compared to the experimental result although the MC result overestimates the critical temperature less than the mean field approximation (this is expected from the basic theory of critical phenomena, see e.g. Ref. [144]). The deviation from the theoretical results

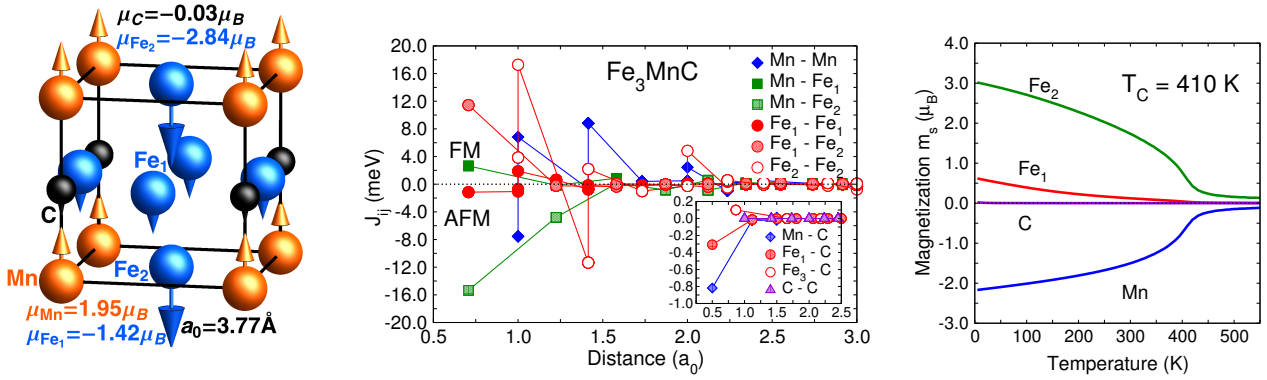

(a) (b) (c)

Figure 4.6: (a) Structure, magnetic moments and (b) magnetic exchange parameters of Fe_3MnC. Magnetic moments as well as exchange coupling constants are enhanced in comparison to γ-Fe_3Mn. As expected, carbon shows only a small moment and small exchange interactions. (c) Variation of the magnetization of the sublattices of Fe_3MnC as a function of temperature. Although the moments and their couplings are stronger compared to Fe_3Mn, the critical temperature is reduced to 410 K. This can be explained by the frustration effect, which originates from the fcc type of lattice and complex exchange interactions.

can be explained by the occurrence of disorder in the real alloys. In order to fortify this assumption, effects of disorder are included by performing calculations using the single-site coherent potential approximation (CPA) [145] as implemented in the SPR-KKR code. The CPA method allows to construct an effective medium corresponding to a mean field like description of a random alloy that consists of 75% iron and 25% manganese. In the construction of the MC simulation cell the two atom types are randomly distributed on the lattice sites. The distribution fulfills the constraint that the system contains approximately 75% Fe and 25% Mn atoms. Due to the introduced disorder the critical temperature is reduced to 320 K which is much closer to the experimental value compared to the T_C of ordered Fe_3Mn. The remaining deviation can be explained by the fact that the lattice constant of the ordered system is used in the CPA calculation and by the intrinsic assumptions made within the single-site CPA. Calculations using the nonlocal CPA (NLCPA) [146], the correct lattice constant and the DLM state as a reference might lead to even better agreement with the experimental T_C-value. But in summary it may be stated that the methods used here are again in reasonable agreement with the experiment.

4.2.4 Fe_3MnC alloys

In order to investigate the influence of carbon on the magnetic properties of Fe-Mn alloys, carbon atoms are added on octahedral interstitial sites. A unit cell with five atoms as it is shown in Fig. 4.6(a) is used during this investigation. It is found that larger relaxation effects are suppressed due to the translational symmetry of the small unit cell. In larger cells with much smaller carbon content strong relaxations of the surrounding octahedrally coordinated atoms are expected. These relaxations are comparable to those found in Ref. [115] for γ-iron with carbon on interstitial sites. For simplicity only the small cells are investigated in the following. An increased lattice constant compared to Fe_3Mn is found which originates from the high carbon concentration on interstitial sites.

The results show that carbon decreases the magnetic moments of the nearest neighbor manganese and iron atoms, whereas the magnetic moment of the next nearest neighbor iron atom, Fe_2, is almost twice as large, see Fig. 4.6(a). This means that the moments of the Fe_2 sublattice is increased by almost the same value as the moments of the other sublattices are decreased. A comparison of the magnetic moments can be found in Table 4.3.

The magnetic exchange parameters of this system show that carbon tends to increase the magnetic interaction between iron and manganese atoms. This can be explained by the larger volume of the cell because due to the larger volume the distance between the atoms is changed. As expected, carbon itself couples weakly to other atoms and the exchange between the carbon atoms is effectively zero. This is explained by the small induced magnetic moment of the carbon atoms. The exchange coupling parameters of Fe_2-Fe_2 and Mn-Mn pairs are strongly oscillating. This originates from the two different pathways connecting these pairs. The Fe_2 atoms can be connected within one Mn-Fe_2 layer or by crossing the C-Fe_1 layer. On the other hand, the Mn atoms can be connected by crossing a C atom, which again means that the C-Fe_1 plane is crossed, or within the Mn-Fe_2 layer without crossing a C atom. The Mn-Fe_2 couplings remain comparable to Mn-Fe couplings in the Fe_3Mn system. The Fe_1-Fe_2 exchange is strong for the direct neighbors but instantaneously reduced for the next nearest neighbors.

The competition of ferro- and antiferromagnetic interactions leads to frustration. This is assured by the MC simulation, where a reduced critical temperature compared to Fe_3Mn is found although the absolute values of exchange couplings are increased. In addition, it should be noted that the Fe_1 magnetization curve exhibits unusual behavior. This sublattice shows no common critical behavior and the increase of the magnetization below T_C is slow and shows an unusual curvature. This is understood by considering that all Fe_1-Fe_1 couplings are small and in addition competing. Therefore, Fe_1 shows no critical behavior itself and aligns only due to its ferromagnetic interaction with the Fe_2 sublattice.

This investigation shows that high carbon content strongly affects the magnetism of the iron-manganese system. This must be connected to the change of the involved exchange mechanism between atom pairs which are now separated by carbon. In addition, the increased volume affects the formation of magnetic moments and the associated exchange interactions.

4.2.5 γ-$FeMn_3$ alloys

From here on, the manganese-rich side of the phase diagram, i.e. $FeMn_3$ in $L1_0$ order is investigated. This means that the sites of iron and manganese atoms are interchanged compared to Fe_3Mn, see Fig. 4.7(a). It turns out that a layerwise antiferromagnetic order is of lowest energy within the collinear *ab initio* formalism. The magnetic moments of all atoms are of comparable size. Similar to the case of Fe_3Mn, the system can be understood as a layered system with pure Mn layer and mixed Fe-Mn layers. Therefore, in analogy to Fe_3Mn different exchange interactions regarding the z- and x-y-directions occur.

Comparing the three systems Fe_3Mn, FeMn, and $FeMn_3$, it is observed that ferromagnetic interactions are more and more suppressed and the antiferromagnetic interactions become dominant with increasing Mn content (see Fig. 4.7(b)). The antiferromagnetic nearest neighbor coupling in $FeMn_3$ is almost by a factor of four stronger than the ferromagnetic interactions. Similar to FeMn, the exchange parameters between the manganese atoms are twice as large compared to the iron-manganese exchange parameters. The exchange between two iron atoms is about a factor of two smaller.

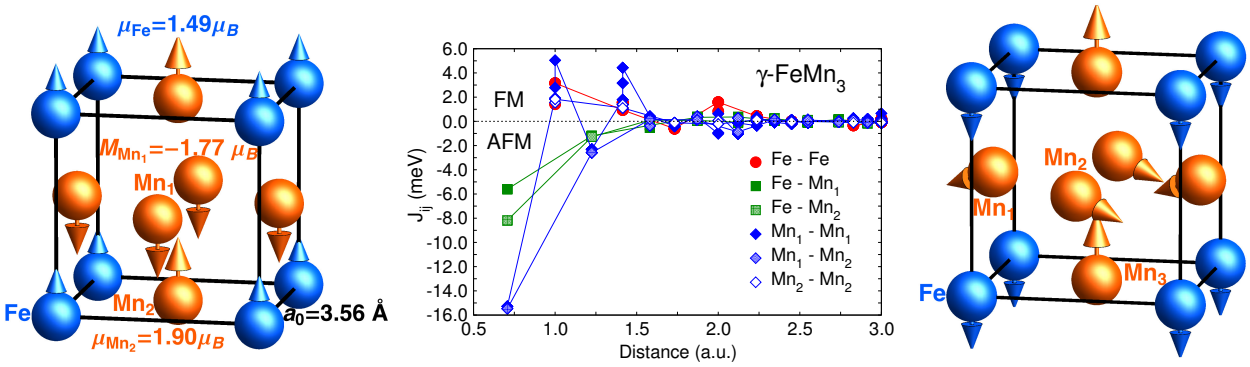

(a) (b) (c)

Figure 4.7: (a) Cubic Structure and magnetic moments of γ-$FeMn_3$ obtained from VASP calculations. (b) Magnetic exchange parameters from SPR-KKR calculations. For this high Mn content the antiferromagnetic interactions become dominant. (c) The non-collinear ground-state of γ-$FeMn_3$ obtained from the MC simulation using the J_{ij} shown in (b).

Due to the antiferromagnetic nearest neighbor interactions this system is frustrated. This is confirmed by the MC simulation, see Fig. 4.8. Despite the large exchange interactions a relatively low transition temperature of $T_C = 440\,K$ is obtained and a ground state spin configuration shown in Fig. 4.7(c), which is non-collinear evolves. The affinity to non-collinear arrangement of magnetic moments is related to the frustration and occurs naturally if the constraint of collinearity is released within the MC simulation. This is analogous to the case of γ-FeMn.

The ground state of the MC simulation is reproduced within a non-collinear VASP calculation. The angles between the moments of the Mn_1 and Mn_2 atoms are 142° in the MC simulation and 141° in the VASP calculation. This is an excellent agreement between the MC simulation and the non-collinear *ab initio* calculation. The total energy difference between the collinear and non-collinear state is $0.31\,meV/f.u.$. In the non-collinear case a slightly increased lattice constant of 3.57 Å is observed. No other collinear state can be stabilized that is comparable to the MC result. Therefore, the iterative scheme for searching the magnetic ground state converged in one step.

Composition	μ_{Fe} (μ_B)	μ_{Mn} (μ_B)	μ_C (μ_B)
$FeMn_3$	1.49 (1.21)	(1) -1.77 (-1.32) (2) 1.90 (1.52)	
$FeMn_3C$	-0.97 (-0.71)	(1) -1.92 (-1.57) (2) 3.54 (3.28)	0.14 (0.10)

Table 4.4: Comparison of the magnetic moments of $FeMn_3$ and $FeMn_3C$, where the enumeration defines the different types of manganese atoms in $FeMn_3C$. The magnetic moments shown in this table are obtained from VASP and the values in the brackets from the SPR-KKR code.

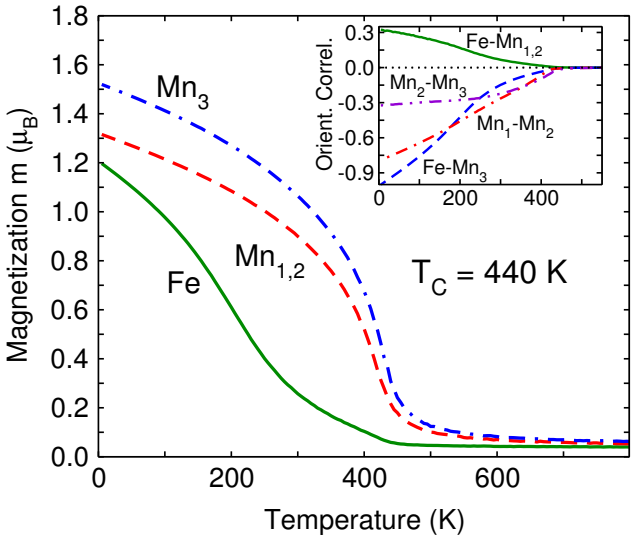

Figure 4.8: Magnetization curves of the four sublattices of $FeMn_3$. The moments of the manganese sublattices start to order first, while those of the iron sublattice order at lower temperatures. This is similar to FeMn. The inset shows the orientation correlation between the different sublattices.

In addition, the magnetization m_{Fe} (see Fig. 4.8) of the iron sublattice evaluated within the MC simulation shows an unusual variation as a function of temperature. The magnetization starts to rise at the critical temperature with a small slope and an unusual curvature which has the opposite sign compared to the magnetization of the other sublattices. In other words, the curvature is convex although a concave curvature is expected at the critical temperature. The slope increases below 300 K and at approximately 250 K the curvature changes its sign and becomes concave. This can be understood from the analysis of the exchange parameters in Fig. 4.7(b). All nearest neighbor interactions of iron are antiferromagnetic which gives rise to strong frustration because the exchange interaction prefers iron to be antiparallel to Mn_1 and Mn_2, which is obviously not possible. With decreasing temperature frustration is decreased due to the non-collinear arrangement of the Mn moments and therefore the iron moments 'know' how to orientate themselves relative to the manganese sublattices if the temperature is low enough. This is confirmed by the orientational correlation function (see Eq. 4.1) shown in the inset of Fig. 4.8. The correlations of the iron sublattice with all manganese sublattices show a sudden change at approximately 250 K. The correlation of Mn_1 and Mn_2 remains unaffected by the changes of the magnetization of the iron sublattice. Therefore, the development of the iron and Mn_3 magnetization is strongly connected to the magnetization of Mn_1 and Mn_2 in the sense that these sublattices 'know' how to order when the Mn_1 and Mn_2 magnetization is strong enough. The correlation function of Fe-Mn_3 and Mn_2-Mn_3 changes its behavior at 250 K because the Mn_3 sublattice changes its orientation.

The $FeMn_3$ system is the second example where the combination of *ab initio* calculations and MC simulations accelerated the search for the magnetic ground state. However, this conclusions is so far only valid for systems with negligible spin-orbit coupling. If spin-orbit coupling would introduce a strong magneto-crystalline anisotropy this contribution has to be included within the MC simulation.

The critical temperature of 440 K obtained here is very close to the experimental value of

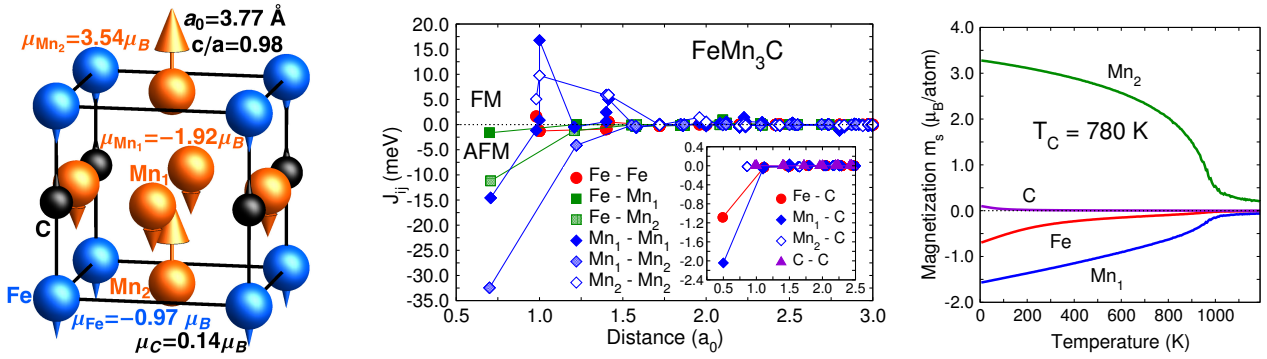

Figure 4.9: (a) Cubic structure and magnetic moments of $FeMn_3C$ obtained from VASP. (b) Magnetic exchange parameters calculated with SPR-KKR. Carbon leads to enhanced magnetic exchange coupling constants compared to $FeMn_3$. Carbon itself exhibits only a small moment and small exchange interactions. (c) Variation of the magnetization of the sublattices of $FeMn_3C$. The MC simulation yields a critical temperature of 780 K.

about 400 K [147] for structurally disordered $FeMn_3$ samples. This indicates that effects of disorder might be less important on the manganese-rich side compared to the iron-rich side. But it can also indicate that the assumption of local moments which is introduced by the Heisenberg model yields better results on this side of the phase diagram.

4.2.6 $FeMn_3C$ alloys

In order to discuss the effect of carbon on the magnetic properties of $FeMn_3$, carbon atoms are added on octahedral sites as shown in Fig. 4.9(a). The collinear magnetic structure changes from the layer-wise configuration of $FeMn_3$ to a more complex configuration. The moments of the Fe atoms are strongly decreased to an unusual value below 1 μ_B whereas the manganese moments are increased.

Attention has to be payed to the moment of the Mn_2 atoms. If the change of the magnetic moment of Mn_2 while passing from $FeMn_3$ to $FeMn_3C$ is compared to the corresponding change of Fe_2 from Fe_3Mn to Fe_3MnC, comparable effects can be observed. The magnetic moment of Mn_2 in Fig. 4.9(a) shows the same strong increase as Fe_2 in Fig. 4.6(a) when compared to the systems without carbon. The difference on the iron rich side is that the magnetic structure of the iron and manganese atoms remains the same when carbon is added whereas the magnetic structure of $FeMn_3C$ differs from the one found in $FeMn_3$.

The exchange parameters of $FeMn_3C$ shown in Fig. 4.9(b) reveal a strong increase of the interaction strength. Ferromagnetic as well as antiferromagnetic interactions are strongly increased compared to $FeMn_3$. But it should be noted that the interactions are almost completely damped for distances beyond two lattice constants. Obviously carbon tends to increase the magnetic exchange onteractions on the iron as well as on the manganese-rich side of the phase diagram.

The critical temperature obtained in the MC simulation is 780 K and therefore strongly increased compared to the system without carbon, see Fig. 4.9(c). This is contrary to the trend found on the iron-rich side of the phase diagram where carbon tends to decrease the critical temperature of the system. Again, as for Fe_3MnC, the magnetization of the iron

sublattice shows a particular behavior, which demonstrates the frustration acting on this sublattice.

The addition of carbon on the Mn rich side leads very strong antiferromagnetic interactions. They are more than 10 meV larger than the largest ferromagnetic interactions. Due to this domination of antiferromagnetism and the high absolute value of the exchange interactions the critical temperature becomes large in $FeMn_3C$. The situation is similar in $FeMn_3$ but the absolute values of the J_{ij} are smaller and therefore T_C is smaller.

4.3 Conclusions

In this chapter a detailed study of the magnetic properties of iron-manganese based binary alloys is carried out by combining *ab initio* methods and Monte Carlo simulations. In a first step the method is adopted to α- and γ-iron in order to check the consistency and validity of this approach. The results for α-iron agree nicely with previous theoretical work and experimental results. The results for γ-iron reproduced the trend for complex magnetic ordering but the critical temperature is about 30% overestimated. This overestimation of T_C is connected with the use of small unit cells in the *ab intio* calculations.

In the next step γ-FeMn is investigated. During this investigation it is shown that the combination of *ab initio* and MC methods accelerates the search for magnetic ground state configurations in particular if they are non-collinear. Therefore, a self-consistent cycle is developed from which the magnetic ground state is obtained by starting from an almost arbitrary configuration. The magnetic configuration which is found agrees accurately with previous theoretical investigations. In addition, the approach gives valuable insight into the temperature dependence of the magnetization below the critical temperature. It turns out that details of the magnetic ordering develop below the critical temperature where reorientations of certain sublattices occur.

Afterwards, results for γ-Fe_3Mn and γ-$FeMn_3$ are presented. It is found that on the iron-rich side of the phase diagram the magnetic order tends to be collinear whereas on the manganese-rich side the magnetic order becomes non-collinear. This originates from decreasing ferromagnetic and increasing antiferromagnetic exchange interactions. The dominance of antiferromagnetic interactions leads to strongly frustrated collinear states. If the constraint of collinearity is removed in the MC simulation of the Heisenberg model, the exchange interactions lead to non-collinear states which can be reproduced in the *ab initio* calculations with excellent agreement. These non-collinear states are found to be of lower energy compared to all possible collinear states and therefore mark the ground state of the small unit cells employed here.

As the FeMn based alloys analyzed in experiments are structurally disordered, an investigation of the influence of disorder required. It is found that while $L1_2$ ordered Fe_3Mn yields a critical temperature which is too high compared to the experiment, the introduction of disorder, using single-site CPA, reduces T_C to a value which is in better agreement with the experimental result. Therefore, it is concluded that disorder is important in order to get a realistic theoretical description of the iron-rich FeMn alloys. Surprisingly, this is different in manganese-rich FeMn alloys where the critical temperature of the ordered system is already close to the experimental critical temperature of the disordered systems. It is carefully concluded that the critical temperature of manganese-rich systems depends less strongly on the chemical order.

In addition, the influence of interstitial carbon on the magnetic properties of Fe_3Mn and $FeMn_3$ is analyzed. It turns out that high carbon concentrations tend to decrease the critical temperature of the alloys on the iron rich side while it enhances the magnetic transition temperature on the manganese rich side. Carbon also leads to the stabilization of collinear states for manganese rich compositions. Therefore, in contrast to $FeMn_3$, $FeMn_3C$ exhibits a collinear ground state

Throughout the entire investigation, attention is paid to the approximations and assumptions that enter the method in particular the approximative nature of the description of itinerant magnets by localized magnetic moment models.

Highlight

This section shows the powerful ability of the combination of first-principles calculations with MC simulations. The evaluated structural and magnetic properties are in excellent agreement with the experimental explorations of the phase diagram of iron-manganese alloys. It turns out that the combination of the both methods leads to an accelerated search for non-collinear ground states and in addition, an outstanding consistency between the *ab initio* calculation and MC simulation is found because both methods predict the same non-collinear ground states with perfect agreement of the angles enclosed by the different moments.

5 Iron-Cobalt

The combination of *ab initio* calculations and MC simulations is now used to study FeCo-alloys. In this chapter, an additional focus is on the occurrence of unusual thermal expansion coefficients known as Invar effect. Therefore, special attention is paid to different magnetic phases of γ-FeCo-alloys. Although, Invar behavior is originally found in iron-nickel alloys (see e.g. Ref. [13] and references therein), the γ-phase of iron-cobalt alloys also show this type of magneto-volume correlation.

So far, no investigation of $Fe_{1-x}Co_x$ comparable to the combined DFT+MC approach is reported in literature. Therefore, the following discussion contributes significantly to the understanding of the connection between zero and finite temperature magnetism and its close relation to the crystal structure.

First, some facts about Fe-Co alloys are presented. Afterwards, an investigation of Fe_3Co, FeCo and $FeCo_3$ is carried out separately. Structural and magnetic properties as well as the influence of disorder are discussed in detail.

5.1 Introduction

Iron-cobalt alloys represent an interesting class of magnetic materials because of the large individual magnetic moments of Fe and Co and their strong ferromagnetic interaction. This gives rise to large saturation magnetizations and high critical temperatures. In addition, magnetic anisotropies are predicted to be very high, which results in a stable orientation of the magnetic moments along a particular crystallographic direction. Alloys exhibiting such properties are of great interest for technological applications where high magnetic flux densities are required.

Due to the additional excellent performance-to-weight ratio of iron-cobalt alloys, they are considered for applications in modern aircrafts where pneumatic, hydraulic and mechanical components are more and more replaced by electric and magnetic analogs [14].

Furthermore, the electronic transport properties of iron-cobalt alloys have attracted much interest (see Ref. [148, 149]). They are, e.g., considered as promising candidates for magneto-resistive devices. Recently, these alloys are experimentally and theoretically investigated from the spin-caloric transport point of view [150].

Iron-cobalt alloys are also investigated because of their magnetostrictive behavior in thin films as reported in Ref. [152]. Since the samples investigated in Ref. [152] exhibit mixed fcc and bcc structure, it is of special interest to study ground state properties of fcc iron-cobalt alloys theoretically even for compositions where the fcc structure is not stable at room temperature because the fcc structure can be stabilized in thin films on certain substrates.

The experimental phase diagram of $Fe_{1-x}Co_x$ is shown in Fig. 5.1. For low temperatures and almost the whole range of composition iron-cobalt alloys exhibit a bcc structure (α-phase). At higher temperatures around 1200 K a transition to the fcc structure (γ-phase) is found again, for almost the whole composition range. There is a small range at around $x = 0.8$ where the α- and γ-phase coexist (note the splitting of the α-γ-transition line). For

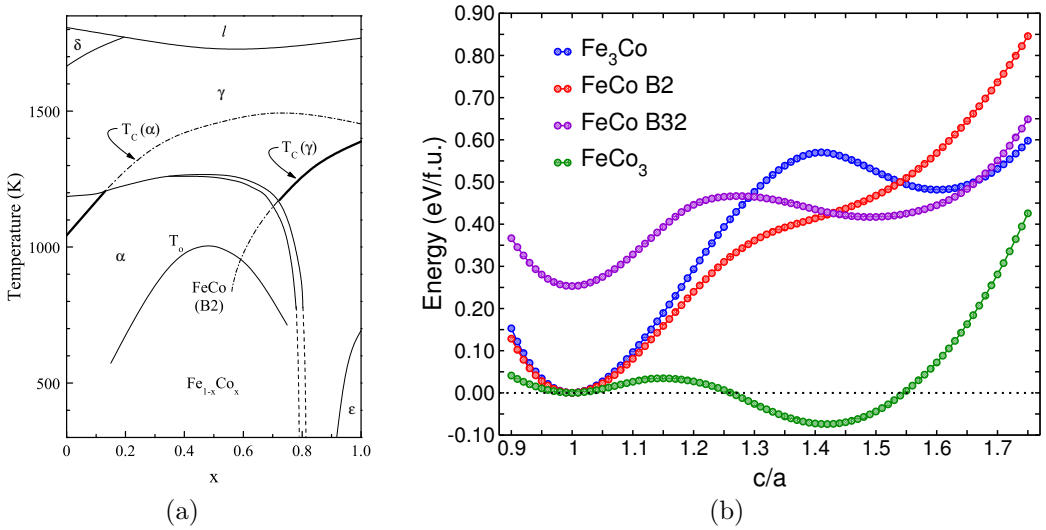

Figure 5.1: (a) Structural and magnetic phase diagram of $Fe_{1-x}Co_x$ alloys [124]. (b) Variation of the total energy of ordered $Fe_{1-x}Co_x$ systems along the Bain path [151]. Concerning FeCo, two types of structure are considered namely the B2 and the B32 structure. For all systems except for the B2 ordered FeCo, two minima at $c/a = 1$ and c/a values between 1.4 and 1.6 are found. This corresponds to the experimental phase diagram which shows that iron-cobalt alloys can exist in bcc or fcc structure depending on the temperature. The energy is normalized to the minimum at $c/a = 1$ except for the B32 structure where the offset at $c/a = 1$ is the energy difference to the B2 structure.

higher Co content the γ-phase is stable for all temperatures until the ϵ-phase becomes the ground state at low temperatures which also transforms to a γ-phase at higher temperatures.

The substitution of cobalt for iron increases the electron concentration, which should lead to the preference of the γ-phase as in the case of FeNi alloys. But, since cobalt strengthens the ferromagnetic interaction, the α-phase remains stable [124]. This indicates a certain connection of the structure of FeCo-alloys to their magnetic properties.

In a broad area around the equiatomic composition the ordered B2-phase or B2-type of phase [1] marks the ground state. At higher temperatures an order-disorder transition takes place which results in a random occupation of the lattice. The associated transition temperature decreases very fast with increasing distance from the equiatomic composition.

The critical temperature of the ferromagnetic-paramagnetic (FM-PM) phase transition is experimentally only accessible in a small range at small Co concentration, because for small Co concentrations the FM-PM transition takes place before the α-phase transforms to the γ-phase. For higher Co concentration the exact determination of the critical temperature is hindered by this α-γ-transition.

At high Cobalt concentration where the α-γ-transition vanishes and the γ-phase is the only stable phase over a wide temperatures range, it is again possible to determine the critical temperature experimentally. The dashed lines in Fig. 5.1 which are associated with $T_C(\alpha)$ and $T_C(\gamma)$ are the extrapolated values for critical temperatures for regions where the corresponding phases are not stable [124].

[1] B2-type means that also compositions that differ from the equiatomic composition exhibit an order comparable to the B2 structure.

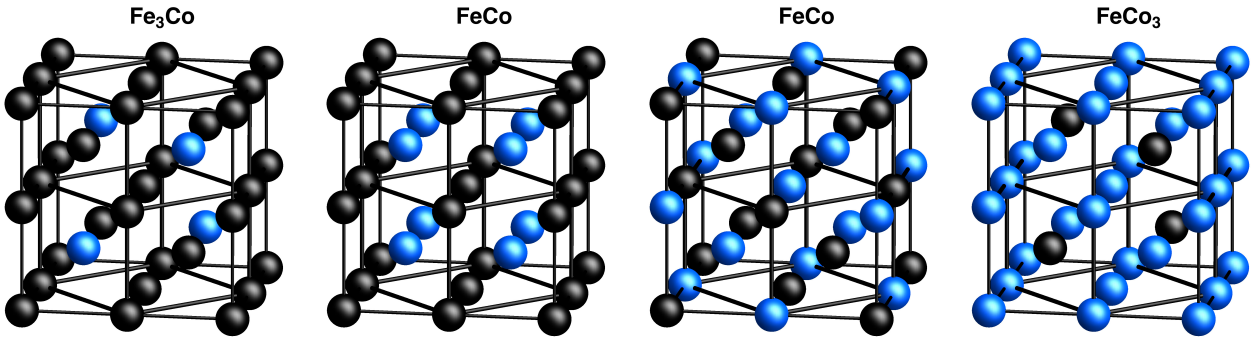

Figure 5.2: Ordered α-phase structures of the iron-cobalt alloys as they are employed in the calculations. Black balls represent Fe atoms and blue balls Co atoms. At the equiatomic composition FeCo, two ordering possibilities are considered: The layerwise B2 structure (b) and the B32 structure (c). For the other two compositions only the $D0_3$ structure (a) and (d) is considered.

As already mentioned, iron-cobalt alloys show extraordinary thermal expansion coefficients. This behavior is connected to spontaneous volume magnetostriction in the α-phase and to magneto-volume instabilities in the γ-phase [124]. In the γ-phase at the iron rich side of the phase diagram the anti-Invar effect causes abnormally high thermal expansion coefficients and at the cobalt rich side they are abnormally small because of the Invar effect (for details see Ref. [153] and references therein). Since the γ-phase is the high temperature phase, methods are needed to stabilize the fcc structure at low temperatures to study its ground state properties. This is achieved by precipitating the iron-cobalt alloy in a copper matrix [154] as mentioned in the discussion of γ-iron in Subsection 4.2.1.

Since the bcc structure is the ground state structure over almost the complete range of composition the investigation presented here starts with VASP calculations of ordered α-Fe_3Co, FeCo and $FeCo_3$. Comparison of the results gives already a first interesting theoretical insight.

The experimental phase diagram (see Fig. 5.1) shows that it is reasonable to consider ordered structures for all three compositions because Fe_3Co, FeCo and $FeCo_3$ lie in the range where B2 structures are preferred. In addition, experimental investigations show that Fe_3Co and $FeCo_3$ crystalize in B2 like $D0_3$ structure [155] and that FeCo shows a preference of the ordered B2-CsCl structure [156, 157]. At the equiatomic composition also the B32 type of order is considered because it is accessible within the same type of unit cell and as seen later this structure helps to gain insight into the α-γ-transition at the equiatomic composition. The structures mentioned here are shown in Fig. 5.2. Like the Heusler structure they all can be understood as a fcc type of structure with a four atom base including the positions (0,0,0), (0.25,0.25,0.25), (0.5,0.5,0.5) and (0.75,0.75,0.75). This is not necessary for the CsCl structure because it can be represented by a unit cell with only two atoms.

It has to be mentioned that the experimental evidence of $D0_3$ structures as well as the B2 has to be taken with care because modern experimental investigations reveal a possible occurrence of superstructures in iron-cobalt alloys. This is theoretically reinforced by cluster expansion calculations which reveal a dense sequence of ground state structures. This can result in an ordered coexistence of different structures which can be interpreted as a superstructure

(for theoretical and experimental details see Ref. [158] and Ref. [14] and references therein). As different structures are also considered in the present investigation and as the energetic relation between them is compared, it turns out that even the investigation of small unit cells sometimes reveals almost degenerated ground states (see further below for details).

The total energy of the considered α-phase systems with varying c/a-ratio is plotted in Fig. 5.1. The Fe_3Co system shows two distinct minima at $c/a = 1$ corresponding to a cubic bcc structure and to a tetragonal fcc structure at $c/a = 1.6$. The energy difference between the two minima is far to high to give a reasonable estimate for the α-γ-transition temperature.

The c/a-curve for the B2-FeCo system shows only one distinct minimum at $c/a = 1$ and an indication for another minimum at about $c/a = 1.4$. In contrast to that, the B32-FeCo structure shows two minima. Besides the minimum at $c/a = 1$, there is a very flat minimum close to $c/a = 1.5$. The offset between the two curves of FeCo corresponds to the energy difference between the B2 and the B32 structure. Together, both curves reveal a nice agreement with the phase diagram because the B2 structure is the ground state structure of FeCo and the structural transition to the γ-phase takes place in the disordered phase. Roughly speaking, the B32 structure is more similar to a disordered structure compared to the layerwise ordered B2 structure because the nearest neighbor environment in both structures is different. In the B2 structure the nearest neighbor shell of every Fe atom contains always eight Co atoms and the same vice versa for the Co atoms. In the B32 structure every atom is surrounded by two atoms of both species. This situation is more comparable to disorder because in a disordered system this is the average situation of a next nearest neighbor shell.

It is concluded that the calculations reproduce the experimental result that the B2 α-phase is the ground state at equiatomic composition, that there is a transition to a more homogeneous structure at higher temperatures and that this more homogeneous structure can transform from bcc to fcc which is not possible in the B2 structure (assuming that the Bain path is the correct transformation path).

In the case of $FeCo_3$ two minima are found at $c/a = 1.0$ and $c/a = 1.42$. In contrast to Fe_3Co the lower lying minimum is the one at $c/a > 1$. Therefore, the calculation reveals the expected trend for fcc structures at higher Co concentrations but, unfortunately, the calculation gives a preference for fcc at $x = 0.75$ where experiment reveals a bcc structure at low temperatures. But as a concentration of $x = 0.75$ is close to the concentration $x = 0.8$ at which bcc and fcc structures can coexist, the calculation is still in good agreement with the experimental results.

The calculations of ordered stoichometric structures reproduce the trend that bcc structures are preferred for Fe rich system, whereas the Co rich systems tend to prefer fcc structures. Table 5.1 summarizes the lattice constants and critical temperatures. Unfortunately no experimental lattice constant of FeCo can be found. In addition, Table 5.2 gives a detailed comparison of calculated and experimentally measured magnetic moments. The theoretical predictions of the moments correspond to the state at the minimum of the c/a-curve of each system. The average magnetic moment per atom is compared to those obtained from neutron diffraction measurements [159] and their g factor corrections [160]. Obviously, the agreement with experiment is excellent. The trend of the single iron and cobalt moments mentioned in Ref. [153] is reproduced correctly. The authors of Ref. [153] state that the Co moment remains almost unchanged with varying concentration and the Fe moment increases. Here, an increase of the Fe moments comparing Fe_3Co and FeCo is found but it is followed by a decreased moment in $FeCo_3$. In addition, the individual magnetic moments are also in good quantitative agreement with previous theoretical studies [160].

Composition	Structure	a (Å)	a_{exp} (Å)	c/a	T_{C}(K)
Fe_3Co	$D0_3$	5.70	5.73	1	1260
FeCo	B2	5.69	-	1	1540
FeCo	B32	5.68	-	1	1400
$FeCo_3$	$D0_3$	5.65	5.68	1.42	1060

Table 5.1: Lattice parameters of ordered iron-cobalt alloys obtained from VASP (GGA) calculations. In addition, the critical temperatures obtained from MC simulations are summarized. Experimental lattice constants of FeCo are not reported in literature. The theoretical data corresponds to the state at the lowest minimum of the c/a variation shown in Fig. 5.1. This is a bcc type of state for Fe_3Co, the B2 bcc state for FeCo and an fcc type of state for $FeCo_3$.

Although the samples in the experiments of Ref. [161] are chemically disordered, the calculated lattice constants are in good agreement. Roughly speaking, the composition has almost no effect on the lattice constant. This is expected because Fe and Co atoms are of comparable size.

The critical temperatures of Fe_3Co and FeCo follow the trend of the extrapolated values of the α-phase shown in the experimental phase diagram (see Fig. 5.1). The critical temperature of $FeCo_3$ which is evaluated for the minimum at $c/a = 1.42$, corresponding to a fcc structure, is also in good quantitative agreement with the extrapolation of the critical temperature for the γ-phase.

In the following a more detailed discussion of the electronic and magnetic properties of the α- and γ-phase is presented and also a comparison of ordered and disordered structures is given.

5.2 Fe_3Co

As already discussed in the introduction above, the low temperature α-phase of Fe_3Co can be considered as an ordered $D0_3$ structure. This structure is shown in Fig. 5.2(a). In Fig. 5.3 the electronic density of states (DOS) corresponding to the two minima in the c/a-curve are shown. The DOS at $c/a = 1$ is comparable to that of pure α-iron, but there are certain differences. Because the core potential of Co is steeper compared to Fe, the density is shifted to lower energies. This results in a small majority density at the Fermi energy and therefore in a higher magnetic moment of Fe because the majority states on the shoulder on the right side of the first peak which are only partially occupied in the case of pure Fe, are now completely occupied. This indicates the transition from weak ferromagnetism in Fe, where the majority d-bands are not completely pushed below the Fermi energy, to strong ferromagnetism where the d-bands lie below E_{F}. There is also a small peak in the minority density at the Fermi energy and the structure of the anti-bonding states above E_{F} is more complex because Fe and Co associated states are located at different energies. These results are in excellent agreement with TB-LMTO calculations presented in Ref. [155]. More details concerning the structure of the density of states are described in Ref. [156] and references therein.

The DOS corresponding to the minimum at $c/a = 1.6$ is of course completely different from

Composition	$\mu_{\mathrm{Fe}}\,(\mu_{\mathrm{B}})$	$\mu_{\mathrm{Co}}\,(\mu_{\mathrm{B}})$	$\langle\mu\rangle\,(\mu_{\mathrm{B}})$	$\langle\mu\rangle_{\mathrm{exp}}\,(\mu_{\mathrm{B}})$	$\langle\mu\rangle_{\mathrm{corr}}\,(\mu_{\mathrm{B}})$
Fe_3Co	2.64 (2.61) 2.39 (2.45)	1.73 (1.74)	2.25	2.45	2.33
FeCo	2.80 (2.76)	1.75 (1.75)	2.28	2.35	2.25
$FeCo_3$	2.68 (2.67)	1.76 (1.75) 1.76 (1.74)	2.07	2.15	1.95

Table 5.2: Comparison of the magnetic moments of ordered structures of $Fe_{1-x}Co_x$. The moments without brackets are taken from VASP calculations where the GGA formulation of Perdew, Burke and Ernzerhof (PBE) [91] is used and those in brackets are taken from SPR-KKR results using LDA in the formulation of Vosko, Wilk and Nusair (VWN) [162]. In addition the average magnetic moment per unit cell calculated with VASP is compared to neutron diffraction experiment (see Ref. [159]) and to those corrected by the corresponding g factors (see Ref. [160]). Please note that in this comparison all calculated values correspond to the bcc structures at $c/a = 1$, even in the case of $FeCo_3$ because the experimental data is obtained from the α-phase.

the one at $c/a = 1$ because it represents the density of states of a tetragonal distorted fcc structure. The majority and the minority densities below the Fermi energy are more similar to each other compared with $c/a = 1$. But the majority density of states is still almost flat and the minority density very structured above E_{f}. The states are more smoothly distributed over the energy range compared to the bcc case where there are many narrow peaks. Please note, that the state at $c/a = 1.6$ is a high-spin state. This means that it shows a high spin polarization compared to other magnetic states which are metastable in the γ-phase of Fe_3Co. A detailed discussion of the different magnetic states occurring in γ-Fe_3Co is discussed below but first the magnetic exchange parameters for different types of order of the α-phase are investigated.

In Fig. 5.4 the magnetic exchange parameters of cubic α-Fe_3Co are shown. The use of Lichtenstein's formula and the MC simulations of the Heisenberg model for the analysis of finite temperature magnetism is particularly justified in the case of iron-cobalt alloys because this method assumes the magnetic moments to be localized and the localized nature of Fe and Co moments in FeCo-alloys is proven by the analysis of the spin density $\rho^{\uparrow}(\boldsymbol{r}) - \rho^{\downarrow}(\boldsymbol{r})$ in Ref. [160]. The authors show that there are only significant contributions to the spin density in a small range around the locations of the atoms. This does not imply iron-cobalt alloys cannot show any signatures of itinerant magnetism.

Figure 5.4(a) shows the exchange interactions in the ordered $D0_3$ phase. Figure (b) and (c) display the interactions for two different types of disorder. In (b) the disordered B2 structure is shown where the sublattices corresponding to (0.25,0.25,0.25) and (0.75,0.75,0.75) are now randomly occupied by iron or cobalt. In the A2 disordered structure all sublattices are occupied randomly. However, the stoichiometry is conserved in all three cases and the disorder is introduced by employing the single-site CPA method. A visualization of the disordered structures is shown in Fig. 5.5.

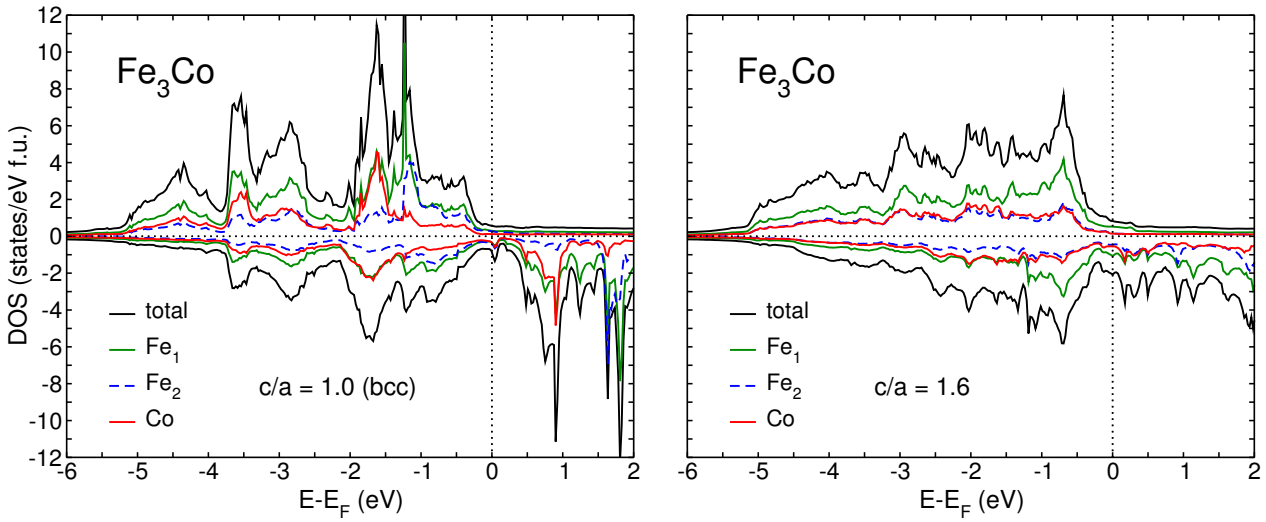

Figure 5.3: Comparison of the electronic densities of states of $D0_3$ ordered Fe_3Co for the two minima in the c/a-curve (see Fig. 5.1). The densities are calculated with VASP using the PBE-GGA exchange-correlation functional.

The exchange interaction between the nearest neighbor pairs Co-Fe_2 and Fe_1-Fe_1 in the $D0_3$ structure mark the strongest contributions (the indices of the atoms correspond to the distinction between atoms with different magnetic moments, see Table 5.2). As cobalt atoms are never nearest neighbors, the Co-Co exchange does not contribute to the interactions between the first two neighboring shells. As the first Co-Co interaction within the third shell is almost zero, it shows that the Co-Co exchange interaction is of short range and gives only strong contributions at small distances. The change in the local environment introduced by structural disorder leads to significant changes of the magnetic exchange parameters. Although there are now next nearest neighbor Co-Co pairs there is still no considerable Co-Co contribution in the B2 structure. The nearest neighbor Co-Fe_1 and Fe_1-Fe_2 contributions remain comparable to those in the ordered $D0_3$ structure, but the next nearest neighbor contributions of Fe-Fe pairs is enhanced. In the A2 structure all three different nearest neighbor pairs exist and they all give a considerable contribution. But this does not increase the critical temperature because the occurrence of Co-Co nearest neighbors in a particular realization of A2 disordered Fe_3Co is of low probability because the cobalt is diluted by iron. Therefore, the occurrence of strong nearest neighbor Co-Co coupling is of low probability and thus this contribution is of lower relevance. The dominant interactions are still the Fe-Fe because of their strength an the high number of pairs. In addition, the Co-Fe pairs are also relevant because of the strength of the interaction and the high number of pairs because on the average cobalt is almost completely surrounded by iron atoms. The two former inequivalent types of Fe atoms are now equivalent because on the average their environment is now the same (this is an implicit assumption of the CPA).

The disordered local moment (DLM) model is often considered to be a better reference state for the determination of the critical temperature because it models the paramagnetic phase and therefore it gives exchange parameters which correspond to temperatures above and close to the critical temperature [97]. Therefore, DLM calculations are carried out for the α-phase with $D0_3$ structure. The magnetic moments obtained for the different types of structural

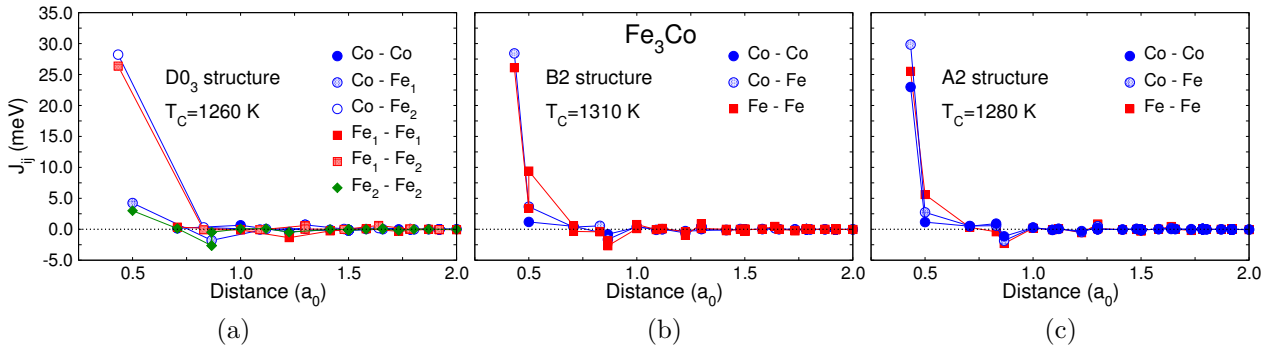

Figure 5.4: Magnetic exchange parameters J_{ij} of α-Fe_3Co. Figure (a) corresponds to the ordered $D0_3$ structure, (b) corresponds to the B2 type of disorder and (c) to complete A2 disorder. The disorder is introduced by employing the single-site CPA method. For each structure the critical temperature obtained from MC simulations is shown.

order of the α-phase as well as those obtained from the DLM calculation are summarized in Table 5.3. The DLM calculation provides quenched cobalt moments of $0.34\,\mu_B$. The iron atoms which have no nearest neighbor Co atoms also show a reduced moment of $1.94\,\mu_B$ and the other reveal an almost unaffected value of $2.53\,\mu_B$. The small Co moment results in a reduced interaction between the Co and Fe atoms and therefore reduces the critical temperature to 900 K. The estimated critical temperature obtained by using the DLM state as a reference is obviously worse compared to the estimate obtained by using the ferromagnetic state. The reason for this are the very small Co moments. The small moments lead to smaller exchange interactions and therefore to smaller critical temperatures. It is carefully concluded that the Co moments is sensitive to the magnetic order of the system under consideration and in particular of its local environment. In a DLM calculation the moment of Co is strongly decreased because its environment represents a magnetically disordered effective medium. Therefore, it may also be tentatively concluded that the Co moments exhibit longitudinal fluctuations of the magnetic moments at high temperatures. This means that not only the direction of the moments fluctuates but also the length. The conclusions are confirmed in subsequent sections where small Co moments are found in metastable antiferromagnetic states of the γ-phase of Fe_3Co and also during the investigation of cobalt-manganese alloys in Chapter 6.

The occurrence of longitudinal fluctuations of the magnetic moment is unfortunately in

	$\mu_{DO_3}\,(\mu_B)$	$\mu_{B2}\,(\mu_B)$	$\mu_{A2}\,(\mu_B)$	$\mu_{DLM}\,(\mu_B)$
Fe	2.61	2.60	2.51	2.53
	2.45	2.40		1.94
Co	1.74	1.76	1.81	0.34

Table 5.3: Comparison of the magnetic moments of α-Fe_3Co for the different ordered and disordered structures including results from disordered local moments (DLM) calculations of the ordered structure. The Results are obtained from SPR-KKR calculations using LDA. It turns out that disorder affects the individual moments only weakly. On the other hand the DLM calculation leads to unrealistically small Co moments.

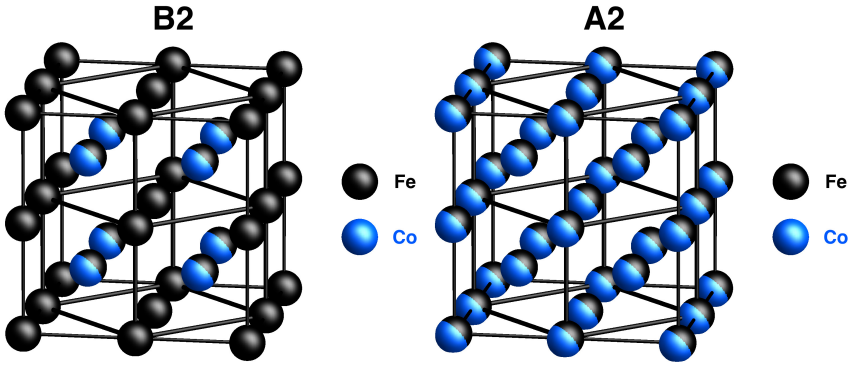

(a) (b)

Figure 5.5: In this figure the structure of the two types of disorder of the α-phase under investigation are shown. In the B2 type disordered structure only one sublattice is randomly occupied and in the A2 type the entire lattice is randomly occupied.

contradiction to the good agreement of the Curie temperature obtained from the MC simulations with the experimental estimation. In the case of strong longitudinal fluctuations the MC simulations should give a bad result because it only takes transverse fluctuations of the magnetic moments into account. This contradiction between good MC results and the strong dependence of the magnetic moment of Co on the local environment cannot be easily resolved. One would have to check the contributions from band magnetism since iron-cobalt alloys seem to be typical band magnets, which are not discussed here (see, e.g. Ref. [163] and references therein).

In the following the γ-phase of Fe_3Co is investigated. Here, special attention is paid to the different magnetic states which can give rise to magneto-volume instabilities.

The structure of the ordered fcc-system is chosen to be $L1_2$ because it can be investigated within a small unit cell and is different from the tetragonal distorted $D0_3$ structure. Therefore, it provides the possibility to investigate another form of order and its properties. On the other hand this structure has already been employed to model binary alloys with the specific composition considered here (see Chapter 4).

In Fig. 5.6, the total energy of four different magnetic states found in VASP calculations is plotted as a function of the lattice constant. The most stable state with lowest total energy, is ferromagnetic and shows a high magnetic moment of $9.25\mu_B$ per formula unit. To adopt the usual terminology used, e.g., for γ-Fe, this state is called the high-spin (HS) state. Besides this state, three different metastable states (states with higher energy than the high-spin state) exist: an antiferromagnetic state, a ferromagnetic state with smaller magnetic moment, called low-spin (LS) state, and a non-magnetic state showing no finite magnetic moments. All these states exhibit higher energies as well as smaller volume.

The energetic order of the states described in the last paragraph suggests an Invar behavior of the thermal expansion because with increasing temperature the antiferromagnetic or the low-spin state with lower volume can be excited which can compensate the regular thermal expansion. Unfortunately, anti-Invar behavior is found in experiments close to this composition [153]. Therefore, one may conclude that there might be a complex AF state with smaller volume and energy than the HS ferromagnetic state. In this case thermal excitation could lead to a transition from the postulated antiferromagnetic state to the high-spin state and therefore to a support of the thermal expansion. This postulated state could not be found

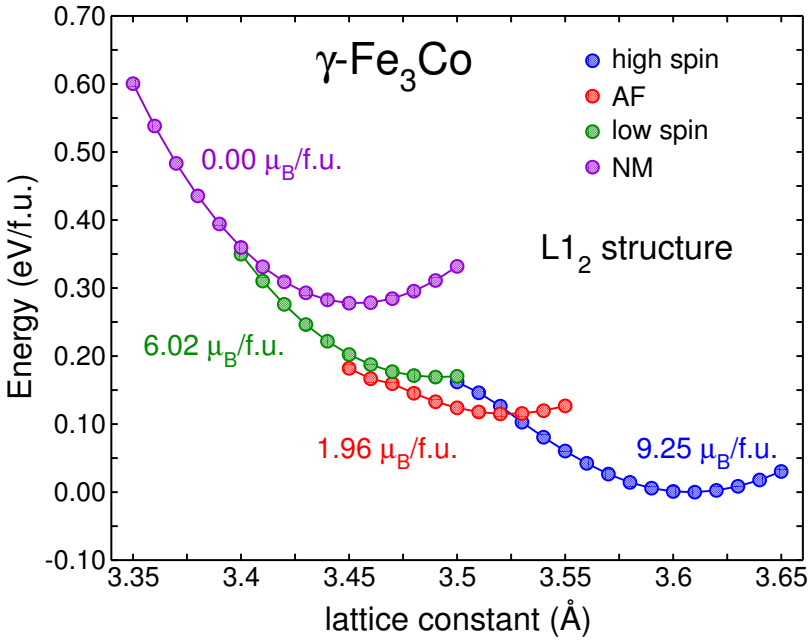

Figure 5.6: Energy dependence of the different magnetic states of γ-Fe_3Co as a function of the lattice constant. The magnetic moments correspond to the total moment per formula unit at the minimum of the particular curve.

in the calculations. This might be connected to the small unit cell which are used. The situation is comparable to the investigation of γ-Fe in Section 4.2.1 where the small unit cell leads to an unsatisfactory description of the ground state. This conclusion is confirmed by MC simulations where the high-spin state and the antiferromagnetic state are taken as a reference (the low-spin state cannot be stabilized in the KKR calculations). Comparable to observations in iron-manganese alloys, the ground state found in MC simulations differs from the state that serves as reference. For both reference states (HS and AF) the MC simulation reveals a complex spin spiral type of ground state. When the high-spin state is taken as the reference, the angle of the spins is tilted in every subsequent layer. If the antiferromagnetic state is chosen the angle is tilted only every second layer. Therefore the wave length of the spiral is twice as large when using the antiferromagnetic state. It is noted that the particular form of the spin spiral state can depend on the size of the simulation cell employed in the MC investigation and is therefore not necessarily a unique feature. In summary: it is very likely that the real groundstate of γ-Fe_3Co is complex antiferromagnetic.

In Fig. 5.7, the magnetic exchange parameters of the high-spin and the antiferromagnetic state are shown. It is a peculiarity that the exchange interactions of the high-spin state lead to a spin spiral type of state in the MC simulations because all nearest neighbor interactions are ferromagnetic. There are some antiferromagnetic interactions in the subsequent neighboring shells but these are more than an order of magnitude weaker compared to the ferromagnetic ones. But one has to keep in mind that with every subsequent neighboring shell the number of atoms contributing in this shell increases significantly and therefore the interactions of all atoms in the shell sum up. This results in a considerable interaction onto the atom which is considered to be in the center of the shells. Considering the exchange interactions in the antiferromagnetic state it is more obvious that a complex magnetic ground state is obtained from the MC simulations because there are ferromagnetic as well as antifer-

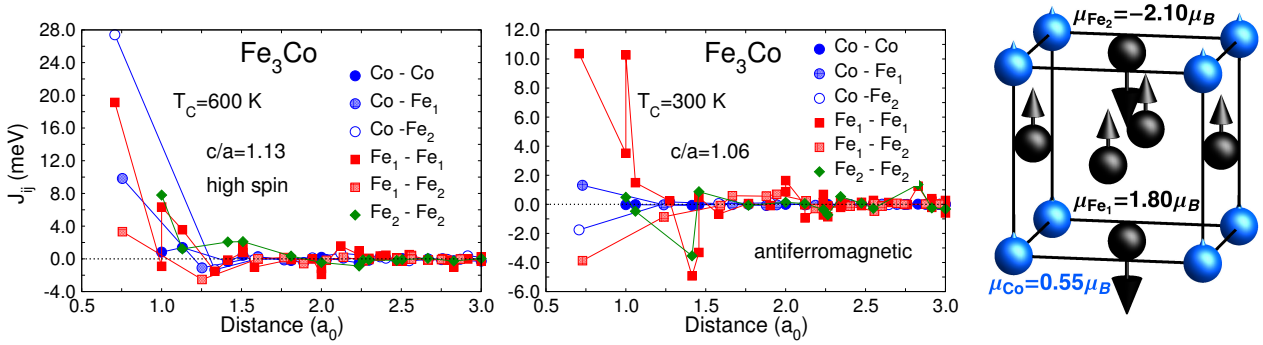

Figure 5.7: Magnetic exchange parameters of the γ-Fe_3Co alloy. Picture (a) shows the exchange interactions of the high-spin state and (b) those of the antiferromagnetic state. The alignment of the moments of the antiferromagnetic state is shown in picture (c).

romagnetic interactions between the nearest neighbors. There are only strong ferromagnetic interactions between the Fe_1-atoms and the strongest antiferromagnetic interactions occur between the Fe_1- and Fe_2-atoms. All other interactions are much weaker. As the interactions in the high spin state are much larger compared to those found in the antiferromagnetic state, the critical temperature is by a factor of two larger.

It should be noted that the magnetic moments of the Co atoms are very small in the antiferromagnetic state (see Fig. 5.7(c)). This is an obvious effect arising from the frustration that the Co atom are subjected to. The Co moments are of comparable size as those found in the DLM calculations because the Co atoms are surrounded by eight Fe atoms with a positive and four Fe atoms with a negative moment. Therefore, the Co atoms are not placed in a simple ferromagnetic environment. This shows again that Co atoms can only develop a large magnetic moment within a ferromagnetic environment and they develop a small moment in an antiferromagnetic environment as, e.g., in the situation discussed here.

Experiments concerning the anti-Invar behavior of $Fe_{1-x}Co_x$ reported in Ref. [153] are carried out for free samples at elevated temperatures beyond the α-γ-transition and samples which show a γ-phase at low temperatures due to the encapsulation within an fcc structured shell. Therefore, it is unclear if the magnetic states found in the calculations play the important role for the understanding of the abnormal expansion, because their energy differences is small compared to the temperature at which the experiments are performed. In addition, the critical temperature of the FM-PM transition is not exactly detected in the experiment and it is therefore not possible to exclude that the anti-Invar behavior is associated with particular magnetic excitations in the PM-phase.

Figure 5.8(a) shows c/a- variations of the high- and low-spin states together with the antiferromagnetic state. It shows that the LS state is sensitive to tetragonal distortions because the magnetization of this state approaches the magnetization of the high-spin state very fast if it is distorted. The remaining energy difference can be explained by considering the volume difference between the HS and LS state which is conserved in the variation of the c/a-ratio. Therefore, it is concluded that the energy surface spanned by the lattice constant and the c/a-ratio is very complex because depending on the volume and the c/a-ratio, the magnetic state changes quickly. The minima on the $c/a < 1$ side of the high-spin and low-spin curve correspond again to the same state, because a volume relaxation of the low-spin state leads

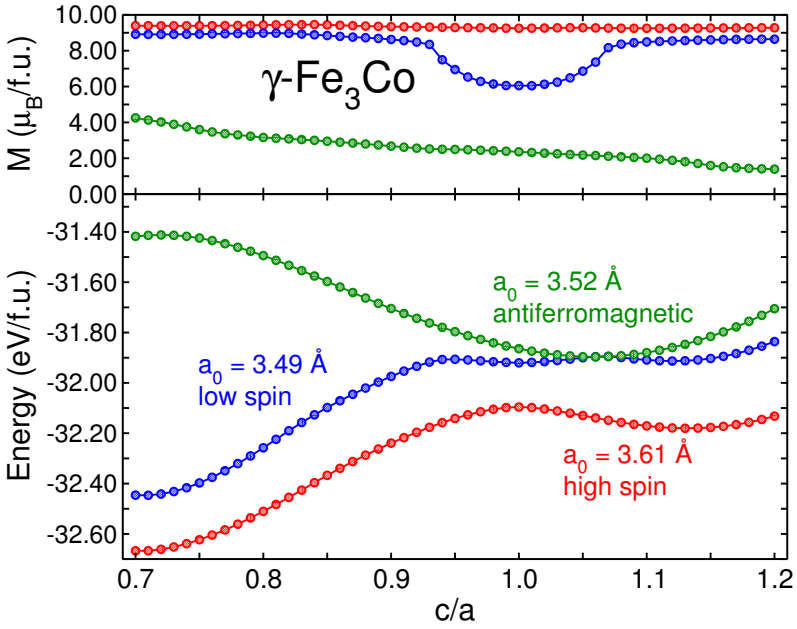

Figure 5.8: Results of the c/a-variation of three different magnetic states of γ-Fe_3Co. The non-magnetic state is skipped.

directly to the high-spin state. The same holds for the minimum of the low-spin curve at $c/a > 1$. In summary: A transition from the LS to the HS state is automatically found by changing the c/a ratio. The interesting point is that tetragonal distortions in combination with volume relaxations can be related to almost continuous changes of the magnetic state. The main conclusion which can by drawn from this observations is that a particular magnetic state of a sample in the γ-phase obtained in an experiment will strongly depend on temperature, pressure and other details of preparation.

In Fig. 5.9(a) the variation of the total energy and the magnetic moment per formula unit along the bcc-hcp path is shown. This particular bcc-hcp path has been proposed in Ref. [164] to study the transformation of the α- to the γ-phase in iron. Besides the bcc associated minimum there is also a minimum which is associated with the hcp structure. The total magnetic moment of the cell changes continuously to smaller values when moving from the bcc to the hcp side of the path. This result implies that a hypothetical hcp phase is found in the theoretical calculations.

In Fig. 5.9(b) the c/a-variations of the $D0_3$ structure and the HS state of the $L1_2$ structure are shown. One has to note that $c/a = 1$ implies a bcc structure for the $D0_3$ curve and an fcc structure for the $L1_2$ curve. Obviously, the fcc and the bcc minimum of both structures is almost at the same energy. This implies that the $D0_3$ structure at c/a=1 and $L1_2$ structure at c/a=0.71 mark two almost degenerated states. This is in perfect agreement with Ref. [158] and Ref. [14] where formation enthalpy sequences of structural phases of $Fe_{1-x}Co_x$ are calculated and compared (see Section 5.1). The authors found almost degenerated states and therefore confirmed the experimental claims about the existence of superstructures (see Ref. [14] for references) which can be understood as a sort of superposition of different almost energetically degenerated structures.

It is particularly interesting that the energy difference between the fcc and bcc structures is an order of magnitude larger than the energy difference between the bcc and hcp structure.

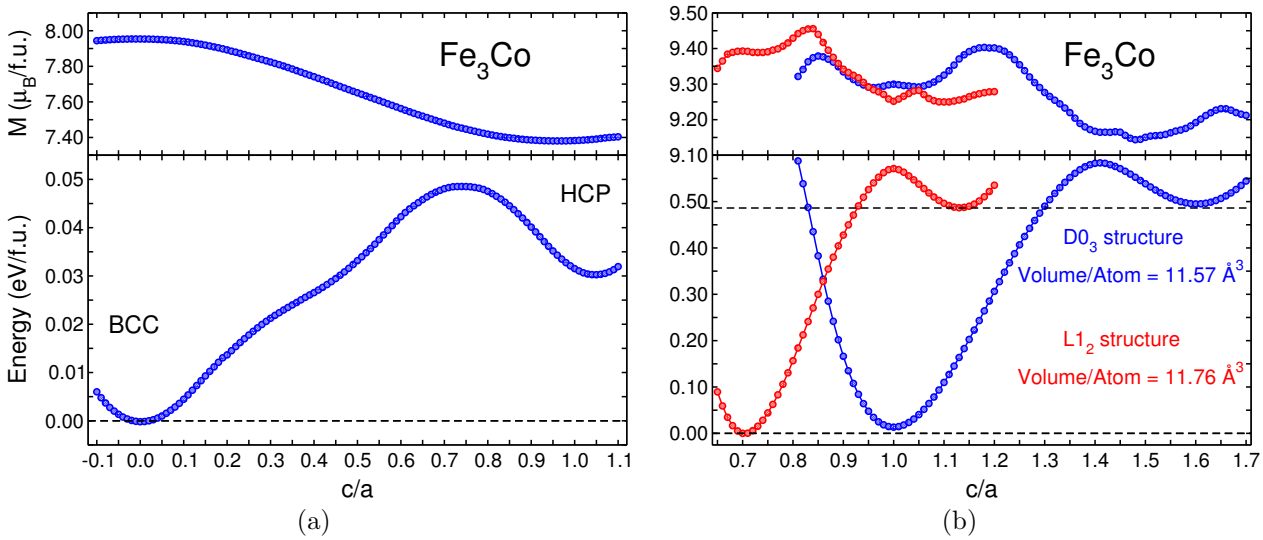

Figure 5.9: (a) Variation of the total energy α-Fe_3Co along the bcc-hcp path. (b) Variation of the total energy along the Bain path of the $D0_3$ and the HS state of the $L1_2$ structure.

As there is no hcp structure found in experiments for the Fe_3Co composition it is concluded that the hcp state predicted here is probably associated with a high pressure state. This conclusion is confirmed by the fact that iron shows a hcp structure called ϵ-phase at high pressures and because the Fe_3Co composition still shows characteristics of pure iron as found throughout the discussion.

5.3 FeCo

Figure 5.1 shows results for systems at the equiatomic composition FeCo. The total energy variation along a path of tetragonal distortion is presented for two different ordered structures namely B2 and B32 which are sketched in Fig. 5.2. In the following the properties of this composition are investigated in more detail.

In Fig. 5.10(a) the electronic DOS of B2 ordered FeCo is shown. Apart from small changes in the details of the structure of the DOS at the Fermi energy, it is simply shifted to higher values compared to the DOS of Fe_3Co. This is expected because the addition of cobalt resembles the addition of electrons. Therefore, more and more states are occupied when Co atoms are added. In addition, as mentioned above the core potential of Co is steeper and therefore induces a shift of the energies. It is interesting to note that the high peak in the majority channel at around -2eV correspond to a peak in the Fe as well as in the Co DOS. This is contrary to Fe_3Co where this peak is spilt into two peaks, one associated with Fe and the other with Co.

Figure 5.10(b) and (c) show the electronic density of states obtained for the B32 structure. Figure (b) corresponds to the minimum at $c/a = 1$ (see Fig. 5.1). An interesting difference compared to the density of states of the B2 structure occurs at the peaks of the majority channel at around $E - E_F = -2$ and in the minority channel around $E - E_F = 1$. In both regions the states are spitted into Fe dominated and Co dominated peaks comparable to the situation found in Fe_3Co. In the B32 structure the Fe states are shifted to lower energies and the Co states are shifted to higher energies. This can be understood by considering the

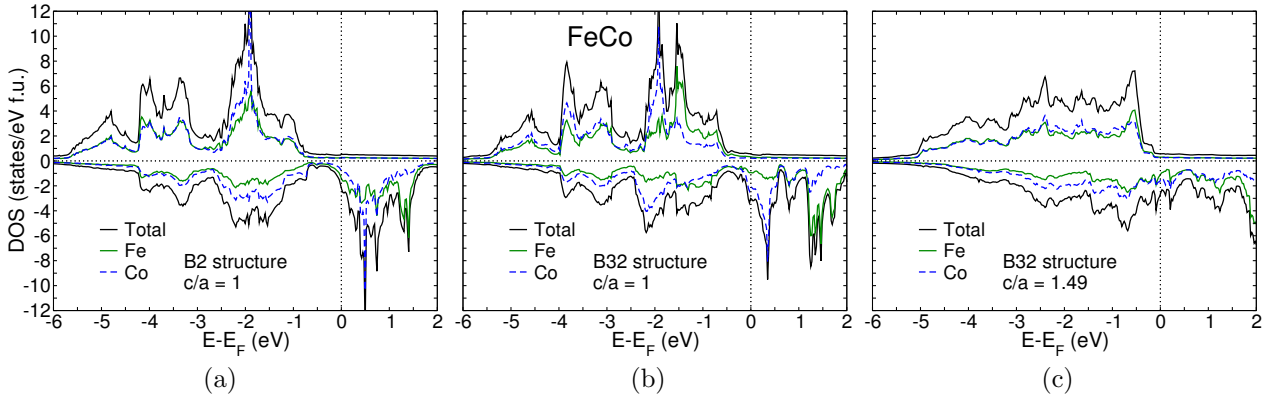

Figure 5.10: Comparison of the electronic densities of states of B2 and B32 ordered FeCo. In the case of B32 order the density of states corresponding to the two minima in the c/a curve (see Fig. 5.1) are shown. The densities are calculated with VASP using the PBE-GGA exchange-correlation functional.

nearest neighbor environment. In the B2 structure there are no Fe-Fe and Co-Co nearest neighbor pairs but these occur in the B32 structure. Therefore, in the B2 structures the overlap between states of Fe and between Co leads to more Fe and Co like states pervading the entire system and as the Co core is stronger attractive the Co like states are shifted to lower and the Fe like states are shifted to higher energies. Similar observations are discussed in Ref. [163] and [160]. The density of states for the tetragonal distorted system at $c/a = 1.49$ is relatively flat and the Fe and the Co states give almost the same contribution to the to the total number of states over the entire energy range. The most obvious feature is that the majority density is completely flat above E_F whereas the minority density is still structured.

In the next step the magnetic exchange interactions of FeCo are investigated. Therefore, the B2, B32 and the fully disordered A2 structure are considered. A discussion of B2 disorder is not needed for the equiatomic composition because any type of disorder is always A2 like. Figure 5.11(a) shows the magnetic exchange parameters of B2 ordered FeCo. The most significant difference compared to the exchange parameters of $D0_3$-Fe_3Co is that there are no nearest neighbor Fe-Fe pairs. Therefore, the high magnetic exchange contribution of these pairs vanishes. The only significant contribution that remains is the one corresponding to the Co-Fe pairs. Interestingly, the critical temperature is not decreased. Instead it is increased up to 1540 K which is about 280 K higher compared to the case of Fe_3Co. This is connected to the higher magnetic moments of the iron atoms and to the higher degree of symmetry in the ordered B2 structure. This means that in the B2 structure every Fe atom has eight Co neighbors and vice versa. Therefore, the Fe-Co interactions sum up to a large contribution.

In Fig. 5.11(b), the magnetic exchange parameters of FeCo with full A2 disorder are shown. As in the case of Fe_3Co there are all three strong nearest neighbor exchange interactions present between the three possible pairs. The nearest neighbor interactions of the three different pairs are of comparable size although the Co-Co interaction is more than 5 eV smaller than the Co-Fe and Fe-Fe interaction. The probability for the existence of a particular pair is much higher compared to the A2 situation in Fe_3Co. Thus, there are many of these strongly interacting neighbors which lead to a significant increase of the critical temperature in A2-FeCo. As expected, the iron moments are reduced in the disordered phase (see Ref. [124]). The difference between the critical temperature of ordered B2 and disordered

	$\mu_{\mathrm{B2}}\,(\mu_{\mathrm{B}})$	$\mu_{\mathrm{B32}}\,(\mu_{\mathrm{B}})$	$\mu_{\mathrm{A2}}\,(\mu_{\mathrm{B}})$	$\mu_{\mathrm{DLM,B2}}\,(\mu_{\mathrm{B}})$	$\mu_{\mathrm{DLM,B32}}\,(\mu_{\mathrm{B}})$
Fe	2.76	2.61	2.58	2.83	2.38
Co	1.76	1.77	1.80	0.00	1.10

Table 5.4: Comparison of the magnetic moments of α-FeCo for the different ordered and disordered structures including DLM calculations for the ordered structures B2 and B32. Most interestingly, the magnetic moment of Co vanishes completely in the DLM calculation of the B2 structures whereas it is finite in the calculation of the B32 structure. The results are obtained from SPR-KKR calculations using LDA of VWN.

A2 is less than 100 K and it is smaller in the disordered case. This is confusing because the exchange parameters are slightly enhanced in the disordered system and the argument which is mentioned above for the disordered Fe_3Co concerning the occurrence of particular pairs does not hold here because on the average an atom of a particular species has four nearest neighbors of the same species and four of the other species. Since all pairs are coupled with comparable strength, one could expect a higher critical temperature. But in the B2 order the nearest neighbor pairs are always of the other species. Therefore, every atom has eight nearest neighbor Co-Fe interactions. In the disordered case, as already mentioned, there are, again speaking in terms of averages, four atoms of both species in the nearest neighbor shell and the Co-Co and Fe-Fe couplings are smaller than the Co-Fe coupling. This leads to the decrease of the critical temperature.

Figure 5.11(c) shows the magnetic exchange parameters of the B32 ordered structure. After the discussion of the disordered A2 system the discussion of the B32 system is very simple. As can be easily seen, the exchange parameters are similar to those of the A2 system. Interestingly the interactions of Co and Fe pairs are almost exactly of the same size. Nearest neighbor pairs for all three combinations do exist but the next nearest neighbors are all of Co-Fe type. The neighborhood of an atom in the B32 structure is the average neighborhood that is expected for a completely disordered system and therefore all arguments brought up in the discussion of the A2 structure are still valid. This is the reason why the critical temperature is almost the same as in the A2 system. Small difference can occur due to the particular realization of the disorder within the finite MC simulation cell in the simulation of the A2 system.

Table 5.4 gives a summary of the individual magnetic moments found in the different calculations of α-FeCo. It shows that there is no big difference between the moments in ordered B2 and B32 structure and disordered A2. In all three cases the individual moments of the atoms are almost of the same size. This changes dramatically when using the DLM formalism. The DLM calculation of B2 ordered α-FeCo reveals zero magnetic moments of cobalt atoms. The iron atoms keep almost the same value of the moment as it is found in the calculation of the ferromagnetic state which is around $2.80\,\mu_{\mathrm{B}}$. No MC simulation is performed employing the exchange parameters of the DLM state because it would it would not bring new insight since there is no contribution of Co atoms due to vanishing moments. In order to perform a reasonable MC simulation there must be a finite contribution of Co but this is not included in the result of the DLM calculation. Obviously, the DLM gives a poor description of the FeCo alloy at least for the B2 structure. This situation is comparable to the results of the Fe_3Co DLM calculation.

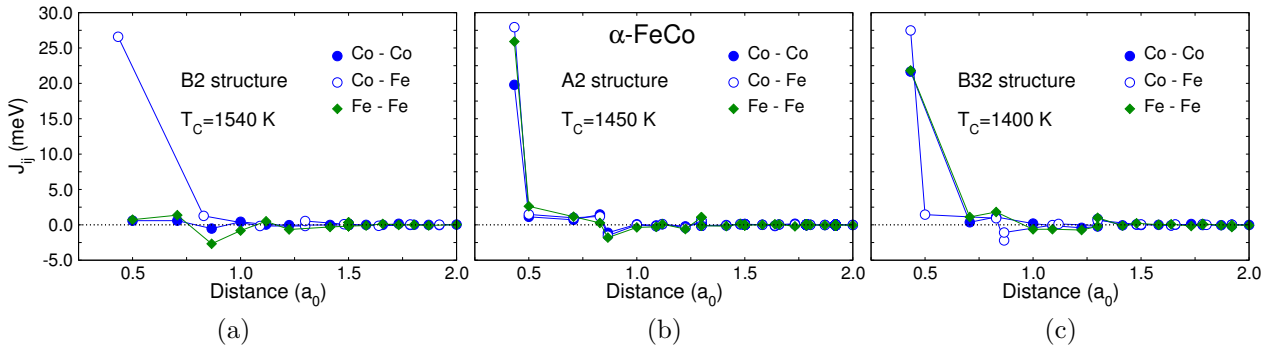

Figure 5.11: Magnetic exchange parameters of ordered and disordered FeCo. In (a) the interactions found in the B2 structure are shown. As expected the exchange parameters of A2 disorder, see (b), are very similar to those found in B23, see (c), because speaking in terms of averages, the chemical environment is the same in both configurations.

In addition, a DLM calculation is carried out for B32 ordered α-FeCo. Here, reasonable results for the magnetic moments are obtained (see Table 5.4). The Fe moment is smaller compared to the calculations of the ferromagnetic state but still realistic and the Co moment is $1.10\mu_B$ which is small but of course much more reasonable than the result of the DLM calculation of the B2 structure. The magnetic exchange parameters obtained from this DLM calculation are shown in Fig. 5.12(c). The interactions are qualitatively comparable to those obtained for the B32 structure with a ferromagnetic reference state. Quantitatively speaking, they are strongly reduced and therefore the critical temperature is also reduced to 920 K. Although the DLM calculation gives quite reasonable results in this case, it does not improve the determination of the critical temperature because the value of 920 K is far away from the extrapolated values obtained from experiment. Therefore, it is concluded that a determination of exchange parameters of FeCo based on a ferromagnetic reference state gives better results compared to the DLM calculation.

It is important to note how strong results of the DLM calculation depend on the underlying structure. The break down found for B2 order is comparable to the result of the DLM calculation for Fe_3Co and therefore supports the interpretation that the Co moment depends sensitively on the local environment. The result of the DLM calculation for the B32 system is in contrast to this interpretation. But this contradiction can be explained if one considers that there are Co-Co nearest neighbor pairs in the B32 structure which are absent in B2-FeCo and $D0_3$-Fe_3Co. It can be concluded that the occurrence of Co-Co nearest neighbor pairs stabilizes the Co moment even in cases where the local environment is not homogeneously ferromagnetic.

In order to investigate ordered γ-FeCo the $L1_0$ structure is employed. Four states are found, for which the energy variations over the volume is shown in Fig. 5.13. As in the case of Fe_3Co a ferromagnetic high-spin state shows the lowest total energy and therefore marks the ground state for the particular configuration chosen here. In contrast to Fe_3Co no antiferromagnetic state is found. Instead, there are two ferromagnetic states with smaller magnetic moment and smaller lattice constant and a non-magnetic state which is also higher in energy and smaller in volume. This can be interpreted as an effect of the increasing cobalt content which suppresses the antiferromagnetic tendencies introduced by iron in the fcc structure. In other words, Cobalt stabilizes ferromagnetic states in the γ-phase. This

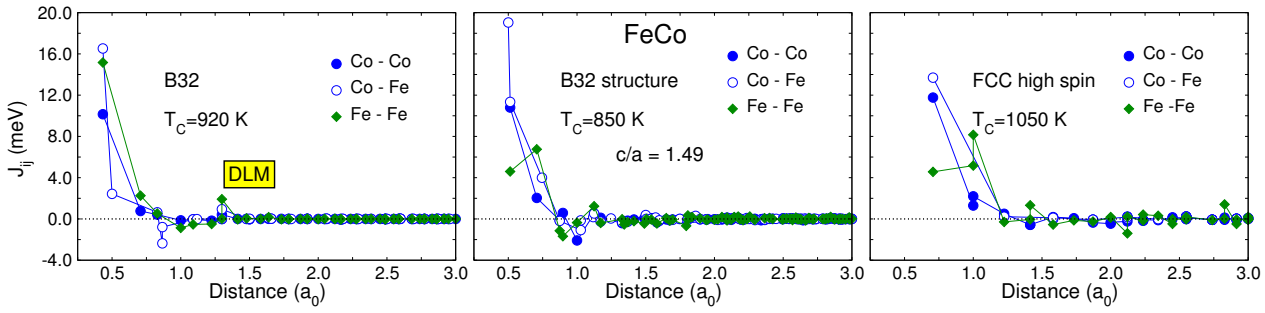

(a) (b) (c)

Figure 5.12: (a) Magnetic exchange parameters obtained from the DLM calculation of FeCo in the B32 structure. (b) Exchange parameters of the tetragonally distorted B32 structure at $c/a = 1.49$ based on a ferromagnetic reference state. In this case the MC simulations lead to a spin spiral type of magnetic state. (c) Magnetic exchange parameters of the high-spin state obtained for the $L1_0$ structure.

is experimentally confirmed by the phase diagram because the critical temperature line of the γ-phase at high cobalt content is increasing with increasing cobalt content. The order of the different magnetic states suggests again an Invar behavior of the thermal expansion coefficient because of a series of states with smaller moment and volume. But it needs to be noted that the energy differences between these states are too small to play an important role in temperature ranges where the γ-phase is stable.

The exchange interactions of γ-FeCo can only be analyzed for the high-spin state because the low-spin states cannot be stabilized within the KKR calculations. Almost all exchange parameters of the high-spin state, which are shown in Figure 5.12(c), are ferromagnetic. They are smaller compared to those of the B2 phase but as there are more nearest neighbors in fcc than in bcc structures, the critical temperature ($T_C = 1050\,K$) is still very high. The extrapolation of the critical temperature in the experimental phase diagram suggests a critical temperature of $T_C = 800\,K$. But since the extrapolation of the experimental results naturally introduces errors and as the theoretical calculation also contains assumptions, the resulting discrepancy is surprisingly small. Unfortunately, it cannot be excluded that some of the errors cancel out.

The calculation of the energy variation of the high-spin state for different c/a-ratios of $L1_0$-FeCo shows that this state is not stable against tetragonal distortions, see Figure 5.13(b). It has only a minimum for bcc like c/a-ratios. The total magnetic moment also approaches the total magnetic moment of the bcc structure. This explains the experimental result that for low temperatures FeCo solidifies in a bcc structure.

These results can be compared to the discussion of the B2 and the B32 structure of α-FeCo because the $L1_0$ structure is connected with the B2 structure by a tetragonal distortion and the B32 structure is connected with the so called $L1_1$ structure (which is also a fcc type of structure) by the same transformation. This means that the c/a-variation of the $L1_0$ structure is associated with the results shown in Fig. 5.1(b) where the c/a-variation of the B2 structure is shown. The results in Fig. 5.1(b) start from bcc and those shown in Fig. 5.13(b) start from fcc. The discussion of the $L1_1$ is skipped because no additional insight can be gained from this. Instead the exchange interactions of the $c/a = 1.49$ case of the B32 structure are discussed in the following.

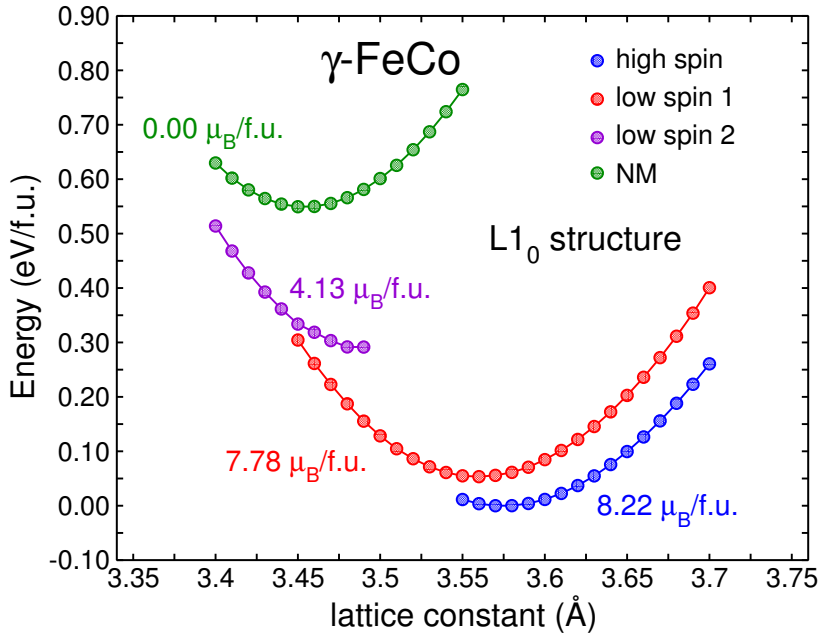

Figure 5.13: Energy dependence of the different magnetic states of $L1_0$ ordered γ-FeCo as a function of the lattice constant.

In Fig. 5.12 the magnetic exchange parameters of the tetragonal distorted B32 structure are shown. The c/a-value of 1.49 implies that this structure corresponds to a $L1_1$ structure with a small tetragonal distortion. In this structure the exchange interaction between the Co-Fe nearest neighbor pairs gives a strong ferromagnetic contribution. The next nearest neighbor Co-Co and Fe-Fe pairs, which are almost the same distance apart from each other, compared to the Co-Fe pairs, give contributions which are at least by a factor of two smaller. The subsequent pairs in the shell at a distance of around one lattice constant give small antiferromagnetic contributions. The antiferromagnetic contributions lead to magnetic frustration of the moments and therefore the critical temperature is decreased compared to the critical temperature of the $L1_0$ structure. The magnetic ground state which is obtain in the MC simulations is a spin spiral state. The moments are tilted by a constant angle from layer to layer when moving along the direction of the tetragonal distortion. Again, the specific form of the spin spiral can depend on details of the simulation but it shows that there is a tendency for complex antiferromagnetic states. Therefore, it is concluded that the smaller Fe content in FeCo reduces the tendency for such states because no simple antiferromagnetic state can be found in the *ab initio* calculations but this tendency does not vanish completely at the FeCo composition because the MC simulation still reveals complex antiferromagnetic ground states.

In Fig. 5.14 the variation of the total energy along the bcc-hcp path [164] is shown where the starting point on the bcc side is the B2 structure. Obviously, the curve has no minimum at the hcp side but only a weak dent. Therefore, it is concluded that at the equiatomic position the occurrence of hcp structure can be excluded even in the case of high pressure. Although, pure iron can develop a hcp ϵ-phase at high pressure and the ground state of pure cobalt is also the ϵ-phase, both trends seem to cancel out for FeCo.

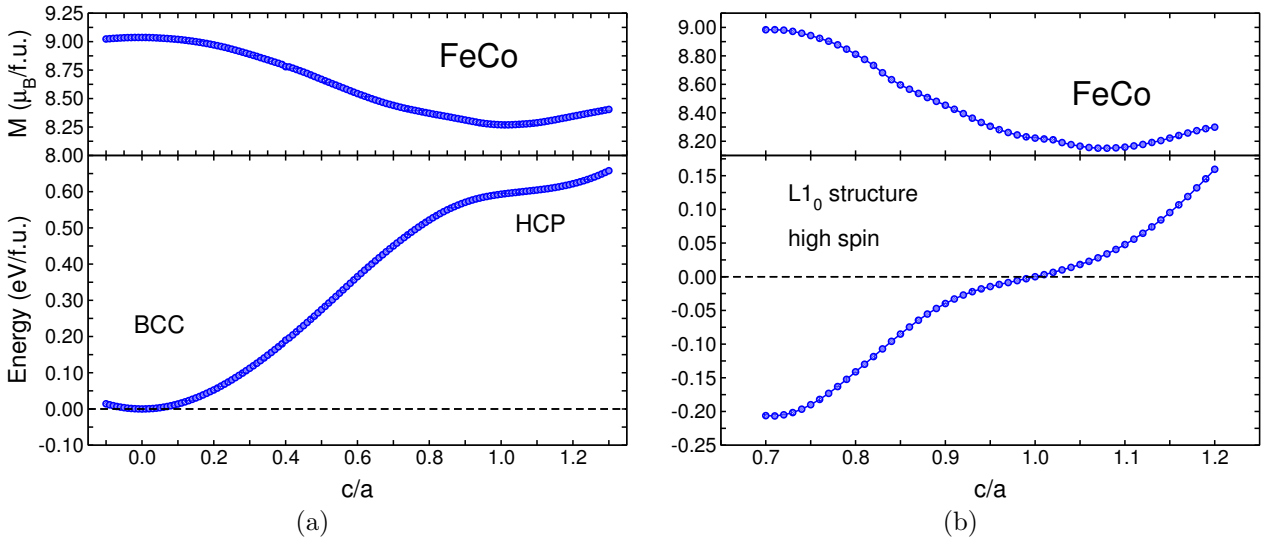

Figure 5.14: (a) Variation of the total energy and the total magnetic moment of FeCo along the bcc-hcp path. The bcc region is associated with the B2 order. (b) Variation of the total energy of the $L1_0$ structure along the Bain path.

5.4 $FeCo_3$

To finish the investigation of iron-cobalt alloys the composition $FeCo_3$ is discussed. In Fig. 5.15 the electronic density of states of $D0_3$ ordered $FeCo_3$ is shown for two different c/a-ratios. These ratios are $c/a = 1$ and $c/a = 1.42$ because for these values minima are found in the c/a-variation shown in Fig. 5.1. In both cases the Fermi energy is again shifted to higher energy values. This is already observed when comparing the DOS of Fe_3Co and FeCo and the trend is continued for $FeCo_3$. For $c/a = 1$ the Fermi energy is located on a high shoulder in the minority DOS and the majority DOS is completely flat around E_F (see Fig. 5.15(a)). As for the B2 structure of FeCo, the highest peak in the majority channel is not spitted into a Fe and a Co contribution. The peaks of both species are always almost at the same energy which shows the high degree of hybridization of Fe and Co states. The DOS for the $c/a = 1.42$ case is of comparable shape as the one obtained for Fe_3Co and FeCo. The main difference is the shift of the DOS to lower values, because with increasing Co content more and more states of higher energy are occupied because the number of electrons per formula unit is increased by increasing the Co concentration. This shows the approximate validity of the rigid band approximation for $Fe_{1-x}Co_x$ systems in the α- as well as in the γ-phase.

Figure 5.16 shows the magnetic exchange parameters of the ordered $D0_3$ structure at $c/a = 1.42$ and of the disordered B2 and A2 structures tetragonally distorted to the same c/a-ratio. Exchange interactions for $c/a = 1$ are not shown because the lower minimum and therefore the ground state is found for $c/a = 1.42$ (see Figure 5.1). The magnetic exchange interactions are decreased by a factor of two compared to Fe_3Co and also compared to the equiatomic composition FeCo. This results in smaller critical temperatures and corresponds to the observations discussed in the preceding sections that for fcc structures of iron-cobalt alloys smaller critical temperatures are obtained. Here, it also fits the experimental phase diagram because the line associated with the critical temperature of the γ-phase ($T_C(\gamma)$)

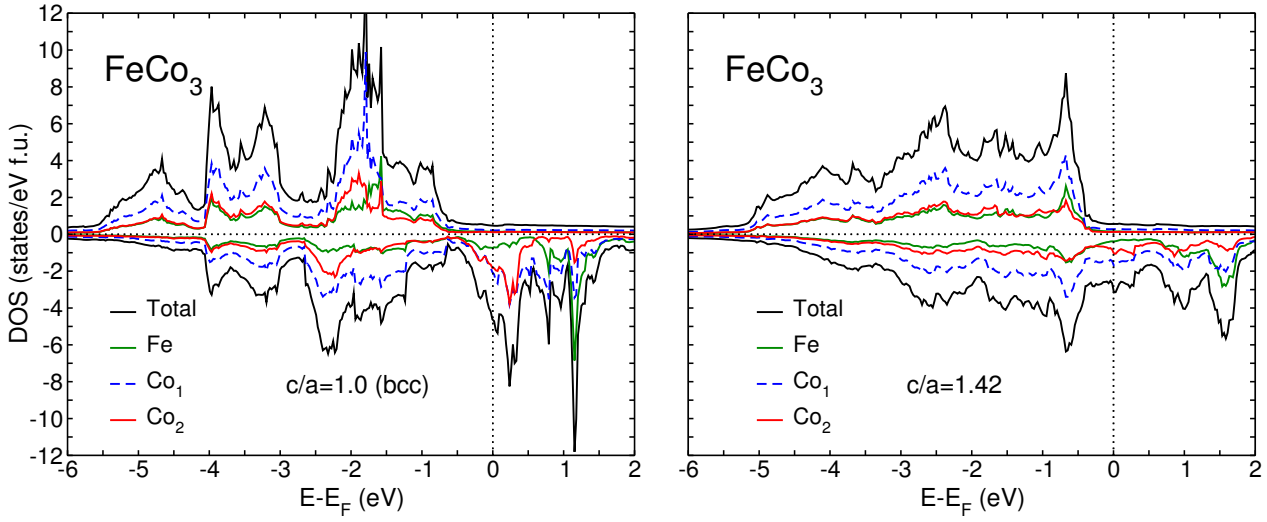

Figure 5.15: Comparison of the electronic densities of states for the ordered iron-cobalt structures calculated with VASP using GGA exchange correlation. (a) shows the DOS of the $D0_3$ structure and (b) the DOS of the tetragonally distorted $D0_3$ structure at $c/a = 1.42$.

drops fast with increasing Fe content. Exactly at $x = 0.75$ it suggests a T_C value of around 1150 K which is only about 100 K higher and is obtained from an extrapolation.

The exchange parameters and the critical temperatures corresponding to the different degrees of disorder, namely the tetragonal distorted B2 and A2 structures, are shown in Fig. 5.16(b) and (c). As in Fe_3Co and FeCo, the interaction between Fe and Co is the strongest interaction. But here, also the Co-Co interactions are strong and play an important role because of the high Co concentration. It turns out that disorder plays a minor role because the differences between the critical temperature of the fully ordered and the two disordered structures are smaller than 100 K. The difference between the two types of disorder is about 10 K. This is comparable to what is found for Fe_3Co where disorder is also less important for the critical temperature. This can be understood if it is taken into account that the magnetic moments of both species are large and that in addition the magnetic exchange between all kinds of nearest neighbor pairs is always strong.

Using the DLM picture to mimic magnetic disorder, the magnetic moments of the Co sublattices are quenched to a value of about 0.3 and $0.8\mu_B$ respectively. The smaller value

	μ_{DO_3} (μ_B)	μ_{B2} (μ_B)	μ_{A2} (μ_B)	μ_{DLM} (μ_B)
Co	1.60	1.59	1.64	0.29
	1.63	1.69		0.78
Fe	2.53	2.48	2.43	2.28

Table 5.5: Comparison of the magnetic moments of $FeCo_3$ for different ordered and disordered structures including the DLM calculation of the ordered structure. The results are obtained from SPR-KKR calculations using LDA of VWN.

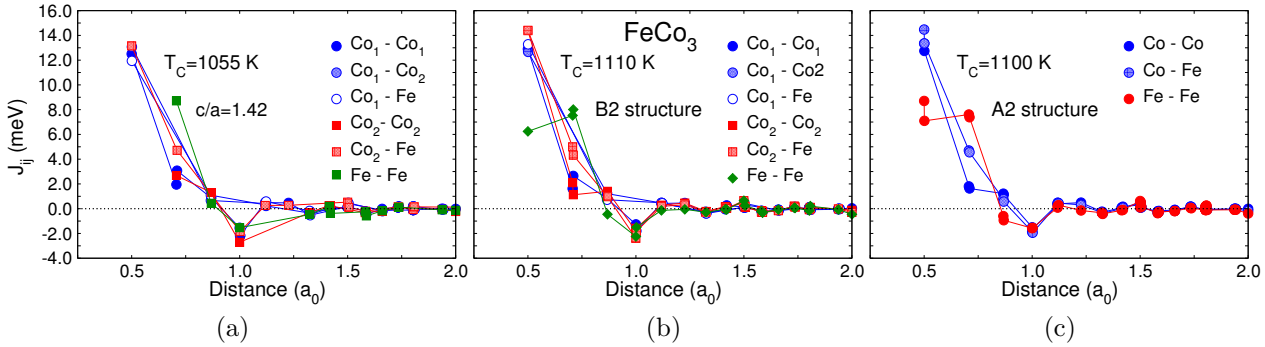

Figure 5.16: Magnetic exchange parameters of ordered and disordered $FeCo_3$. All calculations are performed for $c/a = 1.42$. The B2 and A2 notions only indicate that the same structure for $c/a = 1$ would be B2 or A2 and should not be taken literally.

occurs for Co atoms with Fe nearest neighbors, whereas the larger value belongs to Co atoms with only Co nearest neighbors. The iron moment stays reasonable with a value larger the $2\mu_B$. A comparison of the magnetic moments is given in Table 5.5. This result shows that the DLM picture leads to unrealistic values of the magnetic moments of the Co atoms if they are surrounded by Fe atoms. This supports the conclusion drawn from the results of the DLM calculation of FeCo. It is stated that the DLM picture gives reasonable Co moments in the B32 structure where Co has Co nearest neighbors and fails for the B2 structure because of lacking Co nearest neighbors.

The calculations of the $L1_2$ ordered γ-phase reveal only a ferromagnetic and a nonmagnetic solution (see Fig. 5.17). It is not possible to stabilize a low-spin or an antiferromagnetic solution. Thus, one fails to describe the Invar effect on the cobalt rich side of the phase diagram by the simple two-state model, which assumes two states with finite magnetic moments of different magnitude. But a thermally driven partial occupation of the non magnetic state with smaller volume might contribute to the Invar behavior and also to a reduced net magnetization. But this is unlikely because the energy difference between the ferromagnetic and non-magnetic state is large. In addition, it might be possible that complex antiferromagnetic states which cannot be stabilized in a small unit cell play an important role concerning the Invar effect. But this cannot be verified within the discussion carried out here and is in addition of low probability because the antiferromagnetic tendencies vanish with vanishing iron content and therefore it is possible that antiferromagnetism is only very weak at the $FeCo_3$ concentration.

The c/a-variation of the ferromagnetic state of the $L1_2$ structure shows that it is stable against tetragonal distortions which gives an additional evidence that this structure marks a stable configuration, see Fig. 5.18(b). There is a second minimum at around $c/a = 0.71$ which corresponds to the bcc type of structure, but this minimum is higher in energy. This shows that different types of order, $D0_3$ and $L1_2$, lead to the preference of the γ-phase for this composition.

Figure 5.18 shows the variation of the total energy along the bcc-hcp path. Obviously a stable hcp type of phase can be stabilized in $FeCo_3$. This hcp minimum is found around 1.35. The reason that the minimum is not exactly at 1 can be due to the fact that the hcp structure does not necessarily need to show the ideal c/a-ratio which could be obtained at 1. It can also have a different value and therefore the description of the bcc-hcp path does not

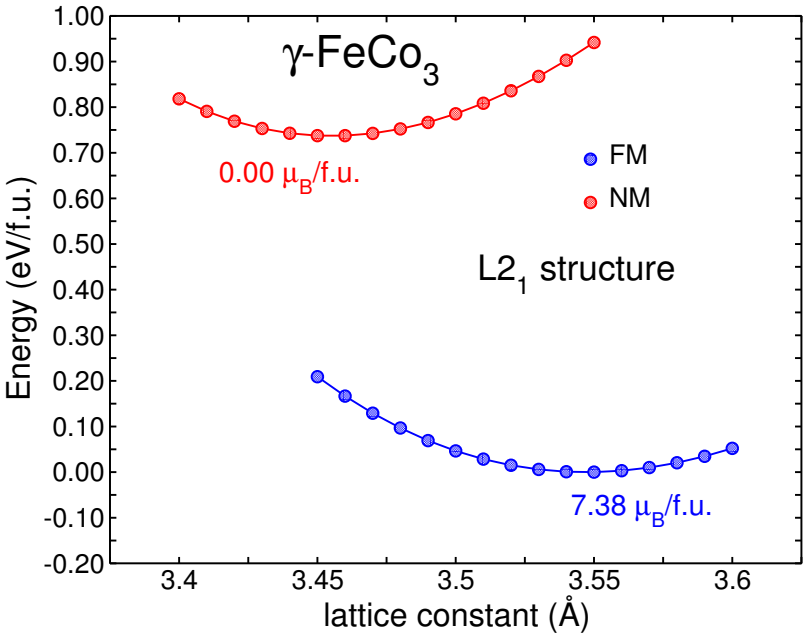

Figure 5.17: Total energy of the different magnetic states of $L1_2$ ordered γ-$FeCo_3$ obtained with VASP.

fit precisely. The magnetization is almost constant along the entire path including only small fluctuations. This shows that by approaching high Co concentrations a hcp state develops which is expected because the hcp phase becomes the ground state for concentrations above 90% Co. But as the energy difference between the bcc and the hcp minimum is an order of magnitude larger compared to Fe_3Co it is concluded the the large Fe content in Fe_3Co leads to a stronger hcp affinity than the large Co content in $FeCo_3$.

5.5 Discussion

A detailed analysis of Fe_3Co, FeCo and $FeCo_3$ is carried out by means of DFT calculations. In addition, MC simulations are carried out to gain insight into finite temperature magnetism and in particular to determine the critical temperature of these systems. Many structural and magnetic features of the experimental phase diagram are nicely reproduced by the calculations. For example, it is found that the α-phase is the ground state of $Fe_{1-x}Co_x$ alloy for $x < 0.75$. At $x = 0.75$ the calculations reveal that the α-phase becomes unstable and the γ-phase becomes the ground state. This structural aspect agrees completely with the experimental phase diagram.

It is confirmed that ordered B2 like structures (e.g. $D0_3$ for $x = 0.25$) are stable over a wide range of compositions around the equiatomic case. The calculations for Fe_3Co reveal that the $D0_3$ structure cannot easily be identified as the ground state order of the system because the tetragonally distorted $L1_2$ structure (with c/a around 1.41) is almost energetically degenerated with the $D0_3$ structure (see Fig. 5.9). The same holds if the $L1_2$ structure is compared with the tetragonally distorted $D0_3$ structure, which are again almost energetically degenerated. It cannot be predicted which structure is more preferable because the energy differences are too small. This fits the modern understanding of the iron-cobalt alloys as discussed in Ref. [14] and references therein. The authors of these publications propose that

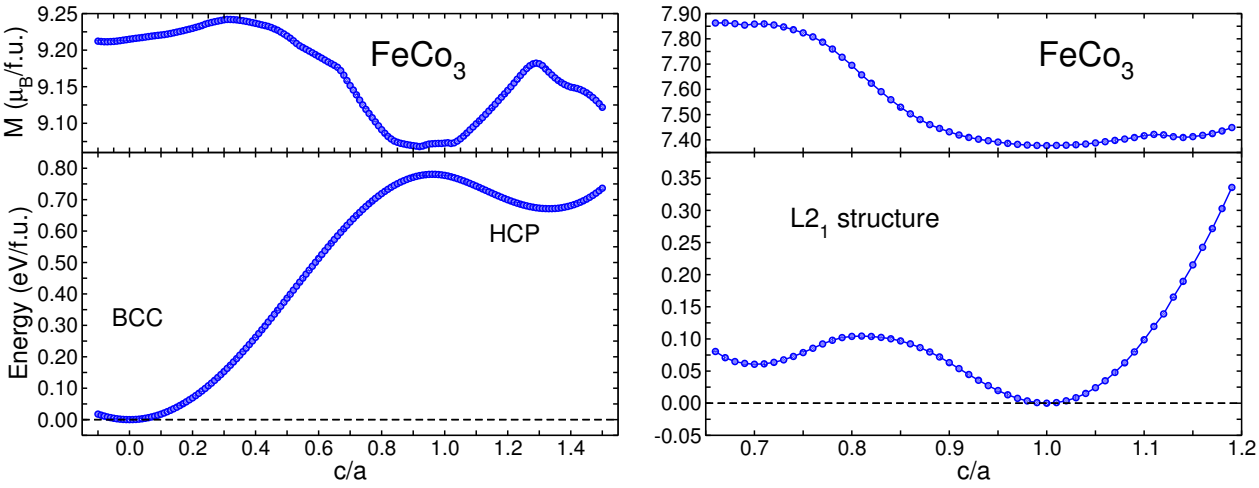

Figure 5.18: (a) Variation of the total energy along the bcc-hcp path. (c) The energy as a function of the c/a-ratio of the magnetic state of $L1_2$ ordered γ-$FeCo_3$.

iron-cobalt alloys exhibit certain superstructures which can be found in experiments and are confirmed by cluster expansion calculations. Therefore, the overall conclusion is that the calculations are consistent with the state-of-the-art knowledge about structural aspects of iron-cobalt alloys because the occurrence of almost degenerated structures is reproduced.

The calculations of fcc structures showed that with increasing Co content the numerous and complex magnetic states which exist in γ-Fe and also in γ-Fe_3Co vanish. The antiferromagnetic tendency on the Fe rich side of the phase diagram vanishes completely on the Co rich side where only ferromagnetic states are stable. This is confirmed by MC simulations of the fcc structures because spin spiral states are found for Fe_3Co, but, simple ferromagenitc states are found for higher Co content. However, there is one exception: the B2 like disordered fcc phase of $FeCo_3$ also shows a spin spiral type of ground state in the MC simulations.

The different magnetic states which are found for γ-Fe_3Co show that one can obtain the basic features of magneto-volume coupling behavior of this phase but on the basis of the present data the anti-Invar effect cannot be explained in the sense of the simple two-state explanation [124]. But as the anti-Invar behavior in this composition is quite weak, there might be subtleties which cannot be gathered by the investigation presented here.

The anomalous behavior of the thermal expansion in the α-phase, which is connected to spontaneous volume magnetostriction [124], cannot be gathered in this analysis and therefore the discussion of this effect is omitted.

The total energy calculations along the bcc-hcp path show that there are stable hcp type states for compositions where the experimental phase diagram does not suggest any ϵ-phase. It can be concluded that the ϵ-phase of $Fe_{1-x}Co_x$ alloys should exist even for $x < 0.9$ but that they are probably high pressure phases as it is the case for pure iron and are therefore difficult to examine within experimental analysis.

The fact that the critical temperature of the iron-cobalt alloys is not sensitive with respect to structural disorder is important for the Fe-Co based Heusler alloys which are discussed in Chapter 7. In such alloys the structural order of the iron and cobalt sublattices is less relevant. It can be shown that only the vicinity of a main group element plays the important

role for the observed changes.

At least, it is an important result that the DLM picture which is generally believed to be a good reference state for the calculation of magnetic exchange parameters and the predictions of critical temperatures has to be taken with care for the case of iron-cobalt alloys. The resulting magnetic moments of the Co atoms can become unrealistically small or even zero if Co is only surrounded by Fe or if the local environment of the Co moment is antiferromagnetic or magnetically disordered. On the other hand, this shows a particular magnetic property of Co and it can be concluded that magnetic fluctuations in the environment of Co atoms lead to strong longitudinal fluctuations of the Co moment.

Highlight

The investigation of $Fe_{1-x}Co_x$ alloys by means of the combined DFT+MC approach reveals a perfect agreement of structural and magnetic properties with the experimental phase diagram. The analysis of the γ-phase allows additional insight into the magneto-volume correlation which is particularly pronounced for Fe rich systems. Since the reported results also contribute to current discussions about superstructures in $Fe_{1-x}Co_x$, this chapter gives an exhaustive overview about basic features of such alloys.

6 Cobalt-Manganese

In this chapter the last binary combination of the three transition metals Mn, Fe and Co namely $Co_{1-x}Mn_x$ is investigated. This binary alloy is of particular experimental and theoretical interest because it is known to show complex magnetic properties including for instance spin glass, superparamagnetic and superantiferromagnetic phases depending on composition and temperature range (see Ref. [15] and references therein). Only few experimental investigations of these systems have been carried out up to now. In these studies the magnetic phases, magnetovolume effects and martensitic transitions have been investigated. Detailed theoretical investigations are missing. Therefore, the combined approach of using DFT calculations together with MC simulations is applied to these alloys in order to gain insight into structure and especially magnetism.

6.1 Introduction

The experimental structural and magnetic phase diagram of cobalt-manganese alloys is shown in Fig. 6.1. Such alloys solidify in a disordered fcc γ-phase or hcp ϵ-phase. The ϵ-phase is only stable for Co rich systems up to Mn concentrations of about 25%. In this Co rich regime, a martensitic phase transition occurs (see, e.g., Ref. [165]) which transforms the ϵ- to the γ-phase when temperature is increased and *vice versa* if it is decreased. In the phase diagram the dependence of the transition temperature range is denoted by the lines marked with $\epsilon \rightarrow \gamma$ and $\gamma \rightarrow \epsilon$. As typical for martensitic transformations, the transition from the low to the high temperature phase takes place at larger temperatures than the reverse transition (this is known as hysteresis). Both transitions vanish quickly at a Mn concentration around 25%. This means that the transition temperature lines drop to zero with increasing Mn content. For higher Mn concentrations (>28%) only the γ-phase is stable for the whole temperature range. In every case the alloy exists only in a disordered solid solution and no ordered structures have been identified in experiments. For manganese concentrations higher than 55% the alloy becomes unstable against decomposition into Co and Mn domains. Therefore, the phase diagram ends at this composition.

In the concentration range up to roughly 25% Mn a ferromagnetic phase (FM) exists. The associated critical temperature decreases fast with increasing manganese content and the magnetic phase transition from ferro- to paramagnetism (PM) vanishes abruptly at around 25% Mn. For compositions including more than 42% Mn the alloys are antiferromagnetic (AFM) and the associated transition temperature increases with increased Mn concentration. In the intermediate concentration range between the ferromagnetic and the antiferromagnetic region (25-42%) complex magnetic phases exist. Depending on the composition a superparamagnetic (SP) or a superantiferromagnetic (SAF) phase occurs. In superparamagnetic and superantiferromagnetic phases ferromagnetically or antiferromagnetically aligned clusters exist within a paramagnetic matrix. At low temperatures these phases show a transition to a spin-glass phase (for details see Ref. [15] and references therein). For concentrations of more than 42% Mn the antiferromagnetic phase changes to a superantiferromagnetic phase before

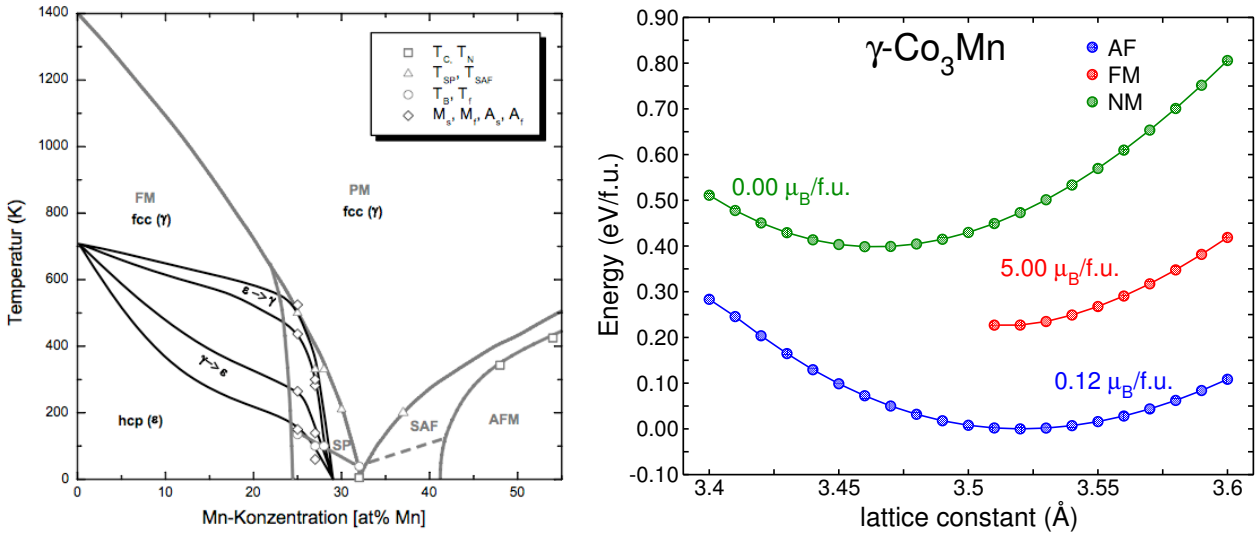

(a) (b)

Figure 6.1: (a) The experimental structural and magnetic phase diagram of $Co_{1-x}Mn_x$ alloys taken from Ref. [15]. (b) The total energy as a function of the lattice constant of the different magnetic states of $L1_2$ ordered γ-Co_3Mn obtained from VASP calculations.

the alloy becomes paramagnetic at higher temperatures. Interestingly, there is a concentration around 33% Mn where no ordered magnetic phase exists.

The thermal expansion coefficients of cobalt-manganese alloys have been investigated and it is found that at Mn concentrations around 48% interesting magneto-volume effects occur. In particular, the system shows Invar behavior below and anti-Invar behavior above the Néel temperature [165, 166]. In addition, a hysteresis in the temperature dependence of the electrical resistivity is observed [167, 166] which is related to the martensitic phase transition between the ϵ- and γ-phase. The most detailed and recent summary of experimental results of these alloys is found in Ref. [15] where elastic and magnetic properties of $Co_{1-x}Mn_x$ alloys are experimentally investigated by the ultrasonic puls-echo-overlap method.

In the following the compositions Co_3Mn and CoMn are investigated by means of *ab initio* calculations and MC simulations. The special focus is again on magnetic properties and how structure and disorder affects these properties. The concentrations are chosen again because they are simple to model and in particular because the Co_3Mn concentration lies in the very interesting composition range where the martensitic transition vanishes, ferromagnetism breaks down and complex magnetism develops. The $CoMn_3$ composition is not considered here because there is no experimental evidence that such system form a homogeneous solution and instead, as already mentioned, both ingredients decompose.

6.2 Co_3Mn

In this section Co_3Mn is discussed. In a first step the ordered $L1_2$ structure is chosen to model the alloy within VASP calculations. This is somewhat hypothetic because no ordered structures are found in the experimental investigations of $Co_{1-x}Mn_x$ alloys but they cannot be completely excluded (in Ref. [166] speculations about ordered structures are mentioned). At this Mn concentration the transition lines of the martensitic phase transformation which

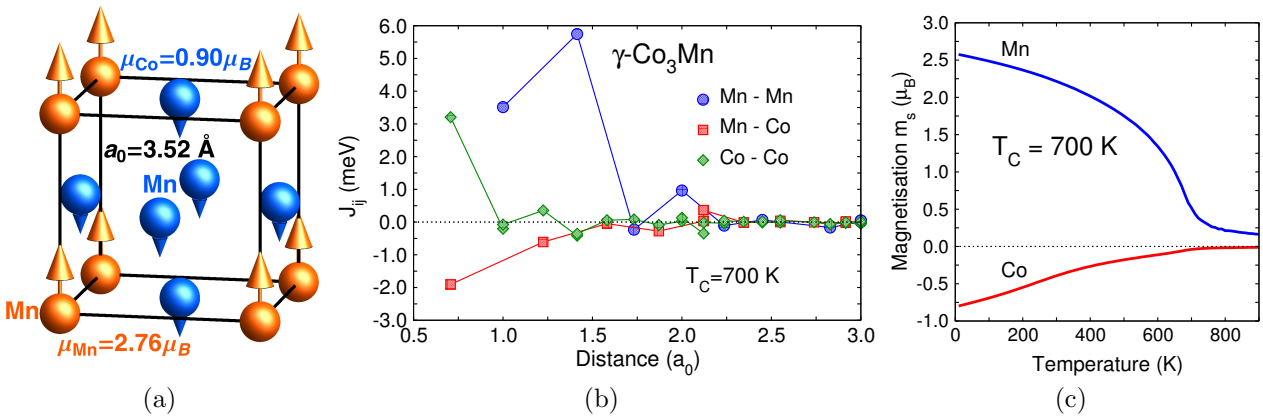

(a) (b) (c)

Figure 6.2: (a) Lattice constant and magnetic moments of $L1_2$ ordered γ-Co_3Mn obtained from VASP calculations. (b) The associated magnetic exchange parameters calculated with SPR-KKR and (c) the result of the corresponding MC simulation.

occurs for small Mn concentrations are about to vanish but can still be found in experiments (see Ref. [15] and reference therein). But as the γ-phase is already stable at room temperature and as the ϵ-phase vanishes completely close to this composition it is not considered here.

Figure 6.1 shows the total energy as a function of the lattice constant of three magnetic states found within the VASP investigation. The state which is of lowest energy shows an antiferromagnetic order. The subsequent state with higher energy is ferromagnetic but no complete calculation can be carried out because this state becomes unstable below a certain lattice constant near the minimum. It is concluded that the ferromagnetic state marks an unstable magnetic configuration at low temperatures. The last state with highest energy is the non-magnetic state.

Concerning the phase diagram of cobalt-manganese alloys, Co_3Mn is located at a critical concentration at which the ferromagnetic phase vanishes and a superparamagnetic state becomes the ground state. In so far, the results shown in Fig. 6.1 reflect that the system is at a point where the ferromagnetic state has not completely vanished but is no more stable and in particular no more the ground state. An antiferromagnetic phase marks the ground state in the ordered $L1_2$ structure, which is modeled with a small unit cell containing 4 atoms. Supercell calculations with more atoms and disordered arrangement of the different atoms might lead to more complex magnetic structures in Co_3Mn.

Figure 6.2(a) shows the magnetic order including the individual moments of the antiferromagnetic state which is of lowest energy in the $L1_2$ structure. The same type of magnetic order is found to be favored for Fe_3Mn (see Subsection 4.2.3). Therefore, the form of the magnetic exchange parameters shown in Fig. 6.2(b) is also comparable to those in the Fe_3Mn system. The Mn-Mn interactions are almost purely ferromagnetic and the Co-Mn interactions are almost completely antiferromagnetic which is also analogue to Fe_3Mn. As expected, the Co-Co interactions are different in Co_3Mn compared to the Fe-Fe interactions in Fe_3Mn. The nearest neighbor Co-Co interaction is ferromagnetic and the subsequent parameters are oscillating around zero. Interestingly, the critical temperature of Co_3Mn is close to the critical temperature of Fe_3Mn although the magnetic exchange parameters are more than a factor of two smaller. The main reason for this is that the nearest neighbor Fe-Fe interaction in Fe_3Mn which is antiferromagnetic, introduces a strong frustration of the Fe sublattice that is only

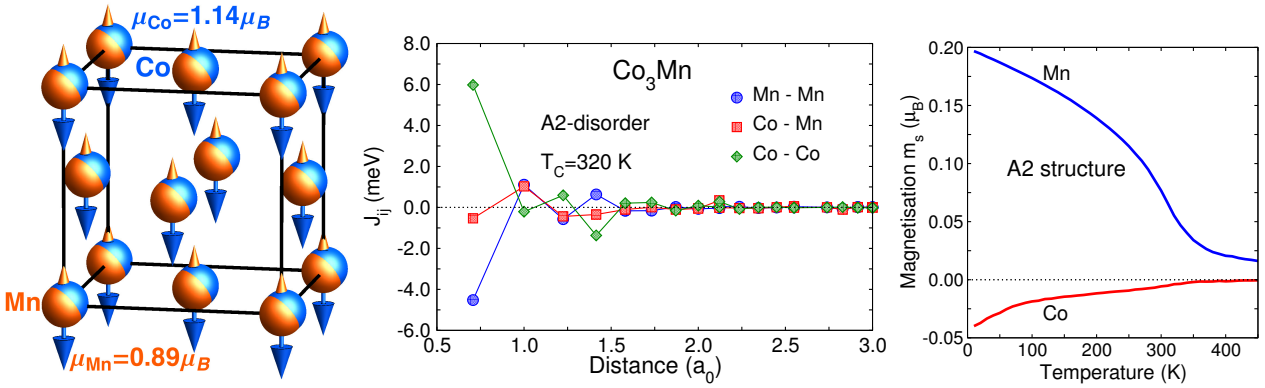

(a) (b) (c)

Figure 6.3: (a) shows a sketch of the fully disordered unit cell and the magnetic moments obtained from the CPA calculation of γ-Co_3Mn. Figure (b) shows the corresponding exchange parameters of the disordered system.

released by next nearest neighbor interactions and the strong antiferromagnetic coupling to the Mn sublattice. This does not occur in Co_3Mn because the interactions in the Co and Mn sublattice are both almost purely ferromagnetic.

Interestingly, the magnetization curves of the Co and Mn sublattice are of the same form as the corresponding curves in Fe_3Mn. A critical behavior of the Mn sublattice is observed but the Co sublattice shows no typical behavior but only a slow almost linear increase of the magnetization with decreasing temperature like the Fe sublattice in Fe_3Mn. This occurs because the Co-Co interactions are small and the coupling to the Mn sublattice is also small. Therefore, the ordering temperature of the Co sublattice is much lower than in the Mn sublattice and due to the small coupling to the Mn sublattice the criticality is not transferred to the Co sublattice. This means that the mechanism responsible for the unusual behavior of the Co magnetization in Co_3Mn is different from the one in Fe_3Mn because in Fe_3Mn the frustration in the Fe sublattice and the strong coupling to the Mn sublattice result in the unusual form of the Fe magnetization. In summary, although there are certain quantitative differences between the exchange interactions of Fe_3Mn and Co_3Mn their finite temperature magnetism is very similar. This is connected to the fact that Fe and Co are similar in the sense that both are ferromagnets with large moments and high Curie temperatures. But certain differences occur because iron exhibits strong antiferromagnetic tendencies in the γ-phase.

The critical temperature of 700 K obtained from the MC simulations represents a good estimate for the experimental result because the line denoting the transition to paramagnetism in the experimental phase diagram is above 600 K at a composition of 25% Mn. This implies that although an ordered structure serves as reference for the calculation of the exchange parameters, the resulting T_C is in agreement with what is found experimentally in disordered samples.

Calculations of exchange parameters of the ferromagnetic state are not possible because this state cannot be stabilized within the KKR calculations. This shows again that the Co_3Mn composition marks a critical point at which the magnetic behavior changes dramatically.

To study the influence of disorder, a CPA calculation of Co_3Mn is performed. In this calculations it is assumed that every lattice site is partially occupied by 75% Co and 25%

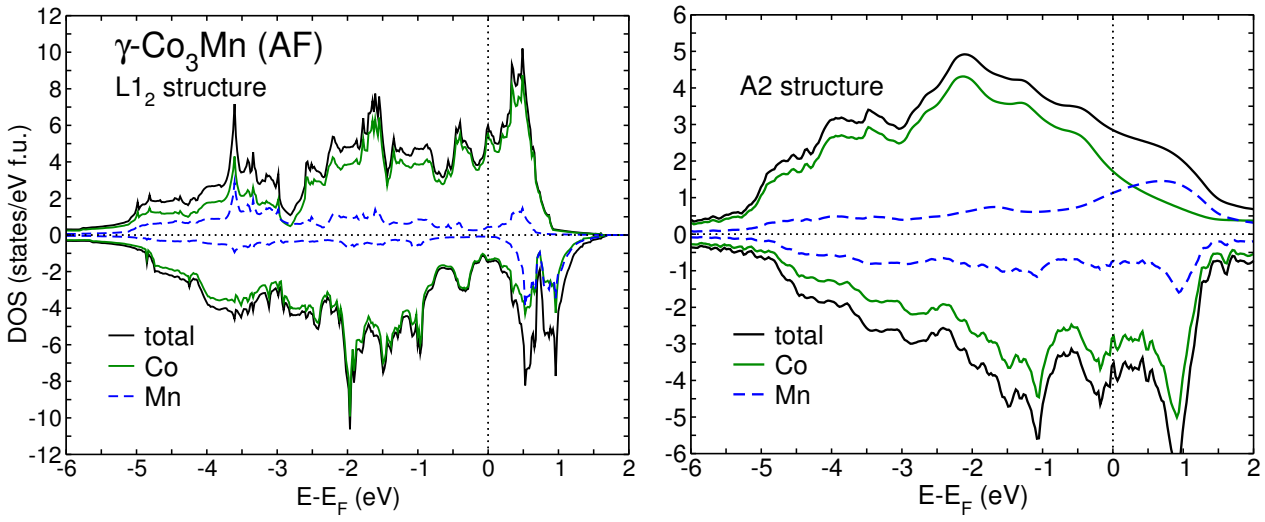

(a) (b)

Figure 6.4: (a) shows the DOS of $L1_2$ structured Co_3Mn in the AF state obtained from VASP and (b) the DOS of the disordered system obtained from a CPA-KKR calculation using SPR-KKR.

Mn. The magnetic state obtained from this calculation is similar to the one in the ordered structure because the moments of Co and Mn are antiparallel aligned with respect to each other (see Fig. 6.3). The moments of Mn are strongly reduced compared to the ordered $L1_2$ structure. This occurs due to the parallel alignment of the nearest neighbor Mn atoms which is very unfavorable because of the antiferromagnetic interaction. In order to reduce the resulting unfavorable energy contributions the moments are quenched.

Figure 6.3(b) shows the magnetic exchange parameters obtained from the CPA calculation. There are competing ferromagnetic and antiferromagnetic couplings of comparable strength. All nearest neighbor Co pairs interact ferromagnetically as in the case of the ordered $L1_2$ structure, but now the Mn pairs interact antiferromagnetically. The antiferromagnetic interaction between nearest neighbor Mn atoms leads to a strong frustration because of the underlying fcc lattice. This leads to a reduction of the critical temperature by more than a factor of two compared to the ordered $L1_2$ system.

The ground state obtained from the MC simulation is the same as shown in Fig. 6.3(a) and the development of the magnetization with decreasing temperature, shown in Fig. 6.3(c), is also similar to the ordered system. The only difference is that the alignment of some of the Mn atoms is disturbed and they are tilted by a small angle compared to the majority of the Mn moments. This depends on the local environment of a particular Mn atom in a particular realization of disorder in the MC simulation cell. The random placement of Co and Mn atoms can lead to a very strong local frustration due to the antiferromagnetic nearest neighbor interaction.

Obviously, the form of the magnetic exchange parameters does not explain the simulated magnetic structure in a simple way because of the antiferromagnetic nearest neighbor interaction between Mn pairs. But it needs to be taken into account that due to the small Mn concentration, the probability for the occurrence of nearest neighbor Mn pairs is small. On the average, every Mn atom is exclusively surrounded by Co nearest neighbors. Therefore,

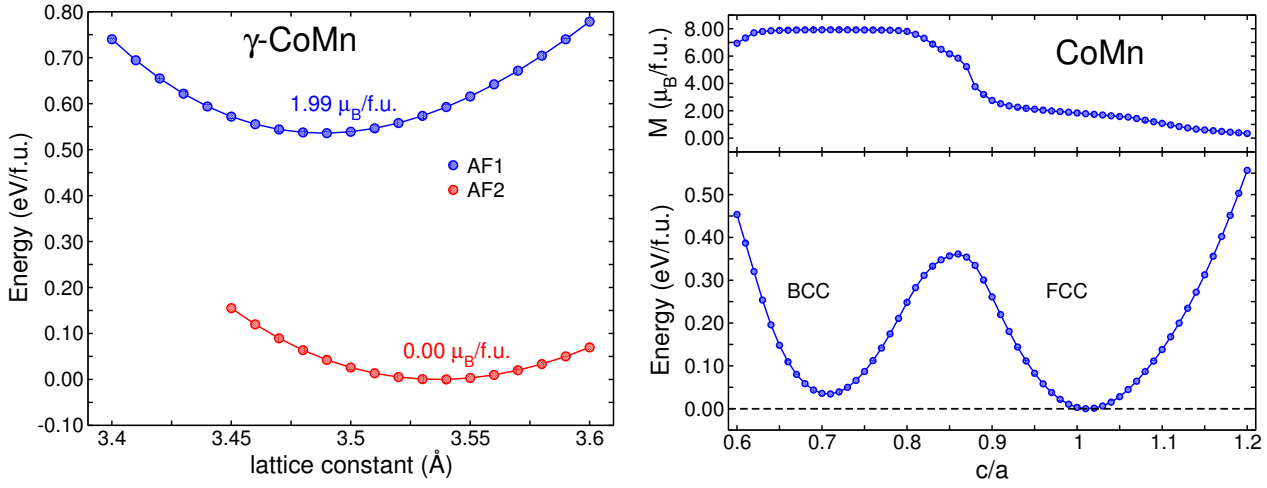

(a) (b)

Figure 6.5: (a) The two different antiferromagnetic states found in VASP calculations of CoMn. (b) The c/a variation of the total energy for the AF1 state.

considering only nearest neighbor interactions, the Co-Co and Co-Mn interactions are the only relevant interactions on the average. The next nearest neighbor interactions between Mn-Mn pairs is more relevant and is ferromagnetic and therefore supports the parallel alignment. Note that the magnetic configuration with antiparallel Co and Mn moments is not strongly preferred because also non-collinear states are possible. Therefore, details of the groundstate found in MC simulations can depend on particular realization of the random composition. This is confirmed by what is mentioned above, that some of the Mn moments are slightly tilted with respect to the majority of the Mn atoms.

Figure 6.4 compares the electronic density of states of the ordered and disordered systems. Due to the high Co concentration, the DOS is almost exclusively determined by Co associated states. The reduction of the valence electron concentration due to manganese pushes the Fermi level to lower energies. Therefore, the states of the high peak in the majority channel at around 0.5 eV above E_F are unoccupied. This explains the small Co moments because in pure γ-Co the Fermi level lies in the flat region which starts at around 1 eV above E_F. As expected, the DOS of the A2 system is strongly smeared out. The fact, that the DOS of the Mn atoms is quite similar for the majority and minority channel explains the small Mn moment in this case. The small increase of the Co moment is connected to the smearing and rearrangement of the states which leads to the dominance of spin-down states.

Considering the later discussion of Co_2MnZ-half-metals it is interesting to note that the Fermi energy of $L1_2$-Co_3Mn lies in a minimum of the minority channel which is completely absent in pure γ-Co. It is carefully concluded the a certain trend for the development of half-metallicity is already present in the binary alloy.

6.3 CoMn

In this section the equiatomic CoMn composition is discussed. The experimental phase diagram suggests an antiferromagnetic γ-phase to be the ground state. Therefore, in the first step the $L1_0$ structure is assumed to perform *ab initio* calculations with VASP. Figure 6.5(a)

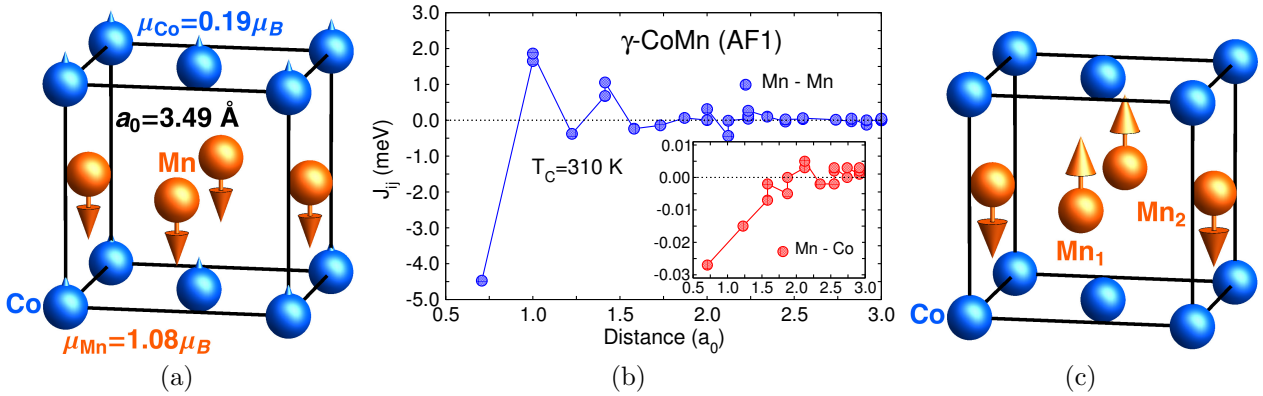

(a) (b) (c)

Figure 6.6: (a) Magnetic order of CoMn in the AF1 state. The magnetic moments are obtained with VASP using the PBE exchange correlation functional. (b) Magnetic exchange parameters of the AF1 state calculated with SPR-KKR using the VWN exchange correlation functional. (c) Magnetic state obtain from the MC simulation.

shows the variation of the total energy as a function of the lattice constant for two antiferromagnetic states found in this ordered structure. The state called AF1 exhibits very small Co moments of 0.19 μ_B and the Mn moments are antiparallel aligned to the small Co moment showing a value of 1.08 μ_B, which is also small compared to usual values of Mn moments in other alloys and in Co_3Mn. The structure and the moments are shown in Fig. 6.6. The strongly quenched moments show that the assumption of an ordered $L1_0$ structure with a layerwise antiferromagnetic order leads to unfavorable results. But as the layerwise antiferromagnetic state can be used as an initial guess for the procedure introduced in Chapter 4, a calculation of exchange parameters and a subsequent MC simulation are performed.

The magnetic exchange parameters of $L1_0$-CoMn in the AF1 state are shown in Fig. 6.6(b). The nearest neighbor Mn atoms show antiferromagnetic coupling and the interactions between Co and Mn are two orders of magnitude smaller. Due to the small Co moments, the Co-Co exchange interactions are small enough that they can be safely neglected and are not shown. The antiferromagnetic interaction between nearest neighbor Mn moments indicates that the magnetic state shown in Figure 6.6(a) is unstable. It indicates in particular that the orientations of nearest neighbor Mn moments must be antiparallel aligned with respect to each other and next nearest neighbors must be parallel. This is obvious regarding the alternation of the Mn exchange parameters from positive to negative values and vice versa and it explains why the Mn moments are strongly quenched to small values, because they are frustrated with respect to the coupling to each other. The moments are reduced to reduce unfavorable energy contributions. As the Co moments are too small, the interaction between Co atoms gives no relevant contribution. The coupling of Co and Mn moments is also very small because of the small moments and this coupling is also is antiferromagnetic.

Within the MC simulation the ground state which is expected from the discussion of the exchange parameters evolves, see Fig. 6.6(c). The Mn moments become antiferromagneticaly aligned in a form which is associated with the alternation of the coupling parameters. Because of the small moments and weak couplings the critical temperature is small. At $T = 310\,\mathrm{K}$ the Mn sublattices start to oder. No ordering of the Co sublattices can be observed at finite temperatures because the interaction is simply too small and the temperature steps in the MC simulation are 5 K. Ordering should be observable at very low temperatures but an

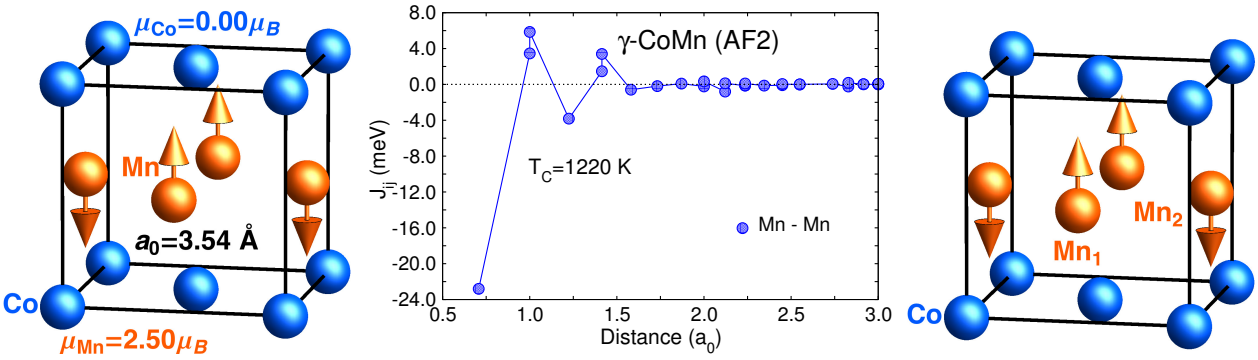

Figure 6.7: (a) Magnetic order of the AF2 state of CoMn. The VASP calculation is performed by using the PBE exchange correlation functional. (b) Magnetic exchange parameters of the AF2 state (again SPR-KKR and VWN functional). (c) Magnetic state obtained from the MC simulation.

estimate for this would be within a range where the accuracy of the entire investigation is not justified. Nonetheless, it should be noted that the critical temperature is in agreement with the experiment which suggests that the antiferromagnetic ordering starts around 400 K. In Fig. 6.6(c) no Co moment is shown because in the MC simulation only the average magnetization of the sublattices is measured which is zero for the Co sublattices due to the lacking order.

The state obtained from the MC simulation using the AF1 state as the reference is also found within a VASP calculation by using the antiparallel alignment of the Mn moments in as initial guess. From now on this state is named AF2. As can be seen from Fig. 6.5(a) this state is of lower total energy compared to the AF1 state. The magnetic moments and the lattice constant are shown in Fig. 6.6(a). The moment of Co is now completely quenched to zero. Interestingly, the moments of Mn take on realistic values because the frustration within the Mn sublattice is avoided by the antiparallel alignment, but, this quenches the moments of Co completely. This effect is similar to what is found in $Fe_{1-x}Co_x$ alloys where it turns out that Co moments are strongly reduced if their local environment is not homogeneously ferromagnetic, see Chapter 5. Therefore, it turns out that choosing an antiparallel alignment of the Mn atoms does not improve the description of the magnetic properties of the entire system but only those of the Mn atoms.

The only finite exchange interactions are those between the Mn atoms shown in Fig. 6.6(b). All interactions between Co or Co and Mn are zero because the magnetic moment of Co is zero. The behavior of the exchange parameters with increasing distance is very similar to that of the AF1 state but the absolute values of the interactions are much larger. This leads to a much higher critical temperature compared to that obtained from the AF1 state. The critical temperature of 1220 K is far to high to be compared to the experimental findings because the experimentally expected value is around 400 K for the equiatomic composition. This means that the value found here is by a factor of three to large. Unfortunately, using the energetically preferred AF2 state as a reference for the calculation of exchange parameters and critical temperature does not improve the theoretical prediction.

In summary, the results obtained for the magnetic state of CoMn in the γ-phase in $L1_0$ structure are up to now unsatisfactory, because the magnetic state of lowest energy is a state

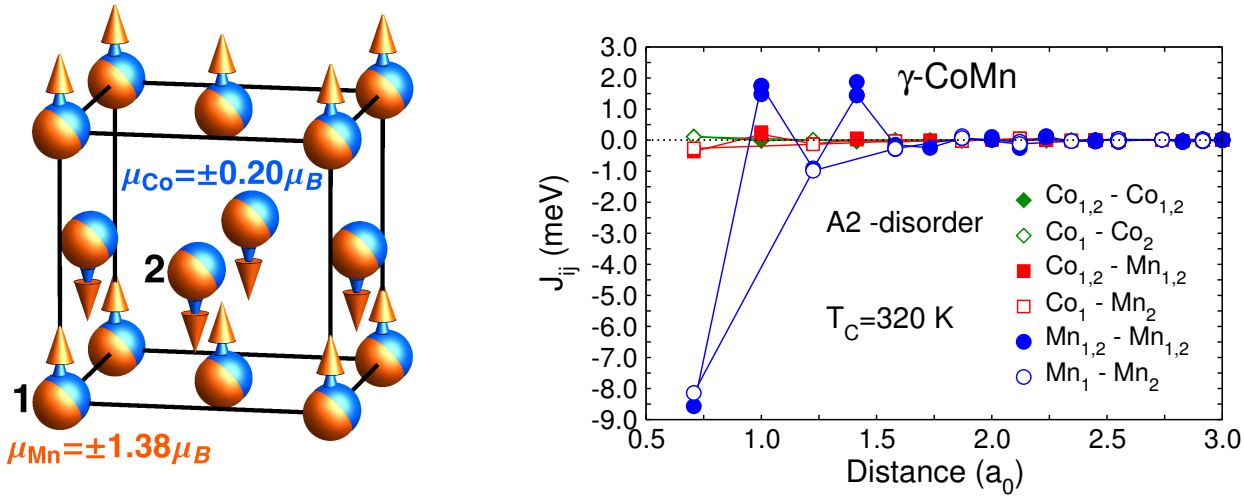

(a) (b)

Figure 6.8: (a) Magnetic structure of the A2 structure. (b) Magnetic exchange parameters of the disordered structure.

where the cobalt moments vanish and also the prediction of the critical temperature does not agree with experiment. These unrealistic results occur due to the assumptions that are made in the calculation. First, the order of the system is artificially introduced because as already mentioned, real systems are known to be solid solutions. And again the small unit cells prevent the search for more complicated ground states. But as already mentioned, the small moments of the Co atom is connected to a physical mechanism that reduces the moment of such atoms in inhomogeneous environments.

In order to check the influence of disorder, a CPA calculation of the disordered A2 structure is carried out. In this calculation all atomic positions are occupied by 50% Co and 50% Mn. The results of this calculation are presented in Fig. 6.8. Part (a) shows the structure, the size of the individual magnetic moments and their orientation with respect to each other. On each site, the moments of Co and Mn are parallel aligned. The Co moments are again very small and the manganese moments are more reasonable although still small. Because of the small Co moments the arrows denoting them in the figure are always shorter than the arrows of the Mn moments. The particular alignment of the moments is layerwise. The first conclusion to be drawn, is that also the CPA description of disorder does not significantly improve the result for the Co moments. The reason for this is again the antiferromagnetic environment.

In Fig. 6.8(b), the magnetic exchange parameters of the A2 structure are shown. The interactions between Mn pairs are large compared to the AF1 state of ordered CoMn but the critical temperature is only slightly increased. On the other hand the interactions are more than a factor of two smaller compared to the AF2 state. But the qualitative form of the Mn-Mn interactions is the same for all three investigated systems. Regarding Fig. 6.8(b) more precisely one finds that the exchange parameters indicate frustration of the magnetic moments. Strong antiferromagnetic interactions are found between Mn in layers with parallel as well as antiparallel aligned moments. Interestingly, this frustration is not released within the MC simulation by the development of a non-collinear state. Instead the result of the MC simulations brings up the same layerwise magnetic configuration.

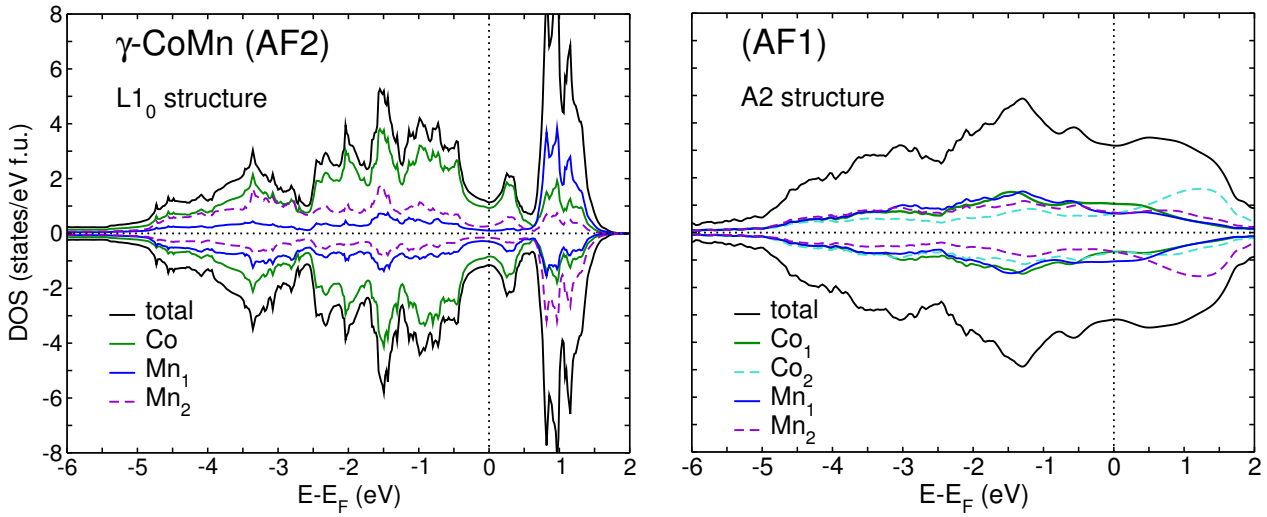

(a) (b)

Figure 6.9: (a) shows the DOS of $L1_0$ ordered CoMn in the AF state and (b) the DOS of the disordered system.

The electronic DOS of the AF2 state of the $L1_0$ structure and the A2 structure are compared in Fig 6.9. The complete symmetry of the Co DOS with respect to the two spin channels is the reason for the totally quenched Co moments. In addition, the Mn moments are pairwise symmetric which is connected to their antiferromagnetic alignment. The total density of states is completely symmetric which results in the vanishing moment of the unit cell. These symmetries are also present in the DOS of the A2 structure which also exhibits no total moment of the unit cell due to the perfect layerwise antiferromagnetism.

An unexpected feature of the ordered CoMn system is shown in Fig. 6.5(b). The c/a-variation of the AF1 state provides a minimum at around $c/a = 0.71$ which is exactly the value of a bcc structure. The minimum is energetically very close to the minimum at $c/a = 1$ and has a large magnetic moment. Obviously, the antiferomagnetic alignment of the fcc system turns into a ferromagnetic one at the bcc associated c/a-value. The occurrence of a α-phase is contrary to what is expected from the experimental phase diagram, because it suggests the fcc γ-phase to be the ground state at this composition and no phase transformation to a bcc structure is found. Therefore, an additional investigation of the hypothetic α-phase is carried out. Calculations of a B2 ordered structure are performed and two magnetic states are found (see Fig. 6.10). The state of lowest energy is a ferromagnetic state and the other is antiferromagnetic and exhibits a magnetic structure analogous to the AF2 state of the γ-phase because the moments of the Co atoms are zero and the Mn moments are of same size and antiparallel aligned.

This implies that surprisingly a α-phase of CoMn is predicted here which has not been found experimentally up to now. In addition, it is interesting that the ferromagnetic α- and the AF1 state of the γ-phase are found to be almost energetically degenerated.

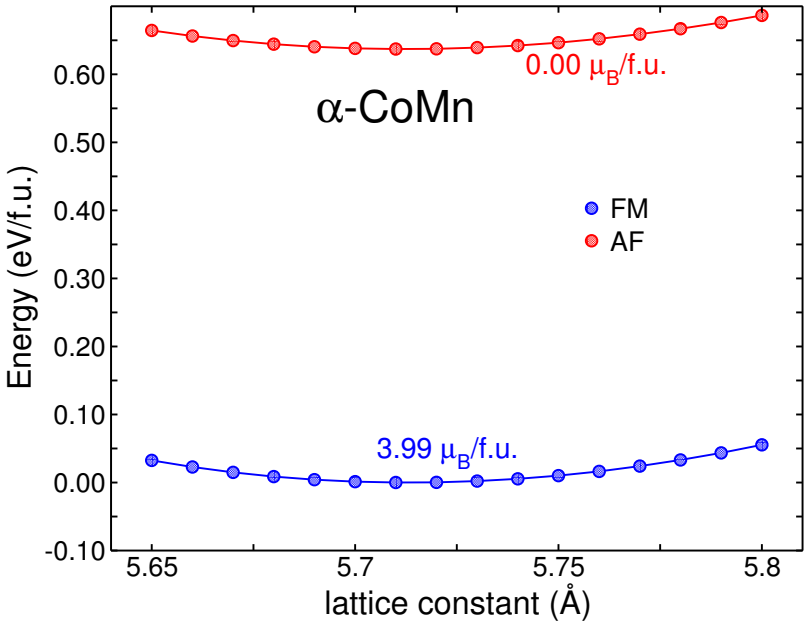

Figure 6.10: The different states of B2 ordered α-CoMn. Surprisingly the ferromagnetic state is energetically preferred.

6.4 Discussion

An analysis of structural and magnetic properties of $Co_{1-x}Mn_x$ alloys is carried out in this chapter in order to contribute to the few existing work concerning these alloys.

The investigation of Co_3Mn reflects the experimentally known fact that this composition marks a critical point a which the magnetic properties change abruptly because the ferromagnetic solution becomes unstable and the antiferromagnetic solution is energetically preferred. The critical temperature obtained from this state can be nicely compared to the experiment. On the other hand the experiments suggest a superparamagnetic ground state which cannot be easily investigated with the methods used here.

The experiments additionally suggest that $Co_{1-x}Mn_x$ alloys do not show structural order but are found in solid solutions. Therefore, a CPA calculation of Co_3Mn is carried out to include a mean field description of disorder. The drawback of this calculation is that the MC simulation reveals a critical temperature which too small in comparison with experiment. Another drawback is that the individual magnetic moments of the Mn atoms are strongly quenched. Therefore, the interesting conclusion is that it is not necessary to include disorder to get reasonable results for finite temperature magnetism. But of course this conclusion has to be taken with care and needs additional investigation to be validated.

During the investigation of the CoMn composition in $L1_0$ structure two antiferromagentic states are found. The first one is a layerwise antiferromagnetic state where the Co and Mn layers are antiparallel aligned. In this state both species exhibit only small moments and, in particular the Co moments are almost zero. In the second state the Mn sublattice is antiferromagnetically ordered with realistic moments and the Co moments are exactly zero. Using the AF1 state as reference state, a critical temperature with good agreement to experiment is found whereas the AF2 state provides a critical temperature which is far to high. The critical temperature obtained in the calculation of a disordered structure employing

the CPA method, leads to almost the same critical temperature as the calculation for the ordered structure with AF1 order which is contrary to the trend found in Co_3Mn

The most interesting result of the investigation of CoMn is that a stable ferromagnetic bcc state is found. This is peculiar because such structures have never been found in experiment and because neither Co nor Mn show tendencies for bcc types structures. In particular, the preference of the ferromagnetic state in a Mn rich alloy is very unusual.

In addition, the calculations presented in this chapter show that there is again the trend that Co moments are strongly reduced in antiferromagnetic environments. It is concluded that there must be a general mechanism which is responsible for this reduction of the Co moments because a similar effect is also found in $Fe_{1-x}Co_x$. In Chapter 5, DLM calculations of α-$Fe_{1-x}Co_x$ are reported which lead to small or even zero moments of the Co atom. A comparison with antiferromagnetic states in α-$Fe_{1-x}Co_x$ is not possible because such states are unstable. But a comparison to γ-Fe_3Co which shows an antiferromagnetic state (see Fig.5.7) is possible and it turns out that in such structures and magnetic configurations the Co moment is also strongly quenched. In summary: Co moments are very sensitive to the magnetic configuration of their local environment. In addition, the chemical environment is also important, because Co moments in Co environments are much more stable.

In the particular case of $Co_{1-x}Mn_x$ alloys one may conclude that the reason for the preference of fully disordered structures found in experiment is closely related to the magnetism of these alloys. All structures investigated here exhibit a certain level of order. Even the CPA calculations include strict translational invariance. This order leads to unfavorable arrangement of the atoms and therefore to quenched magnetic moments. The other way round, one may say that the effort for the development of large moments acts as a driving force for disordered assembly of atoms. This is confirmed by the occurrence of superparamagnetic and superantiferromagnetic phases which show that local clustering occurs which stabilizes the moments.

This discussion shows that conclusions of general interest can be drawn from the presented results and that further theoretical work could lead to a better understanding of the structural and magnetic properties of $Co_{1-x}Mn_x$ alloys.

Highlight

Basic structural and magnetic properties of $Co_{1-x}Mn_x$ alloys are determined in good agreement with experiment. The calculations predict the occurrence of a ferromagnetic α-phase for CoMn which has not been found in experiment. In addition, the study of $Co_{1-x}Mn_x$ alloys reinforces conclusions drawn from the analysis of $Fe_{1-x}Co_x$ in Chapter 5 concerning the magnetic moment of Co: It turns out again that the moment of Co is very sensitive to the chemical composition and magnetic order of its environment.

7 Heusler alloys and half-metallicity

This chapter is devoted to particular classes of functional Heusler alloys which have attracted much attention because of properties that are interesting for a series of technological applications. Special attention is payed to half-metallic ferromagnetism in Heusler alloys based on Mn, Co and Fe. As half-metallicity is connected with the possibility of driving electrical currents with high spin polarization it is of interest in the field of spintronics. An additional focus is on the analysis of details of the magnetic exchange interaction in Ni-Mn based Heusler alloys.

The remainder of this chapter is organized as follows: First, the most important characteristics of Heusler alloys are listed and an introduction to the concept of half-metallic ferromagnetism is given. This introduction follows the review given by Katsnelson et. al. [7]. Afterwards, results obtained for the structural, electronic and magnetic properties of half-metallic Heusler alloys are presented. In addition, results obtained using a new method which allows to distinguish contributions to the total exchange interaction arising from electron states with certain symmetries are presented.

7.1 Heusler alloys

Heusler alloys are ternary intermetallics with stoichiometric composition X_2YZ. The atoms occupy the sites of four interpenetrating face-centered cubic lattices. The X and Y atoms are usually transition metals whereas the Z element belongs to the main group elements. This type of Heusler alloy is called full-Heusler in contrast to the so called half-Heusler alloy with XYZ stoichiometry, where one of the fcc lattices is not occupied. In the following only full-Heusler alloys are considered and the prefix "full" is skipped.

The occupation of the four fcc lattices in Heusler intermetallics can be realized in two different ways which are not symmetrically equivalent. The first one is called conventional Heusler and is shown in Fig. 7.1(a). This structure is designate as the $L2_1$ structure. The second type is shown Fig. 7.1(b) and is called the inverse Heusler [168]. Often, the conventional Heusler structure is denoted by X_2YZ whereas the inverse Heusler structure is denoted by (XY)XZ. The brackets indicate that the two X sublattices of the conventional Heusler are occupied by the X and the Y species in the inverse one.

Throughout the following analysis the total energy of the conventional and the inverse structure of each investigated composition are compared to determine the energetically preferred one. If one of the structures is strongly favored, this gives a clear indication that it is very likely to be the actual ground state structure. If both structures are almost degenerated it indicates that this particular alloy prefers a disordered structure because a mixture of both structures will also have similar energy. *A priori* it is not clear which kind of disorder can be expected. It is possible that only the Y and Z atoms mix and a B2 type of disorder occurs. On the other hand, if all atom types mix, A2 disorder emerges. Formation energy calculations of defects in the $L2_1$ structure show that interchanges of different types of atoms pairs give completely different energies and also depend on the considered composition (for

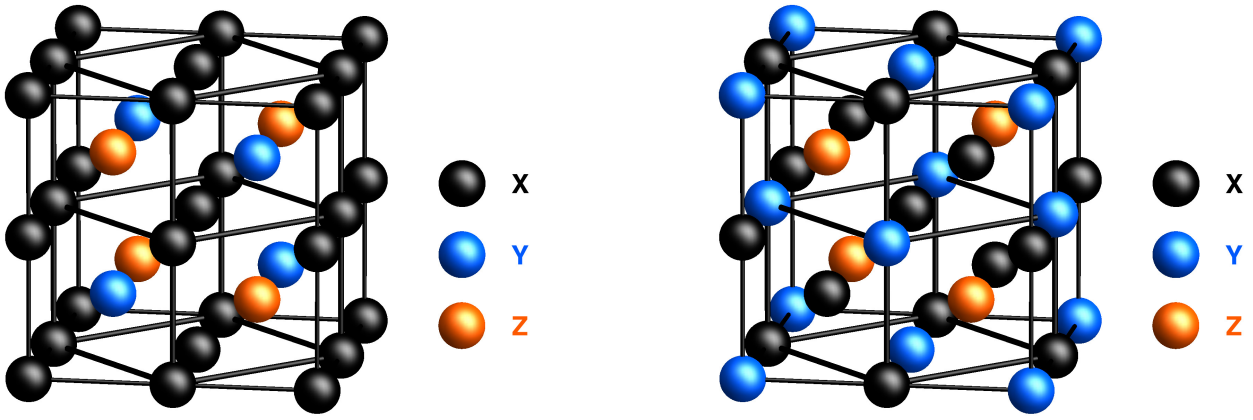

(a) (b)

Figure 7.1: Comparison of the conventional (a) and inverse (b) Heusler structure.

more details see Ref. [169] and references therein). This means that one needs to investigate possible disordered cases very carefully.

In addition, Heusler compounds which crystalize in $L2_1$ structure at low temperatures can exhibit order-disorder transitions. These transitions may also results in an disordered B2 [170] or A2 structure type. The transition to the disordered B2 structure is more likely because in many Heusler alloys the interchanges between the Y and Z species have a lower formation energy [169].

In this chapter calculations for fully ordered as well as for partially and fully disordered cases are presented in order to show a comprehensive investigation.

7.2 Half-metallic ferromagnets

A half-metallic ferromagnet (HMF) is a material in which the DOS at the Fermi energy of one spin channel is that of a metal and the DOS of the other shows a gap like an insulator or a semi-conductor. This results in a 100% spin polarization of the charge carriers at the Fermi energy. The definition does not mean that the gap must necessarily be in the minority spin channel because it can also occur in the majority channel.

Depending on the particular material, the half-metallic gap can have various origins. The different mechanisms which occur in the different material classes are reviewed in Ref. [7]. Since the present work focusses on full-Heusler alloys, only a short description of the origin of the gap in these materials is needed. The authors of Ref. [171] give a detailed group theory based explanation for the example of Co_2MnGe. This explanation can be generalized to other compositions. It concerns the hybridization of Co and Mn orbitals in the minority channel as it is shown in Fig. 7.2(a). The top picture shows how the Co atoms form bonding orbitals associated with the symmetry of the corresponding atomic orbitals. The bottom picture shows how these Co bonding orbitals hybridize in a subsequent step with Mn orbitals. Again, this hybridization follows the underlying symmetry of the original orbitals. As a result, a gap between the highest occupied Co band which is of t_{1u} symmetry and the lowest unoccupied Co band, which is of e_u symmetry opens up. This situation can be identified in the element and symmetry resolved DOS of Co_2MnGe which is shown in Fig. 7.2(b). In this DOS certain

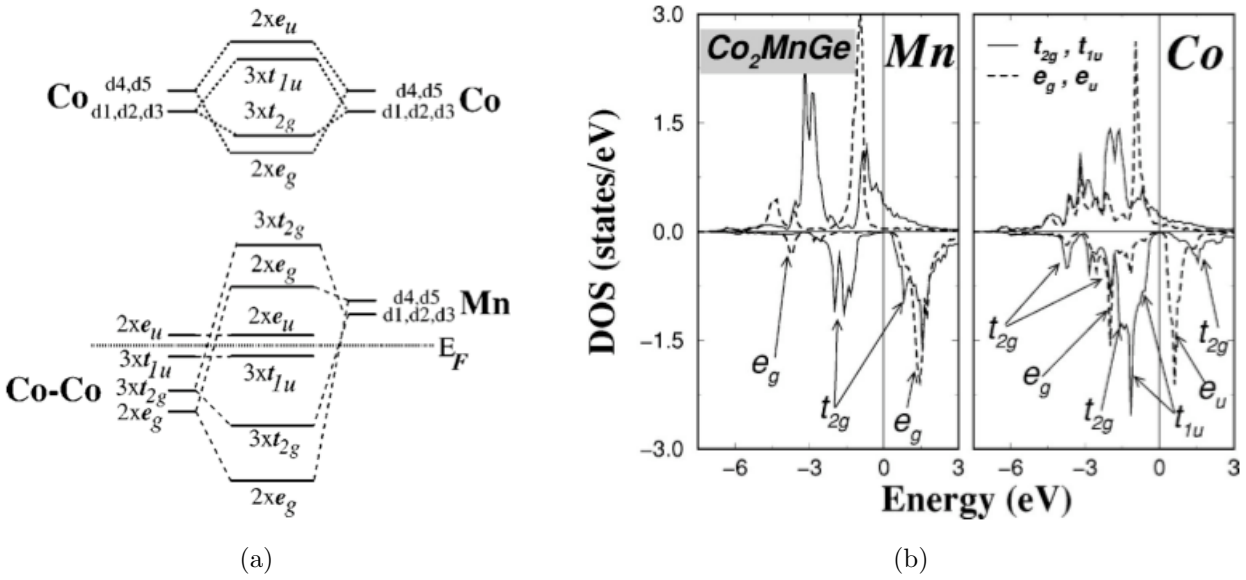

(a) (b)

Figure 7.2: Origin of the half-metallic gap in full-Heusler alloys [171]. The d1, d2 and d3 correspond to the d_{xy}, d_{yx} and d_{zx} orbitals and the d3 and d4 to the d_{z^2} and $d_{x^2-y^2}$ orbitals.

parts can be directly associated with the orbitals shown in Fig. 7.2(a).

This description of the origin of the gap has to be taken with care because it is only an independent electron type of description and the symmetry considerations are only strictly valid at the Γ-point. But this description is still of interest because it gives a simple as well as intuitive understanding of half-metallicity (for more details the reader is referred to Ref. [7]).

Another important feature of half-metallic full-Heusler as well as half-Heusler alloys is their perfect Slater-Pauling behavior. This means that the total magnetic moment of the full-Heusler alloys scales linearly like $M = Z - 24$ where M is the magnetic moment per unit cell and Z is the total number of valence electrons [171]. A similar rule ($M = Z - 18$) holds for the half-Heuslers. This implies that the total magnetic moment per unit cell is an integer value for both classes of systems.

The formal definition of half-metallicity is only valid if it is assumed that the spin of the electron is a good quantum number. This implies that the spin of the electron is a conserved quantity and it requires that spin-orbit interactions can be safely neglected, because due to spin-orbit coupling, the spin-up electrons in the energy range of the half-metallic gap would also have a partial spin-down character. If spin-orbit coupling is small, the resulting spin-down DOS in the gap is small and forms only a weak reflection of the spin-up DOS [172, 173].

On the other hand, finite temperature leads to loss of spin polarization and at the critical temperature of the ferromagnetic-paramagnetic phase transition the polarization vanishes completely together with the net magnetization. At finite temperatures electrons can be excited to occupy states above the gap. This occurs at higher temperatures where the thermal energy becomes comparable to the gap width. But other mechanisms that arise at small temperatures can already lead to loss of polarization. These mechanisms are closely related to magnetic excitations like spin-waves which are already present at low temperatures because the ferromagnetic phase represents a phase of spontaneously broken symmetry and therefore exhibits Goldstone modes [174].

Composition	Magnetic order	a (Å)	c/a	$\mu_{\mathrm{tot}}\,(\mu_{\mathrm{B}})$	$T_{\mathrm{C}}(K)$	$T_{\mathrm{C,exp}}(K)$
Co_2FeAl	FM	5.70	1	5.09	1050	-
Co_2FeSi	FM	5.63	1	5.48	750	1100
(FeCo)FeAl	FM	5.71	1	5.16	790	-
(FeCo)FeSi	FM	5.61	1	5.02	790	-
Co_2MnAl	FM	5.70	1	4.11	480	697
Co_2MnSi	FM	5.63	1	5.02	755	985
Fe_2MnAl	AF	5.68	1	1.99	50	-
Fe_2MnSi	FM	5.59	1	2.99	100	220
(MnFe)MnAl	AF	5.76	1	1.00	140	-
(MnFe)MnSi	AF	5.61	1	1.98	100	-
(MnCo)MnAl	AF	5.74	1	1.99	550	720
(MnCo)MnSi	AF	5.63	1	3.00	270	-

Table 7.1: Lattice parameters and magnetic order of all half-metallic Heusler systems under consideration in this chapter. The results are obtained from VASP (GGA) calculations. In addition, the critical temperatures of the $L2_1$ structure obtained from MC simulations are listed.

An investigation of the thermal collapse of the spin polarization can be approached in two different ways. The first one relies on the fact that the characteristic timescale of magnetic excitations is much longer than the timescales of the electron motion. Therefore, an adiabatic approximation, which decouples the correlation between the magnetic excitation and the electron motion, is justified. This assumption gives the possibility to calculate the electronic structure in a system, which is disturbed by a frozen magnon, self-consistently. In this sense a frozen magnon means that an external constraint enforces the formation of a non-conllinear state which represents a magnon of a certain wavelength. In addition, the influence of short range fluctuations of the magnetization can be studied within the DLM theory. A combination of these approaches has been discussed in Ref. [175] and leads to the result that a non-collinear state of small enough wavelength destroys the hybridizations which are relevant for the formation of the half-metallic gap, and therefore the polarization collapses.

A second approach within the framework of dynamical mean-field theory (DMFT) [176] is carried out in Ref. [177]. This approach leads to the prediction of excitations which are superpositions of spin-up electron states, spin-down electron states and magnons within the gap which are called non-quasiparticle states. They result from dynamic electron-magnon interactions introduced by electron correlations and occur at the edges of the valence and the conduction band. Both approaches clearly show that there are a variety of mechanisms that can destroy half-metallicity at finite temperatures.

How strong temperature affects the gap depends on material specific properties. It can be stated that if E_{F} is directly located at the valence band edge, finite temperature will lead to an immediate loss of polarization because of the non-quasiparticle states. If E_{F} is directly located at the conduction band edge, the polarization gets lost because the minority states in the conduction band are immediately populated at finite temperatures because the excitation

Composition	μ_X (μ_B)	μ_Y (μ_B)	μ_Z (μ_B)
Co_2FeAl	1.18 [1.18] (1.15)	2.77 [3.02] (2.64)	-0.03 [-0.06] (-0.11)
Co_2FeSi	1.34 [1.47] (1.22)	2.81 [3.18] (2.76)	0.01 [0.01] (-0.03)
(FeCo)(FeAl)	(1) 1.60 [2.56] (1.62) (2) 2.56 [2.85] (2.46)	1.04 [1.41] (1.06)	-0.05 [-0.08] (-0.12)
(FeCo)(FeSi)	(1) 1.37 [1.88] (1.67) (2) 2.66 [2.88] (2.68)	1.00 [1.12] (0.92)	-0.01 [-0.03] (-0.07)
Co_2MnAl	0.73 [0.72] (0.76)	2.70 [3.39] (2.67)	-0.04 [-0.07] (-0.13)
Co_2MnSi	1.02 [0.91] (1.00)	2.99 [3.40] (3.03)	-0.01 [-0.03] (-0.07)
Fe_2MnAl	-0.18 (-0.10)	2.36 (2.27)	-0.01 (-0.03)
Fe_2MnSi	0.23 (0.16)	2.54 (2.64)	-0.01 (-0.02)
(MnFe)(MnAl)	(1) -1.77 (-1.44) (2) 0.10 (2.230.35)	2.66 (0.35)	0.01 (-0.05)
(MnFe)(MnSi)	(1) -0.77 (-0.69) (2) 0.35 (2.40)	2.38 (0.27)	0.01 (-0.01)
(MnCo)(MnAl)	(1) -1.56 (-1.28) (2) 2.64 (2.44)	0.96 (0.91)	0.01 (-0.07)
(MnCo)(MnSi)	(1) -0.55 (-0.49) (2) 2.65 (2.62)	0.84 (0.79)	0.01 (-0.01)

Table 7.2: Comparison of the magnetic moments of the different Heusler systems. The moments without brackets are taken from VASP and calculated by using PBE-GGA, those in square brackets are obtained in GGA+U calculations and those in round brackets are taken from SPR-KKR using LDA of VWN. For the conventional Heusler system the positions of the X elements are equivalent and therefore the magnetic moments are equal.

energy needed for this occupation is arbitrarily small. Therefore, HMF materials where the Fermi energy lies somewhere in the middle of the gap are searched [178] because they are most robust against disturbing temperature influence.

Although all effects mentioned above tend to reduce the polarization at E_F and therefore destroy the unique character of a half-metal, some properties deviate considerably enough from those of other materials to justify the introduction of this new material class. One example is the giant TMR ratio that is found in Co_2MnSi/Al-O/Co_2MnSi which can be directly attributed to high polarization at the Fermi level [179].

A serious drawback arises in experimental investigations of half-metals because no distinct property can be determined which decides definitively if a material is half-metallic or not. There is only one almost direct but very expensive method which measures the half-metallic gap. This method is the spin-resolved positron annihilation spectroscopy [180, 181]. Other spin-resolved photo emission spectroscopy experiments are less helpful because they do not probe the bulk but more the surface character. But the electronic structure at the surface can be completely different from that of the bulk and therefore does not necessarily show a gap.

Composition	$L2_1$	B2	A2
Co_2FeAl	1050	840	890
Co_2FeSi	750	700	750

Table 7.3: Critical temperatures of Co_2FeAl and Co_2FeSi for the various types of order.

As half-metallicity is an intrinsic property of a certain material it cannot be identified with the possibility to extract a 100% spin-polarized current from these material. This requires the injection of electrons into a material in which the polarization can be analyzed. But this involves the crossing of a surface or interface. As a consequence, the measured degree of polarization is influenced by the surface or interface and therefore by non-intrinsic properties because the details of the texture of the surface and interface are very important. The effects introduced by interfaces have been studied in detail for half-metallic half-Heusler and full-Heuslers in Refs. [182, 183, 184] and references therein.

Full-Heusler alloys are of special interest in the context of half-metallicity because they often show very high Curie temperatures. This is the main advantage of Heusler alloys compared to other half-metallic system such as CrO_2 or alloys with heavy elements like lanthanides. High Curie temperatures are needed, because ferromagnetism should remain up to technical working temperatures and, in addition, all depolarization effects scale with the reduced temperature T/T_C [7]. Another advantage is the structural similarity to the zinc-blende structure because many technological relevant binary semi-conducturs crystalize in this structure and are therefore epitactically well combinable [169].

Besides the ferromagnetic half-metals also antiferromagnetic half-metals have already been discussed in literature (the very first considerations of such materials are discussed in Ref. [16]). Half-metallic antiferromagnets are very interesting for spintronics applications. Such materials exhibit a 100% polarization at the Fermi level without showing a net magnetization and therefore no magnetic stray fields which is often unfavorable in applications [185]. Following the Slater-Pauling rule, a half-metallic antiferromagnet can be found if the number of valence electrons is exactly 18 in half-Heuslers and 24 in full-Heuslers [186].

In the following sections full-Heusler alloys based on Mn, Fe, and Co are investigated in detail. This means that the X and Y elements are always represented by one of these three $3d$-transition metals. For the Z element Al and Si are chosen. Structural, electronic and magnetic properties are evaluated. Different degrees of disorder and its effect onto the half-metallic gap is considered. In particular, it is investigated how the properties of the binary alloys of Mn, Fe, and Co discussed in the preceding chapters change when the main group element is added and the systems becomes a Heusler compound.

7.3 Co_2FeAl and Co_2FeSi

In this section the cobalt-iron based Heusler alloys Co_2FeAl and Co_2FeSi are investigated and their properties are compared. Since these alloys have already been investigated by various authors, a comprehensive overview of the properties obtained in previous work is given.

Cobalt-iron Heusler alloys are of special interest because they exhibit large magnetic moments as well as high Curie temperatures. The same properties are already known from their binary counterparts (see Chapter 5). This means that Co-Fe based Heusler alloys keep

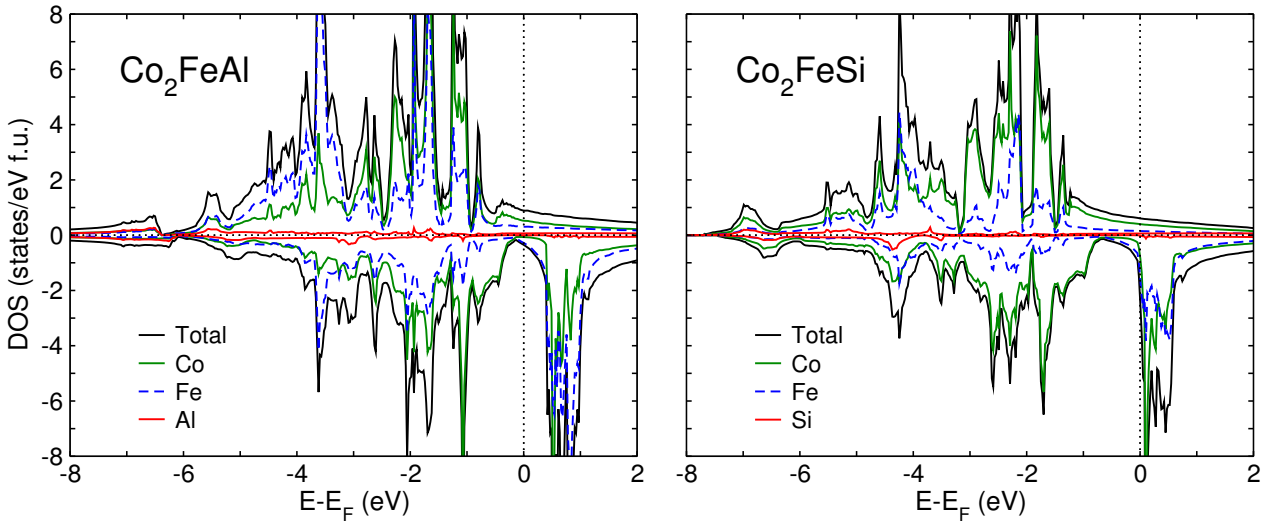

Figure 7.3: Comparison of the calculated electronic densities of states of Co_2FeAl and Co_2FeSi obtained from VASP (GGA). The lattice constant of Co_2FeAl is 5.70 Å and that of Co_2FeSi is 5.63 Å. This comparison shows that GGA leads to a much better description of the half-metallic feature of Co_2FeAl as compared to Co_2FeSi.

the strong ferromagnetic properties of $Fe_{1-x}Co_x$ alloys although 25% of a non-magnetic main group element is added. The strong magnetic properties are of special interest for applications of half-metallic ferromagnets (HMF) at room or more elevated temperatures.

Co_2FeAl and Co_2FeSi have already been considered in transport experiments and are found to show interesting magnetoresistive behavior (see, e.g., Refs. [187, 188]). Other, experimental as well as theoretical investigations have shown that Co_2FeAl and Co_2FeSi reveal the expected integer values of the total magnetic moment per unit cell corresponding to the predicted Slater-Pauling behavior [171]. In addition, the Curie temperatures are found to be very high [11, 189].

Theoretical investigations of Co_2FeSi show that on-site correlations effects of the d-electrons have an essential impact on the description of their electronic structure [190, 191]. If neglected, the expected magnetic moment of $6\mu_B$ is not reproduced and in addition no distinct gap in the minority spin channel at the Fermi energy is found. Therefore, the LDA+U or GGA+U methods have to be employed to account for electronic correlation effects. This leads to a remarkable improvement and a clear gap in the minority DOS as well as the integer value of the magnetic moment is obtained.

The theoretical description of Co_2FeAl is already very good within the standard LDA and GGA. As shown in Ref. [189], the magnetic moment calculated within the framework of KKR is close to $5\mu_B$ and the Fermi energy is located in a minimum of the density of states of the minority spin channel. Although, this minimum is no real gap because a small DOS is still remaining, the description within LDA and GGA is much better compared to results obtained for Co_2FeSi where the Fermi energy is located at a shoulder of a high peak. In Ref. [192], Co_2FeAl is analyzed with the FLAPW method and is found to show a perfect gap at the Fermi energy even without employing the GGA+U method.

The authors of Ref. [178] present a theoretical investigation of $Co_2FeAl_{1-x}Si_x$ over the whole

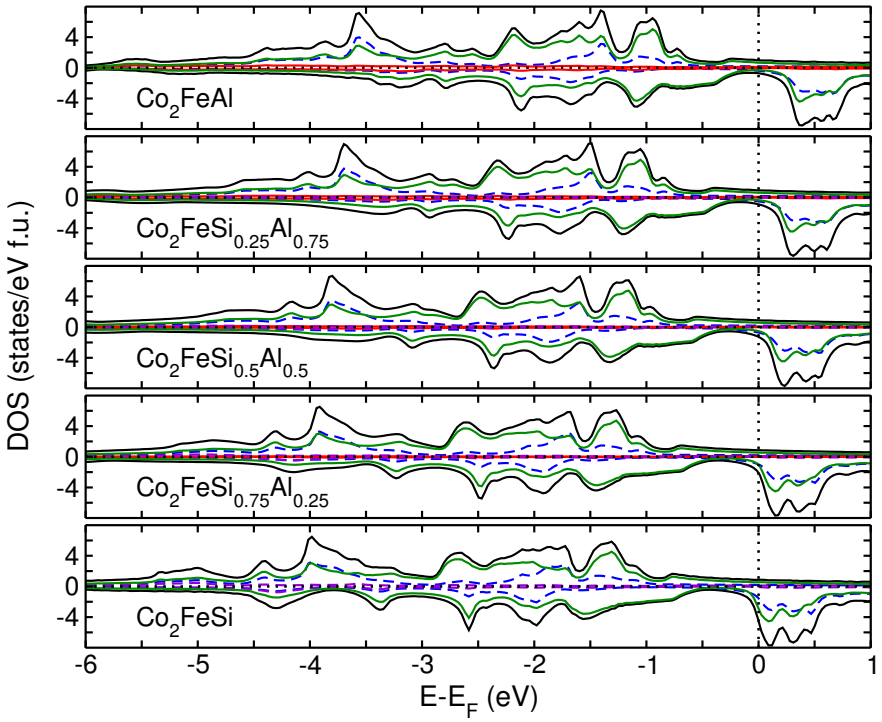

Figure 7.4: Electronic densities of states of $Co_2FeAl_{1-x}Si_x$ alloys. These results are obtained from CPA calculations. The black lines represent the total densities, the green and blue ones the Co and Fe resolved DOS respectively. Red and violet lines correspond to Al and Si.

range of composition. Within this work the band structure of Co_2FeAl calculated with GGA and LDA+U is compared. It is found that within the GGA one minority conduction band touches the Fermi energy but within the LDA+U one reproduces a perfect HMF behavior because the conduction band of the minority channel is shifted to higher energies. In calculations of $Co_2FeAl_{1-x}Si_x$ with different compositions, the U is chosen to have the same value independent of the Si concentration. A perfect HMF DOS is found for all concentrations and the Fermi energy is continuously shifted from the edge of the valence band in the minority channel in Co_2FeAl to the edge of the conduction band in Co_2FeSi. This is why the authors of Ref. [178] conclude that the $x = 0.5$ composition is ideal because in this system the Fermi energy is located in the middle of the gap. As discussed in the introduction this leads to a stronger temperature resistance of half-metallicity.

In the following, calculations of electronic densities of states, magnetic exchange parameters and corresponding predictions of the critical temperatures of the $Co_2FeAl_{1-x}Si_x$ systems are presented. In the discussion of the DOS, special attention is paid to the decomposition into states of t_{2g} and e_g symmetry to compare the results with the explanation of origin of the gap given in Ref. [171] as discussed above.

At first it should be mentioned, that the total energy calculations for Co_2FeAl and Co_2FeSi reveal that the conventional Heusler structure is energetically preferred compared to the inverse one. The large energy differences between conventional and inverse structure of about 696meV/f.u. in Co_2FeAl and 580meV/f.u. in Co_2FeSi indicate a strong ordering tendency in favor of the $L2_1$ structure. It is remarkable that the calculated lattice constant of Co_2FeAl of $a_0 = 5.70\,\text{Å}$ is the same in the conventional as in the inverse structure but the lattice

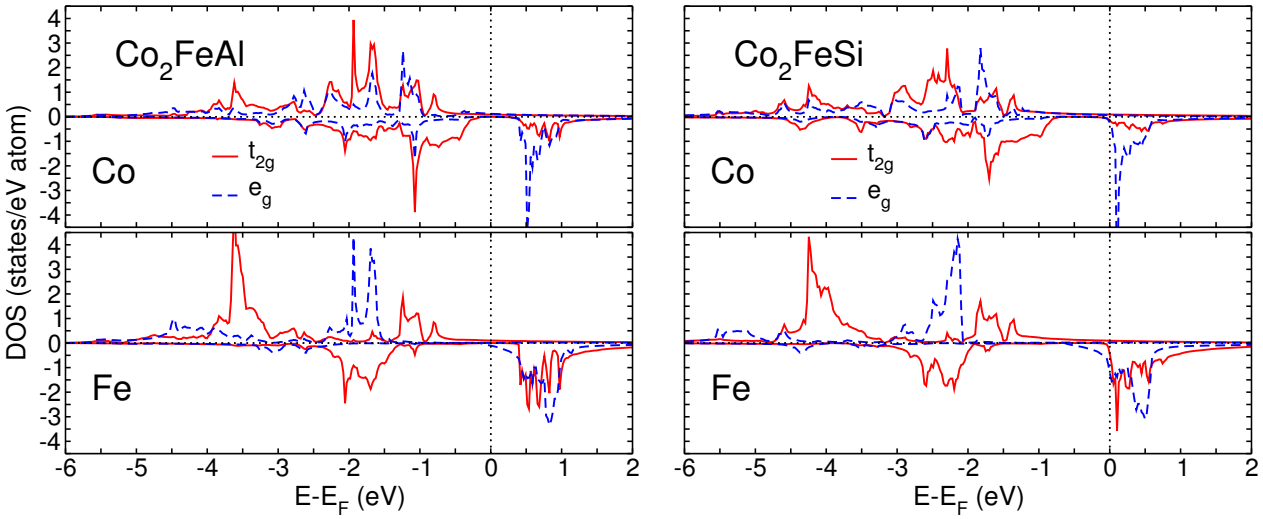

(a) (b)

Figure 7.5: Symmetry resolved DOS of Co_2FeAl and Co_2FeSi obtained from VASP (GGA). Here, only the states with Co and Fe character are plotted.

constant of Co_2FeSi changes from $a_0 = 5.63\,\text{Å}$ in the conventional to $a_0 = 5.58\,\text{Å}$ in the inverse structure.

The structural and magnetic parameters of both systems are outlined in Table 7.1. The total magnetic moment per unit cell obtained from the calculation of Co_2FeAl ($5.09\,\mu_B$) is in good agreement with the expected integer value. The calculation of the magnetic moment of Co_2FeSi reveals $5.48\,\mu_B$ and therefore differs significantly from the expected value of $6.00\,\mu_B$. According to previous results reported above, it is concluded that the description of the expected half-metallic properties of the electronic structure of Co_2FeSi is deficient within GGA. This conclusion is reenforced by regarding the electronic density of states shown in Fig. 7.3. In Co_2FeAl the Fermi energy lies in a region where the minority spin channel shows a gap like dip with a small DOS. A similar dip occurs in the electronic density of states Co_2FeSi, but the Fermi energy is located at the shoulder of a high peak that should belong to the conduction band. The location of the Fermi energy in this region is the reason why the magnetic moment per unit cell is too small compared to the expected integer value. The conduction band is partially filled and the number of unpaired electrons is reduced, therefore, the magnetic moment is decreased. These conclusions have already been proposed in Ref. [190]. It should be noted here that only Fe states are responsible for the incomplete description of the gap because no Co or Al states are found in the gap region. Since the projection of the DOS onto element specific contributions can include minor errors, the total DOS of Co_2FeAl and Co_2FeSi are shown Fig. A.2 in Appendix A.12, but, no significant difference can be found.

In order to investigate the transition from the reasonable description of Co_2FeAl to a bad description of Co_2FeSi, CPA calculations of $Co_2FeAl_{1-x}Si_x$ systems are carried out for increasing x [1]. The results are shown in Fig. 7.4. It is obvious from the figure that the subsequent addition of Si results in an almost constant shift of energy that pushes E_F onto

[1] This is comparable to what is reported in Ref. [178] but here the simple LDA is used instead of the LDA+U in oder to see what changes lead to the deficient description of LDA at $x = 1$.

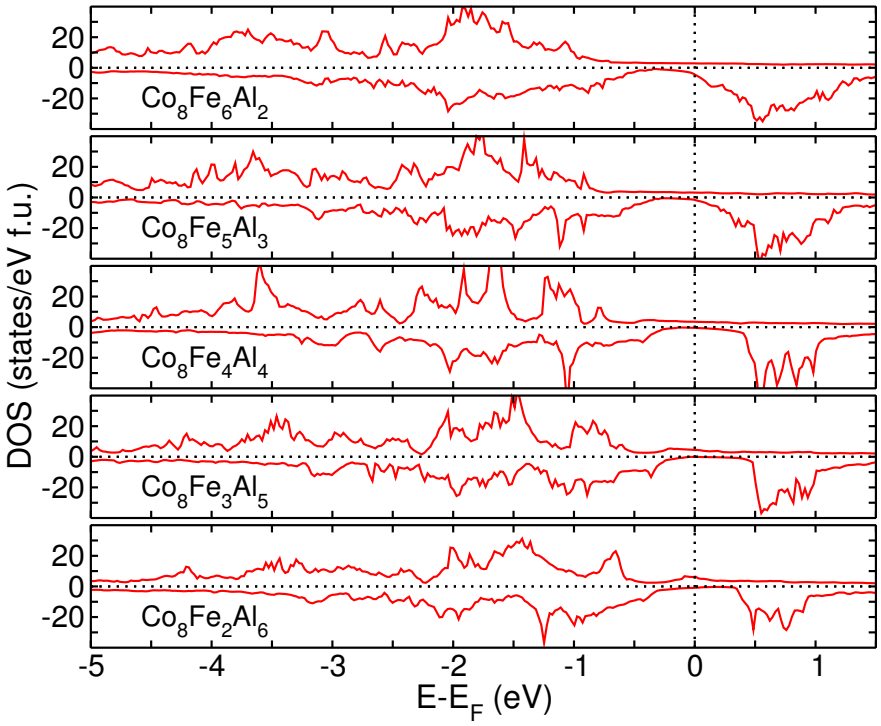

Figure 7.6: Total electronic densities of states of the $Co_8Fe_{6-x}Al_{2+x}$ systems. The results are obtained with VASP by employing a super-cell containing 16 atoms.

the shoulder of the conduction band. Therefore, one concludes that the necessary adaption of the band structure to the increasing number of valence electrons is not correctly captured. It results only in a constant shift of the Fermi energy and therefore in an occupation of states with larger energy. It needs to be noted that the CPA calculation is carried out at the mean lattice constant of Co_2FeAl and Co_2FeSi and is not changed with composition. But it can be checked that small deviations from the equilibrium lattice constant of around 0.035 Å do not introduce relevant changes of the electronic structure.

Figure 7.5(a) and (b) show the atom and symmetry resolved DOS of Co_2FeAl and Co_2FeSi. The Co associated DOS of Co_2FeAl exhibits the same features as shown in Figure 7.2. The Fermi energy lies in a gap between the t_{2g} states at the edge of the valence band and the e_g states at the edge of the conduction band. There is also a gap in the Fe DOS but here the Fermi energy is located at the edge of the anti-bondig states where the number of e_g states is already increasing. This leads to a small finite density at E_f. It is concluded that the situation predicted in Ref. [171] for the cobalt-manganese based Heusler is also found in Co_2FeAl. There are only some minor differences that prohibit the 100% polarization which are obviously connected to the lacking description of iron.

In the case of Co_2FeSi the symmetry resolved Co DOS shows a gap in the minority channel and E_F is located directly at the edge of the e_g peak of the conduction band of the Co states. The resolved Fe DOS uncovers the main reason why the description of Co_2FeSi is insufficient. The Fermi energy is exactly located on a peak in the e_g DOS. Therefore, it is concluded that in particular the description of d-states with e_g symmetry is incorrect within a standart GGA calculation. The important role of electronic correlation effects in iron and iron based alloys and clusters is extensively discussed in literature. A comprehensive overview of literature

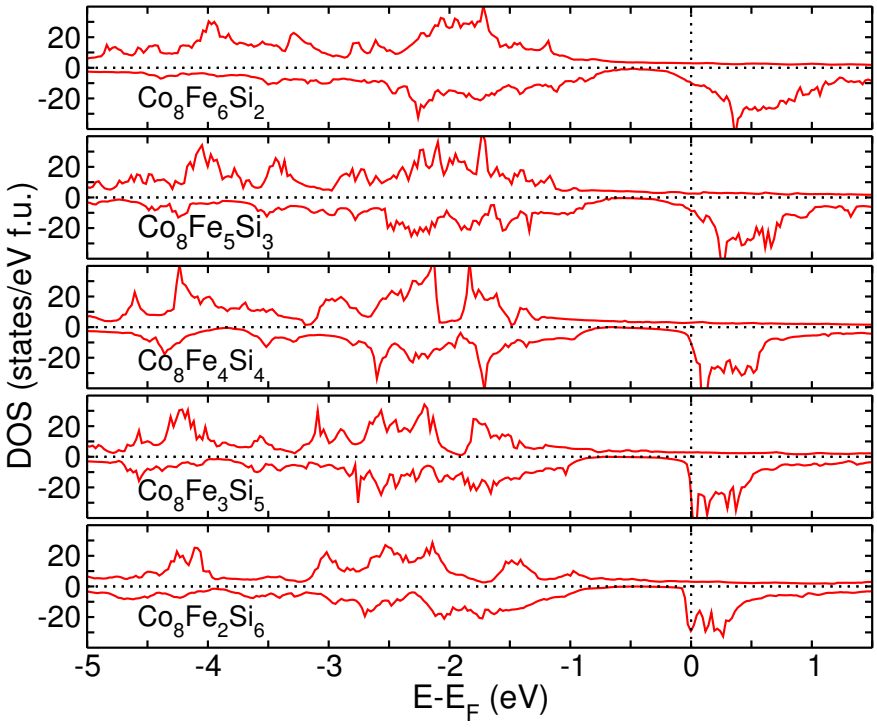

Figure 7.7: Total electronic densities of states of the $Co_8Fe_{6-x}Si_{2+x}$ systems. The results are obtained with VASP by employing a super-cell containing 16 atoms.

concerning the improvement of the description of the electronic structure of iron within the GGA+U method can be found in Ref. [193].

How this lack can be cured and the results may be improved by using the GGA+U scheme in the case of Co_2FeAl and Co_2FeSi is discussed below but, first, an investigation of the magnetic exchange parameters, the influence of disorder and deviations from the stoichiometric composition are discussed.

In order to investigate how deviations from the exact stoichometry of a Heusler system affect the half-metallic features in Co_2FeAl and Co_2FeSi, a super-cell approach is employed. The super-cell chosen here consists of 16 atoms where two of the sublattices are still occupied by Co but the other two are occupied by different amounts of Fe and Al or Si. The precise composition and the corresponding electronic DOS of all $Co_8Fe_{6-x}Al_{2+x}$ systems is shown in Fig. 7.6. Replacing Al by Fe leads to a shift of E_F to higher energies because more valence electrons are contributed by Fe. The gap like dip in the DOS in the vicinity of E_F is found in all investigated systems but is more pronounced on the Al rich side. It is concluded that additional Al affects the half-metallic gap less than additional Fe does. This is of course also connected to the neglected correlation effects introduced by iron. The overall conclusion that can be drawn from this result is that half-metallicity in Co_2FeAl is quiet stable against small changes of the composition in the Fe and Al sublattices.

The corresponding results of $Co_8Fe_{6-x}Si_{2+x}$ are shown in Fig. 7.7. On the Fe rich side the peak of the conduction band as it is present at the exact stoichiometric composition it less sharp and pushed to higher energies. With increasing Fe contend more and more states fill the gap. This is similar to the situation in iron rich $Co_8Fe_{6-x}Al_{2+x}$. On the Si rich side the peak of the conduction band gets sharper and E_F is moving to lower energies and for $Co_8Fe_2Al_6$,

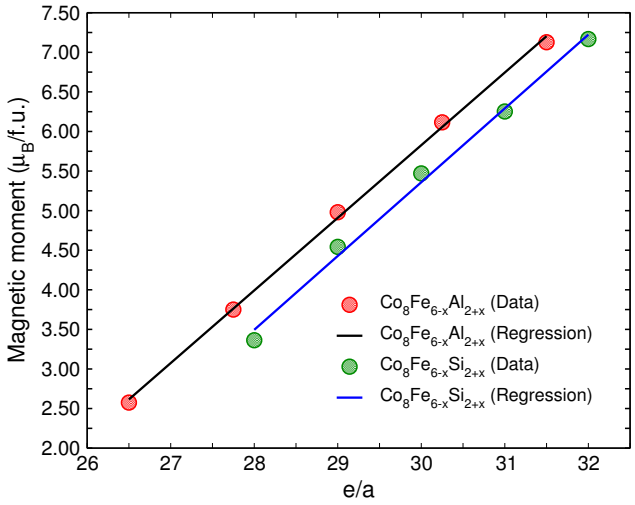

Figure 7.8: Magnetic moment versus valence electron concentration in $Co_8Fe_{6-x}Al_{2+x}$ and $Co_8Fe_{6-x}Si_{2+x}$.

the Fermi energy is exactly located on this peak. Although the gap is very pronounced on the Si rich side half-metallicity is not recovered because E_F is is located in the conduction band. Still, it is concluded that the gap feature is quite stable against compositional changes because the gap remains present over the whole composition range discussed here. It is interesting to note that lowering the valence electron concentration contributed by Fe leads to a more pronounced half-metallic gap in $Co_8Fe_{6-x}Al_{2+x}$ and $Co_8Fe_{6-x}Si_{2+x}$.

The dependence of the magnetic moment on the valence electron concentration of the $Co_8Fe_{6-x}Al_{2+x}$ and $Co_8Fe_{6-x}Si_{2+x}$ systems is shown in Fig. 7.8. The magnetic moments of $Co_8Fe_{6-x}Al_{2+x}$ follow an almost linear behavior whereas those of the $Co_8Fe_{6-x}Si_{2+x}$ are a bit more spread around the corresponding linear regression. This result shows that the Slater-Pauling behavior is also found if the composition is changed.

In the following, disorder and its effects on the DOS and in particular on the magnetic exchange interactions are investigated. The calculated magnetic exchange parameters of $L2_1$ ordered Co_2FeAl are shown in Fig. 7.9(a). The MC simulation reveals a critical temperature of 1050 K. Unfortunately, no exact experimental value of the critical temperature is known. The measurement is difficult because a structural phase transition from the ordered $L2_1$ structure to a disordered B2 or totally disordered A2 structure occurs at high temperatures [187]. As the order-disorder transition is accompanied with the transition from the ferromagnetic to the paramagnetic phase, the features of these transitions cannot be distinguished.

In Ref. [189], where $Co_2Mn_{1-x}Fe_xAl$ alloys in the disordered B2 structure are investigated, two types of phase transitions were found by applying the differential scanning calorimetry method. Only one of these transitions is found during heating and cooling of the sample. The other is supposed to be irreversible because it only occurs in the heating procedure. The authors carefully conclude that the irreversible transition is connected with a structural transition and the reversible with the transition between the ferromagnetic and the paramagnetic phase. For alloys with $x < 0.4$ the magnetic transition takes place before the disorder transition comes up. But for higher values of x both transition switch order and the structure transforms before the Curie temperature is reached. Therefore, the critical temperature of

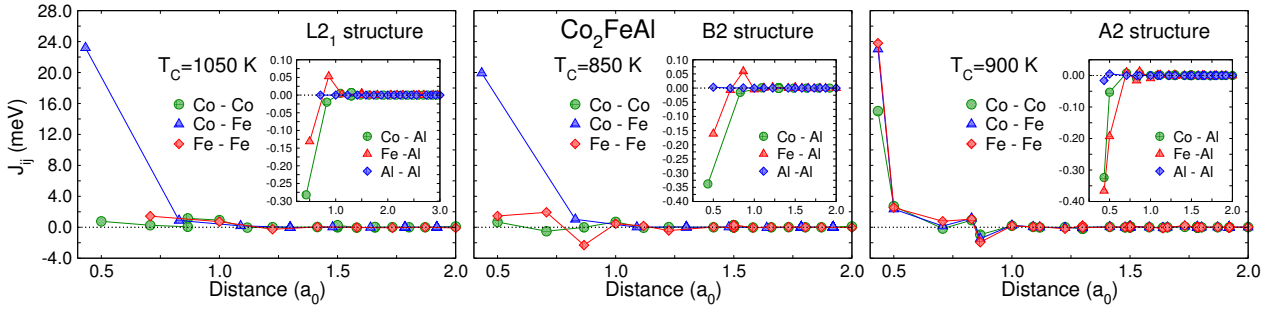

(a) (b) (c)

Figure 7.9: Magnetic exchange parameters J_{ij} of the Co_2FeAl alloy. The first picture shows the interactions in the ordered $L2_1$ structure. The second one corresponds to the B2 type of disorder and the third one to the complete disordered A2 structure.

$L2_1$ ordered Co_2FeAl cannot be determined. But the experiments give evidence that the critical temperature of Co_2FeAl is around 1180 K but the structural phase at that temperature is not determined.

In order to study how the disorder affects magnetism and especially the critical temperature, exchange parameters and critical temperatures of the B2 structure where the Fe and Al sublattices mix and the totally disordered A2 structure where all sublattices mix, are calculated. The exchange parameters of the different structures are compared in Fig. 7.9. Obviously, the Co-Fe coupling plays the most important role in Co_2FeAl because it is always large. This is comparable to what is observed in the Fe_xCo_{1-x} alloys. The Co-Fe coupling is the strongest coupling if only Co and Fe atoms are nearest neighbors as in the case of $L2_1$ and B2 structures. If, in addition, the Co atoms can have Co nearest neighbors and the Fe atoms Fe nearest neighbors, there is also strong coupling between these pairs. This is the case in the totally disordered A2 structure. The exchange interactions between the Al atoms and all other atoms are very small. This coupling is alway antiferromagnetic and thus the induced moment of the Al atoms is always antiparallel aligned to all other atoms.

The critical temperatures of the three structures vary in a range of 200 K. The $L2_1$ structure

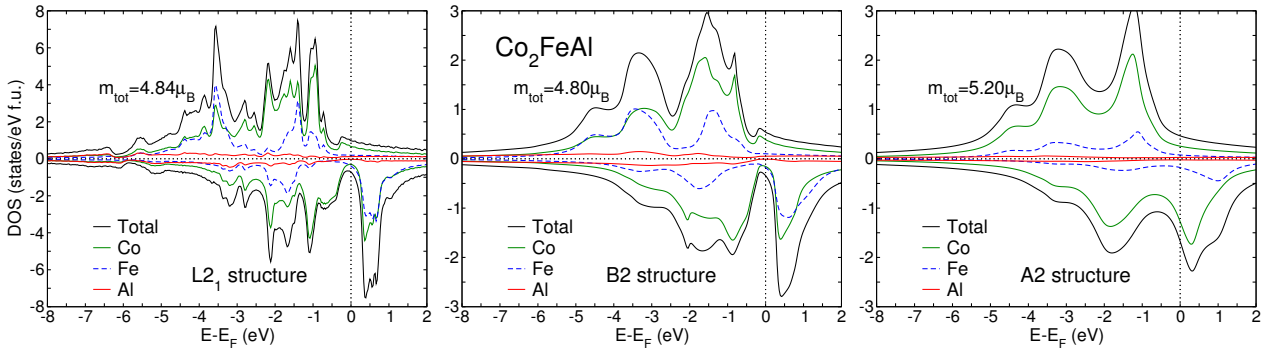

(a) (b) (c)

Figure 7.10: Electronic density of states of the Co_2FeAl Heusler alloy. Figure (a) shows the DOS of the ordered $L2_1$ structure. (b) corresponds to the B2 type of disorder and (c) to the complete disordered A2 structure.

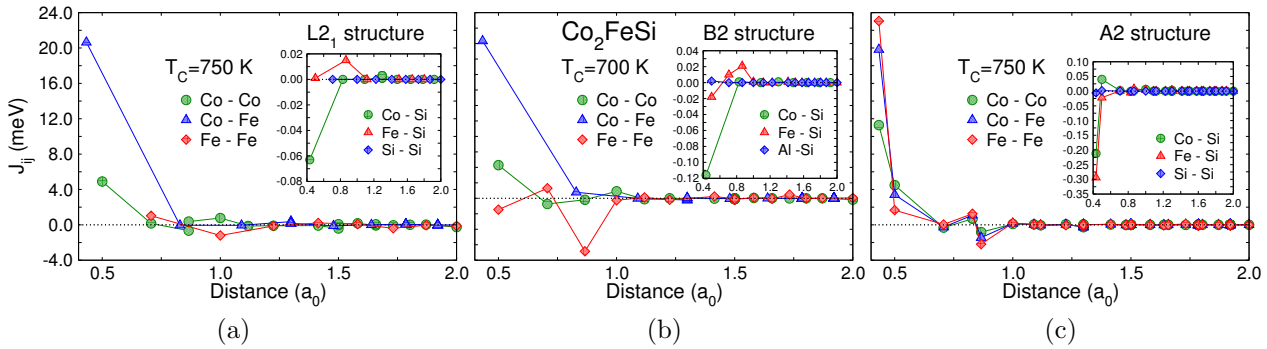

Figure 7.11: Magnetic exchange parameters J_{ij} of the Co_2FeSi Heusler alloy. Figure (a) shows the ordered $L2_1$ structure. (b) corresponds to the B2 type of disorder and (c) to the full A2 disorder.

shows the highest critical temperature. The critical temperature of the B2 structure is 200 K smaller. Two different reasons have to be discussed to understand this decrease of the temperature. First, the exchange parameters of the B2 structure are reduced. This reduction occurs because in the CPA description subsequent Co layers are now separated by a homogeneous Fe-Al layer and therefore the indirect exchange between the Co atoms which is mediated by the Fe atoms, is decreased because there is no pure iron site. Indirect exchange means here that two Co layers interact strongly with the iron atoms in between and are therefore indirectly coupled. A second effect occurs in a certain realization of the the disordered structure in the MC simulation. There is a finite probability that regions exist where many Al atoms are closely together in the Fe-Al layer. This results in a sort of cut between the magnetic interaction which is mainly carried by the Co and Fe atoms. Therefore, an accumulation of Al atoms in a layer leads to a local decoupling of the Co layers because indirect Co-Co coupling via the Fe atoms is locally suppressed. As the probability that such a situation leads to a decoupling of large regions is very small, the critical temperature is not dramatically reduced.

Since Al atoms can occupy every sublattice in the A2 structure and the Co atoms do not form layers, the decoupling mentioned for the B2 structure is impossible. Now, every atom is always surrounded by eight nearest neighbors which all have partial Co as well as Fe character. The magnetic exchange parameters between Co and Fe are of comparable size as in the $L2_1$ structure and the critical temperature is 50 K larger compared with the B2 structure. Due to disorder, the critical temperature is smaller compared to that of the $L2_1$ structure. A more detailed discussion of how disorder affects the magnetic phase transition is given in Section 5.2 where Fe_3Co is discussed for various structures. This discussion can be directly transferred to the case of Co and Fe based Heusler alloys.

It should be noted that as the critical temperature of the $L2_1$ structure is the largest and as the experimental estimate is around 1180 K but for a structurally disordered sample the critical temperature is most probably underestimated by more the 130 K (which is the difference between the experimental estimate and the T_C obtained for the $L2_1$ structure).

The electronic DOS of the $L2_1$, B2 and A2 structure calculated within the KKR formalism are shown in Fig. 7.10. A precise look at the DOS of the $L2_1$ structure reveals that the ASA-KKR formalism gives a quiet bad description of the gap in the minority channel but still a qualitative correspondence to the VASP calculation is found. The DOS of the B2

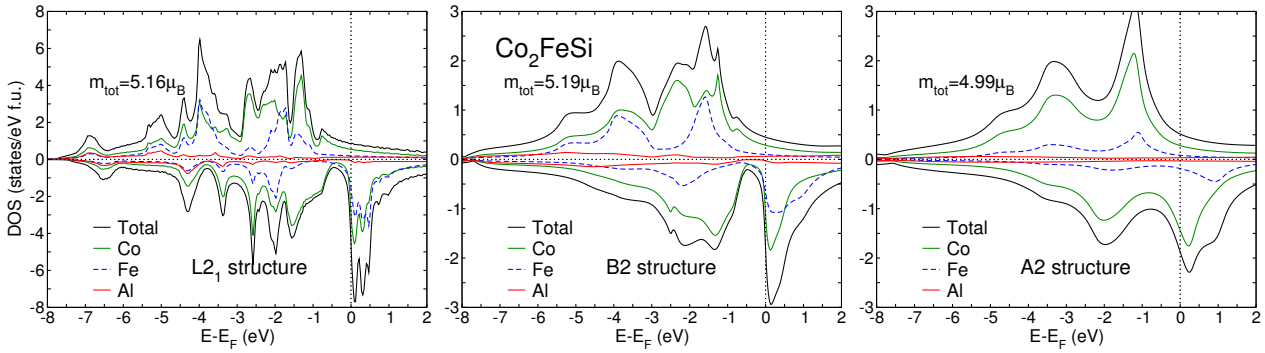

Figure 7.12: Electronic density of states of the Co_2FeSi Heusler alloy. Figure (a) shows the ordered $L2_1$ structure. (b) corresponds to the B2 type of disorder and (c) to the complete A2 type.

system is much more smeared out compared to the $L2_1$ one, but, a deep minimum of the minority channel around the Fermi energy remains. Therefore, it is carefully concluded that B2 disorder does not necessarily destroy the half-metallicity of Co_2FeAl. Regarding the DOS of the A2 structure which is shown in Fig. 7.10(c), it becomes obvious that the occurrence of full disorder destroys all features of half-metallicity. This can be understood from the explanation of the origin of the gap as it is given in the introduction above. As the Co atoms are no longer occupying a simple cubic lattice in the A2 disorder, the formation of the Co *d*-band does not follow the scheme given in Fig. 7.2(a). Therefore, the Co states do not vanish around the Fermi energy.

In order to give an estimate of the transition temperature from the ordered $L2_1$ to the partially disordered B2 phase, the energy of both phases is calculated very accurately within the KKR framework. The difference of these energies is 0.1307eV/atom and therefore reveals a transition temperature of 1516 K. A large error is included because the lattice constant is kept fixed, and therefore effects of thermal expansion are disregarded. Although this estimation is rough, the resulting transition temperature is of the same order of magnitude as the experimental value. Unfortunately, the same method employed for the transition temperature of a possible transition from B2 to the A2 phase gives a completely unrealistic value of more than 12000 K. These results allow the careful conclusion that in a realistic temperature range only an order-disorder transition from the $L2_1$ to the B2 structure can occur. A subsequent transition to A2 disorder is hindered by a large energy barrier that corresponds to temperatures larger than the melting temperature of the Heusler. A more detailed investigation of the development of disorder at high temperatures should include the calculation of displacement energies for the different atoms in different environments but this is beyond the scope of the present analysis.

The same investigation carried out for Co_2FeAl is now presented for Co_2FeSi. Figure 7.11 shows the magnetic exchange parameters of the three different types of order. The determination of the critical temperature of Co_2FeSi with $L2_1$ order shows a significant deviation from experiment. The predicted critical temperature is 750 K whereas the experimentally known value is 1100 K. This shows that the descriptions of the magnetic exchange mechanisms in Co_2FeSi is not accurate. This can be attributed to the inaccurate description of the electronic structure if the influence of on-site correlation effects is neglected. For example, as

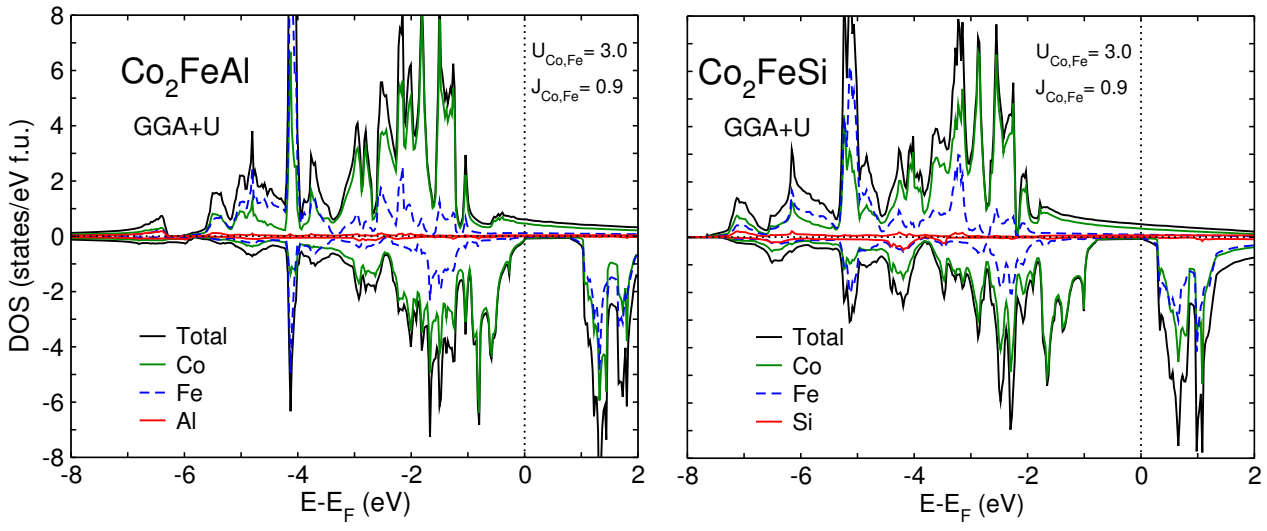

Figure 7.13: Comparison of the electronic densities of states calculated with VASP and the GGA+U formalism. In the GGA+U calculations the lattice constants reveal almost no changes. The GGA lattice constant of Co_2FeAl is 5.70 Å and 5.71 Å for GGA+U. In the case of Co_2FeSi the GGA lattice constant is 5.63 Å and the GGA+U lattice constant is 5.65 Å. The values for U and J are taken from [191].

the deficient description of the electronic structure leads to a reduction of the magnetic moments, this immediately results in reduced exchange parameters. Apart from the quantitative results, the qualitative description is reasonable if it is compared with the results of Co_2FeAl and the binary iron-cobalt systems because, e.g., the dominating Co-Fe interaction is also found here. But the interactions are simply to small to allow a higher critical temperature. Interestingly, disorder seems to have a very small influence on the critical temperature. This is similar to the situation found for Co_2FeAl but here it is even more pronounced because T_C varies only in a range of 50 K. This can be explained by considering that the strong Co-Fe interaction remain almost completely unaffected by the disorder. On the other hand a much stronger Co-Co interaction is found in all types of Co_2FeSi systems compared to Co_2FeAl. Therefore, the indirect exchange interaction of Co mediated by Fe is less important here. The smaller T_C in the B2 structure can be explained by the antiferromagnetic interactions of the Fe atoms which competes with the other ferromagnetic interactions.

The electronic DOS of $L2_1$, B2 and A2 structured Co_2FeSi is shown in Fig. 7.12. The trends found here are comparable to those found in Co_2FeAl. The DOS of the disordered structure of both compositions are of almost the same shape although, as already mentioned, the location of the Fermi energy is not correct. But it is remarkable that even in the B2 structure the Fermi energy is located at the shoulder of a peak in the conduction band as it is found in the $L2_1$ structure. This gives additional evidence that B2 disorder does not relevantly change the mechanisms which are responsible for the occurrence of half-metallicity.

As mentioned above, a short discussion of the influence of on-site correlation effects is given now. The employment of the GGA+U method with the U values given in Ref. [191] leads to an improved description of the electronic structure of Co_2FeAl and Co_2FeSi. Regarding the DOS obtained from such calculations (see Fig. 7.13), one finds that the Fermi energy lies in a

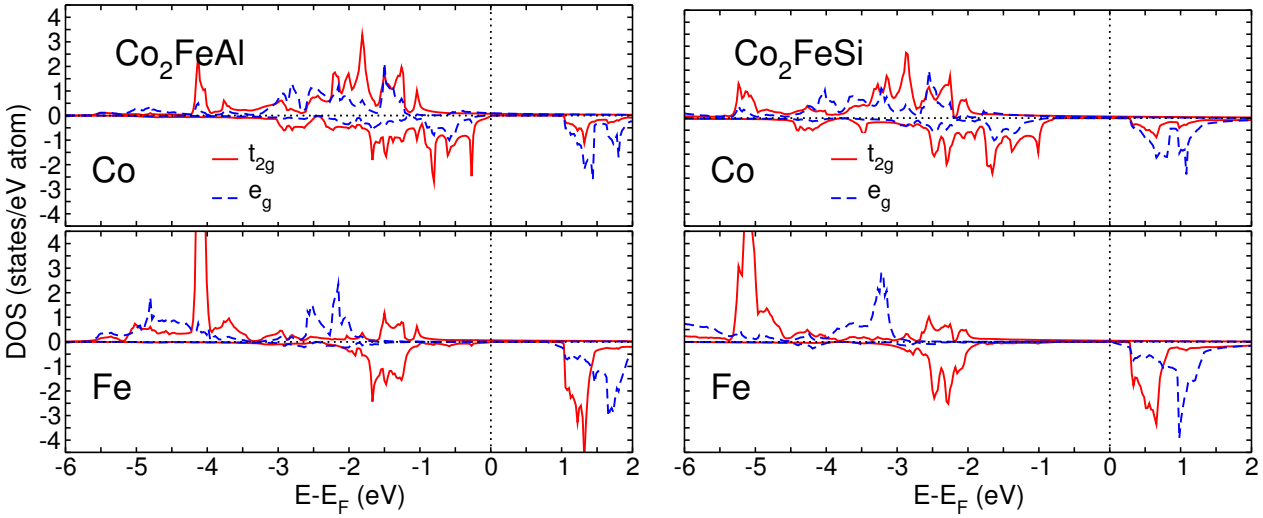

Figure 7.14: Symmetry resolved DOS of Co_2FeAl and Co_2FeSi obtained by employing the GGA+U method.

perfect gap in the minority spin channel. The result for the total magnetic moment in Co_2FeSi is also improved but for Co_2FeAl it is worse compared to GGA without the U (see Table 7.2) which shows that the value of U is not easily transferable between Co_2FeAl and Co_2FeSi. The Fermi energy is now located at the upper edge of the valence band of the minority spin channel in Co_2FeAl and at the lower edge of the conduction band for Co_2FeSi. In both cases the conduction band of the minority channel is pushed to higher energy values and therefore the gap region is broadened. Note, that a main effect of the inclusion of correlation effects is that the iron states are pushed out of the gap.

Obviously the GGA+U calculations can lead to perfect half-metallic gaps in Co_2FeAl and Co_2FeSi but this method has the drawback that U values which are suitable for a particular system are not necessarily transferable to other systems even in the case of two very similar systems. For example, the U values taken from Ref. [191] which are designed for Co_2FeSi lead to larger deviations of the magnetic moment from the expected integer value in Co_2FeAl compared to standard GGA calculations. This shows that even small changes in the composition (in the case here there is only a difference of one valence electron per formula) need an adjustment of the U values. In addition, the U value is designed to improve the half-metallic behavior and the influence onto other electronic features remains neglected. These are the drawbacks of the LDA+U and GGA+U method.

In Fig. 7.14, the symmetry resolved density of states are shown for both systems. It should be noted that in comparison to Fig. 7.5, the e_g states of iron in the Co_2FeSi are pushed out of the gap. This means that the lacking description of the e_g states of iron is improved by the GGA+U method. Therefore, the GGA+U calculations definitively show that correlation effects have to be necessarily included to get a more realistic description of certain Fe states. This is exactly what can be learned from such calculations, no matter what other difficulties are additionally introduced by the method.

In summary: In the case of Co_2FeAl and Co_2FeSi the GGA+U method does not give perfect results and leaves open questions but it shows the importance of correlations effects introduced by iron and in addition gives a quantitative estimate of the corresponding energy.

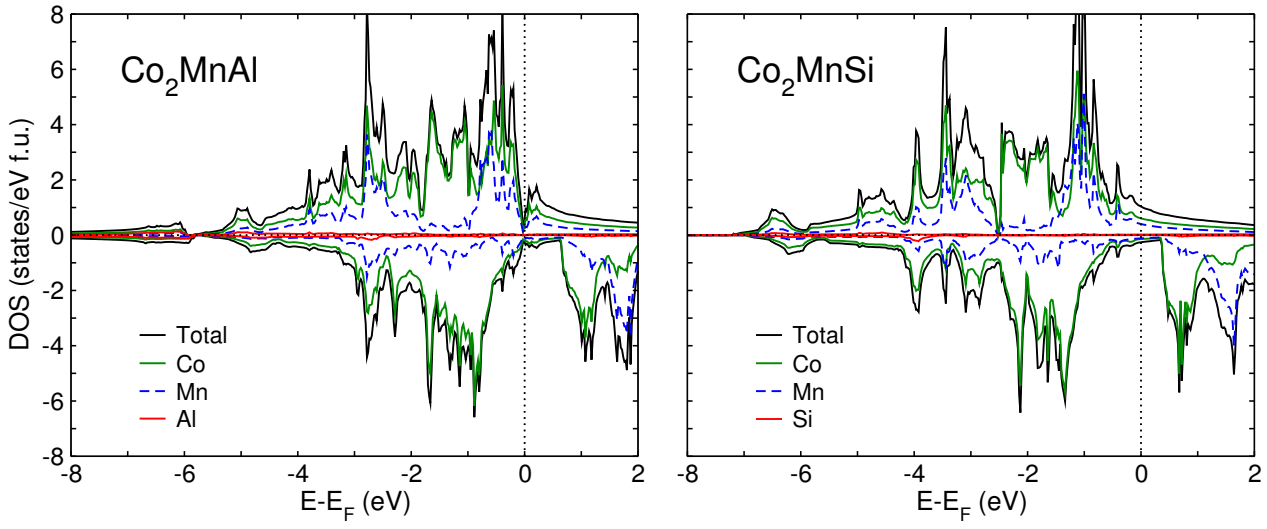

(a) (b)

Figure 7.15: Comparison of the electronic densities of states of Co_2MnAl and Co_2MnSi calculated with VASP (GGA).

7.4 Co_2MnAl and Co_2MnSi

In this section the systems Co_2MnAl and Co_2MnSi are investigated. At first the basic features known from literature are reviewed and afterwards a study similar to the one carried out for Co_2FeAl and Co_2FeSi is presented.

It is known from experiment that Co_2MnSi crystallizes in the $L2_1$ structure [194]. In addition, it is theoretically predicted that within this structure a half-metallic gap is present in the minority density of states [195]. A more detailed experimental investigation of the structure of Co_2MnSi reveals that a certain amount of disorder is always present. The authors of Ref. [196] state that Mn and Co atoms can easily mix because they are electronically similar and also of similar size. The Co_2MnSi Heusler used in magneto-tunnel junctions leads to large TMR ratios [197]. From this results, the conclusion is drawn that half-metallic properties of Co_2MnSi can be of technological use.

The effect of correlation on the electronic structure of Co_2MnSi is also investigated theoretically in Ref. [190] by employing the LDA+U method. It is found that inclusion of correlation effects via the LDA+U method destroys the half-metallic features for U values that are needed to reproduce half-metallicity in Co_2FeSi. In other words, the U values that are sufficient for Co_2FeSi are not transferable to Co_2MnSi and, in addition, the usage of the LDA+U method leads to no significant improvement of the description of the electronic structure of Co_2MnSi.

In Ref. [198], the quaternary system $Co_2Mn_{1-x}Fe_xSi$ is investigated theoretically and experimentally. It is found that a careful tuning of the composition results in a Fermi level which is located in the middle of the gap in the minority spin states as it is desired to ensure that half-metallicity is more stable against temperature induced effects.

There are fewer publications considering Co_2MnAl. Structural and magnetic properties are investigated in Refs. [199, 200]. It is found that an order-disorder transition between $L2_1$ oder and B2 disorder exists. This is comparable to what is found in Co_2FeAl. The Curie temperature of the $L2_1$ structure is found to be about 693 K. In addition, the authors of Ref. [201] investigated how the location of the Fermi level can be tuned in Co_2MnAl by

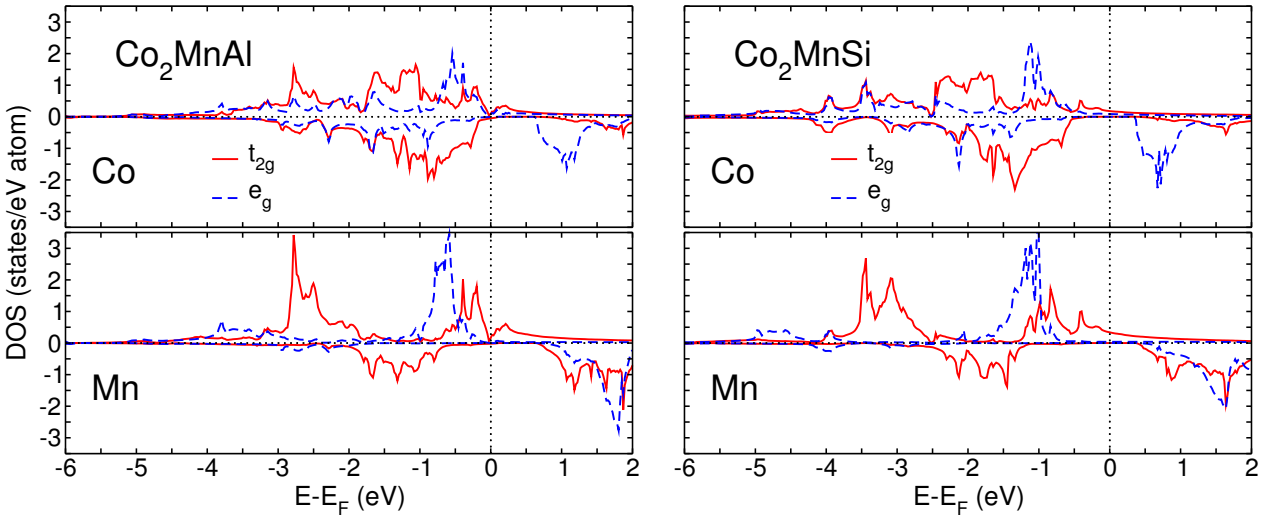

Figure 7.16: Symmetry resolved DOS of Co_2MnAl and Co_2MnSi obtained from VASP (GGA).

doping with As. They found that the Fermi level varies within the half-metallic gap with increasing As concentration in a way comparable to the variation which is found in the $Co_2FeSi_{1-x}Al_x$ systems.

Now, a discussion of the computational results obtained for both systems is given. The first result is that for both compositions the conventional Heusler structure is energetically preferred and therefore a discussion of the inverse structure is skipped.

Figure 7.15 shows the electronic density of states of Co_2MnAl and Co_2MnSi. It is obvious that these calculations reproduce the half-metallic feature in the minority spin channel. The finite density of states in the gap occurs due to small numerical errors in the projection scheme. The total DOS which is obtained without a projection onto element specific contributions shown in Fig. A.2 in Appendix A.12 reveals a clear gap in both systems.

In Co_2MnAl the Fermi energy lies at the upper edge of the valence band. This is the main drawback of this material. Finite temperature can easily destroy half-metallicity in this case because non-quasiparticle states are induced into the gap [177]. The situation is more ideal for Co_2MnSi because the Fermi energy is located almost in the middle of the gap, which is the most stable half-metallic configuration concerning temperature effects (see Section 7.2). The predicted magnetic moments shown in Tab. 7.1 of $4.11\mu_B$ for Co_2MnAl and $5.02\mu_B$ for Co_2MnSi are in agreement with the expected integer values of $4\mu_B$ and $5\mu_B$. Here, one can draw the first conclusions: Obviously, the description of the Co-Mn based Heusler alloys is much better within standard GGA as compared to the Co-Fe based alloys. This shows again that in particular the treatment of Fe states leads to difficulties.

In Fig. 7.16 the symmetry resolved electronic density of states are compared. The minority Co density in both systems shows a contribution of t_{2g}-states below the Fermi energy followed by a gap and a contribution of the e_g-states above the Fermi energy. The manganese contributions show a very broad gap around the Fermi energy. Both densities of states are very similar to those of Co_2MnGe discussed in Ref. [171] and therefore the explanation of the origin of the gap given in Ref. [171] perfectly fits the situation in Co_2MnAl and Co_2MnSi. This is expected beause in particular Co_2MnGe and Co_2MnSi are isoelectronic. This shows

that the contribution of the Mn atoms to the electronic structure is much better captured within the simple GGA as compared to the case of Fe in e.g. Co_2FeSi.

In order to check how half-metallic features can be tuned by changing the composition, the electronic density of states for a series of $Co2MnSi_xAl_{1-x}$ systems are calculated. In Fig. 7.17, the results of these calculations are summarized. With increasing Si content the Fermi energy of the system is shifted to higher values because of successive increase of valence electrons. Therefore, the position of the Fermi energy within the half-metallic gap can be tuned by carefully changing the composition. The result is comparable to that obtained for $Co2FeSi_xAl_{1-x}$ (see Fig. 7.4), where it is also possible to tune the position of E_F. These KKR calculations show again that the description of the electronic structure of Co and Mn based systems is much better than that of Co and Fe based ones even within the ASA-KKR formalism. The DOS in Fig. 7.17 show a perfect gap in the minority channel whereas in $Co2FeSi_xAl_{1-x}$ a finite DOS occurs around the Fermi energy.

Now, the magnetic exchange parameters are investigated and the influence of disorder onto the critical temperature is discussed. Figure 7.18 shows the magnetic exchange parameters of Co_2MnAl in the fully ordered $L2_1$, in the partially disordered B2 and the fully disordered A2 structure. Qualitatively, the exchange parameters in the $L2_1$-phase are completely similar to those of the $L2_1$-phase of Co_2FeAl (see Fig. 7.9). The strong ferromagnetic Co-Fe coupling is replaced by a strong Co-Mn coupling. The Co-Co coupling is very small and also the Mn-Mn coupling is small like the Fe-Fe coupling in Co_2FeAl. Quantitatively, the exchange parameters are more than a factor of two smaller compared to those of Co_2FeAl. This results in a much smaller Curie temperature of only 480 K. This Curie temperature is approximately 200 K smaller than the experimental result of 693 K (see Ref. [202]) which is a serious deviation. To check if this deviation occurs due to the use of the LDA in the calculation of the exchange interactions a calculation using the PBE-GGA functional is carried out but no improvement is found. This implies that the difficulty of finding a good agreement between theoretical prediction and experimental result for the critical temperature of Co_2MnAl seems to be independent of the exchange correlation functional used in the calculation. It can be supposed that the description of the exchange parameters of Co-Mn based system suffers from some serious drawbacks because similar problems are found in the investigation of binary $Co_{1-x}Mn_x$ alloys. Due to the antiferromagnetism in the binary alloys the additional problem of strongly quenched Co moments arises. A similar reduction of the Co moment is also found in Co_2MnAl where the Co moment is about $0.4\,\mu_B$ smaller compared with Co_2FeAl. Therefore, it is concluded that not only the exposure of Co to antiferromagnetic environments reduces its moment but already the proximity to the strong antiferromagnetically interacting element Mn leads to a similar reduction although it is less significant. In particular, the potential antiferromagnetism of Mn leads to the smaller Co-Mn exchange interaction and therefore to the underestimation of the critical temperature.

If disorder is introduced, the modification of the exchange parameters is different from the modification in Co_2FeAl. The main difference is that strong antiferromagnetic couplings occur. These antiferromagnetic couplings are associated with the next nearest neighbor Mn-Mn interactions. In the $L2_1$ ordered system no next nearest neighbor Mn atom pairs exist and therefore there is no antiferromagnetic coupling. It is found in various Heusler alloys which contain Mn that there is a unique dependence of the sign of the magnetic exchange interaction between Mn atoms on the distance between the sites (see for example the review of Siewert *et al.* Ref. [203] and references therein). This dependence of the Mn-Mn interaction on the distance becomes obvious here. The change from a ferromagnetic to antiferromagnetic

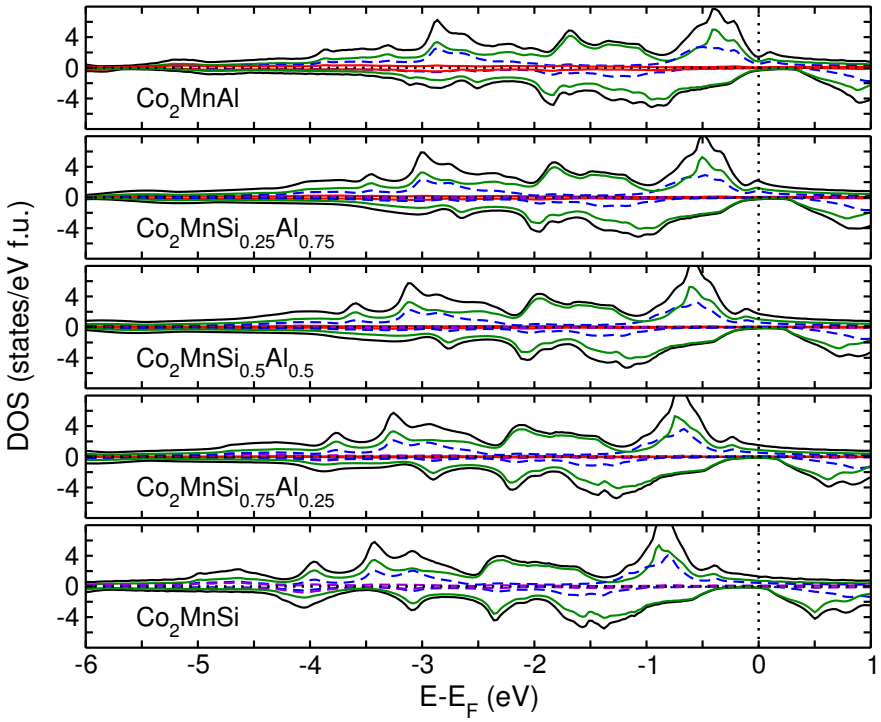

Figure 7.17: Electronic densities of states of $Co_2MnAl_{1-x}Si_x$. The black lines represent the total densities, the green and blue ones the Co and Mn DOS respectively. Red and violet lines correspond to Al and Si.

interaction in case of Heusler alloys is reported in Ref. [204] where the interactions in $L2_1$ and B2 ordered Ni_2MnAl are investigated. In addition, the exchange interaction between Co and Mn and the Co moment are further reduced in the B2 structure (the Co moment of B2 is $0.1\mu_B$ smaller compared $L2_1$).

Although there are a strong antiferromagnetic interactions between the Mn atoms which are almost of the same size compared to the ferromagnetic interaction between Co and Mn the ground state of the B2 phase, which is obtained from the MC simulation is ferromagnetic. This can be understood by adding up the relevant contributions. All Co atoms interact ferromagneticaly with each other and with the Mn atoms. As every Mn atom is surrounded by eight nearest neighbor Co atoms and on the average only by three next nearest neighbor Mn atoms the ferromagnetic coupling dominates and determines the MC ground state. But the Curie temperature is strongly reduced because although the ferromagnetic interactions dominate, the antiferromagnetic couplings introduce frustration of Mn pairs that tends to reduce the critical temperature.

The situation changes again if A2 disorder is considered. The main qualitative change is that nearest neighbor Co-Co interactions occur which are absent in the $L2_1$ and the B2 structure. This leads to an additional ferromagnetic contribution. A second change is that all nearest neighbor interactions are much larger than the largest contributions in the other two structures. This effect can be mainly attributed to the increased Co moments. They are almost a factor of two larger because the environment of the Co atoms contains nearest neighbor Co atoms. This influences the entire magnetism because the total magnetic moment of the unit cell is increased to $4.87\mu_B$ (see Fig. 7.19). Although, the antiferromagnetic Mn-

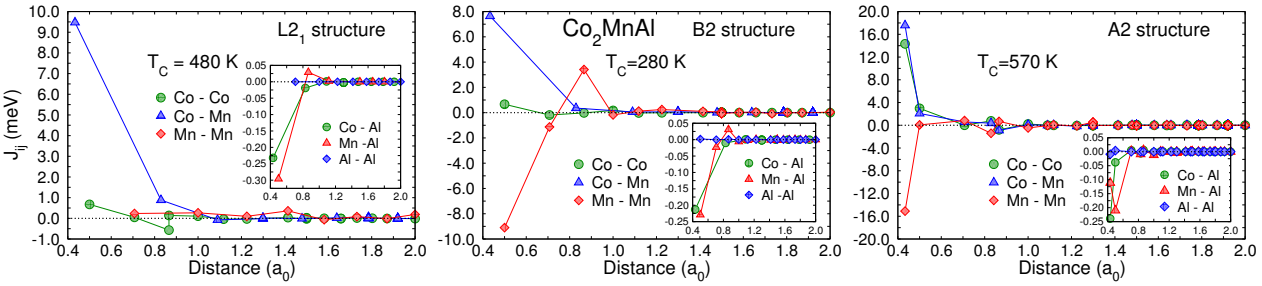

(a) (b) (c)

Figure 7.18: Magnetic exchange parameters calculated with SPR-KKR using the LDA exchange correlation functional of VWN. The critical temperatures are obtained from Monte Carlo simulations.

Mn interactions are also increased, the Curie temperature is now 570 K which is almost 100 K higher than the Curie temperature in the ordered $L2_1$ phase. The MC ground state is ferromagnetic but it has some non-collinear tendencies which are hard to identify and which depend strongly on the particular realization of the system and also on the size of the simulation box. Since the critical temperature of the A2 structure is closer to the experimental result and as it is stated in the introductions that real samples always include a certain degree of disorder the large deviation of the critical temperature of the $L2_1$ structure from the experimental results is partially explained by the influence of disorder.

In Fig. 7.19 the electronic DOS of the three different structures of Co_2MnAl calculated within the KKR-CPA framework are shown. The DOS of the $L2_1$ structure is very similar to the one obtained from VASP calculations. A gap in the minority spin channel is found and the Fermi energy is located at the edge of the valence band. But here, a finite contribution of the Co density of states at E_F remains. The total magnetic moment is also very close to the expected integer value. In the DOS of the B2 structure the features are smeared out but the coarse structure of the DOS is preserved. In particular, the half-metallic gap is not destroyed by introducing B2 disorder. Therefore, it is concluded that small differences in the production of experimental samples, if they only lead to B2 disorder, should have a small effect on half-metallicity. But in the case of A2 disorder the electronic DOS is completely smeared out and also the gap in the minority spin channel vanishes completely. The changes of the DOS introduced by disordering the structure are completely comparable to the changes in Co_2FeAl and Co_2FeSi.

Now, electronic structure and magnetism of Co_2MnSi is discussed. Figure 7.20 shows the magnetic interactions of the three phases with different degree of order. If the couplings obtained in the $L2_1$ structure are compared with those obtained for Co_2FeSi (see Fig. 7.11) a striking similarity is found. As in the comparison of Co_2MnAl with Co_2FeAl, there is only one big difference which concerns the strength of the magnetic couplings. One finds the trend that exchanging Fe by Mn generally leads to smaller exchange parameters. Therefore, the Curie temperature of Co_2MnSi is smaller than that of Co_2FeSi. It is 750 K and therefore about 200 K smaller than the experimentally found value of 985K (see Ref. [202]). This corresponds to the deviation of the theoretical value of Co_2MnAl from the the experimental value which is also found to be 200 K larger. This leads to the conclusion that the general trend of the magnetic interactions and the corresponding Curie temperatures is fairly well reproduced

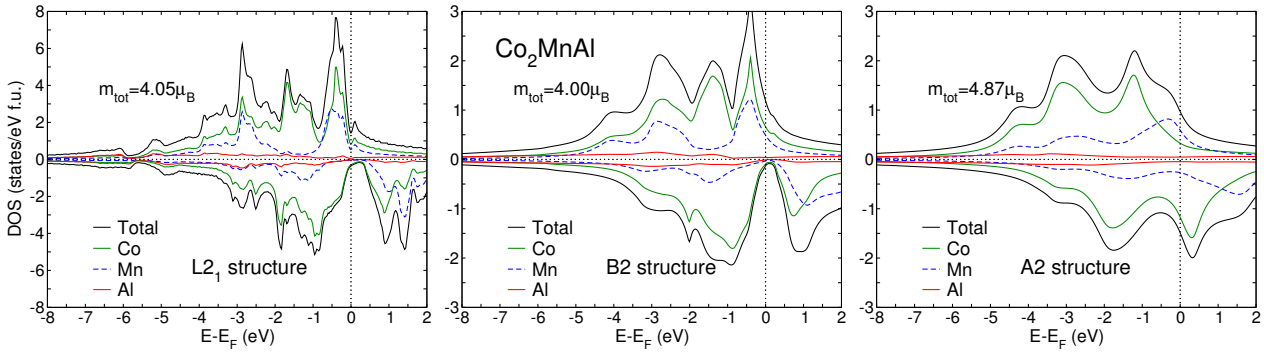

Figure 7.19: Electronic density of states of the Co_2MnAl Heusler alloy. Figure (a) corresponds to the ordered $L2_1$ structure. (b) corresponds to the B2 type of disorder and (c) to the complete A2 disorder.

without employing the GGA+U approach. This also means that, although a larger deviation of the theoretical prediction of the Curie temperature is found, this deviation is not arbitrary but always of the same size. This is the main difference between the description of the Co-Fe and Co-Mn based Heusler compounds investigated here. Possible reasons for the deviation are discussed above for Co_2MnAl.

Introducing B2 disorder leads to comparable changes as in B2-Co_2MnAl. The occurrence of next nearest neighbor Mn atoms leads to antiferromagnetic interactions and the values of all other couplings is slightly reduced. The general decrease of the exchange parameters in combination with the antiferromagnetic Mn-coupling leads to a smaller Curie temperature of 530 K. Despite the antiferromagnetic trend of Mn, the MC ground state remains ferromagnetic. The explanation for this is also the same as given for Co_2MnAl.

The change to A2 disorder has again a similar effect as in Co_2MnAl. But the difference is that the trend of increased magnetic exchange parameters is less pronounced compared to A2-Co_2MnAl. Interestingly, the Curie temperature obtained from the MC simulation is exactly the same as obtained for the $L2_1$ ordered system.

Regarding the electronic density of states of Co_2MnSi for the three structures, the same trends are found as for Co_2MnAl. The Fermi energy is located at the lower edge of the

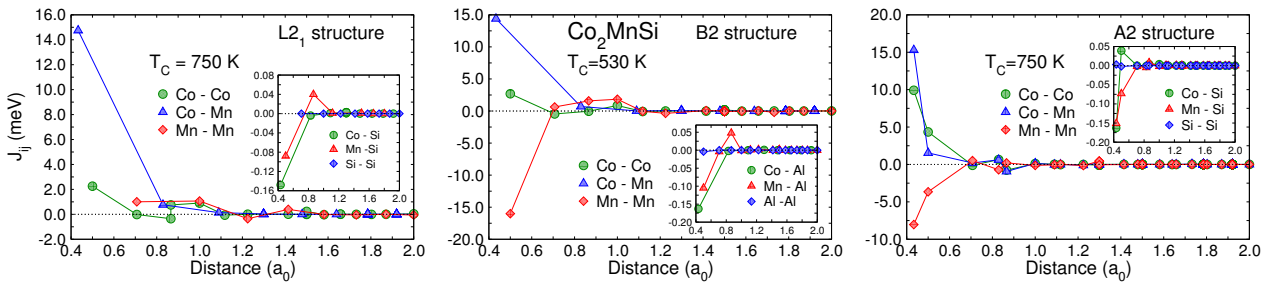

Figure 7.20: Magnetic exchange parameters of Co_2MnSi in $L2_1$, B2 and A2 structure calculated with SPR-KKR using the LDA exchange correlation functional of VWN. The critical temperatures are obtained from Monte Carlo simulations.

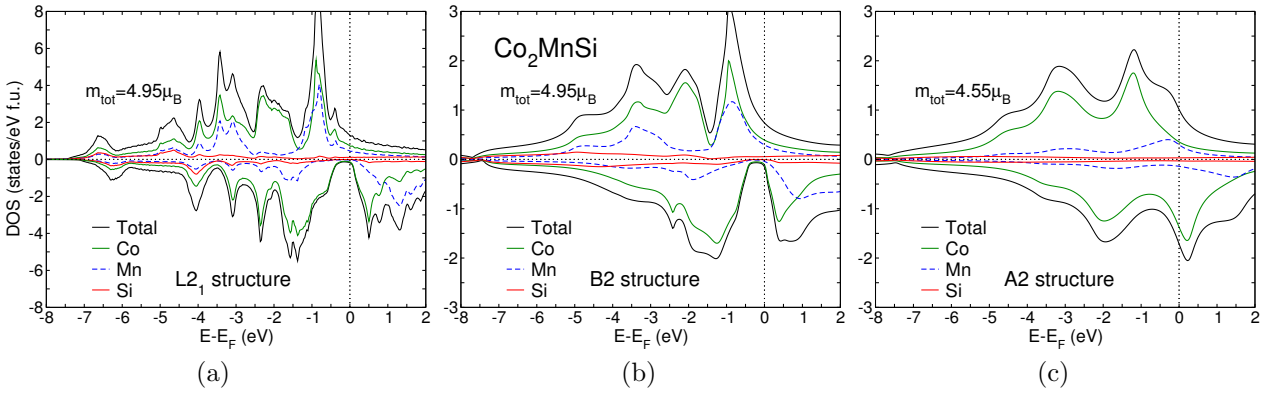

Figure 7.21: Electronic density of states of the Co_2MnSi Heusler alloy. The first picture corresponds to the ordered $L2_1$ structure. The second one corresponds to the B2 type of disorder and the third to the complete A2 type.

conduction band and it remains at this position when B2 disorder is introduced because the gap is still open and only the sharp features of the DOS are smeared out. This changes completely for A2-disorder where half-metallicity is destroyed.

To finish the discussion of Co_2MnAl and Co_2MnSi an exemplary calculation employing the GGA+U method is carried out for both systems. To allow a comparison with results obtained for Co_2FeAl and Co_2FeSi the same U values for Co are used and those for Fe are now used for Mn. Results are shown in Fig. 7.22. As in the Co-Fe based systems the gap in the minority channel becomes much more pronounced. But in the case of Co_2MnAl the position of the Fermi energy is pushed into the valence band. A similar situation is found for Co_2MnSi although in this case the Fermi energy is much closer to the gap. The trend that the inclusion of correlation effects within the GGA+U method leads to poorer results is already described by the authors of Ref. [190]. They conclude that Co_2MnSi should show no half-metallic behavior in experiments because they assume that correlation effects have to be also important for Mn and not only for Fe. This conclusion is supported by the experiments reported in Ref. [205] where the authors have probed the spin polarization by femtosecond spin excitations. They derived demagnetization times and argued that this time scale allows to distinguish metals from half-metals because the dominant Elliot-Yafet spin scattering mechanism [148] is much weaker in half-metals than in normal metals. The authors of Ref. [205] found a two orders of magnitude smaller relaxation time for Co_2MnSi compared to other promising candidates for half-metallic behavior and conclude a spin polarization of only 66%.

This discussion is difficult because it is shown in Ref. [190] that smaller U value lead to improvement of the half-metallic gap without shifting the Fermi energy out of it. In addition, one has to keep in mind that there are a variety of mechanisms that can destroy the 100% spin polarization of half-metal. In the experimental situation the structural order of a sample is not completely controlled, surface effects are present which are also not completely controlled. In particular, the femtosecond spin excitation may probe the surface character of the polarization instead of the bulk property. Therefore, there are a lot of controversies because other experiments, e.g., measurements of TMR ratios on systems with Co_2MnSi electrodes suggests a high degree of spin polarization.

Here, attention should be paid to the Co moments. They show slightly smaller value in the

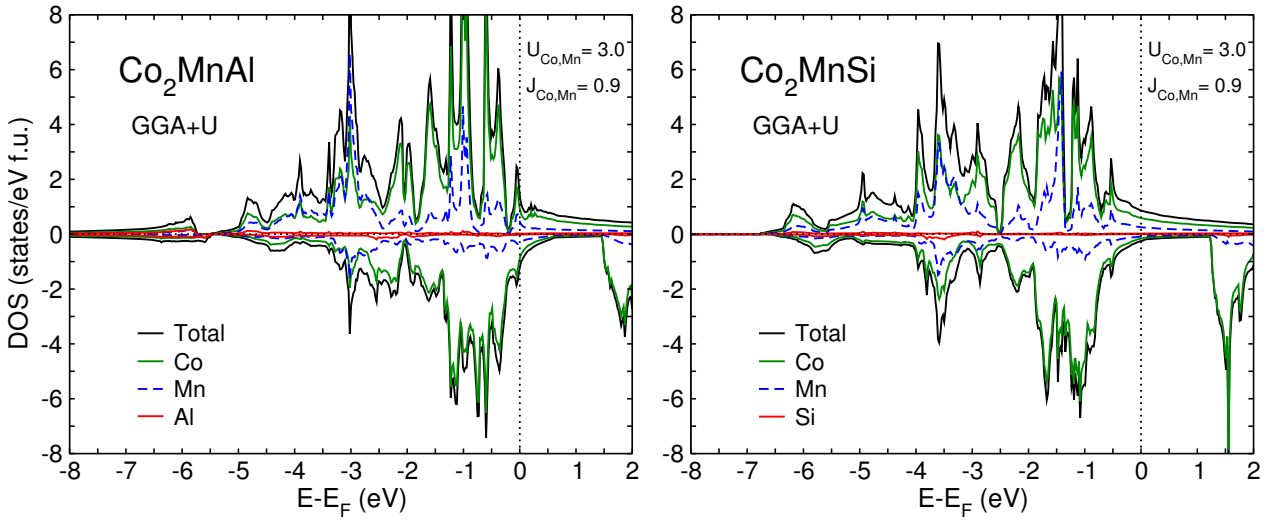

(a) (b)

Figure 7.22: Comparison of the electronic densities of states calculated with VASP and employing the GGA+U method of (a) Co_2MnAl and (b) Co_2MnSi. The values for U and J are taken from [191].

GGA+U method compared to the standard GGA calculations. Therefore, it is concluded that the usage of GGA+U does not necessarily improve the prediction of the critical temperature and instead can lead to an even worse result. This means that although GGA+U gives answers to some questions it poses new ones.

7.5 Fe_2CoAl and Fe_2CoSi

In this section the results of the study of Fe_2CoAl and Fe_2CoSi are presented. Both system are less well investigated compared to Co_2FeX and Co_2MnX (X=Al, Si). Magnetic properties of these systems are studied experimentally by Mössbauer spectroscopy and magneto-optical Kerr effect procedures [206, 207]. Both compounds are also investigated theoretically in the general combinatorial *ab initio* study of Dronskowski *et* al. [168]. The authors found that these alloys are more stable in the inverse Heusler structure compared to the conventional one. In addition, a similar Heusler alloy with the same valence electron concentration namely Fe_2CoGa is studied theoretically in Ref. [163]. It is also found that the inverse Heusler structure is preferred.

In the study reported here, VASP calculations reveal that both systems strongly prefer the inverse Heusler structure. Therefore, the results of the following discussion concern only the inverse structure and their ferromagnetic ground state.

In Fig. 7.23 the electronic densities of states of (FeCo)(FeAl) is compared with that of (FeCo)(FeSi). Since the Fe atoms are no longer symmetrically equivalent in the inverse Heusler structure, they give different contributions and are labeled Fe_1 and Fe_2. The (FeCo)(FeAl) system shows no features of half-metallicity because, although there is a gap like feature in the minority states, the Fermi level is located elsewhere. This is different in (FeCo)(FeSi) where a gap-like feature occurs at E_F (the same features are also found in the total DOS shown in Appendix A.12). It is concluded that small compositional changes in (FeCo)(FeSi), e.g.,

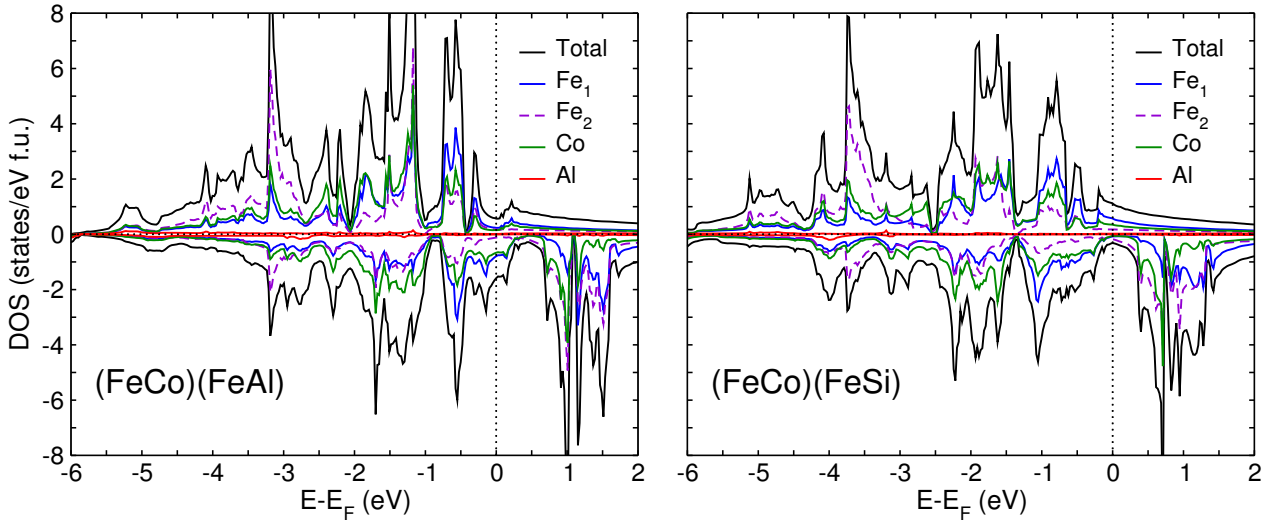

(a) (b)

Figure 7.23: Comparison of the electronic density of states of the inverse Heusler structures (a) (FeCo)(FeAl) and (b) (FeCo)(FeSi) as obtained from VASP.

departing from stoichiometry or doping with another elements, can lead to half-metallicity. In addition, the GGA+U calculation reported below show that there is indeed a trend for a gap in both systems. This can be understood by considering that in both systems the correlation effects of iron can play an important role and therefore the DOS without employing methods to account for correlations is only approximately valid.

It should be noted that the DOS of both systems share similarities with the DOS of FeCo in the B32 structure which is studied in Section 5.3. This occurs because the inverse Heusler structure is very similar to the B32 structure since only the Z component has to be exchanged by the Y component and the B32 is obtained.

It needs to be noted that a possible occurrence of half-metallicity cannot be explained with the arguments given in Section 7.2 because there are no Fe-Fe nearest neighbor pairs that can built up a bonding that can hybridize with Co. Therefore, the mechanism which leads to the possible occurrence of the gap is different.

Figure 7.24 shows the magnetic exchange parameters of Fe_2CoAl for the ordered inverse Heusler structure and the fully disordered A2 structure. The results for the ordered structure are qualitatively comparable to those obtained for α-Fe_3Co investigated in Section 5.2. The exchange parameters of Fe_2CoAl are smaller than those of Fe_3Co due to the difference in the nearest neighbor environment which includes non-magnetic Al atoms and reduces the Co moments by almost $0.7\,\mu_B$. This leads to a strongly reduced critical temperature of 790 K compared to 1260 K observed in α-Fe_3Co. It shows again the sensitive dependence of the Co moment on the local environment. Here, the proximity of non-magnetic atoms reduces the moment drastically. As there are nearest neighbor Fe pairs, the corresponding interaction gives a large contribution comparable to what is found in the B2 structure of Co_2FeAl and Co_2FeSi.

The A2 disorder leads to nearest neighbor Co-Co interactions which are absent in the ordered inverse Heusler structure. Together with a small increase of the Fe-Fe and Fe-Co interactions this results in an increased critical temperature. This trend is again very similar

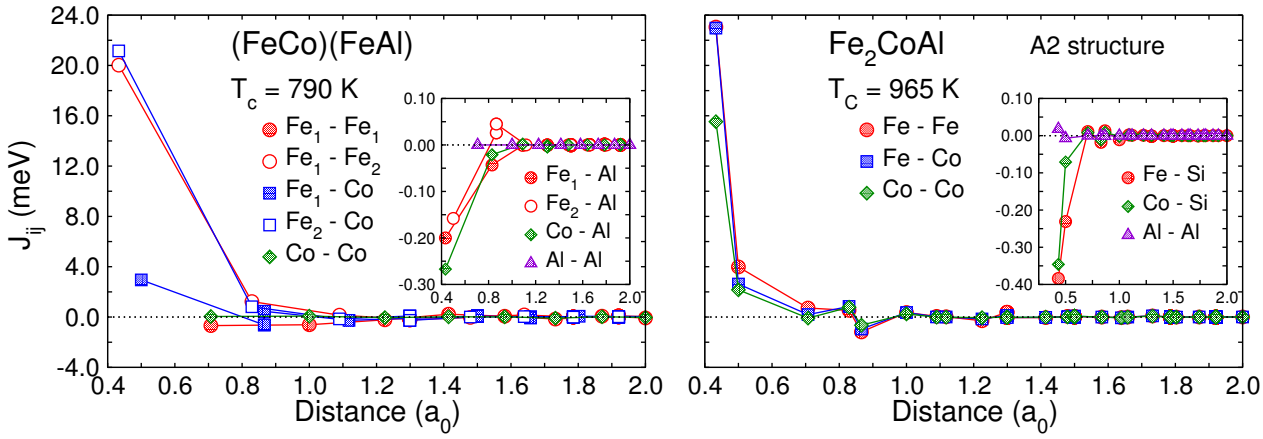

(a) (b)

Figure 7.24: Magnetic exchange parameters of (a) (FeCo)(FeAl) and (b) A2-Fe_2CoAl calculated with SPR-KKR using the LDA exchange correlation functional of VWN. The critical temperatures are obtained from Monte Carlo simulations.

to what is found for Fe_3Co.

An investigation of B2 disorder is neglected because it is more unlikely to occur in systems which prefer an ordered inverse structure. This can be understood by considering that there are no planes in which only one atom type occurs. Therefore, any disordering tendency leads more likely into the direction of A2 than B2.

Figure 7.25 shows the electronic densities of states obtained from SPR-KKR calculations for the inverse and the disordered A2 structure. These calculations confirm that there are no features of half-metallicity. In particular, no gap-like feature remains in the DOS of the inverse structure. The deviations of the SPR-KKR calculation from the VASP calculation

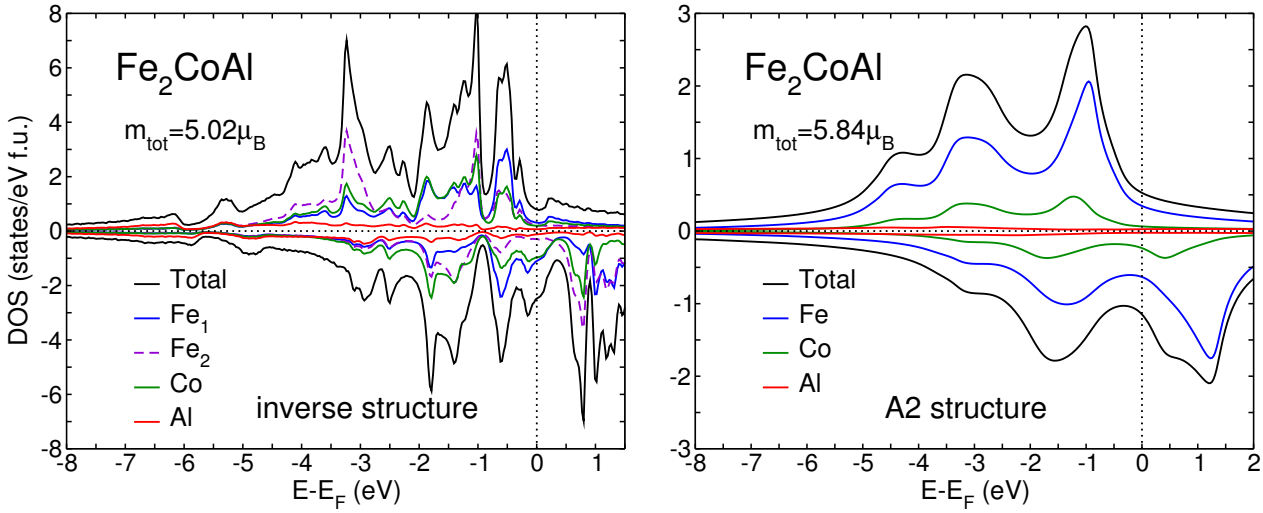

(a) (b)

Figure 7.25: Electronic densitiy of states of the ordered (FeCo)(FeAl) compared with the electronic density of the fully disordered A2 structure. Both DOS are calculated with SPR-KKR.

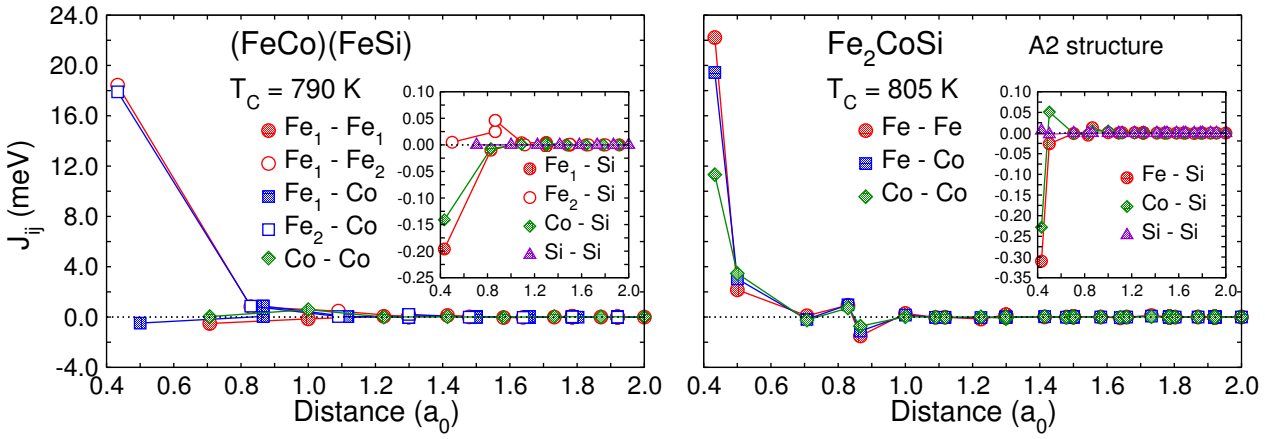

(a) (b)

Figure 7.26: Magnetic exchange parameters of (a) (FeCo)(FeSi) and (b) A2-Fe_2CoSi calculated with SPR-KKR using the LDA exchange correlation functional of VWN. The critical temperatures are obtained from Monte Carlo simulations.

are due to the use of the two different methods with two different exchange correlation functionals. As expected, all sharp features of the DOS are completely smeared out in the A2 structure. Interestingly, the magnetic moment per formula unit is increased.

As already mentioned above, the electronic density of states of (FeCo)(FeSi) shown in Fig. 7.23 exhibits a gap-like region in the minority spin channel in which the Fermi energy is located. In addition, the total magnetic moment of 5.02 μ_B per formula unit is close to the integer value of 5.00 μ_B which is theoretically expected for a half-metal of this particular composition. Therefore, one may conclude that Fe_2CoSi may be half-metallic under certain conditions. For example, a change in the lattice constant or small tetragonal distortions as they can occur if the alloy is grown on a certain substrate might, lead to a half-metallic DOS.

The magnetic exchange parameters of (FeCo)(FeSi) shown in Fig. 7.26 are similar to those obtained for (FeCo)(FeAl) and also comparable to the Fe_3Co results. The critical temperature of the inverse structure has the same value as for Fe_2CoAl with in the range of error bars of the method. This is an interesting result because in all other Heusler alloys discussed so far the interchange of Al by Si leads to different critical temperatures. The occurrence of A2 disorder is also increasing the critical temperature but less stronger compared to Fe_2CoAl. The main reason for this are the smaller the Co-Co and Fe-Co interactions.

The electronic density of states obtained from the KKR calculations (see Fig. 7.27) does not reproduce the integer value of the magnetic moment and the gap-like region in the minority states is less pronounced as compared to the results of the VASP calculations. But there is still a deep minimum of the minority DOS at the Fermi energy. As is known from the previous calculations, A2 disorder destroys all fine structure of the electronic DOS and leaves only strongly broadened features.

In order to investigate how the GGA+U method tends to modify the electronic structure of (FeCo)(FeAl) and (FeCo)(FeSi), calculations have been carried out using the same U-values as previously used during the discussion of Co_2FeX and Co_2MnX with X=Al,Si (see Ref. [191]). The corresponding results are shown in Fig. 7.28. The U affects the electronic structure in a way that a perfect gap opens up in the minority channel in both systems. But in (FeCo)(FeAl) the Fermi level stays in a region of finite density of states and in (FeCo)(FeSi) it is shifted out

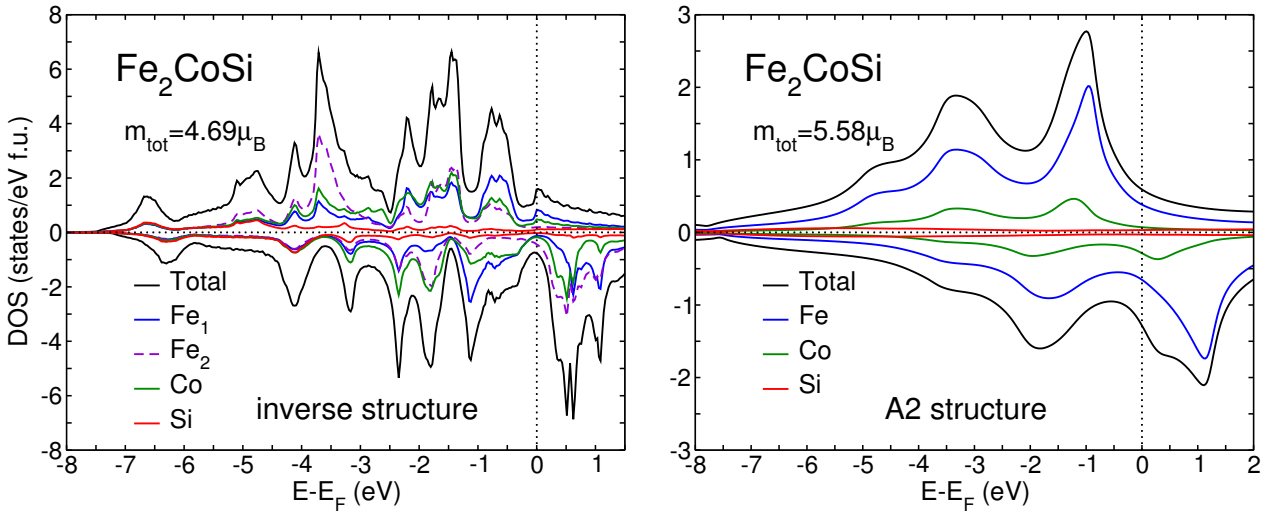

Figure 7.27: Electronic density of states of (a) the ordered inverse Heusler structure of (FeCo)(FeSi) compared with (b) the electronic density of the fully disordered A2 structure.

of the gap region. As the inclusion of correlation effects leads to gap regions in both systems and as the Fermi energy of Fe_2CoSi is very close to this gap, these calculations reinforce the assumption that Fe_2CoSi might become half-metallic if certain additional constraints are fulfilled. But the interesting feature to be noted here is that correlation effects can again lead to gap regions in the minority spin states. This can be explained by considering that the Fe concentration in both alloys is very high and therefore the correlation effects introduced by the iron states play an important role.

The most important result of this section is that (FeCo)(FeAl) and (FeCo)(FeSi) seem to be no intrinsic half-metals although the occurrence of half-metallicity cannot be completely excluded because they still show some features that might be improved by changes of composition or structural constants and possibly develop a gap around the Fermi energy. On the other hand, these systems show high Curie temperatures in the ordered and disordered phases. A conclusion from technological importance is that $Fe_{1-x}Co_x$ samples polluted with Al or Si still show good magnetic properties.

It is already mentioned that the inclusion of correlation effects does not solely affect the gap structure of a promising half-metallic alloy but instead the entire electronic structure. This can also lead to structural changes and therefore the lattice constant obtained from standard GGA and GGA+U of the alloys investigated up to now is compared to the experimental result in Table 7.4. It turns out that the change of the lattice constant induced by correlation effects is quite small but always leads to a better agreement with experiment. But it needs to be reminded that the values of U used in all calculations destroyed the half-metallic features in Co_2MnAl and Co_2MnSi. This shows that the improvement achieved by the GGA+U method for a particular property can lead to the deterioration of other properties. As this needs a careful analysis which is beyond the scope of this work the GGA+U method is not applied to alloys to be discussed in the following sections.

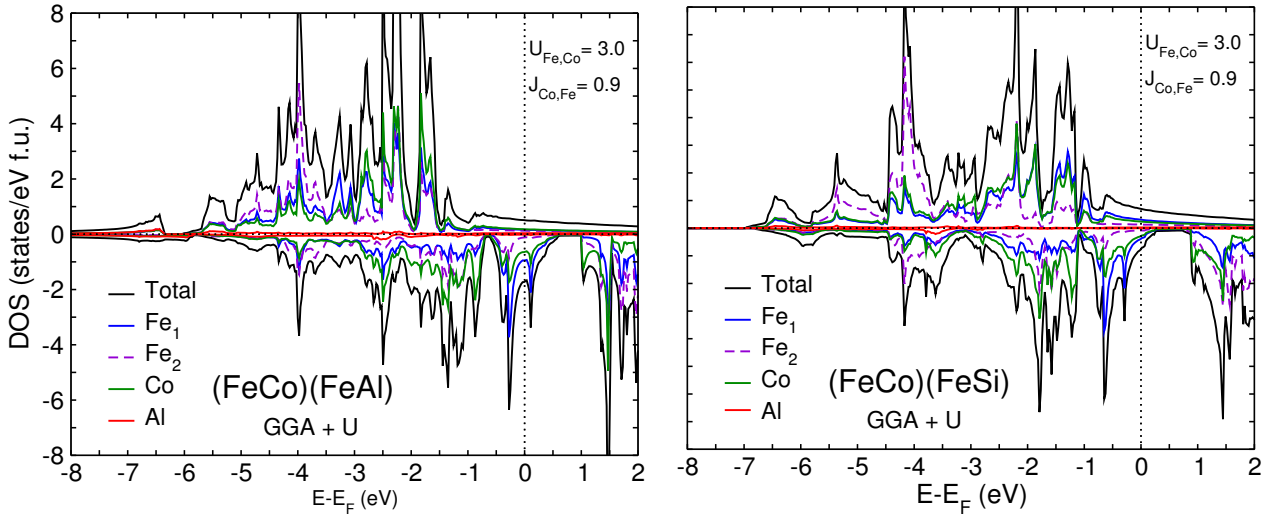

(a) (b)

Figure 7.28: Comparison of the electronic densities of states calculated with VASP within the GGA+U framework. In the GGA+U calculations the lattice constants have changed. The GGA lattice constant of (a) (FeCo)(FeAl) is 5.71 Å and 5.79 Å for GGA+U. In the case of (b) (FeCo)(FeSi) the GGA lattice constant is 5.61 Å and the GGA+U lattice constant 5.63 Å. The values for U and J are taken from [191].

7.6 Fe_2MnAl and Fe_2MnSi

This section is devoted to the analysis of Fe_2MnAl and Fe_2MnSi. Both system are predicted to show half-metallicity together with an antiferromagnetic alignment of the magnetic moments (see Ref. [171]). Such systems are called half-metallic antiferromagnets and are of special technological interest because they combine a polarization of 100% at the Fermi level with a vanishing net magnetization (see Section 7.2).

Experimental studies of Fe_2MnSi show that it exhibits no simple antiparallel alignment of the individual moments but a more complex magnetic structure. It undergoes a phase transition from the paramagnetic phase to ferromagnetic order at about $T = 220\,\mathrm{K}$ and

Composition	a_{GGA} (Å)	$a_{\mathrm{GGA+U}}$ (Å)	a_{exp} (Å)
Co_2FeAl	5.70	5.71	5.73
Co_2FeSi	5.63	5.65	5.64
(FeCo)(FeAl)	5.71	5.79	-
(FeCo)(FeSi)	5.61	5.63	-
Co_2MnAl	5.70	5.74	5.75
Co_2MnSi	5.63	5.64	5.65

Table 7.4: Comparison of the lattice constants obtained with VASP by using GGA and GGA+U. The additional comparison to the experimental values shows that the lattice constants obtained from the GGA+U calculations are more realistic.

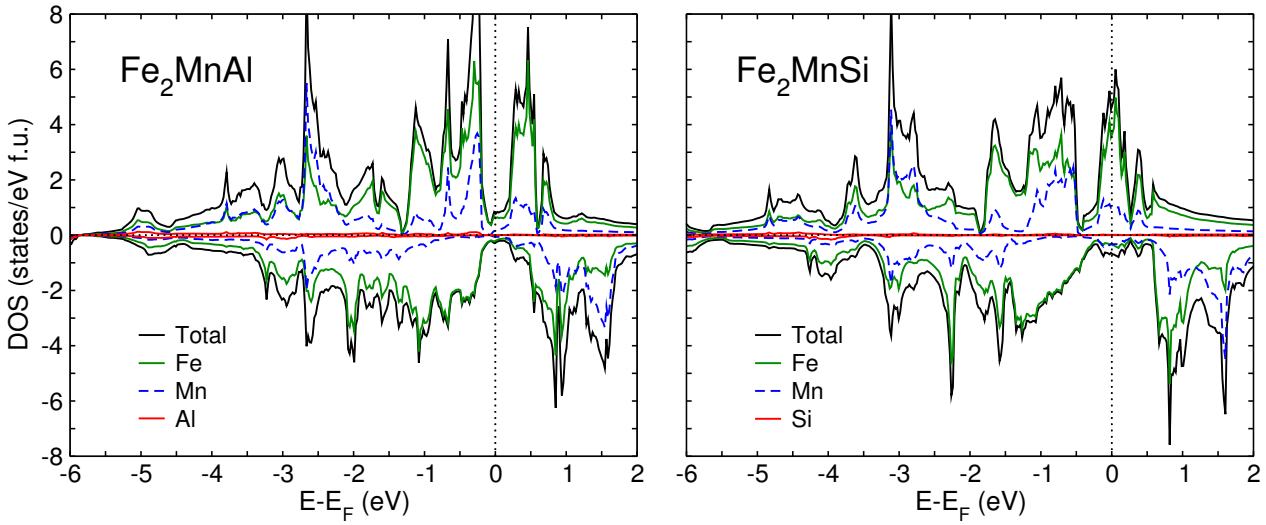

Figure 7.29: Comparison of the electronic densities of states of (a) Fe_2MnAl and (b) Fe_2MnSi. The calculations are carried out with VASP.

a second subsequent transition to a modulated antiferromagnetic phase at about $T = 60\,\mathrm{K}$ [208, 209]. A theoretical investigation is carried out in Ref. [210] where the authors employed a first-principles approach for the calculation of spin-spiral states. They found that a spin-spiral type of state, which is called the spin canted state, seems to be the magnetic ground state. This state is best described by stating that the magnetic moments are not simply antiparallel aligned but also include small canting angles. Interestingly, all collinear calculations (see, e.g., Ref [171]) as well spin-spiral calculations of Fe_2MnSi lead to a very small Fe moment of about $0.2\,\mu_B$, which is very unusual. Due to the small magnetic transition temperature which is below room temperature, Fe_2MnSi is less important for technological considerations but due to the interesting properties mentioned above, it is of great theoretical interest. In particular, MC simulations with *ab initio* exchange interactions are attractive because it allows insight into the finite temperature magnetism and ground state properties.

Figure 7.29 shows the electronic density of states of the conventional Heusler structure of Fe_2MnAl and Fe_2MnSi. Since the inverse structure is energetically unfavorable it is not discussed in the following. The DOS of both alloys are in reasonable agreement with a previous first principles study reported is Ref. [211]. The authors of this article state that both systems show half-metallic behavior because the Fermi energy lies in a gap in the minority states. In this study the investigations where performed within the LMTO-ASA framework using LDA. The element specific DOS obtained with VASP shown in Fig. 7.29 show remaining states in the gap but the total DOS shown in Fig. A.3 in the Appendix show a clear gap in the minority spin channel of both systems and the Fermi energy of both systems is located at the edge of the valence band. This means that the projection onto element associated contributions includes again some small errors. In the majority DOS of Fe_2MnAl a small dip is located close to the Fermi energy. This feature is comparable to what is known as a spin gapless semiconductor. This property is discussed in more detail in Section 7.8 but it should be noted that Fe_2MnAl shows a trend for the occurrence of this feature. The lattice constants obtained using VASP (see Table 7.1) are in excellent agreement

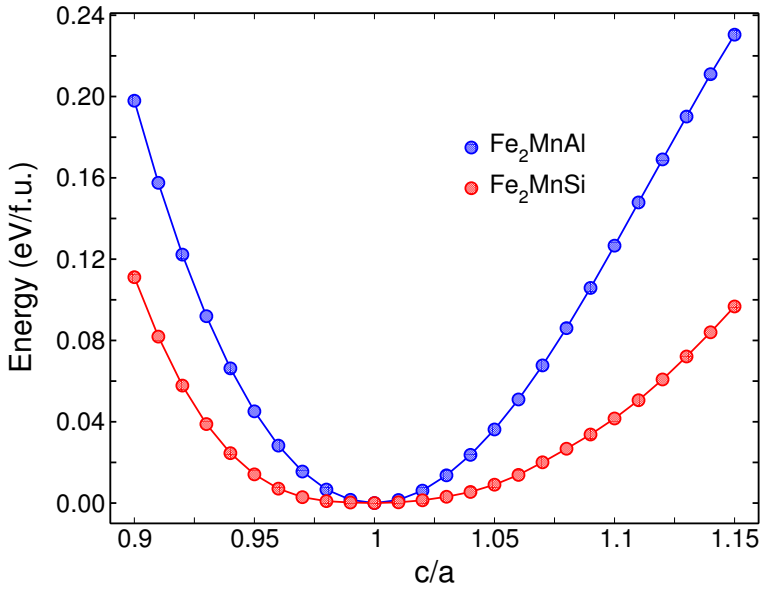

Figure 7.30: Total energy as a function of the c/a-ratio around $c/a = 1$ of Fe_2MnAl and Fe_2MnSi. The curve of Fe_2MnSi shows a very flat minimum at $c/a = 1$

with those found in Ref. [211].

Special attention should be paid to Fig. 7.30 where the variation of the total energy is plotted as a function of the c/a-ratio for both systems. It is obvious that the curve of Fe_2MnSi exhibits a peculiar behavior, because it is flat around the cubic c/a=1 state. This implies, that it should be possible to apply small tetragonal distortions to the system without spending much or even any energy. Additionally, Fe_2MnSi should show small epitaxial stress when grown on surfaces where the lattice constants do not perfectly match. Experiments should be carried out to measure the stress tensor of this system to search for peculiarities that can be associated with this strange energy landscape. The c/a-variation of Fe_2MnAl shows only a steep minimum around $c/a = 1$.

Now, the electronic and magnetic properties of both system are discussed separately. In Fig. 7.31, the magnetic exchange parameters of Fe_2MnAl are shown for the fully ordered $L2_1$ structure as well as for the partially disordered B2 structure. The qualitative form of these interaction parameters is unusual because only the Mn-Mn interactions are of significant size. The interaction between the iron atoms as well as the Fe-Mn exchange is almost zero. This is of course connected with the fact that the magnetic moments of the iron atoms in the $L2_1$ structure are strongly quenched to $0.18\,\mu_B$ in the VASP and $0.10\,\mu_B$ in SPR-KKR calculations. Therefore, no strong interaction between them or with the Mn atoms is possible. Qualitatively, the parameters do not change when B2 type of disorder is introduced but the strength of the Mn-Mn interaction is strongly increased by more than a factor of two because the first Mn-Mn interaction is related to the next nearest Mn pairs in the B2 structure which do not exist in the $L2_1$ structure. This strong antiferromagnetic interaction of next nearest neighbors is also found in the B2 structure of Co_2MnAl and Co_2MnSi. The MC simulation of the $L2_1$ ordered system reveals that the exchange interactions tend to prefer spin-spiral types of magnetic ground states. A critical temperature of 50 K is obtained from a corresponding peak in the heat capacity. The spin-spiral is formed by the magnetic moments of the Mn atoms. The magnetic moments of the Fe and Al atoms remain disordered and

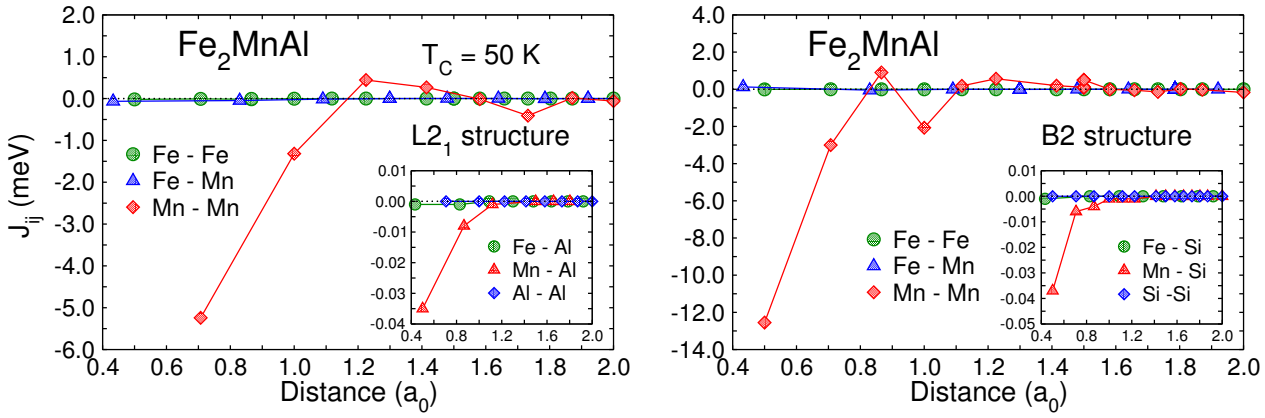

Figure 7.31: Magnetic exchange parameters (a) Fe_2MnAl and (b) Fe_2MnSi calculated with SPR-KKR using the LDA exchange correlation functional of VWN. No critical temperature can be determined for the B2 structure because in this structure no sharp magnetic phase transition occurs. Only a slow transition to frozen disorder is found.

are still fluctuating even at temperatures below 10 K. But this is expected because of the small moment and interactions. The critical temperature obtained here is close the the value where the experiments reveal a transition from the simple ferromagnetic state to the spin canted state. This implies that the zero temperature exchange interactions are not sufficient to capture the phase transition from para- to ferromagnetism at higher temperatures. In addition, the critical temperature can depend on the size of the simulation cell.

As already mentioned, the exchange parameters of the B2 disordered systems are qualitatively similar to those of the ordered system but in this system the next nearest neighbors interaction of Mn-Mn pairs gives an enhanced antiferromagnetic contribution. Therefore, one would expect a larger transition temperature of a possible ordered magnetic state. But the situation turns out to be much more difficult because the system shows a "spin-glass like" behavior. The term "spin-glass like" means that it is not proven here that this system is a true spin-glass because this requires an extended analysis which is beyond the scope of this study. But there are several observations that correspond to expected observations in a spin-glass system. The first observation is that there is no significant magnetization at $T = 0$ K and no spiral type of magnetic structure but the moments of the manganese atoms seem to show a frozen disorder. On the other hand the B2 disordered system fulfills some of the requirements of a spin-glass (see, e.g., Ref. [10] and references therein). Two of these requirements are disorder and dilution. Disorder is present because there is the mixed Mn-Al sublattice and as Mn is the only relevant magnetic moment and the Fe and Al moments are almost zero the system is like a dilute mixture of Mn atoms in a paramagnetic host. The third requirement is the need for competing interactions. This is not directly fulfilled because there are almost only antiferromagnetic interactions. But as the only relevant interactions are antiferromagnetic the system is strongly frustrated. It is therefore concluded that the system is not necessarily a spin-glass but at least the frustration leads to no preference of a certain ordered magnetic state which leads to frozen disorder.

Drastic changes compared to the $L2_1$ and the B2 structure are observed if the magnetic exchange interactions of the fully disordered A2 structure are investigated. The exchange

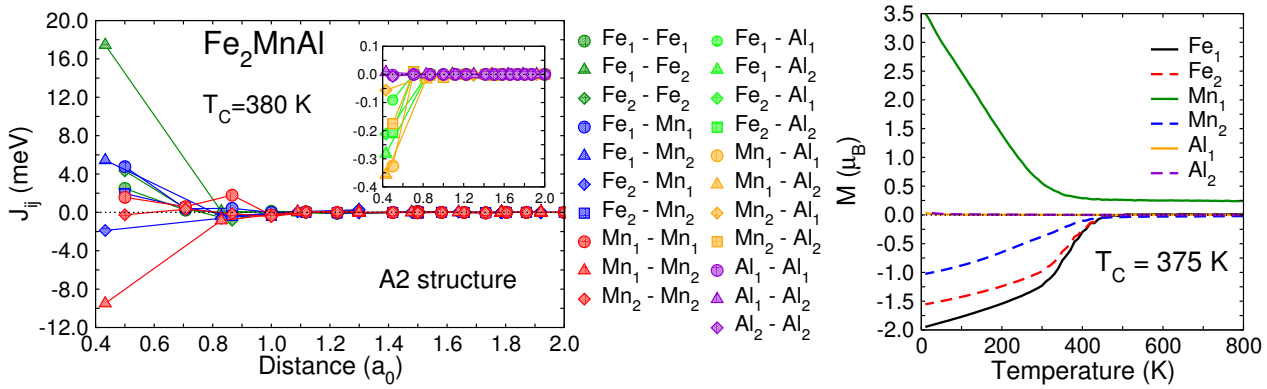

(a) (b)

Figure 7.32: (a) Magnetic exchange parameters of the A2 structure of Fe_2MnAl calculated with SPR-KKR using the LDA exchange correlation functional of VWN. (b) Finite temperature magnetization of the A2 structure obtained from MC simulations.

parameters of this structure are shown in Fig. 7.32(a). To allow antiferromagnetic alignment of the magnetic moments a unit cell consisting of two atoms is used and disorder is included by employing the CPA method to mix 50% Fe, 25% Mn and 25% Al on each site. At one of the sites the Fe moment is parallel to the Mn moment and at the other site the Mn moment is antiparallel to the first Mn atom but the Fe moment is parallel to the first Fe and Mn moment. Therefore, both sites are not symmetrically equivalent. The magnetic moments obtained in the A2 structure are compared to those of the $L2_1$ and the B2 structure in Table 7.5.

The exchange interaction between both types of Fe atoms is now ferromagnetic and the parameters for the two types of Mn atoms are antiferromagnetic but they are by almost a factor of two smaller than the ferromagnetic interactions between the two types of Fe moments. All other interactions are smaller but, all in all, a more ferromagnetic tendency is present in this system. This means, that, e.g., all Fe-Mn interactions except for the Fe_2-Mn_1 exchange are positive. The strong ferromagnetic interactions of Fe are connected to the

	μ_{L2_1} (μ_B)	μ_{B2} (μ_B)	μ_{A2} (μ_B)
Fe	-0.10	-0.08	-1.98 -1.57
Mn	2.27	2.13	-3.96 1.05
Al	-0.03	-0.03	0.07 0.09

Table 7.5: Comparison of the magnetic moments of Fe_2MnAl for different ordered and disordered structures. The different values denoted for the A2 structure correspond to the two symmetrically inequivalent sites used in the calculation. The results are obtained from SPR-KKR calculations using LDA of VWN.

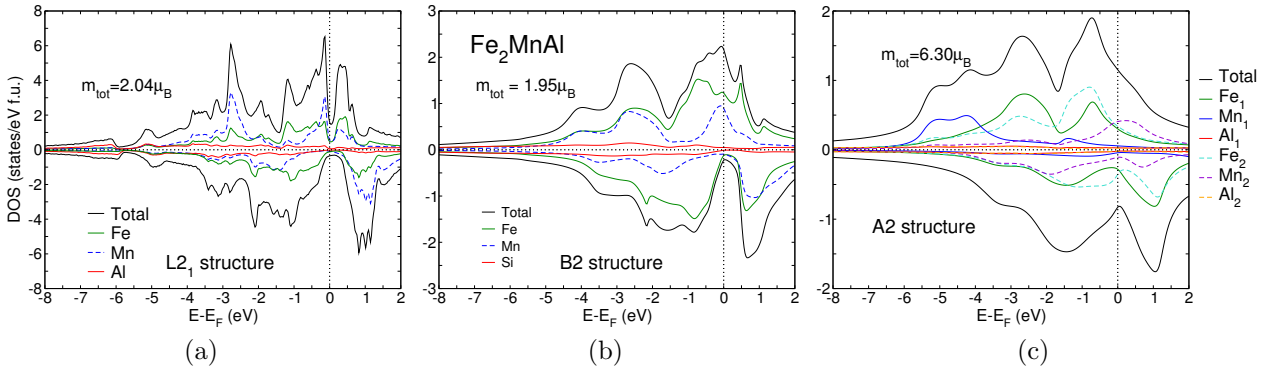

Figure 7.33: Electronic density of states of (a) the ordered Heusler structure of Fe_2MnAl compared with the electronic density of states of (b) the partially disordered B2 and (c) fully disordered A2 structure.

strong increase of the magnetic moments which are $1.98\mu_B$ and $1.57\mu_B$. This increase must be connected to the change in the average environment. In the $L2_1$ and B2 structure the Fe atoms are arranged in layers that are separated by Mn-Al layers. Therefore, Fe atoms cannot be nearest neighbors. In the A2 structure Fe atoms can be nearest neighbors and Fe forms no longer distinct layers.

The development of the magnetization with decreasing temperature obtained from MC simulation is shown in Fig. 7.32(b). Obviously, an antiferromagnetic ground state evolves. This antiferromagnetic state reflects the relations between the exchange interactions. Both iron sublattices are parallel aligned according to their ferromagnetic interaction. The Mn_1 sublattice couples ferromagnetically to the Fe_1 and antiferromagnetically to the Fe_2 sublattice but the Fe_1-Mn_1 interaction is by a factor of two larger. As the Mn_1 moments interact antiferromagnetically with Mn_2 and as they interact ferromagnetically with both Fe sublattices, Mn_2 aligns parallel to Fe and antiparallel to Mn_1. The most interesting feature is that only the two iron sublattices show a typical critical behavior. The manganese sublattices order linearly with decreasing temperature below 350 K. These sublattices exhibit no real phase transition and seem to follow the ordering of the iron atoms according to the interaction between them. This means they behave as if the increasing order of the Fe sublattices acts like an increasing external field on the Mn atoms. This must be connected to the fact that the Mn_1 sublattice interacts ferro- and antiferromagnetically with the different Fe sublattices.

The electronic densities of states of all three structures calculated using the KKR-CPA formalism are compared in Fig. 7.33. The DOS of the $L2_1$ structure shows a valley at the Fermi energy. It is not a perfect half-metallic gap but this is due to small errors introduced by the ASA method. The DOS of the B2 structure shows the same trends that are observed in Heusler alloys discussed in the sections above: The gap-like feature remains and E_F is still located within it and the main change is the smearing of features compared to the ordered structure.

The electronic density of states obtained for the A2 structure is shown in Fig. 7.33(c). The magnetic moment of the cell is much larger compared to the $L2_1$ and B2 structure. This is attributed to the increased Fe moments and the strong Mn_1 moment as discussed above. As usual the details of the DOS are smeared out in the disordered system. The contributions of the iron atoms show qualitative agreement and a rigid band like shift between the majority

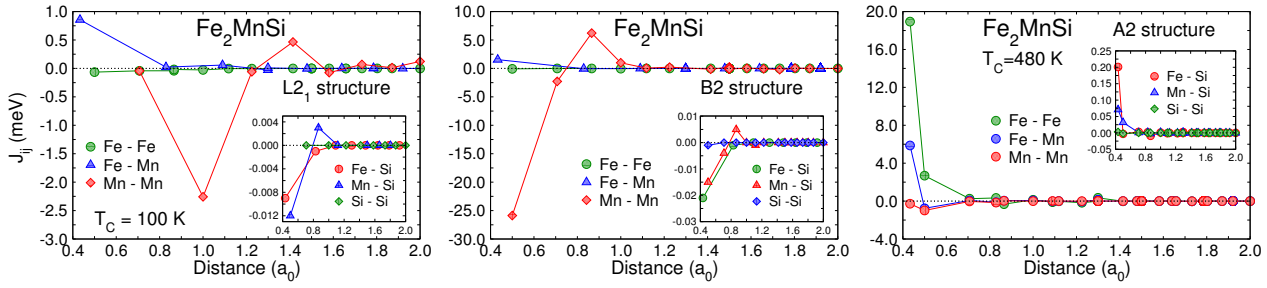

Figure 7.34: Magnetic exchange parameters of Fe_2MnSi for the (a) $L2_1$, (b) B2 and (c) A2 structure calculated with SPR-KKR using the LDA exchange correlation functional of VWN.

and minority spin channels which explains the larger Fe moments. But there is a very strong antisymmetry between the contributions of the manganese atoms comparing the majority and minority spin channels.

In the following Fe_2MnSi is investigated in more detail. In Fig. 7.34, the exchange interactions of the $L2_1$, B2 and A2 structure are shown. In the $L2_1$ structure all interactions are very small and therefore only a small transition temperature to a magnetically ordered state can be expected. Interestingly, the first three neighbor shells give almost no contribution, only the exchange between iron and manganese atoms in the first shell gives a significantly finite contribution around 1 meV. Manganese atoms at a distance of one lattice constant exhibit the strongest and antiferromagnetic interaction. For larger distances the exchange is almost zero except for small oscillations of the Mn-Mn interation. The MC simulation results in spin-spiral type of ground states. As in the case of Fe_2MnAl the term spin-spiral corresponds to the Mn atoms because the small moments of the Fe and Si atoms remain disordered. The details of the shape of this spiral type ground states depend on the size of the simulation cell. In addition, the critical temperature at which a spiral type of order of the manganese moments occurs depends on the size of the simulation cell. This dependence on the size of the simulation cell occurs if the period of the spin-spiral is not commensurable with it. Here, the critical temperature of a simulation cell of $10 \times 10 \times 10$ unit cells is determined by the location of a peak in the specific heat. No detailed investigation of the dependence onto the system size is carried out. It is very interesting that the critical temperature of Fe_2MnSi is by a factor of two higher than the T_C of Fe_2MnAl although the exchange interactions are smaller in Fe_2MnSi. The reason for this can be connected with the dependence of the ordering temperature on the size of the simulation box. On the other hand, the first Mn-Mn interaction which is almost vanishing can lead to a reduction of frustration and a consequent increase of the ordering temperature.

Similar to Fe_2MnAl, large exchange interactions between the Mn atoms occur in the B2 structure because now, the next nearest neighbor Mn-Mn pairs exist. Due to the large antiferromagnetic interaction between the Mn atoms a high transition temperature of the magnetic phase transition is expected. But due to the disorder the formation of ordered magnetic states is hindered. As in Fe_2MnAl the disorder leads to a spin-glass like behavior.

The qualitative and quantitative nature of the exchange interaction changes completely if the A2 structure is considered. Here, the Fe-Fe interactions are no longer almost zero but give the largest contributions which are ferromagnetic (again similar to Fe_2MnAl). In addition,

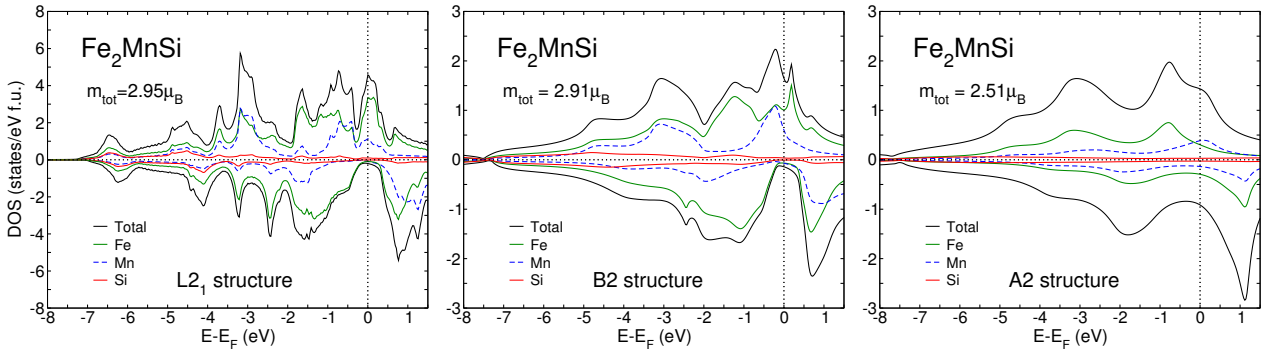

(a) (b) (c)

Figure 7.35: Electronic density of states of (a) the ordered Heusler structure of Fe_2MnSi compared with the electronic density states of (b) the partially disordered B2 and (c) A2 structure.

the exchange interaction between Fe and Mn gives a significant contribution. In contrast to the $L2_1$ and B2 structure, the Mn-Mn interactions is now very close to zero and also the size of the magnetic moment of Fe and Mn changes dramatically compared to the $L2_1$ and B2 structure (see Table 7.6). Obviously, ferromagnetism plays again an important role in the A2 structure. This is reinforced by the high critical temperature of 480 K obtained from the MC simulations. At this temperature a fully ferromagnetic alignment of the moments starts to evolve. The increase of ferromagnetism occurs because the Fe atom occupy 50% of a bcc lattice in A2 disorder.

In Fig. 7.35, the electronic DOS of all three structures is compared. The DOS of the $L2_1$ structure shows a gap like feature in the minority density of states at the Fermi energy which is more pronounced than the one found in Fe_2MnAl. This reinforces the assumption that Fe_2MnSi is also an antiferromagnetic half-metal. The gap remains if B2 disorder is introduced. But half-metallic properties are again completely destroyed if the crystal is fully disordered. Concerning the A2 structure, the total moment of the cell does not change as much as in Fe_2MnAl because the increase of the Fe moments is accompanied with a decrease of the Mn moments and therefore the total moment of the cell is even smaller compared to the total moment in the $L2_1$ and B2 structure.

The investigation of the magnetic exchange parameters of Fe_2MnAl and Fe_2MnSi in different structures shows the complexity of magnetism in this structures. This arises from combining iron with manganese in a fcc type of structure (fcc concerns the sublattices corresponding

	μ_{L2_1} (μ_B)	μ_{B2} (μ_B)	μ_{A2} (μ_B)
Fe	0.16	0.21	1.89
Mn	2.64	2.53	0.69
Si	-0.02	-0.03	-0.06

Table 7.6: Comparison of the magnetic moments of Fe_2MnSi for different ordered and disordered structures. The results are obtained from SPR-KKR calculations using LDA of VWN.

to the $L2_1$ structure). Iron itself shows already a complex magnetism in its γ-phase and if manganese is added, the situation can get even more complicated. This is discussed in more detail in Chapter 4 where binary $Fe_{1-x}Mn_x$ are investigated. But the properties of Fe_2MnAl and Fe_2MnSi cannot be directly compared to the properties of the corresponding binary alloys $Fe_{1-x}Mn_x$ because the addition of Al or Si destroys the trend for well defined antiferromagnetic structures. In addition, the contribution of Fe-Fe and Fe-Mn pairs to the magnetic exchange almost vanishes in the ordered structure. This is explained by considering that the addition of 25% of a main group element leads to dilution.

Considering structural aspects it is very interesting that the addition of Al and Si stabilizes the bcc-like Heusler and B2 structure (bcc concerns the local environment). The addition of Al and Si into Fe-Mn steels is of ongoing discussion because this addition increases the functionality systematically. A systematic analysis of how the addition of Al and Si change the technologically relevant elastic properties is presented in Ref. [103] and references therein. But in this analysis smaller Al or Si concentrations are considered.

7.7 Mn_2FeAl and Mn_2FeSi

In this section the Heusler alloys Mn_2FeAl and Mn_2FeSi are investigated. Up to now only one report can be found which concerns these alloy systems. The authors of Ref. [212] performed a first-principles investigation of the series Mn_2FeZ (Z=Al, Ga, Si, Ge, Sb) and found that this series shows features of half-metallicity although artificial lattice expansions have to be introduced for some of them to find an ideal gap at the Fermi energy in the minority density of states. Unfortunately, the authors only discuss the conventional $L2_1$ structure and they did not check if the inverse Heusler structure is more stable.

A comparison of the total energies obtained from VASP reveals that both systems prefer the inverse Heusler structure. No magnetic state of the conventional structure reveals smaller total energies than any magnetic state of the inverse structure. The energy difference between the magnetic state with the smallest total energy of the conventional and the inverse structure is 0.41 eV per formula unit for Mn_2FeAl and 0.39 eV for Mn_2FeSi. This clearly indicates a strong preference of the inverse Heusler structure. Therefore, only the inverse structure is investigated in the following.

In Fig. 7.36, the electronic DOS of (MnFe)(MnAl) and (MnFe)(MnSi) are compared. The element specific DOS of both systems show a gap like structure of the minority density at the Fermi energy and the total DOS shown in Appendix A.12 reveal a clear gap and show that in both alloys the Fermi energy is located at the upper edge of the conduction band. Therefore, the calculations of both systems indicate that the inverse structure (MnFe)(MnAl) and (MnFe)(MnSi) is half-metallic although the location of the Fermi level indicates a weak resistance of half-metallicity against temperature. It should be noted that as the two symmetrical inequivalent Mn atoms are antiparallel aligned these alloys are examples of half-metallic antiferromagnets. In should be additionally mentioned that the origin of the gap does not follow the simple explanation given in Section 7.2 because the Mn atoms do not form a simple cubic lattice.

It appears to be very strange that the element specific DOS of (MnFe)(MnAl) reveals a peak at the Fermi energy instead of the clear gap obtained in the total DOS which is not calculated by summing the element associated contributions (see Appendix A.12). In order to check if this feature is connected to some artifact arising form the particular choice of the

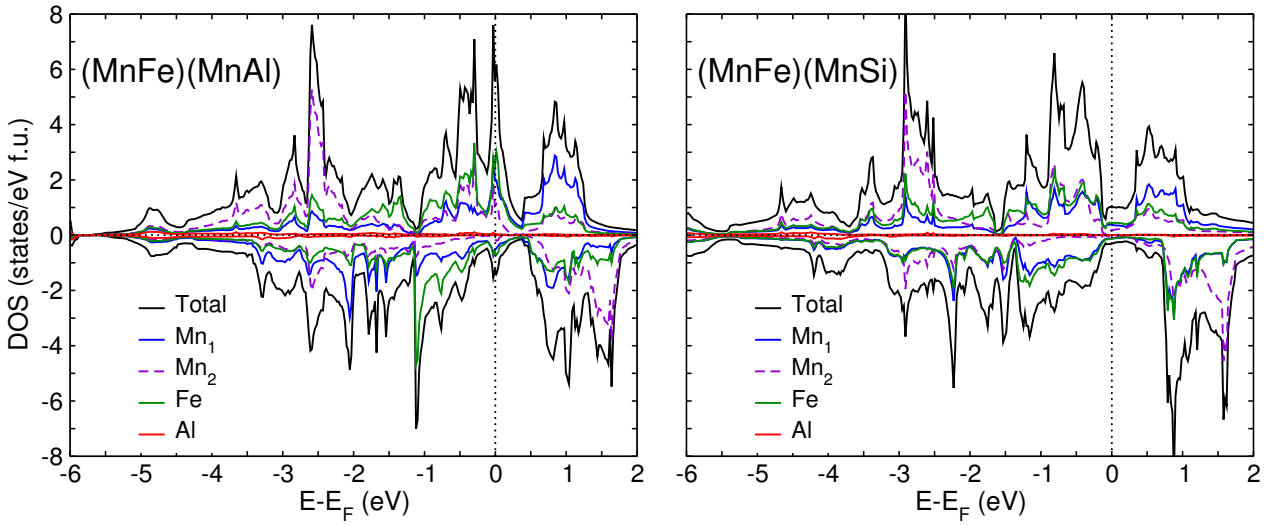

(a) (b)

Figure 7.36: Comparison of the electronic densities of states of (a) (MnFe)(MnAl) and (b) (MnFe)(MnSi) obtain from VASP employing the PBE-GGA.

set of simulation parameters, e.g., the k-point mesh, additional calculations with different parameters are carried out but all reveal a peak at E_F as it is shown in Fig. 7.36(a). But since also the calculation of the DOS within the KKR formalism does not show a peak at E_F the occurrence within the element specific DOS obtained from VASP is attributed to peculiarities arising from the projection scheme.

Concerning the magnetic moments (see Table 7.1), it is noted that the total moment of the unit cell of (MnFe)(MnAl) exhibits exactly the expected integer value of $1.00\,\mu_\mathrm{B}$ and with $1.98\,\mu_\mathrm{B}$ it is very close to the expected $2.00\,\mu_\mathrm{B}$ in (MnFe)(MnSi). Interestingly, the individual moment of one of the Mn types is strongly quenched in both alloys (see Table 7.2). The

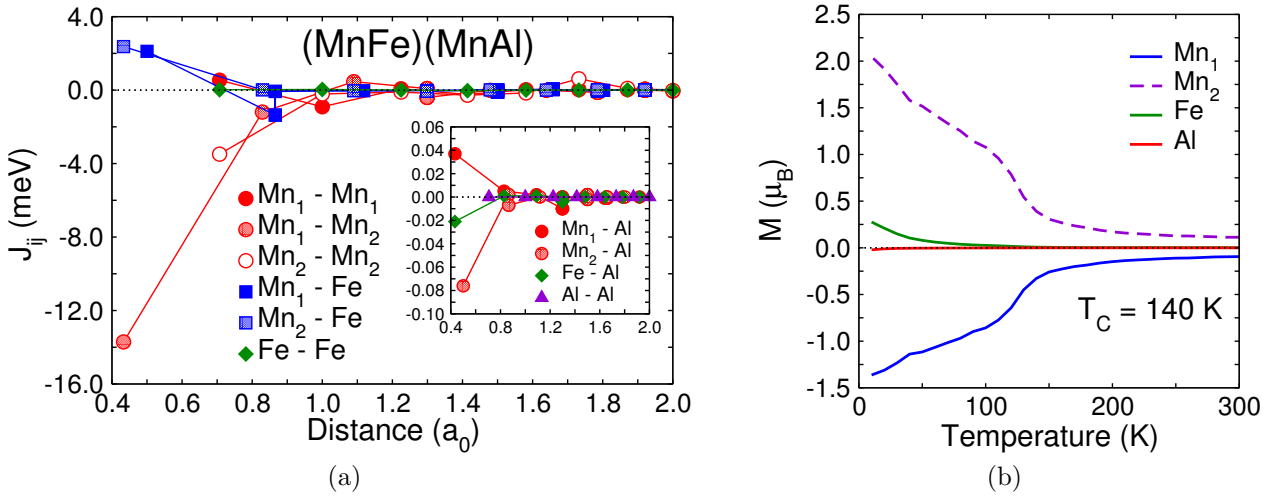

(a) (b)

Figure 7.37: (a) Magnetic exchange parameters of (MnFe)(MnAl) calculated with SPR-KKR using the LDA exchange correlation functional of VWN. (b) Magnetization as a function of temperature obtained from MC simulations.

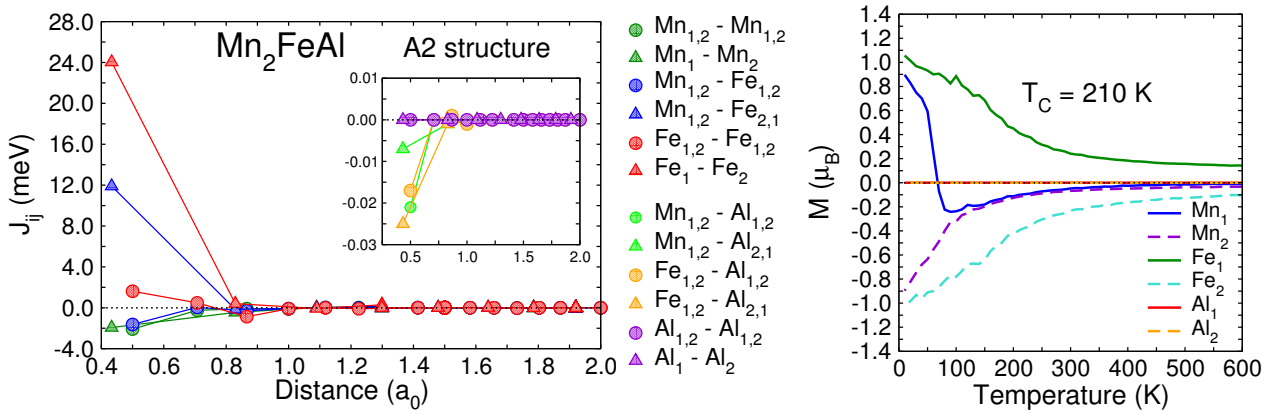

(a) (b)

Figure 7.38: (a) Magnetic exchange parameters of disordered Mn_2FeAl, calculated with SPR-KKR using the LDA exchange correlation functional of VWN. (b) Magnetization curves of the sublattices of Mn_2FeAl.

moment of the iron atoms (2.66 μ_B in (MnFe)(MnAl) and 2.38 μ_B in (MnFe)(MnSi)) gives the dominant contribution to the total magnetic moment per unit cell. The quenched Mn moments indicate frustration of the individual moments in the antiferromagnetic environment. As in the alloys Fe_2MnAl and Fe_2MnSi this quenching of the individual moments is necessary to obtain the expected integer value predicted by the Slater-Pauling behavior.

So far, only the magnetic moments obtained form VASP are discussed. It is interesting to note that the KKR calculations give different results for the individual moments. In particular, the Fe moments are strongly quenched instead of the moment of the second Mn atom (compare Table 7.1). In order to examine the reason for this, additional calculations are carried out. At first it is checked if the different exchange-correlation functionals used in VASP and SPR-KKR are responsible for this results but this is not confirmed by the calculations. In a next step it is analyzed if both states with different individual moments can be obtained in both methods but this is also not possible. An initialization of VASP corresponding to the state found in SPR-KKR leads either to the original state or to serious convergence problems that could not be solved by simply changing the mixing parameters. Comparable problems are found in additional SPR-KKR calculations. It is concluded that both states must be closely related or even degenerated.

The following analysis of the exchange parameters of the inverse structure is based on the reference state which is obtained from the SPR-KKR calculation. Figure 7.37(a) shows the magnetic exchange parameters of (MnFe)(MnAl). The strongest contribution is the antiferromagnetic exchange interaction between Mn_1 and Mn_2. The interactions between both types of Mn atoms and iron are ferromagnetic but by a factor of more than six smaller and the interaction between the Fe atoms is almost zero. This results from the very small Fe moment of only 0.10 μ_B. This particular configuration of interactions leads to the finite temperature behavior of the magnetization shown in Fig. 7.37(b). A small critical temperature of only 140 K is obtained in the MC simulation. Both Mn sublattices align antiferromagnetically but the temperature dependence does not follow the usual manner of the simple Heisenberg model. After a strong increase of the magnetization of both Mn sublattices around the critical temperature, this increase becomes more flat and at around 50 K it becomes again

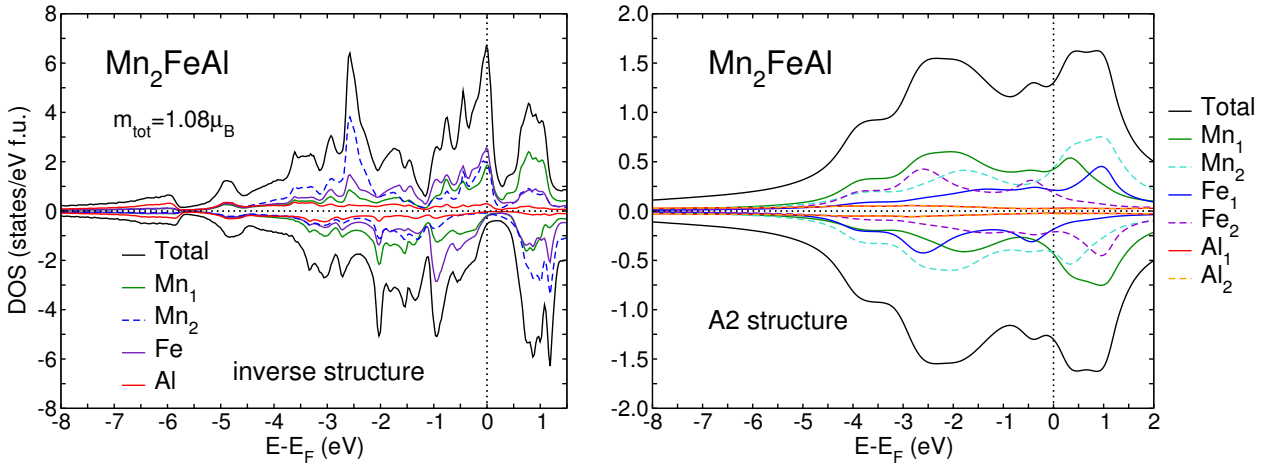

Figure 7.39: Electronic density of states of (a) the ordered (MnFe)(MnAl) and (b) A2 disordered Mn_2FeAl obtained from SPR-KKR.

stronger. This behavior is a result of the interaction with Fe sublattice which introduces frustration because it interacts antiferromagnetically with Mn_1 and Mn_2 and acts against the antiparallel alignment of the Mn moments. Therefore, iron shows only a weak increase of magnetic order but finally aligns parallel to Mn_2 because its interaction with this sublattice is a little bit stronger. The behavior of the Fe sublattice results from the fact that there is no significant interaction between the Fe atoms. In addition, every Mn_1 atom is surrounded by four Mn_2 atoms which are all interacting antferromagnetically with Mn_1. This leads to frustration, non-collinear alignment and small critical temperature. The non-collinear tendency is deduced from the incomplete recovery of the magnetization per atom of the Mn sublattices when compared to the individual magnetic moments. One may conclude that a more sophisticated *ab initio* study of Mn_2FeAl has to include non-collinear calculations since a simple collinear treatment cannot reproduce the realistic electronic structure of this alloy.

A CPA calculation of the A2 structure of Mn_2FeAl reveals a different magnetic structure. As two sublattices are used to model this system (CsCl structure) it is found that on the first sublattice the Mn moments are positive and the Fe moments negative. On the second the situation is the other way around. The Mn moment is $1.40\,\mu_B$ and the Fe moments $1.84\,\mu_B$ on both lattice sites. Therefore, the Fe moments are much larger compared to the case of the inverse structure. As the moments are equal besides the different sign, the total magnetic moment is zero. This indicates that an antiferromagnetic alignment within the Fe and Mn sublattice reduces the frustration significantly.

Figure 7.38(a) shows the magnetic exchange parameters of A2 disordered Mn_2FeAl. These interactions are qualitatively as well as quantitatively different from those found in the ordered inverse Heusler structure. Almost all nearest neighbor interactions are strongly ferromagnetic. Only, the interaction between nearest neighbor Mn atoms is antiferromagnetic but only weak compared to the others. The occurrence of strong Fe-Fe interaction can be immediately understood if it is considered that Fe atoms cannot be nearest neighbors in the inverse Heusler structure but in the A2 structure. But also the interaction of nearest neighbor Mn-Fe pair is strongly enhanced by more than a factor of three which is connected to the stronger Fe moment. But, this configuration of the exchange interaction is unexpected if the

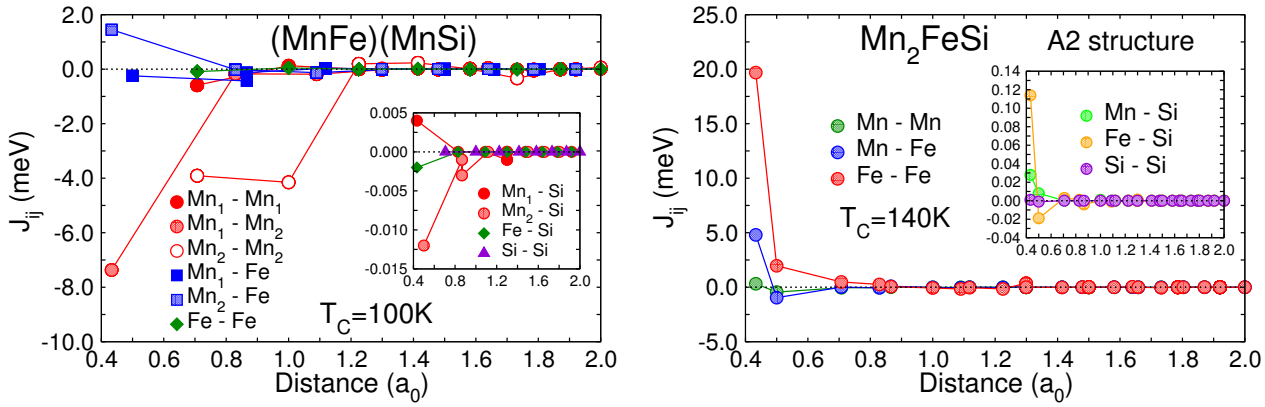

(a) (b)

Figure 7.40: (a) Magnetic exchange parameters of (a) (MnFe)(MnSi) and (b) A2-Mn_2FeSi calculated with SPR-KKR using the LDA exchange correlation functional of VWN.

intrinsic antiferromagnetic alignment of the Fe and the Mn sublattice of the reference state is considered.

Figure 7.38(b) shows the magnetization as a function of temperature obtained from the MC simulation. Although the Fe_1-Fe_2 exchange interactions are strong, the ground state obtained within the MC simulation is a complicated non-collinear antiferromagnetic one (this leads to incomplete recovery of the average magnetic moment at low temperatures). This can be explained with the fact that the nearest neighbor Fe_1-Fe_2 interactions do not occur often because of the small concentration of iron. Instead, the interaction between nearest neighbor Mn-Fe and Mn-Mn pairs occurs very often because Fe and Mn are on the average surrounded by roughly eight Mn atoms. Therefore, the Mn_1 sublattice tends to align parallel with Fe_1 and Mn_2 with Fe_2. As both Mn sublattices interact antiferromagnetically and as this interaction is weak it becomes only important at low temperatures. This leads to the reorientation of the Mn_1 sublattice at around 100 K (see Fig. 7.38(b)). The critical temperature of 210 K is a rough estimate because the transition to the ordered phase does not show the typical features. The fluctuation of the sublattice magnetizations is very strong even at temperatures below 100 K. Therfore, Fig. 7.38(b) shows the magnetization averaged over five MC simulations but still no smooth function of the temperature is obtained.

Figure 7.39 compares the electronic densities of states of the inverse and the A2 structure. The KKR calculation of the inverse structure also shows the trend for a half-metallic gap. As already mentioned above, the element specific DOS obtained from the KKR calculation does not reveal a peak in the minority spin channel at the Fermi energy as it is found in the VASP calculation. Instead it shows the typical minimum with some remaining states around E_F which is connected with the deficient description of the gap within the ASA-KKR. The DOS of the A2 structure is strongly smeared out and reflects the complete antiferromagnetic state of this structure because it is perfectly symmetric. The DOS of the Mn_1 sublattice is compensated by the Mn_2 sublattice and so forth for all other sublattices.

The magnetic exchange interactions of (MnFe)(MnSi) are shown in Fig. 7.40(a). They are qualitatively similar to those of (MnFe)(MnAl) but the interactions in (MnFe)(MnAl) are almost a factor of two larger than those of (MnFe)(MnSi). In addition, the Mn_2-Mn_2 interaction in (MnFe)(MnSi) are qualitatively and quantitatively different from those found

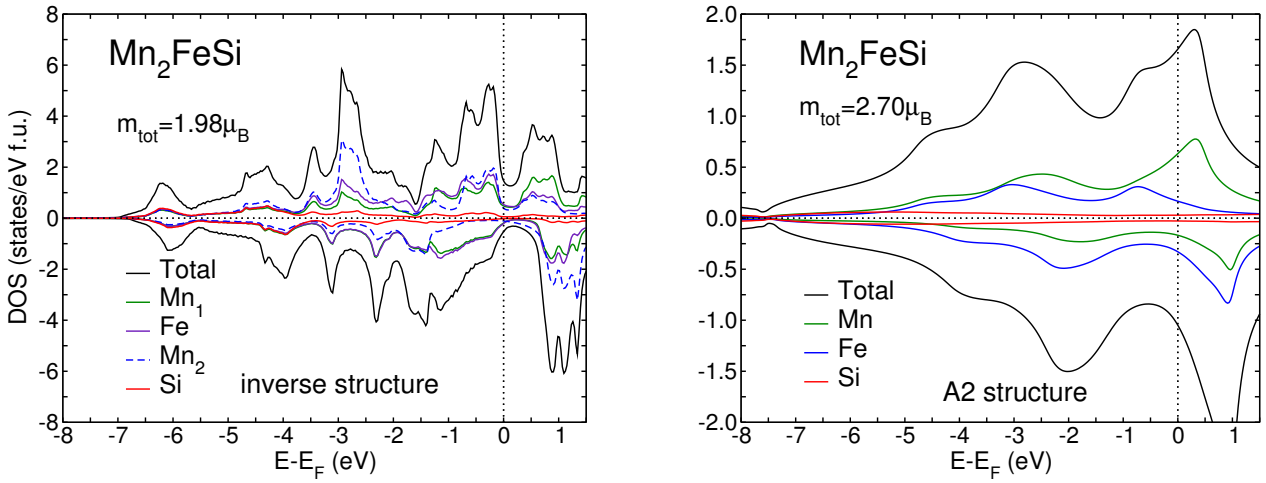

Figure 7.41: Electronic density of states of (a) the ordered structure (MnFe)(MnSi) and (b) A2-Mn_2FeSi.

in (MnFe)(MnAl). The critical temperature of 100 K is also lower than that of Mn_2FeAl but here a spin-spiral type of ground state develops during the MC simulation and therefore the critical temperature is estimated from the specific heat. The main reason for this is the frustration of the Mn sublattices with respect to each other as it is described in the discussion of the exchange interactions of (MnFe)(MnAl). Additionally, the interaction between Mn and Fe is now too small to induce a simpler order.

Figure 7.40(b) shows the magnetic interactions of the A2 structure of Mn_2FeSi. In this structure a simple ferromagnetic state is found in the CPA calculation. All nearest neighbor interactions are ferromagnetic but the Mn-Mn interaction is almost zero. Therefore, only the Fe-Fe and Mn-Fe interactions are important. But, as the probability of the occurrence of nearest neighbor Fe-Fe pairs is small their contribution is small and the critical temperature obtained from the MC simulation is only 140 K because it is almost exclusively determined by the weak Mn-Fe interactions.

In Fig. 7.41 the electronic DOS of (MnFe)(MnSi) and disordered Mn_2FeSi obtained from KKR calculations is shown. As in (MnFe)(MnAl) the DOS of the inverse structure exhibits a gap like minimum around the Fermi energy indicating that also the KKR method reveals (MnFe)(MnSi) to be a half-metallic antiferromagnet. All other features are also comparable to the DOS obtained from VASP but a bit more rounded because of the finite imaginary part. The CPA calculation of the A2 structure leads to a larger magnetic moment due to the ferromagnetic alignment of the moments and the resolution of the quenching. As usual the DOS of the A2 structure is strongly smeared so that it reveals almost no similarities to the DOS of the ordered system.

The discussion of the results obtained for (MnFe)(MnAl) brings up some peculiarities. First of all, the projection scheme used in VASP for the determination of the element specific DOS leads to a pronounced deviation from the result obtained without this scheme. Instead of a clear gap around the Fermi energy, the projection leads to a peak at E_F. The second peculiarity is the occurrence of different magnetic states within the calculations of the different methods which cannot be simply resolved. This leads to the conclusion that the

(MnFe)(MnAl) system requires a more detailed investigation because it cannot be excluded that the peculiarities found here are connected to interesting physics. Interestingly, the (MnFe)(MnSi) system does not lead to any serious open questions and instead the analysis of this system is more straightforward.

7.8 Mn_2CoAl and Mn_2CoSi

In this section Mn_2CoAl and Mn_2CoSi are investigated. Only few studies of this type of Heusler alloys have been carried out yet. The authors of Ref. [213] performed a first-principles investigation and predicted both alloys to be half-metallic ferrimagnets within the inverse Heusler structure. Recently, Mn_2CoAl attracted interest because of its spin gapless semiconductor behavior (see Ref. [214]). Such materials exhibit a gap in the minority density of states and in the majority spin channel the highest valence band touches the Fermi energy from below and the lowest conduction band touches it from above. This results in a gap of zero measure in the majority channel. Therefore, such materials are the limiting case between a half-metal and a semi-conductor. Due to the particular electronic structure experimental investigations of (MnCo)(MnAl) show extraordinary spintronic and thermoelectric properties [214].

Also structural aspect of Mn_2Co-based Heusler alloys are very interesting because during the discussion of $Co_{1-x}Mn_x$ alloys it is mentioned that experiments reveal that these alloys are not stable against spinodal decomposition on the Mn rich side of the phase diagram. In addition, the $Co_{1-x}Mn_x$ alloys are only found in solid solution and not in ordered structure within experimental investigations. But obviously, the addition of a main group element changes this trend completely. The (MnCo)(MnAl) and (MnCo)(MnSi) alloys are examples for completely ordered stable structures of Mn dominated CoMn-based alloys because, although the samples of (MnCo)(MnAl) investigated in Ref. [214] are not single crystals, they exhibit a clear polycrystalline structure.

Again the presentation of the theoretical results obtained during the present study starts with the comparison of the electronic DOS evaluated with VASP. Figure 7.42(a) shows that the spin gapless semiconductor features of (MnCo)(MnAl) are reproduced. There is a clear gap in the minority DOS and a dip of zero measure in the majority DOS at E_F. These features are even more pronounced in the total DOS obtained without the projection scheme shown in Appendix A.12. On the other hand, (MnCo)(MnSi) is no spin gapless semiconductor because in its DOS shown in Fig. 7.42(a) the Fermi energy is located on a pronounced peak in the majority channel. But (MnCo)(MnSi) is a half-metal because is shows the typical gap in the minority density which is again particularly obvious in Fig. A.3 in the Appendix. The projection scheme leads to a peak at the Fermi energy comparable to what is found in the DOS of (MnFe)(MnAl) in Section 7.7. As the DOS of (MnFe)(MnAl) and (MnCo)(MnSi) show a large peak in the majority state at the Fermi energy it is concluded that the artificial occurrence of the peak in the minority channel is connected to some sort of weak mirroring of the majority density of states onto the minority channel. This conclusion is confirmed by analyzing the DOS of other Heusler alloys investigated in this chapter. This reveals that whenever there is a pronounced structure in the majority channel it is weakly reflected by the minority channel.

The magnetic moments per formula unit are in perfect agreement with the expected integer values. For (MnCo)(MnAl) a moment of $1.99\,\mu_B$ and for (MnCo)(MnSi) $3.00\,\mu_B$ is found.

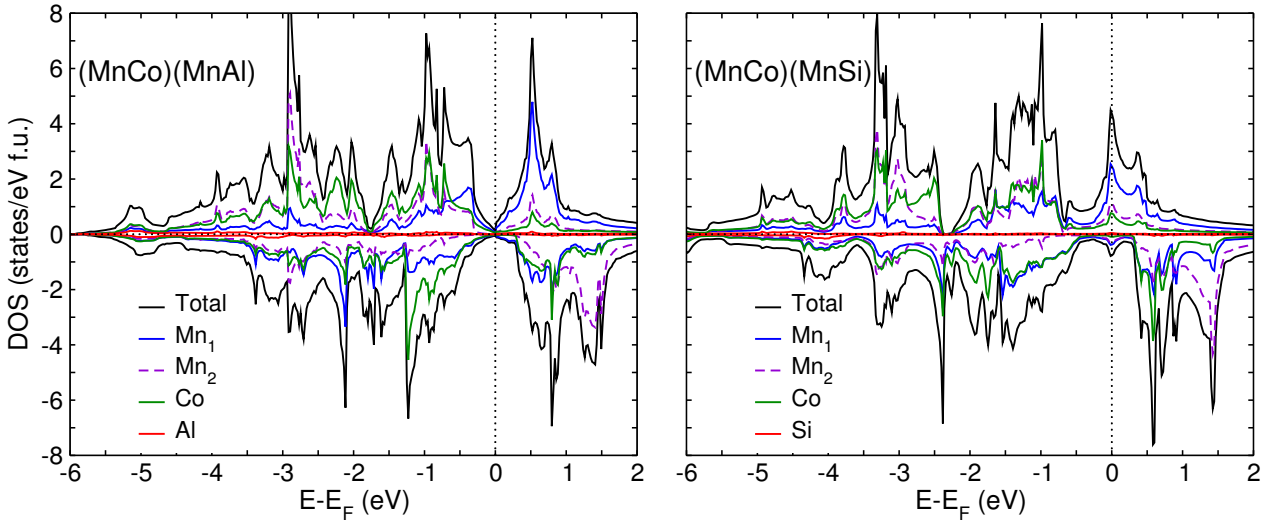

Figure 7.42: Comparison of the electronic densities of states of (a) (MnCo)(MnAl) and (b) (MnCo)(MnSi) obtain from GGA calculations with VASP.

The magnetic structure of lowest energy of both alloys is antiferromagnetic. The moments of the two Mn atoms are antiparallel aligned and of different magnitude. One of the Mn moments in (MnCo)(MnSi) is quenched to $0.55\,\mu_B$. The Co moment is parallel aligned to the Mn moment with the largest magnitude which is also the nearest neighbor of Co (see Table 7.1). According to the results for the binary $Co_{1-x}Mn_x$ alloys it is not expected that the value of the Co moment is close to $1.00\,\mu_B$ ($0.96\,\mu_B$ in (MnCo)(MnAl) and $0.84\,\mu_B$ in (MnCo)(MnSi)) because the antiferromagnetic environment generated by the Mn moments leads to strongly quenched Co moments in the binary alloys.

Figure 7.43(a) shows the magnetic exchange interactions of (MnCo)(MnAl). There are strong ferromagnetic interactions between Mn_2 and Co pairs and a strong antiferromagnetic interaction between Mn_2-Mn_2 pairs. This reflects the magnetic structure described in the last paragraph. As there is only an almost zero interaction between the Co atoms, the finite temperature magnetism of Co is almost exclusively determined by its exchange interaction with the Mn_2 sublattice. The critical temperature obtained from the MC simulations is 550 K which is 170 K below the experimental result of 720 K. This is again a systematic deviation of around 200 K between the theoretical prediction and the experimental finding. It is particularly interesting that the Mn-Co interaction is strong because such interaction occurs in every Heusler alloy investigated so far that contains Co. In other words: If the Heusler alloy contains Co there is always a strong ferromagnetic interaction of Co with the other transition metal atoms if they are nearest neighbors.

The KKR-CPA calculation of the A2 structure of Mn_2CoAl reveals a completely ferromagnetic state. The exchange interactions shown in Fig. 7.43 exhibit ferromagnetic interactions between the Co moments of nearest neighbors and also between nearest neighbor Mn-Co pairs. The value of this interactions is close to the value of the Mn-Co interaction in (MnCo)(MnAl). The Mn-Mn interaction in the A2 structure is antiferromagnetic but smaller compared to what is found in ordered (MnCo)(MnAl). It is remarkable that the form of the J_{ij} of disordered Mn_2CoAl is very similar to the form of the exchange interac-

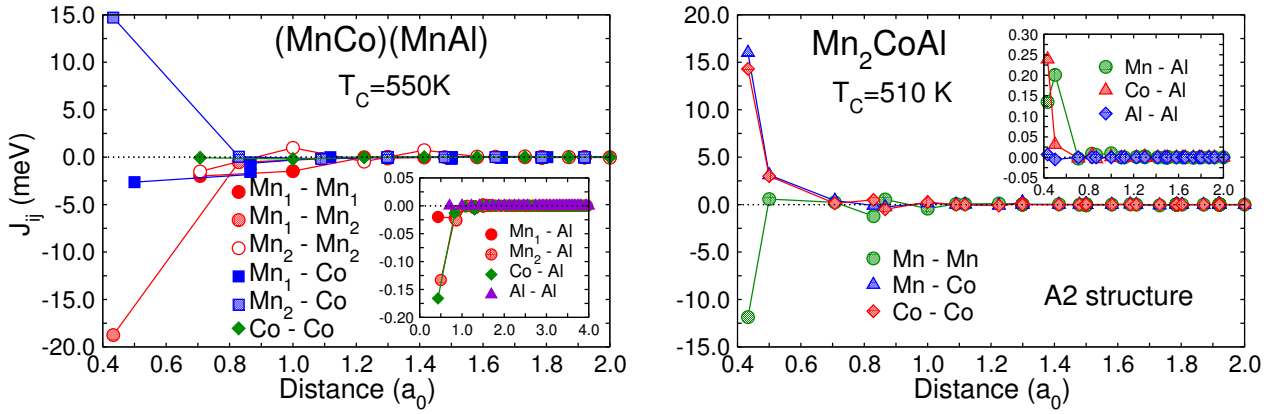

Figure 7.43: Magnetic exchange parameters of (a) (MnCo)(MnAl) and (b) disordered A2-Mn_2CoAl, calculated with SPR-KKR using the LDA exchange correlation functional of VWN.

tions in disordered Co_2MnAl. There is only a quantitative difference because the interactions in Co_2MnAl are stronger. The critical temperature of the A2 structure is only 40 K smaller than the critical temperature of the ordered structure. This is attributed to the comparable strength of the exchange interactions and the analogous competition between ferromagnetic and antiferromagnetic contributions.

Concerning the electronic DOS of (MnCo)(MnAl) obtained from the KKR calculation (see Fig. 7.44(a)) one finds that the KKR calculations nicely reproduce the feature of the spin gapless semiconductor. As expected, the relevant feature are less pronounced compared to the VASP calculation but again this is fully explained by the systematic deviations introduced by the ASA approximation and the finite imaginary part used in the KKR calculation. In particular the finite imaginary part leads to a smearing of the DOS and therefore sharp feature are pronounced. The DOS of the disordered A2 structure shown in Fig. 7.44(b) reveals almost no similarity to the ordered structure and all feature are strongly smeared.

Now, the magnetic exchange interactions and the theoretical predictions of the critical temperatures of (MnCo)(MnSi) and A2-Mn_2CoSi are discussed. In Fig. 7.45(a), the interactions of (MnCo)(MnSi) are shown. These interactions are comparable to those found in (MnCo)(MnAl) although the antiferromagnetic interaction between the two types of Mn atoms is much weaker in (MnCo)(MnSi). Therefore, the critical temperature is reduced to 270 K which is almost half of the value obtained for (MnCo)(MnAl).

The magnetic structure of A2-Mn_2CoSi is completely ferromagnetic and the exchange interactions of this system are shown Fig. 7.45(b). All nearest neighbor interactions are ferromagnetic but the interaction between the Mn atoms is very weak. The Mn-Co interaction is still the strongest but is reduced compared to the inverse structure. Therefore, the critical temperature is reduced to 130 K. It is important to note that the introduction of disorder stabilizes a ferromagnetic ground state. This occurs due to the small Mn-Mn interactions which strongly antiferromagnetic in other Mn-based alloys. This small interaction is also responsible for the very low critical temperature because as the Mn atoms are only weakly interacting, but as Mn occupies 50% of the entire lattice, the occurrence of the strong Mn-Co interactions is partially suppressed. Interestingly, the exchange interactions of A2-Mn_2CoSi are not comparable to the result of Co_2MnSi as it is found in the comparison of Mn_2CoAl

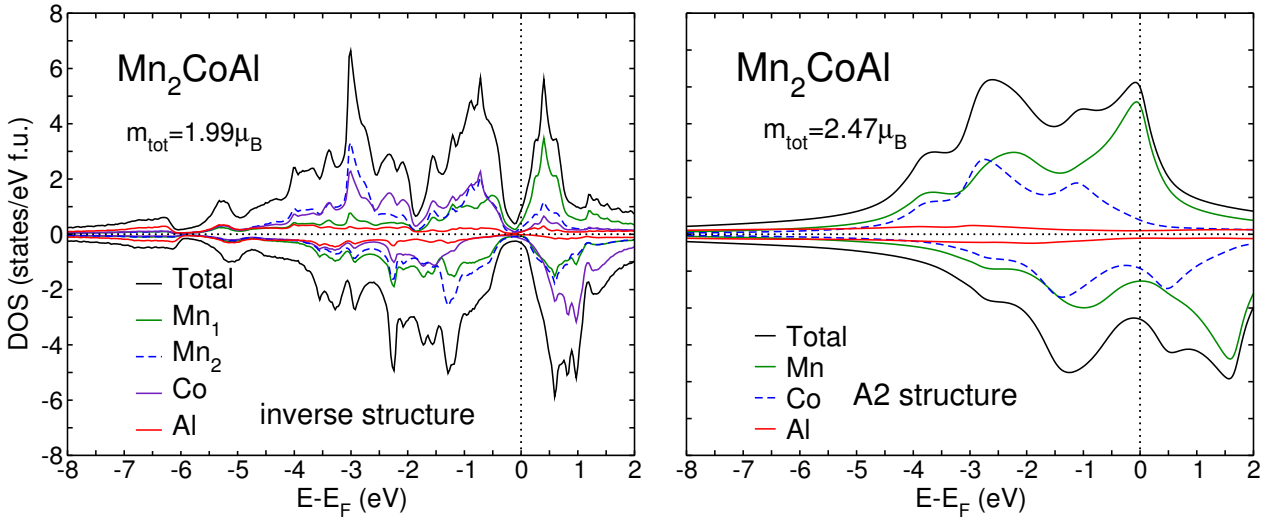

(a) (b)

Figure 7.44: Electronic density of states of the ordered inverse Heusler (MnCo)(MnAl) compared with the electronic density of the fully disordered A2 structure.

and Co_2MnSi.

Figure 7.46 shows the electronic DOS of (MnCo)(MnSi) and A2-Mn_2CoSi obtained from SPR-KKR. As for (MnCo)(MnAl), the KKR calculations of (MnCo)(MnSi) nicely reproduces the result of the VASP calculations. The DOS of A2-Mn_2CoSi shows again that half-metallicity breaks down in the limit of strong structural disorder.

The present investigation succeeds in reproducing the spin gapless semiconductor property of (MnCo)(MnAl). In addition, the strange occurrence of a peak of the minority density as it is found in (MnFe)(MnAl) is also found in (MnCo)(MnSi). It is now attributed to a weak reflection of the of the majority density. The reflection cannot be attributed to the partial inclusion of scalar relativistic effects within the VASP calculations because the total DOS obtained without the projection does not show the reflection. Therefore, the reflection is completely attributed to deviations occurring during the projection of the DOS onto elements specific contributions.

As Mn_2CoAl can also nucleate in the conventional Heusler structure (although the energy difference is quiet large) and as the conventional structure does not reveal the spin gapless semiconductor features, the property is found to be sensitive with respect to the structure.

7.9 Summary of half-metallic Heusler alloys

In the previous sections of this chapter, Heusler alloy based on manganese, iron and cobalt and containing the additional main group element aluminum or silicon are investigated. Half of the investigated systems prefer to nucleate within the conventional Heusler structure and the other half prefers the inverse one. Iron rich alloys in combination with cobalt as well as manganese rich alloys together with iron or cobalt solidify as inverse Heuler alloys. On the other hand, cobalt rich systems strongly prefer the conventional structure. The same holds for iron rich systems with manganese.

All investigated systems, except for (FeCo)(FeAl) and (FeCo)(FeSi) turn out to be half-

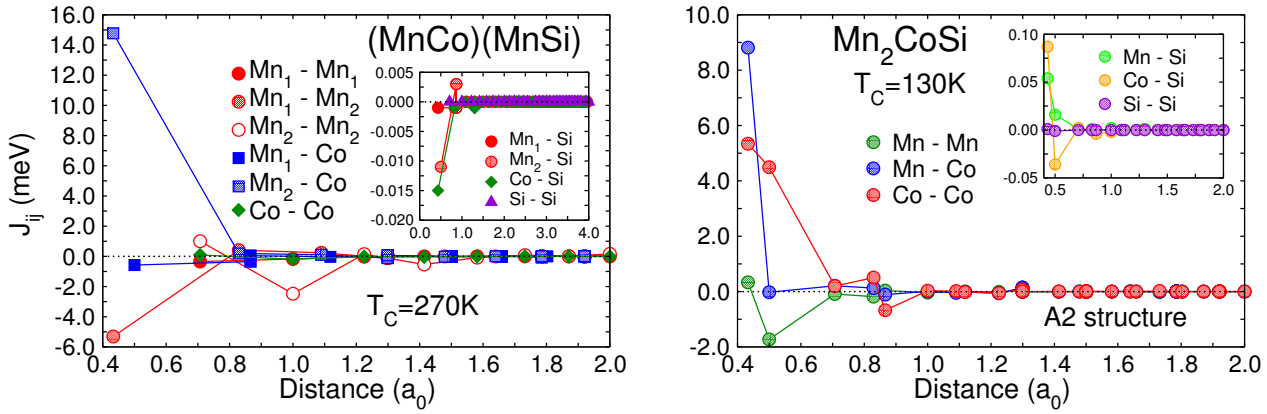

(a) (b)

Figure 7.45: Magnetic exchange parameters of (a) (MnCo)(MnSi) and (b) A2-Mn_2CoSi, calculated with SPR-KKR using the LDA exchange correlation functional of VWN.

metallic. The cobalt-iron and cobalt-manganese based systems are half-metallic ferromagnets whereas iron-manganese, manganese-iron and manganese-cobalt based Heusler alloys are half-metallic antiferromagnets. But concerning the cobalt-iron based Heusler alloys it is found that effects of correlation have to be necessarily included to obtain a distinct half-metallic gap. This is explained by the deficient description of the localized e_g-states of iron. The localization leads to correlations that can only be captured by using the LDA+U or GGA+U method which explicitly accounts for correlations of strongly localized electrons. Such treatment is not necessary for the investigation of the other alloys and in particular the total DOS of (MnFe)(MnAl) and (MnFe)(MnSi) reveal a half-metallic gap without account for correlation effects although they contain iron in the same amount as Co_2FeAl and Co_2FeSi. Therefore, it is carefully concluded that correlation effects of Fe electrons are more pronounced if Fe is combined with Co and in particular in additional combination with Si. This is confirmed by the investigation of Fe_2MnAl and Fe_2MnSi which contain 50% iron, but with a clear half-metallic gap occuring in the minority channel.

It turns out that the half-metallic feature of the DOS is quite stable against B2 disorder but vanishes completely in the limit of strong A2 disorder. In addition, the magnetic properties are sensitive to the type of disorder because it alters the magnetic exchange interaction due to the change of the chemical environment. Therefore, the magnetic ground state as well as the critical temperature can dramatically deviate from what is found in the ordered system.

It is also interesting to note that for many cases the theoretical prediction of the critical temperature as obtained from the MC simulation deviates by 200 K from the experimental result. This shows that the overall trend of the finite temperature magnetism is captured here but also some systematic deviation is found. As already discussed extensively in the previous chapters, this deviations results form the intrinsic approximations of the method but it can be additionally connected with the fact that the critical temperature can rise in the disordered case and that the sample investigated in experiments are never fully ordered.

Some of the properties observed in the Heusler alloys are comparable to the properties of the corresponding binary alloys. In particular the qualitative behavior of the exchange parameters can be very similar. On the other hand, significant deviation occur as, e.g., the fact that the Mn-Co-based Heusler alloys exhibit ordered structures whereas the Co-Mn-based

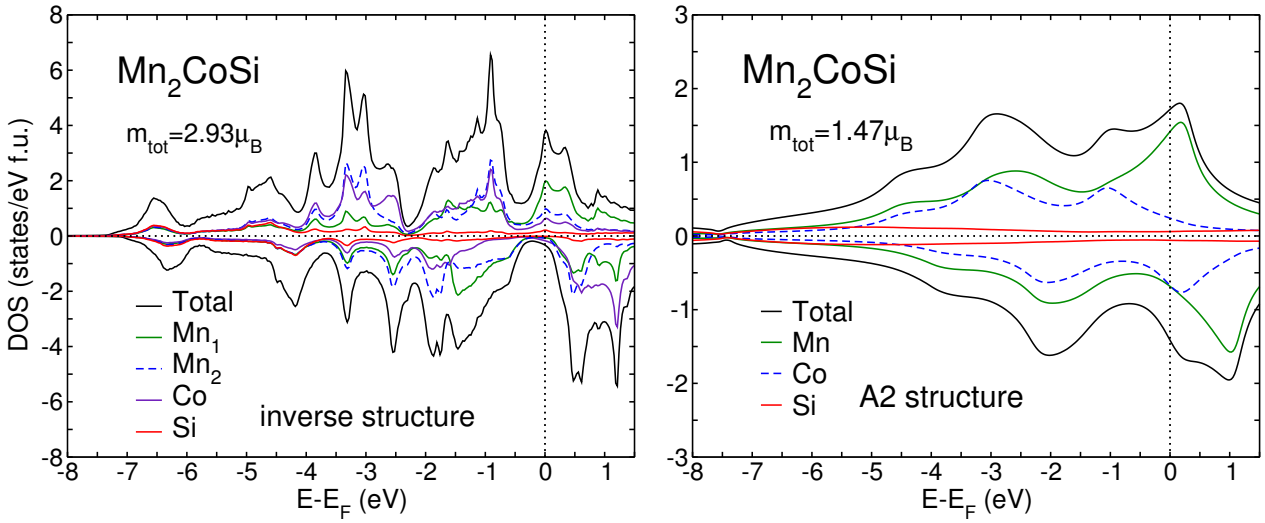

Figure 7.46: Electronic density of states of the ordered inverse Heusler structure of (MnCo)(MnSi) compared with the electronic density of the fully disordered A2 structure.

binary alloys only solidify in solid solutions.

7.10 Magnetic properties of Ni-Mn-based Heusler alloys

In this section a different group of Heusler alloys is investigated. These systems are Ni-Mn based Heusler alloys that reveal magnetic and a martensitic phase transition. Therefore, such materials can show the magnetic shape-memory effect and are also interesting for magnetocaloric applications (see the introduction to Heusler alloys in Section 1.1). An introduction to this field and especially to the connection between shape-memory and magnetocaloric effect is given in Ref. [215]. Here, the focus of the investigation is on the magnetic properties and in particular magnetic exchange parameters. A new method developed to gain a detailed insight into magnetic mechanisms is used. This is the splitting of magnetic exchange parameters into different contribution arising from electrons with special symmetry. These are the e_g and t_{2g} associated electrons. As all these are d-electrons, the interaction of the s- and p-electrons are separately taken into account. The decomposition is achieved by restricting the trace in Eq. (2.253) to the angular momentum indices corresponding to the contribution of interest. Therefore, Lichtenstein's formula corresponding to a certain combination of contributions is given by

$$J_{ij}^{C_1,C_2} = \frac{1}{4\pi}\mathrm{Im}\int_{-\infty}^{E_\mathrm{f}} \mathrm{d}E \sum_{L\in C_1}\sum_{L\in C_2} (t_{i\uparrow}^{-1} - t_{i\downarrow}^{-1})_L \tau_{LL'}^{ij\uparrow} (t_{j\uparrow}^{-1} - t_{j\downarrow}^{-1})_{L'} \tau_{L'L}^{ji\downarrow} \,. \tag{7.1}$$

where the C_i denote the contribution of current interest. This means they can be e_g, t_{2g}, sp or d. The $L = (l, m)$ are composite indices and run over all values associated with the C_i. In how far this decomposition leads to new understanding of the magnetism of such alloys becomes apparent during the following discussion. The calculations performed to obtain the decomposed exchange parameters are carried out by using the Machikaneyama KKR code [216].

Composition	c/a	$\mu_{\mathrm{Ni}}\,(\mu_{\mathrm{B}})$	$\mu_{\mathrm{Co}}\,(\mu_{\mathrm{B}})$	$\mu_{\mathrm{Mn_1}}\,(\mu_{\mathrm{B}})$	$\mu_{\mathrm{Mn_2}}\,(\mu_{\mathrm{B}})$	$\mu_{\mathrm{Sn}}\,(\mu_{\mathrm{B}})$
$Ni_{50}Mn_{39}Sn_{11}$	1.00	0.12	-	3.67	-3.87	-0.04
$Ni_{50}Mn_{39}Sn_{11}$	1.28	0.15	-	3.61	-3.81	-0.05
$Ni_{50}Mn_{39}Sn_{11}$	0.94	0.14	-	3.67	-3.86	-0.04
$Ni_{45}Co_5Mn_{39}Sn_{11}$	1.00	0.14	0.79	3.64	-3.87	-0.04
$Ni_{45}Co_5Mn_{39}Sn_{11}$	1.28	0.15	0.51	3.60	-3.80	-0.05
$Ni_{45}Co_5Mn_{39}Sn_{11}$	0.94	0.14	0.72	3.64	-3.86	-0.04

Table 7.7: Comparison of the magnetic moments. The calculations are performed using the specx code [216] and GGA. The atomic volume is given by 54.62 $\mathrm{Å}^3$ in all cases.

In a first step, $Ni_{50-x}Co_xMn_{39}Sn_{11}$ alloys are analyzed for $x = 0$ and 5. They are of special interest concerning a spin-glass type of behavior in their low temperature phase. The authors of Ref. [9] present a detailed experimental investigation of $Ni_{50-x}Co_xMn_{39}Sn_{11}$ over a range of x reaching from 0 to 10. They established a complex phase diagram. For all compositions a paramagnetic austenite is found. For small Co concentrations up to $x = 4$, the martensitic transformation takes place before a magnetic phase transition occurs. In the same concentration range the martensite undergoes a phase transition to a superparamagnetic phase followed by a subsequent transition to a so called superspin-glass state. For compositions between $x = 5$ and 9 the austenite becomes ferromagnetic and during the martensitic transformation the superparamagnet evolves, again followed by a transition to a superspin-glass state. Above $x = 9$ the martensitic transition vanishes and only a ferromagnetic austenite state is found at low temperatures. The term "super" indicates that the corresponding phase are not homogeneous but cluster exist which show a certain type of magnetic structure and interact to form a certain type of "super"-structure. An introduction to the field of supermagnetism can be found in Ref. [217].

In the following, always three types of structures are considered for each concentration. First, the cubic structure is considered because this structure is supposed to be the high temperature phase (austhenitic phase) across the entire composition range considered here. In addition, two tetragonal distorted structures are considered. One corresponds to a c/a-ratio of 0.94 and the other to 1.28. The atomic volume and c/a-ratios are extrapolated from VASP calculations at slightly different composition. The question which of both minima in the c/a-variation is connected to the structural ground state in the martensitic phase can differ for different types of Heusler alloys and is still a matter of ongoing discussion (for details see Ref. [5]).

Only the conventional Heusler structure is considered where the excess manganese is placed onto the site of the Z-element by using the CPA formalism and additional Co is mixed onto both Ni sublattices.

A summary of individual magnetic moments found in $Ni_{50}Mn_{39}Sn_{11}$ and $Ni_{45}Co_{45}Mn_{39}Sn_{11}$ is given in Table 7.7. Figure 7.47 shows the magnetic exchange parameters of $Ni_{50}Mn_{39}Sn_{11}$ for $c/a = 1.00$, $c/a = 1.28$ and $c/a = 0.94$ together with their decomposition into different contributions. Comparing the total exchange interactions in Fig. 7.47(a), (b) and (c) it becomes apparent that a tetragonal distortion leads to a strong increase of the antiferromagnetic

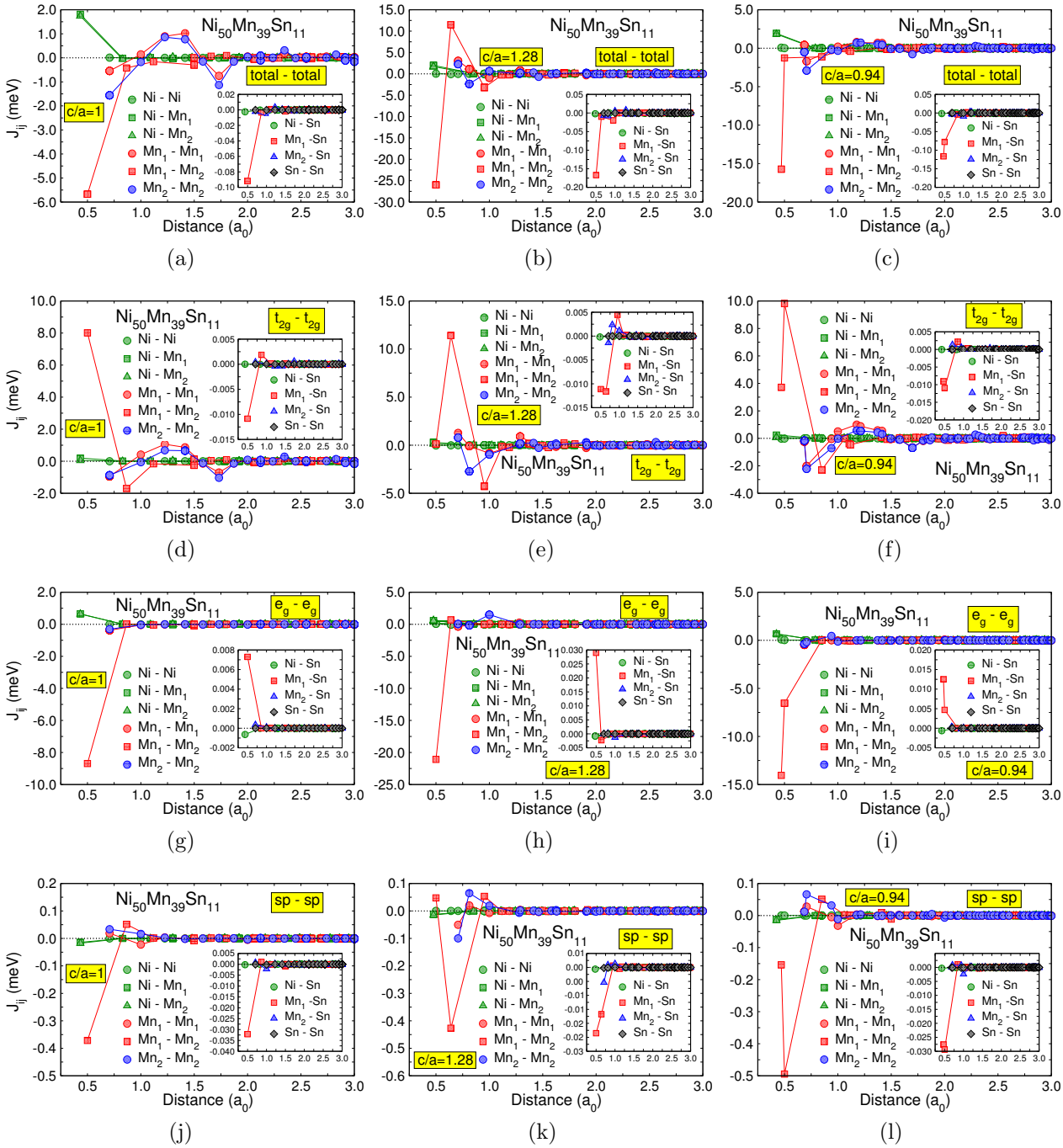

Figure 7.47: Magnetic exchange parameters of $Ni_{50}Mn_{39}Sn_{11}$, calculated with the specx code using the GGA exchange correlation functional.

interaction between the Mn_1 and Mn_2 moments. All other interactions are much smaller but an RKKY type of oscillation of the Mn-Mn exchange interactions is always present. This oscillation seems to be much more pronounced in the $c/a = 1$ case but this is misleading because the energy scale is much smaller compared to the tetragonal distorted cases.

The origin of the increase of the strong next nearest neighbor Mn_1-Mn_2 interaction is now analyzed by investigating the contributions from different classes of electrons. Regarding t_{2g}-t_{2g} and e_g-e_g contributions in the case of $c/a = 1.00$ (Fig. 7.47(a) and (g)) a very surprising

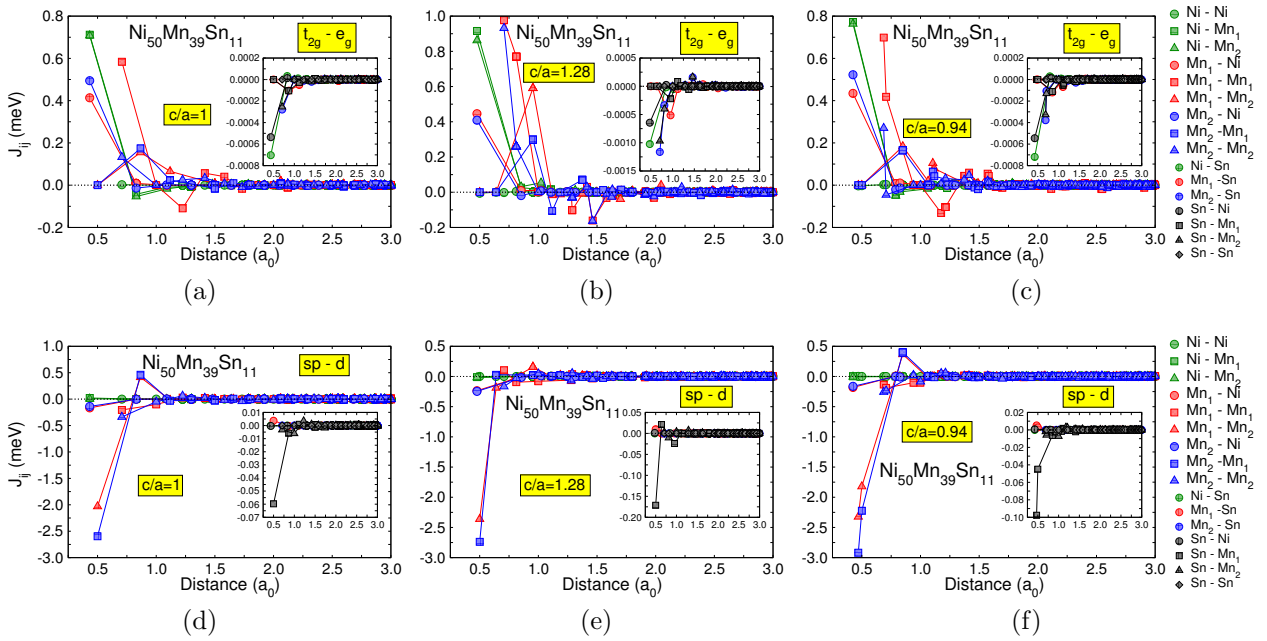

Figure 7.48: Magnetic exchange parameters of $Ni_{50}Mn_{39}Sn_{11}$, calculated with specx using the GGA exchange correlation functional. Here the mixed contributions are presented.

property is observed: Both contribution are almost of the same size but with opposite sign. Therefore, these contributions cancel out. In addition, the contribution of the interaction between the *sp*-electrons does not explain the antiferromagnetic interaction between Mn_1 and Mn_2 because it is too small. To find the contribution which is responsible for this interaction the t_{2g}-e_g and *sp*-*d* interactions have to be taken into account. These are shown in Fig. 7.48. This brings up another surprise because the origin of the Mn_1-Mn_2 interaction in the cubic structure is the *sp*-*d* contribution. This is unexpected because it is generally believed that the exchange interaction between the *d*-electrons is usually the origin of strong magnetism in transition metal alloys. The canceling of t_{2g}-t_{2g} and e_g-e_g contributions can be interpreted as the evidence of an instability. In other words: A change of the structure which resolves the canceling could be energetically preferred. This resolution of the canceling occurs when a tetragonal distortion is applied (see the different contributions of the $c/a = 1.28$ and $c/a = 0.94$ case shown in Fig. 7.47). In both both cases ($c/a = 1.28$ and $c/a = 0.94$) the largest contribution to the dominating antiferromagnetic nearest neighbor interaction between Mn_1 and Mn_2 is given by the e_g-e_g contribution. The ferromagnetic contribution arising from the t_{2g}-t_{2g} electrons is strongly reduced in both cases.

The conclusion drawn from this observations is that magnetism possibly acts as a driving force of the martensitic transition of $Ni_{50}Mn_{39}Sn_{11}$. This means that the intrinsic cancelation of the t_{2g}-t_{2g} and e_g-e_g contributions leads to a kind of magneto-structural instability of the austhenitic phase because the unfavorable cancelation of the different contributions to the magnetic exchange interaction is resolved by a tetragonal transformation. This conclusion is completely new and differs significantly from other modern theories concerning the formation of the martensitic phase in magnetic Heusler alloys (see e.g. Ref. [218]). It is not claimed that magnetism is the only driving force responsible for the martensitic transition but gives an important contribution that has to be taken into account to achieve a complete

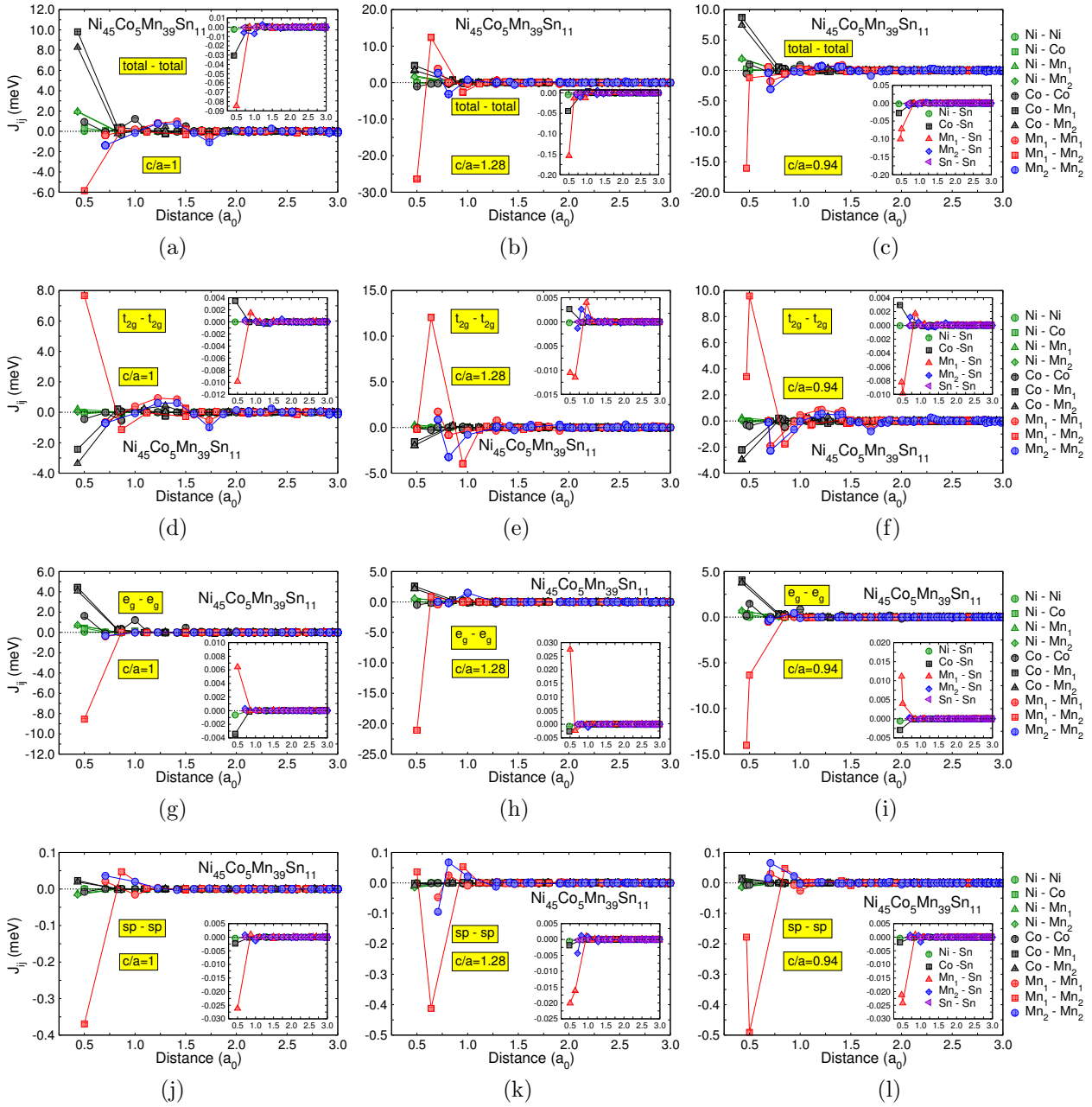

Figure 7.49: Magnetic exchange parameters of $Ni_{45}Co_5Mn_{39}Sn_{11}$, calculated with specx using the GGA exchange correlation functional.

understanding.

Another interesting observation is that interactions of longer range (beyond one lattice constant) are almost exceptionless evoked by the t_{2g}-t_{2g} contribution. The e_g-e_g contributions vanish completely beyond the next nearest neighbor shell. Smaller contributions to long range interactions are given by t_{2g}-e_g and *sp*-*d* fractions. This must be connected to the degree of localization of the electrons of different symmetry. The t_{2g} electrons are more delocalized because speaking in terms of atomic orbitals the orbitals of t_{2g}-symmetry of neighboring atoms share a stronger overlap compared to orbitals of e_g-symmetry. The more delocalized the electrons are the more they can lead to interactions with long range. Contributions to

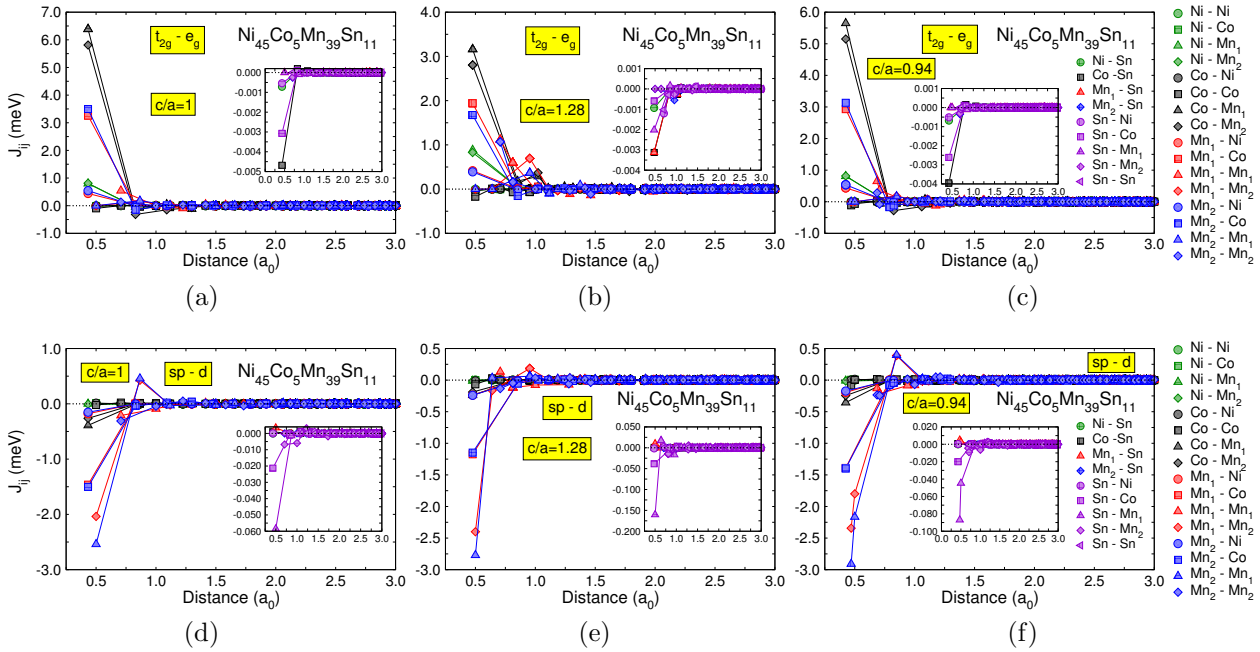

Figure 7.50: Magnetic exchange parameters of $Ni_{45}Co_5Mn_{39}Sn_{11}$, calculated with specx using the GGA exchange correlation functional.

the long range behavior of the t_{2g}-e_g part arise from the interaction of the delocalized t_{2g} electrons with localized e_g electrons.

Speaking in terms of localization, the canceling of the t_{2g}-t_{2g} and e_g-e_g contributions implies that the interaction between localized electrons overrides the interaction between the delocalized electrons in the cubic case.

Now, changes of the magnetic exchange introduced by the addition of Co on the Ni sublattice are investigated. Figure 7.49 shows the magnetic interaction in $Ni_{45}Co_5Mn_{39}Sn_{11}$. In this alloy the additional Co is placed on the two Ni sublattices and leads to additional and strong ferromagnetic next nearest neighbor interactions of the Co moments with the Mn moments (see Fig. 7.49(a), (b) and (c)). This immediately leads to the conclusion that a strong increase of the Co content leads to a ferromagnetic ground state of the cubic phase as it is found in experiment.

It is interesting to note that except for the occurrence of the Co related interactions, the qualitative form of the magnetic exchange interactions is the same as in the system without Co. In particular, the same canceling of the t_{2g}-t_{2g} and e_g-e_g contributions to the nearest neighbor Mn exchange found in cubic $Ni_{50}Mn_{39}Sn_{11}$ is observed in cubic $Ni_{45}Co_5Mn_{39}Sn_{11}$. This canceling is again resolved if the system is tetragonally distorted.

In addition, the t_{2g}-t_{2g} and e_g-e_g contributions of the interactions of Co with both Mn sublattices almost cancel because the t_{2g}-t_{2g} contribution is negative whereas the e_g-e_g contribution is positive (note that the signs are oppositely distributed compared to the Mn_1-Mn_2 interaction). The contribution which is responsible for the large total interactions between cobalt and manganese is almost exclusively given by the t_{2g}-e_g interaction (see Fig. 7.50). In contrast to what is found for the Mn_1-Mn_2 interaction the canceling is not resolved if the system is tetragonally distorted. Therefore, the interactions between Co and Mn do not vary as strong as the Mn_1-Mn_2 interactions when the system is tetragonally distorted.

Composition	c/a	$\mu_{\mathrm{Ni}}\,(\mu_{\mathrm{B}})$	$\mu_{\mathrm{Co}}\,(\mu_{\mathrm{B}})$	$\mu_{\mathrm{Mn_1}}\,(\mu_{\mathrm{B}})$	$\mu_{\mathrm{Mn_2}}\,(\mu_{\mathrm{B}})$	$\mu_{\mathrm{In}}\,(\mu_{\mathrm{B}})$
$Ni_{50}Mn_{34}In_{16}$	1.00	0.21	-	3.63	-3.85	-0.04
$Ni_{50}Mn_{34}In_{16}$	1.29	0.22	-	3.59	-3.79	-0.05
$Ni_{50}Mn_{34}In_{16}$	0.94	0.25	-	3.64	-3.81	-0.05
$Ni_{45}Co_5Mn_{34}In_{16}$	1.00	0.25	0.93	3.60	-3.85	-0.04
$Ni_{45}Co_5Mn_{34}In_{16}$	1.29	0.21	0.60	3.57	-3.78	-0.04
$Ni_{45}Co_5Mn_{34}In_{16}$	0.94	0.23	0.84	3.60	-3.85	-0.04

Table 7.8: Comparison of the magnetic moments. The calculations are performed using the specx code and GGA. The atomic volume is given by $54.00\,\text{Å}^3$ in all cases.

In order to see how the results obtained for $Ni_{50}Mn_{39}Sn_{11}$ and $Ni_{45}Co_{45}Mn_{39}Sn_{11}$ can be generalized to other compositions, the two systems $Ni_{50}Mn_{34}In_{16}$ and $Ni_{45}Co_{45}Mn_{34}In_{16}$ are now analyzed. A summary of the corresponding individual moments is given in Table 7.8. Comparing the total exchange interactions of austhenitic ($c/a = 1$) $Ni_{50}Mn_{34}In_{16}$ shown in Fig. 7.51(a) to those of $Ni_{50}Mn_{39}Sn_{11}$, a qualitative similarity is immediately observed. The most important interactions are again given by the strong antiferromagnetic coupling between the Mn_1 and Mn_2 moments. In addition, the ferromagnetic interaction of both Mn sublattices is found in $Ni_{50}Mn_{34}In_{16}$ but both are about 1 meV larger compared to $Ni_{50}Mn_{39}Sn_{11}$. Also, the long range oscillation of the manganese coupling are present. Concerning the tetragonal distorted cases, the strong increase of the antiferromagnetic interactions between the two Mn sublattices is found.

The most interesting fact is that the cancellation of the t_{2g}-t_{2g} and e_g-e_g contributions to the total exchange is also found for $Ni_{50}Mn_{34}In_{16}$. As in $Ni_{50}Mn_{39}Sn_{11}$ the antiferromagnetic interaction of Mn_1 and Mn_2 is dominated by the contribution arising from the coupling of *sp*- and *d*-electrons (see Fig. 7.52). This changes again when tetragonal distortions are introduced.

The conclusion drawn from this observations is that the basic magnetic mechanisms do not change if the main group element Sn is replaced by In in combination with a decrease of the Mn concentration. On the one hand, this can explained by the fact that the main group element atoms are of comparable size and the valence electron density is not dramatically changed by switching between both compositions. On the other hand this shows again the striking feature of this kind of Heusler alloys that the details of the properties can be carefully tuned by tuning the composition.

Now, the influence of Co placed on the Ni sites is investigated. Similar to $Ni_{45}Co_{45}Mn_{39}Sn_{11}$ the alloy system $Ni_{45}Co_{45}Mn_{34}In_{16}$ is considered. The results of the magnetic exchange interaction are shown in Fig. 7.53 and 7.54. Again, ferromagnetic interactions between the Mn and Co moment come into play. In $Ni_{45}Co_{45}Mn_{34}In_{16}$ these interactions are slightly larger compared to $Ni_{45}Co_{45}Mn_{39}Sn_{11}$ as it is additionally observed for the coupling between the Mn and Ni sublattices. Still, there is the approximate canceling of the t_{2g}-t_{2g} and e_g-e_g contributions to the Mn_1-Mn_2 and Co-Mn interactions which is resolved in the Mn_1-Mn_2 case for tetragonal distortions but remains for the Co-Mn couplings.

The main observation is that the magnetic exchange interactions are very similar for all

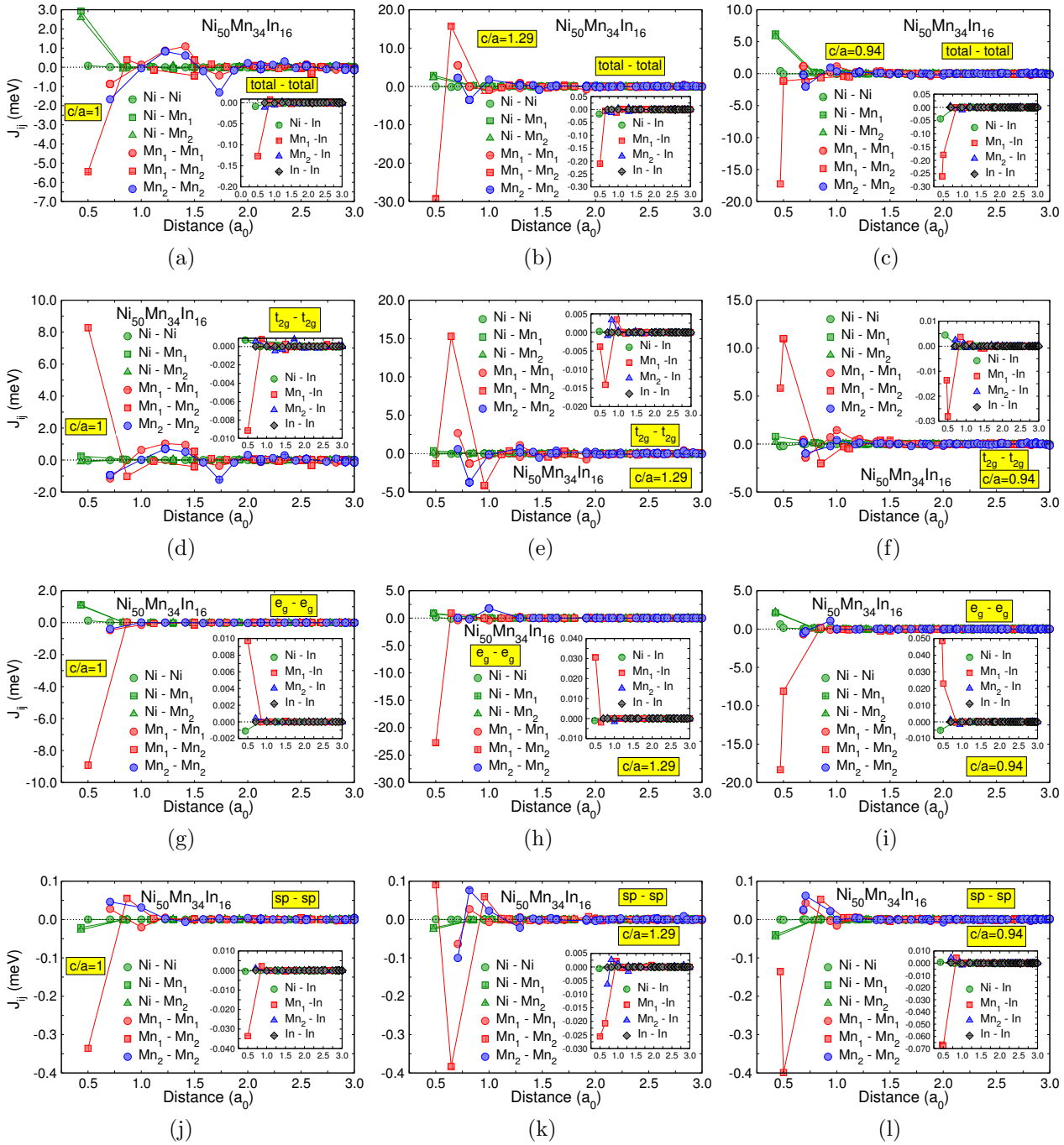

Figure 7.51: Magnetic exchange parameters of $Ni_{50}Mn_{34}In_{16}$, calculated with specx using the GGA exchange correlation functional.

four systems which are investigated here. Since certain properties of this mechanism are proposed to be connected with the occurrence of the martensitic transition, it implies that, in addition, the driving force of the martensitic transition in all systems show the same contribution arising from magnetism.

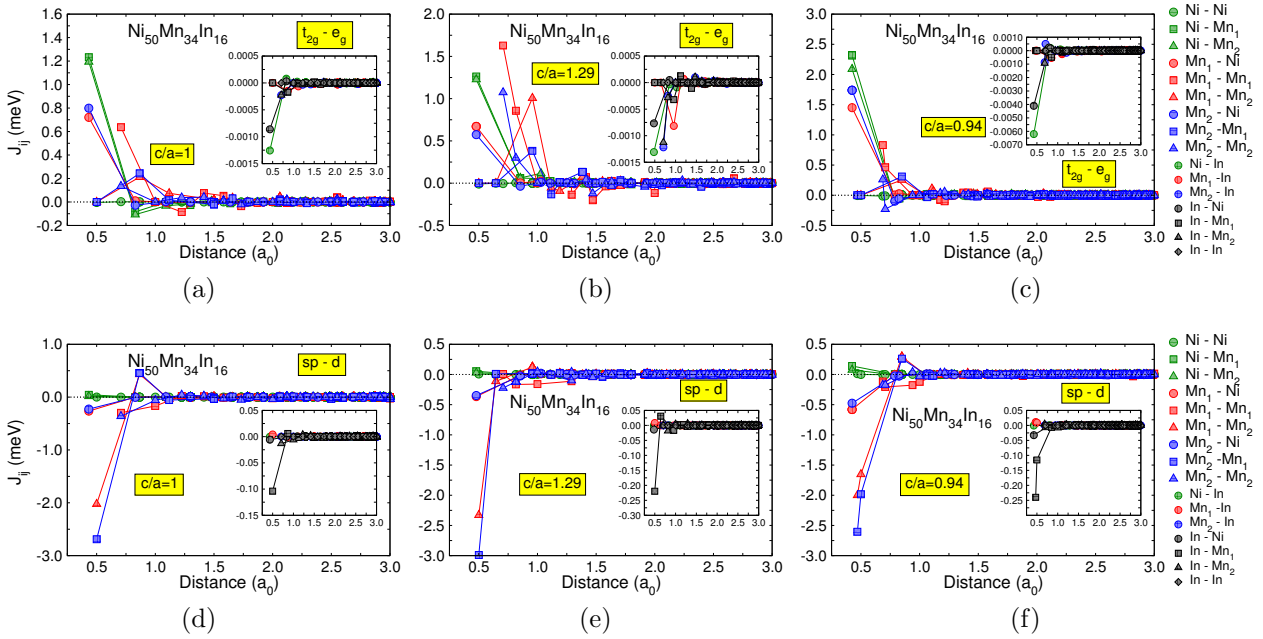

Figure 7.52: Magnetic exchange parameters of $Ni_{50}Mn_{34}In_{16}$, calculated with specx using the GGA exchange correlation functional.

7.11 Summary of Ni-Mn-based Heusler alloys

The last last section shows that the decomposition of the magnetic exchange interaction into symmetry associated contributions gains valuable insight into the magnetism of the Ni-Mn based Heusler alloys. It turns out that in some cases the interaction can be attributed almost exclusively to certain contributions. The most obvious examples are is the interaction between the Mn sublattices as well as the interaction between Mn and Co. It it also clearly shown that long range interactions and the associated RKKY oscillations arise from the t_{2g} contribution to the total exchange which corresponds to the more delocalized type of electrons.

In addition, the analysis leads to new evidence that the martensitic transition in Ni-Mn based Heusler alloys is closely related to magnetism and that magnetism can act as a driving force of this transition. This results from the observation that canceling of large exchange interaction contributions arising from different symmetries indicates a certain kind of instability which is resolved by tetragonal distortions.

It would be of particular interest if by a more extensive study of a great ensemble of different magnetic Heusler alloys showing the martensitic transition a quantitative connection between the canceling of exchange contributions and the martensitic temperature can be found. One might guess for example that if the t_{2g} and e_g contributions are larger that the instability connected with their canceling leads to higher or lower transition temperatures.

It needs to be noted again that the lattice parameters used here, are extrapolated from VASP calculations at slightly different compositions, but it can be shown that the essential physics described in the last section does not change if small deviations of the lattice structure are considered.

It is concluded that the method presented here is an interesting tool for the theoretical

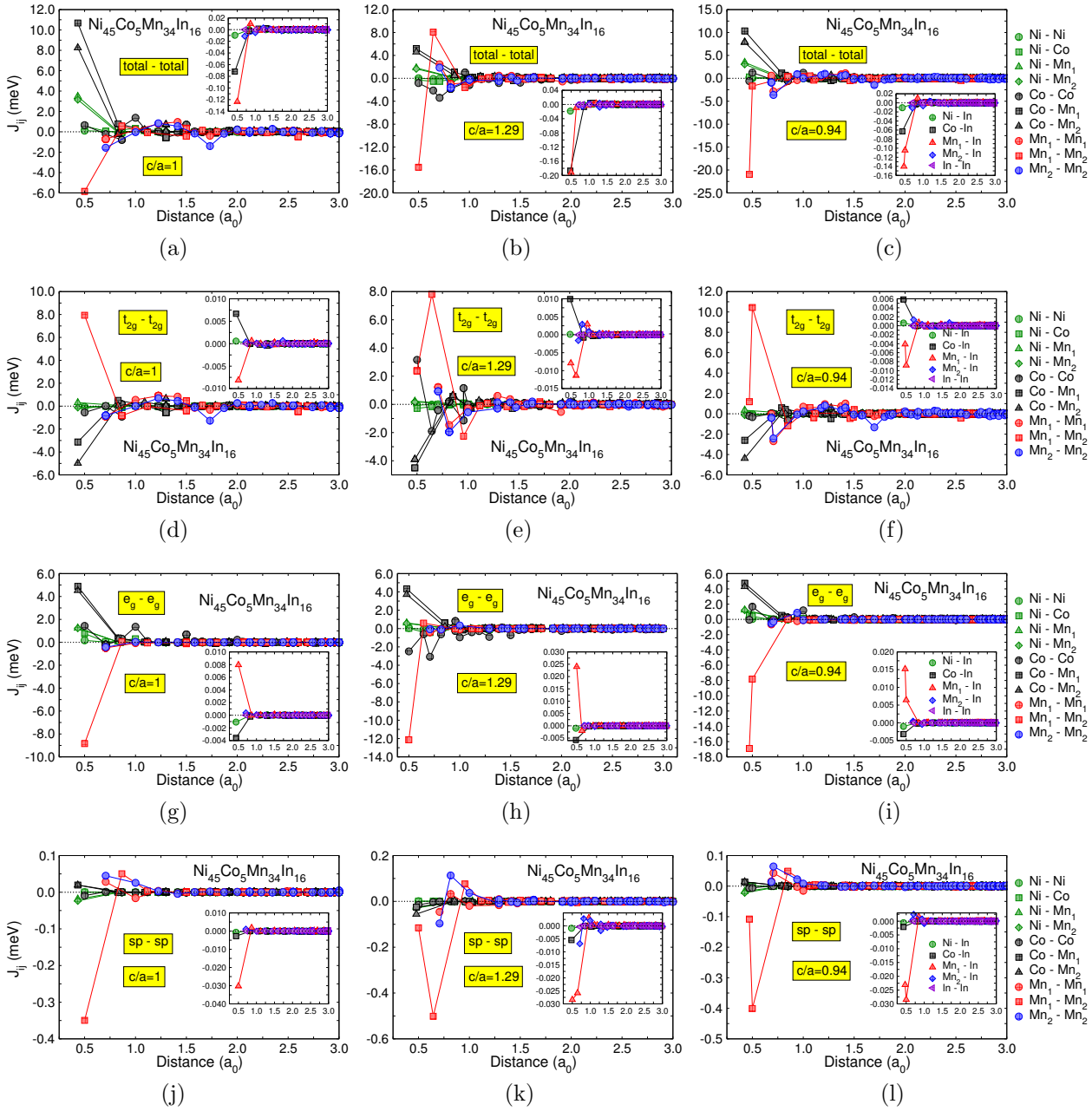

Figure 7.53: Magnetic exchange parameters of $Ni_{45}Co_5Mn_{34}In_{16}$, calculated with specx using the GGA exchange correlation functional.

design of functional magnetic materials which show a pronounced "metamagnetic" behavior.

Highlight

The major part of this chapter is devoted to an extensive study of half-metallic Heusler alloys based on Mn, Fe and Co. The combination of *ab initio* calculations and MC simulations leads to deeper insight into the magnetism of such systems and it dependence on temperature and structural disorder. In particular, Heusler alloys based on Co and Fe reveal correlation effects that have to be treated with exchange-correlation contributions beyond GGA. Some of the

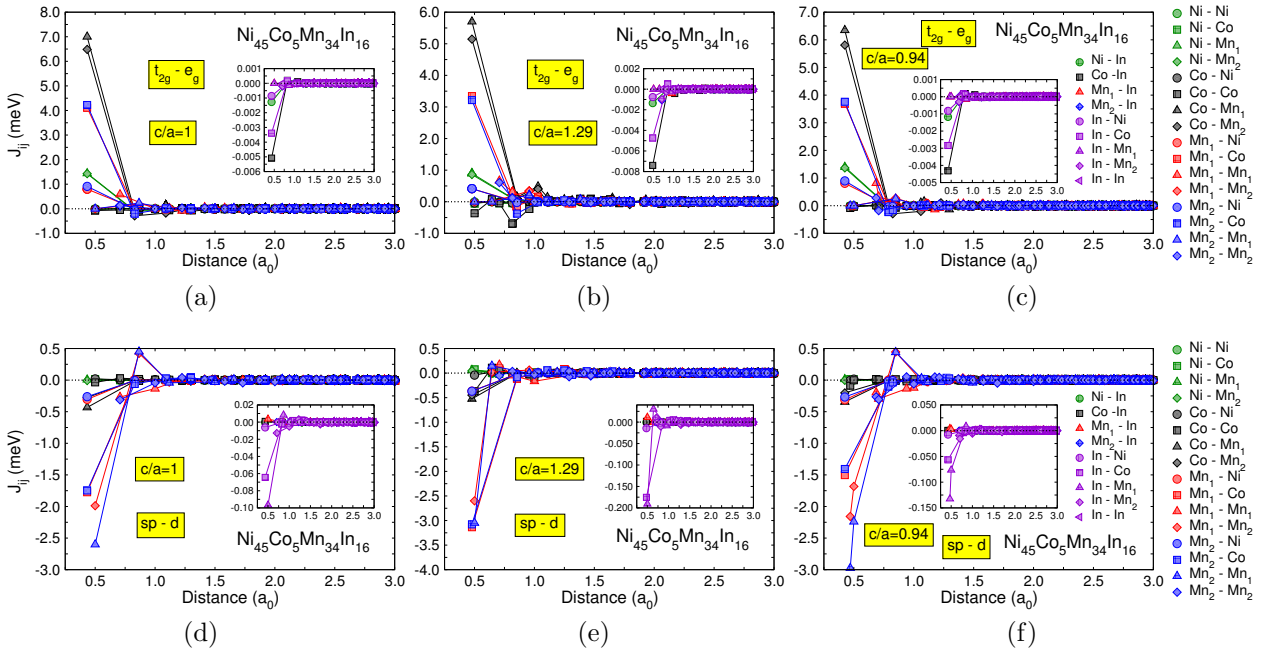

Figure 7.54: Magnetic exchange parameters of $Ni_{45}Co_5Mn_{34}In_{16}$, calculated with specx using the GGA exchange correlation functional.

investigated system turn out to be complex antiferromagnetic half-metals. In the end of the chapter, the magnetic exchange interactions of Ni-Mn based Heusler systems are investigated using a decomposition scheme that allow to distinguish between contributions arising from different types of electron states. This reveals that magnetism can play an important role concerning the driving force of the martensitic transition which occurs in this systems.

8 Spin caloritronics

In this chapter results of transport calculations concerning the field of spin caloritronics are discussed. Therefore, basic concepts of this field are introduced first. It is described which types of effects belong to this field and how they can be classified. Afterwards results obtained by employing the linear response formalism for the determination of electronic transport generalized to describe thermoelectric properties and their spin dependence are presented. The particular focus is on calculations of spin-dependent Seebeck coefficients for systems containing half-metallic Heusler alloys.

8.1 Introduction

It is almost immediately obvious from the name that spin caloritronics is a generalization of spintronics to spin and temperature dependent transport effects and concerns the interplay between spin, charge and heat currents. This field basically emerged from the observation of the so called spin Seebeck effect by Uchida *et al.* as reported in Ref. [219]. The authors found that a thermal gradient subjected to an iron-nickel layer drives a spin current into attached platinum stripes. This spin current is detected by measuring the inverse-spin-Hall voltage generated in the Pt stripes by the injected spin current. The first and intuitive interpretation is that both spin channels act like a thermocouple and therefore, instead of driving a thermo-current, drive a thermo-spin-current. The most interesting as well as surprising feature of the observation of the spin Seebeck effect is that the effect can be shown to persist over length scales that exceed the typical spin-scattering length scales by orders of magnitude. As this cannot be explained within a conventional two current model this observations led to a vivid research for spin and temperature dependent effects that opened the field of spincaloritronics.

A review as well as a classification scheme to organize the different types of spin caloritronic effects is given by Bauer *et al.* in Ref. [86]. The classifications scheme distinguishes between collective, relativistic, and spin-dependent thermoelectric effects (called independent electron effects). The spin Seebeck effect is a prominent example of collective effects. They are called collective because they are closely related to collective excitations like magnons. In fact, a theory that describes the magnon driven spin Seebeck effect is reported in Ref. [220]. On the other hand the role of phonons driving spin by the spin-dependent phonon drag is a matter of ongoing discussion (see Ref. [86] and references therein). The relativistic effects are basically based on spin-orbit coupling that leads to spin-dependent transport properties like, e.g., the anomalous- or spin-Hall effect. The thermal generalization of these effects are the anomalous- and spin-Nernst effect. The last field which is the field of spin-dependent thermoelectrics concerns in the simplest form the spin polarization of the thermo-current driven by the usual Seebeck effect. This spin polarization results from the polarization of the electronic density of states and variations of the mobility in the two spin channels. In other words: It is possible that one spin channel gives a much stronger contribution to the total Seebeck coefficient than the other. This leads to thermally driven spin injection and is for example reported in Ref. [221]. In addition the thermal generalization of the well known spintronic effects like the TMR is reported in Ref. [150].

Here, the focus is on the possibility that a strong spin dependence of the Seebeck coefficient can be used to generate spin accumulation by applying a temperature gradient. This spin accumulation could be used to drive spin currents into functional devices. In other words, the present study is an attempt to design a thermally driven spin current generator from first-principles.

The ferromagnetic half-metals are promising candidates in the field of spin caloritronics because, as extensively discussed in the last chapter, they exhibit a 100% spin-polarization of the electronic density of states (DOS) at the Fermi level. This means that there is a gap in the DOS of one of the spin channels and it should, in principle, be possible to extract a 100% spin-polarized current out of these materials. Unfortunately, the sensitive dependence of half-metallicity on details like interfaces and interface defects has up to now hindered a simple generation of currents with high spin-polarization from the half-metals [7]. Therefore, theoretical investigations of promising thermoelectric devices which can inject currents of high spin-polarization, is of great importance.

In this chapter, results of *ab initio* based transport simulations of Co, Fe and Mn based Heusler alloys are reported. As shown in the last chapter these alloys are half-metallic ferromagnets and have already been considered for spintronics applications (see, e.g., Ref. [7]). Structural, electronic and magnetic properties as well as the Curie temperature of the alloys are determined in Chapter 7. The Curie temperature is of special interest because it is required to be sufficiently high in order to allow the design of devices which keep the ferromagnetic half-metallicity beyond room temperature.

More precisely, this chapter is devoted to the first-principles analysis of thermoelectric transport properties of Co_2FeAl, Co_2FeSi, Co_2MnAl and Co_2MnSi layers with Pt contacts. It turns out that a strong dependence on layer thickness and composition is found. Furthermore, the contributions of the two spin-channels reveal the possibility that spin-polarized currents can be generated by applying a thermal gradient.

The Heusler layer in between the platinum leads can be considered as an analog to the copper-cobalt multilayers investigated by Gravier *et al.* [222]. The authors report interesting spin-dependent electronic and thermoelectric properties such as the magneto-resistance and magneto-thermopower. Recently, such system are investigated theoretically by means of *ab initio* calculations focussing on the magnetic anisotropy of the Seebeck coefficient [223].

In the present work, the role of the non-magnetic copper is taken over by platinum that introduces strong spin-orbit coupling and the magnetic Co is replaced by Co based Heusler alloys which can be arranged within the platinum including only a very small lattice mismatch. The usage of the magnetic Heusler alloys leads to far more degrees of freedom to tune the properties of the system (see discussion in Chaper 7).

In order to determine the transport properties a fully relativistic description of the electronic structure within the screened Korringa-Kohn-Rostoker (SKKR) [66] method in combination with the Kubo-Greenwood formalism is employed. This ensures that the spin-orbit coupling introduced by platinum is implicitly taken into account. The relativistic spin-projection operator introduced by Lowitzer *et al.* [81] is used to evaluate the spin-dependent contributions. This operator allows the projection of current contributions onto the two spin channels in the relativistic framework (for details see Section 2.7.1).

The main goal of this chapter is to evaluate the possibility to drive a highly spin-polarized current by applying a thermal gradient to composite platinum-Heusler systems. As it is difficult to grow large crystals of Heusler alloys with perfect $L2_1$ structure, a direct application of such alloys as half-metallic spin injectors is hindered because half-metallicity is suppressed

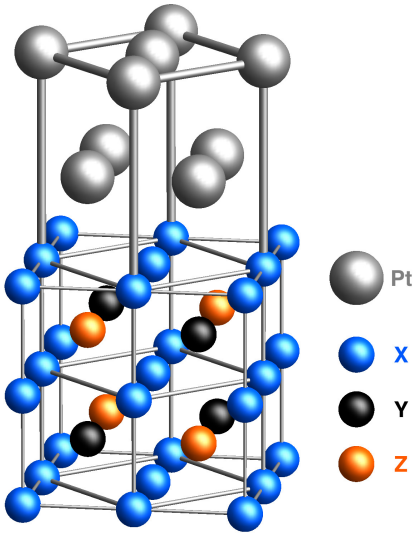

Figure 8.1: Schematic view of the interface between platinum leads and layers. The platinum lattice is rotated with respect to the Heusler lattice because the length of the diagonal of the platinum lattice is comparable to the lattice constants of the Heusler alloys. This ensures that the lattice mismatch between both metals is between 0.06 and 0.11 Å depending on the particular Heusler system.

by disorder. It is much easier to grow thin layers of Heusler alloys with perfect $L2_1$. Therefore, if it turns out that a thin film of half-metallic Heusler between two leads already induces a high spin-polarization of the current, the systems under consideration here are of special interest. It is shown throughout the next section that exactly this is possible.

First, details of the transport calculations and the modeling of the Pt-Heusler-Pt systems are presented. Afterwards, a detailed investigation of transport properties and electronic structure of the Pt-Heusler-Pt systems is carried out.

8.2 Details of the calculations

Calculations of transport properties are carried out using the fully relativistic screened KKR method [66] and the linear response formalism in the formulation of Baranger and Stone [77] as first implemented by Mavropoulos *et al.* [224]. This formalism is introduced in Chapter 2. In order to ensure an accurate determination of the transport properties, more than 90,000 k-points within the irreducible wedge of the two-dimensional Brillouin zone are used. The imaginary part is set to 0.0001 Ry and the energy grid for the calculation of the Seebeck coefficient is 0.001 Ry.

A sketch of the geometry used in the transport calculations is shown in Fig. 8.1. The layer distance at the interface is the average of the layer distance of platinum and of the Heusler alloy. No lattice relaxations in the interface region are included.

Within the SKKR method the system is assumed to be translational invariant in the x- and y-direction and in the z-direction the system is terminated on both sides by two semi-infinite leads. The magnetization direction points along the z-axis as well as the direction of the current. Therefore, transport perpendicular to the planes in a system with out-of-plane magnetization is considered here.

Due to the two dimensional translational invariance a two-dimensional lattice constant a_{2d} is defined by

$$a_{2d} = \sqrt{2} a_{bcc} \tag{8.1}$$

where $a_{bcc} = a_{\mathrm{3d,Heusler}}/2$ is the three-dimensional lattice constant of the underlying bcc lattice of the Heusler part of the system and thus a_{2d} is its diagonal. Hence, the distance between

two subsequent Heusler monolayers is given by

$$d = \frac{a_{\mathrm{bcc}}}{2} = \frac{\sqrt{2}}{4} a_{2d}\,. \tag{8.2}$$

The platinum and the Heusler lattices are rotated by 45° with respect to each other. This ensures the smallest possible lattice mismatch between the two structures. For example, the lattice constant of the Heusler cell of Co_2FeSi is 2.81 Å (which is half of the lattice constant of the 16 atoms cell $a_{3\mathrm{d,Heusler}}/2$) and the lattice constant of Pt is 3.92 Å. This is of the same order as the diagonal of the Heusler structure which is 3.97 Å and therefore close to the Pt lattice constant. This results in a small lattice mismatch between 0.06 to 0.11 Å depending on the particular Heusler alloy.

To simplify the construction of the system it is assumed that the lattice constant of Pt is the same as that of the two-dimensional lattice constant of the Heusler system:

$$a_{\mathrm{3d,Pt}} = a_{\mathrm{2d}}\,. \tag{8.3}$$

The atomic volume of the Heusler is $a_{bcc}^3/2 = a_{2d}^3/4\sqrt{2}$, hence, the (average) Wigner-Seitz radius is given by

$$\begin{aligned} \frac{4\pi}{3} R_{ws}^3 = \frac{a_{2d}^3}{4\sqrt{2}} \Rightarrow R_{ws}^H &= \frac{1}{4\sqrt[6]{32}} \left(\frac{3}{4\pi}\right)^{1/3} a_{2d} \\ &\simeq 0.138\; a_{2d}\,. \end{aligned} \tag{8.4}$$

In the fcc Pt lattice the atomic volume is $a_{fcc}^3/4 = a_{2d}^3/4 = 2a_{bcc}^3 = a_{2d}^3/\sqrt{2}$, thus,

$$\begin{aligned} \frac{4\pi}{3} R_{ws}^3 = \frac{a_{2d}^3}{4} \Rightarrow R_{ws}^{Pt} &= \frac{1}{\sqrt[3]{4}} \left(\frac{3}{4\pi}\right)^{1/3} a_{2d} \\ &\simeq 0.391\; a_{2d} \end{aligned} \tag{8.5}$$

Four layers of Pt are included in the interaction region to join smoothly to the two semi-infinite bulk regions. The Heusler layer is always terminated by a Co monolayer on both sides. Therefore, the interface between Pt and the Heusler system is always metallic. The distance between the Pt and Co monolayer in the interface is taken to be the average of the Pt and the Heusler interlayer distances, i.e. $(1/2 + \sqrt{2}/4)/2 = (2 + \sqrt{2})/8$. In this way, the atomic radii for all Pt atoms can be taken as R_{ws}^{Pt} and all the atoms in the Heusler alloy can have an atomic radius of R_{ws}^{H} (H=Heusler) as above, irrespective of their atomic positions.

Assuming such interface structures between platinum and Heusler alloy turns out to be reasonable because structural relaxation calculations using Quantum Espresso [225] do not reveal strong changes. Instead the relaxations obtained from such configurations are very small. Therefore, it is concluded that the description of the interface chosen here serves as an excellent approximation.

Details of the theoretical formalism used to obtain the transport properties are explained in Section 2.7, 2.7.1 and 2.7.2.

8.3 Transport properties

In this section transport properties, in particular the Seebeck coefficient and its spin dependence of Pt-Heusler-Pt systems are discussed. For every type of Heusler, systems containing

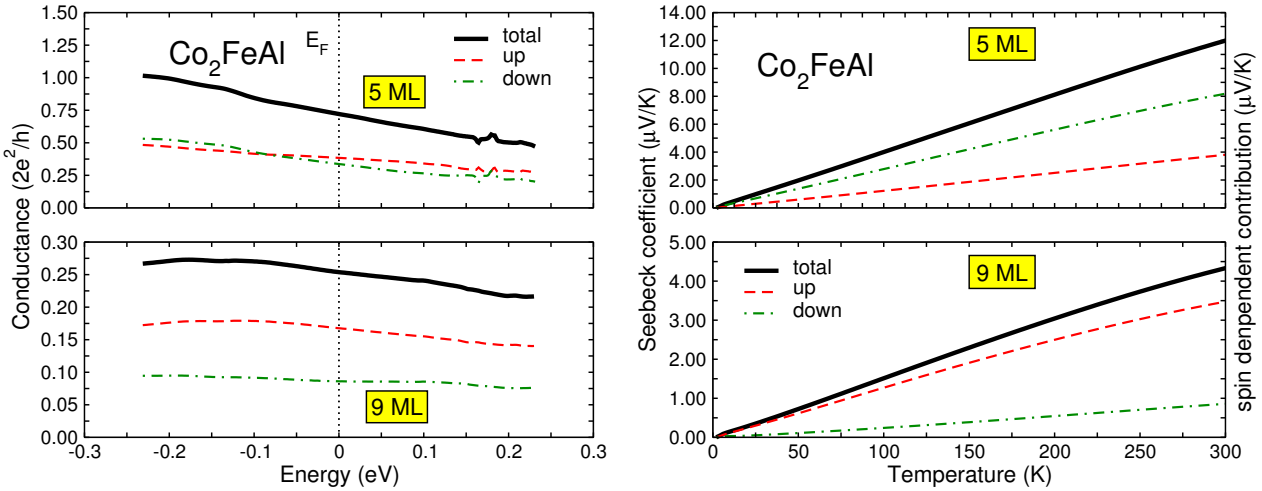

(a) (b)

Figure 8.2: (a) Energy dependence of the conductance near the Fermi energy of the Pt-Co_2FeAl-Pt system with five and nine monolayers. The black lines denote the total conductance whereas the green and red denote the contributions from the two spin channels. (b) Temperature dependence of the Seebeck coefficient and the contributions from the spin channel associated with the systems in (a). The colors also correspond to (a)

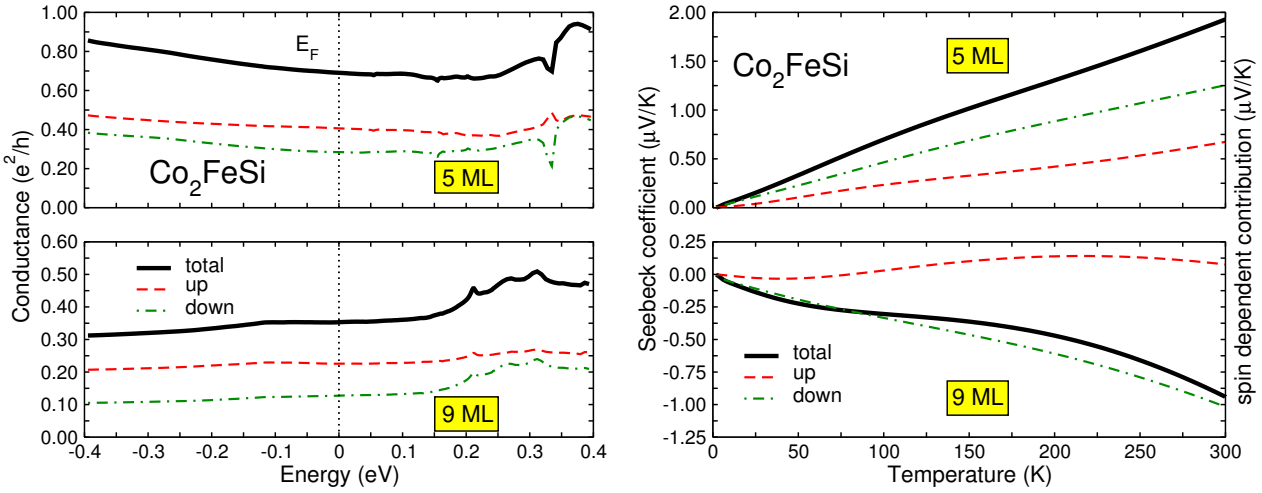

(a) (b)

Figure 8.3: (a) Energy dependence of the conductance near the Fermi energy of the Pt-Co_2FeSi-Pt system with five and nine monolayers. (b) Seebeck coefficient and the contributions from the spin channels associated with the systems in (a).

five monolayers are compared to systems containing nine monolayers of Heusler. The number of monolayers is chosen in a way that the Pt-Heusler interface is purely metallic in the sense that the first Heusler monolayer on both sides contains only cobalt.

In the upper panel of Fig. 8.2(b) the calculated temperature dependence of the Seebeck coefficient of Pt-Co_2FeAl-Pt with five Heusler monolayers is shown. The Seebeck coefficient increases linear with temperature. The contribution of the spin-down channel is almost by

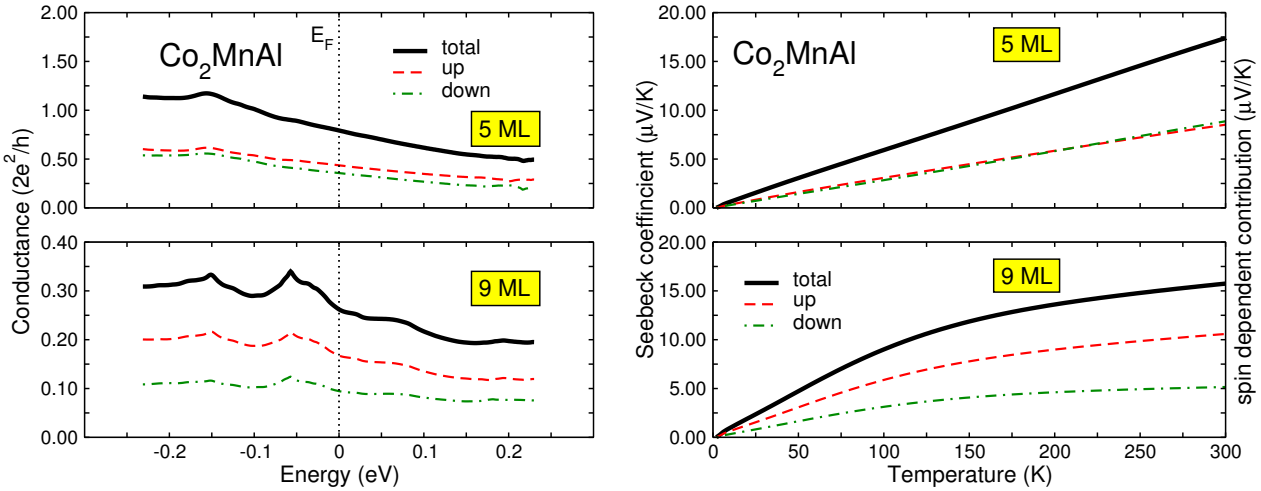

(a) (b)

Figure 8.4: (a) Energy dependence of the conductance near the Fermi energy of the Pt-Co_2MnAl-Pt system with five and nine monolayers. (b) Seebeck coefficient and the contributions from the spin channesl associated with the systems in (a).

a factor of two larger than the one of the spin-up channel. The upper panel of Fig. 8.2(a) shows the energy dependence of the conductance. Around the Fermi energy the energy dependence is linear which leads to the linear increase of the Seebeck coefficient with increasing temperature. Both spin channels give almost the same contribution to the total conductance but as the slope of the spin-down part is stronger its contribution to the Seebeck coefficient is more pronounced.

As shown in the lower panel of Fig. 8.2(b), the Seebeck coefficient of a system containing nine monolayers of Co_2FeAl is smaller compared to the system with five monolayers. In addition, there is a much larger difference between the contributions of the two spin channels to the total Seebeck coefficient. This can again be explained with the energy dependence of the conductance where the spin-up channel reveals a slope comparable to that of the total conductance and the energy dependence of the spin-down channel is almost flat. A flat energy dependence leads to small Seebeck coefficients because the slope of this dependence determines the size of the Seebeck coefficient.

The first conclusion which can be drawn from the results for Pt-Co_2FeAl-Pt is that the Seebeck coefficient of the layered system depends strongly on the thickness of the layer. This basically arises from the different shapes of the energy dependence of the conductance. The fact that conductance is very sensitive to the thickness of layers is well known and is described, e.g., in Ref. [224]. It is especially interesting that one spin channel can contribute strongly to the total Seebeck coefficient for five layers and gives only a minor contribution for nine layers.

Now, the Pt-Co_2FeSi-Pt systems are discussed. This gives insight into how far compositional changes affect the Seebeck coefficient. In particular, the replacement of Al by Si introduces one more valence electron. It should also be kept in mind that pure Al is a metal whereas Si is a semiconductor.

Regarding the upper panel of Fig. 8.3(b) which shows the temperature dependence of the Seebeck coefficient of a system containing five monolayers of Co_2FeSi, it is immediately

noticed that the Seebeck coefficient is by more than a factor of three smaller compared to the Pt-Co_2FeAl-Pt system with five monolayers. In addition, small deviations from the linear behavior of the Seebeck coefficient are found in this system.

The energy dependence of the conductance of the Pt-Co_2FeSi-Pt systems shown in the upper panel of Fig. 8.3(a) is almost linear around E_F but reveals a distinct structure above the Fermi energy and is still quite flat below. There is a pronounced peak above E_F which is connected with numerical inaccuracies which can occur if strong changes of the electronic structure appear during the energy sampling. In such cases the k-point mesh used within the calculation can be commensurate with important features in the two dimensional Brillouin zone at a certain energy but can miss some features at another energy. As such structures affect the calculation of the Seebeck coefficient only very weakly the enormous numerical effort which is required to cure this lack is not necessary.

Turning to the results of the Pt-Co_2FeSi-Pt system with nine monolayers shown in the lower panel of Fig. 8.3(b), a strong change occurs in comparison to the system with five monolayers. The Seebeck coefficient of this system is negative and the evolution with temperature is not linear as for the system with five monolayers. In addition, the two additive contributions to the total Seebeck coefficient have opposite signs. The contribution of the spin-down channel which gives the strongest contribution, is negative whereas the contribution of the spin-up channel is small and positive. Therefore, the resulting total Seebeck coefficient is very small and negative. This can be understood by considering the energy dependence of the conductance around the Fermi level (see lower panel of Fig. 8.3(a)) which is almost flat and therefore gives only small contributions to the Seebeck coefficient. This behavior changes around 0.1 eV away from the Fermi energy when more structure comes into play. But this structure is again in an energy region which contributes only weakly to the Seebeck coefficient at temperatures up to 300 K.

Concerning the discussion of systems containing a Co_2FeSi layer it should be remembered that the description of the electronic structure of Co_2FeSi does not reveal a half-metallic gap at the Fermi energy without accounting for correlation effects (see Section 7.3).

In a next step the Y-component of the Heusler compound is changed from iron to manganese. This results in a larger Seebeck coefficient for systems containing five monolayers of Co_2MnAl (see upper panel of Fig. 8.4(b)). Here, the additive contributions of the spin channels to the total Seebeck coefficient are almost of the same size and exhibit a comparable structure. The energy dependence of the conductivity of this system is shown in the upper panel of Fig. 8.4(a). It reveals a strong slope of the total conductance and both spin-dependent contributions. The conductance of both spin channels exhibits almost the same slope which results in almost the same contribution to the total Seebeck coefficient. Interestingly, the qualitative shape of the energy dependence of the conductance and its spin-dependent contributions of the Pt-Co_2FeAl-Pt system with five monolayers is comparable to that of the Pt-Co_2MnAl-Pt with the same number of layers.

In the system containing nine monolayers of Co_2MnAl between the platinum leads (see lower panel of Fig. 8.4(b)), the total Seebeck coefficient is increased. This is contrary to the Co_2FeZ (Z=Al, Si) systems where the Seebeck coefficient is smaller in the nine layer case. But here there is a sizable slope at low temperatures and it seems to saturate for larger temperatures. This saturation stems from the flat regions of the energy dependence of the conductivity at more than 1.5 eV away from the Fermi energy. Although there is a pronounced structure below the Fermi energy the average slope in this region is small and therefore this region gives almost no contribution to the Seebeck coefficient. This system is a perfect example of a

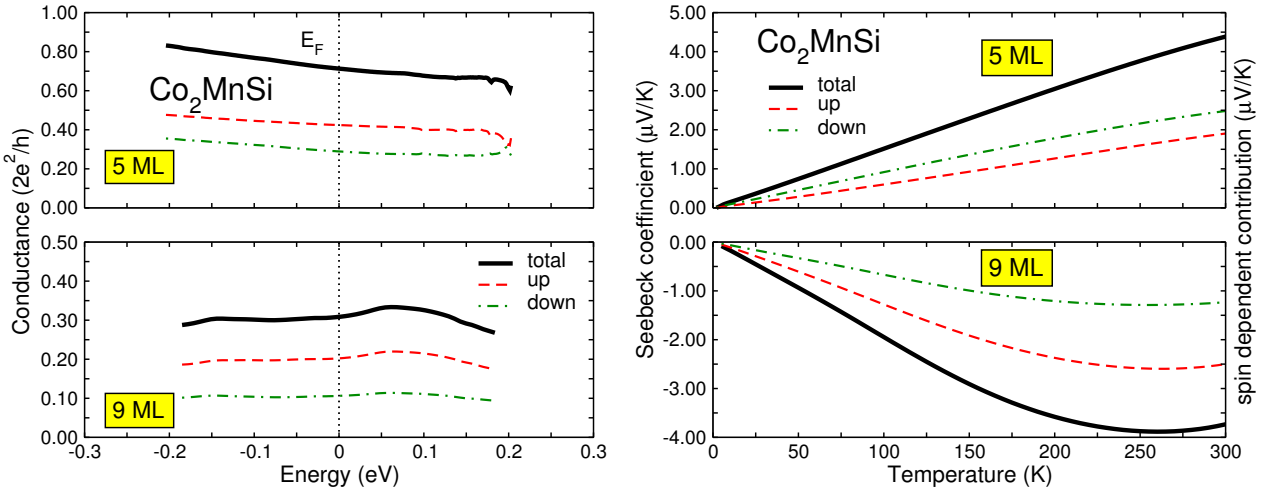

Figure 8.5: (a) Energy dependence of the conductance near the Fermi energy of the Pt-Co_2MnSi-Pt system with five and nine monolayers. (b) Seebeck coefficient and the contributions from the spin channels associated with the systems in (a).

system with small conductivity (speaking in terms of ballistic conductance at the Femi level) but with a large Seebeck coefficient. This shows again that the Seebeck coefficient depends almost exclusively on the slope of the conductance and much lesser on its absolute value.

To finish the discussion of the transport properties the Seebeck coefficient of Pt-Co_2MnSi-Pt systems is discussed now. The upper panel of Fig. 8.5(b) shows its temperature dependence for the system containing five monolayers Heusler. The absolute value is decreased compared to the Pt-Co_2MnAl-Pt system. This is analogous to the decrease found in the Co-Fe based system where the exchange of Al by Si reduces the Seebeck coefficient strongly. The evolution of the additive contributions from the spin channels to the total Seebeck coefficient with temperature for Pt-Co_2MnSi-Pt is qualitatively comparable to the one of Pt-Co_2MnAl-Pt because they are almost of the same size. The energy dependence of the conductance shown in the upper panel of Fig. 8.5(a) is linear with almost no structure.

The last system that has to be discussed is the system which contains nine monolayers of Co_2MnSi. Its Seebeck coefficient is shown in the lower panel Fig. 8.5(b). Obviously this system exhibit a very interesting behavior because the Seebeck coefficient is negative and has a minimum and around 275K.

The energy dependence of the conductance shows a bump above the energy and is flat

	Al		Si	
	5ML	9ML	5ML	9ML
Fe	+	+	+	-
Mn	+	+	+	-

Table 8.1: This table summarizes which combination of elements and layer thickness leads to positive or negative Seebeck coefficients.

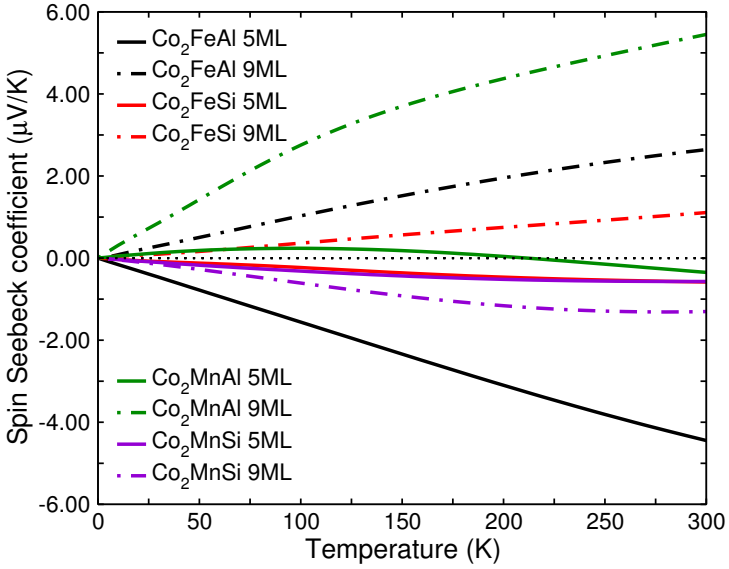

Figure 8.6: Comparison of the temperature dependence of the spin Seebeck coefficient of all systems under consideration.

behavior below. This asymmetry leads to the unusual temperature dependence of the Seebeck coefficient. The slope at energies above the energy of the bump is negative and therefore has a positive contribution to the Seebeck coefficient. This results in the minimum of the temperature dependence oft the Seebeck coefficient.

Table 8.1 summarizes the sign of the Seebeck coefficient of all systems studied here. It shows a systematic difference between systems containing Al and those containing Si. All systems containing Al considered here exhibit a positive Seebeck coefficient for both layer thicknesses in combination with Fe and also with Mn. The systems that contain Si show a positive Seebeck coefficient for 5 monolayers of Heusler for the case of Fe and Mn and a negative Seebeck coefficient for 9 monolayers.

Figure 8.6 shows the spin Seebeck coefficient defined in Eq. (2.322) of all systems investigated throughout this chapter. Obviously, the systems with five monolayers of Co_2FeAl and nine monolayers Co_2MnAl lead to the largest effect but in the first case the spin Seebeck coefficient is negative and in the second it is positive. Therefore, the thermoelectric current in this systems exhibits the strongest spin-polarization but with opposite sign.

8.3.1 Electronic structure of the transport systems

In order to get a deeper insight into how the thermoelectric properties depend on the layer thickness and the composition, the electronic structure of the Pt-Heusler-Pt systems discussed here, has to be understood in more detail. Therefore, this subsection is devoted to the discussion of the electronic DOS of the Heusler layers between platinum leads. The main question is if there are signatures of half-metallicity in the small Heusler layers and how they influence the Seebeck coefficient and its spin dependence. Therefore, the DOS of the Heusler layer is discussed here, but for completeness Appendix A.13 is devoted to the discussion of the DOS of the Pt leads close to the interface.

In Fig. 8.7 the electronic DOS of the two Pt-Co_2FeAl-Pt systems is shown. The DOS of only the first three and five Heusler layers is presented because the subsequent layers reveal

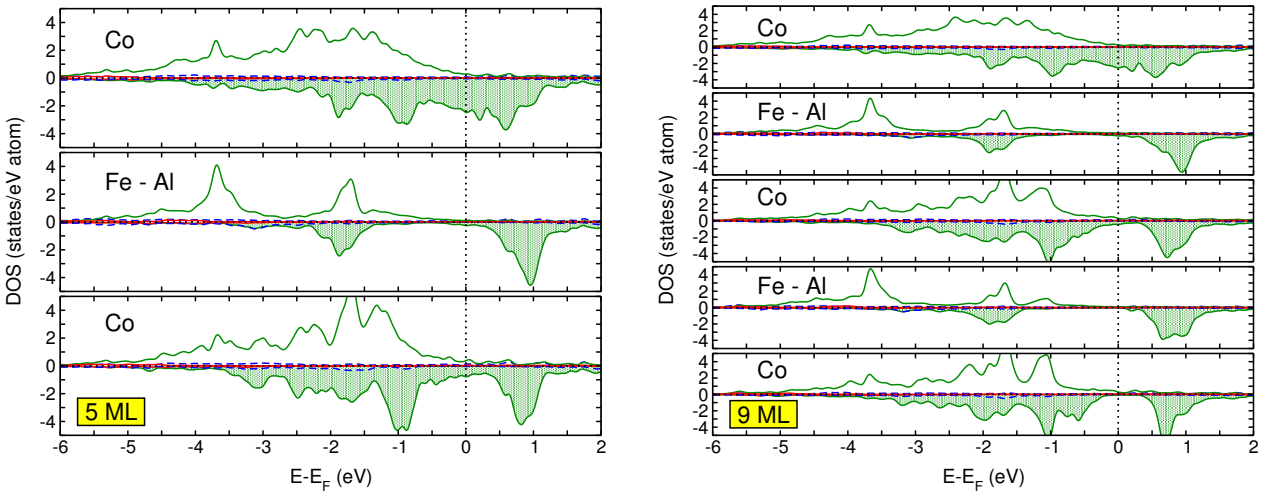

Figure 8.7: DOS of the Pt-Co_2FeAl-Pt system with (a) five and (b) nine monolayers of Heusler between the platinum leads.

the same DOS because of the reflection symmetry of the system. The green lines correspond to the *d*-state and blue and red to *p*- and *s*-states. One easily observes that in the system containing only five monolayers of Heusler the half-metallic gap is absent even in the Co layer in the middle. But obviously the DOS becomes more similar to that of bulk Co_2FeAl in the middle of the Heusler layer compared to the DOS in the monolayer which is directly connected to the Pt lead. This shows that the influence of the interface decays very fast.

If the DOS of the system containing nine monolayers of Co_2FeAl is examined, one observes that the half-metallic gap is recovered in the middle of the system. This means that the influence of the Pt interface is almost completely decayed after four layers. The occurrence of this gap is responsible for certain differences of the Seebeck coefficient between the system with five and nine monolayers.

Comparing the energy dependent conductances in the upper and lower panel of Fig. 8.2 to the DOS in Fig. 8.7 it becomes apparent why the contribution of the two spin channels are different for different numbers of monolayers. For five monolayers both spin channels give almost the same contribution to the conductance whereas for nine layers the contribution of the spin-up channel is almost twice as large. This results from the occurrence of the half-metallic gap in the spin-down DOS of the system with nine Heusler layers. The absence of states in the spin-down channel in the middle of the system reduces the transmission probability of spin-down electrons significantly. The remaining transmission can be explained by the occurrence of electrons that flipped their spin on the way through the system and by the occurrence of spin-down electrons that tunnel through the small region where there is no spin-down state. The reduction of the total conductance is a general trend observed in all systems. This general thickness dependence can be attributed to the occurrence of interference due to multiple reflection within the Heusler (for detail see Ref. [224]).

The same arguments given to explain the energy dependent conductance of Pt-Co_2FeAl-Pt are also valid for the Pt-Co_2FeSi-Pt systems. Their DOS are shown in Fig. 8.8. Again, the occurrence of the gap in the spin-down channel in the nine layer system leads to a 50% smaller contribution of this channel compared to the spin-up channel. The sudden increase

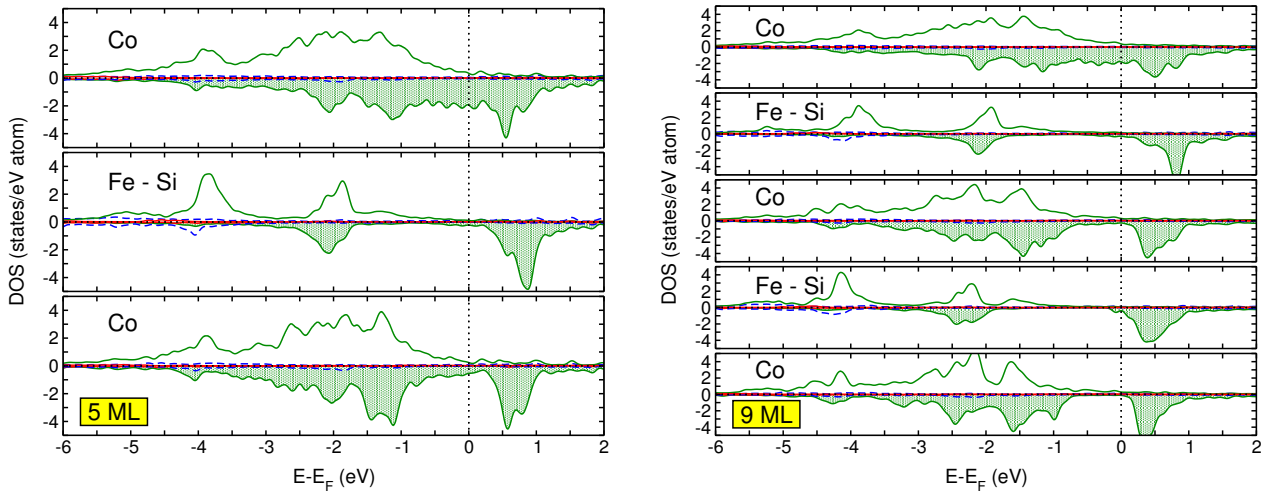

Figure 8.8: DOS of the Pt-Co_2FeSi-Pt system with (a) five and (b) nine monolayers of Heusler between the platinum leads.

of the conductance above the Fermi energy in the nine monolayer system can be related to the peak in the DOS above the Fermi energy. The sudden occurrence of states in the middle of the system leads to the occurrence of many new transmission channels. Therefore, the conductance of the spin-down channel increases which of course leads to an increase of the total conductance.

The energy dependence of the five layer Pt-Co_2MnAl-Pt system can also be described by features of the DOS which is shown in Fig. 8.10(a). The DOS of both spin channels is relatively large at the Fermi energy which leads to the occurrence of many transmission channels and therefore to a quite large conductance. In the nine layer system (see Fig. 8.4)

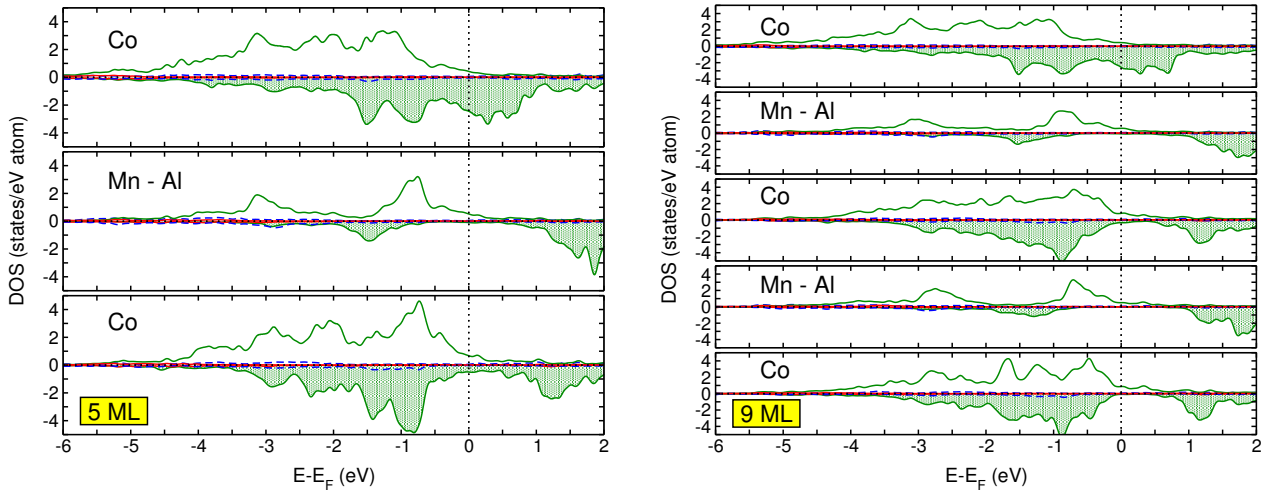

Figure 8.9: DOS of the Pt-Co_2MnAl-Pt system with (a) five and (b) nine monolayers of Heusler between the platinum leads.

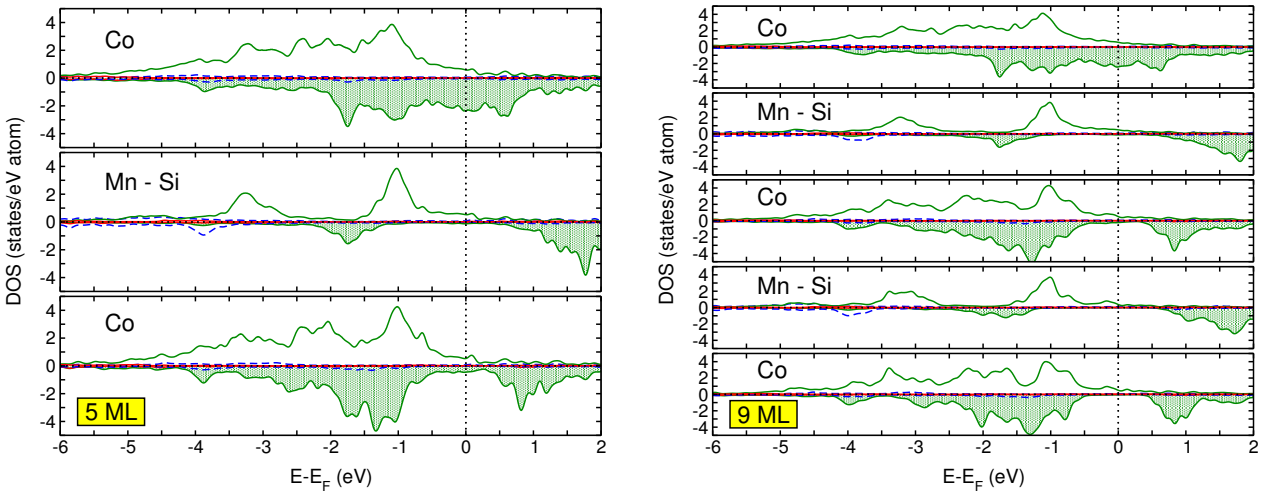

Figure 8.10: DOS of the Pt-Co_2MnSi-Pt system with (a) five and (b) nine monolayers of Heusler between the platinum leads.

the total conductance is again reduced and also the spin-down conductance is again about a factor of two smaller. This is again connected to the occurrence of the half-metallic gap (see Fig. 8.10(b)).

Concerning the DOS of the Pt-Co_2MnSi-Pt systems the results are similar to those of the other systems. The half-metallic gap is fully recovered in the nine monolayer system. Therefore, the small conductance contribution of the spin-down channel in this system can be attributed to this feature. Although the Fermi level of this system is almost exactly in the middle of the gap the conductance is only small but not zero. This shows that there must be enough channels through which electrons can travel from one side to the other by tunneling through the monolayers without spin-down states. Besides the tunneling, other channels must be connected to relativistic effects.

The systematic behavior of the sign of the Seebeck coefficient as summarized in Table 8.1 can also be related to the features of the electronic DOS. The DOS of the Pt-Co_2FeAl-Pt and Pt-Co_2MnAl-Pt systems show that the Fermi energy has the tendency to be located closer to the valence edge of the spin-down channel. This is different in Pt-Co_2FeSi-Pt and Pt-Co_2MnSi-Pt where the Fermi energy shows a tendency for the conduction edge of the spin-down channel. A Fermi energy at the edge of the valence band leads to a large conductance below because of the large number of channels and a Fermi energy at the edge of the conduction band leads to a large conductance above. This has a strong effect on the slope of the energy dependence of the conductance which determines the Seebeck coefficient. Negative slope is connected to a Fermi energy at the valence band and a positive slope to a Fermi energy at the conduction band.

Another summarizing comparison is given in Table 8.2 where the polarization of the total DOS at the Fermi energy of the systems is compared to the polarization of the associated conductance. This polarization is defined by $(\uparrow - \downarrow)/(\uparrow + \downarrow)$ where the arrows represent the actual spin-up or spin-down contributions. The most interesting observation is that the polarization of the DOS is negative for all systems whereas the polarization of the conductance is always positive. This is connected with the large peak in the minority channel of the total

	Conductance		DOS	
	5ML	9ML	5ML	9ML
Co_2FeAl	0.07	0.32	-0.27	-0.27
Co_2FeSi	0.18	0.28	-0.25	-0.26
Co_2MnAl	0.10	0.28	-0.21	-0.17
Co_2MnSi	0.19	0.31	-0.24	-0.20

Table 8.2: Comparison of the polarization of the conductance and the total electronic density of states of the entire system.

DOS at the Fermi energy that is mainly associated with the DOS of the platinum leads (see Appendix A.13 where the electronic DOS of the first three layers of the leads are shown). Since the states associated with this peak are localized and as in addition there are only very few states within this energy range in the Heusler layer, their contribution to the conductance of the minority channel is only small. Therefore, the DOS of the Heusler layer determines the spin-dependence of the conductance almost completely. It shows that the Heusler layer acts as a spin filter even if relativistic effects are taken into account within the calculation of the transport coefficients.

8.4 Summary

The transport calculations presented here are carried out for the ballistic regime. Therefore, no inelastic scattering of electrons is considered. The temperature dependence enters the calculation only through the derivative of the Fermi function. Therewith, the additional activation of transport channels with increasing temperature is taken into account. Effects of phonons and magnetic excitations are neglected.

The transport calculations show that the Seebeck coefficient strongly depends on the details of the system. Therefore, small changes of the layer thickness and the composition can result in strong changes of the behavior of the Seebeck coefficient. This allows a precise tuning of the thermoelectric properties.

It can be stated that the Seebeck coefficient does almost solely depend on coarse properties of the energy dependence of the conductance. The main contribution is given by the averaged slope of this property. In particular, a small conductance can lead to large Seebeck coefficients if its slope is large enough. This is consistent with the fact that the method used here can be understood as a generalization of the Mott formula (see e.g. Ref. [86]). The Mott formula determines the Seebeck coefficient from the logarithmic derivative of the conductance with respect to the energy directly at the Fermi level.

If the calculated Seebeck coefficients of the composite Pt-Heusler-Pt systems are compared to the experimental measurements of bulk Seebeck coefficients of Co-based Heusler alloys (see Ref. [202]) fundamental differences are observed. The most obvious fact is that all except the nine layer Co_2FeSi and Co_2MnSi system show positive Seebeck coefficients over the whole temperature range. The experimental observation of Seebeck coefficients of the corresponding Heusler bulk materials reveal negative values for all systems. It is even more surprising that the composite systems exhibit positive Seebeck coefficients because Pt shows also a negative

Seebeck coefficient above 200K.

It clearly turns out that thin films of half-metallic Heusler alloys between platinum leads give rise to strong spin-polarized currents and in addition to spin-polarized thermoelectric currents. They only need to consist of nine monolayers because from nine monolayers on half-metallicity is recovered within the Heusler film. This leads to a significant suppression of the conductance of the spin-down channel together with a slope that differs strongly from that of the spin-up channel. This leads to a large difference between both contributions to the total Seebeck coefficient. Therefore, the systems investigated here can act as electrically as well as thermally driven spin filter devices.

The only drawback of this interpretation is the fact that half-metallicity of Co-based Heusler alloys is strongly temperature dependent. Therefore, the spin-polarization in such Heusler alloys is strongly reduced at higher temperatures. Therefore, large spin Seebeck coefficients at temperatures above 200 K seem to be promising but might be suppressed in real experiments.

In addition, it should be noted that the choice of the Pt-Co interface between the platinum leads and the Heusler layer has a particular influence on the transport properties. This interface is strongly responsible for size of the conductance as well as for the degree of spin-polarization of the electric current in such systems. Further investigation could include the analysis of interfaces between platinum and Fe-Z and Mn-Z (Z=Al, Si) layers. Such layers can be used on both sides and also the combination of mixed and pure Co layers is of interest. In addition, Pt-based Heusler alloy could be considered in order to give almost perfect interfaces between lead and Heusler. A systematic analysis of the effect of the interface between Heusler alloys and semiconductors are reported in Ref. [226].

On the other hand, the influence of collective excitations could be included by using the adiabatic approach or the DLM picture (see Ref. [175]). This means that frozen magnons are prepared in the systems or that paramagnetic tendencies are introduced by using the CPA method. In addition, the effect of frozen phonons could be considered. On the other hand, the properties of systems with larger Heusler layers have to be carried out and in addition the k-point resolved density of states needs to be taken into account to give a more detailed insight into the transport mechanisms. A systematic investigation including all the different contributions is beyond the scope of the present work.

In summary, a consistent theoretical description of cobalt based Heusler alloys in Pt-Heusler-Pt composite systems is presented here. These composite systems have turned out to be promising candidates for the generation of spin polarized currents by applying a thermal gradient.

Highlight

This chapter gives a contribution to the modern field of spincaloritronic as a possibility to design thermally driven spin generators is proposed. Trilayer structures of platinum and Heusler alloys exhibit strongly spin dependent Seebeck coefficients. Therefore, the application of a thermal gradient automatically leads to a spin accumulation in such systems. This property is understood from analyzing the electronic structure and is attributed to the recovery of the half-metallic gap in the Heusler layer if it is large enough. Interestingly, large enough turns out to be nine or more monolayers.

9 Summary and Conclusions

A comprehensive study of Mn, Fe and Co based alloys, including all binary combinations and corresponding Heusler alloys, containing additional Al or Si has been carried out in this treatise. A combined approach using first-principles methods together with Monte Carlo simulations is employed. This approach leads to interesting new insights into the magnetism at zero and finite temperature. In addition, the influence of disorder on certain properties is taken into account by incorporating the coherent potential approximation.

During the investigation of $Fe_{1-x}Mn_x$, the combination of *ab intio* and Monte Carlo methods leads to a fast evaluation of non-collinear ground states as well as insight into possible reorientation transitions of the magnetic structure at finite temperature which is attributed to the different inter- and intra-sublattice exchange coupling constants. Non-collinear ground states occur on the Mn rich side of the phase diagram due to the strong antiferromagnetic tendencies of Mn and frustration of the moments arranged on the fcc lattice. The addition of carbon at interstitial sites leads to the stabilization of collinear magnetism even in Mn rich alloys. Critical temperatures of the magnetic phase transitions obtained from Monte Carlo simulations by employing exchange parameters calculated with *ab initio* methods, are in excellent agreement with experimental findings.

Results of the analysis of $Fe_{1-x}Co_x$ alloys agree with the experimental phase diagram of structural and magnetic properties. The theoretical description of the structural properties is based on the comparison of the total energy of different structures. This comparison reveals a series of almost energetically degenerated structures. This corresponds to the modern understanding of super-structured iron-cobalt-alloys. The investigation of the γ-phase of $Fe_{1-x}Co_x$ alloys shows the existence of complex magneto-volume correlations on the iron rich side of the phase diagram. In addition, it is observed that the moment of Co atoms strongly depends on the local environment. Magnetic disorder tends to decreases the moment significantly. This effect is even stronger if the nearest neighbor environment is chemically inhomogeneous. On the other hand, the vicinity of other Co atoms in the nearest neighbor shell stabilizes the Co moment.

In particular, the investigation of $Co_{1-x}Mn_x$ alloys reveals entirely new understanding of these systems because they have not been extensively studied theoretically. The results are in good agreement with the structural and magnetic phase diagram obtained from experiments and show the complex nature of magnetic properties of such alloys although details of supermagnetism occurring in $Co_{1-x}Mn_x$ cannot easily be described by the methods used here. The study reinforces the conclusions drawn form the investigation of $Fe_{1-x}Co_x$ that the Co moment is sensitive to the local environment because the same trends are found in $Co_{1-x}Mn_x$. For example, the VASP calculations reveal that the Co moment vanishes completely if Co is subjected to an environment including antiferromagnetically aligned Mn atoms. But the most remarkable result is that the investigation predicts the existence of a bcc phase at the equiatomic composition. Such phases have not been found in experiment and are therefore unexpected. As the energy difference between the fcc and bcc phases obtained here is not large, a coexistence of both phases might be the possible reason why bcc structures of CoMn are unknown up to now.

After the discussion of binary alloys the focus is on Heusler alloys and in particular on half-metallic ferro- and antiferromagnetism of such systems. In the first part of this analysis attention is paid to effects of electron correlation. The actual persuasion represented in literature which states that accounting for such effects is particularly important for Co_2FeAl and Co_2FeSi is reinforced and additional insight is gained. In these systems, and especially in the latter, the description of localized e_g-states of iron is found to be deficient within standard GGA because these states tend to fill the half-metallic gap. This lack can be cured by employing the GGA+U method, but, it is also discussed that employing this method can lead to deficiency of other properties. It is particularly interesting that in, e.g., Fe_2MnAl and Fe_2MnSi, the inclusion of correlation effects is not necessary to obtain the half-metallic behavior, which seems to be unexpected, because these alloys include 50% iron. Instead, it can be concluded that if Fe is located in a Co rich environment it leads to the deficiency of standard GGA. The hybridization of Fe and Co states at the edge of the conduction band is not correctly captured and therefore the e_g-states of Fe are pushed to lower energies and into the gap. This conclusion supported by the investigation of $Fe_{1-x}Co_x$. In Fe rich binary systems a tendency for the occurrence of a half-metallic gap is already present whereas the DOS of Co rich systems is large around E_F. Therefore, the mechanism responsible for the development of the gap must be more subtle for Co rich Heusler alloys. On the other hand, these arguments suggest the prediction of a half-metallic tendency of Fe_2CoZ alloys which is not confirmed by the investigation of Fe_2CoAl and Fe_2CoSi. This reveals the particular role of the main group element. It is carefully concluded that the semiconducting element Si carries additional responsibility for the problematic description of the electronic structure of Co_2FeSi.

Calculations of the electronic structure of Co_2MnAl and Co_2MnSi reveal no problems when using GGA, instead their half-metallic property can be destroyed by employing the GGA+U method. The half-metallic feature of these systems is found to be very robust against the occurrence of B2 disorder, but, due to antiferromagnetic tendencies introduced by Mn the Curie temperature is strongly affected by disorder. The change of the average nearest neighbor environment is responsible for the change of the Curie temperature because the strength and the sign of the exchange interactions reveals a strong dependence on the local setting.

As already mentioned, the only combinations of the elements considered here which do not show a pronounced half-metallic tendency, are Fe_2CoAl and Fe_2CoSi. This conclusion has to be taken with care because Fe_2CoSi shows at least a minimum in the minority spin channel of the density of states around the Fermi energy. It cannot be excluded that a more developed investigation, including better treatment of electron correlations, determines Fe_2CoSi to be half-metallic. On the other hand, the electronic structure of Fe_2CoAl shows features which seem to prevent this system from being half-metallic. It is interesting to note that in contrast to Co_2FeZ alloys the Fe_2CoZ systems prefer to nucleate in the inverse Heusler structure.

The combination of 50% Fe with Mn, e.g., Fe_2MnAl as well as 50% Mn with Fe and Co, e.g., Mn_2FeAl or Mn_2CoAl, leads to the formation of half-metallic antiferromagnetism. More than that, magnetism of such systems becomes very complex leading to non-collinear structures and complicated finite temperature magnetism. The most outstanding examples are Fe_2MnAl and Fe_2MnSi because they show spin-glass like behavior in the B2 structure.

As noticed for the case of Co_2MnAl and Co_2MnSi the investigation of the influence of disorder on the half-metallic gap shows that this property is quite stable if only the Y and Z sublattices reveal disorder as in the B2 structure. On the other hand, the occurrence of A2 type of disorder, where all sublattices mix destroys half-metallicity. This is found for all

systems that prefer the conventional Heusler structure because in the inverse structure any disorder leads to the A2 structure.

Comparing Heusler alloys to the corresponding binary alloys it turns out that the addition of the main group element significantly alters many properties. For example, the addition of the main group element leads to the stabilization of ordered structures of Co-Mn-based alloys with high Mn content. On the other hand, high Curie temperatures are found for binary $Fe_{1-x}Co_x$ as well as for Co_2FeZ alloys. Both results show the outstanding properties of Heusler alloys.

The investigation of Ni-Mn based Heusler alloys employing a new method of decomposing the magnetic exchange interaction into symmetry associated contributions and analyzing these contributions separately gains interesting insight into details of the exchange mechanisms in such alloys. It is found that qualitatively the exchange mechanisms are very stable against compositional changes. In fact, all system analyzed here, reveal a particular from of the magnetic exchange interactions as a function of the distance. It is also explicitly shown how localized states lead to short range and delocalized states to long range interaction. In addition, the results obtained with this method suggest that the magnetic exchange interactions act as an additional driving force of the martensitic transition in such systems. This is one of the most outstanding results reported in this treatise because it allows a entirely new perception of the martensitic transitions in magnetic alloys.

The discussion closes with the investigation of Seebeck coefficients and their spin-dependence in Heusler layers between two platinum leads. Such systems exhibit the possibility to drive a thermocurrent with high spin polarization because the half-metallic Heusler layers act as a spin filter above a certain film thickness. Therefore, they are promising candidates for the design of thermally driven spin generators. Since this investigation contributes to the field of spincaloritronics it is of actual relevance.

A Appendix

A.1 The solutions of the Dirac equation for a free particle

Here, more details, of how the solutions of the U_i are justified, are shown. Therefore, only the two equations for U_1 and U_4 are considered because the procedure is the same for the other two equations. This system of equations is given by

$$\begin{aligned} \left(mc^2 - W\right) U_1 + c\left(p_x - ip_y\right) U_4 &= 0 \\ c\left(p_x + ip_y\right) U_1 - \left(mc^2 + W\right) U_4 &= 0 \,. \end{aligned} \tag{A.1}$$

A standard way to find the solution is to express one variable in term of the other, e.g.,

$$U_4 = -\frac{\left(mc^2 - W\right)}{c\left(p_x - ip_y\right)} U_1 \tag{A.2}$$

when starting from the first equation. Inserting this into the second equation gives

$$\frac{c^2\boldsymbol{p}^2 + m^2c^4 - W}{c\left(p_x - ip_y\right)} U_1 = 0 \tag{A.3}$$

where the denominator is zero according to the relativistic energy relation. Therefore, all pairs of U_1 and U_4 satisfying Eq. A.2 are valid solutions. To express these possible solutions in terms of known quantities one sets $U_1 = c\left(p_x - ip_y\right)$ from which immediately $U_4 = W - mc^2$ follows. Repeating this procedure by replacing U_1 in the first equation or by replacing U_1 or U_4 in the second equation one finds two linear independent pairs of expressions for U_1 and U_4.

A.2 Normalization for the solutions of the Dirac equation for a free particle

In this Appendix the evaluation of the normalization constant for spin-up and down as well as for positive and negative energies is summarized. Starting from

$$U_i^{\pm} = N_{\pm} \begin{pmatrix} \chi^i \\ \frac{c\hat{\boldsymbol{\sigma}}\boldsymbol{p}}{mc^2 \pm W} \chi^i \end{pmatrix} \tag{A.4}$$

where $i = \pm 1/2$ and $N_\pm$ is the normalization constant for the positive $(+)$ and negative $(-)$ energies respectively, the normalization requirement gives

$$\left(U_i^\pm\right)^\dagger U_i^\pm = |N_\pm|^2 \left(\chi_i^\dagger \chi_i + \frac{c^2 \left(\boldsymbol{\sigma} \cdot \boldsymbol{p}\chi_i\right)^\dagger \boldsymbol{\sigma} \cdot \boldsymbol{p}\chi_i}{\left(mc^2 \pm W\right)^2} \right) \tag{A.5}$$

$$\overset{(1)}{=} |N_\pm|^2 \left(1 + \frac{c^2 \chi_i^\dagger \boldsymbol{\sigma} \cdot \boldsymbol{p}\boldsymbol{\sigma} \cdot \boldsymbol{p}\chi_i}{\left(mc^2 \pm W\right)^2} \right) \tag{A.6}$$

$$\overset{(2)}{=} |N_\pm|^2 \left(1 + \frac{c^2 \boldsymbol{p}^2}{\left(mc^2 \pm W\right)^2} \right) \tag{A.7}$$

$$\overset{(3)}{=} |N_\pm|^2 \frac{m^2c^4 \pm 2mc^2W + W^2 + c^2\boldsymbol{p}^2}{\left(mc^2 \pm W\right)^2} \tag{A.8}$$

$$= |N_\pm|^2 \frac{2W^2 \pm 2mc^2W}{\left(mc^2 \pm W\right)^2} = 1 \tag{A.9}$$

where in (1) the propertiy $\sigma_i^\dagger = \sigma_i$ and in (2) $\boldsymbol{\sigma} \cdot \boldsymbol{p}\boldsymbol{\sigma} \cdot \boldsymbol{p} = \boldsymbol{p}^2$ and in (3) $W^2 = c^2p^2 + m^2c^4$ is used. Positive energies give

$$|N_+|^2 \frac{2W^2 + 2mc^2W}{\left(mc^2 + W\right)^2} = 1 \tag{A.10}$$

$$|N_+|^2 \frac{2W\left(mc^2 + W\right)}{\left(mc^2 + W\right)^2} = 1 \tag{A.11}$$

$$|N_+|^2 \frac{2W}{\left(W + mc^2\right)} = 1 \tag{A.12}$$

and for negative energies one obtains

$$|N_-|^2 \frac{2W^2 - 2mc^2W}{\left(mc^2 - W\right)^2} = 1 \tag{A.13}$$

$$-|N_-|^2 \frac{2W\left(mc^2 - W\right)}{\left(mc^2 - W\right)^2} = 1 \tag{A.14}$$

$$|N_-|^2 \frac{2W}{\left(W - mc^2\right)} = 1\,. \tag{A.15}$$

These equations determine the normalization factor.

A.3 Approximate exchange correlation functionals

It is shown in Chapter 2.1.6 that in the non-relativistic case the Kohn-Sham ansatz gives the possibility to solve a many-body problem by means of solving independent particle Schrödinger equations with an effective external potential determined self-consistently. The only intricate is that one part of the effective potential which is the exchange-correlation contribution is unknown. In this Appendix, the two most famous approximate schemes which are frequently used in practical calculations are presented but at first some exactly known properties of the exchange-correlation functional are derived because the approximate

functionals need to fulfill these properties in order to give reasonable results. Details of the following considerations can be found, e.g., in Ref. [52].

First, the so called sum rules are introduced. Therefore, the definition of the two electron density is needed, which is given by

$$\rho_2(\boldsymbol{r}', \boldsymbol{r}) = N\,(N-1) \sum_{\sigma_1,\ldots,\sigma_N} \int \mathrm{d}^3 r_3 \,\ldots \int \mathrm{d}^3 r_N \,|\Psi(\boldsymbol{r}', \sigma_1; \boldsymbol{r}, \sigma_2; \boldsymbol{r}_3, \sigma_3; \ldots; \boldsymbol{r}_N, \sigma_N)| \;. \quad \text{(A.16)}$$

This quantity determines the joint probability of finding one particle at point $\boldsymbol{r}$ and another at point $\boldsymbol{r}'$ and can be decomposed into

$$\rho_2(\boldsymbol{r}', \boldsymbol{r}) = n(\boldsymbol{r}) n_2(\boldsymbol{r}, \boldsymbol{r}') \quad \text{(A.17)}$$

where the density $n\,(\boldsymbol{r})$ gives the probability to find a particle at $\boldsymbol{r}$ given by

$$n(\boldsymbol{r}) = N \sum_{\sigma_1,\ldots,\sigma_N} \int \mathrm{d}^3 r_2 \,\ldots \int \mathrm{d}^3 r_N \,|\Psi(\boldsymbol{r}, \sigma_1; \boldsymbol{r}_2, \sigma_2; \boldsymbol{r}_3, \sigma_3; \ldots; \boldsymbol{r}_N, \sigma_N)| \quad \text{(A.18)}$$

and $n_2\,(\boldsymbol{r}, \boldsymbol{r}')$ which gives the conditional probability to find another particle at $\boldsymbol{r}'$ when there is one at $\boldsymbol{r}$. A simple integration of Eq. (A.17) over $\boldsymbol{r}'$ gives

$$\int \mathrm{d}^3 r' n_2(\boldsymbol{r}, \boldsymbol{r}') = N - 1 \,, \quad \text{(A.19)}$$

because $N-1$ particles are left to be found in space when there is one particular at $\boldsymbol{r}$. By separating out the exchange-correlation part of the conditional probability

$$n_2(\boldsymbol{r}, \boldsymbol{r}') = n(\boldsymbol{r}') + n_{\mathrm{xc}}(\boldsymbol{r}, \boldsymbol{r}') \;, \quad \text{(A.20)}$$

one finds in comparison to Eq. A.19 that the exchange correlation part has to fulfill

$$\int \mathrm{d}^3 r' \, n_{\mathrm{xc}}(\boldsymbol{r}, \boldsymbol{r}') = -1 \;. \quad \text{(A.21)}$$

This means that if there is a particle at $\boldsymbol{r}$ it leaves a hole in the rest of the system which is often termed exchange-correlation hole.

As the expectation value of the Coulomb operator can be written in terms of the two electron density ρ_2 one finds

$$\langle U \rangle = \int \mathrm{d}^3 r \int \mathrm{d}^3 r' \, \frac{\rho_2(\boldsymbol{r}, \boldsymbol{r}')}{|\boldsymbol{r}' - \boldsymbol{r}|} = \int \mathrm{d}^3 r \int \mathrm{d}^3 r' \, \frac{n(\boldsymbol{r}) n(\boldsymbol{r}')}{|\boldsymbol{r}' - \boldsymbol{r}|} + \int \mathrm{d}^3 r \int \mathrm{d}^3 r' \frac{n(\boldsymbol{r}) n_{\mathrm{xc}}(\boldsymbol{r}, \boldsymbol{r}')}{|\boldsymbol{r}' - \boldsymbol{r}|} \quad \text{(A.22)}$$

which contains a particular expression for the exchange-correlation energy given by

$$E_{\mathrm{xc}} = \int \mathrm{d}^3 r \int \mathrm{d}^3 r' \, \frac{n(\boldsymbol{r}) n_{\mathrm{xc}}(\boldsymbol{r}, \boldsymbol{r}')}{|\boldsymbol{r}' - \boldsymbol{r}|} \;. \quad \text{(A.23)}$$

In the next step $n_{\mathrm{xc}}\,(\boldsymbol{r}, \boldsymbol{r}')$ is split into an exchange and a separate correlation part

$$n_{\mathrm{xc}}(\boldsymbol{r}, \boldsymbol{r}') = n_{\mathrm{x}}(\boldsymbol{r}, \boldsymbol{r}') + n_{\mathrm{c}}(\boldsymbol{r}, \boldsymbol{r}') \;. \quad \text{(A.24)}$$

Now, an artificial parameter λ is introduced which can switch the particle interaction on ($\lambda = 1$) and of ($\lambda = 0$) in the sense that

$$\hat{H}_\lambda = \hat{T} + \lambda \hat{V}_{\text{int}} \,, \tag{A.25}$$

neglecting the external potential for the moment. Following the arguments above and defining $\rho_2^\lambda(\boldsymbol{r}', \boldsymbol{r})$ by Ψ^λ which is the the groundstate of $\hat{H}_\lambda$, it becomes apparent that the result of the integral in Eq. (A.21) remains -1 and does not depend on λ. But as there is no correlation in a non-interacting system the two important sum rules for the exchange and the correlation part are

$$\int \mathrm{d}^3 r' \, n_{\text{x}}(\boldsymbol{r}, \boldsymbol{r}') = -1 \tag{A.26}$$

$$\int \mathrm{d}^3 r' \, n_{\text{c}}(\boldsymbol{r}, \boldsymbol{r}') = 0 \,. \tag{A.27}$$

Therewith, two general properties of the exchange and the correlation part are derived, which have to be fulfilled by every reasonable approximation of the exchange-correlation functional.

Another set of important features are the so called scaling relations. The derivation of all these relations is too much involved to be presented here but details can be found in Ref. [52] and references therein.

The scaling concerns, e.g., a uniform scaling of the coordinates. Therefore, one defines a scaled wave function by

$$\Psi_\gamma(\boldsymbol{r}_1, \sigma_1; \ldots; \boldsymbol{r}_N, \sigma_N) = \gamma^{3N/2} \Psi(\gamma \boldsymbol{r}_1, \sigma_1; \ldots; \gamma \boldsymbol{r}_N, \sigma_N) \tag{A.28}$$

where the norm of the wave function is conserved. This implies that the density obeys the relation

$$n_\gamma(\boldsymbol{r}) = \gamma^3 n(\gamma \boldsymbol{r}) \,. \tag{A.29}$$

Using this expression it can be shown that the kinetic energy of non-interacting particles T_0, the Hartree energy E_{H} (which is the Coulomb part) and the exchange contribution E_{x} obey the relations

$$T_0[n_\gamma] = \gamma^2 T_0[n] \quad , \quad E_{\text{H}}[n_\gamma] = \gamma E_{\text{H}}[n] \quad , \quad E_{\text{x}}[n_\gamma] = \gamma E_{\text{x}}[n] \,. \tag{A.30}$$

The contribution arising from the correlation does not reveal such a simple scaling behavior but inequalities can be derived and are given by

$$E_{\text{c}}[n_\gamma] > \gamma E_{\text{c}}[n] \;\; (\gamma > 1) \quad , \quad E_{\text{c}}[n_\gamma] < \gamma E_{\text{c}}[n] \;\; (\gamma < 1) \,. \tag{A.31}$$

The last important relation to be mentioned here concerns the spin-dependent case and is the so called spin scaling relation given by

$$E_{\text{x}}[n_\downarrow, n_\uparrow] = \frac{1}{2} E_{\text{x}}[2n_\downarrow] + \frac{1}{2} E_{\text{x}}[2n_\uparrow] \,. \tag{A.32}$$

The sum rules as well as the scaling relations are the main constraints for the construction of exchange-correlation functionals. Whenever one or more of these constraints are violated the corresponding functional must lead to unreasonable results.

Now, the basic approximation of the exchange-correlation functional, which was already proposed by Kohn and Sham [44], is introduced. This approximation relies on the assumption

that the exchange-correlation contribution can locally be described by the corresponding contribution of an uniform and homogenous electron gas with the same density. Therefore, this approximation is called local (spin) density approximation (L(S)DA). This functional is give by

$$\begin{aligned} E_{\mathrm{xc}}^{\mathrm{LSDA}}\left[n^{\uparrow}, n^{\downarrow}\right] &= \int \mathrm{d}^3 r\, n(\boldsymbol{r}) \epsilon_{\mathrm{xc}}^{\mathrm{hom}}\left(n^{\uparrow}(\boldsymbol{r}), n^{\downarrow}(\boldsymbol{r})\right) \\ &= \int \mathrm{d}^3 r\, n(\boldsymbol{r}) \left[\epsilon_{\mathrm{x}}^{\mathrm{hom}}\left(n^{\uparrow}(\boldsymbol{r}), n^{\downarrow}(\boldsymbol{r})\right) + \epsilon_{\mathrm{c}}^{\mathrm{hom}}\left(n^{\uparrow}(\boldsymbol{r}), n^{\downarrow}(\boldsymbol{r})\right)\right] \end{aligned} \tag{A.33}$$

where $\epsilon_{\mathrm{xc}}^{\mathrm{hom}}$ is the exchange-correlation energy per particle of a homogeneous electron gas. It only depends on the densities of the two spin channels at point $\boldsymbol{r}$ and not on the complete density. Therefore, $\epsilon_{\mathrm{xc}}^{\mathrm{hom}}$ is only a nested function and no longer a functional. The quantization axis of the spin is assumed to be the same at all points in space. This can be generalized to allow for non-collinear arrangement of the spins by introducing a position dependent unitary transformation which rotates the coordinate system locally. A detailed derivation can be found in Ref. [52].

As the exchange and the correlation part can be decomposed in the sense that

$$E_{\mathrm{xc}} = E_{\mathrm{x}} + E_{\mathrm{c}} \ , \tag{A.34}$$

the exchange part of $\epsilon_{\mathrm{x}}^{\mathrm{hom}}$ is separated and replaced by the exchange energy of the homogeneous electron gas which is exactly known from Hartree-Fock theory [52]. It is given by

$$\epsilon_{\mathrm{x}}^{\mathrm{hom}}\left(n_{\uparrow}, n_{\downarrow}\right) = -3\left(\frac{3}{4\pi}\right)^{1/3} \frac{1}{n}\left(n_{\uparrow}^{4/3} + n_{\downarrow}^{4/3}\right) \ . \tag{A.35}$$

Unfortunately, no analytical representation of the correlation energy of the homogeneous electron gas is known. But a variety of parameterizations exist, which rely on different approximate and numerical methods. One example is the parameterization of Hedin and Lunqvist [227], which is based on local field correction calculations of Singwi *et al.* [228] and is given by

$$\epsilon_c^{HL}\left(r_s\right) = -0.0225\left\{\left[1 + \left(\frac{r_s}{21}\right)^3\right]\log\left(1 + \frac{21}{r_s}\right) - \left(\frac{r_s}{21}\right)^2 + \frac{r_s}{42} - \frac{1}{3}\right\} \tag{A.36}$$

where $\frac{4}{3}\pi r_s^3 = n^{-1}$. A widely used representations proposed by Volko, Wilk and Nusair [162] is based on the random phase approximation (RPA) method [229]. The same authors give another representation based on very accurate quantum Monte-Carlo simulations of Ceperley and Alder [230]. The most recent and probably most accurate parameterization was given by Perdew and Wang [231] which is also based on the results of Ceperley and Alder.

The LSDA leads to reasonable results in many cases and of course especially for system where a slowly varying electron density is expected. Problems arise for intrinsically inhomogeneous cases like system with surfaces and molecules or system where electrons are strongly correlated. The theory of strongly correlated electrons is still a matter of ongoing debate today and a modern review of this field is given in Ref. [232] (some additional remarks concerning the inclusion of correlations effects within this treatise are given at the end of this Appendix).

A technical reason for the success of the LSDA is that it fulfills all sum rules and scaling relations and by definition the important limit of the homogeneous electron gas. Apart from the good properties, it has to be mentioned that the LSDA suffers from the artificial introduction of a self-energy contribution. In the Hartee-Fock formalism (see Section 2.1.2) this contribution cancels out but in the LSDA this cancelations is only approximative.

To improve the LSDA it seems to be natural to consider gradients of the local density. This results in an expansion by means of the magnitude of density gradients ∇n^σ. Such a gradient expansion approximation (GEA) was already suggested by Kohn and Sham [44] and carried out be various groups (see Ref. [233] and references therein). For example, in the limit of a still slowly varying density the second order gradient expansion approximation of the form

$$E_{\mathrm{xc}}^{\mathrm{GEA}}\left[n_\uparrow, n_\downarrow\right] = E_{\mathrm{xc}}^{\mathrm{LSDA}}\left[n_\uparrow, n_\downarrow\right] + \sum_{\sigma,\sigma'} \int \mathrm{d}^3 r\, C_{\mathrm{xc}}^{\sigma,\sigma'}(n_\uparrow, n_\downarrow)\, \frac{\nabla n_\sigma \nabla n_{\sigma'}}{n_\sigma^{2/3}\, n_{\sigma'}^{2/3}} \tag{A.37}$$

is proposed. Unfortunately, the GEA approximation leads to no improvement. It violates sum rules and scaling relations and often the obtained results are even worse compared to LSDA. This illustrates the importance of the exactly known features of the exchange correlation functional.

To cure the lacks of the gradient expansion a series of modified gradients which preserve the most important requirements was proposed. They are called generalized gradients and therefore the approximation is termed generalized gradient approximation (GGA). Many different approaches to this GGA have been presented and some of them are reviewed in Ref. [234]. Here, the focus lies on the most recent as well as most successful approach that has been introduced by Perdew and co-workers. One great feature of this approach is that it only relies on fundamental constants and not on empirical assumptions. According to Ref. [233] a starting point of this approximation of the exchange-correlation energy is given by

$$E_{\mathrm{xc}}^{\mathrm{GGA}}\left[n_\uparrow, n_\downarrow\right] = \int \mathrm{d}^3 r\, f\left(n^\uparrow, n^\downarrow, \nabla n^\uparrow, \nabla n^\downarrow\right) \tag{A.38}$$

where the f includes first order gradient corrections to the homogenous density. In contrast to the LDA the input quantity f is not unique as the exchange-correlation energy of the homogenous electron gas. In order to get a reasonable form of the function f it is subsequently decomposed into different contributions. First, it is written as a product of the local density, exchange energy per particle of the unpolarized uniform electron gas $\epsilon_{\mathrm{x}}^{\mathrm{P}}$ and a so called enhancement factor F_{xc}

$$E_{\mathrm{xc}}^{\mathrm{GGA}}\left[n_\uparrow, n_\downarrow\right] = \int \mathrm{d}^3 r\, n(\boldsymbol{r}) \epsilon_{\mathrm{x}}^{\mathrm{P}}(r_S) F_{\mathrm{xc}}(r_S, \zeta, s)\ . \tag{A.39}$$

This enhancement factor depends on the density parameter r_s (introduced in the discussion of the LSDA), the local spin polarization

$$\zeta\left(\boldsymbol{r}\right) = \frac{n_\uparrow(\boldsymbol{r}) - n_\downarrow(\boldsymbol{r})}{n(\boldsymbol{r})} \tag{A.40}$$

and the reduced density gradient

$$s\left(\boldsymbol{r}\right) = \frac{|\nabla n|}{2 k_{\mathrm{F}} n} = \frac{3}{2\alpha} |\nabla r_s|\,. \tag{A.41}$$

Here, $\alpha = (9\pi/4)^{1/3}$ and the so called local Fermi radius k_F is given by $k_\mathrm{F} = \alpha/r_S$. This decomposition into subsequent products is not trivial and only exact under certain conditions [91]. In the next step, the enhancement factor is decomposed into its exchange and correlation contribution

$$F_\mathrm{xc}(r_S, \zeta, s) = F_\mathrm{x}(\zeta, s) + F_\mathrm{c}(r_S, \zeta, s)\,. \tag{A.42}$$

Both contributions are given in terms of complicated functions which are founded on considerations based on sum rules, scaling and the requirement to fulfill certain physical limits. Here, only the functional form is given but details can be found in Ref. [91, 233]. The functional form of the exchange contribution is given by

$$F_\mathrm{x}(\zeta, s) = \frac{1}{2}\left[(1+\zeta)^{4/3}\, F_\mathrm{x}\Big(s/\left(1+\zeta^{1/3}\right)^{1/3}\Big) + (1-\zeta)^{4/3}\, F_\mathrm{x}\Big(s/\left(1-\zeta^{1/3}\right)^{1/3}\Big)\right] \tag{A.43}$$

where

$$F_\mathrm{x}(s) = 1 + \kappa - \frac{\kappa}{1 + \mu s^2/\kappa} \tag{A.44}$$

with $\kappa = 0.804$ and $\mu = 0.21952$. To obtain the correlation contribution the function

$$H = 2c_0\phi^3 \ln\left\{1 + \frac{\beta}{c_0}\left[\frac{1+At^2}{1+At^2+A^2t^4}\right]t^2\right\} \tag{A.45}$$

is defined. Here, A is given by

$$A = \frac{\beta}{c_0}\left[\exp\left(-\frac{\epsilon_\mathrm{c}\left(r_S, \zeta\right)}{2c_0\phi^3}\right) - 1\right]^{-1} \tag{A.46}$$

and

$$\phi\left(\zeta\right) = \frac{(1+\zeta)^{2/3} + (1-\zeta)^{2/3}}{2}\,. \tag{A.47}$$

In addition, another type dimensionless density gradient is introduced by

$$t = \frac{|\nabla n|}{2\phi k_s n} = \frac{\left(3\pi^2/16\right)^{1/3} s}{\sqrt{r_S}\phi}\,. \tag{A.48}$$

The $k_s = 2\sqrt{k_\mathrm{F}/\pi}$ is the Thomas-Fermi screening wave number, $\beta = 0.066725$ and $c_0 = (1 - \ln(2))/\pi$. Now, the complete expression for the enhancement function is given by

$$F_\mathrm{xc}(r_S, \zeta, s) = F_\mathrm{x}(\zeta, s) + \frac{\epsilon_\mathrm{c}(r_S, \zeta) + H\left[r_S, \zeta, t\left(s\right)\right]}{\epsilon_\mathrm{x}^\mathrm{P}(r_S)}\,. \tag{A.49}$$

With this, the discussion of non-relativistic approximations to the exchange-correlation functional is closed. It becomes obvious that a systematic improvement of such functionals is far from trivial. Therefore, the development of new functionals is still a vivid research topic. In addition to the GGA also non-local approximations of the exchange-correlation functional are part of actual research but their discussion is beyond the scope of this introduction.

Concerning the description of the electronic structure of strongly correlated systems the LDA as well as the GGA tend to miss important features, e.g., insulators can turn out to be metallic. Among the many methods that have been proposed to cure this lack the so called

LDA+U method is shortly introduced here because it is used in some of the investigation carried out in this work. The LDA+U method employs the Hubbart model [235] which is particularly designed for treating effects of correlated electrons, within an additional term in the exchange-correlation functional. This method was first proposed by Anisimov *et al.* [236] in 1993 and the achievements that have been acquired by using this approach are extensively reviewed in Ref. [237]. Today the method is usually used in the form derived by Dudarev *et al.* [238] which is also used in the present work. Within this method two free parameters have to be appropriately chosen. Therefore, this method is not a full *ab initio* method. But recently methods are developed that allow to determine the free parameters of the LDA+U method again from the first-principles level (see e.g. Ref. [204]). Here, only a particular set of values is used which is explicily given in the sections where correlation effects are taken into account. In particular the GGA+U method is used throughout this treatise to combine the good features of the GGA with additional inclusion of correlation introduced by the Hubbard term.

A.4 Relativistic exchange correlation functionals

This section is devoted to a short discussion of relativistic exchange-correlation functionals. As this topic involves complicated derivations and in addition a more detailed knowledge about particularities of relativistic many-body theory, the discussion is restricted to some comments and references concerning relativistic LDA.

Corresponding to the development of non-relativistic LDA it is possible to design the relativistic analogue. It can be written in the same form as shown in Eq. A.33 but the determination of the different local contributions to the exchange energy of the homogeneous relativistic electron gas is far more complicated because it starts directly from quantum electrodynamics and involves renormalization considerations which cannot be discussed here (see Ref. [33]). Interestingly, the final result of such calculation is that the relativistic exchange energy can be replaced by a product of the non-relativistic expression multiplied by a correction factor (see Ref. [239] and references therein). The same can be shown for the correlation part [240]. Unfortunately, the use of the relativistic functional does not necessarily lead to improved results compared to calculations carried out within relativistic DFT in combination with non-relativistic exchange-correlation functionals. Therefore, the relevance of relativistic exchange-correlation contributions in calculations of the electronic structure of molecules has been investigated in Ref. [241]. The authors performed calculations using the relativistic LDA as well as GGA and concluded that the LDA contributions are only very small and those of the GGA are negligible.

Therewith, the discussion is finished and the interested reader is referred to the cited literature and reference therein for more details.

A.5 Projector augmented plane waves

In this Appendix the projector augmented plane wave (PAW) method invented by P. Blöchel is outlined [90]. The derivation presented here follows Ref. [242].

The underlying idea of the PAW method is that, apart from the periodicity of a solid two different regions of the lattice can be identified: The first one is the region between the atoms which is usually called bonding region and the second is the region close to the nucleus. The

first is characterized by a quite flat potential whereas close to the nucleus the potential is very steep. This twofold character of the potential leads to two types of states. There are core states which are localized around the core because of the steep potential and are zero in the bonding region. In addition, there are valence states which are less localized and can even be delocalized within the whole solid and are non-zero in the core and bonding region. It turns out to be very difficult to describe both regions and the associated states on the same footing with same accuracy.

A serious problem arises because the one-particle Kohn-Sham wave functions have to oscillate very strongly close to the nucleus to fulfill the requirement of orthogonality of the many non-zero states (core and valence) in this region. On the other hand, the wave functions are much smoother in the bonding region because here the potential is slowly varying and the number of non-zero states is much smaller. For a plane wave expansion this means that a large set has to be used to gather the oscillations around the core whereas a small set would be more appropriate to achieve smooth solutions in the bonding region. Practically, the plane wave ansatz fails to give sufficient results for band structures of real solids.

The problem can be overcome by dividing the wave function into two parts. One part is calculated close to the nucleus in a certain well defined sphere. In this sphere the wave function is appropriately expanded in spherical functions. Outside the sphere it is still expanded in plane waves. Both parts are matched continuously on the surface of the sphere. The PAW method is inspired by such considerations.

The additional idea of the PAW method is to define a linear transformation $\hat{\mathcal{T}}$ which connects the true Kohn-Sham wave function $|\psi_n\rangle$ to an auxiliary wave function $|\tilde{\psi}_n\rangle$ which is smooth around the nuclei by

$$|\psi_n\rangle = \hat{\mathcal{T}}|\tilde{\psi}_n\rangle \; . \tag{A.50}$$

The n is a composite index including band index, k-point and spin variable. With this transformation a transformed Kohn-Sham equation can be derived,

$$\hat{\mathcal{T}}^\dagger \hat{H} \hat{\mathcal{T}} |\tilde{\psi}_n\rangle = \epsilon_n \hat{\mathcal{T}}^\dagger \hat{\mathcal{T}} |\tilde{\psi}_n\rangle \tag{A.51}$$

which is the central equation for the determination of the $|\tilde{\psi}_n\rangle$. As the solutions of this equation are smooth functions the application of numerical methods it is much more convenient.

The open question is how the transformation $\hat{\mathcal{T}}$ has to be defined to ensure that the auxiliary functions $|\tilde{\psi}_n\rangle$ calculated from Eq. A.51 are smooth. As the wave functions $|\psi_n\rangle$ are naturally smooth in the bonding region the transformation needs to operate only in a certain region around the cores. Therefore, one defines

$$\hat{\mathcal{T}} = 1 + \sum_a \hat{\mathcal{T}}^a \tag{A.52}$$

where a is the atom index. Inside a region of $|\boldsymbol{r} - \boldsymbol{R}^a| < r_c^a$ the wave function $|\psi_n\rangle$ is given by $|\tilde{\psi}_n\rangle$ and an additional part which is transformed by the atom centered transformation ($|\psi_n\rangle = |\tilde{\psi}_n\rangle + \hat{\mathcal{T}}^a|\tilde{\psi}_n\rangle$). Outside this region both functions are equal ($|\psi_n\rangle = |\tilde{\psi}_n\rangle$ for $|\boldsymbol{r} - \boldsymbol{R}^a| > r_c^a$). The region within r_c^a is termed augmentation region and r_c^a is a cut-off radius which is chosen in a way to ensure that different augmentation regions do not overlap.

In order to determine the local transformation $\hat{\mathcal{T}}^a$ the true wave function $|\psi_n\rangle$ is expanded inside the augmentation spheres by partial waves $|\phi_i^a\rangle$ with coefficients that are unknown up to now. For each partial wave a corresponding smooth partial wave $\tilde{\phi}_i^a$ is defined and both

sets are connected via

$$|\phi_i^a\rangle = (1 + \hat{\mathcal{T}}^a)|\tilde{\phi}_i^a\rangle \quad \Leftrightarrow \quad \hat{\mathcal{T}}^a|\tilde{\phi}_i^a\rangle = |\phi_i^a\rangle - |\tilde{\phi}_i^a\rangle \tag{A.53}$$

for all i in all augmentation spheres a. The transformation is completely defined by the two sets of wave functions ϕ_i^a and $\tilde{\phi}_i^a$. As the transformation should not operate outside the augmentation sphere, Eq. A.53 implies that the partial wave functions need to be identical outside the sphere in the sense that

$$\phi_i^a(\boldsymbol{r}) = \tilde{\phi}_i^a(\boldsymbol{r}) \quad , \quad \text{for } r > r_c^a \, . \tag{A.54}$$

Assuming the set of smooth partial wave functions to be complete, one can expand the smooth wave function,

$$|\tilde{\psi}_n\rangle = \sum_i P_{n,i}^a |\tilde{\phi}_i^a\rangle \quad , \quad \text{for } |\boldsymbol{r} - \boldsymbol{R}^a| < r_c^a \tag{A.55}$$

where the $P_{n,i}^a$ are expansion coefficients which are, up to now, undetermined. This implies that the true wave functions can be expanded by

$$|\psi_n\rangle = \hat{\mathcal{T}}|\tilde{\psi}_n\rangle = \sum_i P_{n,i}^a |\phi_i^a\rangle \quad , \quad \text{for } |\boldsymbol{r} - \boldsymbol{R}^a| < r_c^a \tag{A.56}$$

where the expansion coefficients are exactly the same as in the expansion of the auxiliary wave function. As it is required that the transformation is linear, the expansion coefficients $P_{n,i}^a$ have to be linear functionals of $|\tilde{\psi}_n\rangle$. Therefore, they can be defined by

$$P_{n,i}^a = \langle \tilde{p}_i^a | \tilde{\psi}_n \rangle = \int \mathrm{d}r \, \tilde{p}_i^{a*}(\boldsymbol{r} - \boldsymbol{R}^a) \tilde{\psi}_n(\boldsymbol{r}) \, , \tag{A.57}$$

and the $|\tilde{p}_i^a\rangle$ are fixed functions which are called smooth projector functions. The projections $|\tilde{\phi}_i^a\rangle\langle\tilde{p}_i^a|$ have to fulfill the completeness relation

$$\sum_i |\tilde{\phi}_i^a\rangle\langle\tilde{p}_i^a| = 1 \tag{A.58}$$

to ensure that the expansion $\sum_i |\tilde{\phi}_i^a\rangle\langle\tilde{p}_i^a|\tilde{\psi}_n\rangle$ is identical to $|\tilde{\psi}_n\rangle$ inside the augmentation region, which additionally requires that

$$\langle \tilde{p}_{i_1}^a | \tilde{\phi}_{i_2}^a \rangle = \delta_{i_1,i_2} \quad , \quad |\boldsymbol{r} - \boldsymbol{R}^a| < r_c^a \, . \tag{A.59}$$

This means that the projection functions are orthonormal to the partial wave functions. It should be noted that there are no restrictions for the $|\tilde{p}_i^a\rangle$ outside the augmentation sphere. According to Ref. [90] the most general form of the projector functions is given by

$$\langle \tilde{p}_i^a | = \sum_j \left(\left\{ \langle f_k^a | \tilde{\phi}_l^a \rangle \right\}_{i,j}^{-1} \langle f_j^a | \right) \tag{A.60}$$

where the $|f_j^a\rangle$ are elements of an arbitrary set of linear independent functions.

By applying the completeness relation Eq. A.58, the operator $\hat{\mathcal{T}}^a$ can be written in terms of the partial waves and projector functions as

$$\hat{\mathcal{T}}^a = \sum_i \hat{\mathcal{T}}^a |\tilde{\phi}_i^a\rangle\langle\tilde{p}_i^a| = \sum_i (|\phi_i^a\rangle - \tilde{\phi}_i^a\rangle)\langle\tilde{p}_i^a| \tag{A.61}$$

and the total transformation is given by

$$\hat{\mathcal{T}} = 1 + \sum_a \sum_i (|\phi_i^a\rangle - |\tilde{\phi}_i^a\rangle)\langle\tilde{p}_i^a| \,. \tag{A.62}$$

Therefore, the true wave function is given by

$$\psi_n(\boldsymbol{r}) = \tilde{\psi}_n(\boldsymbol{r}) + 1 + \sum_a \sum_i (\phi_i^a(\boldsymbol{r}) - \tilde{\phi}_i^a(\boldsymbol{r}))\langle\tilde{p}_i^a|\tilde{\psi}_n\rangle \;, \tag{A.63}$$

where the smooth auxiliary wave function $\tilde{\psi}_n(\boldsymbol{r})$ is obtained by solving Eq. A.51 and the rest of the transformation is determined by the partial waves and projector functions.

As there is freedom to choose the projector functions, they are chosen to make the expansion converge fast and the $|\tilde{\psi}_n\rangle$-functions as smooth as possible. As the functions are independent of the particular system under considerations they can be pre-calculated for each element.

A.6 Preliminary comments about partial wave representations

In Chapter 2.2, multiple scattering theory is introduced. In this Appendix a representation of the Green's function in terms of spherical functions is introduced. All practical calculations of MST are carried out within this representation because the spherical representation is most convenient due to the spherical symmetry of the single-site scattering problem which is usually assumed to have muffin tin geometry. Therefore, angular momentum is conserved, which allows to treat contributions arising from partial spherical waves independently. The introduction of the partial wave representation follows the discussion of Ref. [243].

A.6.1 Partial wave representation and the radial Schrödinger equation

At first the solution of the Schrödinger equation for a constant potential is discussed in terms of spherical functions. Therefore, spherical coordinates are introduced which leads to the following form of the Schrödinger equation

$$\left[-\frac{\hbar^2}{2m}\left(\frac{\partial^2}{\partial r^2} + \frac{2}{r}\frac{\partial}{\partial r}\right) + \frac{\boldsymbol{L}^2}{2mr^2} + V(r)\right]\psi(r,\vartheta,\varphi) = E\psi(r,\vartheta,\varphi) \;, \tag{A.64}$$

where $V(r) = V$. In spherical coordinates the wave function can be separated into the radial and angular part by $\psi(r,\vartheta,\varphi) = R(r)\,Y_{lm}(\vartheta,\varphi)$ where the Y_{lm} are the spherical harmonics. As the Y_{lm} fulfill $\boldsymbol{L}^2 Y_{lm} = \hbar^2 l(l+1) Y_{lm}$ the radial part of Eq. (A.64),

$$\left\{-\frac{\hbar^2}{2m}\left[\frac{\mathrm{d}^2}{\mathrm{d}r^2} + \frac{2}{r}\frac{\mathrm{d}}{\mathrm{d}r} - \frac{l(l+1)}{r^2}\right] + V\right\} R(r) = ER(r) \tag{A.65}$$

can be treated independently and the angular momentum enters as a parameter. The additional definition $k = \sqrt{2m(E-V)}/\hbar$ leads to

$$\left[\frac{\mathrm{d}^2}{\mathrm{d}r^2} + \frac{2}{r}\frac{\mathrm{d}}{\mathrm{d}r} - \frac{l(l+1)}{r^2} + k^2\right] R(r) = 0 \tag{A.66}$$

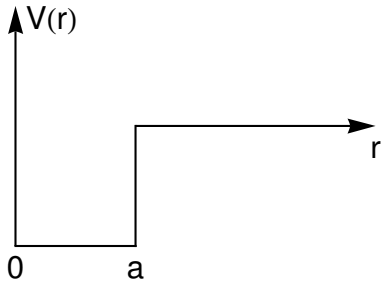

Figure A.1: The spherical potential well.

and a substitution $\rho = kr$ gives

$$\left[\frac{\mathrm{d}^2}{\mathrm{d}\rho^2} + \frac{2}{\rho}\frac{\mathrm{d}}{\mathrm{d}\rho} - \frac{l(l+1)}{\rho^2} + 1\right] R(\rho) = 0\,. \tag{A.67}$$

This equation can be solved by introducing the spherical Bessel $j_l(\rho)$ and Neumann $n_l(\rho)$ functions which are defined by

$$\begin{aligned} j_l(\rho) &= (-\rho)^l \left(\frac{1}{\rho}\frac{\mathrm{d}}{\mathrm{d}\rho}\right)^l \frac{\sin(\rho)}{\rho} \\ n_l(\rho) &= -(-\rho)^l \left(\frac{1}{\rho}\frac{\mathrm{d}}{\mathrm{d}\rho}\right)^l \frac{\cos(\rho)}{\rho}\,. \end{aligned} \tag{A.68}$$

As the j_l vanish at the origin they fulfill the right boundary conditions and are called regular solutions. The Neumann functions are called irregular solutions because they diverge at the origin. Physically, the right boundary condition means that the solution of Eq. (A.67) has to be zero at $r = 0$ because the centrifugal term $l(l+1)/\rho^2$ dominates at small distances which leads to a vanishing probability density at the origin.

For later purposes also the spherical Hankel functions are introduced as a superposition of spherical Bessel and Neumann functions by

$$h_l^{\pm}(\rho) = j_l(\rho) \pm i n_l(\rho)\,. \tag{A.69}$$

Now, the spherical potential well of width a and depth V_0 centered around the origin is discussed which is a simple example of a spherical scattering potential of finite range. The discussion of this problem introduces the procedure which is also used to evaluate the single-site scattering problem. A sketch of the potential is shown in Fig. A.1. First, the bound states and afterwards the continuous set of unbound states of this potential are constructed.

In order to find the bound states, the problem is split into two parts. The first part is the solution of

$$\left[\frac{\mathrm{d}^2}{\mathrm{d}r^2} + \frac{2}{r}\frac{\mathrm{d}}{\mathrm{d}r} - \frac{l(l+1)}{r^2} + q^2\right] R(r) = 0\,. \tag{A.70}$$

where $q = \sqrt{2m(V_0 + E)}/\hbar$ with $-V_0 < E < 0$, which is the solution inside the well with $r < a$. As mentioned above, this solution has to be regular at the origin and therefore

$$R(r) = A j_l(qr)\,, \quad 0 \le r \le a\,. \tag{A.71}$$

Outside the potential well the equation

$$\left[\frac{\mathrm{d}^2}{\mathrm{d}r^2} + \frac{2}{r}\frac{\mathrm{d}}{\mathrm{d}r} - \frac{l(l+1)}{r^2} - \kappa^2\right] R(r) = 0 \tag{A.72}$$

has to be solved, where $\kappa = \sqrt{2m(-E)}/\hbar$. The definition of κ implies that the wave function vanishes exponentially with increasing r. This part of the solution is given by

$$R(r) = Bh_l^+(i\kappa r) \quad , \quad 0 \leq r \leq a\,. \tag{A.73}$$

Requiring that both parts and their first derivatives with respect to r are equal at $r = a$, the full solutions of the bound states are defined and the free parameters can be determined.

Now, free continuum solutions for energies $E > 0$ are evaluated. As these functions must also fulfill the boundary condition of being regular at the origin the general solution is again twofold and given by

$$R_l(r) = \begin{cases} Aj_l(qr) & r < a \\ Bj_l(kr) + Cn_l(kr) & r > a \end{cases} , \tag{A.74}$$

where $q = \sqrt{2m(V_0 + E)}/\hbar$ and $k = \sqrt{2mE}/\hbar$. Within the radius of the potential well the solutions is only given by regular spherical Bessel functions. Outside this radius the general solution also includes irregular spherical Neumann functions. From the continuity requirement at $r = a$ and the normalization the coefficients can be determined.

It can be shown that the free solutions have an asymptotical behavior for large r given by

$$R_l(r) \simeq \frac{B}{kr}\left[\sin\left(kr - \frac{l\pi}{2}\right) - \frac{C}{B}\cos\left(kr - \frac{l\pi}{2}\right)\right] \tag{A.75}$$

where by defining $C/B = -\tan\delta_l(k)$ one obtains

$$R_l(r) \simeq \frac{B}{kr\cos(\delta_l(k))}\sin\left(kr - \frac{l\pi}{2} + \delta_l(k)\right)\,. \tag{A.76}$$

The quantity $\delta_l(k)$ is called phase shift and describes the deviation of the asymptotical behavior of the free solutions ($E > 0$) of the potential well from the behavior of free waves.

This illustrates the essence of stationary scattering theory which aims to calculate scattered states in an asymptotically region of space far away from the scatterer. In the next subsection it is shown that this state is obtained from an incident wave which is well defined asymptotically far away from the scattering center and the stationary solutions of the potential. Asymptotically, both states differ only by a phase shift. Therefore, the influence of the scattering potential is fully determined by this phase shift. The other way around it implies that a scattering potential itself is already fully determined by the phase informations of the incident and scattered wave.

For later purposes it is important to note that the solutions R_l always involve a factor r^{-1} and thus may be written as $R_l = r^{-1}u_l$.

A.6.2 Stationary scattering

In this subsection the preliminary considerations of the last section are used to solve a general spherical scattering problem. In order to find the stationary scattering solution the following

assumptions are taken into account. Far away from the scatterer the incident waves are plane waves given by

$$\psi_0(\boldsymbol{r}) = \frac{1}{(2\pi)^3} \mathrm{e}^{i\boldsymbol{k}\boldsymbol{r}} \,. \tag{A.77}$$

The exact eigenfunctions of the Hamiltonian of the scatterer are given by

$$\left[-\frac{\hbar}{2m}\nabla^2 + V(\boldsymbol{r}) \right] \psi_{\boldsymbol{k}}(\boldsymbol{r}) = E_{\boldsymbol{k}} \psi_{\boldsymbol{k}}(\boldsymbol{r}) \,. \tag{A.78}$$

Both types of functions are uniquely defined by the wave vector $\boldsymbol{k}$. This is obvious for the incident wave ψ_0. In the case of the stationary solutions $\psi_{\boldsymbol{k}}$ it indicates that they can be represented by an incoming or outgoing scattering solution where only a phase shifted plane wave part will remain in the asymptotic region. All details of the scattering part vanish asymptotically due to the finite range of the potential. It is implicitly assumed that for every incident plane wave there is a stationary scattering solution with the same k-vector (describing the asymptotic behavior). In addition, it is assumed that the potential vanishes faster than $1/r$. The case of a bare Coulomb potential which vanishes exactly with $1/r$ is excluded because in solids the bare Coulomb potential of the core is partially screened by the core electrons.

The Schrödinger equation is now written in the following form

$$\left[\nabla^2 + \frac{2m}{\hbar} E_{\boldsymbol{k}} \right] \psi_{\boldsymbol{k}}(\boldsymbol{r}) = V(\boldsymbol{r}) \psi_{\boldsymbol{k}}(\boldsymbol{r}) \tag{A.79}$$

where $E_{\boldsymbol{k}} = \hbar^2 k^2 / 2m$ in the asymptotic region (the energy of the state determines the wave vector in the asymptotic region). Equation (A.79) is interpreted as an inhomogeneous differential equation with inhomogeneity $V(\boldsymbol{r})\,\psi_{\boldsymbol{k}}(\boldsymbol{r})$. Such differential equations can be solve by employing the Green's function of the free system which is determined by the differential equation

$$\left[\nabla^2 + k^2 \right] G^+(\boldsymbol{r}, \boldsymbol{r}') = \delta(\boldsymbol{r}) \,. \tag{A.80}$$

(here only G^+ is considered). The full solution of Eq. (A.79) is therefore given by the combination

$$\psi_{\boldsymbol{k}}(\boldsymbol{r}) = \psi_0(\boldsymbol{r}) + \frac{2m}{\hbar} \int \mathrm{d}^3 r \, G^+(\boldsymbol{r}, \boldsymbol{r}') V(\boldsymbol{r}') \psi_{\boldsymbol{k}}(\boldsymbol{r}') \tag{A.81}$$

which is the Lippman-Schwinger equation. As shown, e.g., in Ref. [243] the free Green's function is given by

$$G^+(\boldsymbol{r} - \boldsymbol{r}') = \frac{1}{4\pi} \frac{\mathrm{e}^{ik|\boldsymbol{r}-\boldsymbol{r}'|}}{|\boldsymbol{r} - \boldsymbol{r}'|} \,. \tag{A.82}$$

Inserting the right hand side of Eq. (A.82) into the Lippmann-Schwinger equation one gets

$$\psi_{\boldsymbol{k}}(\boldsymbol{r}) = \psi_0(\boldsymbol{r}) - \frac{m}{2\pi\hbar^2} \int \mathrm{d}\boldsymbol{r} \, \frac{\mathrm{e}^{ik|\boldsymbol{r}-\boldsymbol{r}'|}}{|\boldsymbol{r} - \boldsymbol{r}'|} V(\boldsymbol{r}') \psi_{\boldsymbol{k}}(\boldsymbol{r}') \,. \tag{A.83}$$

In the asymptotic limit where $|\boldsymbol{r}| \gg |\boldsymbol{r}'|$ the approximation

$$k|\boldsymbol{r} - \boldsymbol{r}'| \sim kr - \boldsymbol{k}\boldsymbol{r}' \tag{A.84}$$

with $\boldsymbol{k} = k\boldsymbol{r}'/r$ is valid and implies that the k-vector is parallel to the unit vector of the point one is looking at when the origin is the center of the scattering potential. Therefore, the solution is of the following form

$$\psi_{\boldsymbol{k}}(\boldsymbol{r}) = \mathrm{e}^{i\boldsymbol{k}\boldsymbol{r}} + \frac{\mathrm{e}^{ikr}}{r} f_{\boldsymbol{k}}(\vartheta, \varphi) \tag{A.85}$$

and the so called scattering amplitude is given by

$$f_{\boldsymbol{k}}(\vartheta, \varphi) = -\frac{m}{2\pi\hbar} \int \mathrm{d}^3 r \, \mathrm{e}^{i\boldsymbol{k}\boldsymbol{r}'} V(\boldsymbol{r}') \psi_{\boldsymbol{k}}(\boldsymbol{r}') \, . \tag{A.86}$$

Now, the asymptotic form of the scattering solution is formally determined. Therefore, a partial wave representation of the scattering amplitude $f_{\boldsymbol{k}}$ in terms of spherical functions must be evaluated. But first, an important identity, namely the Bauer identity has to be introduced. This identity gives a plane wave in terms of spherical functions in the following way

$$\mathrm{e}^{i\boldsymbol{k}\boldsymbol{r}} = 4\pi \sum_{l=0}^{\infty} \sum_{m=-l}^{l} i^l j_l(kr) Y_l^{*m}(\hat{\boldsymbol{k}}) Y_l^m(\hat{\boldsymbol{r}}) \, . \tag{A.87}$$

If the plane wave propagates in z-direction, as it will be assumed in the following, this formula simplifies to

$$\mathrm{e}^{ikz} = \mathrm{e}^{ikr\cos\theta} = \sum_{l=0}^{\infty} (2l+1) i^l j_l(kr) P_l(\cos\theta) \, , \tag{A.88}$$

where $P_l(\cos\theta)$ denotes the Legendre polynomials (see Ref. [243]). Therewith, the scattering amplitude $f_{\boldsymbol{k}}$ can be calculated. As already mentioned, the z-direction is chosen to be the symmetry axis and in addition the polar axis. Due to this assumption the stationary states of the scattering potential and the scattering amplitude can be expanded in terms of Legendre polynomials in the following way

$$\psi(r, \theta) = \sum_{l=0}^{\infty} \frac{u_l(r)}{r} P_l(\cos\theta) \tag{A.89}$$

$$f(\theta) = \sum_{l=0}^{\infty} f_l P_l(\cos\theta) \, . \tag{A.90}$$

It is shown in Appendix A.6.1 that the asymptotic form of the solutions $u_l = rR_l$ of the radial Schrödinger equation is given by

$$u_l(r) = a_l \sin\left(kr - \frac{l\pi}{2} + \delta_l\right) \tag{A.91}$$

where the constant a_l is chosen in order to fulfill the boundary conditions. By employing Bauer's identity and the expansion of the scattering amplitude (Eq. (A.90)) one obtains

$$\mathrm{e}^{i\boldsymbol{k}\boldsymbol{r}} + f(\theta)\frac{\mathrm{e}^{ikr}}{r} = \sum_l \left((2l+1) i^l j_l(kr) + f_l \frac{\mathrm{e}^{ikr}}{r} \right) P_l(\cos\theta) \, . \tag{A.92}$$

Using the asymptotic form of the spherical Bessel functions j_l gives

$$r\psi(r,\theta) \sim \sum_l \left((-1)^{l+1} \frac{(2l+1)}{2ik} \mathrm{e}^{-ikr} + \left(\frac{(2l+1)}{2ik} + f_l \right) \mathrm{e}^{ikr} \right) P_l(\cos\theta) \tag{A.93}$$

and as the asymptotic form of u_l has to be equal to the expression in the brackets one finds

$$a_l = i^l \frac{(2l+1)}{k} \mathrm{e}^{i\delta_l} \tag{A.94}$$

$$f_l = \frac{(2l+1)}{k} \mathrm{e}^{i\delta_l} \sin\delta_l \, . \tag{A.95}$$

Now, the scattering amplitude is fully determined by

$$f(\theta) = \frac{1}{k}(2l+1)\mathrm{e}^{i\delta_l} \sin\delta_l \, P_l(\cos\theta) \tag{A.96}$$

and the scatting problem is solved.

A.7 Functions of operators

Given an arbitrary linear operator with corresponding eigenfunctions and eigenvalues obtained from

$$\hat{L}|\phi_i\rangle = l_i|\phi_i\rangle \, , \tag{A.97}$$

every well behaved function F fulfills the equation

$$F(\hat{L})|\phi_i\rangle = F(l_i)|\phi_i\rangle \, . \tag{A.98}$$

As the function F, when acting on real or complex numbers z, can be expanded in a series

$$F(z) = \sum_{n=1}^{\infty} f_n z^n \, , \tag{A.99}$$

the same holds when F is acting on an operator as

$$F(\hat{L}) = \sum_{n=1}^{\infty} f_n \hat{L}^n \tag{A.100}$$

where the coefficients f_n are by definition the same as in Eq. (A.99). As $\hat{L}^n$ means that the operator is acting on a function n times it follows that

$$\hat{L}^n|\phi_i\rangle = l_i^n|\phi_i\rangle \tag{A.101}$$

the expansion of the function of the operator is well defined and therefore Eq. (A.98) is justified.

A.8 Bauer's identity

Here, the following notation is used

$$j_L\left(\epsilon;\boldsymbol{r}\right)=j_l\left(pr\right)Y_{l,m}\left(\hat{\boldsymbol{r}}\right)\,. \tag{A.102}$$

Therefore, Bauer's identity is of the form [63]

$$\mathrm{e}^{i\boldsymbol{k}(\boldsymbol{r}_n-\boldsymbol{r}_m)}=4\pi\sum_L i^l j_L\left(\epsilon;\boldsymbol{r}_n-\boldsymbol{r}_n\right)^\times Y_L(\hat{\boldsymbol{k}})\,. \tag{A.103}$$

This can be rewritten as expansion of j_L in terms of plane waves and spherical harmonics. If one multiplies both sides with $Y_{L'}(\hat{\boldsymbol{k}})^*$

$$\frac{1}{4\pi}\mathrm{e}^{i\boldsymbol{k}(\boldsymbol{r}_n-\boldsymbol{r}_m)}Y_L(\hat{\boldsymbol{k}})^*=\sum_L i^l j_L\left(\epsilon;\boldsymbol{r}_n-\boldsymbol{r}_n\right)^\times Y_L(\hat{\boldsymbol{k}})Y_{L'}(\hat{\boldsymbol{k}})^* \tag{A.104}$$

and integrates over $\hat{\boldsymbol{k}}$

$$\frac{1}{4\pi}\int \mathrm{d}\hat{\boldsymbol{k}}\mathrm{e}^{i\boldsymbol{k}(\boldsymbol{r}_n-\boldsymbol{r}_m)}Y_L(\hat{\boldsymbol{k}})^*=\sum_L i^l j_L\left(\epsilon;\boldsymbol{r}_n-\boldsymbol{r}_n\right)^\times\int \mathrm{d}\hat{\boldsymbol{k}}Y_L(\hat{\boldsymbol{k}})Y_{L'}(\hat{\boldsymbol{k}})^*=\sum_L i^l j_L\left(\epsilon;\boldsymbol{r}_n-\boldsymbol{r}_n\right)^\times\delta_{LL'} \tag{A.105}$$

this leads to

$$j_L\left(\epsilon;\boldsymbol{r}_n-\boldsymbol{r}_n\right)^\times=\frac{i^{-l}}{4\pi}\int \mathrm{d}\hat{\boldsymbol{k}}\mathrm{e}^{i\boldsymbol{k}(\boldsymbol{r}_n-\boldsymbol{r}_m)}Y_L(\hat{\boldsymbol{k}})^*\,. \tag{A.106}$$

A.9 The full structural Green's function

In Section 2.2.3, the operator equation

$$\hat{\mathcal{G}}^{nm}=\hat{G}_0(1-\delta_{nm})+\sum_{k,j}\hat{G}_0(1-\delta_{nk})\hat{\tau}^{kj}\hat{G}_0(1-\delta_{jm}) \tag{A.107}$$

is given which introduces the resolvent of the full structural Green's function. The same relation holds for the real space representation giving

$$\mathcal{G}^{nm}(z,\boldsymbol{r}_n,\boldsymbol{r}_m)=G_0(z,\boldsymbol{r}_n,\boldsymbol{r}_m)\left(1-\delta_{nm}\right)+\sum_{k(\neq n)}\sum_{j(\neq m)}G_0(z,\boldsymbol{r}_n,\boldsymbol{r}_k)\tau^{kj}(z,\boldsymbol{r}_k,\boldsymbol{r}_j)G_0(z,\boldsymbol{r}_j,\boldsymbol{r}_m) \tag{A.108}$$

where the indices of the spatial variables indicate the affiliation to different distinct regions D_{V_i}. Now, the free Green's functions are expanded according to Eq. (2.165) and (2.183)

$$\begin{aligned}\mathbf{j}(\epsilon,\boldsymbol{r}_n)\boldsymbol{\mathcal{G}}^{nm}\mathbf{j}(\epsilon,\boldsymbol{r}_m)^\times=&\,\mathbf{j}(\epsilon,\boldsymbol{r}_n)\boldsymbol{\mathcal{G}}_0^{nm}\mathbf{j}(\epsilon,\boldsymbol{r}_m)^\times(1-\delta_{nm})\\&+\sum_{k(\neq n)}\sum_{j(\neq m)}\mathbf{j}(\epsilon,\boldsymbol{r}_n)\boldsymbol{\mathcal{G}}_0^{nm}\mathbf{j}(\epsilon,\boldsymbol{r}_k)^\times\tau^{kj}(z,\boldsymbol{r}_k,\boldsymbol{r}_j)\mathbf{j}(\epsilon,\boldsymbol{r}_j)\boldsymbol{\mathcal{G}}_0^{nm}\mathbf{j}(\epsilon,\boldsymbol{r}_m)^\times\end{aligned} \tag{A.109}$$

where an integration over $\boldsymbol{r}_k$ and $\boldsymbol{r}_j$ leads to

$$\boldsymbol{\mathcal{G}}^{nm}(\epsilon)=\boldsymbol{\mathcal{G}}_0^{nm}(\epsilon)(1-\delta_{nm})+\sum_{k(\neq n)}\sum_{j(\neq m)}\boldsymbol{\mathcal{G}}_0^{nk}(\epsilon)\boldsymbol{\tau}^{kj}(\epsilon)\boldsymbol{\mathcal{G}}_0^{jm}(\epsilon)\,. \tag{A.110}$$

A.10 Scalar relativistic approximation

As many of the calculations in this treatise employ an approximation of relativistic MST, namely the scalar relativistic formulation, this formalism is shortly introduced in this Appendix.

For a non-magnetic system a slightly different Kohn-Sham-Dirac Hamiltonian is considered where the identity is subtracted from the rest energy term which leads to ($\hbar = m = 1$)

$$\mathcal{H}(\boldsymbol{r}) = c\,\boldsymbol{\alpha}\cdot\boldsymbol{p} + (\beta - \mathsf{I}_4)\,c^2 + V\mathsf{I}_4\ . \tag{A.111}$$

Using the property that relativistic wave functions can be written in terms of two bi-spinors and writing $|\psi\rangle = |\phi, \chi\rangle$ the eigenvalue equation corresponding to Eq. (A.111) is automatically split into two equations

$$c\,\boldsymbol{\alpha}\cdot\boldsymbol{p}|\chi\rangle - V|\phi\rangle = \epsilon|\phi\rangle \tag{A.112}$$

$$c\,\boldsymbol{\alpha}\cdot\boldsymbol{p}|\phi\rangle + \left(V - 2c^2\right)|\chi\rangle = \epsilon|\chi\rangle\ . \tag{A.113}$$

This allows to express the spinor $|\chi\rangle$ in terms of $|\phi\rangle$ as

$$|\chi\rangle = (1/2c)\,\mathcal{B}^{-1}\boldsymbol{\sigma}\cdot\boldsymbol{p}|\phi\rangle \tag{A.114}$$

where $\mathcal{B} = 1 + (1/2c^2)\,(\epsilon - V)$. This yields the following equation for $|\phi\rangle$

$$\left[(1/2)\,\boldsymbol{\sigma}\cdot\boldsymbol{p}\mathcal{B}^{-1}\boldsymbol{\sigma}\cdot\boldsymbol{p} + V\right]|\phi\rangle = \mathcal{D}|\phi\rangle = \epsilon|\phi\rangle\ . \tag{A.115}$$

In a central field the operator $\mathcal{D}$ reveals the same constants of motion as the full Dirac Hamiltonian. Therefore, Eq. (A.115) is separable with respect to radial and angular variables and can be treated in the same way shown for the Schrödinger and full Dirac equation. The radial equation is of the form

$$\begin{aligned}&\left[\frac{1}{2}\left(-\frac{\mathrm{d}^2}{\mathrm{d}r^2} + \frac{l(l+1)}{r^2}\right) + V(r) - \epsilon\right]R_\kappa(r) = \\ &\left\{\frac{1}{4c^2}\mathcal{B}^{-2}\frac{\mathrm{d}V(r)}{\mathrm{d}r}\frac{\kappa}{r} + \frac{1}{4c^2}\left[[\epsilon - V(r)]\right]\mathcal{B}^{-1}\left(-\frac{\mathrm{d}^2}{\mathrm{d}r^2} + \frac{l(l+1)}{r^2}\right) + \frac{1}{4c^2}\mathcal{B}^{-2}\frac{\mathrm{d}V(r)}{\mathrm{d}r}\frac{\mathrm{d}}{\mathrm{d}r}\right\}R_\kappa(r)\,.\end{aligned} \tag{A.116}$$

This equation shows some remarkable properties: In the limit $c = \infty$, it reduced to the radial Schrödinger equation. Using the approximation $\mathcal{B} = 1$ the Pauli-Schrödinger equation is obtained. Therefore, Eq. (A.116) can be regarded as a justified approximation of the Dirac equation.

Regarding the case $\mathcal{B} = 1$ in more detail and neglecting the κ-dependent term, an equation is obtained which depends only on the eigenvalue l of the square of the angular momentum operator and is given by

$$\left[\frac{1}{2}[1-(1/2c^2)(\epsilon-V(r))]\left(-\frac{\mathrm{d}^2}{\mathrm{d}r^2}+\frac{l(l+1)}{r^2}\right)+V(r)-\frac{1}{4c^2}\frac{\mathrm{d}V(r)}{\mathrm{d}r}\frac{\mathrm{d}}{\mathrm{d}r}-\epsilon\right]R_\kappa(r)=0\ . \tag{A.117}$$

The formal structure of this equation is the same compared to the radial Schrödinger equation and is the basis of scalar relativistic calculations. This equations contains already some of important features obtained from the relativistic theory but as the simpler symmetry of the Schrödinger equation is conserved it is much easier to handle.

A.11 Gradient formula

In this Appendix a formula for carrying out the gradient of a product of a radial function and a general spherical harmonics is derived. The main purpose is to derive the gradient formula which is used in Section 2.7.1 for the calculation of the matrix elements of the current operator. This formula is given by

$$\begin{aligned}\frac{\partial}{\partial z} f(r) Y_{l,m}(\hat{r}) = &\sqrt{\frac{(l+m)(l-m)}{(2l+1)(2l-1)}} \left[\frac{\mathrm{d}f(r)}{\mathrm{d}r} + \frac{l+1}{r} f(r)\right] Y_{l-1,m}(\hat{r}) \\ &+ \sqrt{\frac{(l+m+1)(l-m+1)}{(2l+1)(2l+3)}} \left[\frac{\mathrm{d}f(r)}{\mathrm{d}r} - \frac{l}{r} f(r)\right] Y_{l+1,m}(\hat{r}) \ . \end{aligned} \tag{A.118}$$

The derivation starts by writing nabla in spherical coordinates

$$\begin{aligned}\nabla &= \hat{r}(\hat{r}\cdot\nabla) - \hat{r}\times(\hat{r}\times\nabla) \\ &= \hat{r}\frac{\partial}{\partial r} - \frac{i}{r}(\hat{r}\times\mathbf{L}) \ . \end{aligned} \tag{A.119}$$

Therewith, the considered gradient can be written as follows

$$\nabla\left(f(r) Y_L(\hat{r})\right) = \frac{\mathrm{d}f(r)}{\mathrm{d}r}\hat{r} Y_L(\hat{r}) - \frac{i}{r} f(r)\ (\hat{r}\times\mathbf{L}) Y_L(\hat{r}) \ . \tag{A.120}$$

Next, the spherical harmonics for $l = 1$ namely

$$Y_{1,0}(\hat{r}) = \left(\frac{3}{4\pi}\right)^{1/2} \cos\vartheta \tag{A.121}$$

$$Y_{1,1}(\hat{r}) = -\left(\frac{3}{8\pi}\right)^{1/2} \sin\vartheta e^{i\varphi} \quad , \quad Y_{1,-1}(\hat{r}) = \left(\frac{3}{8\pi}\right)^{1/2} \sin\vartheta e^{-i\varphi} \tag{A.122}$$

are combined and rewritten and the following way

$$\begin{aligned} Y_{1,-1}(\hat{r}) - Y_{1,1}(\hat{r}) &= 2\left(\frac{3}{8\pi}\right)^{1/2} \sin\vartheta\cos\varphi = \sqrt{2}\left(\frac{3}{4\pi}\right)^{1/2}\frac{x}{r} \\ -Y_{1,-1}(\hat{r}) - Y_{1,1}(\hat{r}) &= 2i\left(\frac{3}{8\pi}\right)^{1/2} \sin\vartheta\sin\varphi = i\sqrt{2}\left(\frac{3}{4\pi}\right)^{1/2}\frac{y}{r} \\ Y_{1,0}(\hat{r}) &= \left(\frac{3}{4\pi}\right)^{1/2}\frac{z}{r} \, . \end{aligned} \tag{A.123}$$

Now, the quotients of the spatial components and the absolute value r are written as

$$\begin{aligned}\frac{x}{r} &= \left(\frac{4\pi}{3}\right)^{1/2}\frac{\sqrt{2}}{2}\left(Y_{1,-1}(\hat{r}) - Y_{1,1}(\hat{r})\right) \\ \frac{y}{r} &= i\left(\frac{4\pi}{3}\right)^{1/2}\frac{\sqrt{2}}{2}\left(Y_{1,-1}(\hat{r}) + Y_{1,1}(\hat{r})\right) \\ \frac{z}{r} &= \left(\frac{4\pi}{3}\right)^{1/2} Y_{1,0}(\hat{r}) \end{aligned} \tag{A.124}$$

and the following vectors are introduced

$$\xi_1 = \frac{\sqrt{2}}{2}(-1, i, 0) \ , \xi_{-1} = \frac{\sqrt{2}}{2}(1, i, 0) \ , \xi_0 = (0, 0, 1) \ . \tag{A.125}$$

With this, the quotients are rewritten as

$$\begin{aligned}
\frac{x}{r} &= \left(\frac{4\pi}{3}\right)^{1/2} \left(Y_{1,-1}(\hat{r}) [\xi_{-1}]_x + Y_{1,1}(\hat{r}) [\xi_1]_x\right) \\
\frac{y}{r} &= \left(\frac{4\pi}{3}\right)^{1/2} \left(Y_{1,-1}(\hat{r}) [\xi_{-1}]_y + Y_{1,1}(\hat{r}) [\xi_1]_y\right) \\
\frac{z}{r} &= \left(\frac{4\pi}{3}\right)^{1/2} Y_{1,0}(\hat{r}) [\xi_1]_z \ .
\end{aligned} \tag{A.126}$$

Using the latter, the radial unit vector can be written as

$$\hat{r} = \left(\frac{4\pi}{3}\right)^{1/2} \sum_{\mu=-1}^{1} Y_{1,\mu}(\hat{r}) \xi_\mu \ , \tag{A.127}$$

and therefore the product of the radial unit vector and a general spherical harmonic is given by

$$\hat{r} Y_L(\hat{r}) = \left(\frac{4\pi}{3}\right)^{1/2} \sum_{\mu=-1}^{1} Y_{1,\mu}(\hat{r}) Y_L(\hat{r}) \xi_\mu = \left(\frac{4\pi}{3}\right)^{1/2} \sum_{\mu=-1}^{1} \sum_{\ell'=\ell\pm1} C_{L,(1,\mu)}^{\ell',m+\mu} Y_{L'}(\hat{r}) \ \xi_\mu \tag{A.128}$$

with the Gaunt coefficient

$$C_{LL'}^{L''} = \int \mathrm{d}\hat{r} Y_L(\hat{r}) Y_{L'}(\hat{r}) Y_{L''}^*(\hat{r}) \ . \tag{A.129}$$

Inserting the definitions of the vectors ξ_μ yields

$$\begin{aligned}
\hat{r} Y_L(\hat{r}) &= \left(\frac{4\pi}{3}\right)^{1/2} \\
&\times \left[\frac{\sqrt{2}}{2}\left(C_{(l,m),(1,-1)}^{l-1,m-1} Y_{l-1,m-1}(\hat{r}) + \underbrace{C_{(l,m),(1,-1)}^{l,m-1}}_{=0} Y_{l,m-1}(\hat{r}) + C_{(l,m),(1,-1)}^{l+1,m-1} Y_{l+1,m-1}(\hat{r})\right)\begin{pmatrix}1\\ i\\ 0\end{pmatrix}\right. \\
&+ \left(C_{(l,m),(1,0)}^{l-1,m} Y_{l-1,m}(\hat{r}) + \underbrace{C_{(l,m),(1,0)}^{l,m}}_{=0} Y_{l,m}(\hat{r}) + C_{(l,m),(1,0)}^{l+1,m} Y_{l+1,m}(\hat{r})\right)\begin{pmatrix}0\\ 0\\ 1\end{pmatrix} \\
&\left.+\frac{\sqrt{2}}{2}\left(C_{(l,m),(1,1)}^{l-1,m+1} Y_{l-1,m+1}(\hat{r}) + \underbrace{C_{(l,m),(1,1)}^{l,m+1}}_{=0} Y_{l,m+1}(\hat{r}) + C_{(l,m),(1,1)}^{l+1,m+1} Y_{l+1,m+1}(\hat{r})\right)\begin{pmatrix}-1\\ i\\ 0\end{pmatrix}\right] \\
&= \frac{1}{2}\left[\left(\frac{(l-m+2)(l-m+1)}{(2l+3)(2l+1)}\right)^{1/2} Y_{l+1,m-1}(\hat{r})\right.
\end{aligned}$$

$$
\begin{aligned}
&- \left(\frac{(l+m)(l+m-1)}{(2l-1)(2l+1)} \right)^{1/2} Y_{l-1,m-1}(\hat{r}) \Bigg] \begin{pmatrix} 1 \\ i \\ 0 \end{pmatrix} \\
&+ \left[\left(\frac{(l-m)(l+m)}{(2l-1)(2l+1)} \right)^{1/2} Y_{l-1,m}(\hat{r}) + \left(\frac{(l-m+1)(l+m+1)}{(2l+3)(2l+1)} \right)^{1/2} Y_{l+1,m}(\hat{r}) \right] \begin{pmatrix} 0 \\ 0 \\ 1 \end{pmatrix} \\
&+ \frac{1}{2} \left[\left(\frac{(l+m+2)(l+m+1)}{(2l+3)(2l+1)} \right)^{1/2} Y_{l+1,m+1}(\hat{r}) \right. \\
&\left. - \left(\frac{(l-m)(l-m-1)}{(2l-1)(2l+1)} \right)^{1/2} Y_{l-1,m+1}(\hat{r}) \right] \begin{pmatrix} -1 \\ i \\ 0 \end{pmatrix} . \qquad \text{(A.130)}
\end{aligned}
$$

In a next step the components of the angular momentum operator are rewritten by

$$
L_x = \frac{1}{2}(L_1 + L_{-1}) \ , L_y = \frac{1}{2i}(L_1 - L_{-1}) \ , L_z = L_0 \qquad \text{(A.131)}
$$

$$
\begin{aligned}
L_x &= \frac{\sqrt{2}}{2}\left(-[\xi_1]_x L_1 + [\xi_{-1}]_x L_{-1} \right) \\
L_y &= \frac{\sqrt{2}}{2}\left(-[\xi_1]_y L_1 + [\xi_{-1}]_y L_{-1} \right) \\
L_z &= [\xi_0]_z L_0 \qquad \text{(A.132)}
\end{aligned}
$$

and thus the complete angular momentum operator can be written as the sum

$$
\mathbf{L} = \sum_{\mu=-1}^{1} a_\mu L_\mu \xi_\mu \qquad \text{(A.133)}
$$

with the coefficients

$$
a_1 = -\frac{\sqrt{2}}{2} \ , a_{-1} = \frac{\sqrt{2}}{2} \ , a_0 = 1 \ . \qquad \text{(A.134)}
$$

Combining Eq. (A.127) with this sum representation of the angular momentum operator, the cross product of the radial unit vector and the angular momentum operator is given by

$$
\begin{aligned}
\hat{r} \times \mathbf{L} &= \left(\frac{4\pi}{3} \right)^{1/2} \left(\sum_{\mu=-1}^{1} Y_{1,\mu}(\hat{r}) \, \xi_\mu \right) \times \left(\sum_{\mu'=-1}^{1} a_{\mu'} L_{\mu'} \xi_{\mu'} \right) \\
&= \left(\frac{4\pi}{3} \right)^{1/2} \sum_{\mu=-1}^{1} \sum_{\mu'=-1}^{1} Y_{1,\mu}(\hat{r}) \, a_{\mu'} L_{\mu'} \left(\xi_\mu \times \xi_{\mu'} \right) \ . \qquad \text{(A.135)}
\end{aligned}
$$

Carrying out the sums gives

$$
\hat{r} \times \mathbf{L} = \left(\frac{4\pi}{3} \right)^{1/2} \left[Y_{1,-1}(\hat{r}) \begin{pmatrix} \frac{i}{\sqrt{2}} L_0 \\ -\frac{i}{\sqrt{2}} L_0 \\ -\frac{\sqrt{2}i}{2} L_1 \end{pmatrix} + Y_{1,0}(\hat{r}) \begin{pmatrix} \frac{i}{2}(L_1 - L_{-1}) \\ \frac{i}{2}(L_1 + L_{-1}) \\ 0 \end{pmatrix} + Y_{1,1}(\hat{r}) \begin{pmatrix} \frac{i}{\sqrt{2}} L_0 \\ \frac{i}{\sqrt{2}} L_0 \\ -\frac{\sqrt{2}i}{2} L_{-1} \end{pmatrix} \right] . \qquad \text{(A.136)}
$$

At first the z-component is investigated to derive the formula in Eq. (A.118) that is mentioned in the beginning of this Appendix. Restricting to this z-component one obtains

$$\begin{aligned}\left[\nabla\left(f\left(r\right)Y_L\left(\hat{r}\right)\right)\right]_z = &\left(\frac{4\pi}{3}\right)^{1/2}\left(C^{l-1,m}_{(l,m),(1,0)}\,Y_{l-1,m}\left(\hat{r}\right)+C^{l+1,m}_{(l,m),(1,0)}\,Y_{l+1,m}\left(\hat{r}\right)\right)\frac{\mathrm{d}f\left(r\right)}{\mathrm{d}r}\\ &-\frac{\sqrt{2}}{2r}\left(\frac{4\pi}{3}\right)^{1/2}f\left(r\right)\Big(\sqrt{l\left(l+1\right)-m\left(m+1\right)}\,Y_{1,-1}\left(\hat{r}\right)Y_{l,m+1}\left(\hat{r}\right)\\ &+\sqrt{l\left(l+1\right)-m\left(m-1\right)}Y_{1,1}\left(\hat{r}\right)Y_{l,m-1}\left(\hat{r}\right)\Big)\,. \end{aligned} \tag{A.137}$$

The product of two spherical harmonics can be represented in terms of a sum of products between Gaunt coefficients and a single spherical harmonic as

$$Y_L\left(\hat{r}\right)Y_{L'}\left(\hat{r}\right)=\sum_{L''}C^{L''}_{L,L'}Y_{L''}\left(\hat{r}\right) \tag{A.138}$$

where

$$\left|l-l'\right|\leq l''\leq l+l' \tag{A.139}$$

and

$$m''=m+m'\,, \tag{A.140}$$

or by writing out the composite index L,

$$Y_{l,m}\left(\hat{r}\right)Y_{l',m'}\left(\hat{r}\right)=\sum_{l''}C^{l'',m+m'}_{(l,m),(l',m')}Y_{l'',m+m'}\left(\hat{r}\right)\,. \tag{A.141}$$

In the case considered here, only two types of products of spherical harmonics occur which are given by

$$Y_{1,-1}\left(\hat{r}\right)Y_{l,m+1}\left(\hat{r}\right)=C^{l-1,m}_{(l,m+1),(1,-1)}\,Y_{l-1,m}\left(\hat{r}\right)+C^{l+1,m}_{(l,m+1),(1,-1)}\,Y_{l+1,m}\left(\hat{r}\right) \tag{A.142}$$

$$Y_{1,1}\left(\hat{r}\right)Y_{l,m-1}\left(\hat{r}\right)=C^{l-1,m}_{(l,m-1),(1,1)}\,Y_{l-1,m}\left(\hat{r}\right)+C^{l+1,m}_{(l,m-1),(1,1)}\,Y_{l+1,m}\left(\hat{r}\right)\,. \tag{A.143}$$

Inserting this result into Eq. (A.137) one obtains

$$\begin{aligned}\left[\nabla\left(f\left(r\right)Y_L\left(\hat{r}\right)\right)\right]_z = &\left(\frac{4\pi}{3}\right)^{1/2}\left(C^{l-1,m}_{(l,m),(1,0)}Y_{l-1,m}\left(\hat{r}\right)+C^{l+1,m}_{(l,m),(1,0)}Y_{l+1,m}\left(\hat{r}\right)\right)\frac{\mathrm{d}f\left(r\right)}{\mathrm{d}r}\\ -&\left(\frac{4\pi}{3}\right)^{1/2}\frac{\sqrt{2}}{2}\sqrt{l\left(l+1\right)-m\left(m+1\right)}\Big(C^{l-1,m}_{(l,m+1),(1,-1)}Y_{l-1,m}\left(\hat{r}\right)+C^{l+1,m}_{(l,m+1),(1,-1)}Y_{l+1,m}\left(\hat{r}\right)\Big)\frac{f\left(r\right)}{r}\\ -&\left(\frac{4\pi}{3}\right)^{1/2}\frac{\sqrt{2}}{2}\sqrt{l\left(l+1\right)-m\left(m-1\right)}\Big(C^{l-1,m}_{(l,m-1),(1,1)}Y_{l-1,m}\left(\hat{r}\right)+C^{l+1,m}_{(l,m-1),(1,1)}Y_{l+1,m}\left(\hat{r}\right)\Big)\frac{f\left(r\right)}{r}\,. \end{aligned} \tag{A.144}$$

A simple rearrangement leads to

$$\begin{aligned}
\left[\nabla\left(f\left(r\right)Y_L\left(\hat{r}\right)\right)\right]_z = & \left(\frac{4\pi}{3}\right)^{1/2}\left(C^{l-1,m}_{(l,m),(1,0)}\,Y_{l-1,m}\left(\hat{r}\right)+C^{l+1,m}_{(l,m),(1,0)}\,Y_{l+1,m}\left(\hat{r}\right)\right)\frac{\mathrm{d}f\left(r\right)}{\mathrm{d}r}\\
& -\left(\frac{4\pi}{3}\right)^{1/2}\frac{\sqrt{2}}{2}\left(\sqrt{l\left(l+1\right)-m\left(m-1\right)}C^{l-1,m}_{(l,m-1),(1,1)}\right.\\
& \left.+\sqrt{l\left(l+1\right)-m\left(m+1\right)}C^{l-1,m}_{(l,m+1),(1,-1)}\right)Y_{l-1,m}\left(\hat{r}\right)\,\frac{f\left(r\right)}{r}\\
& -\left(\frac{4\pi}{3}\right)^{1/2}\frac{\sqrt{2}}{2}\left(\sqrt{l\left(l+1\right)-m\left(m-1\right)}C^{l+1,m}_{(l,m-1),(1,1)}\right.\\
& \left.+\sqrt{l\left(l+1\right)-m\left(m+1\right)}C^{l+1,m}_{(l,m+1),(1,-1)}\right)Y_{l+1,m}\left(\hat{r}\right)\,\frac{f\left(r\right)}{r} \qquad \text{(A.145)}
\end{aligned}$$

and writing out the Gaunt coefficients gives

$$\begin{aligned}
&\left[\nabla\left(f\left(r\right)Y_L\left(\hat{r}\right)\right)\right]_z =\\
&\left(\left(\frac{\left(l+m\right)\left(l-m\right)}{\left(2l+1\right)\left(2l-1\right)}\right)^{1/2}Y_{l-1,m'}\left(\hat{r}\right)+\left(\frac{\left(l-m+1\right)\left(l+m+1\right)}{\left(2l+1\right)\left(2l+1\right)}\right)^{1/2}Y_{l+1,m'}\left(\hat{r}\right)\right)\frac{\mathrm{d}f\left(r\right)}{\mathrm{d}r}\\
&+\frac{1}{2}\left\{\left[\left(l\left(l+1\right)-m\left(m-1\right)\right)\frac{\left(l-m+1\right)\left(l-m\right)}{\left(2l-1\right)\left(2l+1\right)}\right]^{1/2}\right.\\
&\left.+\left[\left(l\left(l+1\right)-m\left(m+1\right)\right)\frac{\left(l+m+1\right)\left(l+m\right)}{\left(2l-1\right)\left(2l+1\right)}\right]^{1/2}\right\}Y_{l-1,m}\left(\hat{r}\right)\,\frac{f\left(r\right)}{r}\\
&-\frac{1}{2}\left\{\left[\left(l\left(l+1\right)-m\left(m-1\right)\right)\frac{\left(l+m+1\right)\left(l+m\right)}{\left(2l+3\right)\left(2l+1\right)}\right]^{1/2}\right.\\
&\left.+\left[\left(l\left(l+1\right)-m\left(m+1\right)\right)\frac{\left(l-m+1\right)\left(l-m\right)}{\left(2l+3\right)\left(2l+1\right)}\right]^{1/2}\right\}Y_{l+1,m}\left(\hat{r}\right)\,\frac{f\left(r\right)}{r}\,. \qquad \text{(A.146)}
\end{aligned}$$

This can be further simplified to obtain

$$\begin{aligned}
&\left[\nabla\left(f\left(r\right)Y_L\left(\hat{r}\right)\right)\right]_z =\\
&\left(\left(\frac{\left(l+m\right)\left(l-m\right)}{\left(2l+1\right)\left(2l-1\right)}\right)^{1/2}Y_{l-1,m}\left(\hat{r}\right)+\left(\frac{\left(l-m+1\right)\left(l+m+1\right)}{\left(2l+1\right)\left(2l+1\right)}\right)^{1/2}Y_{l+1,m}\left(\hat{r}\right)\right)\frac{\mathrm{d}f\left(r\right)}{\mathrm{d}r}\\
&+\frac{1}{2}\left\{\left[\frac{\left(l-m+1\right)^2\left(l+m\right)\left(l-m\right)}{\left(2l-1\right)\left(2l+1\right)}\right]^{1/2}\right.\\
&\left.+\left[\frac{\left(l+m+1\right)^2\left(l+m\right)\left(l-m\right)}{\left(2l-1\right)\left(2l+1\right)}\right]^{1/2}\right\}Y_{l-1,m}\left(\hat{r}\right)\,\frac{f\left(r\right)}{r}\\
&-\frac{1}{2}\left\{\left[\frac{\left(l+m+1\right)\left(l-m+1\right)\left(l+m\right)^2}{\left(2l+3\right)\left(2l+1\right)}\right]^{1/2}\right.
\end{aligned}$$

$$+\left[\frac{(l+m+1)(l-m+1)(l-m)^2}{(2l+3)(2l+1)}\right]^{1/2}\Bigg\} Y_{l+1,m}(\hat{r})\ \frac{f(r)}{r} \tag{A.147}$$

and

$$\begin{aligned}
&[\nabla(f(r)Y_L(\hat{r}))]_z = \\
&\left(\left(\frac{(l+m)(l-m)}{(2l+1)(2l-1)}\right)^{1/2} Y_{l-1,m}(\hat{r}) + \left(\frac{(l-m+1)(l+m+1)}{(2l+1)(2l+1)}\right)^{1/2} Y_{l+1,m}(\hat{r})\right)\frac{\mathrm{d}f(r)}{\mathrm{d}r} \\
&+\left(\frac{(l+m)(l-m)}{(2l-1)(2l+1)}\right)^{1/2}(l+1)\ Y_{l-1,m}(\hat{r})\ \frac{f(r)}{r} \\
&-\left(\frac{(l+m+1)(l-m+1)}{(2l+3)(2l+1)}\right)^{1/2} l\, Y_{l+1,m}(\hat{r})\ \frac{f(r)}{r}\,.
\end{aligned} \tag{A.148}$$

In the end one finds the formula for the z-component

$$\begin{aligned}
[\nabla(f(r)Y_L(\hat{r}))]_z = &\left(\frac{(l+m)(l-m)}{(2l-1)(2l+1)}\right)^{1/2}\left(\frac{\mathrm{d}f(r)}{\mathrm{d}r}+\frac{(l+1)}{r}f(r)\right) Y_{l-1,m}(\hat{r}) \\
&+\left(\frac{(l+m+1)(l-m+1)}{(2l+3)(2l+1)}\right)^{1/2}\left(\frac{\mathrm{d}f(r)}{\mathrm{d}r}-\frac{l}{r}f(r)\right) Y_{l+1,m}(\hat{r})\,.
\end{aligned} \tag{A.149}$$

In the following the x-component is derived and therefore one starts with

$$\begin{aligned}
&[\nabla(f(r)Y_L(\hat{r}))]_x = \\
&\frac{1}{2}\Bigg[\left(\frac{(l-m+2)(l-m+1)}{(2l+3)(2l+1)}\right)^{1/2} Y_{l+1,m-1}(\hat{r}) - \left(\frac{(l+m)(l+m-1)}{(2l-1)(2l+1)}\right)^{1/2} Y_{l-1,m-1}(\hat{r}) \\
&-\left(\frac{(l+m+2)(l+m+1)}{(2l+3)(2l+1)}\right)^{1/2} Y_{l-1,m-1}(\hat{r}) + \left(\frac{(l-m)(l-m-1)}{(2l-1)(2l+1)}\right)^{1/2} Y_{l-1,m+1}(\hat{r})\Bigg]\frac{\mathrm{d}f(r)}{\mathrm{d}r} \\
&+\left(\frac{4\pi}{3}\right)^{1/2}\frac{f(r)}{r}\left(\frac{m}{\sqrt{2}}Y_{1,-1}(\hat{r})\,Y_{l,m}(\hat{r}) + \frac{1}{2}\sqrt{l(l+1)-m(m+1)}\,Y_{1,0}(\hat{r})\,Y_{l,m+1}(\hat{r})\right. \\
&\left.-\frac{1}{2}\sqrt{l(l+1)-m(m-1)}\,Y_{1,0}(\hat{r})\,Y_{l,m-1}(\hat{r}) + \frac{m}{\sqrt{2}}Y_{1,1}(\hat{r})\,Y_{l,m}(\hat{r})\right)\,.
\end{aligned} \tag{A.150}$$

The products of the spherical harmonics can be written as

$$\begin{aligned}
Y_{1,-1}(\hat{r})\,Y_{l,m}(\hat{r}) &= C^{l-1,m-1}_{(l,m),(1,-1)}\,Y_{l-1,m-1}(\hat{r}) + C^{l+1,m-1}_{(l,m),(1,-1)}\,Y_{l+1,m-1}(\hat{r}) \\
Y_{1,0}(\hat{r})\,Y_{l,m+1}(\hat{r}) &= C^{l-1,m+1}_{(l,m+1),(1,0)}\,Y_{l-1,m+1}(\hat{r}) + C^{l+1,m+1}_{(l,m+1),(1,0)}\,Y_{l+1,m+1}(\hat{r}) \\
Y_{1,0}(\hat{r})\,Y_{l,m-1}(\hat{r}) &= C^{l-1,m-1}_{(l,m-1),(1,0)}\,Y_{l-1,m-1}(\hat{r}) + C^{l+1,m-1}_{(l,m-1),(1,0)}\,Y_{l+1,m-1}(\hat{r}) \\
Y_{1,1}(\hat{r})\,Y_{l,m}(\hat{r}) &= C^{l-1,m+1}_{(l,m),(1,1)}\,Y_{l-1,m+1}(\hat{r}) + C^{l+1,m+1}_{(l,m),(1,1)}\,Y_{l+1,m+1}(\hat{r})\,.
\end{aligned} \tag{A.151}$$

Writing out the Gaunt coefficients

$$
\begin{aligned}
Y_{1,-1}(\hat{r})\,Y_{l,m}(\hat{r}) = &-\left(\frac{3}{4\pi}\right)^{1/2}\frac{1}{\sqrt{2}}\left[\left(\frac{(l+m)(l+m-1)}{(2l-1)(2l+1)}\right)^{1/2}Y_{l-1,m-1}(\hat{r})\right.\\
&\left.-\left(\frac{(l-m+2)(l-m+1)}{(2l+3)(2l+1)}\right)^{1/2}Y_{l+1,m-1}(\hat{r})\right]\\
Y_{1,0}(\hat{r})\,Y_{l,m+1}(\hat{r}) = &\left(\frac{3}{4\pi}\right)^{1/2}\left[\left(\frac{(l-m-1)(l+m+1)}{(2l-1)(2l+1)}\right)^{1/2}Y_{l-1,m+1}(\hat{r})\right.\\
&\left.+\left(\frac{(l-m)(l+m+2)}{(2l+3)(2l+1)}\right)^{1/2}Y_{l+1,m+1}(\hat{r})\right]\\
Y_{1,0}(\hat{r})\,Y_{l,m-1}(\hat{r}) = &\left(\frac{3}{4\pi}\right)^{1/2}\left[\left(\frac{(l-m+1)(l+m-1)}{(2l-1)(2l+1)}\right)^{1/2}Y_{l-1,m-1}(\hat{r})\right.\\
&\left.+\left(\frac{(l-m+2)(l+m)}{(2l+3)(2l+1)}\right)^{1/2}Y_{l+1,m-1}(\hat{r})\right]\\
Y_{1,1}(\hat{r})\,Y_{l,m}(\hat{r}) = &-\left(\frac{3}{4\pi}\right)^{1/2}\frac{1}{\sqrt{2}}\left[\left(\frac{(l-m)(l-m-1)}{(2l-1)(2l+1)}\right)^{1/2}Y_{l-1,m+1}(\hat{r})\right.\\
&\left.-\left(\frac{(l+m+2)(l+m+1)}{(2l+3)(2l+1)}\right)^{1/2}Y_{l+1,m+1}(\hat{r})\right]
\end{aligned}
\tag{A.152}
$$

the x-component of the gradient formula is given by

$$
\begin{aligned}
&\left[\nabla\left(f(r)\,Y_L(\hat{r})\right)\right]_x =\\
&\frac{1}{2}\left[\left(\frac{(l-m+2)(l-m+1)}{(2l+3)(2l+1)}\right)^{1/2}Y_{l+1,m-1}(\hat{r})-\left(\frac{(l+m)(l+m-1)}{(2l-1)(2l+1)}\right)^{1/2}Y_{l-1,m-1}(\hat{r})\right.\\
&\left.-\left(\frac{(l+m+2)(l+m+1)}{(2l+3)(2l+1)}\right)^{1/2}Y_{l+1,m+1}(\hat{r})+\left(\frac{(l-m)(l-m-1)}{(2l-1)(2l+1)}\right)^{1/2}Y_{l-1,m+1}(\hat{r})\right]\frac{\mathrm{d}f(r)}{\mathrm{d}r}\\
&+\frac{1}{2}\frac{f(r)}{r}\left\{m\left[\left(\frac{(l-m+2)(l-m+1)}{(2l+3)(2l+1)}\right)^{1/2}Y_{l+1,m-1}(\hat{r})-\left(\frac{(l+m)(l+m-1)}{(2l-1)(2l+1)}\right)^{1/2}Y_{l-1,m-1}(\hat{r})\right]\right.\\
&+m\left[\left(\frac{(l+m+2)(l+m+1)}{(2l+3)(2l+1)}\right)^{1/2}Y_{l+1,m+1}(\hat{r})-\left(\frac{(l-m)(l-m-1)}{(2l-1)(2l+1)}\right)^{1/2}Y_{l-1,m+1}(\hat{r})\right]\\
&+\sqrt{l(l+1)-m(m+1)}\left[\left(\frac{(l-m-1)(l+m+1)}{(2l-1)(2l+1)}\right)^{1/2}Y_{l-1,m+1}(\hat{r})\right.\\
&\qquad\left.+\left(\frac{(l-m)(l+m+2)}{(2l+3)(2l+1)}\right)^{1/2}Y_{l+1,m+1}(\hat{r})\right]\\
&-\sqrt{l(l+1)-m(m-1)}\left[\left(\frac{(l-m+1)(l+m-1)}{(2l-1)(2l+1)}\right)^{1/2}Y_{l-1,m-1}(\hat{r})\right.
\end{aligned}
$$

$$+\left(\frac{(l-m+2)(l+m)}{(2l+3)(2l+1)}\right)^{1/2} Y_{l+1,m-1}(\hat{r})\Bigg]\Bigg\}. \tag{A.153}$$

An completely analogous calculation gives the y-component

$$\begin{aligned}
&[\nabla(f(r)Y_L(\hat{r}))]_y = \\
&\frac{i}{2}\Bigg[\left(\frac{(l-m+2)(l-m+1)}{(2l+3)(2l+1)}\right)^{1/2} Y_{l+1,m-1}(\hat{r}) - \left(\frac{(l+m)(l+m-1)}{(2l-1)(2l+1)}\right)^{1/2} Y_{l-1,m-1}(\hat{r}) \\
&+\left(\frac{(l+m+2)(l+m+1)}{(2l+3)(2l+1)}\right)^{1/2} Y_{l+1,m+1}(\hat{r}) - \left(\frac{(l-m)(l-m-1)}{(2l-1)(2l+1)}\right)^{1/2} Y_{l-1,m+1}(\hat{r})\Bigg]\frac{\mathrm{d}f(r)}{\mathrm{d}r} \\
&+\frac{1}{2}\frac{f(r)}{r}\Bigg\{m\Bigg[\left(\frac{(l+m)(l+m-1)}{(2l-1)(2l+1)}\right)^{1/2} Y_{l-1,m-1}(\hat{r}) + \left(\frac{(l-m+2)(l-m+1)}{(2l+3)(2l+1)}\right)^{1/2} Y_{l+1,m-1}(\hat{r})\Bigg] \\
&-m\Bigg[\left(\frac{(l-m)(l-m-1)}{(2l-1)(2l+1)}\right)^{1/2} Y_{l-1,m+1}(\hat{r}) - \left(\frac{(l+m+2)(l+m+1)}{(2l+3)(2l+1)}\right)^{1/2} Y_{l+1,m+1}(\hat{r})\Bigg] \\
&+\sqrt{l(l+1)-m(m+1)}\Bigg[\left(\frac{(l-m-1)(l+m+1)}{(2l-1)(2l+1)}\right)^{1/2} Y_{l-1,m+1}(\hat{r}) \\
&\qquad\qquad + \left(\frac{(l-m)(l+m+2)}{(2l+3)(2l+1)}\right)^{1/2} Y_{l+1,m+1}(\hat{r})\Bigg] \\
&+\sqrt{l(l+1)-m(m-1)}\Bigg[\left(\frac{(l-m+1)(l+m-1)}{(2l-1)(2l+1)}\right)^{1/2} Y_{l-1,m-1}(\hat{r}) \\
&\qquad\qquad + \left(\frac{(l-m+2)(l+m)}{(2l+3)(2l+1)}\right)^{1/2} Y_{l+1,m-1}(\hat{r})\Bigg]\Bigg\}.
\end{aligned} \tag{A.154}$$

It is used that the Gaunt coefficients can be written as (taken from the book of Strange, Appendix C)

$$C^{l''m''}_{lm,l'm'} = \left(\frac{(2l+1)(2l'+1)}{4\pi(2l''+1)}\right)^{1/2} C(ll'l'';m,m')\,C(ll'l'';0,0)\,\delta_{m'',m'+m}$$

A.12 Total density of states of promising Half-Metals

Due to inherent assumptions in the projection of the total DOS onto element specific contributions within the PAW formalism subtle but important features are sometimes inaccurately reproduced compared to the total DOS which is obtained without employing the projection scheme. In particular, the half-metallic gap is sometimes filled with elemental states that are absent in the total DOS. Therefore, this Appendix shows the total DOS of the promising half-metallic alloys obtained from VASP within standard GGA

A.13 DOS of the platinum interface

This Appendix is devoted to the electronic structure of the Pt leads of the systems analyzed in Section 8.3 and 8.3.1. All figures show the first three layers of the platinum leads which are

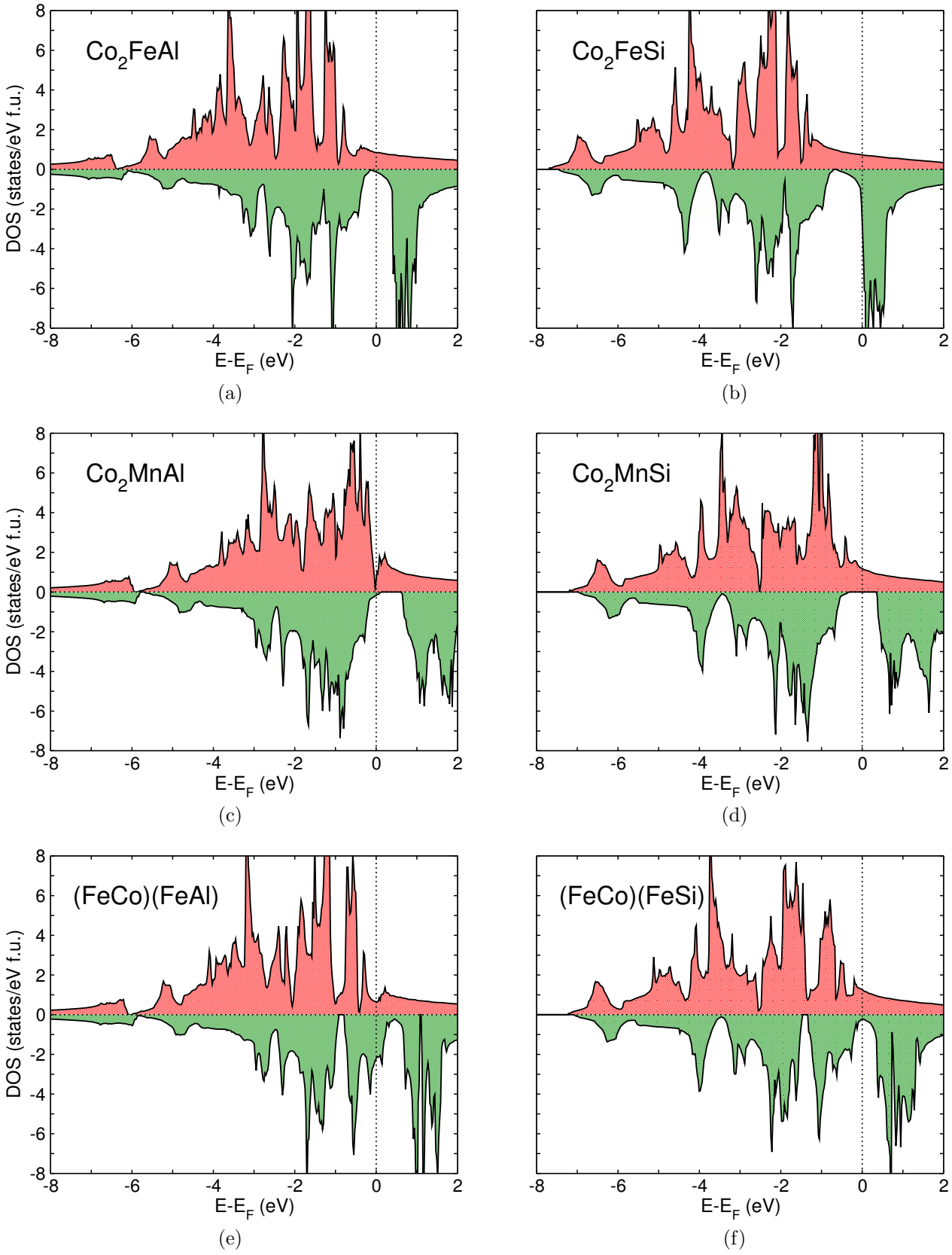

Figure A.2: Comparison of the total electronic densities of states of the first three pairs of alloys.

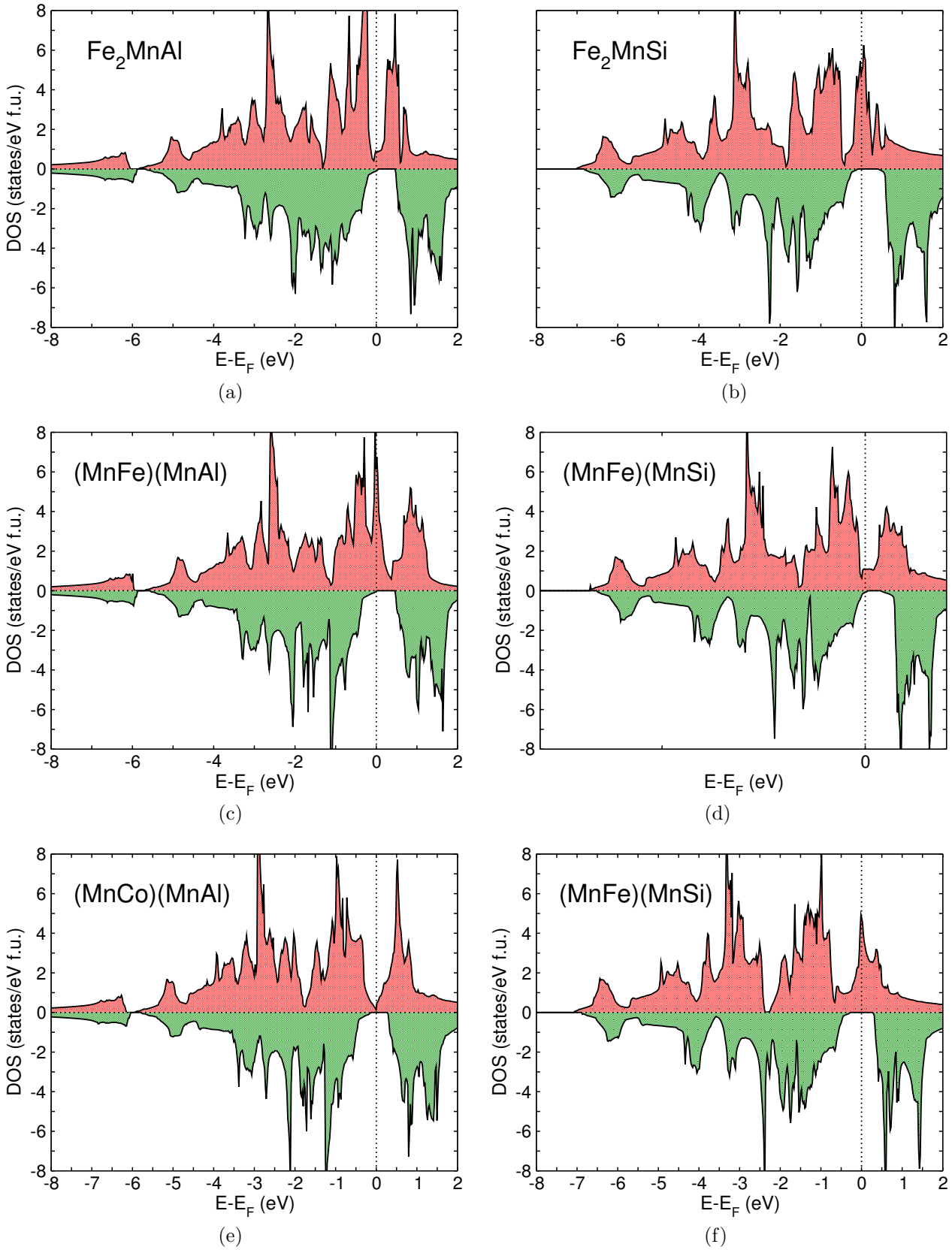

Figure A.3: Comparison of the total electronic densities of states of the last three pairs of alloys.

equal on both sides because of the reflection symmetry of the systems. This means that the DOS denoted with Pt_1 corresponds to the layer which is directly connected to the Heusler. The DOS denoted with Pt_2 and Pt_3 correspond to subsequent layers deeper in the lead.

Figure A.4 shows the DOS of the Pt leads of the Pt-Co_2FeAl-Pt and Pt-Co_2FeSi-Pt systems with five and nine monolayers of Heusler. The same is shown in Fig. A.5 for the Pt-Co_2FeAl-Pt and Pt-Co_2FeSi-Pt systems. The main feature which occurs in all systems is the induced magnetization of the first Pt layers of the lead. This can be immediately deduced from the asymmetry of the DOS of the majority and minority spin channel. In all cases the majority DOS of the first layer is small and quiet flat at E_F whereas the minority DOS shows a peak. In the subsequent layers an additional peak in the majority DOS develops. This peaks is shifted into the Fermi energy in deeper layers of leads and the DOS becomes that of pure Pt. The DOS of deeper layers are not shown here because the main change is only the shift in the majority channel. The difference in the Pt DOS of systems with five and nine monolayers is very small. In addition, the DOS of the third Pt layer denoted with Pt_3 is the comparable for all system but especially when comparing the systems including Co_2FeAl and Co_2FeSi as well as those containing Co_2MnAl and Co_2MnSi.

Most interestingly, the DOS of the minority channel of the Pt leads is large close to the interface but the contribution of this channel to the total conductance is smaller in each system considered here (see Table 8.2). Therefore, one can conclude that the Pt states at the Fermi energy are more localized and the resulting small mobility leads to the small contributions to the conductance.

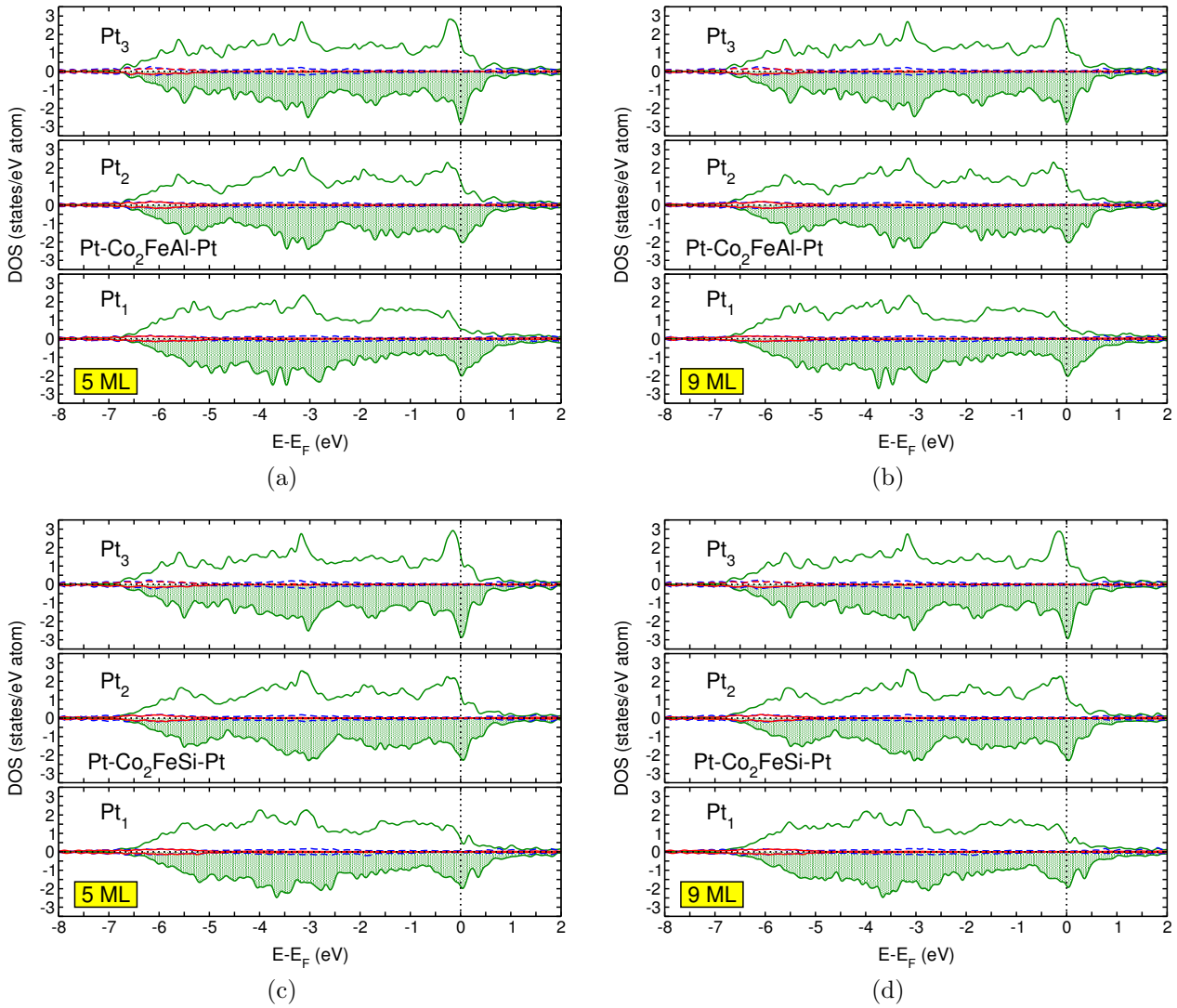

Figure A.4: DOS of platinum leads of the Pt-Co_2FeAl-Pt and Pt-Co_2FeSi-Pt systems with five and nine monolayers of Heusler.

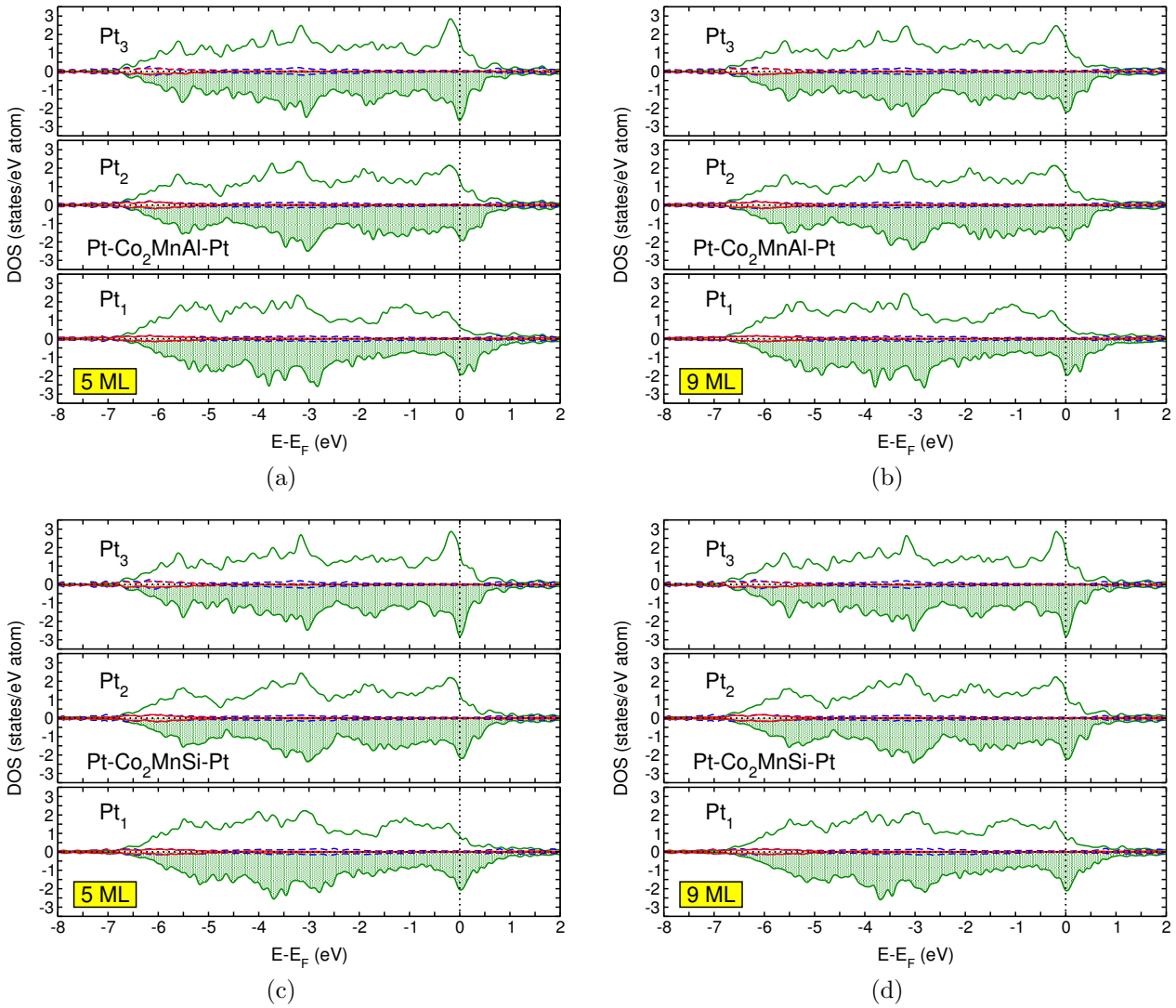

Figure A.5: DOS of platinum leads of the Pt-Co_2MnAl-Pt and Pt-Co_2MnSi-Pt systems with five and nine monolayers of Heusler.

Bibliography

[1] F. Heusler. *Über magnetische Manganlegierungen.* Verhandlungen der deutschen Physikalischen Gesellschaft, **5** (1903).

[2] Z. Nishiyama. *Martensitic transformations* (Academic Press, INC., London, Great Britain, 1971).

[3] K. Otsuka and C. M. Wayman. *Shape memory materials* (Cambridge University Press, Cambridge, Great Britain, 1998).

[4] K. Ullakko, J. K. Huang, C. Kantner, and R. C. O'Handley. *Large magnetic-field-induced strains in Ni_2MnGa single crystals.* Appl. Phys. Lett., **69** (1996).

[5] M. Siewert, et al. *Designing shape-memory Heusler alloys from first-principles.* Appl. Phys. Lett., **99**, 191904 (2011).

[6] R. A. de Groot, F. M. Mueller, P. G. van Engen, and K. H. J. Buschow. *New class of materials: Half-metallic ferromagnets.* Phys. Rev. Lett., **50** (1983).

[7] M. I. Katsnelson, V. Y. Irkhin, L. Chioncel, A. I. Lichtenstein, and R. A. de Groot. *Half-metallic ferromagnets: From band structure to many-body effects.* Rev. Mod. Phys., **80**, 315 (2008).

[8] J. M. D. Coey, M. Venkatesan, and M. A. Bari. *Lecture notes in physics*, vol. 595 (Springer Verlag Berlin, Berlin, Germany, 2002).

[9] D. Y. Cong, S. Roth, and L. Schulz. *Magnetic properties and structural transformations inNi-Co-Mn-Sn multifunctional alloys.* Acta Materialia, **60**, 5335 (2012).

[10] K. Binder and A. P. Young. *Spin glasses: Experimental facts, theoretical concepts and open questions.* Rev. Mod. Phys., **58**, 801 (1986).

[11] S. Wurmehl, et al. *Geometric, electronic, and magnetic structure of Co_2FeSi: Curie temperature and magnetic moment measurements and calculations.* Phys. Rev. B, **72**, 184434 (2005).

[12] D. Comtessse, H. C. Herper, A. Hucht, and P. Entel. *A first-priciples study aided with Monte Carlo simulations of carbon doped iron-manganese alloys.* Eur. Phys. J. B, **85**, 343 (2012).

[13] M. van Schilfgaarde, I. A. Abrikosov, and B. Johansson. *Origin of the Invar effect in iron-nickel alloys.* Nature, **400**, 46 (1999).

[14] A. Díaz-Ortiz, R. Drautz, M. Fähnle, H. Drosch, and J. M. Sanchez. *Structure and magnetism in bcc-based iron-cobalt alloys.* Phys. Rev. B, **73**, 224208 (2006).

[15] E. Arnscheidt. *Untersuchung der elastischen und magnetischen Eigenschaften von CoMn-Legierungen mit Ultrschall.* Ph.D. thesis, Ruhr-Universität Bochum (2004).

[16] H. van Leuken and R. A. de Groot. *Half-metallic antiferromagnets.* Phys. Rev. Lett., **74** (1995).

[17] L. D. Landau and E. M. Lifschitz. *Lehrbuch der Theoretischen Physik*, vol. 3 (Akademie-Verlag Berlin, Berlin, Germany, 1979), 1 edn.

[18] E. Rebhan. *Theoretische Physik, Band 2* (Elsevier GmbH, Munich, Germany, 2005).

[19] M. Born and J. R. Oppenheimer. *Zur quantentheorie der molekeln.* Ann. Phys., **389**, 457 (1927).

[20] L. D. Landau and E. M. Lifschitz. *Lehrbuch der Theoretischen Physik*, vol. 4 (Akademie-Verlag Berlin, Berlin, Germany, 1991), 7 edn.

[21] A. Messiah. *Quantenmechanik*, vol. 2 (Walter de Gruyter, Berlin, Germany, 1990), 3 edn.

[22] D. R. Hartree. *The wave mechanism of an atom with a non-coulomb central field. Part i. Theory and methods.* Proc. Camb. Phil. Soc., **24**, 89 (1928).

[23] D. R. Hartree. *The wave mechanism of an atom with a non-coulomb central field. Part ii. Some results and discussion.* Proc. Camb. Phil. Soc., **24**, 111 (1928).

[24] V. Fock. *Näherungsmethode zur Lösung des quantenmechanischen Mehrkörperproblems.* Z. Phys., **61**, 126 (1930).

[25] F. Jensen. *Introduction to Computational Chemistry* (John Wiley & Sons Ltd, West Sussex, England, 1999).

[26] C. C. J. Roothaan. *New developments in molecular orbital theory.* Rev. Mod. Phys., **23**, 69 (1951).

[27] G. G. Hall. *The molecular orbital theory of chemical valency VIII: A method for calculating ionization potentials.* Proc. Roy. Soc., **205**, 541 (1951).

[28] J. A. Pople and R. K. Nesbet. *Self-consistent orbitals for radicals.* J. Chem. Phys., **22**, 571 (1954).

[29] E. Rebhan. *Theoretische Physik, Band 1* (Elsevier GmbH, Munich, Germany, 1999).

[30] T. Koopmans. *Über die Zuordnung von Wellenfunktionen und Eigenwerten zu den einzelnen Elektronen eines Atoms.* Physica, **1**, 104 (1934).

[31] R. M. Martin. *Electronic Structure* (Cambridge University Press, Cambridge, United Kingdom, 2004).

[32] P. Strange. *Relativistic quantum mechanics* (Cambridge University Press, Cambridge, England, 1998).

[33] R. P. Feynman. *Quantum electrodynamics* (W. A. Benjamin, Inc., Massachusetts, USA, 1962).

[34] E. M. Rose. *Relativistic electron theory* (John Wiley & Sons, New York, USA, 1971).

[35] I. M. Benn and R. W. Tucker. *An introduction to spinors and geometry with applications in physics* (Adam Hilger, Bristol, England, 1988).

[36] P. A. M. Dirac. *Quantum theory of the electron. Part II.* Proc. Roy. Soc. Series A, **118**, 351 (1928).

[37] J. Schwinger. *Quantum Electrodynamics. I. A Covariant Formulation.* Phys. Rev., **74**, 1439 (1948).

[38] J. Schwinger. *Quantum Electrodynamics. II. Vacuum Polarization and Self-Energy.* Phys. Rev., **75**, 651 (1949).

[39] L. H. Thomas. *The calculation of atomic fields.* Proc. Cambridge Phil. Roy. Soc, **23**, 542 (1927).

[40] E. Fermi. *Un methodo statistico per la determinazione di alcune priorieta dell' atome.* Accad. Naz. Lincei., **6**, 602 (1927).

[41] P. A. M. Dirac. *Note on exchange phenomena in the Thomas-Fermi atom.* Proc. Cambridge Phil. Roy. Soc, **26**, 376 (1930).

[42] P. Hohenberg and W. Kohn. *Inhomogenous electron gas.* Phys. Rev., **136**, B864 (1964).

[43] R. M. Dreizler and E. K. U. Gross. *Density functional Theory* (Springer-Verlag, Berlin, Germany, 1990).

[44] W. Kohn and L. J. Sham. *Self consistent equations including exchange and correlation effects.* Phys. Rev., **140**, A1133 (1965).

[45] E. S. Kryachko and E. V. Ludeña. *Energy density functional theory of many-electron systems* (Kluwer Academic Publishers, Dordrecht, Netherlands, 1990).

[46] M. Levy. *Universal variational functionals of electron densities, first order density matrices, natural spin orbitals and solution of the n-representability problem.* Proc. Nat. Acad. Sci., **76**, 6062 (1979).

[47] M. Levy. *Electron densities in search of Hamiltonians.* Phys. Rev. A, **26**, 1200 (1982).

[48] E. Lieb. *Density functional for coulomb systems.* Int. J. Quant. Chem., **24**, 243 (1983).

[49] T. L. Gilbert. *Hohenberg-Kohn theorem for nonlocal external potentials.* Phys. Rev. B, **12**, 2111 (1975).

[50] U. von Barth and L. Hedin. *A local exchange-correlation potential for the spin polarized case: I.* J. Phys. C, **5**, 1629 (1972).

[51] M. M. Pant and A. K. Rajagopal. *Theory of inhomogeneous magnetic electron gas.* Solid State Commun., **10**, 1157 (1972).

[52] J. Kübler. *Theory of itinerant electron magnetism* (Oxford, University Press, Oxford, United Kingdom, 2000).

[53] J. D. Bjorken and S. D. Drell. *Relativistic quantum fields* (Mc Graw-Hill, Inc, New York, USA, 1965).

[54] A. K. Rajagopal and J. Callaway. *Inhomogeneous electron gas.* Phys. Rev. B, **7**, 1912 (1973).

[55] A. K. Rajagopal. *Inhomogeneous relativistic electron gas.* J. Phys. C, **11**, L943 (1978).

[56] A. H. M. Donald and S. H. Vosko. *A relativistic density functional formalism.* J. Phys. C, **12**, 2977 (1979).

[57] H. Eschrig. *The fundamentals of density functional theory* (Teubner, Stuttgart, Germany, 1996).

[58] H. Dreyssé. *Electronic structure and physical properties of solids* (Springer Verlag, Berlin, Germany, 2000).

[59] G. Kresse and J. Furthmüller. *Efficient iterative schemes for ab initio calculations using a plane wave basis set.* Phys. Rev. B, **54**, 11169 (1996).

[60] G. Kresse and J. Furthmüller. *Efficiency of ab initio total energy calculations for metals and semiconductors using a plane wave basis set.* Comp. Mat. Sci, **6**, 15 (1996).

[61] J. Korringa. *On the calculation of the energy of a Bloch wave in a metal.* Physica, **13**, 392 (1947).

[62] W. Kohn and N. Rostoker. *Solution of the Schrödinger equation in periodic lattices with an application to metallic lithium.* Phys. Rev., **94**, 1111 (1954).

[63] J. Zabloudil, R. Hammerling, L. Szunyogh, and P. Weinberger. *Electron Scattering in Solid Matter* (Springer Verlag, Berlin, Germany, 2005).

[64] P. Weinberger. *Electron scattering theory for ordered and disordered matter* (Oxford University Press, New York, USA, 1990).

[65] A. Gonis. *Green Functions of Ordered and Disordered Systems* (Elsevier Science Publishers, Amsterdam, Netherlands, 1992).

[66] L. Szunyogh, B. Újfalussy, P. Weinberger, and J. Kollár. *Self-consistent localized KKR scheme for surfaces and interfaces.* Phys. Rev. B, **49**, 2721 (1994).

[67] R. Zeller, P. H. Dederichs, B. Újfalussy, L. Szunyogh, and P. Weinberger. *Theory and convergence properties of the screened Korringa-Kohn-Rostoker method.* Phys. Rev. B, **52**, 8807 (1995).

[68] P. Weinberger and L. Szunyogh. *Perpendicular magnetism in magnetic multilayer systems.* Comp. Mat. Sci., **17**, 414 (2000).

[69] P. Weinberger. *Multilayer systems and symmetry.* Phil. Mag. B, **75**, 509 (1997).

[70] E. M. Godfrin. *A method to compute the inverse of an n-block tridiagonal quasi-hermitian matrix.* J. Phys.: Condens. Matter, **3**, 7843 (1991).

[71] A. I. Liechtenstein, M. I. Katsnelson, and V. A. Gubanov. *Exchange interactions and spin-wave stiffness in ferromagnetic metals.* J. Phys. F: Met. Phys., **14**, L125 (1984).

[72] A. I. Liechtenstein, M. I. Katsnelson, V. P. Antropov, and V. A. Gubanov. *Local spin density functional approach to the theory of exchange interactions in ferromagnetic metals and alloys.* J. Magn. Magn. Mater., **67**, 65 (1987).

[73] V. Heine. *Electronic structure from the point of view of the local atomic environment.* Solid State Phys., **35**, 1 (1980).

[74] P. Lloyd and P. V. Smith. *Multiple scattering theory in condensed materials.* Adv. Phys., **21**, 69 (1972).

[75] W. M. Termmerman. *On the generalization of the impurity problem.* J. Phys. F: Met. Phys., **12**, L25 (1982).

[76] R. Kubo. *Statistical-mechanical theory of irreversible processes. I. General theory and simple applications to magnetic and conduction problems.* J. Phys. Soc. Jpn., **12**, 570 (1957).

[77] H. U. Baranger and A. D. Stone. *Electrical linear-response theory in an arbitrary magnetic field: A new Fermi-surface formation.* Phys. Rev. B, **40**, 8169 (1989).

[78] Y. Imry and R. Landauer. *Conductance viewed as transmission.* Rev. Mod. Phys., **71**, S308 (1999).

[79] D. A. Greenwood. *The Boltzmann equation in the theory of electrical conduction in metals.* Proc. Phys. Soc., **71**, 585 (1958).

[80] H. W. Butler. *Theory of electronic transport in random alloys: Korringa-Kohn-Rostoker coherent-potential approximation.* Phys. Rev. B, **31**, 3260 (1985).

[81] S. Lowitzer, D. Ködderitzsch, and H. Eber. *Spin projection and spin current density within relativistic transport calculations.* Phys. Rev. B, **82**, 140402 (2010).

[82] P. Weinberger, P. M. Levy, J. Banhart, L. Szunyogh, and B. Újfalussy. *Band structure and electrical conductivity of disordered layered system.* J. Phys.: Condens. Matter, **8**, 7677 (1996).

[83] S. Wimmer, D. Ködderitzsch, K.Chadova, and H. Ebert. *First-principles linear response description of the spin Nernst effect.* Phys. Rev. B, **88**, 201108(R) (2013).

[84] U. Sivan and Y. Imry. *Multichannel Landauer formula for the termoelectric transport with application to thermopower near the mobility edge.* Phys. Rev. B, **33**, 551 (1986).

[85] J. M. Luttinger. *Theory of thermal transport coefficients.* Phys. Rev., **135**, A1505 (1964).

[86] G. E. W. Bauer, E. Saitoh, and B. J. van Wees. *Spin caloritronics.* Nature Mat., **11**, 391 (2012).

[87] L. Smrčka and P. Středa. *Transport coefficients in strong magnetic fields.* J. Phys. C: Solid State Phys., **10**, 2153 (1977).

[88] M. Jonson and G. D. Mahan. *Mott's formula for the thermopower and the wiedemann-franz law.* Phys. Rev. B, **21**, 4223 (1980).

[89] H. Ebert. *Magneto-optical effectsin transition metal systems.* Rep. Prog. Phys., **59**, 1665 (1996).

[90] R. E. Blöchel. *Projector augmented-wave method.* Phys. Rev. B, **50**, 17953 (1994).

[91] J. P. Perdew, K. Burke, and M. Ernzerhof. *Generalized gradient approximation made simple.* Phys. Rev. Lett., **77**, 3865 (1996).

[92] O. K. Andersen. *Simple approach to the band structure problem.* Solid State Commun., **13**, 133 (1973).

[93] S. H. Vosko, L. Wilk, and M. Nusair. *Accurate spin-dependend electron liquid correlation energies for local spin density calculations: A critical analysis.* Can. J. Phys., **58**, 1200 (1980).

[94] A. V. Ruban and I. A. Abrikosov. *Configurational thermodynamics of alloys from first principles: Effective cluster interactions.* Rep. Prog. Phys., **71**, 046501 (2008).

[95] H. E. Stanley. *Introduction to phase transitions and critical phenomena* (Oxford Univ. Pr., New York, 1987).

[96] N. M. Rosengaard and B. Johansson. *Finite-temperature study of itinerant ferromagnetism in Fe, Co, and Ni.* Phys. Rev. B, **55**, 14975 (1997).

[97] A. V. Ruban, S. Shallcross, S. I. Simak, and H. L. Skiver. *Atomic and magnetic configurational energetics by the generalized pertubation method.* Phys. Rev. B, **70**, 125115 (2004).

[98] S. Shallcross, A. E. Kissavos, V. Meded, and A. V. Ruban. *An ab initio effective hamiltionian for magnetism including longitudinal spin fluctuations.* Phys. Rev. B, **72**, 104437 (2005).

[99] A. V. Ruban, S. Khmelevsky, P. Mohn, and B. Johanssom. *Temperature-induced longitudinal spin fluctuations in Fe and Ni.* Phys. Rev. B, **75**, 054402 (2007).

[100] M. Pajda, J. Kudrnovský, I. Turek, V. Drchal, and P. Bruno. *Ab initio calculations of exchange interactions, spin-wave stiffness constants, and Curie temperatures of Fe, Co and Ni.* Phys. Rev. B, **64**, 174402 (2001).

[101] F. Körmann, A. Dick, T. Hickel, and J. Neugebauer. *Pressure dependence of the Curie temperature in bcc iron studied by ab initio simulations.* Phys. Rev. B, **79**, 184406 (2009).

[102] T. Gebhardt, et al. *Ab initio lattice stability of fcc and hcp Fe-Mn random alloys.* J. Phys.: Condens. Matter, **22**, 295402 (2010).

[103] T. Gebhardt, et al. *The influence of additions of Al and Si on the lattice stability of fcc and hcp Fe-Mn random alloys.* J. Phys.: Condens. Matter, **24**, 246003 (2011).

[104] T. C. Schulthess, W. H. Butler, G. M. Stocks, S. Maat, and G. J. Mankey. *Noncollinear magnetism in substitutionally disordered face-centered-cubi FeMn.* J. Appl. Phys., **85**, 4842 (1999).

[105] G. M. Stocks, et al. *On the magnetic structure of γ-FeMn alloys.* J. Appl. Phys., **91**, 7355 (2002).

[106] D. Spišák and J. Hafner. *Magnetic structures in ordered and disordered γ-FeMn alloys: Ordering due to disorder.* Phys. Rev. B, **61**, 11569 (2000).

[107] CALPHAD: Computer Coupling of Phase Diagrams and Thermochemistry.

[108] T. Hickel, B. G. A. Dick, and, F. Körmann, and J. Neugebauer. *Steel design from fully parameter-free ab initio computer simulations.* Steel Res. Int., **80**, 4 (2009).

[109] A. Dick, T. Hickel, and J. Neugebauer. *The effect of disorder on the concentration-dependece of stacking fault energies in* $Fe_{1-x}Mn_x$ *- A first principles study.* Steel Res. Int., **80**, 603 (2009).

[110] B. Hallstedt, et al. *Thermodynamic properties of cementite Fe_3C.* CALPHAD, **34**, 129 (2010).

[111] J. Rezende, et al. *Prediction of microstructure and microsegregation in a Fe-Mn-C austenitic steel based on phase-field microstructure simulations.* Steel Res. Int., **80**, 609 (2009).

[112] H. J. Bargel and G. Schulze. *Werkstoffkunde* (Springer, Berlin, 1999), 6st edn.

[113] F. Körmann, A. Dick, T. Hickel, and J. Neugebauer. *Rescaled Monte Carlo approach for magnetic system: Ab initio thermodynamics of bcc iron.* Phys. Rev. B, **81**, 134425 (2010).

[114] F. Körmann, A. Dick, T. Hickel, and J. Neugebauer. *Role of spin quantization in determining the thermodynamic properties of magneitv transition metals.* Phys. Rev. B, **83**, 165114 (2011).

[115] D. W. Boukhvalov, Y. N. Goronstyrev, M. I. Katsnelson, and A. I. Liechtenstein. *Magnetism and local distortions near carbon impurity in γ-iron.* Phys. Rev. Lett, **99**, 247205 (2007).

[116] C. Jiang, S. G. Srinivasan, A. Caro, and S. A. Maloy. *Structural, elastic, and electronic properies of* Fe_3C *from first priciples.* J. Appl. Phys., **103**, 043502 (2008).

[117] J. von Appen, B. Eck, and R. Dronskowski. *A density-functional study of the phase diagram of cementite-type* $(Fe, Mn)_3C$ *at absolute zero temperature.* J. Phys.: Condens. Matter, **22**, 316002 (2010).

[118] N. I. Medvedeva, D. V. Aken, and J. E. Medvedeva. *Magnetism in bcc and fcc Fe with carbon and manganese.* J. Phys.: Condens. Matter, **22**, 316002 (2010).

[119] G. Kresse and D. Joubert. *From ultrasoft pseudopotentials to the projector augmented-wave method.* Phys. Rev. B, **59**, 1758 (1999).

[120] H. Ebert. In H. Dreyssé, ed., *Lecture Notes in Physics Vol. 535*, 191 (Springer, Berlin, 1999).

[121] I. Turek, J. Kudrnovsky, V. Drchal, and P. Brumo. *Exchange interactions, spin waves, and transition temperatures in itinerant magnets.* Phil. Mag., **86**, 1713 (2006).

[122] P. Yu, X. F. Jin, J. Kudrnovsky, D. Wang, and P. Bruno. *Curie temperatures of fcc and bcc nickel an permalloy: Supercell and Green's function methods.* Phys. Rev. B, **77**, 054431 (2008).

[123] P. Bruno. *Exchange interactions parameters and adiabatic spin-wave spectra of ferromagnets: A "renormalized magnetic force theorem".* Phys. Rev. Lett., **90**, 087205 (2003).

[124] W. Pepperhoff and M. Acet. *Constitution und Magnetism of Iron and its Alloys* (Springer, Berlin, 2001).

[125] S. Chadov, et al. *Orbital magnetism in transition metal systems: The role of local correlation effects.* EPl, **82**, 37001 (208).

[126] M. A. Ruderman and C. Kittel. *Indirect exchange coupling of nuclear magnetic moments by conduction electrons.* Phys. Rev., **96**, 99 (1954).

[127] T. Kasuya. *A theory of metallic ferro- and antiferromagnetism on Zener's model.* Prog. Theor. Phys., **16**, 45 (1956).

[128] K. Yosida. *Mangetic properties of Cu-Mn alloys.* Phys. Rev., **106**, 893 (1957).

[129] G. Bihlmayer. *Computational nanoscience: Do it yourself!* 447 (John Neuman Institute for Computing, Jülich, 2006).

[130] E. C. Stoner and E. P. Wohlfarth. *A mechanism of magnetic hysteresis in heterogeneous alloys.* Phil. Trans. R. Soc. A, **240**, 599 (1948).

[131] M. Ležaić, P. Mavropoulos, and S. Blügel. *First-principle prediction of high Curie temperature of ferromagnetic bcc-Co and bcc-FeCo alloys and its relevance to tunneling magnetoresistance.* Appl. Phys. Lett., **90**, 082504 (2007).

[132] F. J. Pinski, J. Staunton, B. L. Gyorffy, D. D. Johnson, and G. M. Stocks. *Ferromagnetism versus antiferromagnetism in face-centeres-cubic iron.* Phys. Rev. Lett., **56**, 2096 (1986).

[133] O. N. Mryasov, A. I. Lichtenstein, L. Sandratskii, and V. A. Gubanov. *Magnetic structure of fcc iron.* J. Phys.: Condens. Matter, **3**, 7683 (1991).

[134] O. N. Mryasov, V. A. Gubanov, and A. I. Lichtenstein. *Spiral-spin-density-wave states in fcc iron: Linear-muffin-tin-orbitals band-structure approach.* Phys. Rev. B, **45**, 12330 (1992).

[135] V. P. Antropov, M. I. Katsnelson, M. van Schilfgaarde, and B. N. Harmon. *Ab initio spin dynamics in magnets.* Phys. Rev. Lett., **75**, 729 (1995).

[136] E. Sjöstedt and L. Nordström. *Noncollinear full-potential studies of γ-Fe.* Phys. Rev. B, **66**, 014447 (2002).

[137] Y. Tsunoda. *Spin-density wave in cubic γ-Fe and γ-$Fe_{100-x}Co_x$ precipitates in Cu.* J. Phys.: Condens. Matter, **1**, 10427 (1989).

[138] H. C. Herper, E. Hoffmann, and P. Entel. *Ab initio full-potential study of the structural and magnetic phase stability of iron.* Phys. Rev. B, **60**, 3839 (1999).

[139] P. James, O. Eriksson, B. Johansson, and I. A. Abrikosov. *Calculated magnetic properties of binary alloys between Fe, Co, Ni, and Cu.* Phys. Rev. B, **59**, 419 (1999).

[140] H. Dreyssé, ed. *Lecture Notes in Physics Vol. 535* (Springer, Berlin, 1999).

[141] J. S. Kouvel and J. S. Kasper. *Long-range antiferromagnetism in disordered Fe-Ni-Mn alloys.* J. Phys. Chem. Solids., **24**, 529 (1963).

[142] J. Staunton, G. L. Gyorffy, A. J. Pindor, G. M. Stocks, and H. Winter. *The disordered docal doment picture of itinerant magnetism at finite temperatures.* J. Magn. Magn. Mater., **45**, 15 (1984).

[143] J. Staunton, G. L. Gyorffy, G. M. Stocks, and J. Wadsworth. *The static, paramagnetic, spin susceptibility of metals at finite temperatures.* J. Phys. F: Met. Phys., **16**, 1761 (1986).

[144] H. Kleinert and V. Schulte-Frohlinde. *Critical properties of ϕ^4-Theories* (World Scientific, London, United Kingdom, 2001).

[145] P. Soven. *Coherent-potential model of substitutional disordered alloys.* Phys. Rev, **156**, 809 (1967).

[146] D. Ködderitzsch, H. Ebert, D. A. Rowlands, and A. Ernst. *Relativistic formulation of the Korringa-Kohn-Rostoker nonlocal coherent-potential approximation.* New J. Phys., **9**, 81 (2007).

[147] H. C. Herper, E. Hoffmann, and P. Entel. *Ab inito investigations of iron-based martensitic systems.* J. Physique IV, **7**, C5 (1997).

[148] I. Žutić, J. Fabian, and S. D. Sarma. *Spintronics: Fundamentals and applications.* Rev. Mod. Phys., **76**, 323 (2004).

[149] C. Ahn, K. H. Shin, R. Loloee, J. Bass, and W. P. Pratt. *Current-perpendicular-to-plane spin transport properties of CoFe alloys: Spin diffusion length and scattering asymmetry.* J. Appl. Phys., **108**, 023908 (2010).

[150] M. Walter, et al. *Seebeck effect in magnetic tunnel junctions.* Nat. Mat. Lett., **10**, 742 (2011).

[151] E. C. Bain. *The nature of martensite.* Trans. AIME, **70**, 25 (1924).

[152] D. Hunter, et al. *Giant magnetostiction in anneald $Co_{1-x}Fe_x$ thin films.* Nat. Commun., **2**, 518 (2011).

[153] B. Gehrmann, M. Acet, H. C. Herper, E. Wassermann, and W. Pepperhoff. *The invar property of fcc Co and larger spontanous magnetostriction of bcc Fe-Co.* Phys. Stat. Sol. B, **214**, 175 (1999).

[154] Y. Nakamura, M. Shiga, and S. Santa. *Invar behavior of face-centered cubic FeCo alloys precipitated from copper.* J. Phys. Soc. Japan, **26**, 210 (1969).

[155] K. J. Kim, S. J. Lee, and J. M. Park. *Electronic structure of $D0_3$-ordered Fe_3Co and Co_3Fe studied by spectroscopic ellipsometry.* J. Magn. Magn. Mater., **241**, 6 (2002).

[156] A. Y. Liu and D. Singh. *General-potential study of the electronic and magnetic structure of FeCo.* Phys. Rev. B, **46**, 11145 (1992).

[157] K. J. Kim, S. J. Lee, and D. W. Lynch. *Study of optical properties and electronic structure of ferromagnetic FeCo.* J. Magn. Magn. Mater., **241**, 6 (2002).

[158] R. Drautz, A. Díaz-Ortiz, M. Fähnle, and H. Drosch. *Ordering and magnetism in Fe-Co: Dense sequence of ground-state structures.* Phys. Rev. Lett., **93**, 067202 (2004).

[159] D. I. Bardos. *Mean magnetic moments in bcc FeCo alloys.* J. Appl. Phys., **40**, 1371 (1969).

[160] K. Schwarz, P. Mohn, P. Blaha, and J. Kübler. *Electronic and magnetic structure of bcc Fe-Co alloys from band theory.* J. Phys. F: Met. Phys., **12**, 2659 (1984).

[161] K. H. J. Buschow, P. G. van Engen, and R. Jongebreur. *Magneto-optical properties of metallic ferromagnetic materials.* J. Magn. Magn. Mat., **38**, 1 (1983).

[162] S. J. Vosko, L. Wilk, and M. Nusair. *Accurate spin-dependent electron liquid correlation energies for local spin density calculations: A critcal analysis.* Can. J. Phys., **58**, 1200 (1980).

[163] A. Dannenberg, M. Siewert, M. E. Gruner, M. Wuttig, and P. Entel. *Competing structural ordering tendencies in Heusler-type alloys with high Curie temperatures: $Fe_2CoGa_{1-x}Zn_x$ studied by first-principles calculations.* Phys- Rev. B, **82**, 214421 (2010).

[164] M. Friák and M. Šob. *Ab initio study of the bcc-hcp transformation in iron.* Phys. Rev. B, **77**, 174117 (2008).

[165] C. John, et al. *Magnetovolume effects and structural transformations in CoMn alloys.* J. Appl. Phys., **67**, 5268 (1990).

[166] M. Acet and E. F. Wassermann. *Magnetism and structural stability in CoMn alloys.* J. Appl. Phys., **70**, 6556 (1991).

[167] W. Bendick and W. Pepperhoff. *Thermally excited states in cobalt and cobalt alloys.* J. Phys. F: Mat. Phys., **9**, 2185 (1979).

[168] M. Gillessen and R. Dronskowski. *A combinatorial study of inverse Heusler alloys by first-principles computational methods.* J. Comput. Chem., **31** (2009).

[169] I. Galanakis and P. Mavropoulos. *Spin-polarization and electronic properties of half-metallic Heusler alloys calculated from first principles.* J. Phys.: Condens. Matter, **19**, 315213 (2007).

[170] T. Ohoyama, P. J. Webster, and R. S. Tebble. *The ordering temperature of Cu_2MnAl.* J. Phys. D: Appl. Phys., **1**, 951 (1968).

[171] I. Galanakis, P. H. Dederichs, and N. Papanikolaou. *Slater-pauling behavior and origin of the half-matallicity of the full-Heusler alloys.* Phys. Rev. B, **66**, 174429 (2002).

[172] P. Mavropoulos, et al. *Effect of the spin-orbit interaction on the band gap of half metals.* Phys. Rev. B, **69**, 054424 (2004).

[173] P. Mavropoulos, I. Galanakis, V. Popescu, and P. H. Dederichs. *Influence of the spin-orbit interaction on the band gap of Heusler alloys.* J. Phys.: Condens. Matter, **16**, S5759 (2004).

[174] J. Goldstone, A. Salam, and S. Weinberg. *Broken symmetries.* Phys. Rev., **127**, 965 (1962).

[175] M. Ležaić, P. Mavropoulos, J. Enkovaara, G. Bihlmayer, and S. Blügel. *Thermal collapse of spin polarization in half-metallic ferromagnets.* Phys. Rev. Lett, **97**, 026404 (2006).

[176] A. Georges, G. Kotliar, W. Krauth, and M. J. Rozenberg. *Dynamic mean-field theory of strongly correlated fermion systems and the limit of infinite dimensions.* Rev. Mod. Phys., **68**, 13 (1996).

[177] L. Chioncel, E. Arrigoni, M. I. Katsnelson, and A. I. Lichtenstein. *Electron correlations and the minority-spin band gap in half-metallic Heusler alloys.* Phys. Rev. Lett., **96**, 137203 (2006).

[178] G. H. Fecher and C. Felser. *Substituting the main group element in cobal-iron based alloys $Co_2FeAl_{1-x}Si_x$.* J. Phys. D: Appl. Phys., **40**, 1582 (2007).

[179] Y. Sakuraba, et al. *Giant tunneling magnetoresistance in Co_2MnSi/Al-O/Co_2MnSi magnetic tunnel junctions.* Appl. Phys. Lett., **88**, 192508 (2006).

[180] K. E. H. M. Hanssen and P. E. Mijnarends. *Positron-annihilation study of the half-metallic ferromagnet NiMnSb: Theory.* Phys. Rev. B, **34**, 5009 (1986).

[181] K. E. H. M. Hanssen, P. E. Mijnarends, L. P. L. M. Rabou, and K. H. J. Buschow. *Positron-annihilation study of the half-metallic ferromagnet NiMnSb: Experiment.* Phys. Rev. B, **42**, 1533 (1990).

[182] I. Galanakis. *Towards half-metallic interfaces: Co_2CrAl/InP contacts.* J. Phys.: Condens. Matter, **16**, 8007 (2004).

[183] M. Ležaić, I. Galanakis, G. Bihlmayer, and S. Blügel. *Structural and magnetic properties of the (011) and (111) surfaces of the half-metal NiMnSb.* J. Phys.: Condens. Matter, **17**, 3121 (2005).

[184] I. Galanakis, M. Ležaić, G. Bihlmayer, and S. Blügel. *Interface properties of NiMnSb/InP and NiMnSb/GaAs contacts.* Phys. Rev. B, **71**, 214432 (2005).

[185] X. Hu. *Half-metallic antiferromagnets as a prospective material for spintronics.* Adv. Mater., **24**, 294 (2012).

[186] I. Galanakis, K. Özdoğan, and E. Şaşioğlu. *Half-metallic antiferromagnets in $Cr_{2+x}Se$ ($0 \leq x \leq 1$): A first-principles study.* Phys. Rev. B, **86**, 134427 (2012).

[187] S. Okamura, A. Miyazaki, S. Sugimoto, N. Tezuka, and K. Inomata. *Large tunnel magnetoresistance at room temperature with a Co_2FeAl full-Heusler alloy electrode.* Appl. Phys. Lett., **86**, 232503 (2005).

[188] C. H. H. Schneider, and, G. Jakob, and W. W. H. Adrain. *Structural, magnetic and transport properties of Co_2FeSi Heusler films.* J. Phys. D: Appl. Phys., **42**, 1548 (2007).

[189] V. Jung, G. H. Fecher, B. Balke, V. Ksenofontov, and C. Felser. *Electronic structure, magnetic properties and order-disorder phenomena in $Co_2Mn_{1-x}Fe_xAl$.* J. Phys. D: Appl. Phys., **42**, 084007 (2009).

[190] H. C. Kandpal, G. H. Fecher, C. Felser, and G. Schönhense. *Correlations in the transition-metal-based Heusler compound Co_2MnSi and Co_2FeSi.* Phys. Rev. B, **73**, 094422 (2006).

[191] J. Thoene, S. Chadov, G. Fecher, C. Felser, and J. Kübler. *Exchange energies, Curie temperatures and magnons in Heusler compounds.* J. Phys. D: Appl. Phys., **42**, 084013 (2009).

[192] G. H. Fecher, et al. *Design of magnetic materials: The electronic structure of the ordered, doped Heusler compound $Co_2Cr_{1-x}Fe_xAl$.* J. Phys.: Condens. Mater., **17**, 7237 (2005).

[193] G. Rollmann. *Ab initio Simulationen eisenhaltiger Systeme: Vom Festkörper zum Cluster.* Ph.D. thesis, Universität Duisburg-Essen (2007).

[194] P. J. Webster. *Magnetic and chemical order in Heusler alloys containing cobalt and manganese.* J. Phys. Chem. Solids, **32**, 1221 (1971).

[195] S. Ishida, T. Masaki, S. Fujii, and S. Asano. *Theoretical search for half-metallic films of Co_2MnZ (Z=Si,Ge).* Physica B, **245**, 1 (1998).

[196] B. Ravel, M. P. Raphael, and V. G. Harris. *EXAFS and neutron diffraction study of Heusler alloy Co_2MnSi.* Phys. Rev. B, **65**, 184431 (2002).

[197] J. Schmalhorst, S. Kämmerer, M. Sacher, G. Reiss, and A. Hütten. *Interface structure and magnetism of magnetic tunnel junctions with a Co_2MnSi electrode.* Phys. Rev. B, **70**, 024426 (2004).

[198] B. Balke, G. H. Fecher, H. C. Kandpal, and C. Felser. *Properties of the quaternary half-metal-type Heusler alloy $Co_2Mn_{1-x}Fe_xSi$.* Phys. Rev. B, **74**, 104405 (2006).

[199] A. F. R. Y. Umetsu, K. Kobayashi, R. Kainuma, and K. Ishida. *Magnetic properties and stability of $L2_1$ and B2 phases in the Co_2MnAl Heusler alloy.* J. Appl. Phys., **103**, 07D718 (2008).

[200] R. Yilgin, Y. Sakuraba, M. Oogane, Y. Ando, and T. Miyazaki. *Magnetic properties of single crystalline Co_2MnAl Heusler alloy thin films.* J. Supercond. Nov. Magn., **25**, 2659 (2012).

[201] W. Q. Li, J. X. Cao, J. W. Ding, and X. H. Yan. *Tuning Fermi level within half-metallic gap in Co-based Heusler alloys.* Eur. Phys. J. B, **85**, 250 (2012).

[202] B. Balke, et al. *Seebeck coeffiecients of half-metallic ferromagnets.* Solid State Commun., **150**, 529 (2010).

[203] M. Siewert, et al. *A irst-principles investigation of the compositional dependent properties of magnetic shape memory Heusler alloys.* Adv. Eng. Mat., **14**, 530 (2012).

[204] I. Galanakis and E. Şaşıoğlu. *Structural-induced antiferromagnetism in Mn-based full Heusler alloys: The case of ni_2mnal.* Appl. Phys. Lett., **98**, 102514 (2011).

[205] G. M. Müller, et al. *Spin polarization in half-metals probed by femtosecond spin excitation.* Nature Mat., **8**, 56 (2008).

[206] K. Szymański, et al. *Mössbauer and magnetic studies of $Fe_{3-x}CoAl$.* J. Magn. Magn. Mater., **210**, 150 (2000).

[207] Y. Maede, et al. *Magnetooptical properties of iron based Heusler alloy epitaxial films on Ge (111).* Physics Procedia, **11**, 200 (2011).

[208] T. Ersez, G. D. Etheridge, and T. J. Hicks. *Determination of the direction of the antiferromagnetic modulation below the low-temperature re-ordered regime in Fe_2MnSi.* J. Phys.: Condens. Mat., **7**, 8423 (1995).

[209] T. Ersez, G. D. Etheridge, and T. J. Hicks. *Investigation of magnetic anisotropy in the complex low-temperature phase in Fe_2MnSi.* J. Magn. Magn. Mat., **177**, 1351 (1998).

[210] P. Mohn and E. Supanetz. *Spin ordering in $Fe_{3-x}Mn_xSi$ Heusler alloys.* Phil. Mag. B, **78**, 629 (1998).

[211] S. Fujii, S. Ishida, and S. Asano. *A half-metallic band structure and Fe_2MnZ (Z=Al,Si,P).* J. Phys. Soc. Jpn., **64**, 185 (1995).

[212] H. Z. Luo, et al. *Half-metallic properties of the Mn_2FeZ (Z=Al, Ga, Si, Ge, Sb) Heusler alloys: A first-priciples study.* J. Appl. Phys., **103**, 083908 (2008).

[213] N. Xing, H. Li, J. Dong, R. Long, and C. Zhang. *First-principle prediction of half-metallic ferrimagnetism of the Heusler alloys Mn_2CoZ (Z=Al, Ga, Si, Ge) with a high-ordered structure.* Comp. Mat. Sci., **42**, 600 (2008).

[214] S. Ouardi, G. H. Fecher, C. Felser, and J. Kübler. *Realization of spin gapless semiconductors: The Heusler compound Mn_2CoAl.* Phys. Rev. Lett., **110**, 1004001 (2013).

[215] A. Planes, L. Manosa, and M. Acet. *Magnetocaloric effect and its relation to shape-memory properties in ferromagnetic Heusler alloys.* J. Phys.: Condens. Matter, **21**, 233201 (2009).

[216] M. Ogura, C. Takahashi, and H. Akai. *Calculated electronic structures and Néel temperaturesof half-metallic diluted antiferromagnetic semiconductors.* J. Phys.: Condens. Matter, **19**, 3865 (2007).

[217] S. Bedanta and W. Kleemann. *Supermagnetism.* J. Phys. D: Appl. Phys., **42**, 013001 (2009).

[218] S. Kaufman, et al. *Adaptive modulations of martensites.* Phys. Rev. Lett., **104**, 145702 (2010).

[219] K. Uchida, et al. *Observation of the spin Seebeck effect.* Nature, **455**, 778 (2008).

[220] J. Xiao, G. E. W. Bauer, K. Uchida, E. Saitoh, and S. Maekawa. *Theory of magnon-driven spin Seebeck effect.* Phys. Rev. B, **81**, 214418 (2010).

[221] A. Slachter, F. L. Bakker, J.-P. Adam, and B. J. van Wees. *Thermally driven spin injection from a ferromagnet into a non-magnetic metal.* Nature Phys., **6**, 879 (2010).

[222] L. Gravier, S. Serrano-Guisan, F. Reuse, and J.-P. Ansermet. *Spin-dependent Peltier effect of perpendicular currents in multilayered nanowires.* Phys. Rev. B, **73**, 052410 (2006).

[223] V. Popescu and P. Kratzer. *Large magnetic anisotropy in thin Co films embedded in Cu determined by ab initio investigations.* Phys. Rev. B, **80**, 104425 (2013).

[224] P. Mavropoulos, N. Papanikolaou, and P. H. Dederichs. *Korringa-Kohn-Rostoker Green-function formalism for ballistic transport.* Phys. Rev. B, **69**, 125104 (2004).

[225] P. Giannozzi, et al. *Quantum Espresso: A modular open-source software project for quantum simulations of materials.* J. Phys.: Condens. Mat., **21**, 395502 (2009).

[226] S. Chadov, et al. *Efficient spin injector scheme based on Heusler materials.* Phys. Rev. Lett., **107**, 047202 (2011).

[227] B. I. L. L. Hedin, and. *Explicit local exchange-correlation potential.* J. Phys. C: Solid State Phys., **4**, 2064 (1971).

[228] K. S. Singwi, A. Sjölander, M. P. Tosi, and R. H. Land. *Electron correlations at metallic densities. iv.* Phys. Rev. B, **1**, 1044 (1970).

[229] G. D. Mahan. *Many-particle physics* (Plenum Press, London, United Kingdom, 1990).

[230] D. M. Ceperley and B. J. Alder. *Ground state of the electron gas by a stochastic method.* Phys. Rev. Lett., **45**, 566 (1980).

[231] J. P. Perdew and Y. Wang. *Accurate and simple analytic representation of the electron gas correlation energy.* Phys. Rev. B, **45**, 13244 (1992).

[232] W. Metzner, M. Salmhofer, C. Honerkamp, V. Meden, and K. Schönhammer. *Functional renormalization group approach to correlated fermion systems.* Rev. Mod. Phys., **84**, 299 (2012).

[233] J. P. Perdew, K. Burke, and Y. Wang. *Generalized gradient approximation for the exchange-correlation hole of a many-electron system.* Phys. Rev. B, **54**, 16533 (1996).

[234] J. P. Perdew and K. Burke. *Comparison shopping for a gradient-corrected density functional.* Int. J. Quant. Chem., **57**, 309 (1996).

[235] J. Hubbart. *Electron correlations in narrow energy bands.* Proc. Roy. Soc., **276**, 238 (1965).

[236] V. I. Anisimov, I. V. Solovyev, M. A. Korotin, M. T. Czyźyk, and G. A. Sawatzky. *Density-functional theory and NiO photoemission spectra.* Phys. Rev. B, **48**, 16929 (1993).

[237] V. I. Anisimov, F. Aryasetiawan, and A. I. Lichtenstein. *First-principles calculations of the electronic structure and spectra of strongly correlated systems: the LDA+U method.* J. Phys.: Condens. Matter, **9**, 767 (1997).

[238] S. L. Dudarev, G. A. Botton, S. Y. Savrasov, C. J. Humphreys, and A. P. Sutton. *Electron-energy-loss spectra and the structural stability of nicke oxide: An LSDA+U study.* Rhys. Rev. B, **57**, 1505 (1998).

[239] B. X. Xu, A. K. Rajagopal, and M. V. Ramana. *Theory of spin-polarized inhomogenous relativistic electron systems.* J. Phys. C, **17**, 1339 (1984).

[240] M. V. Ramana and A. K. Rajagopal. *Inhomogenous relativistic electron gas: Correlation potential.* Phys. Rev. A, **24**, 1689 (1981).

[241] M. Mayer, O. D. Häberlen, and N. Rösch. *Relevance of relativistic exchange-correlation functionals and of finite nuclei in molecular density-functional calculations.* Phys. Rev. A, **54**, 4775 (1996).

[242] C. Rostgaard. *The projector augmented-wave method.* arXiv:0910.1921v2 (2009).

[243] F. Schwabl. *Quantenmechanik* (Springer Verlag, Berlin, Germany, 1998).

Publications

Parts of the results presented in this thesis have been published in the following articles:

P. Entel, D. Comtesse, H. C. Herper, M. E. Gruner, M. Siewert, S. Sahoo, and A. Hucht. *Ab-inition modeling of Fe-Mn based alloys and nanoclusters.* MRS Proceedings, **1296**, 80 (2011)

D. Comtesse, H. C. Herper, A. Hucht, and P. Entel. *A first-principles study aided with Monte Carlo simulations of carbon doped iron-manganese alloys.* Eur. Phys. J. B, **85**, 343 (2012)

P. Entel, M. Siewert, M. E. Gruner, H. C. Herper, D. Comtesse, R. Arróyave, N. Singh, A. Talapatra, V. V. Sokolovskiy, V. D. Buchelnikov, A. Albertini, L. Righi, and V. A. Chernenko. *Complex magnetic ordering as a driving mechanism of multifunctional properties of Heusler alloys from first principles.* Eur. Phys. J. B, **86**, 65 (2013)

D. Comtesse, B. Geisler, P. Entel, P. Kratzer, and L. Szunyogh. *First-principles study of spin-dependent thermoelectric properties of half-metallic Heusler thin film between platinum leads.* Phys. Rev. B, **89**, 094410 (2014)

A. Grünebohm, D. Comtesse, A. Hucht, M. E. Gruner, A. Malovskaya, and P. Entel. *Optimizing the magnetocaloric effect in Ni-Mn-Sn by substitution: A first-principles study.* submitted to IEEE Trans. Magn.

D. Comtesse, M. E. Gruner, M. Ogura, V.V. Sokolovski, V. D. Buchelnikov, A. Grünebohm, R. Arróyave, N. Singh, T. Gottschall, O. Gutfleisch, V. A. Chernenko, F. Albertini, S. Fähler, and P. Entel. *First-principles calculation of the instability leading to giant inverse magnetocaloric effects.* Phys. Rev. B, **89**, 184403 (2014)

P. Entel, M. E. Gruner, D. Comtesse, V.V. Sokolovski, and V. D. Buchelnikov. *Interacting magnetic spin-cluster glasses and strain glasses in Ni-Mn based Heusler structured intermetallics.* Physica Status Solidi B, **DOI** 10.1002/pssb.201451059

Following articles have been published in relation with this thesis:

P. Entel, S. Sahoo, M. Siewert, M. E. Gruner, H. C. Herper, D. Comtesse, M. Acet, V. D. Buchelnikov, and V. V. Sokolovskiy. *First-principles investigations of caloric effects in ferroic materials.* AIP Conference Proceedings, **1461**, 11 (2011)

R. Meyer, and D. Comtesse. *Vibrational density of states of silicon nanoparticles.* Phys. Rev. B, **83**, 014301 (2011)

P. Entel, A. Dannenberg, M. Siewert, H. C. Herper, M. E. Gruner, D. Comtesse, H.- J. Elmers, and M. Kallmayer. *Basic properties of magnetic shape-memory materials from first-principles calculations.* Metallurgical and Materials Transactions A, **43**, 2891 (2012)

A. Grünebohm, A. Hucht, R. Meyer, D. Comtesse, and P. Entel. *Simulation of cluster sintering, dipolar chain formation, and ferroelectric nanoparticulate systems.* NanoScience and Technology, **79**, 139 (2012)

P. Entel, V. V. Sokolovskiy, V. D. Buchelnikov, D. Comtesse, and M. Acet. *Interaction of phase transformation and magneto- and elastocaloric properties of Heusler alloys.* MRS Proceedings, **1581** (2013)

P. Entel, M. E. Gruner, D. Comtesse, and M. Wuttig. *Interaction of phase transformation and magnetic properties of Heusler alloys: A density functional theory study.* JOM, **65**, 1540 (2013)

Miscellaneous:

D. Comtesse, A. Hucht, D. Grüneberg. *Thermodynamic Casimir Effect in the large-n limit.* arxiv:0904.3661v2 (2009)

Danksagung

An dieser Stelle möchte ich allen danken, die mir beim Erstellen dieser Arbeit von großer Hilfe waren. Dabei möchte ich zuerst Prof. Dr. Entel für die Möglichkeit, in den letzten Jahren in seiner Gruppe zu arbeiten und die Betreuung bei der Anfertigung dieser Arbeit, danken.

Ich möchte Dr. Heike Herper für die vielen Diskussionen über Inhalte dieser Arbeit, sowie für Ihre Anregungen, die meine Forschungarbeit maßgeblich beeinflusst haben danken. Weiterhin möchte ich Dr. Markus Gruner dafür danken, dass er mir sein Wissen über Materialphysik und seine Erfahrung im Bereich der Computer Simulationen jederzeit zur Verfügung gestellt hat.

Ein ganz besonderer Dank geht an Dr. Alfred Hucht, der schon in den letzten zwei Jahren meines Studiums meine Arbeit und wissenschaftliche Entwicklung unterstützt hat, indem er mir jederzeit mit Rat und Tat zur Seite stand und von dessen besonderer Art, Probleme anzugehen, ich sehr viel gelernt habe.

Ich möchte aber auch Dr. Ralf Meyer für die Zusammenarbeit danken, durch die ich vor allem viel über Programmierung gelernt habe.

Darüber hinaus möcht ich Dr. Mario Siewert dafür danken, dass er mir über Jahre ein guter Büro Partner war, für den Spass, den wir bei der Arbeit hatten und nicht zu letzt für die unzähligen Diskussion und Hilfestellungen, die unsere Zusammenarbeit geprägt haben. Für Diskussionen und Hilfe, sowie für die tolle Zusammenarbeit gilt mein Dank aber auch Dr. Anna Grünebohm.

Ganz besonders möchte ich aber an dieser Stelle meinen Eltern Ingrid und Klaus Comtesse danken. Ohne Ihre Liebe und Ihren unermüdlichen Einsatz hätte ich den Weg, der mich hierhin geführt hat niemals bestreiten können.

Ebenso möchte ich meinem Bruder Frank Comtesse dafür danke, dass er mich dazu inspiriert hat Physiker zu werden, indem er mir in meiner Jugend erklärte was das Periodensystem der Elemente ist und was es bedeutet.

Erklärung

Ich versichere, dass ich diese Arbeit selbständig verfasst, keine anderen als die angegebenen Quellen und Hilfsmittel benutzt und alle wörtlich und inhaltlich übernommen Stellen als solche kenntlich gemacht habe.

Duisburg, im März

Denis Comtesse